Max Planck Institute for Astronomy

Astrophysics and Instrumentation

Report for the Meeting of the Scientific Advisory Board
March 23-25, 2010

Edited by Klaus Jäger, Thomas Henning, and Hans-Walter Rix

MAX-PLANCK-GESELLSCHAFT

Front cover:
The massive star forming region S255 in our galaxy. This image was taken during one of the first scientific observations with the new LUCIFER1-instrument at the Large Binocular Telescope (LBT). Colour-coded in green is emission from H_2.
(Credit: W.Brandner et al., LBTO/LUCIFER-Team)

Preface

Activities at the MPIA encompass astrophysical research, both observational and theoretical, and instrumentation and technology development.
Complementing the “Status Report”, this booklet tries to give a comprehensive, although not complete, overview over the activities at the MPIA in the period 2007-2009. The contributions were written by the PIs on behalf of the teams involved. Complementing these brief summaries, the Annual Reports of the last three years offer much more detailed descriptions of the major research and instrumentation efforts.

February 2010,

Klaus Jäger

Table of Contents

11 Instrumentation 265

1 Highlights

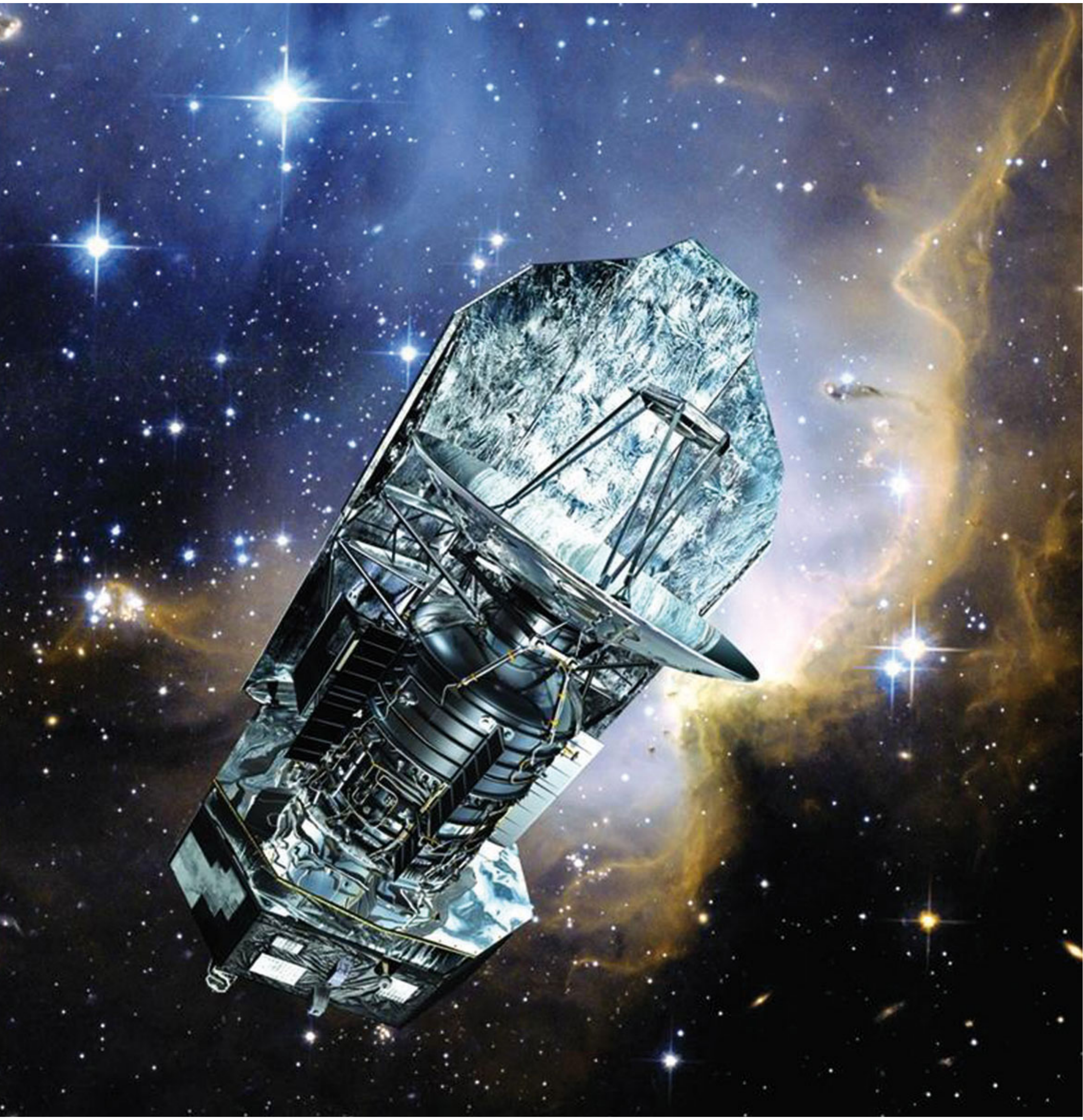

Image on previous page:
The HERSCHEL Infrared Space Telescope with its 3.5m mirror was launched on 14th May 2009 and is operated about 1.5 million km away from Earth in anti-solar direction. It performs observations in the far-infrared and sub-millimetre range and is equipped with three instruments. Among those, the MPIA was engaged in the development of PACS, a camera and spectrometer for wavelengths from 60 to 210 µm.
(Credit: ESA)

Towards first results from HERSCHEL Key Programs

Oliver Krause, Eva Schinnerer, Klaus Meisenheimer, Thomas Henning

The highly successful commissioning and performance verification phase of HERSCHEL led to first observations within the “Science Demonstration Phase” in September 2009. MPIA's guaranteed time share of 15% (corresponding to 285 hours) has been mainly invested into two Guaranteed Time Key Programmes led by the institute on “The earliest phases of star formation (EPOS)” (PI: O. Krause) and “The Dusty Young Universe” (PI: K. Meisenheimer). Our technical expertise with PACS and scientific interest led to a successful MPIA involvement in nine more HERSCHEL key programs. The wide distribution of these programs in galactic (EPOS, DIGIT, MESS, DUNES, Gould Belt, Cold Cores, HOPS) and extragalactic astronomy (Dusty Young Universe, KINGFISH, SHINING, HERCULES) - reflects the significance of HERSCHEL for the core science fields of our institute. The total observing time granted to these HERSCHEL programs is 2600 hours, the MPIA being responsible for many key areas of data reduction and analysis.

The EPOS program, the Earliest Phases of Star Formation, is a 112 hour Guaranteed Time Key Program aimed at studying the initial conditions and early stages of star formation in our Galaxy. We use HERSCHEL PACS and SPIRE scan maps (Fig. 1) to construct spatially resolved spectral energy distributions of low- to high-mass star-forming cores and protostars, covering the full peak of thermal dust emission. These data allow us to determine dust temperatures, density profiles and the mass distribution with an unprecedented accuracy. Of particular interest are a number of deeply embedded protostars which appear only in the long wavelength PACS bands.

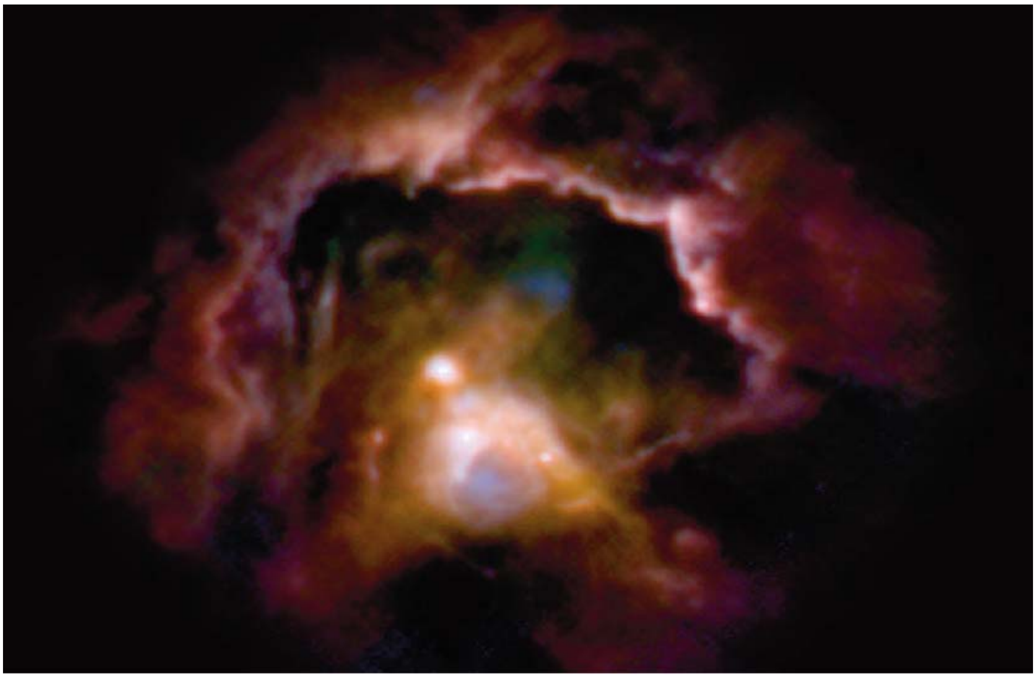

Figure 1: Image of the high-mass star forming region ISOSS J22164+6003 taken with the PACS instrument aboard HERSCHEL at 70 µm (blue), 100 µm (green) and 160 µm (red).

The detection of a significant fraction of the highest redshift quasars (z > 5) in the (sub-)milimeter wavelength range indicates that a substantial amount of dust has been synthesized already during the first billion year since the Big Bang. Recent 24 µm observations with Spitzer have shown that very hot dust is present close to the QSO core in most z > 5 quasars. However, both the (sub-)mm and mid infrared observations can only catch tails of the dust emission spectrum, at $\lambda_{rest} > 200$ µm, and at $\lambda_{rest} < 5$ µm, respectively. Measuring the peak of the dust emission has been beyond the capabilities of FIR satellites or ground-based sub-mm telescopes. Thus, critical properties, such as FIR luminosity, dust temperatures and mass, remain unconstrained.

The first PACS observations of two luminous sources at the edge of the universe, the most distant known quasar SDSS J1148+5251 at z = 6.42 and the mm-loud quasar BR 1202-0725 at z = 4.69, by the MPIA-led 164 hours Guaranteed Time Key Program "The Dusty Young Universe" have clearly detected the sources. In both cases the PACS photometry indicates a very continuous distribution of dust temperatures between T~1000 K and T ~ 50 K.

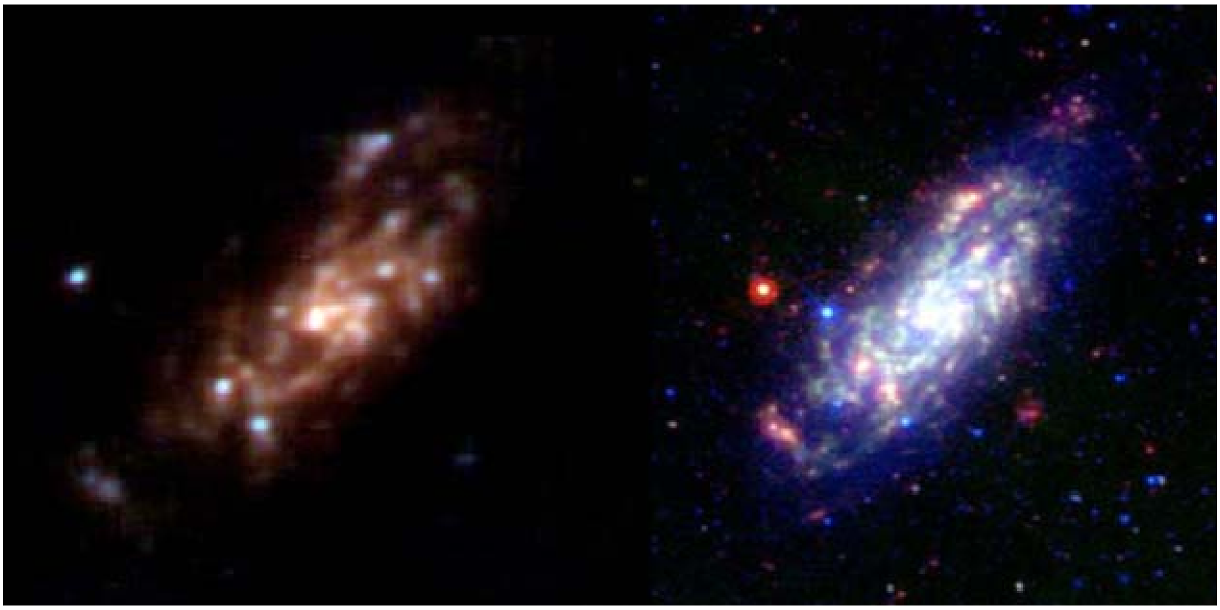

Figure 2: (a) PACS 70, 100, 160 µm composite image of the first KINGFISH SDP-target NGC 4559 at a distance of 15 Mpc. (b) Spitzer 3.6, 8 and 24 µm composite for comparison.

KINGFISH (Key Insights on Nearby Galaxies: a Far-Infrared Survey with HERSCHEL) is a 536 hours Open Time Key Program with significant participation from the MPIA, being responsible for the PACS imaging section of the survey. KINGFISH will provide for, the first time, imaging across the peak of the dust SED at a spatial resolution that matches individual SF complexes, and spectroscopic maps of key diagnostic lines to constrain the cooling and heating processes of the warm neutral medium and the obscured ionized ISM. The PACS and SPIRE imaging from 70 to 500 µm is expected to produce the first comprehensive census of dust in different galactic environments on a spatially resolved basis. Our PACS images of NGC 4559 demonstrate the capabilities of HERSCHEL in resolving individual star forming regions in the far infrared (Fig. 2).

The Open Time Key Program DIGIT (Dust, Ice, and Gas In Time) is aimed on observations of circumstellar disks in order to understand the processes that govern the formation of stars and planets. The MPIA team is particularly interested in full range spectroscopy using PACS which enables SED fitting and a spectral decomposition to identify the mass fraction of individual dust components. As one of the first targets of the DIGIT program, the Herbig Ae/Be star HD 100546 was observed. The PACS spectrum clearly detected the 69µm forsterite emission feature, the shape and central position of which is currently used to measure the dust temperature and to search for hints of non–random orientation of the crystals in this system.

First results from the different programs will be submitted for publication in the dedicated A&A HERSCHEL Special Issue by March 31, 2010.

Direct imaging search for extrasolar planets - from SEEDS to SPHERE

Markus Feldt, Christian Thalmann, Joe Carson, Wolfgang Brandner, Micaela Stumpf, Miwa Goto, Thomas Henning

Introduction

Direct imaging and indeed characterization of extrasolar planets is becoming increasingly important these days, even before the next, dedicated generation of exoplanet imagers, spectrographs and polarimeters starts being commissioned.

At MPIA, such bservations are being carried out both in preparatory programs for the large SPHERE survey, as well as independently as searches for brown dwarf or planetary companions, and both from ground and space.

Space-Based Programs

We are using mid-infrared photometry from Spitzer IRAC archival data in combination with follow-up near-infrared photometry from ground-based telescopes, to search the wide-separation (>100AU) orbital space around stars that are already known to have inner (like <5AU) planets, as determined from previous Doppler spectroscopy studies. Our goal is to expand our knowledge of exoplanet characteristics, including an improved understanding of the connection between wide-separation substellar companions and the existence of narrow-separation inner planets.

Also in this context, a high-resolution spectral differential imaging survey with HST/NICMOS has revealed a companion to the L 4 dwarf 2MASS0337-1758[1], which with its estimated mass 10 10-15 M_{Jup} assigns to the system the uncommonly low mass ratio of $q = 0.2$. If the physical companionship of this object is confirmed in the proposed follow-up observations, this will be the closest ($0\farcs087$) companion ever directly imaged

Ground-Based Programs

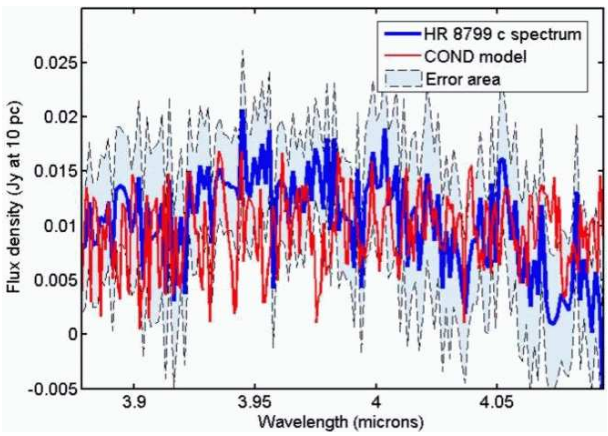

Figure 1: *Spectrum of HR 8799 c.*

On the ground, VLT/NACO was used to observe the HR 8799 planetary system. Here, we obtained the first spatially resolved spectrum of an exoplanet orbiting another star (See fig. 1). The spectrum of the planet HR 8799 c covers the wavelength range from 3.88 to 4.10μm. A model spectrum by Baraffe et al. (2003, A&A 402, 701) without dust opacities for an age of 100 Myr, and with $T_{\rm eff} = 1100$ K, logg = 4.0, and $R_{\rm pl} = 1.3\ R_{\rm Jup}$, corresponding to a planetary mass of 6.4 $M_{\rm Jup}$, reproduces the integrated flux, though not the observed spectral shape. Since including dust opacities also cannot reproduce the observed spectrum, non-equilibrium chemistry in the planetary atmosphere of HR 8799 c is likely the explanation for the observations [2].

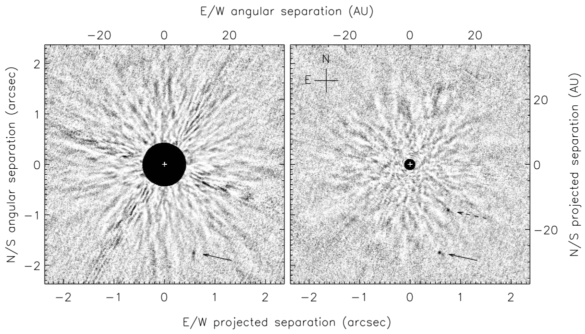

Figure 2: *Signal-to-noise map of the GJ 758 B discovery images from May 2009 (left) and August 2009 (right). A possible second companion to GJ 758 is pointed out by a dashed arrow in the right image.*

A new detection was achieved during a commissioning run of the HiCiao instrument at the Subaru Telscope, where MPIA researchers are involved in the corresponding "Subaru Strategic Exploration of Exoplanets and Disks with HiCIAO/AO188" (SEEDS) program. Here we discovered a brown dwarf or possible planet at a projected separation of 1.9 = 29 AU and a contrast of $\Delta H = 14.5$ mag around the star GJ 758 (see Fig. 2), placing it between the separations at which substellar companions are expected to form by core accretion (5 AU) or direct gravitational collapse (typically about 100 AU). At 10 to 40 times the mass of Jupiter and a temperature of 550 to 640 K, GJ 758 B constitutes one of the few known T-type companions, and the coldest ever to be imaged in thermal light around a sun-like star.

The experience gained in the described programs, particularly during the "Angular Differential Imaging" application that led to GJ 758 B's discovery, will next be applied in the large SPHERE preparation survey, commencing in the ongoing semester with initially 6 Nights using H-band coronagraphic imaging with NACO. In this program, a total of 110 stars will be observed with a total integration time of about 1.5 hrs each, leading to expected contrast limits of about 9 mag at $0\farcs5$ and 15 mag at $2''$.

References

[1] Micaela B. Stumpf; Wolfgang Brandner; Viki Joergens; Thomas Henning; Herve Bouy; Rainer Köhler; Markus Kasper, 2010, ApJ, submitted: The search for planetary mass companions to field brown dwarfs with HST/NICMOS

[2] Markus Janson;, Carolina Bergfors; Miwa Goto; Wolfgang Brandner; David Lafrenière, 2010, ApJ, 710, L35: Spatially resolved spectroscopy of the exoplanet HR 8799c

[3] Christian Thalmann; Joe Carson; Miwa Goto; Michael McElwain; Sebastian Egner; Christoph Mordasini; Markus Feldt; Jun Hashimoto; Yutaka Hayano; Thomas Henning; Klaus W. Hodapp; Ryo Kandori; Hubert Klahr; and 6 more Authors, 2009, ApJL 707: Discovery of the coldest imaged companion of a sun-like star

The earliest stages of massive star formation

Henrik Beuther, Thomas Henning & Oliver Krause

Understanding the initial conditions that lead to the formation of massive stars remains one of the key questions in high-mass star formation research. At MPIA we follow several approaches to study these earliest stages of high-mass star formation. While the scientific goals of these different studies are similar, they nevertheless differ a lot by their initial target selection as well as by their observational approach. We briefly outline 3 different studies here.

Infrared Dark Clouds (IRDCs) in the vicinity of High-Mass Protostellar Objects (HMPOs) Correlating mid-infrared extinction maps from the MSX satellite with 1.2 mm dust continuum data from the IRAM 30 m telescope towards a sample of HMPOs, we serendipitously identified more than 40 IRDCs (Sridharan et al. 2005). These IRDCs are on average colder and have lower levels of turbulence than the HMPOs. This indicated that the IRDCs are not solely less luminous, but that they likely represent an earlier evolutionary stage than the HMPOs. However, samples like this likely consist of sources in different evolutionary stages, e.g., high-mass starless cores, and high-mass cores with embedded low- to intermediate-mass protostars that may be destined to become massive at the end of their evolution.

To better characterize these differences, we observed this sample with the IRAM 30 m telescope covering spectral line tracers of low-density gas, high-density gas, molecular outflows/jets and temperature effects [1]. The SiO(2–1) observations reveal detections toward 18 sources. Assuming that SiO is exclusively produced by sputtering from dust grains, this implies that at least in 40% of this sample star formation is ongoing. The $H^{13}CO^+$ line width is on average 1.5 times larger than that of previously observed NH_3(1,1). This is indicative of more motion at the denser core centers, due to either turbulence or beginning star formation activity. Furthermore, estimates of the CH_3CN and CH_3OH abundances are low, consistent with chemical models at the earliest evolutionary stages of high-mass star formation. In addition to this, the CH3OH abundances compare well to recently reported values for low-mass starless cores.

Physical properties of Southern IRDCs To enlarge the sample of well-characterised IRDCs in the southern hemisphere, where ALMA will play a major role soon, we correlated 1.2 mm continuum data from SIMBA@SEST with Spitzer/GLIMPSE images to establish the connection between mm emission sources and the IRDCs we see at 8 μm in absorption [2].

The morphology of the 1.2 mm continuum emission is in all cases in close agreement with the mid-infrared extinction (Fig. 1). The total masses of the IRDCs were found to range from 150 to 1150 $M_\odot$ (emission data) and from 300 to 1750 $M_\odot$ (extinction data). We derived peak column densities between 0.9 and 4.6 $\times$ 10^{22} cm^2 (emission data) and 2.1 and 5.4 $\times$ 10^{22} cm^2 (extinction data). It is demonstrated that the extinction method fails for very high extinction values (and column densities) beyond A_v values of roughly 75 mag. By taking the spatial resolution effects into account and restoring the column densities derived from the dust emission back to a linear resolution of 0.01 pc, peak column densities of 3-19$\times$$10^{23}$ cm^2 are obtained, much higher than typical values for low-mass cores. Furthermore, these column densities are beyond the column density threshold of 3.0×10^{23} cm^2 required by theoretical considerations for massive star formation. We conclude that the values of derived column densities make these objects excellent candidates for objects in the earliest stages of massive star formation.

The earliest stages of massive star formation identified by ISOSS In a different approach, we used the ISOPHOT Serendipity Survey (ISOSS) at 170 μm to identify massive molecular clumps with 100 to a few 1000 $M_\odot$, dust temperatures below 18 K and low bolometric luminosities. A suite of follow-up observations has been carried out to constrain the initial conditions for the formation of high-mass stars in this sample. Single dish follow-up observations

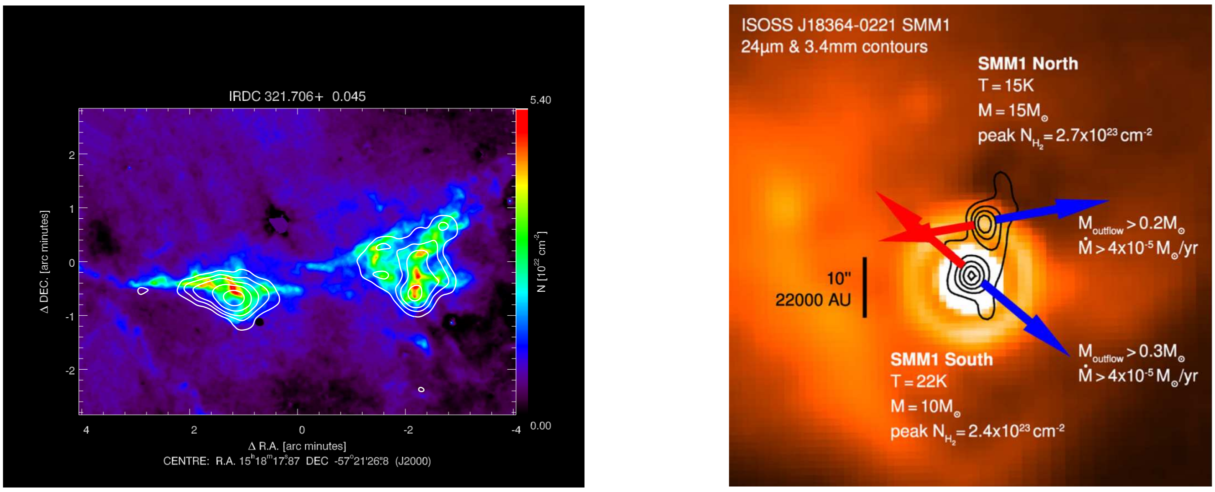

Figure 1: *The left panel shows in color an H_2 column density map derived from the Spitzer 8 μm extinction data. The contours present 1.3 mm dust continuum emission from the SEST observatory. The right panel shows a deep Spitzer 24 μm image of the central region of ISOSS J18364-0221. Two high-mass cores are detected in the 3 mm dust continuum (contours) with the Plateau de Bure Interferometer. Properties of the cores and their outflows are highlighted.*

in the submm continuum and in molecular lines (e.g., NH_3) confirm the low temperatures of gas and dust down to 11 K, as well as low levels of turbulence and the presence of infall motions. These compact objects, candidates for high-mass starless cores and protostars, have been characterized in detail with interferometry.

A recent study confirms the onset of star formation in the region ISOSS J183640221 [3]. The contracting clump has fragmented into two compact cores, SMM1 North and South (Fig. 1) with radii of 0.05 pc, interferometric masses of 15 and 10 $M_\odot$, and luminosities of 20 $L_\odot$ and 180 $L_\odot$. SMM1 South harbors a source traced at 24 and 70 μm, drives an energetic molecular outflow, and appears supersonically turbulent at the core center. SMM1 North has no infrared counterparts and shows lower levels of turbulence, but also drives an outflow. Both outflows appear collimated, and parsec-scale near-infrared features probably trace the outflow-powering jets. Mass outflow rates of at least $4 \times 10^{-5} M_\odot yr^{-1}$ and outflow dynamical timescales of less than 10^4 yr were derived. Our HCN(1—0) modeling for SMM1 South yielded an infall velocity of 0.14kms^1 and an estimated mass infall rate of $3 \times 10^5 M_\odot yr^{-1}$. Both cores may harbor seeds of intermediate or high-mass stars. Comparing the core properties with recent simulations of massive core collapse indicates very early stages dominated by accretion luminosity.

Far infrared and submillimeter observations with the recently launched HERSCHEL space observatory will shed new light on the high-mass starless cores and protostars identified by the three strategies aboves: They constitute the core sample of EPOS, a dedicated HERSCHEL key program on the earliest phases of star formation.

References

[1] Beuther, H., Sridharan, T.K., 2008, ApJ 668, 348

[2] Vasyunina, T., Linz, H., Henning, Th., Stecklum, B., Klose S., Nyman L.-A., 2009, A&A, 499, 149

[3] Hennemann, M., Birkmann, S., Krause,O., Lemke, D., Pavlyuchenkov, Y., More, S., Henning, Th., 2009, ApJ 693, 1379

Quasar host galaxies: Formation and evolution

Knud Jahnke, Mauricio Cisternas, Katherine J. Inskip & Eva Schinnerer

Formation of quasars: The curious case of HE0450–2958

HE0450–2958 is a luminous quasar at $z = 0.186$, apparently interacting with a nearby companion galaxy. It is also known to emit large quantities of infrared (IR) radiation, on the level of an Ultraluminous Infrared Galaxy (ULIRG). Since HST imaging has so far failed to detect a host galaxy, this system could have been in a potentially very special state. It would have been lying strongly off the scaling relation between black hole (BH) and bulge mass of normal galaxies [1].

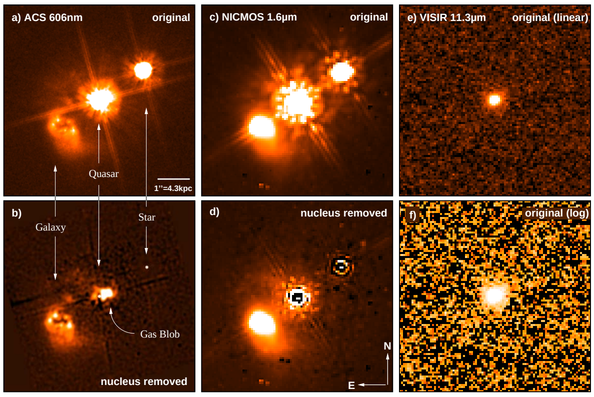

Figure 1: *The HE0450–2958 system at high spatial resolution [2]: optical HST/ACS V-band (left), near-infrared HST/NICMOS H-band (center), and mid-infrared ESO VLT/VISIR at 11.3μm (right). HST images are shown as observed (top) and with quasar light removed (bottom); the VISIR image is in linear and log stretch. Optical/NIR: Quasar is in the center, the companion galaxy 1.″5 (6.5 kpc) to the SE and a foreground star to the NW.*

We then investigated the system with hitherto unmatched spatial resolution and depth in the near IR and mid IR, using HST/NICMOS and the VISIR imager on the ESO VLT ([2], see Fig. 1). While we only detect a possible off-center extension of the host galaxy but not the bulk system itself, we study the companion galaxy in detail. We find that it is clearly interacting with the quasar and it contains optically thick dust, distorting its morphology at visible wavelengths. The companion forms large amounts of stars ($\sim$350 $M_\odot$/year) and is a star-formation powered ULIRG. By heating moderate amounts of dust in its vicinity, the quasar is emitting as an AGN-powered ULIRG. While the quasar system is now proven to be consistent with the local BH–bulge scaling relation, its star-formation and AGN accretion are located in physically disjoint locations – a possible "coevolution" of BHs and galaxies can thus only happen with spatial and temporal offsets.

In addition, the quasar has a radio jet, pointing almost exactly at the companion galaxy. While this could be coincidence, we laid out a possible scenario [3], in which some or all of the star-formation in the companion galaxy might be induced by the radio jet. The quasar would trigger formation of stars that would inevitably end up in the quasar's host galaxy once the host and companion eventually merge. While such systems are rare today, they would have been much more common in the earlier universe, opening a new path in which BHs could influence the formation of their own host galaxies, with implications on their joint evolution.

Evolution of AGN scaling relations: Star formation vs. assembly

While HE0450–2958 is a prominent example of how BHs and galaxies are not independent in their evolution, we started several projects to statistically trace the evolution of BHs and galaxies across 2/3 of cosmic time. The first result is a study of the BH and bulge mass ($M_{\rm BH}$–$M_{\rm bulge}$) relation at $z \sim 1.3$ [4]. We constrained the stellar masses for 10 quasars in the COSMOS field using ACS I-band and NICMOS H-band observations. By adding BH masses, obtained in two different optical spectroscopic campaigns within the COSMOS collaboration (Fig. 2), we were able to compare these 10 quasars to the local $M_{\rm BH}$–$M_{\rm bulge}$-relation.

We find that they fall directly onto the local scaling relation, however not with their bulge mass, but with the measured *total* stellar mass. Two different interpretations are possible: (i) If our quasar hosts are bulge dominated, the $M_{\rm BH}$–$M_{\rm bulge}$-relation did not evolve over the last 10 Gyr. (ii) Since we have strong indications that substantial disk components are present in the hosts, they would lie off the local $M_{\rm BH}$–$M_{\rm bulge}$-relation by a factor of 2–3. Since the host galaxies at $z = 1.3$ have to evolve onto the local BH–bulge-relation by $z = 0$ which they already match with their total stellar mass, all mass to form the bulges by $z = 0$ has already to be present in the galaxies at $z = 1.3$. Only a conversion of disk into bulge mass needs to and can occur, no (substantial) addition of solely new stars or solely increased BH mass is possible. Major galaxy mergers, as above for HE0450–2958 could be responsible for this, but also minor mergers or secular processes. Our finding shows that the formation of bulge stars and the assembly of bulges occurs at different times. Since this is a path not open to black hole formation, this might drive the observed evolution of the $M_{\rm BH}$–$M_{\rm bulge}$-relation since $z > 6$.

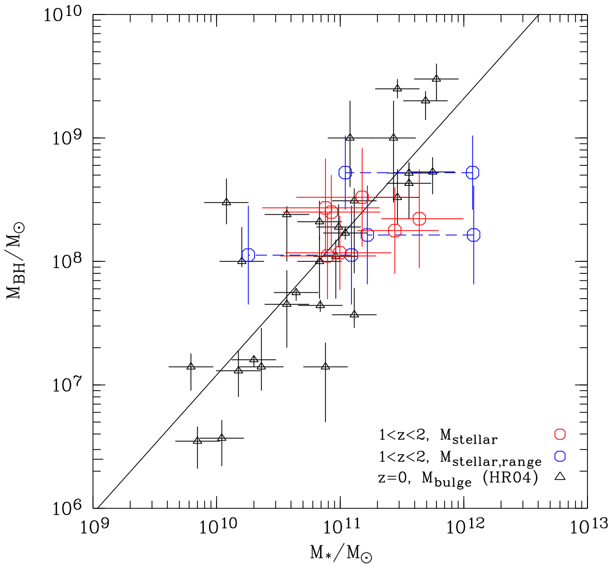

Figure 2: *Black hole vs. stellar mass. Shown are the BH to bulge mass relation at $z \sim 0$ (Häring & Rix 2004, ApJ, 604, 89; triangles and regression line), and our total stellar masses at $z \sim 1.4$. Points with ranges bracket the masses for the three host galaxies unresolved in I-band. Stellar masses are computed using M/L from the general COSMOS stellar mass catalog (Ilbert et al. 2009, ApJ in press, arXiv:0903.0102) given the nucleus-removed host galaxy colours. BH masses were derived in two separate projects [5, 6] using a virial approach.*

Main collaborators on HE0450–2958 are David Elbaz, Eric Pantin and Pierre-Olivier Lagage (CEA-Saclay, France), Geraldine Letawe (Liege, Belgium) and Lutz Wisotzki (AIP Potsdam, Germany). On COSMOS AGN scaling relations main collaborators are Angela Bongiorno, Marcella Brusa and Andrea Merloni (MPE Garching, Germany), Mara Salvato (MPI Plasmaphysik Garching, Germany), Jonathan Trump (Arizona, USA), and Olivier Ilbert (IfA Hawaii, USA). Knud Jahnke, Katherine J. Inskip and Mauricio Cisternas are members of the Emmy Noether-Group "Coevolution of Galaxies and Black Holes" at MPIA, funded by the German DFG.

References

[1] Magain, P., et al. (incl. Jahnke, K.) 2005, Nature, 437, 381

[2] Jahnke, K., Elbaz, D., et al. 2009, ApJ, 700, 1820

[3] Elbaz, D., Jahnke, K., et al. 2009, A&A in press, arXiv:0907.2923

[4] Jahnke, K., et al. (incl. Cisternas M., Inskip K. J., Schinnerer E.) 2009, ApJ, 706, L215

[5] Trump, J. R., et al. (incl. Jahnke, K., Schinnerer, E.) 2009, ApJ, 696, 1195

[6] Merloni, A., et al. (incl. Jahnke, K.) 2009, ApJ in press, arXiv:0910.4970

The faintest galaxies

Nicolas Martin, Sergey Koposov

How faint can a galaxy be? All galaxies, large or small, are concentrations of stars and gas at the center of a massive dark matter halo. But were the conditions met in all dark matter halos for stars to form? Over the last few years, the discovery of numerous extremely faint dwarf galaxies, which sometimes contain only a few hundred stars, has challenged our views on what a galaxy could be and how they could form.

Dwarf galaxies play an essential role in the formation of large galaxies. Throughout time, it is their absorption by their more massive counterparts that helped create galaxies that we observe today, such as our own Milky Way. The stellar content, the dynamical and kinematic properties, the spatial distribution around and the rate of infall of dwarf galaxies onto their host can all be linked to the cosmological properties of the Local Group. The small number of known dwarfs have, however, been a persistent conundrum: not only does a sample of 10–20 objects limit the amount of reliable information that one can extract on the cosmology, but comparisons with dark matter simulations reveal that there is a significant discrepancy between the number of expected dark matter sub-halos and the number of observed Local Group satellites (that is, dark matter sub-halos containing stars).

The discovery of the darkest galaxies

Systematic surveys of both the Milky Way (the Sloan Digital Sky Survey) and the Andromeda galaxies (the Pan-Andromeda Archaeological Survey) have however revolutionized our view of these two galaxies' satellite systems, revealing tens of new dwarf galaxies with unexpectedly low luminosities [7]. Figure 1 highlights the newly found galaxies around the Milky Way and, given that the SDSS only covers the northern Galactic cap, underlines that numerous other dwarf galaxies remain to be discovered.

Over the last couple of years, a careful analysis of the new Milky Way satellites based on SDSS data enabled us to:

- robustly characterize the detectability of these system, an invaluable piece of information for any comparison with simulations [2];
- derived their star formation histories, metallicities and constrain their distance from the analysis of their color-magnitude diagram showing they are in majority old and metal-poor system [1];
- build a comprehensive database of their structural parameters and luminosities, bypassing the difficulties that came from comparing the structure of these systems discovered by many different group, with different techniques [6]

Towards a better agreement with CDM simulations

The discrepancy of observed Local Group satellites with the number of dark matter sub-halos in simulations of Milky Way-like halos has been a major issue of the last ten years: hundreds (and not tens) of dwarf galaxies should have been discovered if every sub-halo were to contain stars. However, it is now becoming apparent that the recent discoveries within the Local Group play a significant role in bridging observations and theory, thereby alleviating this so-called 'missing-satellite problem'. Using semi-analytical models with simple physical recipes to populate dark matter simulations with stars, we are able to reproduce the luminosities, sizes and depth of the gravitational potential well of close-by dwarf galaxies, as well as their radial distribution from Galaxy [3, 4, 5].

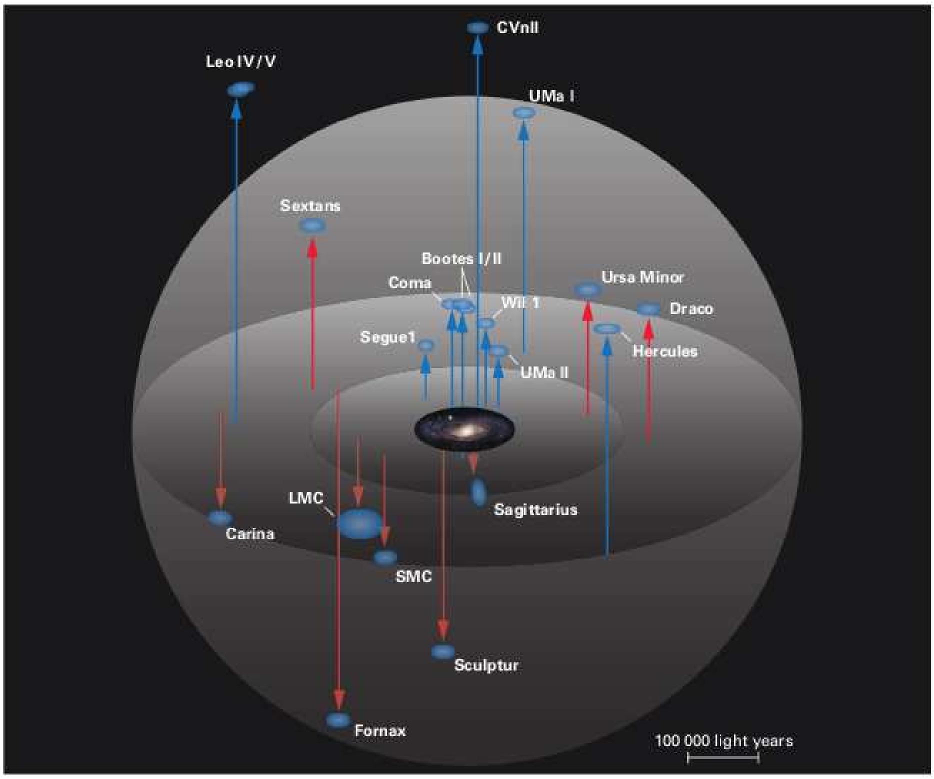

Figure 1: *The distribution of satellite dwarf galaxies around the Milky Way. Systems known before the 21st century are indicated with red arrows whilst the numerous newly discovered systems found within the Sloan Digital Sky survey since 2004 are indicated with blue arrows. The coverage of the survey (covering only one quarter of the sky) explains the anisotropic distribution of these satellites and highlights how incomplete our knowledge of the Milky Way satellites system is in other regions of the sky.*

References

[1] de Jong J. T. A., Rix H.-W., Martin N. F., Zucker D. B., Dolphin A. E., Bell E. F., Belokurov V., Evans, N. W., 2008, AJ 135, 1361

[2] Koposov S., Belokurov V., Evans N. W., Hewett P. C., Irwin M. J., Gilmore G., Zucker D. B., Rix H.-W., Fellhauer M., Bell E. F., Glushkova E. V., 2008, ApJ 686, 279

[3] Koposov S. E., Yoo J., Rix H.-W, Weinberg D. H., Macciò A. V., Escudé J. M., 2009, ApJ 696, 2179

[4] Macciò A. V., Kang X., Moore B., 2009, ApJ 692, L109

[5] Macciò A. V., Kang X., Fontanot F., Somerville R. S., Koposov S. E., Monaco P., 2009, MNRAS, in press, arXiv:0903.4681

[6] Martin N. F., de Jong J. T. A., Rix H.-W., 2008, ApJ 684, 1075

[7] Martin N. F., McConnachie A. W., Irwin M. J., Widrow L. M. *et al.*, ApJ 705, 758

The heart of Active Galactic Nuclei

Klaus Meisenheimer, Leonard Burtscher, Marc Schartmann, Konrad Tristram

Resolving the dust distribution on parsec scale

The *unified scheme* for Active Galactic Nuclei (AGN) explains various types by a line-of-sight effect: it postulates that the central engine – an accreting super-massive black hole – is embedded in a doughnut-shaped torus of gas and dust. Thus, the hot accretion disk and the Broad Line Region are only visible when looking along the torus axis. This is the case in Seyfert 1 galaxies. In an edge-on case, however, the direct view onto the core is blocked by the dusty torus and only narrow emission lines from regions above and below the torus are visible. The object then appears as Seyfert 2 galaxy. The UV-optical light which is trapped by dust in the torus should heat the dust to a few hundred Kelvin, and the dust should re-radiate in the mid infrared.

Already in its first year of operation, the MID-infrared interferometric Instrument (MIDI) at the VLTI was able to resolve a parsec scale dust structure in the Seyfert 2 galaxy NGC 1068. [2] A very detailed study of the closest Seyfert galaxy in Circinus [3] revealed that the dust structure consists of two components: a compact, disk-like component of 2 pc diameter and more extended component (see Fig. 1). The dust disk coincides with a rotating disk of water masers. The total flux and the rapid change of the interferometric signal (visibilities) with baseline indicates that the extended component is not smooth but has a patchy or filamentary structure. In fact, when modifying a smooth gaussian brightness distribution by a screen of patchy transmission a better fit to the data can be obtained (right panel in Fig. 1). An interferometric snapshot survey of the mid-infrared brightest AGN during the MIDI Guaranteed Time Observations (GTO) successfully observed ten more sources (including the quasar 3C 273) and resulted in a first size measurement of their dust distribution [4]. As a general result we find that the effective size at 10 μm scales as $r_{10} \sim L^{1/2}$ as expected either from constant surface brightness of a black body at $T = 300\,\mathrm{K}$ or from an optical thin dust distribution, which is heated by radiation from a central source. During GTO also the nearest Seyfert 1 galaxy, NGC 4151 could be observed. Despite a very limited $uv-$coverage (the source is at $\delta = +40°$) a dust distribution of 2 pc diameter is resolved [1]. It seems that the structure is rather similar to that in equally bright Seyfert 2 galaxies, thus supporting the unified scheme.

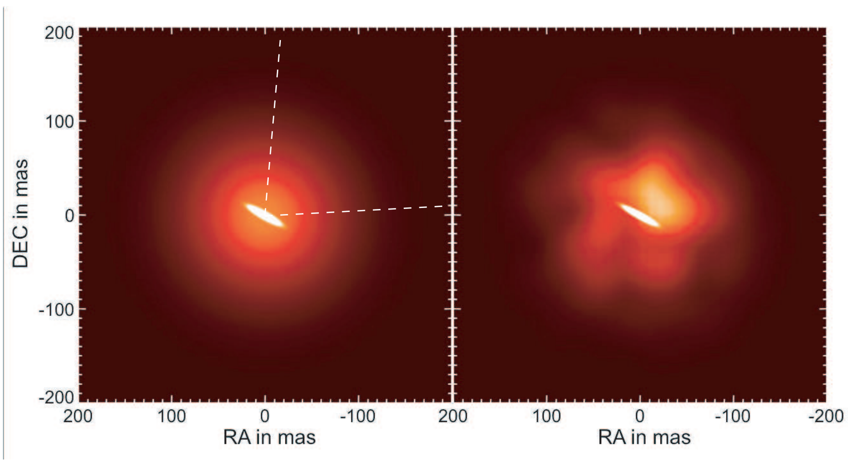

Figure 1: *The dust torus in the Circinus galaxy. The* left panel *shows the smooth model (composed of two Gaussian brightness distributions), the* right panel *visualises the best-fitting patchy model. Dashed lines indicate the ionization cone as derived from emission lines on larger scale.*

Modeling the dusty torus

Independently from the observations reported here, theoretical considerations led to the conclusion that a geometrically thick, smoothly filled molecular cannot be stable (Krolik & Begelman 1988). Therefore, we investigated a torus model in wich a nuclear star cluster of intermediate age (5×10^7 yr) injects both mass (stellar mass loss in AGB phase and planetary nebulae) and kinetic energy (supernovae) into the core region [5]. Under these circumstances a sytem of radially stretched, cooling filaments evolves (see Fig. 2). Along the filaments the gas is inflowing towards a dense turbulent disk. Although the size of the disk resembles that of the observed dust disks (Fig. 1), it is such dense that it does not appear as emitting disk but as dark band.

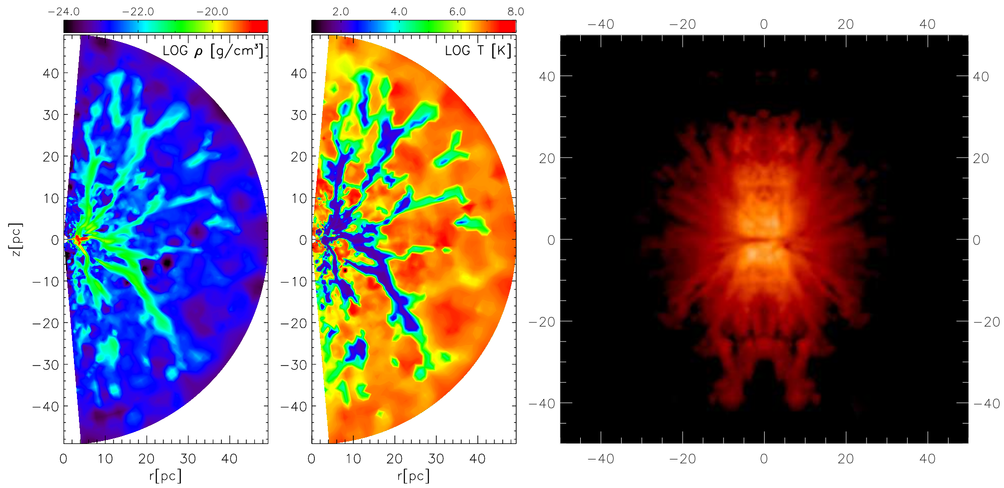

Figure 2: *Hydrodynamical torus model. The* left *and middle panels show the gas density and temperature in a meridional slice. The right panel displays the image at $\lambda = 12\,\mu m$ which would be observed from an edge-on view onto this torus. Note that the dense disk appears as dark band.*

ESO Large Programme: The diversity of dusty molecular tori

The detailed MIDI observations of a handful of AGN, as well as the theoretical models indicate that a "standard torus" does not exist. The diversity among the observed Seyfert 2 galaxies is such large that it will be impossible to test the Seyfert 1/2 unification with a few AGN. Therefore we proposed a Large Programme at the VLTI with the aim to obtain sufficiently detailed observations for all those AGN which have been shown to be bright enough for such a study during the GTO snapshot survey. The granted time (13 nights with *two* UTs) will allow us to harvest most of MIDI's capabilities for AGN research before the next generation of instruments (PRIMA+MIDI, MATISSE) become operational.

Collaborators of the MIDI AGN program are Walter Jaffe, David Raban and Huub Röttgering (Leiden); Sebastian Hönig, Makoto Kishimoto and Gerd Weigelt (Bonn). The models are developed with Hubert Klahr, Thomas Hennig, Max Camenzind (ZAH) and Sebastian Wolf (Kiel).

References

[1] Burtscher, L., Jaffe, W., *et al.* 2009, ApJL, 705, L53.

[2] Jaffe, W., Meisenheimer, K., *et al.* 2004, Nature, 429, 47.

[3] Tristram, K. R. W., Meisenheimer, K., *et al.* 2007, A&A, 474, 837

[4] Tristram, K. R. W., Raban, D., Meisenheimer, K., *et al.* 2009, A&A, 502, 67

[5] Schartmann, M., Meisenheimer, K., Klahr, H., *et al.* 2009, MNRAS, 393, 759

2 Star Formation

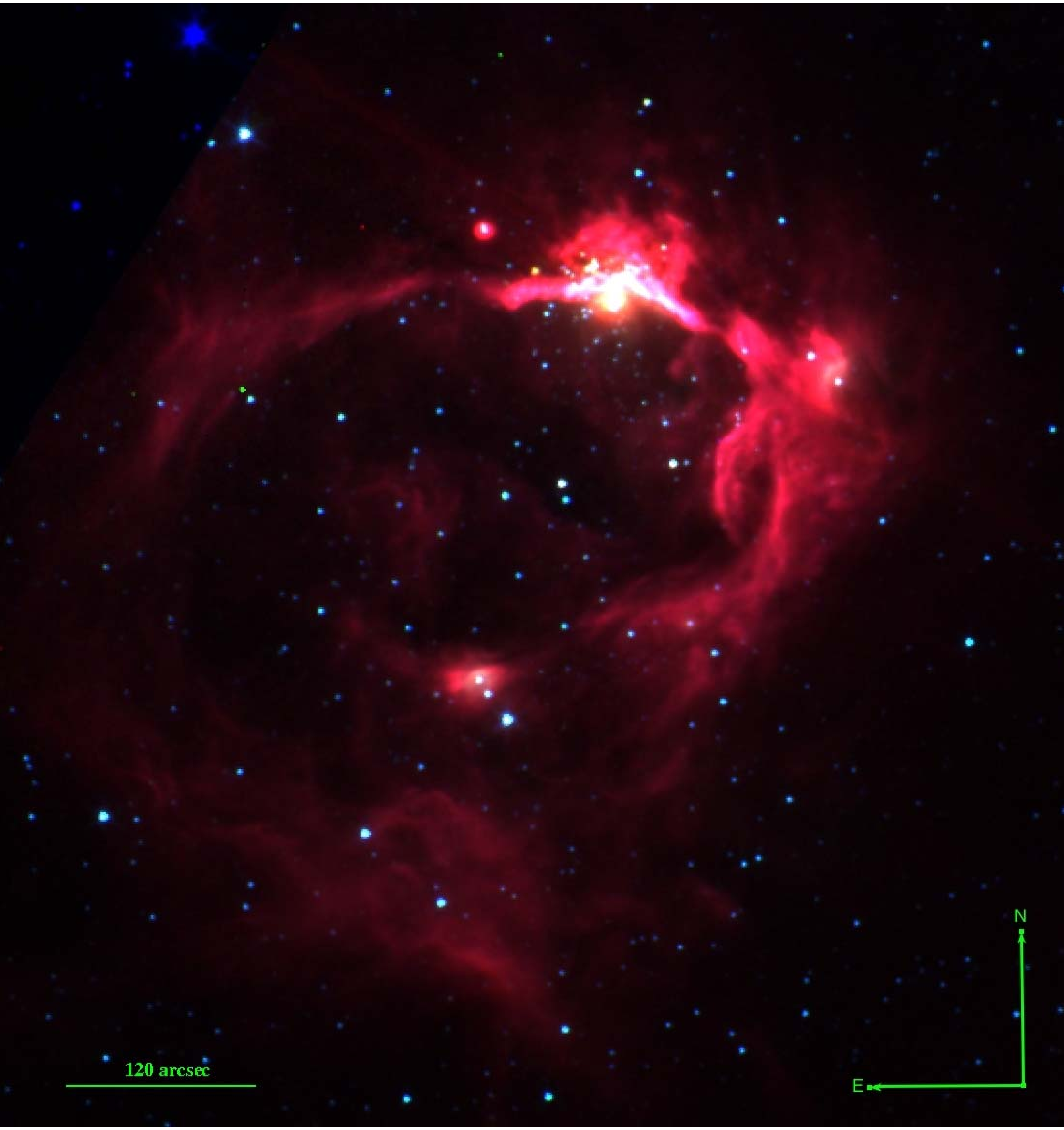

Image on previous page:
Spitzer/IRAC image of RCW 34, a massive star-forming region located in the Vela Molecular Cloud (see page 53 for details).

Isolated star formation in Bok globules

Ralf Launhardt, Amelia Stutz, Markus Schmalzl, and Thomas Henning

Low mass stars are the most numerous stars in the universe. However, despite their high relative numbers, key aspects of their early formation stages remain hidden, enshrouded by large amounts of dust, short time-scales, and the complex and messy processes which can dominate in clustered regions. While larger star-forming complexes are well-suited to investigate the origin of the stellar mass spectrum, many of the difficulties in studying the properties of individual cores can be partially overcome by observing relatively simple nearby and isolated star-forming regions, such as Bok Globules. Bok globules often reside in the filamentary outskirts of larger cloud complexes and mostly contain only one single star-forming core. In order to investigate their star-forming potential, we have studied a large number of globules for signs of star-forming cores and their evolutionary stages [1], chemical evolution [2], kinematic structure [3], and fragmentation [4], using as tracers, e.g., MIR shadows [5], MIR and FIR emission [6], (sub)mm dust emission [1], as well as molecular lines from various species like CO, CS, HCO^+, or $N2H^+$ [2].

Looking into the darkness: the earliest stages of star formation

At the very earliest stages of formation, the identification and detailed characterization of truly pre-stellar cores – cores that are forming or will soon form stars – is the fist step towards revealing the low–mass star-formation process. [5] present a sample of 14 starless cores observed with *Spitzer* and selected be seen in absorption at 24 μm. The observed absorption features, or shadows, are cast by the most embedded and dense core material at the heart of the clouds (Fig. 1). Using a simple Jeans mass criterion, [5] find that about 2/3 of cores producing 24 μm shadows are collapsing or near collapse, a result that is supported by millimeter line observations. Of this subset at least half of the cores have indications of 70 μm shadows. All cores observed to produce absorption features at 70 μm are close to collapse. [5] conclude that 24 μm shadows, and even more so the 70 μm ones, are useful markers of cloud cores that are approaching collapse, and place detailed observational constraints on starless core properties.

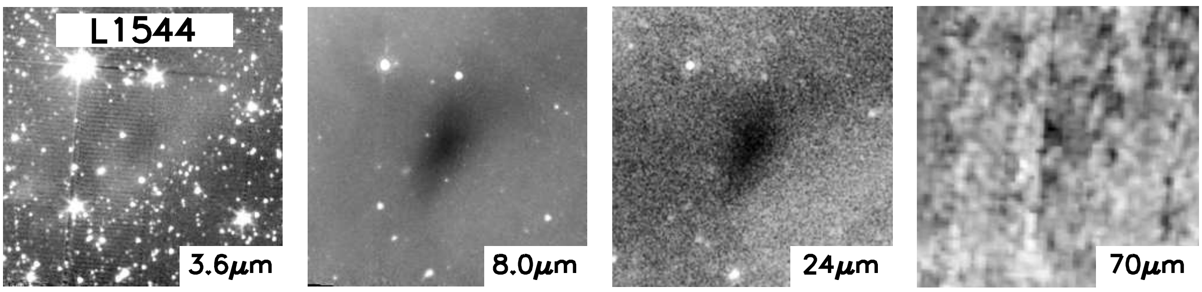

Figure 1: *5' × 5' images of starless core L 1544. The densest core material is seen in absorption at 8.0 μm and 24 μm, and marginally at 70 μm; at 3.6 μm faint emission is observed.*

The star-forming hearts of Bok globules: unexpected complexity

We have studied 32 Bok globules at NIR and submm wavelengths (Fig. 2) and compiled and fitted spectral energy distributions (SEDs) of the embedded sources to derive their evolutionary stages [1]. While the evolutionary stage of visible YSOs can be derived from their NIR colors, other means are necessary for characterizing dust-enshrouded protostars, the most active phase of stellar mass accretion. The sparse data available for only a handful of protostars has made it difficult to establish reliable criteria that trace their evolution. This has dramatically changed during the past few years with the advance of submm bolometer cameras and FIR space facilities,

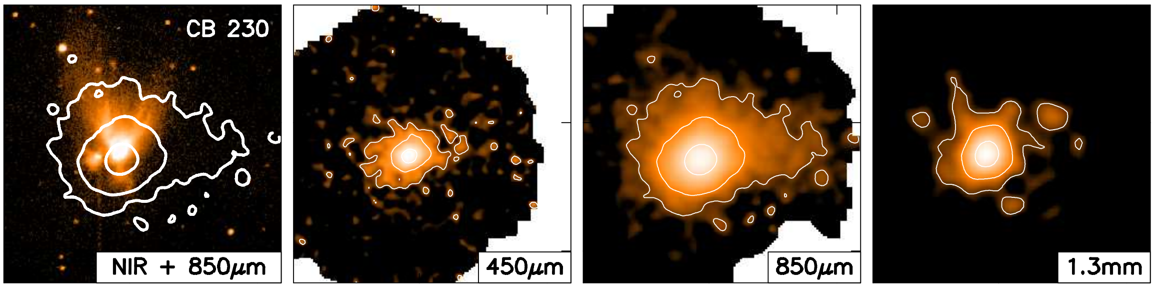

Figure 2: *2' images of the binary star-forming core in the Bok globule CB 230. From left to right: NIR (K-band) image with 850 μm contours; submm dust emission at three wavelengths.*

like *Spitzer* and *Herschel*, that now allow us for the first time to compile complete and spatially resolved SEDs of protostars. We find that the bolometric temperature is the most reliable tracer to discriminate between Class 0 protostars and Class I YSOs (Fig. 3). The Class I YSOs in our sample split up into two distinct groups, one with NIR nebulosities and extended envelopes but no visible stars and with $L_{\rm smm} / L_{\rm bol} > 1.9\%$, and one with visible, very red stars and $L_{\rm smm} / L_{\rm bol} < 1\%$. This bifurcation could hint towards a very quick envelope dispersal, but our sample is too small to draw a reliable conclusion. We also find that at least two thirds of the star-forming globules show evidence of forming multiple stars on scales between 1,000 and 50,000 AU. Surprisingly, the majority of them contain sources at different evolutionary stages, e.g., prestellar or protostellar cores with nearby Class I or II YSOs. This widespread non-coevality possibly suggests a picture of slow and sequential star formation in isolated globules.

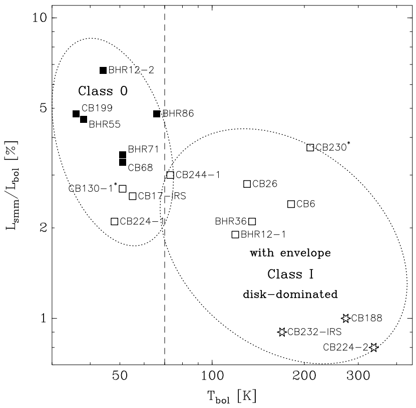

Figure 3: *Ratio of submm to bolometric luminosity vs. bolometric temperature for sources embedded in Bok globule cores. The vertical dashed line marks the $T_{\rm bol} = 70\,K$ boundary between Class 0 and Class I sources proposed by Myers et al. (1998, ApJ 492, 703). Sources without any NIR counterparts are marked by filled squares. Sources associated NIR nebulosities or jets, but no star-like objects, are marked by empty squares. Sources with star-like NIR counterparts are marked by asterisks.*

Collaborators in this project are Ya. Pavlyuchenkov and D. Wiebe (INASAN Moscow, RU), T. Bourke (CfA, Cambridge, USA), X. Chen (Yale University, USA), D. Ward-Thompson and D. Nutter (Cardiff University, UK), G. Rieke and J. Bieging (Steward Obs., USA), R. Zylka (IRAM, FR), and S. Wolf (Kiel University, GE).

References

[1] Launhardt, R., Nutter, D., Ward-Thompson, D., et al. 2009, submitted to ApJ

[2] Pavlyuchenkov, Ya., Wiebe, D., Launhardt, R., Henning, Th. 2006, ApJ 645, 1212

[3] Chen, X., Launhardt, R., & Henning, Th. 2007, ApJ 669, 1058

[4] Chen, X., Launhardt, R., Bourke, T. L., et al. 2008, ApJ 683, 862

[5] Stutz, A.M., Rieke, G.H., Bieging, J.H., et al., 2009, ApJ 707, 137

[6] Stutz, A.M., Rubin, M., Werner, M.W., et al., 2008, ApJ 687, 389

Low-turbulence cores close to high-mass stars

Henrik Beuther & Thomas Henning

Introduction

Although our understanding of massive star formation has improved tremendously over the last decade, most studies were targeted toward relatively evolved regions like high-mass protostellar objects (HMPOs), hot molecular cores (HMCs) or ultracompact HII regions (UCHIIs). Toward even earlier evolutionary stages prior or at the onset of massive star formation, in recent years significant progress has been made in identifying large samples of infrared dark clouds (IRDCs) via absorption studies in the mid-infrared with the MSX, ISO and Spitzer satellites (see also contribution by Beuther, Krause & Henning). However, in spite of this, real high-mass starless cores (HMSCs) have been rarely identified. To overcome this obvious missing link, here we report high-spatial-resolution Plateau de Bure Interferometer observations and analysis of two excellent HMSC candidates in the dust continuum and the line emission of N_2H^+(1–0) and ^{13}CS(2–1) to investigate their physical properties prior to any star formation activity [1]. These data are complemented with Spitzer and IRAM 30 m observations.

A multi-wavelength study with Spitzer and the IRAM facilities

Correlating the Spitzer mid- to far-infrared data at 24 and 70 μm wavelength with the IRAM 30 m 1.2 mm dust continuum observations, we identify two strong mm emission peaks that are clearly associated with mid-infrared shadows at least up to 70 μm wavelength (Figure 1). With a total gas mass of about 90 $M_\odot$, these cores are very good candidates of intermediate-mass star-forming regions prior to any active star formation activity. Furthermore, the two regions are only about $1'$ apart from the luminous HMPO IRAS 19175+1357. Hence the target regions are still within the large-scale environment of this much more evolved source.

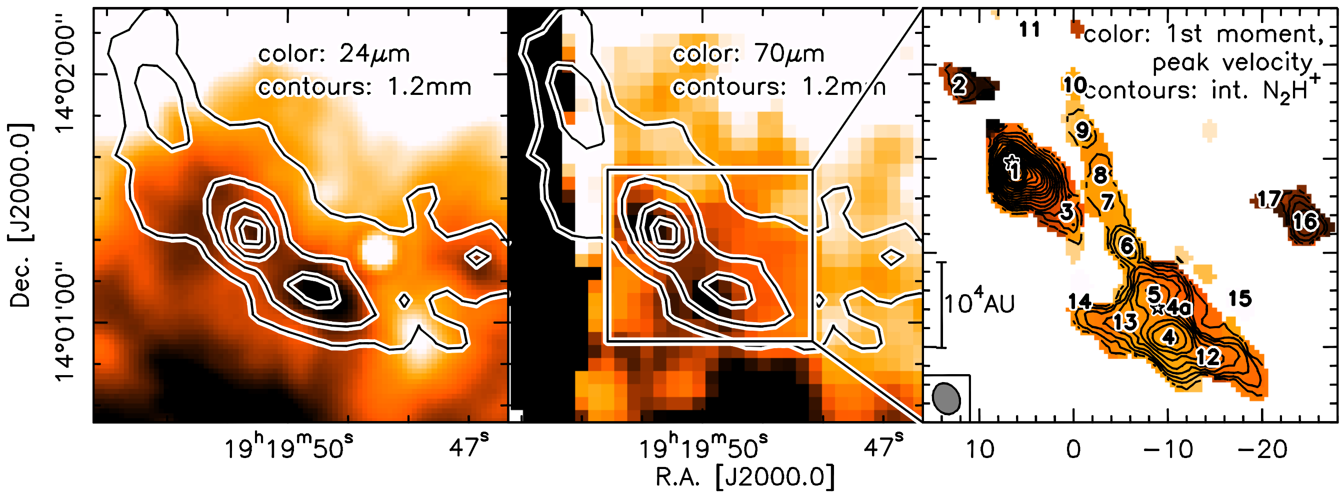

Figure 1: *The left and middle panel show in color-scale the Spitzer 24 and 70 µm data, respectively. The contours present the corresponding 1.2 mm continuum data from the IRAM 30 m telescope. The righ panel shows the zoom in of N_2H^+(1–0) data from the Plateau de Bure Interferometer. The color-scale presents the peak velocity distribution and the contours outline the integrated N_2H^+ emission. Numbers mark the identified sub-sources.*

To get a better handle on the physical small-scale structure of this two regions – IRDC 19175-4 and IRDC 19175-5 –, we observed them with the Plateau de Bure Interferometer in the 3.23 mm dust continuum as well as the N_2H^+(1–0) and ^{13}CS(2–1) line emission.

While IRDC 19175-4 is clearly detected in the 3.23 mm continuum emission, the second source in the field, IRDC 19175-5, is only barely observable above the 3σ continuum detection threshold. However, the N_2H^+(1–0) observations reveal 17 separate sub-sources in the vicinity of the two IRDCs (Figure 1). Most of them exhibit low levels of turbulence ($\Delta v \leq 1\,\mathrm{km\,s^{-1}}$), indicating that the fragmentation process in these cores may be dominated by the interplay of thermal pressure and gravity, but not so much by turbulence. Combining the small line widths with the non-detection up to 70 μm and the absence of other signs of star formation activity, most of these 17 cores with masses between sub-solar to $\sim$10 $\mathrm{M_\odot}$ are likely still in a starless phase. The N_2H^+ column density analysis indicates significant abundance variations between the cores. Furthermore, we find a large CS depletion factor of the order 100. Although the strongest line and continuum peak is close to virial equilibrium, its slightly broader line width compared to the other cores is consistent with it being in a contraction phase potentially at the verge of star formation. Based on the 3.23 mm upper limits, the other cores may be gravitationally stable or even transient structures. The relative peak velocities between neighboring cores are usually below $1\,\mathrm{km\,s^{-1}}$, and we do not identify streaming motions along the filamentary structures. Average densities are between 10^5 and $10^6\,\mathrm{cm^{-3}}$ (one to two orders of magnitude larger than for example in the Pipe nebula) implying relatively small Jeans-lengths that are consistent with the observed core separations of the order 5000 AU.

These observations show that multiple low- to intermediate-mass low-turbulence starless cores can exist in the proximity of more turbulent active intermediate- to high-mass star-forming regions. While masses and levels of turbulence are consistent with low-mass starless core regions, other parameters like the densities or Jeans-lengths differ considerably. This may be due to environmental effects. The quest for real high-mass starless cores prior to any star formation activity remains open.

References

[1] Beuther, H., Henning, Th., 2009, A&A, 503, 859

Probing the evolution of molecular cloud structure: From quiescence to birth

Jouni Kainulainen, Henrik Beuther, Thomas Henning

What stirs up star formation in molecular clouds?

Star formation is known to take place exclusively in the most extreme density enhancements of molecular clouds. In the current view, the structure of molecular clouds, and thereby the occurrence of the density enhancements, is heavily affected by the motions induced by supersonic turbulence. In parallel, the cloud structure is also crucially affected by the self-gravity of gas and magnetic fields in the clouds. Determining the relative strengths of these cloud-shaping mechanisms is regarded as one of the critical open questions of the interstellar medium.

The understanding of the above mentioned mechanisms derives from extensive numerical simulations that have yielded predictions for characteristics of molecular cloud structure. Such predictions are directly used by analytic theories of star formation. Contrasting this understanding, observational description of the large-scale molecular cloud structure is crucially lacking. This is due to the general difficulty of measuring the gas distribution in molecular clouds.

Molecular cloud complexes viewed by dust extinction

To tackle the above issues, we have undertaken a study in which we examine the large-scale structures of nearby molecular clouds by employing a novel near-infrared dust extinction mapping technique. For nearby clouds, this technique provides sensitivity over a relatively wide dynamical range ($A_V \approx 0.5 - 25$ mag) and a robust method to map clouds over their full extent.

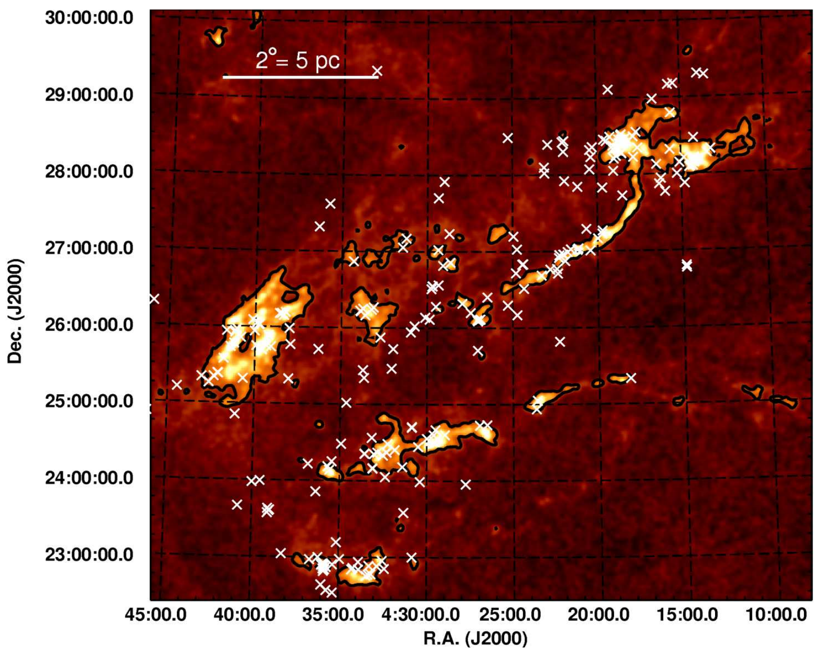

Figure 1: *Near-infrared dust extinction map of the Taurus molecular cloud complex [1]. The crosses show the known pre-main-sequence stars in the cloud. The contour is drawn at $A_V = 4$ mag, marking the region above which the PDF deviates from a lognormal function (see Fig. 2).*

We used this technique in conjunction with data from 2MASS survey to derive dust extinc-

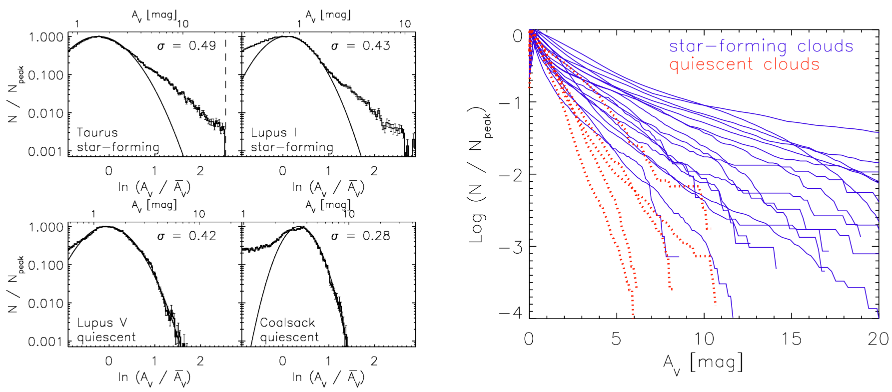

Figure 2: *Left: Probability distributions of column density in two star-forming clouds and two quiescent clouds. Right: Cumulative mass functions of 23 nearby molecular cloud complexes [1].*

tion maps for a large sample of molecular clouds. The sample forms a complete set of prominent cloud complexes closer than $d \leq 200$ pc. As an example, Fig. 1 shows the wide-field extinction map derived for the well-known Taurus star-forming complex.

Bringing molecular clouds from quiescence to birth

While the derived maps can be used to examine several structural parameters, we first focused on the probability density functions (PDFs hereafter) of column density in the clouds [1]. This distribution plays a fundamental role in current theories of star formation: it is used to explain, for example, the initial mass function of stars, and the star formation rates and efficiencies of molecular clouds. In particular, the numerical simulations predict the distribution to take a log-normal shape in isothermal, turbulent, non-gravitating media.

The column density PDFs derived for the clouds in our study show that simple log-normal functions fit the PDFs of most clouds rather poorly. Instead, excess "wings" at higher column densities are persistent features of the molecular cloud structure (Fig. 2, left). Most intriguingly, the PDFs show a clear trend. All clouds with active star formation show strong excess of higher column densities. In contrast, almost all quiescent clouds have PDFs that either are well described by log-normal functions, or show only low excess of high column densities. These observations are in agreement with a picture in which the molecular cloud in the early stage of its evolution is decisively shaped by turbulent motions. As the cloud evolves, local density enhancements can become self-gravitating, which assembles a growing fraction of gas to higher column densities. This is strongly reflected in the cumulative PDFs, describing the fraction of material above a certain column density (Fig. 2, right). In the low column density regions, turbulent motions prevail as the dominant structure shaping mechanism. Interestingly, these observations then suggest that self-gravity has a strong role in shaping the cloud structure starting from a very early stage, corresponding to the onset of active star formation in the cloud.

We are currently comparing our data to the most recent numerical simulations in order to directly constrain the crucial parameters in them and in the analytic theories of star formation. This work is being done in collaboration with Rene Plume (University of Calgary, Canada).

References

[1] Kainulainen, J., Beuther, H., Henning, T., Plume, R., 2009, accepted to A&A Letters.

Brown dwarfs and very low-mass stars in the Praesepe open cluster: A dynamically unevolved Mass Function

Steve Boudreault, Coryn A. L. Bailer-Jones, Bertrand Goldman, Thomas Henning & José A. Caballero

Introduction

Several publications in the past decade have been concerned with the mass function of low mass stellar and substellar populations in open clusters. Studies of relatively old open clusters (age$>$100 Myr) are important for the following two reasons in particular. First, they permit a study of the intrinsic evolution of brown dwarfs, e.g. their luminosity and effective temperature, which constrains structural and atmospheric models. Second, together with younger clusters we can investigate how brown dwarf populations as a whole evolve and thus probe the efficiency with which brown dwarfs evaporate from clusters to populate the Galactic field. Numerical simulations of cluster evolution have demonstrated that the mass functions can evolve through dynamical interaction. These interactions result in a decrease of the open cluster brown dwarf (and low-mass star) population. This has been observed by from a comparison of the Pleiades (120 Myr) and Hyades (625 Myr) mass functions [2].

Many earlier studies of the substellar mass function have focused on young open clusters with ages less than $\sim$100 Myr, and in many cases much younger ($<$ 10 Myr). However, youth presents difficulties. First, intra-cluster extinction plagues the determination of the intrinsic luminosity function from the measured photometry. Second, at these ages the brown dwarf models have large(r) uncertainties and estimates of the substellar mass function in very young clusters (age $\sim$1 Myr) might be unreliable due to these modelling uncertainties. brown dwarfs in older clusters suffer less from these problems.

The old open cluster Praesepe is an interesting target considering its age and distance. Here we present the results of a photometric survey to identify low mass and brown dwarf members of this cluster from which we estimate its mass function and compare this with that of other clusters.

Observations

Our survey consists of 47 Omega 2000 (O2k) fields each of size 15.4$\times$15.4 arcmin^2 observed in J and K_s, plus the same region observed in nine I_c Wide Field Imager (WFI) fields each of size 34$\times$33 arcmin^2. This gives a total coverage of 3.1 deg^2 observed in all three bands. The near-infrared (NIR) observations were made on the 3.5m telescope at Calar Alto, Spain (with observation runs of several nights from February 2005 to January 2007). The optical observations were carried out with the Wide Field Imager (WFI) on the MPG/ESO 2.2m telescope at La Silla, Chile during 17–22 March 2007. The 5σ detection limits of our survey are I_c=23.4 mag, J=20.0 mag and K_s=18.6 mag (which correspond to $\sim$0.05 $M_\odot$).

Results and future work

The mass function rises from 0.6 $M_\odot$ down to 0.1 $M_\odot$ (a power law fit of the mass function gives α=1.8$\pm$0.1; $\xi(M) \propto M^{-\alpha}$), and then turns over at $\sim$0.1 $M_\odot$. This rise agrees with the mass function inferred by previous studies, including a survey based on proper motion and photometry (Fig. 1). In contrast, the mass function differs significantly from that measured for the Hyades (Fig. 1), an open cluster with a similar age ($\tau \sim$ 600 Myr). Possible reasons are that the clusters did not have the same initial mass function, or that dynamical evolution (e.g. evaporation of low mass members) has proceeded differently in the two clusters. Although different binary fractions could cause the observed (i.e. system) mass functions to differ, there is no evidence for differing binary fractions from measurements published in the literature.

The results from our work on Praesepe are presented in a publication in press at journalthe Astronomy & Astrophysics [1].

We plan to continue our study of Praesepe clusters with the analysis of additional $rizY$-band photometry obtained using the LBC blue and red cameras at the LBT telescope at Mt. Graham, obtained in March and December of 2008. The area of the LBT is $0.61\,\mathrm{deg}^2$ and completely overlaps with our existing NIR photometry. We reach a 5σ detection limit at $45\,\mathrm{M_J}$. We are currently analyzing these data and a publication is expected in the near future.

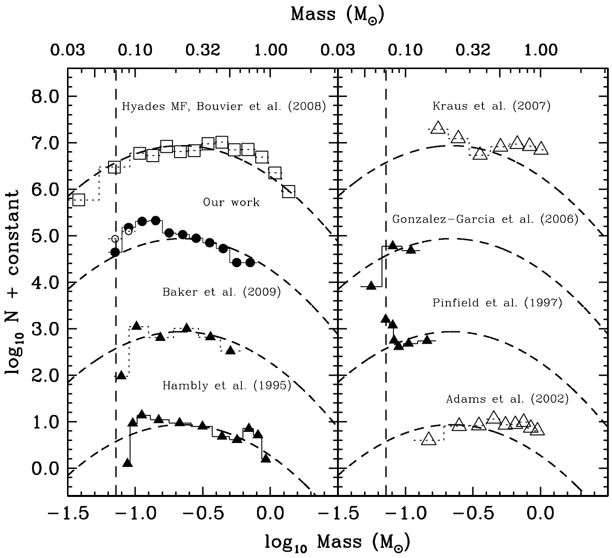

Figure 1: *Mass function of Praesepe from our present work (open dots assuming a dusty atmosphere and filled dots assuming a dust-free atmosphere), from previous work (open triangles for survey using proper motion and filled triangles for survey using photometry only), as well as the mass function from the Hyades [2] (open squares). We also show the log-normal fit of the galactic field star mass function as a thin dashed line and the substellar limit as a thick dashed line.*

References

[1] Boudreault, S, Bailer-Jones, C. A. L., Goldman, B., Henning, T. & Caballero, J. A., 2009, A&A, in press (*arXiv:0910.4529*).

[2] Bouvier, J., Kendall, T. T., Meeus, G., et al., 2008, A&A, 481, 661

Dust coagulation and fragmentation in molecular clouds

Chris W. Ormel

Dust coagulation in molecular cloud cores.

Understanding the behavior of dust in molecular clouds (cores) is important since it plays a pivotal role in observational studies that try to assess the physical and evolutionary state of the cloud, through, for example, dust extinction, near-IR, and, far-IR/sub-mm emission measurements. However, in the dense and cold environments of cores, the dust properties are expected to change. First, ices condense out, producing a mantle of ∼100 Å in size. However, a more potent mechanism for grain growth is coagulation among dust grains. In this study we have assessed the importance of coagulation by combining several state-of-the art theoretical models [1].

Numerical simulations

First, we conducted a parameter study to obtain the outcome of a collision between two dust aggregates (see Fig. 1). Collisions between dust grains often produce fractal aggregates, which

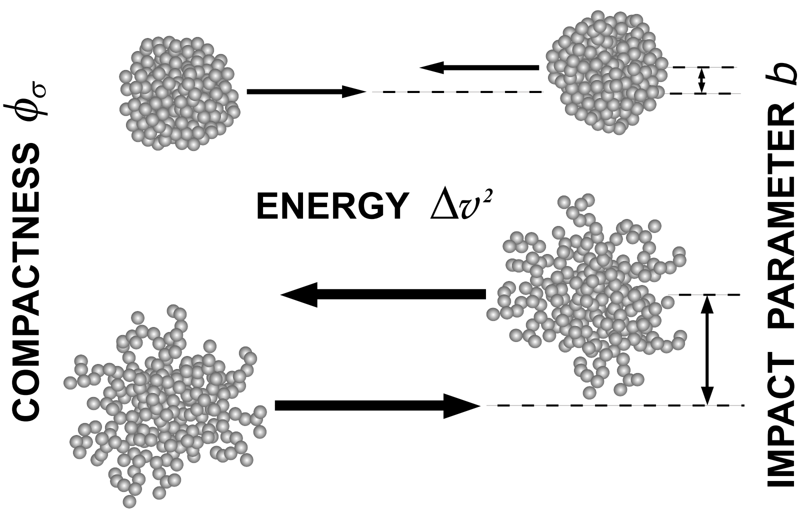

Figure 1: *The setup for a numerical collision between two dusty aggregates. The collisional outcome depends, among others, on (i) mass ratio, (ii) collision velocity, (iii) aggregate porosity, and (iv) impact parameter.*

internal structure can be very fluffy (1993, Ossenkopf, A&A, 280, 637). However, when collision velocities increase the fluffy structure collapses or even fragment. All these factors (mass ratio, fluffiness, impact parameter, & velocity) have been taken into account, resulting in a 'look-up table' for the outcome of the collisions (2009, Paszun & Dominik, A&A, 507, 1023).

Second, a *collisional evolution* study was performed. We have used a Monte Carlo code (2007, Ormel et al., A&A, 461, 215) to follow the particle internal structure and the collision parameters. The resulting dust size distributions are plotted in the left panel of Fig. 2 for a case where the dust grains are coated by fine ice mantles. The *left* panel shows the distribution function at various times. Here, N is the number of grains per aggregate where the grains are 0.1 μm in radius. It can be seen that due to coagulation most of the mass becomes locked up in

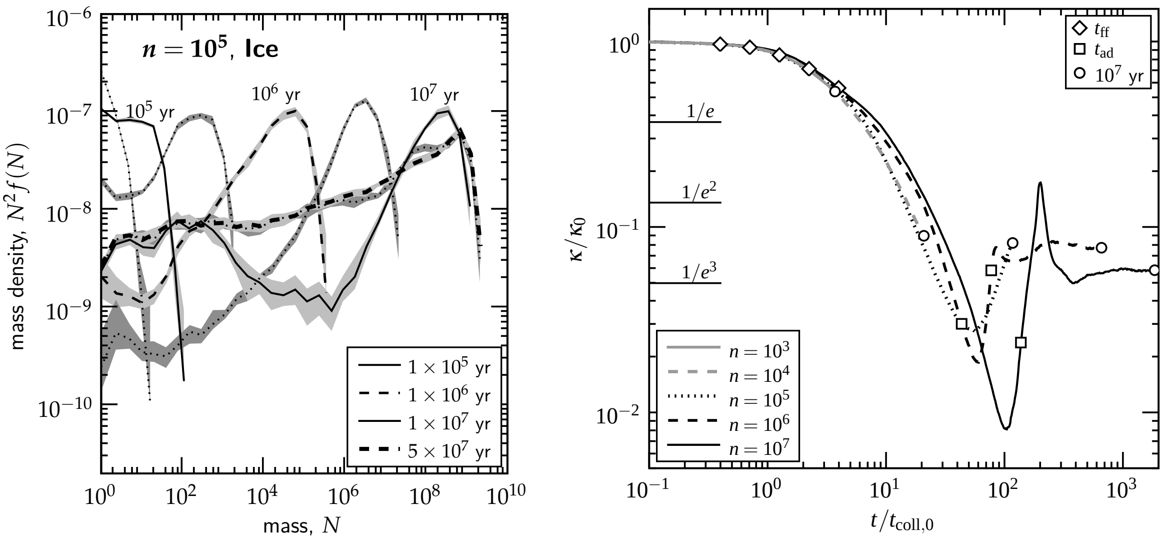

Figure 2: *(left) The size distribution at various times during the evolution. (right) The reduction of the dust opacity as function of time and cloud density.*

big aggregates, reaching $N \sim 10^8$ (or ~ 100 μm size grains) by 10^7 yr. However, after this time fragmentation stalls any further growth. The size distribution then evolves to a steady state and becomes rather flat, a feature also seen in a similar coagulation-fragmentation simulations in protoplanetary disks [2].

Growth timescales

However, it is unlikely that cores will survive for these long timescales. In reality, the lifetime of the cloud will determine how much coagulation takes place and to which extent the observational characteristics (dust opacities) are affected.

This is illustrated in Fig. 2 where we have plotted the reduction in the geometrical opacity κ/κ_0, which is valid at, e.g., visible wavelengths. The outcome of the simulation is shown at five different densities. Markers indicate three key points during the evolution: the free-fall timescale $t_{\rm ff}$, the ambipolar diffusion timescale $t_{\rm ad}$ and $t = 10^7$ yr. Thus, it can be seen that when clouds collapse on the free-fall timescale (*diamonds*) the imprints of coagulation will be very modest; however, when clouds exist on the ambipolar diffusion timescale (*squares*) there is a significant potential for growth (decreasing κ/κ_0) or even fragmentation (increasing κ/κ_0) for the highest densities.

Collaborators are D. Paszun, C. Dominik (both Amsterdam) and A. Tielens (Leiden).

References

[1] Ormel, C.W., Paszun, D., Dominik, C, &, Tielens, A.G.G.M, 2009, A&A, 502, 845

[2] Brauer, F., Dullemond, C.P., Henning Th., 2008, A&A, 480, 859

Direct evidence for dust growth in L183 from MIR light scattering seen by Spitzer

Jürgen Steinacker

Measuring changing dust properties in molecular clouds

Cold and dense cores of molecular clouds are commonly considered to be a favorable place for the growth of dust particles. Evidence for the existence of grains being larger than commonly observed interstellar medium grains have been gathered in different wavelength regions. But disentangling spatial variations in dust properties, density, and temperature is a challenge given the many parameters needed to describe the often clumpy or filamentary cloud structures.

Extinction measurements at optical to MIR wavelengths have the advantage that the temperature of the dust grains no longer influences the results. But the method requires a radiation source like scattered light, diffuse emission from small grains or molecules, or background stellar or extragalactic emission. Moreover, the exponential extinction limits the method to moderate optical depths.

Aside from the thermal emission of the grains in the cloud gas, and their absorption, they also efficiently scatter radiation. This so-called NIR cloudshine can be used as a general tracer of the outer column density of dense clouds and is very sensitive to the outer density structure. However, the scattering cross section of the ISM dust particles drops with wavelength once the wavelength is much larger than the particle size. Scattered light from cores at MIR wavelengths therefore was not reported so far.

L183 (also known as L134N) is a starless dark cloud high above the Galactic plane (36^o) with a distance of about110 pc and a gas mass of about 80 $M_\odot$. It contains an elongated ridge of dense material with two pre-stellar cores and the main pre-stellar core has a peak extinction of A_V=150 mag with a dust temperature close to 7 K. Fig. 1 shows the images of L183 obtained by Spitzer at 3.6, 4.5, and 8 μm.

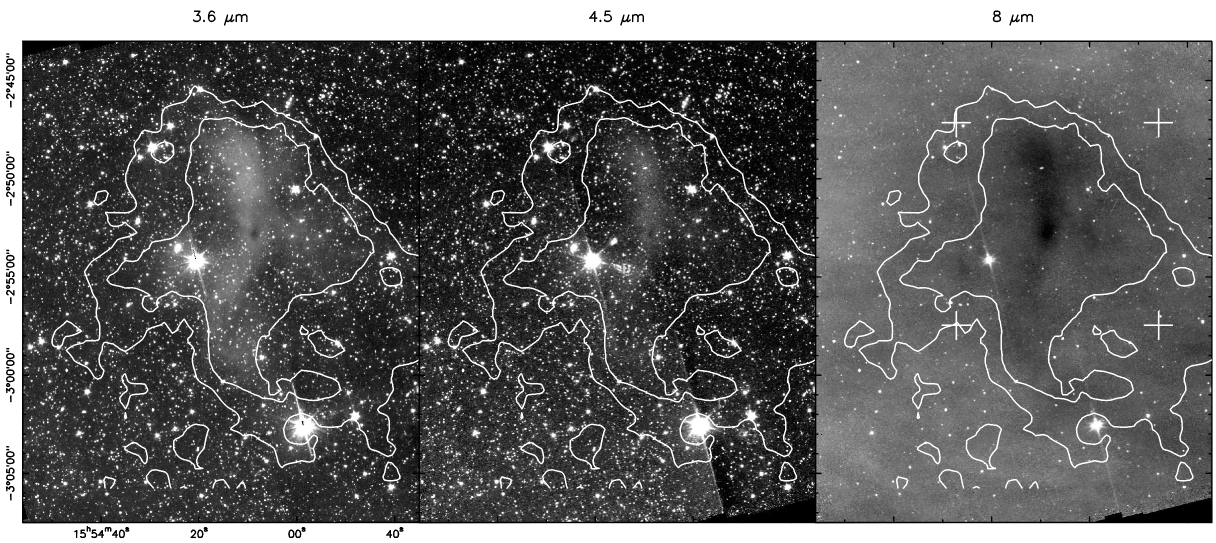

Figure 1: *IRAC 3.6, 4.5, and 8 μm long exposure mosaics. Superposed to each image are the A_V=5 and 10 mag contours. The white crosses in the 8 μm image mark the region which has been further modeled.*

Grain growth visible in the dense regions of L183

Several reasons suggest that the emission seen at 3.6 and 4.5 μm can not be attributed to thermal black body emission of larger dust grains (temperature too low), or emission of stochastically heated particles (it should originate from an outer layer where most of the interstellar radiation field is absorbed, there should be more flux from 5.8 than from 4.5 μm, and holes are not consistent with the observed extinction map when applying a 3D modeling radiative transfer analysis).

We therefore suggested that this emission is scattered interstellar radiation. To test this hypothesis, we have performed 3D radiative transfer calculations producing scattered light images of the central dense region where emission is seen (Steinacker et al. 2009). The model included a realistic direction-dependent interstellar radiation field based on the DIRBE data which did not introduce new unknowns. Using simple silicate dust grains without growth, the produced scattered light flux was not sufficient to reproduce the observed image. Using a simple dust growth model with the size scaling with the gas density,the main features of the Spitzer observation in the 3.6, 4.5, and 8 μm bands can be reproduced. The existence of this new MIR window to study the growth of grains in the dense parts of cores is due to an interplay of several effects: At MIR wavelengths, the moderate optical depth allows to observe dense regions where growth is expected. The MIR scattering efficiency of smaller grains is too low to detect them, but larger grains scatter more efficiently and become observable again.

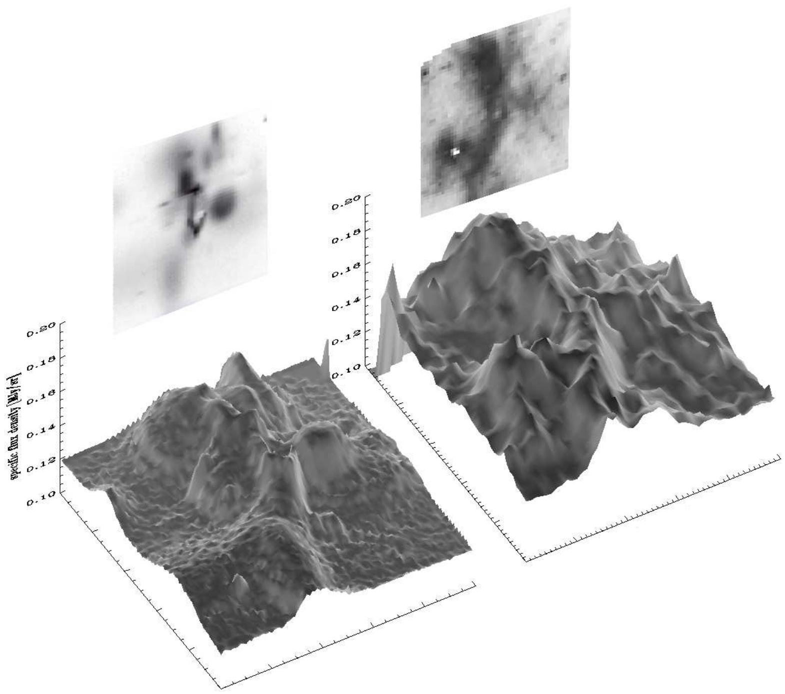

Figure 2: *Comparison of the specific flux density (z-axis) of the 3.6 μm Spitzer image of the inner 66000 AU of L183 (right), processed through a star removal routine, with the scattered light model image (left).*

Collaborators are Laurent Pagani (Observatoire de Paris, France), Aurore Bacmann (LAOG, France), and Sylvain Guieu (Spitzer SC, USA).

Reference: Steinacker, J., Pagani, L., Bacmann, A., & Guieu, S. 2009, arXiv:0912.0145

Bipolar jets from a close T Tauri star binary

Reinhard Mundt

Scientific Background

So far all models proposed for driving jets and outflows from young stars have only considered single stars as the central source (e.g. Pudritz et al. 2007; Protostars and Planets V, 277). Furthermore it has not been investigated whether any of these models can be applied to a close binary system, such as KH 15D, where the spectroscopic signature of a bipolar outflow has been found in the [OI]λ6300 line in 2003 [1]. A small-scale bipolar jet of $\sim$70 AU length in [SII]λ6731 is also known for the close 19 d T Tauri star (TTS) binary UZ Tau E [2]. In a recent study [3] we have presented for the first time in the astrophysical literature simple models for jet formation in close TTS binary systems and hope that our study will initiate detailed theoretical and observational follow-up studies of this challenging astrophysical problem.

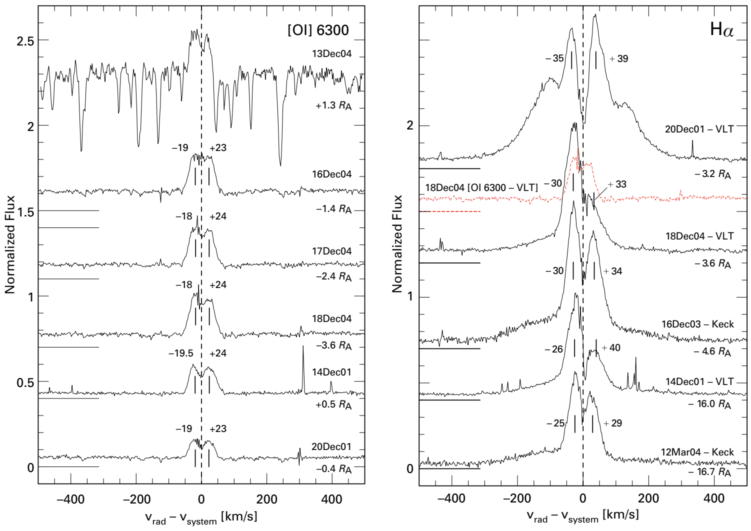

Figure 1: *The left hand part of the figure shows five UVES/VLT [OI]λ 6300 line profiles of KH 15D taken during full eclipse by the circumbinary disk together with an out of eclipse profile (top) for comparison purposes. The right hand part shows five fully "eclipsed" Hα line profiles taken with UVES/VLT and HIRES/Keck and obtained in part at different epochs than the [OI] profiles. Please note that the velocities of the two jet components (indicated in km s^{-1}) are nearly symmetric relative to the systemic velocity [3].*

Methods and Results

Our study is based on high-resolution Hα and [OI]λ 6300 line profiles of the TTS spectroscopic binary KH 15D (P=48.4 d, ϵ $\sim$0.6, periastron separation $\sim$18 R_A, M_A=0.6$M_\odot$, M_B=0.7$M_\odot$) obtained during eclipses by the circumbinary disk (CBD). KH 15D (age$\sim$2 Myr, d=760 pc) has been the subject of many detailed observational and theoretical studies (e.g. Herbst et al. 2008, Nature 452, 194). It first got attention for its unique photometric variability with deep and practically grey eclipses every 48.4 days that have become deeper and wider with each passing year. The following model describes the available data. A nearly edge-on binary system is surrounded by a CBD which is inclined to the binary plane by $\approx$10-20°. Since more than a decade the CBD has been totally occulting the orbit of star B and has been increasingly occulting that of star A. This is due to its precession on a $\sim 10^3$ yr time scale, which causes the occulting edge to cover the orbit of the binary. During the epoch of observations discussed here, only eclipses of star A are observed, which result from the disappearance of this star behind the occulting edge. Without this sharp edge acting as a "natural coronagraph" it would have been practically impossible to trace in Hα or [OI] the much fainter emission from the outflowing gas analyzed here and shown in Fig. 1. One quite important result of our study is that the radial velocities of the two spectroscopically identified jet components are nearly *symmetric to the systemic velocity* of the binary system.

Possible simple models

Due to the high excentricity ($\sim$0.6) of the KH 15D binary system the two stars approach as close as $\sim 18\,R_A$ (R_A=1.3 $R_\odot$) during periastron. We find it of great astrophysical interest that such a close binary system can launch jets, and it remains as a large theoretical challenge to model such a system, or even closer systems like UZ Tau E. One important guidance for any launching model of the KH 15D jets is the fact that the redshifted and blueshifted jet components in Hα and [OI] show a symmetric velocity shift relative to v_{sys}=+18.6 km s^{-1}. In the following we discuss two possible models which could explain this important result. In the first model the jets are launched from the innermost part of the CBD. A problem with this idea is the large inferred inner radius of the CBD ($\sim$0.6 AU; Herbst et al. 2008, Nature 452, 194), since at this radius the CBD is rotating with only v_{rot} $\sim$45 km s^{-1} (P=145 d, 3:1 inner Lindblad resonance). Magneto-hydrodynamic simulations (e.g. Fendt 2006, ApJ 651, 272) for various magnetic field strengths and magnetic field configurations have shown that jet velocities of v_{jet} $\sim$1-1.5 v_{rot} are normal, although $v_{jet}$$\sim$2 v_{rot} is not unusual. This means that v_{jet}=100 km s^{-1} is not implausible and we adopt this value for the CBD launching model, which would be consistent with the inclination angle of the binary system and the measured radial velocities of the jets. The CBD launching model predicts higher jet velocities for shorter period TTS binaries, which is consistent with [OI] line profiles of UZ Tau E (P=19 d) and DQ Tau (P=15.8 d), in which the edge of their blue wing indicate v_{jet} $\geq$150km s^{-1} and $\geq$120km s^{-1}, respectively (Huerta et al. 2005, AJ 129, 985).

Although the CBD jet launching idea is attractive we also consider the following second model, which produces higher jet speeds. This model requires that each of the two binary stars launches a magneto-hydrodynamically driven outflow with $\sim$200 km s^{-1} from each of the circumstellar disks and that each of these two outflows is of similar mass flux and velocity. At some distance from the system these two outflows merge to form a common jet. Whether this rather speculative idea would work in the end requires detailed modeling.

This project is done in collaboration with C. Hamilton (Dickinson College), W. Herbst (Wesleyan University), C M. Johns-Krull (Rice University), J.N. Winn (MIT)

References

[1] Hamilton, C, Herbst, W., Bailer-Jones, C., Mundt, R. 2003, ApJ 591, L45

[2] Hirth, G. A., Mundt, R., & Solf, J. 1997, A&A Supp. 126, 437

[3] Mundt, R., Hamilton, C, Herbst, W., Johns-Krull, C.M., Winn, J.N. 2010, ApJ 708, L5

An outflow origin of the [NeII] emission in the T Tau Triplet

Roy van Boekel & Thomas Henning

The evolution of protoplanetary disks

After the main accretion phase (Class 0/I) is over, young stars are still surrounded by a circumstellar disk of gas and dust with a typical mass of about 1% of the stellar mass. During the class II phase, planets are thought to form in the disk midplane, while the disk is being dissipated within a few Myr on average. The disk dissipation process is still very poorly understood, and the roles and relative importance of various proposed dissipation mechanisms, e.g. viscous evolution, photo-evaporation, and planet formation, are essentially unknown. The photo-evaporation process has been well studied theoretically, and there is convincing observational evidence of disks being eroded by external UV fields from nearby O-stars clusters, as well as less conclusive evidence of isolated disks being evaporated by UV photons from their own central star. However, it is extremely difficult to assess the effectiveness of photo-evaporation since the energetic radiation responsible for the disk erosion is strongly absorbed by even small columns of foreground material, and we cannot measure the relevant UV fields directly.

The [NeII] 12.81 μm line, a tracer for ionizing radiation?

Motivated by numerous detections of the 12.81 μm fine structure line of singly ionized Neon in infrared spectra of protoplanetary disks made with the Spitzer Space Telescope, several authors have developed theoretical models to explain this emission. The first ionization potential of Neon is high (21.6 eV) and only EUV or X-ray photons are energetic enough to create the ions. Models of disks whose surface layers are irradiated by X-rays (Glasgold et al. 2008, Ercolano et al. 2008) or EUV radiation (Hollenbach & Gorti 2009) from the central star have been successful in explaining the [NeII] line fluxes in typical Spitzer detections. High spectral resolution ground based observations have yielded examples of narrow [NeII] line profiles (<20 km/s) centered at the stellar velocity or blue-shifted by a few km/s, consistent with a disk surface or photo-evaporative disk wind origin (Herzceg et al. 2008, Pascucci & Sterzik 2009). Thus, energetic radiation may well explain the [NeII] emission from circumstellar disks. Vice versa, the [NeII] line may provide a long sought observational tracer for energetic radiation fields at the disk surface, allowing to constrain models of photo-evaporation. However, the low spectral and spatial resolution Spitzer spectra do not allow the detected [NeII] emission to be unambiguously attributed to the disk surface or a disk wind, and other potential origins of the [NeII] emission need first to be ruled out. In particular, high velocity shocks in jets have been proposed as sources of [NeII] emission in YSOs (e.g. Van den Ancker et al. 1998).

High resolution VISIR spectroscopy of T Tau: an ideal test case

The T Tau multiple system constitutes a good environment to investigate the nature of the [NeII] emission mechanism: it is nearby, it contains three young stars with circumstellar disks of which at least one is a strong X-ray source, it has at least two jets and complex structures of shocked gas within a few arcseconds of the central stars, and it shows a strong [NeII] line in infrared spectra taken with ISO and Spitzer. However, in the existing space-based detections there is no meaningful kinematic information due to insufficient spectral resolution, and all potential origins lie within a single spatial resolution element. Thus the nature of the emission mechanism remains undetermined and high resolution observations are required.

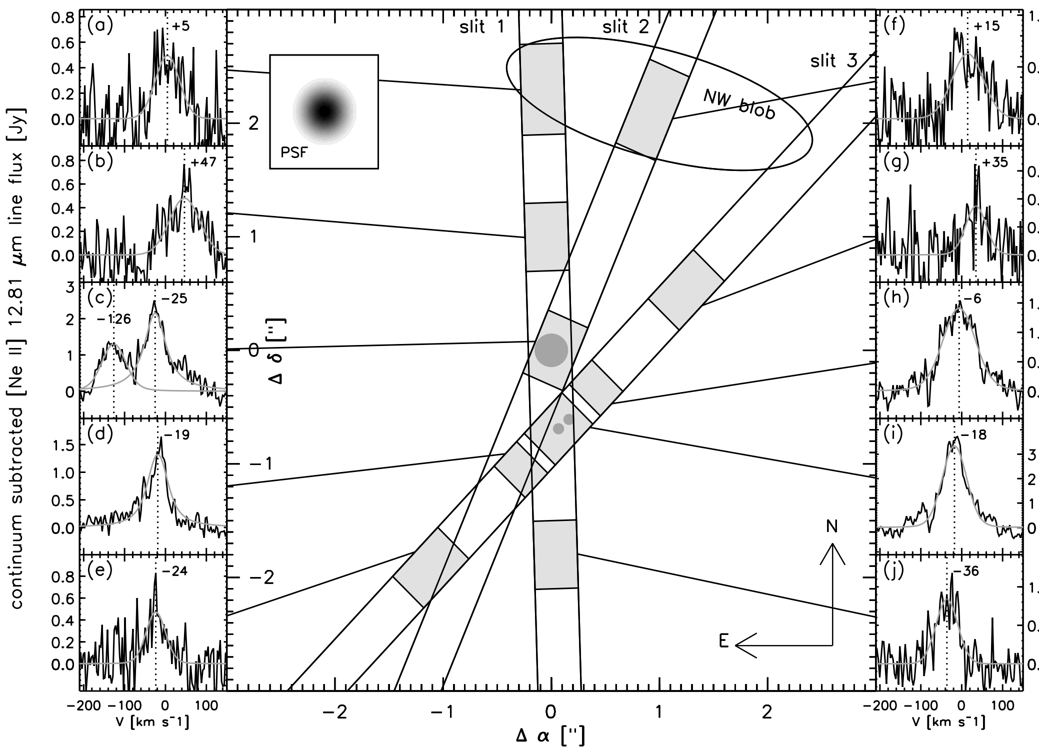

Figure 1: *VISIR spectra showing the 12.81 μm [NeII] emission line in the T Tau system.*

We have observed the T Tau system with VISIR at the VLT, offering a spectral resolution of $R \approx 30000$ and a spatial resolution of $\approx 0\farcs4$, through several longslits covering the main system components. Figure 1 provides an overview of our observations. The [NeII] line is detected at many positions in the system, both at the positions of the stars as well as in more extended diffuse regions that also light up in shocked H_2 (e.g. Beck et al. 2008, Gustafsson et al 2008).

Our main findings are: 1) the strongest [NeII] emission peak is centered on T Tau S and not on the X-ray bright northern component (note that T Tau S is in fact a close binary consisting of components Sa and Sb, which are not spatially separated in the VISIR observations); 2) there is blue-shifted extended toward the sout-east, and redshifted emission toward the north-west that comes to a halt at the position of the "NW blob", a well known feature thought to be the terminal bow-shock of a jet arising from T Tau S; 3) the spatial extent of the bright [NeII] component centered on T Tau S is ≈20 times larger than either of the disks in the southern binary. We conclude that the vast majority of the [NeII] emission in the T Tau system arises in a jet launched from T Tau S. These results have appeared in A&A [1].

[NeII] emission from disks or outflows?

In a parallel study, we have compared the [NeII] line fluxes of ∼80 young stars to their X-ray luminosities. We find a positive correlation between both, with, however, very large source to source scatter. In particular, the sources with known jets are strongly over-luminous in [NeII]. The picture that emerges is that the [NeII] line may well be a good tracer of energetic radiation at the disk surface, except in stars that drive a jet (Güdel et al. 2009, 2010).

Collaborators are Manuel Güdel (Zürich), Fred Lahuis (Leiden), and Eric Pantin (Paris)

References

[1] R. van Boekel, M. Güdel, Th. Henning, F. Lahuis, and E. Pantin, A&A, 497, 137V

3D model of bow shocks

Maiken Gustafsson

The model

Outflows from young stars are driven by jets or winds and are frequently the most dramatic and distinct manifestation of a newborn star. Down the axis of jets, shocks are often observed as bow shaped structures in which the H_2 line strength and morphology are characteristic of the physical and chemical environment and the velocity of the impact. Thus, the study of bow shocks reveals valuable information concerning the ambient medium as well as the launching mechanism of the jets and winds from protostars. The morphology of a bow shock projected into the plane of the sky naturally depends on the viewing angle, but also the orientation of the magnetic field. Also the line brightness and line ratios can change quite drastically with viewing angle. Thus, in order to model the shocks in detail and extract the underlying physical conditions convincingly, we need a full 3D model that incorporates the effects of the geometry of the system.

We present a 3D model of bow shocks propagating in a homogeneous medium with a uniform magnetic field inclined at an arbitrary angle to the propagation axis of the shock [1]. We focus on the molecular hydrogen emission lines in the near-infrared, but the morphology of atomic species can also be predicted by the model. The 3D model is constructed by associating a planar shock with every point on a 3D bow skeleton. The shock conditions vary along the bow surface and we let the widths of the planar shocks determine the thickness of the bow shell. The planar shocks are modeled with a highly sophisticated chemical reaction network which is essential for predicting accurate line emission. The bow shock can move at an arbitrary inclination and we model the projected morphology and line emission brightness in the plane of the sky.

Bow shocks appear in many different guises

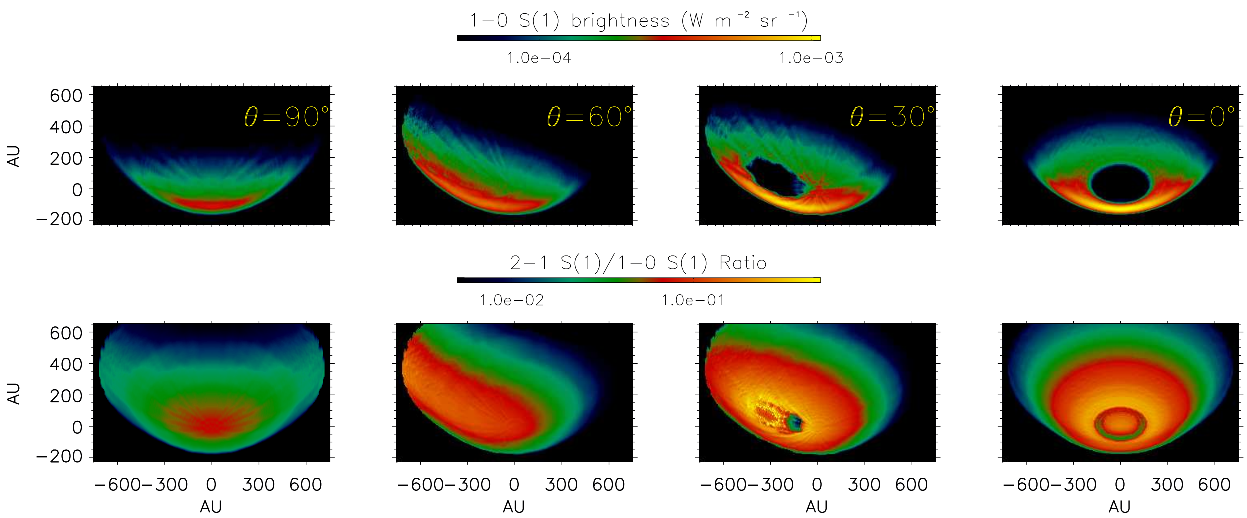

Figure 1: *Brightness of the H_2 v=1-0 S(1) emission line (upper row) and the v=2-1 S(1)/v=2-1 S(1) line ratio (lower row) of a series of shocks with different orientation of the magnetic field. θ is the angle of the magnetic field direction to the axis of shock propagation. The shocks are moving at an inclination to the line of sight of 50°.*

The morphology of the emission from a bow shock is highly dependent on the orientation of the magnetic field (Fig. 1) and the inclination of the flow. The planar shocks are strongest on the part of the bow surface that faces towards the magnetic field. The result is that the morphology can be highly asymmetric. Together with inclination effects this means that bow shocks can appear in many different guises and they do not necessarily - or even generally - show a characteristic bow shape. Thus broadly speaking we can state that the somewhat confused appearance of shocked zones in star forming regions may be due to shocks moving at a variety of angles to the observer and to the direction of the magnetic field.

The ratio of the H_2 v=2-1 S(1) line to the v=1-0 S(1) line is variable across the flow (Fig. 1) and the spatial offset between the peaks of the lines may be used to estimate the inclination of the flow. The radial velocity peaks behind the apparent apex of the bow shock when the flow is seen at an inclination different from face-on or edge-on. Under certain circumstances the radial velocity of an expanding bow shock can show the same signatures as a rotating flow. In this case a velocity gradient perpendicular to the outflow direction is a projection effect of an expanding bow shock lighting up asymmetrically due to the orientation of the magnetic field.

Reproducing observations

With the 3D model we reproduce the brightness levels in three observed H_2 lines as well as the shape and size of a chosen bow shock in OMC1 (Fig. 2). Previous modeling involving 1D and 2D models has not been able to reproduce both the brightness and the shock width - and naturally not the appearance of the shock to the observer. The 3D model thus enables us to determine the pre- and post-shock conditions with a degree of certainty that was not previously possible. Furthermore, it allows us to estimate the viewing angle and the direction of the magnetic field with respect to the shock propagation in addition to density, shock velocity, and magnetic flux density.

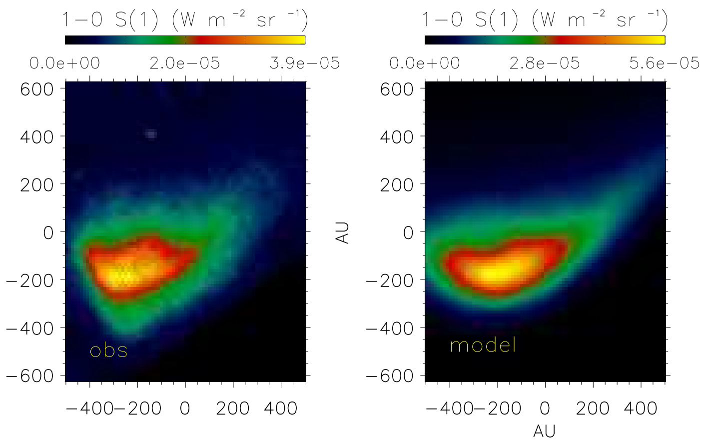

Figure 2: *H_2 v=1-0 S(1) line emission map of a bow shock in OMC1 observed at ESO-VLT (left) compared to the best fit 3D model (right).*

Collaborators are Lars Kristensen (Leiden Obs, The Netherlands), Thomas Ravkilde, David Field (Aarhus U., Denmark), Sylvie Cabrit (Obs Paris, France), Guillaume Pineau des Forêts (IAS, France)

References

[1] Gustafsson, M. *et al.*, 2010, A&A, *in Press*

Fragmentation in high-mass star formation: A core mass function resembling the IMF

Javier A. Rodón, Henrik Beuther

Introduction

The Core Mass Functions (CMFs) of low-mass star-forming regions are found to resemble the shape of the Initial Mass Function (IMF). A similar result is observed for the dust clumps in high-mass star-forming regions, although at spatial scales that do not resolve the substructure of these massive clumps, but that rather trace cluster-forming scales. The massive star-forming region IRAS 19410+2336 is one exception, having been observed at spatial scales on the order of ~ 2500 AU, sufficient to resolve the clump substructure and derive its CMF, which resembles the Salpeter IMF (Beuther & Schilke 2004). To derive the CMF, they assumed a constant average temperature for all the cores detected. To test and improve these results, we investigate the protostellar content of IRAS 19410+2336 at high spatial resolution at 1.4 mm and 3 mm in spectral line and dust continuum emission, this time determining the temperature structure of the region and deriving a more detailed CMF [1].

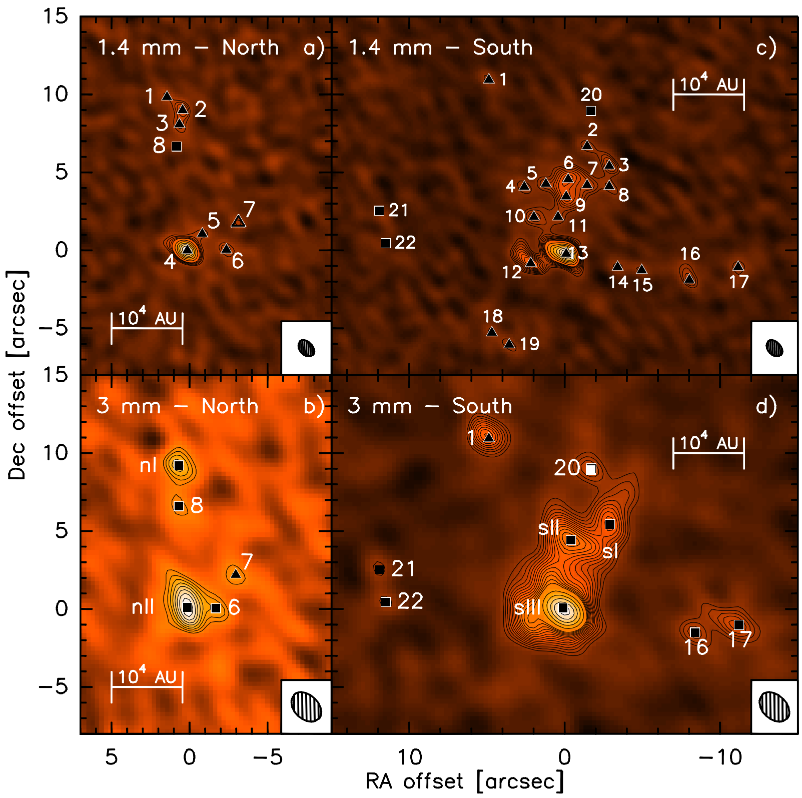

Figure 1: *Continuum maps of IRAS 19410+2336 obtained with the PdBI. In the top row are the 1.4 mm maps of the Northern (panel a) and Southern (panel c) (proto)clusters. Similarly, in the bottom row are the 3 mm maps of the Northern and Southern (proto)clusters in panels b) and d) respectively. The contouring starts at the 4σ level in all the panels, increasing in 1σ steps first and in 4σ steps afterwards. The triangles mark the position of the sources detected at 1.4 mm while the squares are the sources detected at 3 mm . A square appearing in a 1.4 mm map indicates a source that is only detected at 3 mm . Similarly, a triangle in a 3 mm map signals a source detected at the same position in a 1.4 mm map.*

The CMF of IRAS 19410+2336

IRAS 19410+2336 was mapped with the Plateau de Bure Interferometer (PdBI) at 1.4 mm and 3 mm in the BCD configurations, tuning the receivers to observe the continuum and several molecular transitions of formaldehyde (H_2CO) and methyl cyanide (CH_3CN). The formaldehyde transitions were also observed with the IRAM 30 m Telescope.

We detected 26 continuum sources at 1.4 mm with a spatial resolution down to $\sim$ 2200 AU, several of them with counterparts at NIR and MIR wavelengths, distributed in two (proto)clusters (see Fig. 1). With the PdBI CH_3CN and PdBI/IRAM 30 m H_2CO emission we derived the kinetic temperature of the observed cores, ranging from 35 to 90 K. Using these temperatures we calculated the circumstellar masses of the detected sources, ranging from ~ 0.7 to $\sim 8\,M_\odot$. These masses were strongly affected by the spatial filtering of the interferometer, filtering out a common envelope with $\sim 90\%$ of the single-dish flux. Accounting for binning effects as well as cumulative distributions, we derived a power-law CMF, with a power-law index $\beta = -2.3 \pm 0.2$ (see Fig. 2). We resolve the Jeans length of the (proto)clusters by one order of magnitude, and also find minimal evidence of velocity dispersion in the (proto)clusters.

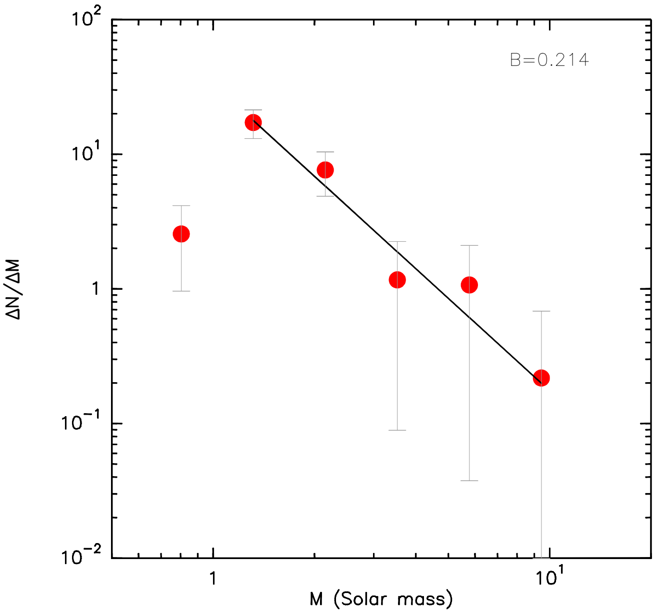

Figure 2: *CMF of IRAS 19410+2336 for core masses above* $1\,M_\odot$. *The solid red line represent the best power-law fit with a power-law index* $\beta = -2.3 \pm 0.2$. *This CMF corresponds to a mass binning* $\Delta M = \log M_k - \log M_{k-1} = B = 0.214$ *(see [1]).*

We find that the slope of the CMF of IRAS 19410+2336 is in agreement with the Salpeter IMF, and we discuss different scenarios for the formation of the Initial Mass Function. From the virial and Jeans analysis of the cores they are likely collapsing, and the (proto)clusters appear to be in a stage of weak dynamical evolution.

Collaborator is Peter Schilke (University of Cologne, Germany).

References

[1] Rodón, J. A., Beuther, H. & Schilke, P. 2010, A&A, *submitted*

Sequential star formation in RCW 34: A spectroscopic census of the stellar content of high-mass star-forming regions

Arjan Bik, Thomas Henning, Tatiana Vasyunina, Henrik Beuther, Hendrik Linz

The formation and early evolution of high-mass stars occurs in deeply embedded clustered environments, where the forming stars and molecular clouds are mutually interacting. Therefore, to study the early evolution of the massive stars, a full census of the stellar content as well as a characterization of its environment are required to disentangle the different processes. We are carrying out a program aiming at a spectroscopic classification of all the high- and intermediate mass cluster members of a well selected sample of 10 clusters. Using the technique of integral field spectroscopy, we obtain an unbiased census of the stellar content. Supporting longer wavelength observations (Spitzer/IRAC) are added to study the environment and detect the more deeply embedded objects. The 10 regions were selected to cover a range in luminosity as well as evolutionary stage.

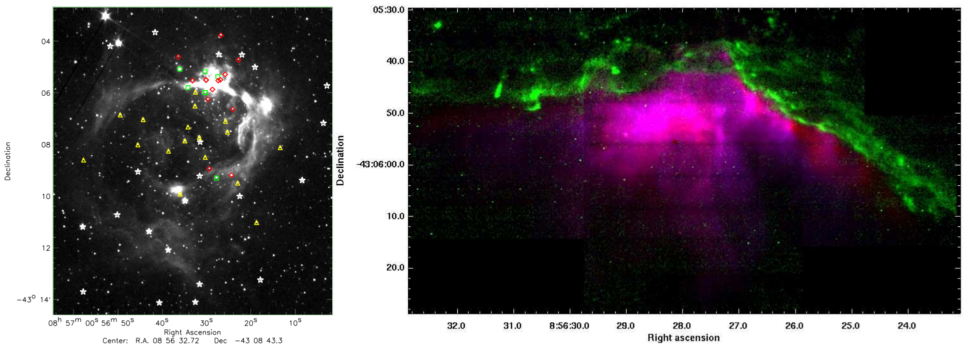

Figure 1: *left: Spitzer/IRAC 3.6 μm image of RCW 34 and its surroundings. Overplotted are the class II sources (yellow triangle), class I/II sources (green squares), class 0/I sources (red diamonds). A cluster of class II sources inside the bubble becomes apparent. right: 3 color line map extracted from the SINFONI data high lighting the location of the HII region and the ionization front and the interation with the molecular cloud (blue: HeI, green: H_2, red: Brγ)*

A near-infrared spectroscopic census of RCW 34

We obtained VLT/SINFONI integral field spectroscopy of the high-mass star-forming region RCW 34, along with *Spitzer*/IRAC photometry of the cluster surroundings. RCW 34 consists of three different regions. A large bubble has been detected on the IRAC images in which a cluster of intermediate- and low-mass class II objects is found (Fig. 1, left). Surprisingly, no massive stars are detected in the bubble. At the northern edge of the bubble an HII region is identified in the SINFONI data (Fig. 1, right). The SINFONI spectra are classified to reveal the stellar content of the HII region. Apart from the O8.5V ionizing source, 2 other B stars are identified, allowing the determination of a accurate spectro-photometry distance of 2.5 ± 0.2 kpc for RCW 34. The remaining stars are identified as G- and K type stars. These stars are in the pre-main-sequence (PMS) phase, still contracting towards the main sequence. By comparing the position of the PMS stars in a Herzsprung-Russell Diagram (HRD) with evolutionary models for PMS stars, we derive an age of 2 ± 1 Myr for the stars in the HII region (Fig. 2). Also visible in the SINFONI data is the interacting region (H_2 emission) between the HII region and a dense molecular cloud north of the HII region. Inside this molecular cloud several class 0/I stars as well as outflows are found, suggesting the presence of recent star formation.

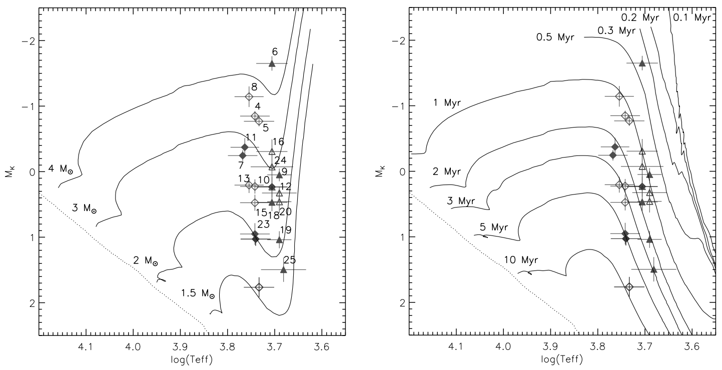

Figure 2: *The extinction corrected K vs log(T_{eff}) HRD. The K-band magnitude has been corrected for the distance modulus. The plotted symbols reflect the different spectral types, diamonds: G stars, triangles: K stars. The filled symbols represent objects with infrared excess. Over-plotted with a dotted line is the 2 Myr main-sequence isochrone, with as solid lines PMS evolutionary tracks.* Right*: HRD with overplotted as solid lines the PMS isochrones between 0.1 and 10 Myr.*

Triggered star formation?

The observed geometry suggests that triggered star formation could play a role here. The presence of the class 0/I sources in the molecular cloud suggests that the objects inside the molecular cloud are significantly younger than the objects in the HII region. Between the class II sources in the bubble and the PMS stars in the HII region no age difference could be detected with the present data. The most likely scenario for the formation of the three regions is that star formation propagated from south to north. First the bubble is formed producing only intermediate- and low-mass stars, after that, the HII region is formed from a dense core at the edge of the molecular cloud, resulting in the expansion as a champagne flow. More recently, star formation occurred in the rest of the molecular cloud. Two different formation scenarios are possible. (a) The bubble with the cluster of low- and intermediate mass stars triggered the formation of the O star at the edge of the molecular cloud which in its turn induces the current star-formation in the molecular cloud. (b) An external triggering is responsible for the star-formation propagating from south to north.

Collaborators are Elena Puga (CSIC, Spain), Rens Waters, Lex Kaper, Alex de Koter (Univ. Amsterdam, The Netherlands), Matthew Horrobin, Andrea Stolte (Cologne, Germany), Mario van den Ancker, Fernando Comerón (ESO, Germany), Ed Churchwell (Madison, USA), Stan Kurtz (UNAM, Mexico), Thijs Kouwenhoven (KIAA, China), Wing-Fai Thi (ROE, United, Kingdom), Christoffel Waelkens (Univ. Leuven, Belgium).

References

[1] Bik, A, Puga, E, Waters, L B F M, Horrobin, M, Henning, Th, Vasyunina, T, Beuther, H, Linz, H., Kaper, L, van den Ancker, M E, Lenorzer, A, Churchwell, E B, Kurtz, S, Kouwenhoven, M B N, Stolte, A, De Koter, A, Thi, W.-F, Comeron, F, Waelkens, Ch, 2010, accepted by ApJ.

A Trapezium in the making: Millimeter interferometry of W3 IRS5

Javier A. Rodón, Henrik Beuther

Introduction

Although most young massive stars appear to be part of multiple systems, it is poorly understood how this multiplicity influences the formation of massive stars. The high-mass star-forming region W3 IRS5 is a prime example of a young massive cluster where the cluster center is resolved into multiple subsources at cm and infrared wavelengths, a potential proto-Trapezium system. We investigate with the Plateau de Bure Interferometer the protostellar content of W3 IRS5 in the 1.4 mm and 3.4 mm continuum, down to subarcsecond scales and study the compact outflow components, also tracing the outflows back to their driving sources via the shocktracing SiO emission [1].

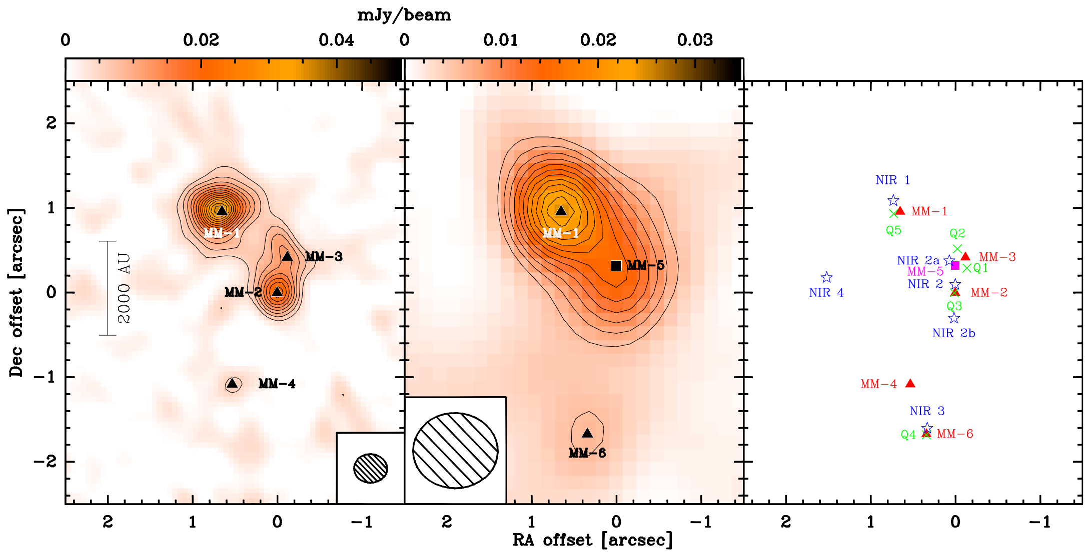

Figure 1: *Continuum maps of W3 IRS5 at 1.4 mm (left) and 3.4 mm (middle). Beams are shown at the bottom left of each panel. Filled triangles mark the mm sources detected. Right panel: Relative positions of the different sources in W3 IRS5. Filled triangles are as before, stars are the known NIR sources and crosses are the known radio sources. The square marks source MM5, the joint contribution of sources MM2 and MM3.*

The W3 IRS5 Proto-trapezium

In the continuum maps of W3 IRS5 we detect 5 individual sources. Their calculated absolute masses range between ~ 0.3 to $\sim 40\,M_{\odot}$, although they are strongly affected by the spatial filtering inherent to the interferometric technique. Nevertheless, from the relative separations of the three strongest sources we propose the scenario of a Trapezium-like system, with at least 3 objects enclosed within a $\sim$2000 AU radius, with a high (proto)stellar density of $\sim 5 \times 10^{6}$ protostars pc^{-3}, and sharing a common envelope from which they may still be accreting gas. Four of the five mm sources are identified as counterparts of sources previously detected at NIR, MIR and radio wavelengths. The remaining fifth source (labeled MM4) is a new detection (see Fig. 1).

Thanks to the obtained high spatial resolution of $\sim 0.36''$ we can for the first time trace the small-scale flows, detecting five molecular outflows and identifying the driving source of three of them (see Fig. 2). Although we find on short spatial scales the same alignment and axes as the outflows on large spatial scales previously detected in SiO and CO, within our accuracy we do not find strong evidence to support that we are tracing the inner and denser regions of those outflows, but we cannot rule out that possibility. Rather in contrast to this, these small-scale outflows appear to be different features.

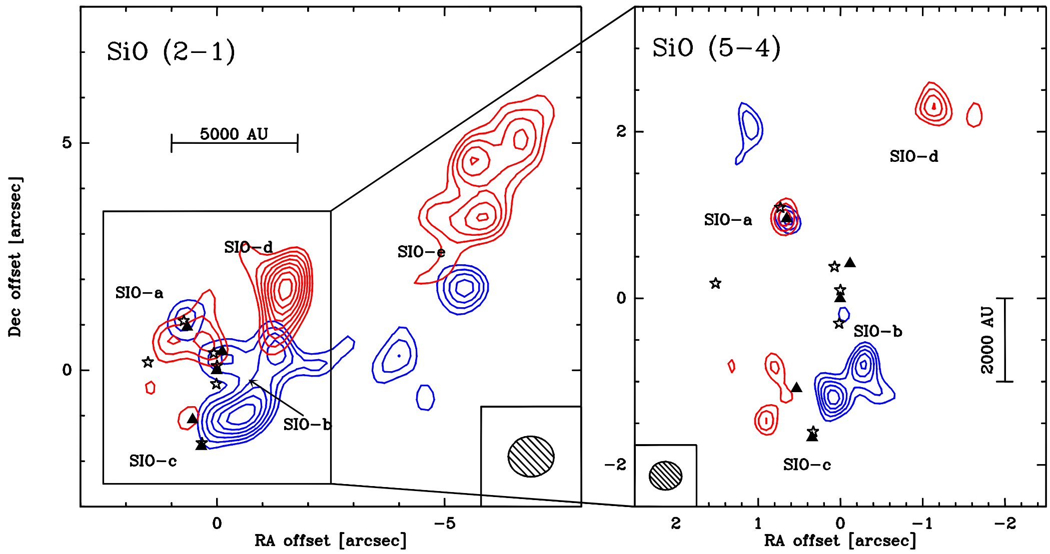

Figure 2: *Left: 3.4 mm SiO (2–1) transition. Blue contours outline the blueshifted emission and red contours the redshifted emission. Right: The corresponding 1.4 mm SiO (5–4) transition. The beams are represented at the bottom right corner of each panel. Labeled SIO-a through -e are the five outflows detected, triangles are the detected mm sources and the stars mark the known NIR sources.*

Two of the SiO outflows are close to the line-of-sight (l.o.s.) direction and each one is driven by one of the stronger mm sources detected. This configuration explains why these two objects are detected from NIR to radio wavelengths because cavities being carved out by outflows nearly along the l.o.s. have lower extinction, allowing the detection in the NIR and MIR of the hot dust near the collapsing protostar, while the long wavelength emission traces the dusty envelope that still surrounds it.

Collaborators are Tom Megeath (University of Toledo, USA) and Floris F. S. van der Tak (SRON, The Netherlands).

References

[1] Rodón, J. A., Beuther, H., Megeath, S. T., & van der Tak, F. F. S. 2008, A&A, 490, 213

Rotational structure and outflow in the infrared dark cloud 18223-3

Cassandra Fallscheer, Henrik Beuther

Massive star formation in its infant stage

Massive stars ($M > 8M_{\odot}$) are paramount constituents of galaxies, yet their formation is significantly less well understood than low-mass star formation. Theories of massive star formation predict massive accretion disks and indirect evidence for disks is prevalent, but observational evidence for such structures is rare. Outflows appear to be widespread in massive star formation regions and must be powered and fed by a (massive) accretion disk. Evidence of rotation and infall that hint at the presence of disks has been detected in several systems, although further study is required.

A large rotating structure perpendicular to the outflow

In this case study, we have observed the infrared dark cloud (IRDC) 18223-3 with the Submillimeter Array (SMA), IRAM 30 m and the Plateau de Bure Interferometer (PdBI) [1]. The combined SMA and 30 m data reveal a well defined northwest-southeast outflow orientation (See Fig. 1). To the southeast of the 1.3 mm continuum peak, we see a cone-like blueshifted component, and the northwest is dominated by a broader blueshifted component. While it is less clear what is happening in the redshifted regime, the blueshifted components indicate that we are likely looking at a system that is roughly in the plane of the sky. From this we deduce that the likely disk orientation would be approximately edge on and that the associated velocity gradient would be in the northeast-southwest direction.

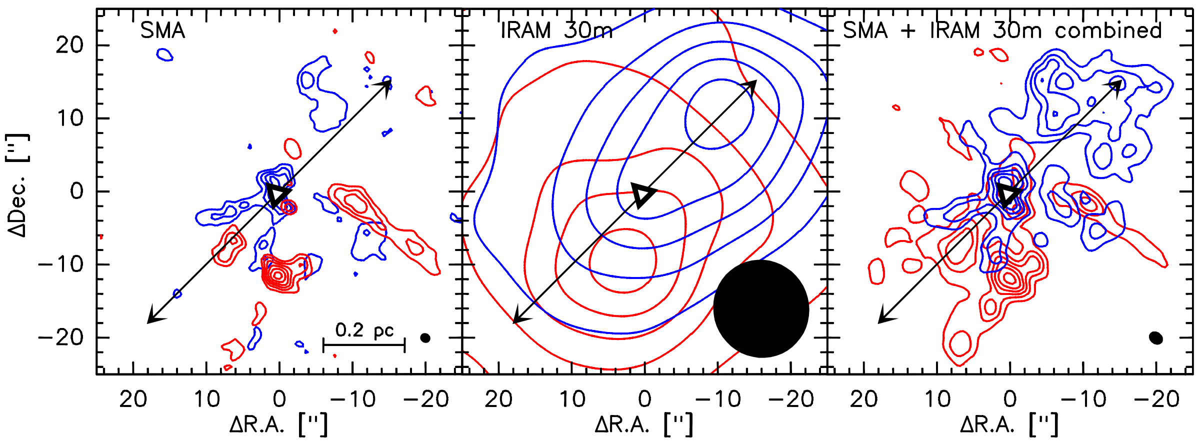

Figure 1: *$^{12}CO(2\text{–}1)$ blue- and redshifted maps of IRDC 18223-3 from SMA, IRAM 30 m, and SMA + IRAM 30 m combined in the left, center, and right panels respectively. In each panel, the 1.3 mm continuum peak is indicated by the triangle, and the beam is included in the lower right corner.*

We detect velocity gradients perpendicular to the outflow in CH_3OH and N_2H^+, although they are observed over a very large spatial distance and a relatively small velocity range. The velocity gradient seen in CH_3OH is shown in the right panel of Fig. 2. On the order of 20,000 AU in size, the large rotating core we currently detect is much larger than other disk or disk-like structures around similar low-luminosity intermediate- to high-mass star forming regions published in the literature. We thus suspect that CH_3OH and N_2H^+ are actually tracing the

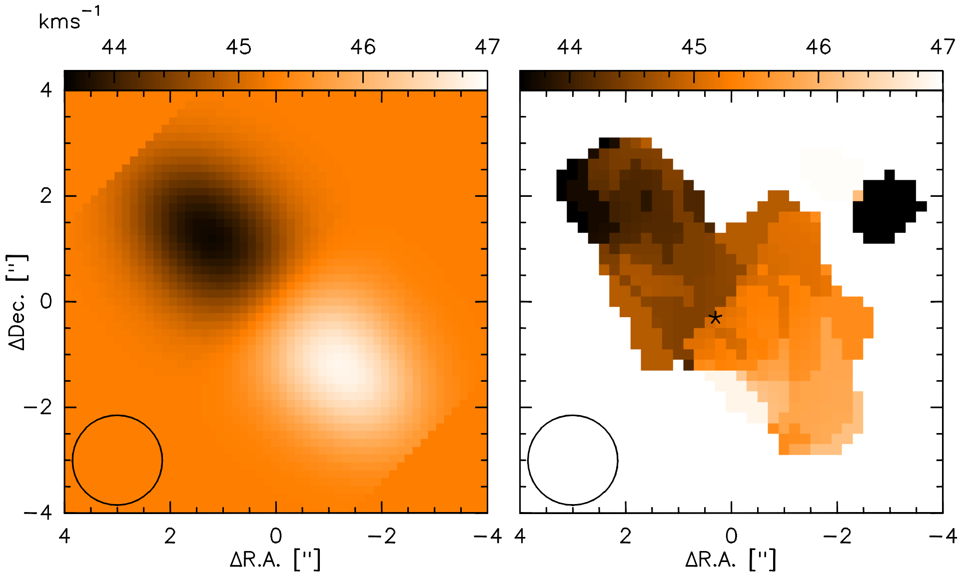

Figure 2: *Left: the model after convolving to the 1.7" resolution of the data Right: the CH_3OH velocity moment map (velocity weighted by intensity). The SMA beam size is shown in the lower left corner.*

outer parts of an infalling toroid. This rotating toroid likely plays an important role in feeding an accretion disk within the unresolved central region and may decrease in size over time as the outer edges dissipate or contract leading to growth of the disk. Hence we see here potentially the earliest stages of the disk formation process. As there is not much known about CH_3OH as a tracer of massive disks, one possibility is that it may be a good tracer for disk kinematics only at very early evolutionary stages, but that other hot core molecules such as CH_3CN, for example, may be better for more evolved massive star formation regions.

Using the Ulrich Model for mass infall which conserves angular momentum, we have successfully reproduced the velocity gradient observed in CH_3OH. The modeled density distribution combined with the velocity field is shown in the left panel of Fig. 2. This agreement between model and observations enhances the argument that the rotation we see results from a single flattened rotating entity rather than multiple sources or other scenarios.

The results we have presented further support the idea that IRDCs are sources undergoing the early stages of high-mass star formation. IRDC 18223-3 likely represents one of the earliest stages of disk formation. We suspect that the large rotating and flattened envelope structure is one of the earliest detectable stages in the evolutionary sequence of accretion disks. In this framework, the structure we see and have described here feeds an inner accretion disk and will continue contracting into a true accretion disk as time passes.

Collaborators are Qizhou Zhang, Eric Keto, and T.K. Sridharan, all at the Harvard-Smithsonian Center for Astrophysics.

References

[1] Fallscheer, C., Beuther, H., Zhang, Q., Keto, E., & Sridharan, T.K. 2009, A&A, 504, 127

The Rosette Eye: A key transition phase in the birth of a massive star

Roland Gredel

The Rosette Molecular complex (RMC)

The Rosette Molecular Complex (RMC) is one of the most massive giant molecular cloud complexes in the Galaxy. It is located at a distance of 1.39 kpc and harbors a gas reservoir of 10^5 M⊙. Its central cluster NGC 2244 contains several O-type stars with a total luminosity of 1000 L⊙. The stars drive an expanding HII shell into the interstellar medium may be responsible for triggered star formation, as several embedded stellar clusters are located along its ionization front. One of these clusters, located to the South-East of NGC2244, contains the brightest infrared source in the RMC, AFGL 961. This well-studied high-mass protostellar binary system drives a powerful molecular outflow into the gas. The present study focuses on AFGL 961II which is located some 30’’ to the West of AFGL 961. Both objects are located along a broad ridge of molecular emission.

The `Rosette Eye’

We have performed deep optical and near-infrared imaging and spectroscopy of the region around AFGL 691II using the NTT, UKIRT, and the 4m KPNO telescope. The mass of AFGL 691II has been estimated to 20 M⊙ (Li & Smith 2005, AJ 130, 721), which is somewhat larger than the recently constrained value of 6 M⊙ obtained from its spectral energy distribution (Williams et al. 2009, ApJ 699, 1300).

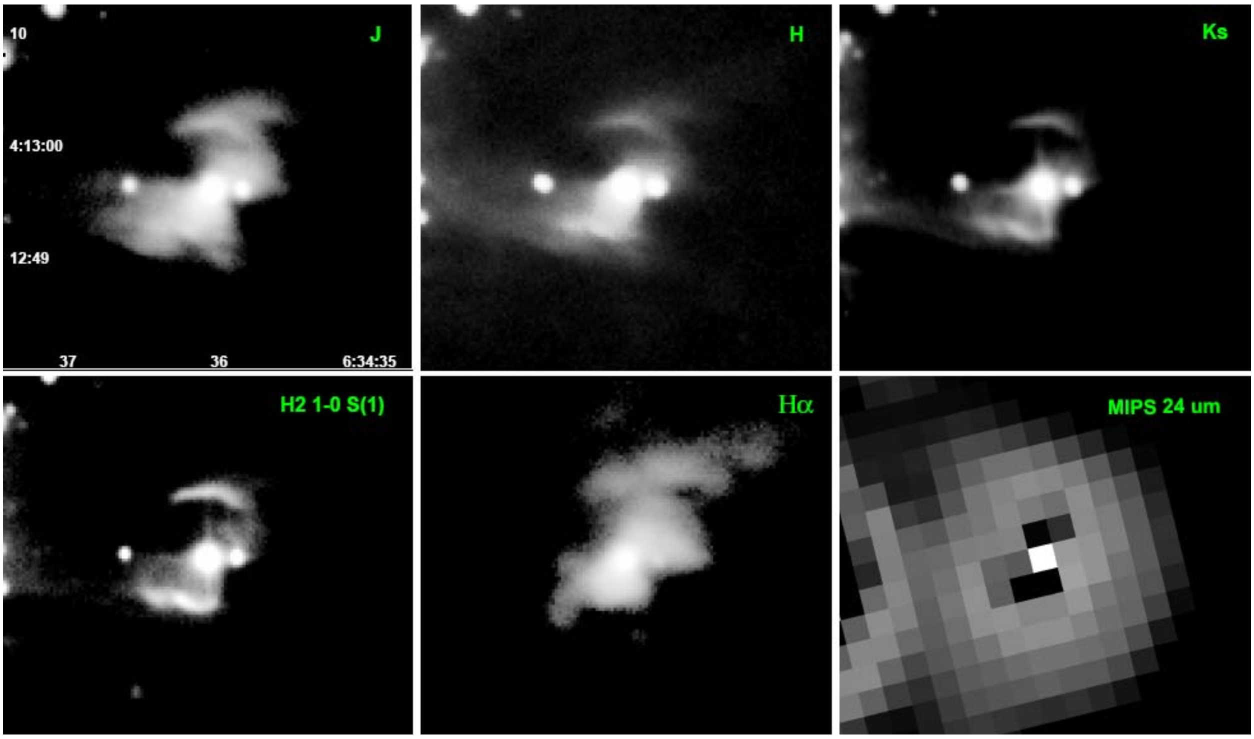

Figure 1: Greyscale images of the Rosette Eye in J, H, Ks (upper panels) and H_2, Hα, and MIPS 24μm. AFGL 691II is the bright point source in the center of each image.

The compact, hour-glass shaped diffuse HII region seen in the Hα image has an extent of less than 0.1 pc in size, which is a typical size of massive star-forming clumps. AFGL 691II shows very strong Hα emission with an equivalent width of 170 A and a FWHM of some 500 km s^{-1}. A bipolar nebula emerges from our near-infrared data, most prominently seen in the J-band image (cf. Fig. 1). In the H_2 image, prominent arcs appear in the North and South. The H_2 emission spectrum of the Northern arc is shown in Figure 2. The spectrum contains emission from v' = 9, and is explained in terms of fluorescently excited H_2 in a strong UV radiation field, consistent with the conclusions drawn from the optical Hα data. The 24 mm Spitzer/MIPS data show that AFGL 961II is clearing out its surrounding material. The MIPS 24 μm image indicates a dumbbell shaped nebula that encompassed the bipolar cavity detected in the NIR. The cavity is devoid of dust emission, probably due to the dissociation of dust in the ionized flows. We have also obtained a high resolution long-slit spectrum of the H_2 (1,0) S(1) line across AFGL 961II using CGS4 ([2]). The radial velocity of the H_2 emission across the region is constant and does not show the velocity gradient expected from shocked gas,

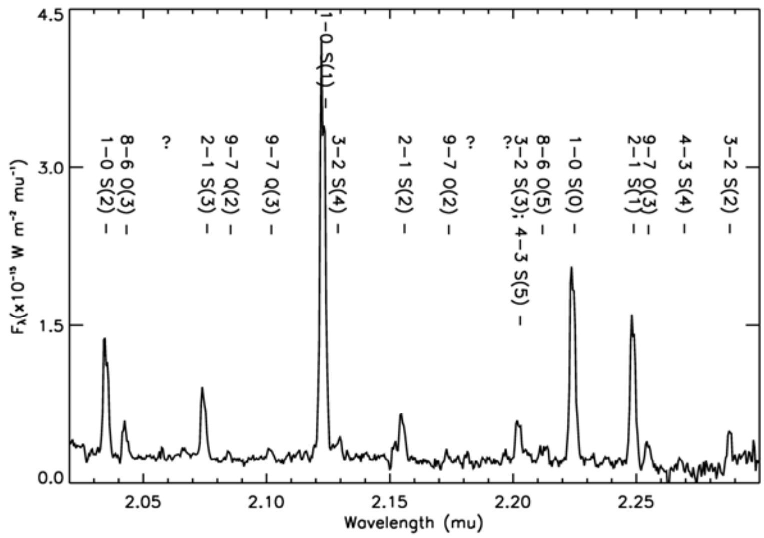

Figure 2: K-band spectrum of the northern arc. The ro-vibrational emission from v'=8 and 9 is caused by fluorescent excitation of H_2 in the UV radiation field from the protostar.

We propose that the `Rosette Eye' represents the spectacular case of a massive star in its very early stage of formation. The central YSO has finished its original collapse and the new born star has turned on an intense UV radiation field and ionizing wind. AFGL961II is not detected at 1.4mm (Williams et al. 2009), which places it into a more advanced evolutionary state than AFGL 961, lacking a cold dusty envelope. Our findings provide evidence that the formation of a 6 - 20 $M_\odot$ star proceeds through disk accretion. Evidence exists that the outflows observed from high-mass protostars are scaled-up versions of their low-mass counterparts (eg. [2]). The observations support a scenario where high-mass star formation proceeds via the same physical processes that govern low-mass star formation, yet at significantly increased accretion rates.

Collaborators are Jin Zeng Li, Michael D. Smith, Christopher J. Davis, and Travis A. Rector

References

[1] Li, J.Z., Smith, M.D., Gredel, R., Davis, C.J., Rector, T.A., 2008, ApJL 679, L101
[2] Gredel, R., 2006, A&A 457, 157

A massive YSO scrutinised by MIR interferometry. Diagnosis: Adiposity!

Hendrik Linz, Thomas Henning, Markus Feldt, Roy van Boekel

The inner structure of massive young stellar objects

High-mass stars predominantly form in clustered environments much farther away from the Sun, on average, than typical well-investigated low-mass star-forming regions. Thus, high spatial resolution is a prerequisite for making progress in the observational study of high-mass star formation. Furthermore, all phases prior to the main sequence are obscured by dense circumstellar environments. This forces observers of deeply embedded massive young stellar objects (MYSOs) to move to the mid-infrared (MIR) where the resolution of conventional imaging is limited to $> 0\overset{''}{.}25$ even with 8-m class telescopes. Hence, one traces linear scales still several hundred AU in size even for the nearest MYSOs, and conclusions on the geometry of the innermost circumstellar material remain ambiguous. Still, we need this information about the structure within the inner 100 AU in order to decide whether high-mass stars form similar to low-mass stars, and how in detail they attain their mass.

A way to overcome the diffraction limit of single telescopes is to employ interferometric techniques. We have set up a program to utilise the mid-infrared interferometer MIDI at the VLTI to access the structure of the warm circumstellar dust around massive YSOs down to scales of 20 milli-arcseconds. Thirteen massive YSOs have been observed to date with this instrument that had been built eight years ago under the leadership of the MPIA.

Mid-infrared interferometry of the enigmatic object M8E-IR

The object M8E-IR, a prominent high-mass YSO well investigated at lower angular resolution since the 1980's, was one of the prime targets we have collected data for. However, since MIDI as a two-element interferometer does not allow to deduce images directly, but only visibilities (spectrally dispersed fringe contrast measurements), subsequent modelling is necessary for interpretation. We first use the SED fitting tool of Robitaille et al. (2007, ApJS 169, 328) to identify parameter setups from a large grid of models where the resulting continuum emission well fits the known SED of the observed YSO. Then, the underlying Monte Carlo radiative transfer code of Whitney et al. (2003, ApJ 591, 1049) is used to produce high-resolution mid-infrared maps for those model setups. Comparing the resulting synthetic visibilities with the observed ones indicates which models can simultaneously account for the observed SED and visibilities. Our investigation [1] finally led to some interesting conclusions (Fig. 1).

According to our best SED fit, the source comprises a very compact circumstellar disk (< 50 AU), a larger envelope with small bipolar cavities, and a cool central object ($T_{\rm eff} < 5{,}000$ K). We mention explicitly, that among the well-fitting models there are also configurations without a disk (axisymmetric flattened envelope plus outflow cavities only), but also including a cool bloated central star. The standard description for such an object – hot star ($T_{\rm eff} > 20{,}000$ K) + envelope – can fit the SED as well (cf. Fig. 1 left), but fails to reproduce the measured visibilities (Fig. 1 right). This suggests that in the case of M8E-IR, the choice of the central object actually governs the resulting visibility levels.

A bloated central star – signature of the accretion history

The best-fitting models for M8E-IR in the Robitaille model grid feature central stars of 10–15 $M_\odot$ which are strongly bloated (120–150 $R_\odot$) and, therefore, have relatively low effective temperatures. It was already known that accretion with high rates onto main sequence stars can

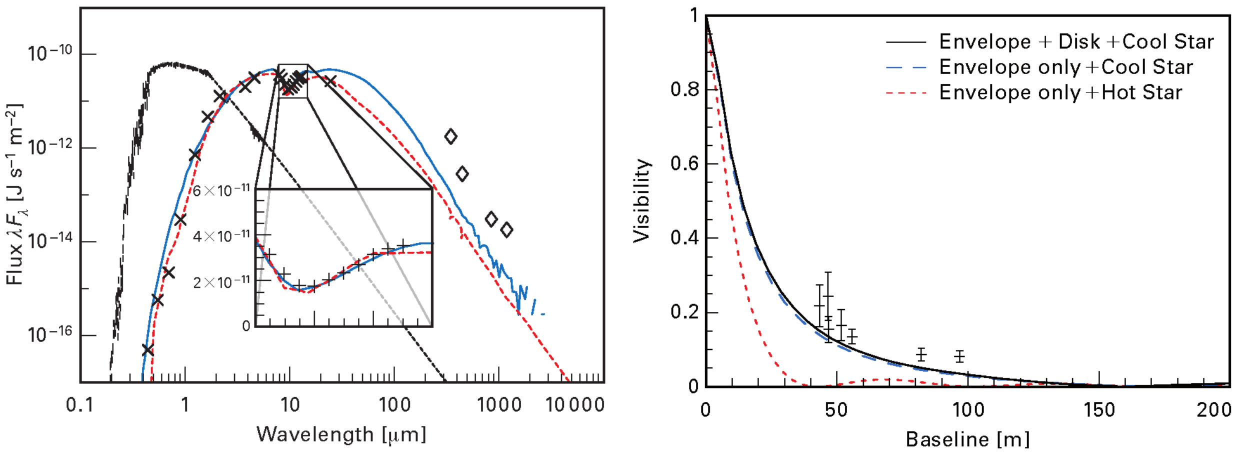

Figure 1: *Left: SED fits for M8E-IR. The blue continuous line is the model with cool bloated central star (unreddened stellar SED as black curve), while the model with hot central star is given as red dotted line. Both fit the SED very well. Right: Comparison between models and observed visibilities (plus signs with error bars). The canonical hot-star model (red dotted line) fails to come close to the measurements, while the cool-star models show a reasonable agreement.*

temporarily puff up such stars. Recent simulations confirm this assessment (Hosokawa & Omukai 2009, ApJ 691, 823; Yorke & Bodenheimer 2008, ASP Conf. Ser. 387, 189). These groups find that for accretion rates of the order 10^{-3} $M_\odot$/yr, the protostellar radius can temporarily increase to over 100 $R_\odot$, in accordance with our findings. Interestingly, there have been reports in the literature which revealed high-velocity molecular outflows from M8E-IR based on M-band CO absorption spectra. One therefore can speculate on recent (∼120 yr) FU Ori-type outbursts for this object. If these multiple outflow components trace recent strong accretion events, the central star certainly can have been affected.

Conclusions – Visibilities break the SED-fitting ambiguity

We have observed the massive young stellar object M8E-IR with the MIDI interferometer at the VLTI. We find substructures with mid-infrared sizes of around 30 mas. The measured elevated visibilities indicate that the usual approach for such objects (spherically symmetric envelope with hot central star) fails in the case of M8E-IR. Most interestingly, our data are consistent with M8E-IR harbouring a 10–15 $M_\odot$ central star that has been bloated ($R > 100\,R_\odot$) by recent strong accretion events. While we can exclude the existence of a large circumstellar disk, the presence of a compact disk (< 50 AU) is likely, but needs further confirmation. Our results show that IR interferometry, combined with radiative transfer modelling, can be a viable tool to reveal crucial structure information on embedded massive young stellar objects and to resolve ambiguities arising from fitting the SED.

Collaborators on this project have been Ilaria Pascucci (Johns Hopkins University), Alexander Men'shchikov (CEA Saclay), Thorsten Ratzka (LMU München), Sascha Quanz (ETH Zürich), Rens Waters (Universiteit van Amsterdam), and Hans Zinnecker (Astrophysikalisches Institut Potsdam).

References

[1] Linz, H., Henning, Th., Feldt, M., et al., 2009, A&A, 505, 655

High-mass accretion disks: theory and observations

Henrik Beuther, Hubert Klahr & Rolf Kuiper

Introduction

High-mass stars play a crucial role in determing the energy budget and molecular/atomic content of the interstellar medium (ISM). Throughout their whole life-time they inject energy into their environment starting with molecular outflows during their formation, continuing with copious UV photons during their entire main sequence, and finishing with the final supernovae events. Furthermore, they are the cradle of all heavy elements, and their formation is the only star formation mode observable in distant galaxies.

Although different high-mass star formation scenarios are discussed in the literature, there is a growing concensus that massive stars form via disk-mediated accretion qualitatively similar to their lower-mass siblings. However, the details are still poorly constrained. At MPIA, we are following diverse approaches to study the formation and evolution of high-mass accretion disks from an observational as well as theoretical perspective.

Observations

To investigate the evolutionary changes of rotating structures and accretion disks in high-mass star formation, we selected several target regions as representative examples of their evolutionary class: infrared dark clouds (IRDC) for the earliest evolutionary stages [2], high-mass protostellar objects (HMPO) for the main evolutionary phase, and hot cores for chemically more evolved regions [1]. Here we just outline the results for the hot core sample.

For a general understanding of rotational and disk properties a solid statistical base is required. Therefore, we conducted a large program at the Australia Telescope Compact Array to investigate a sample of 12 high-mass disk candidates in highly excited ammonia lines (NH_3(4,4) and (5,5)), to filter out the cold envelope and to mainly trace the inner rotating structures.

Except for one, all other sources were detected in both NH_3 transitions (Figure 1 left). From the eleven mapped sources, six show clear signatures of rotation and/or infall motions. These signatures vary from typical velocity gradients perpendicular to the outflows, to infall signatures in absorption against ultracompact HII regions, to more spherical infall signatures in emission. Although our spatial resolution is 1000AU, we do not find clear Keplerian signatures in any of the sources. Furthermore, we also do not find flattened structures. This implies that typical Keplerian accretion disks - if they exist as expected - should be confined to regions usually smaller than 1000AU. It is likely that these disks are fed by the larger-scale rotating envelope structure we observe here.

Theory

We are conducting analytic massive disk studies [4] as well as 3D simulations of the formation of massive stars and the related phenomena like the formation of disks and outflows [3]. For the code development we have chosen the modern Magneto-Hydro (MHD) code PLUTO that was originally developed in the jet community. It contains a variety of hydro and MHD solvers, all of a Godunov/Riemann solver type and it includes the possibility for using a spherical grid which we think is most suited for simulations that involve rotating material, e.g. collapsing clouds and forming disks. Rolf Kuiper introduced radiation transport and self-gravity into the PLUTO code as part of his PhD thesis. Especially the radiation transport has to be accurate and fast. For that purpose a hybrid radiation scheme was implemented into PLUTO. In this scheme first the radiation from the central region of the grid, e.g. the newly formed star is treated via frequency dependent ray tracing to get the proper radiation pressure and gas temperature especially around the dust destruction zone. The absorbed and reemitted radiation is then treated via flux-limited diffusion in the optical thick parts in the forming disk around the star.

Since 2D models will always suffer from the need that viscosity, e.g., angular momentum transport has to be parameterized and can not be studied per se, ongoing work is pushing for 3D simulations. We start with a high-mass core slightly perturbed from axis symmetry. The grid has now a maximum resolution of 15AU per grid cell down at 80AU from the star, yet still extends out to 20000AU. Also this simulation treats the full thermodynamics plus radiation transport and needed only a few hundred CPU hours for the studied low-resolution cases. Yet even at the low resolution we find very interesting effects. The massive disk whose formation we already observed in the 2D run is now prone to self gravity and the related spiral arm forming instabilities. As the collapse proceeds (e.g., after 33000 years) the two-peaked structure merges into a one armed spiral and one can see a single condensed clump in the density maximum (Fig. 1 right). At the same time the radiation pressure begins to push the gas up along the rotation axis creating an outflow and a cavity, yet still not as evolved as in the 2D case, which was after 50000 years.

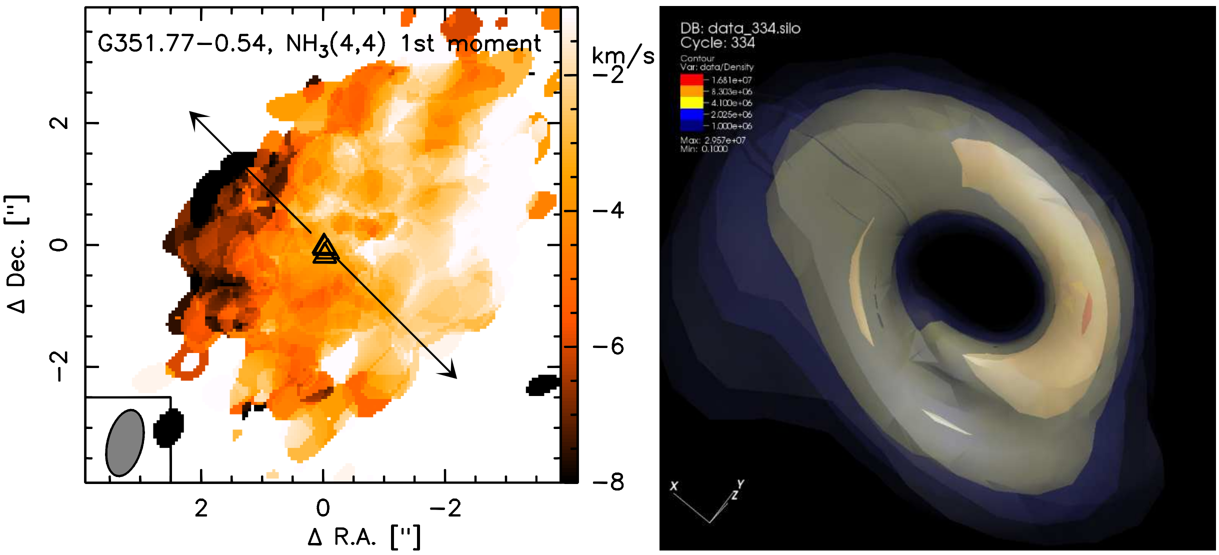

Figure 1: **left:** *The colour-scale presents the intensity weighted velocity structure (1st moment map) toward the hot molecular core G351.77-0.54 measured in NH3(4,4). The arrows show the orientation of the molecular outflow, the triangles mark the CH3OH maser positions, and the synthesized beam is shown at the bottom-left.* **Right:** *After 33000 years a m=1 mode has formed from the m=2 mode and more mass has been accreted onto the star in the center. This m=1 mode could potentially be the onset of a companion that fragments from the disk.*

References

[1] Beuther, H., Walsh, A.J., Longmore, S.N., 2009, ApJ, 184, 366

[2] Fallscheer, C., Beuther, H., Zhang, Q., Keto, E., Sridharan T.K., 2009, A&A, 504, 127

[3] Kuiper, R., Klahr, H., Dullemond, C., Kley, W., and Henning, Th., 2009, A&A, in press

[4] Vaidya, B., Fendt, C., Beuther, H., 2009, ApJ, 702, 567

3 Protoplanetary Disks and Planet Formation

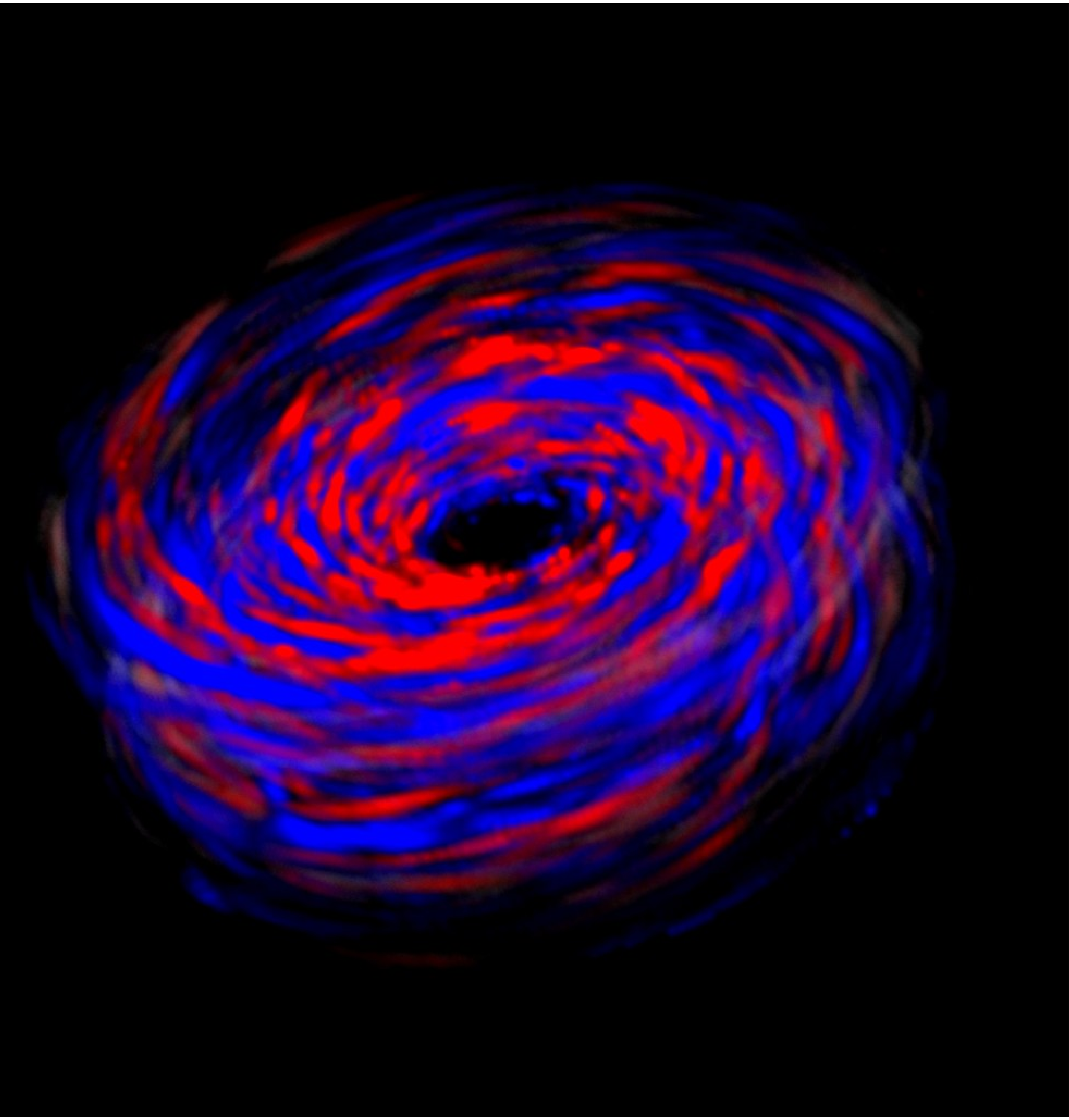

Image on previous page:

Turbulent motions in a protostellar disk model. The gas in the disk atmosphere moves up (blue) and down (red) as fast as the speed of sound, driven by magnetic forces. The Doppler shifts in the spectral lines of the gas molecules may be detectable with future millimetre interferometers (Credit: M. Flock et al. (MPIA))

Star and protoplanetary disk properties in Orion's suburbs

Min Fang, Roy van Boekel, Wei Wang, Aurora Sicilia-Aguilar, and Thomas Henning

Introduction

Knowledge of the evolution of circumstellar accretion disks is pivotal to our understanding of star and planet formation; but despite intensive theoretical and observational studies, the disk dissipation process is not well understood. When properties of circumstellar disks, such as their geometry and accretion rate, are correlated with stellar and environmental parameters, global trends may be found but the source-to-source scatter is almost always very large. Star formation appears to be a very complex process controlled by many entangled parameters, which may not all be accessible observationally at the current time. If we carefully observe large and well characterized samples of young stars, trends may emerge from the "noise" and dependencies on specific parameters may become clear. Superb infrared observations of such samples are now available from various surveys performed with the Spitzer Space telescope. These provide a good measure of evolutionary state of the dusty disk, i.e. its presence and geometry, but provide no information on the stellar properties and the disk accretion behavior. These require supplementary observations, in particular optical and/or near-infrared spectroscopy and imaging. Only the combined multi-wavelength data set allows to reliably correlate star and disk properties, and a better understanding of the star formation process. In this contribution we highlight several results from a large campaign aimed at determining the stellar properties and accretion behavior of hundreds of stars in two large regions of low-mass star formation in the Orion molecular cloud that were surveyed with Spitzer. These results have appeared in A&A [1].

An optical spectroscopy and imaging survey of L1630N and L1641

The Lynds 1630N and 1641 clouds (Fig. 1), located in the Orion complex at a distance of ≈450 pc, have been imaged with Spitzer, detecting ∼60 000 sources of which many hundreds are young stars associated with the clouds. We observed both regions with VLT's multiple-object optical spectrograph VIMOS, targeting a total of 715 stars. Optical SDSS and Calar Alto LAICA imaging was combined with 2MASS JHK photometry and the Spitzer data to obtain spectral energy distributions from 0.4 to 24 μm. We performed automated spectral typing following Hernandez et al. (2004), reaching an accuracy of ∼1 sub-type. Reddened model atmospheres were fitted to the optical/NIR photometric data, keeping $T_{\rm eff}$ fixed at the spectroscopic value, thus having only the extinction and angular diameter as free parameters. Mass and age estimates of individual objects were made through placement in the HR diagram and comparison to several sets of pre-main sequence evolutionary tracks. Numerous optical emission lines are detected in our VIMOS spectra, such as Hα, Hβ, He I 5876Å, [O I] 6300Å, [N II] 6583Å, Ca II 8498Å, etc. In particular the broad Hα, Hβ, and He I lines are used to estimate the accretion rates.

We classified each star in our spectroscopic sample as a cluster member if it complied with any of the following criteria: 1) IR excess; 2) Li I 6707Å absorption; 3) Hα emission. We thus identified 132 confirmed young stars in L1630N and 267 such objects in L1641. We identify 28 transition disk systems, 20 of which were previously unknown, as well as 42 new transition disk candidates for which we have broad-band photometry but no spectroscopy. We provide a catalogue of 399 YSOs, for each of which we give mass and age estimates, the equivalent widths of optical emission lines, the extinction, and measures of the evolutionary state of the dusty disk. In addition we provide a photometric catalogue of ≈22 000 sources detected both in the optical and infrared but for which we have no spectroscopy.

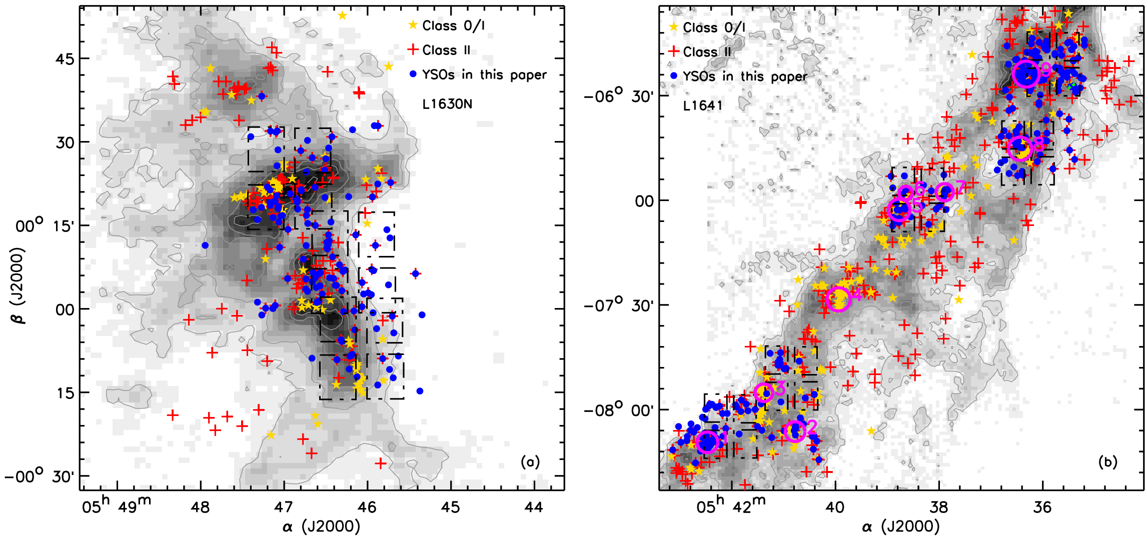

Figure 1: *The positions of Spitzer-detected YSOs and our VIMOS sample (on ^{13}CO contours).*

The scaling law of the accretion rate with stellar mass

In existing studies of how the accretion rate scales with stellar mass a strong dependence is found of roughly $\dot{M}_{\rm acc} \propto M_*^{\alpha}$, with $\alpha \approx 2$, and very large source-to-source scatter. This M_*^2 behavior is predicted from Bondi-Hoyle theory, but this theory applies only to mass gathering from the molecular cloud onto the disk (and even there is very simplified) and there is no a-priori reason to assume that accretion onto the star should happen at the same rate. We find a dependence of $\alpha \sim 2$ if the whole mass range of $0.04 M_\odot \leq M_* \leq 5 M_\odot$ is included, but a steeper dependence of $\alpha \sim 3.1$ in the sub-solar regime. Thus, the scaling law of $\dot{M}_{\rm acc}$ with M_* appears *not to be the same across the whole mass regime.* Going back to the literature, we in fact find the same behavior if we include *only* stars with spectroscopically determined properties.

Accretion in transition disk systems

The fraction of stars with transition disks that show significant accretion activity is relatively low compared to stars with still optically thick inner disks (26±11% and 57±6%, respectively). However, those transition disks that *do* show significant accretion have the same median accretion rate as normal optically thick disks of $3{-}4 \times 10^{-9} M_\odot {\rm yr}^{-1}$. This puts important constraints on the role of accretion in the evolution and dissipation of disks.

Age distribution of various populations

We find that the ages of CTTSs and WTTSs with disks are statistically indistinguishable. WTTS without disks are substantially older than the CTTSs, and the ages of the transition disks systems and the disk-less WTTSs are statistically indistinguishable. The notion that disk-less systems and transition disks are more evolved than sources with (still) full-fledged disks has long been around, but to our knowledge this is the first time that actual age differences between the different populations have been detected for a substantial number of sources, and thus direct observational evidence for this hypothesis is given.

References

[1] M. Fang, R. van Boekel, W. Wang, A. Carmona, A. Sicilia-Aguilar, and Th. Henning 2009, A&A, 504, 461

Accretion history of protoplanetary disks

Davide Fedele, Aurora Sicilia-Aguilar, Thomas Henning

Introduction

A substantial amount of the final mass of a star is accreted during the pre main sequence phase through a circumstellar disk. Such a disk forms during the collapse of the molecular cloud to conserve the angular momentum and is the natural environment where planet formation occurs. The physics behind such a *protoplanetary disk* is in turn important to understand how planets form. In this perspective, mass accretion is one of the most fundamental properties of a young star, modulating many of the most physically interesting processes, including those that affect planet formation. Accretion controls disk dissipation timescales, brakes stellar rotation, drives powerful outflows, may inhibit some of the hard X-ray emission but also produce soft X-ray and UV emission, and heats the disk surface. In order to sustain mass accretion a substantial mass of gas has to be present in the disk. The mass accretion rate ($\dot{M}_{acc}$) is then an indirect tracer of the gas reservoir in protoplanetary disks. Moreover, accretion seems to relate to the disk properties as in the case of *transitional objects* – stars with an optically thin inner disk surrounded by an optically thick outer disk. Measurements of $\dot{M}_{acc}$ are an essential tool for evaluating theories of disk evolution.

A main research activity pursued at MPIA is the study of the mass accretion properties in young stars. We present in this report some of the results obtained in the last year in this field based on the work of Fedele et al. [1] and Sicilia-Aguilar et al. [2].

Evolution of the mass accretion rate

We obtained accretion rates for a large number of solar-type stars in the Cep OB2 region by measuring the UV excesses with broad band optical photometry. The presence of accretion at very low rates was also constrained by high-resolution Hα spectroscopy (sensitive to $\dot{\mathrm{M}}\geq 10^{-11}\mathrm{M}{-}\odot\mathrm{yr}^{-1}$). The stars display different disk morphologies, with most of them being surrounded by evolved and flattened disks, and up to 20% of the disks having no or very reduced near-IR excesses. We find that accretion rates are systematically lower than in younger regions (Fig. 1) and roughly consistent with viscous evolution. Nevertheless, the fact that at any age we find non-accreting objects reveals that viscous evolution is not the only mechanism leading to disk dissipation: photoevaporation may be an important process to remove substantial amounts of disk mass. The correlations between $\dot{\mathrm{M}}$ and disk structure in these evolved objects are nevertheless weak. About half of the "transition" disks with presumably optically thin disks are found to be accreting, but the typical accretion rates of accreting TD and "normal" CTTS are not statistically different. This points out to grain growth/settling as the main cause of the low IR excess of these accreting "transition" objects.

Mass accretion vs dust dissipation

We performed a large spectroscopic survey aimed at measuring the timescale of mass accretion in young, pre-main-sequence stars in the spectral type range K0 – M5. Using multi-object spectroscopy with VIMOS at the VLT we identified the fraction of accreting stars in a number of young stellar clusters and associations of the ages of between 1 – 30 Myr. The fraction of

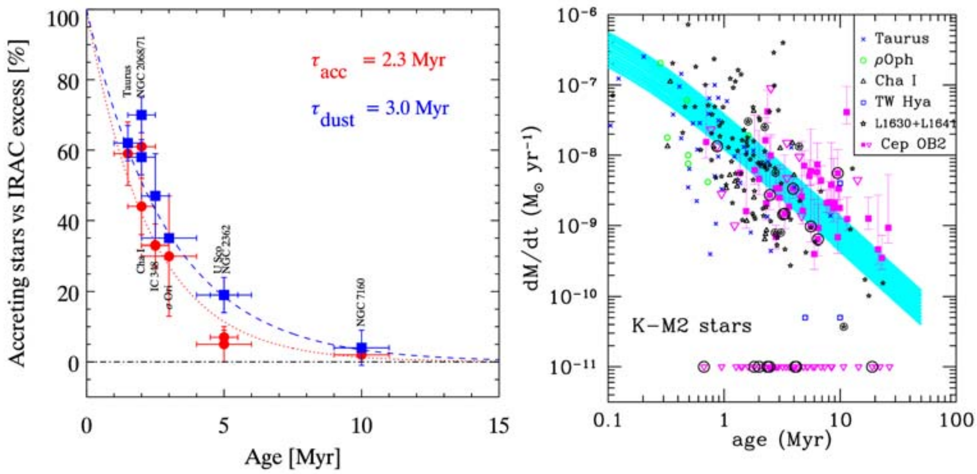

Figure 1: *(left)* f_{acc} *(dots) versus* f_{IRAC} *(squares) and exponential fit (dotted line) for* f_{acc}*, dashed line for* f_{IRAC}*. (right) Evolution of the accretion rate versus age in different regions. The global picture is consistent with viscous evolution models (cyan area), but many stars with different ages do not appear to be accreting (inverted triangles are upper limits,* $\dot{M}< 10^{-11} M_{\odot} yr^{-1}$*)*

accreting stars decreases from ~ 60 % at $1.5 - 2$ Myr to ~ 2 % at 10 Myr. No accreting stars are found after 10 Myr at a sensitivity limit of 10^{-11} $M_{\odot} yr^{-1}$. We compared the fraction of stars showing ongoing accretion (f_{acc}) to the fraction of stars with near-to-mid infrared excess (f_{IRAC}). In most cases we find $f_{acc} < f_{IRAC}$, i.e., mass accretion appears to cease (or drop below detectable level) earlier than the dust is dissipated in the inner disk. At 5 Myr, 95 % of the stellar population has stopped accreting material at a rate of $> 10^{-11}$ $M_{\odot} yr^{-1}$, while ~ 20 % of the stars show near-infrared excess emission. Assuming an exponential decay, we measure a mass accretion timescale (τ_{acc}) of 2.3 Myr, compared to a near-to-mid infrared excess timescale (τ_{IRAC}) of 3 Myr. A possible explanation is that in these systems accretion is stopped by the formation/migration of giant planets at scale of a few AU from the central star while dust beyond the planet's orbit may still emit detectable infrared excess in the IRAC bands.

Collaborators are: L. Hartmann (University of Michigan), R. Jayawardhana (Toronto University), J. M. Oliveira (Keele University), M.E. van den Ancker (ESO)

References

[1] Fedele, D. et al. 2009 A&A accepted

[2] Sicilia-Aguilar, A., Henning, Th., Hartmann, L., submitted to ApJ

Gas in protoplanetary disks

Thomas Henning, Andres Carmona, and Davide Fedele

During the last two decades the properties of protoplanetary disks have been explored through studies of dust emission and scattering. However, most of the mass in protoplanetary disks is contained in molecular hydrogen. The gas determines the disk dynamics, regulating angular momentum and mass transport and determining the conditions for dust evolution through mutual particle collisions. In addition, the gas is the ingredient for giant planet formation. The gas content of the outer disk can be constrained by (sub)millimetre observations of the CO molecule and its isotopologues. UV and near-infrared lines probe the innermost hot regions of disks. Mid-infrared emission lines of molecular hydrogen could be potential tracers to probe the warm gas in regions of giant planet formation.

We performed a very sensitive search for mid-infrared molecular hydrogen emission at 12.278 and 17.035 μm [1], using the high-resolution modes of the ESO-VLT instrument VISIR. Altogether we observed a variety of disks around Herbig Ae/Be stars and T Tauri stars. In none of the objects we could detect emission from molecular hydrogen. We had to conclude that the disks contain less than a few tenths of Jupiter mass of optically thin molecular hydrogen at 150 K and less than a few Earth masses of such gas at 300 K and higher temperatures. Most of the molecular hydrogen is located in the optically thick part of the disk. Molecular hydrogen emission from the disk surface layers can only be expected in the presence of additional heat sources for the gas (see, e.g., Bitner et al. 2007, ApJ 661, L69). With the high-resolution near-infrared VLT spectrograph CRIRES [2], we were able to detect the 1-0 S(1) and 1-0 S(0) NIR lines of molecular hydrogen, coming from the disk around the classical T Tauri star LKHα 264. The observation implies the presence of a few lunar masses of hot gas in the very inner disk (at about 0.1 AU). The line ratio indicates that the hydrogen molecules are most likely thermally excited by UV photons.

For the first time, we attempted a direct comparison of the dust and gas distribution in the planet-forming regions of protoplanetary disks around intermediate-mass stars [3]. As a tracer for the gas, we used the [OI] 630 nm emission line; the dust distribution was investigated by mid-infrared interferometry in the 10 μm silicate emission feature. The oxygen emission line is thought to be produced by photodissociation of OH molecules by stellar UV photons and traces only the surface layer of the disk that is directly exposed to the stellar radiation field. In the two objects HD 101412 and HD 135344 B, we found a compact 10 μm emission (smaller than 2 AU), while the oxygen brightness profile shows a double peaked structure. The inner peak is strongest and consistent with the location of the dust, the outer peak is fainter and is located at 5-10 AU. These two disks appear strongly flared in the gas, but self-shadowed in the dust beyond 2 AU, indicating gas-dust decoupling. The disk around HD 179218 is flared in the dust; the oxygen emission seems also to come from a flared disk. The observations suggest that we see an evolutionary sequence from HD 179218 to HD 135344B and HD 101412, where the disk initially flared becomes flat under the combined action of gas-dust decoupling, grain growth and dust settling (see Fig. 1).

Observations with the Spitzer satellite have now opened a new frontier in the investigation of the gas in inner regions of protoplanetary disks. Lines from water, carbon monoxide and a variety of organic molecules have been detected. We performed a comparative study of the gas (and dust) properties of disks around young Sun-like stars (K1-M5) and cool stars/brown dwarfs (M5-M9) [4]. For the first time, we detected organic molecules in disks around brown dwarfs. In addition, we found a striking difference in the detection rate statistics and the line flux ratios of HCN and C_2H_2 between the two samples, demonstrating a significant underabundance of HCN relative to C_2H_2 in the disk surface of cool stars. We propose this difference to originate from the large difference in the UV irradiation around the two types of sources. The different chemistry of preplanetary gas may influence the bulk composition and volatile content of the

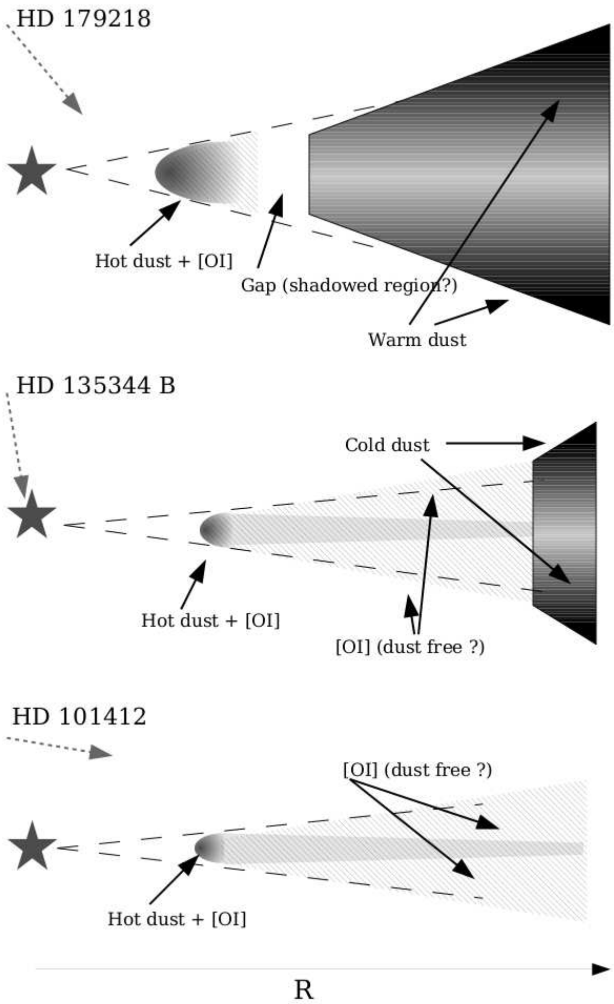

Figure 1: *Simplified sketch of the dust and gas distribution in the disks around the stars HD 179218, HD 135344B and HD 101412. The inclination of the disk to the line of sight is shown by the dashed line. After [3].*

forming planets.
Main Collaborators are M. van den Ancker (ESO, Garching) and I. Pascucci (JHU, Baltimore).

References

[1] Carmona, A., van den Ancker, M.E., Henning, Th. et al.: 2008, A Search for Mid-infrared Molecular Hydrogen Emission from Protoplanetary Disks. A&A, 477, 839.

[2] Carmona, A., van den Ancker, M.E., Henning, Th. et al.: 2007, A Search for Near-infrared Molecular Hydrogen Emission in the CTTS LkHα 264 and the Debris Disk 49 Ceti. A&A 476, 853.

[3] Fedele, D., van den Ancker M.E., Acke B. et al.: 2008. The Structure of the Protoplanetary Disks Surrounding Three Young Intermediate Mass Stars. II. Spatially Resolved Dust and Gas Distribution. A&A 491, 809.

[4] Pascucci, I., Apai, D., Luhmann K., Henning, Th. et al. 2009. The Different Evolution of Gas and Dust in Disks around Sun-like and Cool Stars. ApJ 696, 143.

Death as a condition for life: planet formation and the dead zone in protoplanetary disks

Mario Flock, Natalia S. Dzyurkevich, Dmitry Semenov, Neal J. Turner, Hubert Klahr

In nature, death is essential for new life. The same is true in protoplanetary disks. Many of the key unresolved issues in planet formation hinge on a region inside the disk called the "dead zone", where the low conductivity prevents magnetic forces from driving turbulence. In this region, thermal ionization is ineffective due to the low temperatures, while non-thermal ionization is weak because the stellar X-rays and interstellar cosmic rays are blocked by the disk matter. Protoplanetary disks thus consist of a laminar dead zone embedded in turbulent surroundings.

The dead zone in the Solar nebula spanned the modern-day orbits of the planets, so we infer that it provided the environment for the assembly of the primordial interstellar dust into larger bodies.

The next generation of telescopes, including ALMA and Herschel, have as a major objective the measurement of the gas kinematics and the dust properties in the surface layers and interiors of protoplanetary disks. Our goal is to apply our advanced theoretical tools, to construct models for use in interpreting the coming flood of data. Among the tools available are detailed chemical codes incorporating the knowledge of reaction processes and rates gleaned from interstellar chemistry studies and laboratory measurements (Semenov), and magnetohydrodynamical codes capable of following the flows through a large portion of a protoplanetary disk while accurately tracking the localized development of the turbulence (Flock, Dzyurkevich). The chemical calculations yield the electron abundance and the degree of coupling between the magnetic fields and the gas, while the dynamical calculations follow the movements of the gas under the influence of the magnetic forces. The resulting changes in gas density may lead in turn to shifts in the electron abundance. Combining these two tools will enable global models of protoplanetary disks in which the dead zone changes size and shape over time. Our view is that the evolving dead zone will prove to govern the accumulation of solid material, the flow of gas to the star (including episodic accretion events), and the eventual dispersal of the disk.

Distribution of Turbulence In Protoplanetary Disks

As a beginning step, we have made the first global 3-D resistive MHD calculations of protostellar disks, using a static ionization profile (Figure 1). The results demonstrate the formation of a local radial gas presure maximum near the inner boundary of the dead zone, capable of trapping small solid particles. The resistivity increases sharply passing outward through 4.5 AU, and as seen in the figure, the predominantly magnetic accretion stresses decline from as much as 10% of the local gas pressure in the disk atmospheres, to as little as one part in 10^5 of the gas pressure in the dead zone well outside the boundary.

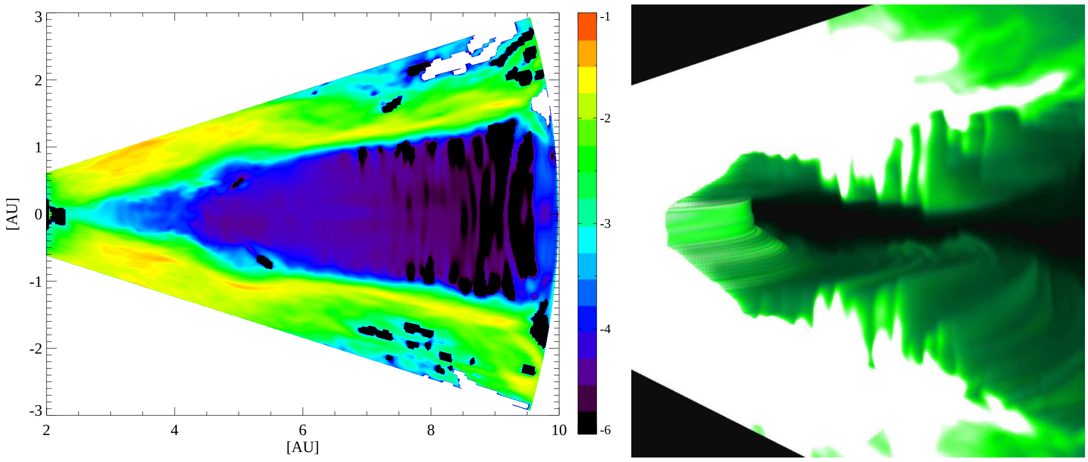

Figure 1: *Left: Shakura-Sunyaev accretion stress parameter in a 3-D resistive-MHD calculation of a protoplanetary disk. The star lies to the left and the disk is viewed in cross-section. Outside* 4.5 *AU lies a midplane dead zone where the weak coupling of the magnetic fields to the gas yields a ratio* α *of the accretion stress to the gas pressure just* 10^{-5}. *Meanwhile the disk atmospheres above and below show vigorous turbulence and large stresses, with* α *approaching* 0.1. *The stress has been averaged along the orbital direction and over time. Right: Volume rendering of the dust density in a 3-D global resistive MHD calculation of a protostellar disk, about 50 local orbits after a small cloud of dust was inserted at radius* < 4.5 *AU. The star lies out of the image to top left and only a sector of the disk is shown (from 3 to 8 AU). Vigorous turbulence in the disk atmospheres at top and bottom carries the cloud of dust toward and away from the star, while barely penetrating the dead zone where turbulence is weak.*

Transport In And Around the Dead Zone

We have also tracked the dispersal of a passive contaminant in the gas flows in and around the dead zone. The contaminant is a model for the behaviour of both fine dust grains, and trace gas-phase molecular species. We placed a cloud of the contaminant in the turbulent zone inside 4.5 AU. Figure 2 shows a snapshot of the cloud about 50 local orbits later. The cloud has spread a great distance radially through the disk atmosphere where the turbulence is strong, while largely avoiding the laminar dead zone interior. Fingers of contaminated material extending vertically into the dead zone indicate that some slower exchange of material occurs across the upper and lower boundaries.

References

[1] Trapping of Solids at the Inner Edge of the Dead Zone: 3-D Global MHD Simulations. Dzyurkevich N., Flock M., Turner N. J., Klahr H. & Henning Th., Astron. & Astrophys., in press.

[2] Flock M. et al. A&A, submitted.

[3] Chemical and Thermal Structure of Protoplanetary Disks as Observed with ALMA. Semenov D., Pavlyuchenkov Ya., Henning Th., Wolf S. & Launhardt R., 2008, Astrophys. J. 673, L195

Water in protoplanetary disks

Cornelis Dullemond, Anton Vasyunin, Thomas Henning and Tilman Birnstiel

Introduction

Water is the basic ingredient of life. It is quite abundant in interstellar space. But how water was brought to Earth is still a matter of debate. Studying where water resides in protoplanetary disks is one way of seeking an answer to this question. Moreover, it is believed that water ice played a pivotal role in the formation of planets. The precise location of the so-called "snow line" in these disks is an important parameter for planet formation theories. If there are ways to find observational clues to the location of the snow line, that would help our quest for an understanding of how planet form.

Infrared spectra of a number of protoplanetary disks taken with Spitzer-IRS reveal a rich landscape of water lines on top of the dust continuum (Carr & Najita 2008, Science, 319, 1504; Salyk et al. 2008, ApJ 676, L49). It turns out that most protoplanetary disks feature such water lines. The interpretation of these lines is, however, rather tricky. It is known that water lines are notoriously non-LTE because of the large critical densities of water rotational levels. The only way by which a quantitative analysis of such lines can be done is by use of detailed non-LTE radiative transfer and/or detailed gas phase and dust-surface chemistry. In this contribution we discuss two projects that were done, entirely or in part, at the MPIA on this topic. In the first project we use radiative transfer without chemistry to constrain the abundance distribution of water in disks from the observed Spitzer-IRS spectra. In the second project we use the surface chemistry of water on dust grains to predict the abundance distribution ab initio, and how it depends on grain growth.

Radiative transfer models and the location of the snow line

The purpose of our radiative transfer study is not to create perfect fits to individual source spectra, but rather to find a fiducial model that reproduces the overall properties of the water line spectra from the Carr & Najita and Salyk et al. samples of T Tauri stars (hereafter called "the sample"). Our radiative transfer analysis is carried out with a new radiative transfer code that we developed specially for the purpose of infrared molecular/atomic lines from protoplanetary disks ([2]). This code overcomes various numerical difficulties experienced by conventional radiative transfer codes in models with a large ratio of systematic velocity to intrinsic thermal or turbulent line width.

We start our study ([1]) by setting up a generic disk structure model that is roughly consistent with the disks around the T Tauri stars we are comparing to. The dust temperature is then computed with continuum radiative transfer using the RADMC code. As a first attempt to create a consistent model, a standard equilibrium abundance of water is taken, $x_{\mathrm{H_2O}} = 3 \times 10^{-4}$. The resulting models show that the low excitation lines from the sample sources are reproduced reasonably well, but the high excitation lines are strongly underpredicted, partly due to non-LTE effects. Our second attempt is to increase the gas temperature in the disk surface layers well beyond the dust temperatures, as is predicted by more detailed models of disk surface layers (e.g. Gorti & Hollenbach 2008, ApJ 683, 287). This now reproduces the high-excitation water lines of the sample, but overpredicts the low-excitation lines. Only if, as our third and final attempt, we reduce the abundance of water drastically beyond 1 AU, can all lines be approximately reproduced. This radius happens to be the location of the snowline at the midplane. We speculate that freeze-out near the midplane on large grains combined with vertical mixing depletes the gaseous water not only from the midplane region, but also from the surface layers. If confirmed by future more detailed models, this may be a way to spot the midplane snow line, even though this is normally hidden from view by the large optical depth of the disk.

Impact of grain growth on water abundance in the disk

Chemical processes occurring on the surfaces of grains are of crucial importance for the formation of key molecules such as molecular hydrogen, water and complex organic species. In our work, we utilized a detailed model of grain evolution in the disk which includes processes of grain growth, fragmentation and sedimentation, to study the impact of these processes on the chemical composition of protoplanetary disks around a DM Tau-like star.

Among the most interesting results we found is the enhancement of gas phase water abundance in the inner part of the disk (R $\leq$ 100 AU). We found that due to processes of grain evolution the total surface area of grains gets smaller and the disk becomes less opaque for the UV radiation of the central star. A stronger UV field causes efficient photodesorption of water from grain mantles (where it has been formed) to the gas phase. Since grains evolve more quickly in the dense inner part of the disk, the strongest enhancement of gas phase water abundance also happens in the inner disk where terrestrial planets may possibly be formed (see Fig. 1). Also, the effect of enhancement of gas phase abundances of species may be used as an independent observational tracer of grain growth in protoplanetary disks.

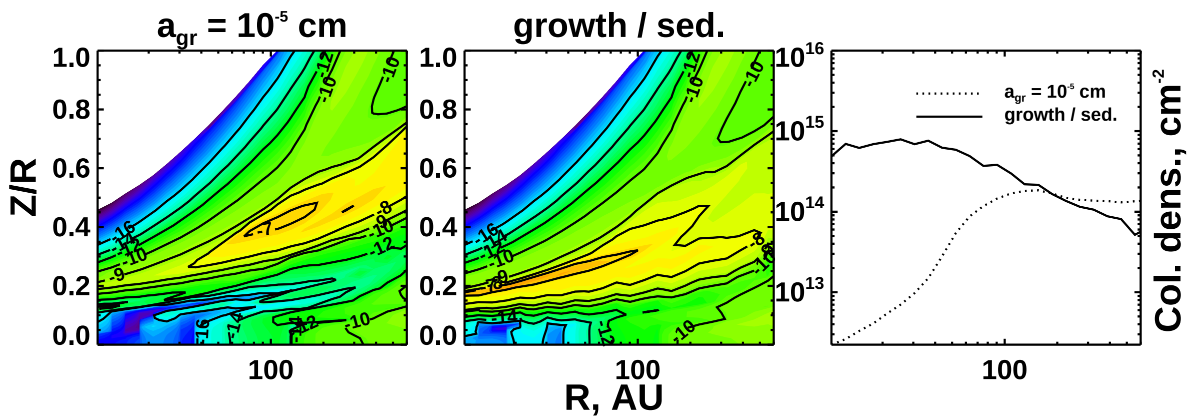

Figure 1: *H_2O abundance across the disk. Left panel: model with standard grains of size 10^{-5} cm, middle panel: model with account for grain growth and sedimentation, one can see an enhanced water abundance at R $\leq$ 100 AU, Z/R $\sim$ 0.2. Right panel: radial distribution of column density of water in corresponding models.*

Collaborator is Dmitry Wiebe (INASAN, Russia)

References

[1] Meijerink, R., Pontoppidan, K.M., Blake, G.A., Poelman, D.R. & Dullemond, C.P., 2009, ApJ, 704, 1471

[2] Pontoppidan, K.M., Meijerink, R., Dullemond, C.P. & Blake, G.A., 2009, ApJ, 704, 1482

Smoothed or layered? Protoplanetary disks as observed with ALMA

Dmitry Semenov, Thomas Henning, and Ralf Launhardt

Molecules as probes of planet-formation processes

One of the most exciting questions in astrophysics is to understand the origin of planetary systems. Nowadays the planet formation is studied by observing protoplanetary disks in dust continuum and in lines of abundant molecules, both at infrared and (sub-) millimeter wavelengths. A few nearby disks around T Tauri and Herbig Ae stars have been spatially resolved in a handful of molecular lines (e.g. [1]). As demonstrated by [2], excitation of molecular lines in disks with strong gradients of physical conditions and chemical structure can be hard to interpret. The observations coupled to advanced modeling allowed to derive basic disk parameters such as size, mass, temperature and density distribution, kinematics, and chemistry (e.g., [3, 4, 5]).

The situation will change dramatically when the Atacama Large Millimeter Array (ALMA), equipped with 50 12-m antennas, will come into operation in 2012. ALMA will be capable of imaging disks at spatial resolutions up to $\sim 0.005''$ in a 30-950 GHz frequency range. The physical and chemical structure of protoplanetary disks will become accessible in lines of molecules which we can only dream of now. The analysis of the ALMA data will require a thorough re-evaluation and adjustment of modern models of disk evolution. Thence, in [6] we studied the potential of ALMA to distinguish between temperature gradients and chemical effects in disks.

ALMA as a tool to study protoplanetary disks

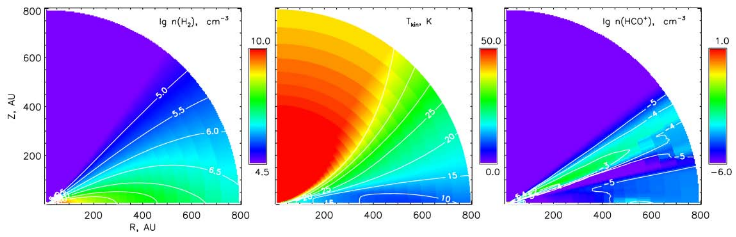

Figure 1: *Distributions of the particle density (left panel), temperature (middle panel), and absolute abundances of HCO$^+$ at 5 Myr (right panel) for the DM Tau disk model.*

We adopt a flared model of a DM Tau disk with a radius of 800 AU, an accretion rate $\dot{M} = 10^{-8}\,M_\odot\,\mathrm{yr}^{-1}$, a viscosity parameter $\alpha = 0.01$, and a mass of $M = 0.07\,M_\odot$ (see Fig. 1). To mimic the case when the vertical temperature gradient is absent, the same disk model with isothermal vertical temperature distribution is used. The 5 Myr of evolution is modeled with a large gas-grain chemical model ([7]). The HCO$^+$ absolute abundances (molecules cm^{-3}) in the DM Tau disk at 5 Myr (Fig. 1). A layered structure with the maximal HCO$^+$ concentration reached at intermediate heights is apparent. Transport processes can smooth these abundance gradients, leading to uniformly distributed abundances ([8]). Thus, we consider a model with an uniform HCO$^+$ abundance of 10^{-9} relative to H_2.

Using these 3 models, and the 2D non-LTE line radiative transfer code of [2], noise-free beam-unconvolved channel maps of HCO$^+$(4-3) were synthesized. At the 60° inclination the integrated line width is ~ 3 km s^{-1}, with a peak intensity reached at ~ 0.8 km s^{-1}. To simulate the ALMA observations, we use these synthetic maps as an input to the GILDAS software.

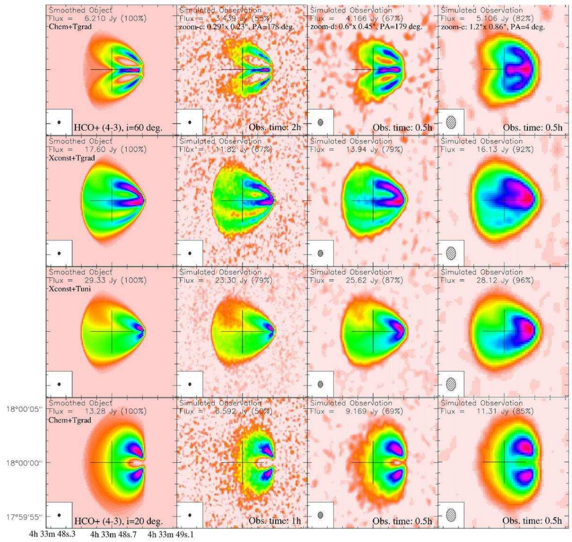

Figure 2: *(From 1st to 3rd row) The ALMA HCO$^+$ (4-3) synthetic map at the* $V = +0.77$ *km s*$^{-1}$ *velocity channel and the* 60° *inclination angle for the disk models: with chemical stratification and temperature gradients (1st column), the disk model with the uniform abundances (2nd column), and the vertically isothermal model with the uniform abundances (3rd column). Three ALMA configurations are shown: "zoom-c" (*$\sim 0.25''$ *beam,* $t_{\rm obs} = 2$ *h), "zoom-b" (*$\sim 0.5''$ *beam,* $t_{\rm obs} = 0.5$ *h), and "zoom-e" (*$\sim 1''$ *beam,* $t_{\rm obs} = 0.5$ *h). (4th column) The HCO$^+$ (4-3)* $V = +0.3$ *km s*$^{-1}$ *channel for the disk model with chemical gradients and the inclination angle of* 20°.

The simulated ALMA channel maps of HCO$^+$(4-3) at various spatial resolutions for the 3 adopted models at 2 inclinations are shown in Fig. 2. Similar modeling was done for other molecules and transitions. Clearly, the ALMA interferometer will be capable of distinguishing the effects of physical structure and chemical stratification, in particular for highly-inclined disks, using compact array configurations with baselines of $\lesssim 1$ km and 0.5–10 hours of integration time.
Other Collaborators: Yaroslav Pavlyuchenkov (INASAN Moscow), Sebastian Wolf (Kiel Univ.)

References

[1] Bergin, E. A. 2009, arXiv:0908.3708

[2] Pavlyuchenkov, Y., Semenov, D., Henning, T., & et al. 2007, ApJ, 669, 1262

[3] Semenov, D., Pavlyuchenkov, Y., Schreyer, K., & et al. 2005, ApJ, 621, 853

[4] Qi, C., Wilner, D. J., Calvet, N., & et al. 2006, ApJL, 636, L157

[5] Schreyer, K., et al. 2008, A&A, 491, 821

[6] Semenov, D., Pavlyuchenkov, Y., Henning, T., & et al. 2008, ApJL, 673, L195

[7] Vasyunin, A. I., Semenov, D., Henning, T., & et al. 2008, ApJ, 672, 629

[8] Semenov, D., Wiebe, D., & Henning, T. 2006, ApJL, 647, L57

What is in the hole of the transition disks?

Aurora Sicilia-Aguilar, Thomas Henning, Veronica Roccatagliata, Johny Setiawan, Jeroen Bouwman, Ralf Launhardt, Min Fang, Roy van Boekel

Transition Disks: How to open an inner hole

Transition disks (TD) are protoplanetary disks thought to be in an intermediate stage between Class II and Class III objects. They show very weak or no near-IR excesses down to certain wavelengths ($\lambda \leq 6\mu$m for solar-type stars) but "normal" Class II-like spectral energy distributions (SEDs) in the mid-IR (Fig.1). This suggest that the inner disk is optically thin or even totally depleted from dust. Some TD are still accreting (Fig.1), having thus gas-rich inner disks [1]. Studying the origin and evolution of TD is important to understand disk dissipation and planet formation. Several mechanisms have been proposed to explain TD: differential grain growth and settling in the inner disk, UV photoevaporation from the central star, dynamical clearing by stellar companions, and planet formation. The timescales for these mechanisms to operate and the lifetimes of the resulting TD are not the same, so TD observed in clusters with different ages may be physically different objects. The various mechanisms also leave different imprints on the disk (accretion, disk mass, presence of small dust). Examining disk and accretion properties and searching for companions (stellar or substellar), we can infer which mechanisms dominate disk dissipation at a given age. Finally, not all objects need to go through the TD phase: some may undergo a more global evolution, due, for instance, to external photoevaporation.

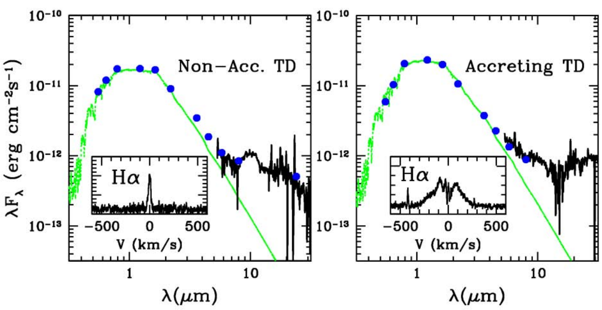

Figure 1: *Spectral energy distributions (SEDs) and Hα profiles of non-accreting (left) and accreting(right) transition disks around two young (∼4 Myr), $M_* \sim 0.8\ M_\odot$ stars.*

Grain growth, dust settling, and photoevaporation

Determining the presence of accretion (e.g. via Hα spectroscopy) and the accretion rates (e.g. via UV excess) in TD and evolved disks helps to reveal the processes responsible for the inner holes. Measures of the accretion rates in evolved CTTS and accreting TD in the 4 Myr-old cluster Tr 37 [1] show no significant differences in $\dot{M}$ for these two types of objects, with median values of $\dot{M}\sim$3-2$\times 10^{-9} M_\odot yr^{-1}$, respectively. This suggests that photoevaporation is not always efficient in opening an inner hole, even if the accretion rate is very low ($<10^{-9}$-$10^{-10} M_\odot yr^{-1}$ [1]). The lack of differences between CTTS and TD also suggests that most accreting TD found at 4 Myr age are objects where strong grain growth and settling has rendered the inner disk optically thin/flat, while the gas content is comparable to that of evolved CTTS [1]. Nevertheless, planet formation may be the leading process in the formation of TD in younger clusters. In addition, a large number of TD appear not to be accreting. These objects are more frequent at older ages:

~50% of TD at 4 Myr are not accreting [1], while the fraction is only ~30% at 1-2 Myr [2]. The inner holes of these objects are thus most likely related to photoevaporation, which becomes more efficient at older ages, although giant planet formation may also render accretion undetectable in evolved disks with initially low $\dot{\mathrm{M}}$ [1].

Binaries and planets

The fact that TD are older than CTTS in Orion L 1630 and L 1641 clouds suggests that binarity is not the main cause of TD [2]. Nevertheless, some TD are found to be binaries. GW Ori is an accreting K0 star surrounded by a very massive disk (M_{disk} ~0.5-1.3 $M_\odot$). It is variable in the IR, displaying sometimes low near-IR fluxes characteristic of TD. A binary companion with a period ~240 days had been previously detected. We obtained new radial velocity measurements using FEROS/La Silla during last year. Our data confirm the period, but we find a lower mass ($M sini$ ~0.17$M_\odot$) and higher eccentricity of the companion than previous studies. The low mass of the companion embedded in a massive disk suggests that the system could be gravitationally unstable, and might even point to binary formation within the disk.

GM Aur is a K7 star aged 3 Myr. Its reduced near-IR excess suggested the presence of an inner hole. Recent observations in ^{13}CO and C^{18}O with IRAM/PdB reveal the presence of a gas cavity with a ~20 AU radius [3]. This hole could be explained by the presence of a very low-mass companion or a 5-10 M_J planet orbiting at about 15 AU. The hole is almost devoid of dust, which suggests that, if a planet is the cause, planet formation must start very early, probably during the Class I phase.

Are all TD "in transition"? Do all disks dissipate via a TD phase?

Observations of some young low-mass star-forming regions like the Coronet cluster reveal a surprisingly high fraction of TD [4]. Moreover, the SEDs and silicate features of disks in the Coronet suggest a high degree of grain growth and dust settling, even in the cases without inner holes. A large TD fraction in a young cluster suggests that the SED morphology may also depend on the initial conditions in the star-forming regions or the mass of the central star (disks around M-type stars and BD being typically flatter than around solar-type stars). Large fractions of TD observed in regions with different ages [4, 5, 6] also suggest long TD lifetimes (≥1 Myr). Since many disks suffer from strong grain growth/settling without getting inner holes, disk dissipation via generalized dust evolution throughout the disk may be a possible evolutionary path.

Collaborators are Anne Dutrey (Observatoire de Bordeaux, France), Lee Hartmann (University of Michigan, USA), Warrick Lawson (School of PEMS, USF@ADFA, Canberra, Australia), Gwendolyn Meeus (Universidad Autónoma de Madrid, Spain).

References

[1] Sicilia-Aguilar, A.; Henning, Th.; Hartmann, L. 2010, ApJ 710, 597

[2] Fang, M.; van Boekel, R.; et al., 2009, A&A 504, 461

[3] Dutrey, A.; Guilloteau, S.; Piétu, V.; Chapillon, E.; Gueth, F.; Henning, Th.; Launhardt, R.; et al., 2008, A&A 490, L15

[4] Sicilia-Aguilar, A.; Henning, Th.; Juhász, A.; Bouwman, J., et al. 2008, ApJ 687, 1145

[5] Sicilia-Aguilar, A.; Bouwman, J.; Juhász, A., et al., 2009, ApJ 701, 1188

[6] Meeus, G.; Juhasz, A.; Henning, Th.; Bouwman, J.; et al. 2009, A&A 497, 379

Dust growth and fragmentation: The first stages of planet formation

Cornelis Dullemond, Frithjof Brauer, Til Birnstiel, Andras Zsom, Thomas Henning

Introduction

Planets such as the Earth are formed through the aglomeration of solids in a protoplanetary disk. Starting as small dust particles no larger than a micrometer, dust aggregates grow as these dust particles hit each other and stick to each other. However, as particles/aggregates grow larger, their collision velocities increase. Once they are as large as a few decimeters, their collision velocities are so large that they no longer stick but instead fragment, producing smaller aggregates again. This constitutes what is often called the "meter size barrier", because collisions of particles of a meter in size happen at the largest velocities. Once particles somehow grow well beyond a meter in size, the collision velocities go down again and growth is possible again. The meter size barrier is actually two barriers: the "fragmentation barrier", meaning that aggregates of this size will destroy each other upon collisions, and the "radial drift barrier", meaning that even if they are not destroyed, they tend to radially drift toward the star so quickly that we lose all our planetary raw material before we can form full-grown planets.

We know that planets have formed, despite the meter-size barrier. But we also know that disks tend to remain strongly dust-rich for their entire life, which is consistent with the existence of a fragmentation barrier. So we must now find a way to allow some material to cross the meter size barrier, but not too efficiently, otherwise all the solids would be turned into planets with 10^5 years and disks would become dust-free, which is inconsistent with observations.

We have developed in the last few years a number of methods and codes to model this process in detail. The first type of method is one that solves the dust particle distribution function $N(m, r, z)$ as a function of particle mass m and the radial and vertical location in the disk r, z. This method has the advantage of solving the evolution of the dust over the entire disk efficiently. This work has been published in [1, 2, 4].

But the distribution function method has the drawback that it does not allow easily to follow the *structure* of the aggregates: are they compact or fluffy? This is important because this structure has a strong influence on the coupling to the gas, and thus on the growth process itself. We therefore developed a complementary method: A Monte Carlo method for solving the aggregation, fragmentation and structure-modification process [3]. Now, a collision can have not only the effect of breaking up aggregates or letting them stick: now one can also model the compaction of aggregates and evaluate whether they will bounce or stick if they do not break up.

Example 1: Planetesimal formation near the snow line

In a 2007 paper, Kretke & Lin proposed that rapid radial drift and large collision velocities could be prevented if a local pressure bump is present. They suggested that the snow line in the disk, i.e. the radius where the temperature of the disk drops below the water freeze-out temperature, would be the location where such a long-lived pressure bump would reside. Frithjof Brauer used his model to compute the behavior of the solids in such a disk. The result is shown in Fig. 1. In this figure, growth would be represented by a gradual upward moving of the colored area. Shown there is a still of this evolution, at the time when a fraction of the material has already broken through the barrier. For most part of the disk, near 1 meter, the growth is stalled. Only at the snow line the growth can break through and move to the top of the diagram. We showed here that the presence of such pressure bumps may indeed help to overcome the meter-size barrier.

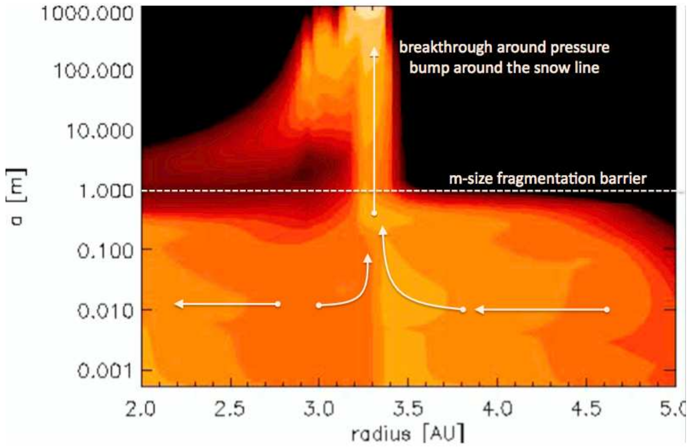

Figure 1: *Formation of planetesimals and breakthrough through the "meter size barrier". Color: Amount of dust aggregates at location r and particle size a. Shown is a snapshot.*

Example 2: The growth-fragmentation cycle

Using the Monte Carlo code we were able to demonstrate how the growth and fragmentation cycle produces an equilibrium distribution of aggregates that have a relatively narrow distribution of porosities (Fig. 2). This is important information, because it may help to later include porosity in a simpler way into the distribution function code.

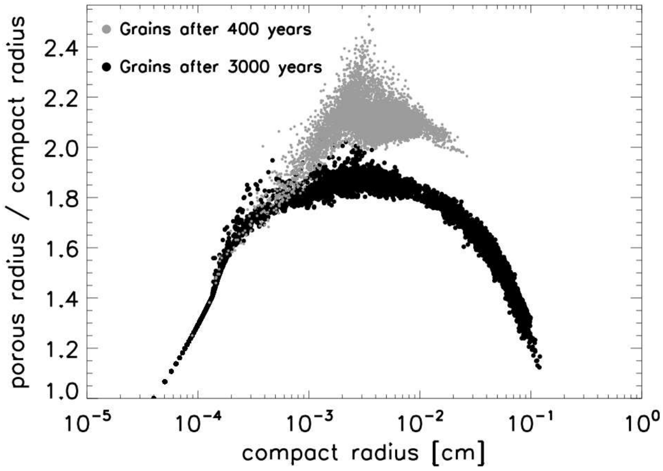

Figure 2: *The growth-fragmentation equilibrium calculated using the Monte Carlo method of [3].*

References

[1] Brauer, F., Dullemond, C.P. & Henning, Th., 2008, A&A,480,859

[2] Brauer, F., Henning, Th. & Dullemond, C.P., 2008, A&A,487,L1

[3] Zsom, A. & Dullemond, C.P., 2008, A&A,489,931

[4] Birnstiel, T., Dullemond, C.P. & Brauer, F., 2009, A&A,503,L5

The mineralogy of dust grains in T Tauri and transition disks.

Jeroen Bouwman, Thomas Henning, Aurora Sicilia-Aquilar, Attila Juhász

Infrared spectra of disks

Spectroscopic observations of the thermal infrared emission of circumstellar disks have proven to be crucial in our understanding of the physical processes governing the disk structure and chemical processing and growth of dust grains (for a review on this subject see [4]). With the launch of the *Spitzer Space Telescope* in the fall of 2003, for the first time, a large sample of protoplanetary disks around lower mass stars could be observed. With its involvement in the "Formation and Evolution of Planetary Systems" (FEPS) science legacy program and leading multiple open time program on *Spitzer*, the MPIA is at the fore-front of infrared spectroscopy of protoplanetary disks. Our efforts of the last few years have lead to a substantial number of publications concerning the mineralogy of dust grains in T Tauri and transition disks [1, 2, 3, 4, 5, 6, 7, 8, 9]. An example of *Spitzer* spectroscopy can be seen in Fig. 1. These spectra show multiple emission features from crystalline silicate dust species.

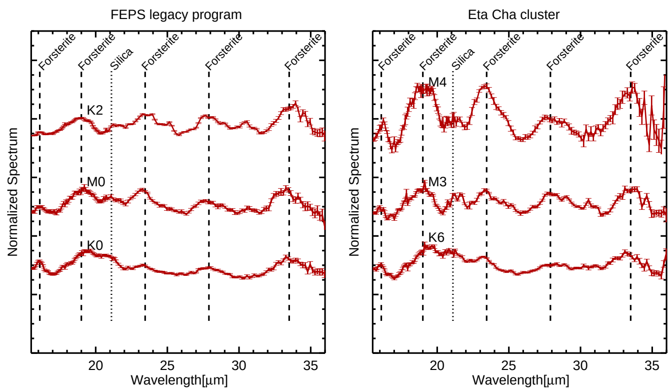

Figure 1: *Example of* Spitzer *spectra of the disks around low-mass pre-main sequence stars. The left panel shows three spectra observed within the FEPS legacy program [1], the right panel three spectra of low mass pre-main sequence systems in the η Chamaeleontis cluster [9]. The vertical lines in each panel indicate the peak positions of forsterite (Mg_2SiO_4) and Silica (SiO_2), two of the main crystalline silicate dust species.*

Dust processing and evolution

Comparing the spectra of Fig. 1 to those of the intermediate mass Herbig Ae/Be systems (see the contribution of Attila Juhász in this report) identical crystalline (high temperature) silicates can be observed. This suggest that similar physical processes occur in circumstellar disks independent of the mass of the central star. A key focus of our research activities are disks of pre-main-sequence stars located in small and nearby associations [5, 8, 9]. The key aspect of associations - a group of coeval and cospatial stars - allows us to disentangle stellar and disk properties from age in driving the evolution of the dust in these systems. Surprisingly, a similar mineralogy can be observed between ~1 Myr and ~8 Myr, the age of youngest and oldest cluster in our study. This implies that dust evolution is not a simple function of stellar age. This is also suggested by the observed spread in dust properties between the coeval systems of one

association, showing that other intrinsic star-disk properties must govern the dust evolution. One of these properties could be binarity. Bouwman et al (2006, ApJ 653, 57) noticed that close binaries have a strong influence on the disk evolution. However, medium separation binaries seem not to influence the dust composition and behave in a simmilar fashion as single star systems [6]. Apart from binary compagnions, the formation of a giant planet could also influence the dust evolution. A developing planet, opening a gap in the disk, would produce shock waves through tidal interaction with the disk and heat dust grains to high enough temperatures for crystallization to occur. We propose that this scenario applies for RECX 5, a systems in the η Cha cluster ([2]; see also the top right spectrum of Fig. 1). Next to the formation of crystals one should also consider amorphization. We show that the stellar X-ray fluxes around 1 AU and ion energies of the present solar wind are sufficient to amorphize the upper layer of dust grains very efficiently, leading to an observable reduction of the crystalline mass fraction of the circumstellar, sub-micron sized dust [3]. The above discussed processes demonstate the complex nature of dust processing and evolution in disks. The combined effect on the dust composition could erase relations between crystallinity and parameters such as age or spectral type.
Collaborators are Gwendolyn Meeus (UNAM, Spain), Sebastion Wolf (University Kiel, Germany), Ilaria Pascucci, Daniel Apai, Christine Chen (STScI, USA), Eric Feigelson, Kevin Luhman (Penn State, USA), Michael Meyer (ETH, Switzerland), Fred Lahuis (SRON, Netherlands), Antonella Natta (Arcetri, Italy), John Carpenter, Lynne Hillenbrand (CallTech, USA), Warrick Lawson (University of New South Wales, Australia), Bram Acke (University of Leuven, Belgium), Rens Waters, Carsten Dominik (University of Amsterdam, Netherlands), Alexander Tielens (Leiden Observatory, Netherlands), Dean Hines (Space Science Institute, USA), Serena Kim, (University of Arizona, USA), Murray Silverstone (Eureka Scientific, USA), David Hollenbach (NASA/Ames, USA), Adrian Glauser (UK Astronomy Technology Centre, UK), Martin Güdel (University of Vienna, Austria), Dann Watson (University of Rochester, USA)

References

[1] Bouwman, J.; Henning, Th.; Hillenbrand, L. A.; Meyer, M. R.; Pascucci, I.; Carpenter, J.; Hines, D.; Kim, J. S.; Silverstone, M. D.; Hollenbach, D.; Wolf, S. 2008, ApJ 683, 479

[2] Bouwman, J.; Lawson, W. A.; Juhász, A.; Dominik, C.; Feigelson, E. D.; Henning, Th.; Tielens, A. G. G. M.; Waters, L. B. F. M. 2010, ApJ, submitted

[3] Glauser, A. M.; Güdel, M.; Watson, D. M.; Henning, Th.; Schegerer, A. A.; Wolf, S.; Audard, M.; Baldovin-Saavedra, C. 2009, A&A 508, 247

[4] Henning, Th ; Meeus, G. 2010

[5] Meeus, G.; Juhász, A.; Henning, Th.; Bouwman, J.; Chen, C.; Lawson, W.; Apai, D.; Pascucci, I.; Sicilia-Aguilar, A. 2009, ApJ 497, 379

[6] Pascucci, I.; Apai, D.; Hardegree-Ullman, E. E.; Kim, J. S.; Meyer, M. R.; Bouwman, J. 2008, ApJ 673, 477

[7] Pascucci, I.; Apai, D.; Luhman, K.; Henning, T.; Bouwman, J.; Meyer, M. R.; Lahuis, F.; Natta, A. 2009, ApJ 696, 143

[8] Sicilia-Aguilar, A.; Henning, T.; Juhász, A.; Bouwman, J.; Garmire, G.; Garmire, A. 2008, ApJ 687, 1145

[9] Sicilia-Aguilar, A.; Bouwman, J.; Juhász, A.; Henning, Th.; Roccatagliata, V.; Lawson, W. A.; Acke, B.; Feigelson, E. D.; Tielens, A. G. G. M.; Decin, L.; Meeus, G. 2009, ApJ 701, 1188

Formation of diamond in protoplanetary disks under the influence of high energy particles

Miwa Goto, Thomas Henning

The Herbig Ae star Elias 1 has a circumstellar disk as seen in the large infrared excess in the spectral energy distribution. The dust emission is spatially resolved recently by mid-infrared interferometry, which sets lower limit of the disk size at 20–30 AU (Liu et al. 2007, ApJ, 658, 1164). Elias 1 is one of a handful young stellar objects that shows diamond emission in the protoplanetary disk. We used Subaru Telescope and the spectrograph IRCS to obtain medium resolution spectra of Elias 1 at 3.0–3.8 μm in order to shed light on the formation of diamond in a disk using high angular resolution afforded by the adaptive optics system. The FWHM of the point spread function (PSF) was 80 mas at 3.3 μm, which is 11 AU at the distance of 140 pc. We extracted 17 strips of the spectra along the slit, each offset by 10 AU, in order to see the variation of PAH and diamond emission features in the disk as a function of the distance from the central star (Fig. 1). The central part of the disk is almost devoid of PAH emission with the equivalent width becoming larger toward the outer disk, while diamond emission is compact and concentrated near the star.

The first diamond emission from a protoplanetary disk is found by Whittet et al. in 1983 (A&A, 123, 301) in HD 97048, as an identified emission at 3.53 μm. Since then, only three young stars are known to date that show diamond emission from the circumstellar disks - HD 97048, Elias 1, and MWC 297. Recent survey of diamond features over 60 young stellar objects (YSO) with an 8-m class telescope did not add a clear detection of a new diamond star (Acke et al. 2006, ApJ, A&A, 457, 171). Diamond is the most common substance in meteorites in the Solar System. It is yet to be understood why the stars with diamond emission form disks are so rare.

These diamond YSOs are indeed special, being the only Herbig Ae/Be stars that show x-ray flares. Giardino et al. (2004, A&A, 413, 669) used XMM Newton and Chandra x-ray observatory to monitor Elias 1, and detected x-ray flares with exponential decay similar to the Sun. Hamaguchi et al. (2000, ApJ, 532, 1111) also found a similar x-ray flare in MWC 297. No monitoring observation is available for HD 97048, but it is the hardest x-ray source in the cluster (Stelzer et al. 2004, A&A, 423, 1029). X-ray emission from a Herbig Ae/Be star, let alone its flare, is intriguing enough, as a Herbig Ae/Be star is not supposed to be an x-ray source in the first place. High-mass and low-mass stars are bright x-ray sources, as the former produces x-ray emission in the high-velocity stellar winds, and the latter in the magnetic activity similar to the Sun. Herbig Ae/Be stars fall in between - the stellar wind is too weak to produce x–ray, but too strong to keep the surface convective zone required to drive the magnetic dynamo. Elias 1 has a companion at 4″ away, and further resolved into a binary recently (Smith et al. 2005, A&A, 431, 307). Either of the low-mass companions naturally explain the x-ray flare from Elias 1. MWC 297 also has a low-mass companion, and Hamaguchi et al. attribute the x-ray flare to that companion.

What does the presence of x-ray active low-mass companions have to do with the production of diamond in a protoplanetary disk? Diamond is hard to produce in the ultra-low pressure environment in the interstellar medium. A material scientist Banhart demonstrated in 1996 (Banhart & Ajayan 1996, Nature, 382, 433) that the core of carbon onions transforms into diamond at the incidence of high energy electrons. Carbon onions are concentric graphitic shells nested like an onion. When put under the electron beam, carbon atoms in outer shells are knocked on. In consequence, the outer shells shrink, and ultra-high pressure (50–100 GPa) builds up at the core of the onions, where the graphitic structure naturally transforms into diamond.

We propose a novel path of diamond formation in protoplanetary disks by drawing parallel with the laboratory experiment. The new production path naturally explains why the diamond emission is rare, why the presence of x-ray active low-mass companion is critical, why the emission features have been seen only in Herbig Ae/Be stars and not in T-Tauri stars, and why the diamond emission is concentrated near the star where the PAH emission is missing. The x-ray flare from low-mass companions accompanies with the particle acceleration following magnetic reconnection. The particle precipitation works as the electron beam in the experiment of Banhart et al. The influx of the electron current to a carbon onion at 10 AU away in a typical solar flare is consistent with 2-200 A cm^{-2} of the laboratory experiment [1]. The presence of carbon onions in the disk of Elias 1 is unclear. However, PAH is the low-mass end of graphene. The presence of PAH implies the presence of small graphite particles. The Banhart experiment actually started with nano-meter size graphite particles which are further converted to carbon onions by electron irradiation. The absence of PAH at the center of the disk implies graphitic material consumed in the production of diamond particle.

T-Tauri stars are natural x-ray sources. Therefore, their protoplanetary disks should be more subject to the particle precipitation than Herbig Ae/Be stars. Why do we not see diamond emission in T-Tauri stars? Banhart continued the electron beam experiment to find that the conversion of carbon onions to diamond proceeds to the surface of the onions without high pressure once the diamond core is formed; as long as the ambient temperature is warm (Zaiser & Banhart, 1997, PRL, 79, 3680). This is because diamond has higher threshold energy than graphite against the displacement by the particle hit. The graphite layers in the carbon onion are therefore gradually converted to diamond in the long run under the extreme inequilibrium condition induced by the particle irradiation. The threshold energy of diamond is highest with respect to graphite at the temperature of 600 K. The surfacing of diamond proceeds most efficiently at this temperature. The size of the disk that reaches 600 K in a T-Tauri star is 0.1–1 AU while it is significantly larger in Herbig Ae/Be stars. T Tauri stars might indeed have plenty of diamonds inside graphitic particles, but the disk temperature is so low that they do not surface to the dust grains to produce diamond emission features.

Collaborators are Akira Kouchi (Hokkaido University), C. Jäger (Friedrich-Schiller-Universität Jena), A.C. Andersen (Dark Cosmology Centre), Hiroshi Terada, Tomo Usuda (Subaru Telescope).

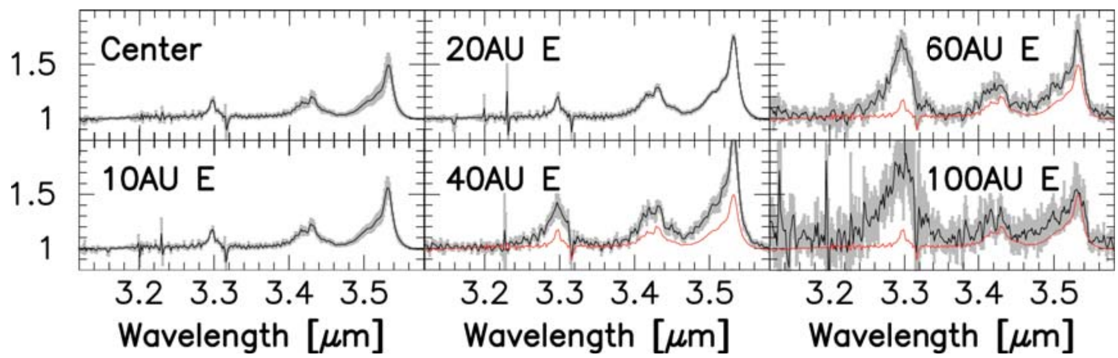

Figure 1: *Spectra of Elias 1 as a function of distance from the central star. The central part of the disk is devoid of PAH (3.3 μm), while diamond emission is compact (3.53 μm). Note that that sharp emission line at 3.28 μm is Pfund δ.*

References

[1] Goto, M., Henning, Th., Kouchi, A., Takami, H., Hayano, Y., Usuda, T., Takato, N., Terada, H., Oya, S., Jäger, C., Andersen, A. C. 2009, ApJ, 693, 610

Caught in the act: Following the large outburst of the T Tauri Star Ex Lupi with a multi-wavelength campaign

Attila Juhász, Roy van Boekel, Cornelis Dullemond, Jeroen Bouwman, Aurora Sicilia-Aguilar, Thomas Henning

Young eruptive stars and dust evolution

EX Lup-type stars (or EXors) are young eruptive stars undergoing 1–5 mag outbursts at optical wavelengths. The duration of these outburst can vary between several months to a year and although they occur randomly, eruptions are on average separated by several years of quiescent periods. These outburst are thougth to be related to runaway accretion in the innermost regions of protoplanetary disks. Apart from the presence of outburst, no other difference has been found between normal T Tauri stars and EXors. It is therefore likely, that EXors are, in fact, normal T Tauri stars in a stage of the early stellar evolution, that most if not all of the young stars go through. EXor outbursts can also play a role in the thermal processing of protoplanetary dust. The enhanced luminosity of the inner regions of the disk during outbursts can cause massive crystal formation in the disk. Crystalline silicates are known to be essentially missing from the interstellar medium (ISM), yet are abundant in protoplanetary disks and Solar System comets. Although these facts suggest that silicate crystals form in disks around young stars, in the lack of direct observations, it is still unknown when and where exactly crystallization occurs.

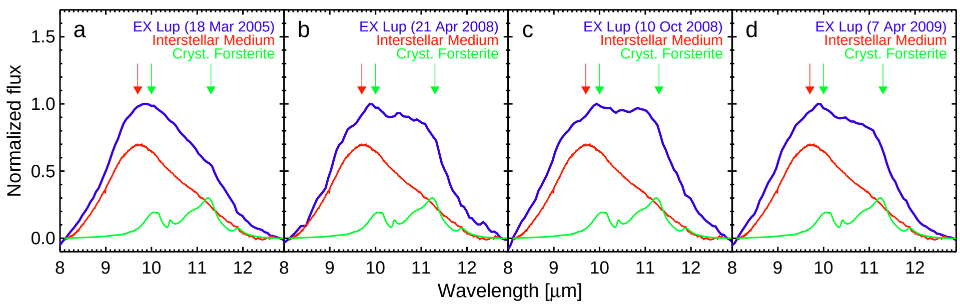

Figure 1: *Evolution of the 10 µm silicate feature of EX Lup during the 2008 outburst. For comparison the 10 µm silicate profile of the interstellar dust as well as that of crystalline forsterite is shown (both scaled to the figure), while arrows mark the peak positions of these materials.*

The 2008 outburst of EX Lup

At the beginning of 2008 EX Lup went into its most recent outburst, which was the largest since 1950s, brightening 5 mag above its quiescent brightness at optical wavelengths. We observed EX Lup with the Infrared Spectrograph (IRS) onboard the Spitzer Space Telescope at three epochs after the beginning of the outburst. While in the pre-outburst spectrum from the literature showed no contribution from crystalline silicates (Fig. 1*a*), bands of crystalline forsterite (10.0 μm, 11.3 μm, 16.1 μm) appeared in the spectrum taken during the outburst (Fig. 1*b*). The only possible explanation for the appearance of crystalline bands is the in situ formation of forsterite crystals in the innermost hot regions of the disk. This was the first direct observation of the crystal formation process in protoplanetary disks [1]. In the Spitzer IRS spectrum taken right after the end of the outburst forsterite bands also longwards of 20 μm became visible while

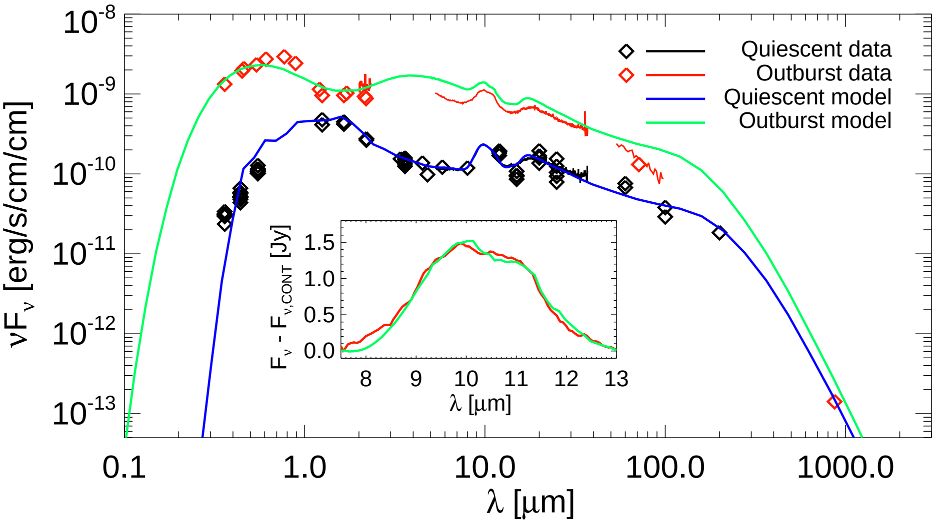

Figure 2: *SED of EX Lup in the quiescent phase (Sipos et al. 2009) and in the 2008 outburst. By increasing the accretion rate we are able to reproduce the outburst SED using all other parameters from the quiescent phase disk model. This indicates no structural changes in the disk during the outburst. The inset shows how well the shape of the silicate feature is reproduced by our model.*

forsterite features shortwards of 13 μm became stronger (Fig. 1*c*). The shape of the spectrum, taken six months after the end of the outburst, did not change longwards of 20 μm compared to the previous spectrum. Shortwards of 20 μm, however, the strength of the crystalline features suprisingly became weaker. On the same day when the outburst Spitzer IRS spectrum was taken we observed EX Lup also with various ground- and space-based instruments from optical to sub-millimeter wavelengths (Fig. 2). The Spectral Energy Distribution (SED) of EX Lup was modeled 2D radiative transfer code and a 1+1D turbulent mixing/settling code. We used the parameters of the quiescent phase disk model of Sipos et al. (2009) and increased the accretion rate ($2{\cdot}10^{-7}M_\odot$/year, estimated from Br γ emission). The modeling revealed that crystals formed in the uppermost surface layers of the disk within about 1.2 AU from the central star, where the temperature exceeded 1000 K. Our radiative transfer model is able to reproduce the shape of the outburst Spitzer IRS spectrum (Fig. 2), but crystalline features longwards of 20 μm are stronger in the post-outburst Spitzer spectra than our model predicts. Our calculations show that the decrease of crystallinity in the 10 μm silicate feature between the two post-outburst spectra is likely caused by the transportation of crystals to larger radii by a wind, rather than vertical turbulent mixing. This study showed that the value of crystallinity in protoplanetary disks, derived from mid-infrared spectroscopy, can be a function of time. The random nature of EXor outbursts predicts also large diversity in crystal yield on long time-scale even among systems with similar parameters.

Collaborators are Péter Ábrahám (Konkoly Observatory, Hungary), Ágnes Kóspál (Leiden Observatory, The Netherlands), Attila Moór (Konkoly Observatory, Hungary), László Mosoni (Konkoly Observatory, Hungary), Zs. Regály (Konkoly Observatory, Hungary), Nikoletta Sipos (Konkoly Observatory, Hungary)

References

[1] Ábrahám, P., Juhász, A., van Boekel., R., Henning, Th., Kóspál, Á, Mosoni, L, Sicilia-Aguilar, A., Sipos, N. 2009, Nature, 459, 224

Dust mineralogy in the disks around Herbig Ae stars – The Spitzer Legacy

Attila Juhász, Jeroen Bouwman, Thomas Henning

Herbig Ae stars

Herbig Ae stars (hereafter HAe stars) are young stars (1–10 Myr) in their later stages of the pre-main sequence evolution. The observed infrared excess above the photospheric emission of these stars arises from a protoplanetary disk and in many case from an envelope as well. Planet formation theories suggests that this evolutionary stage (1–10 Myr) is exactly where the formation of planetary embryos is likely to occur. HAe stars, being also more massive and brighter than low-mass T Tauri stars, are natural candidates to study processes which play an important role in planet formation. In this study we analyzed the spectra of a comprehensive set (45 sources) of Herbig Ae stars taken with the Infrared Spectrograph (IRS) onboard the Spitzer Space Telescope. The signal-to-noise ratio (S/N) of these spectra is among the highest ever has measured towards young stars (typically several hundreds). We studied mid-infrared emission features of various dust species, to derive the composition and physical properties of protoplanetary dust grains.

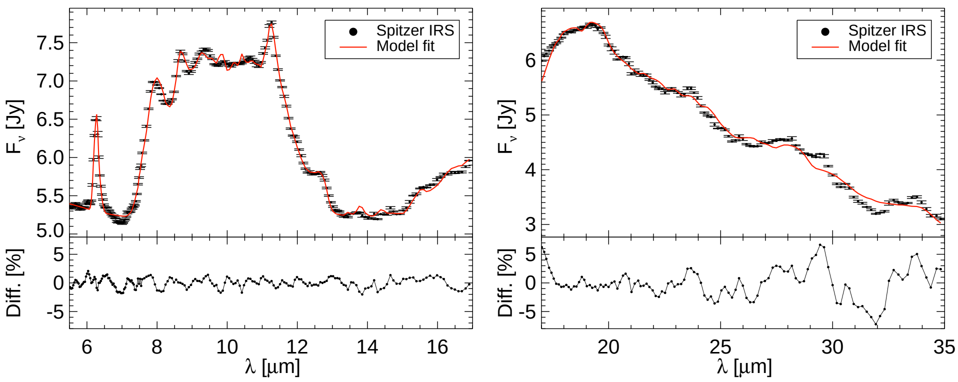

Figure 1: *An example of the fits to the Spitzer IRS spectra (HD 95881). Our model can reproduce the observed spectra typically on a percentage level in the 5–17 µm region (Left) and on a few percent level in the 17–35 µm region (Right). The average S/N is 650 and 350 in the shorter and longer wavelength interval, respectively.*

What Spitzer spectra tell us about protoplanetary dust

As a first step we identified the dust species showing features in the Spitzer IRS spectra. The identification revealed that the major components of protoplanetary dust are amorphous silicates with olivine and pyroxene stoichiometry, crystalline forsterite and enstatite and silica. Bands of Polyciclic Aromatic Hydrocarbons (PAHs) are also commonly seen in the spectra. Apart from the aforementioned dust species no features of other dust components has been found in the extreme high S/N spectra. The Spitzer IRS spectra were then analyzed using the Two-Layer Temperature Distribution method [1]. Mass absorption coefficients of the aforementioned dust species were calculated for the analysis using DHS theory and three discrete grain sizes (0.1 μm, 2.0 μm, and 5.0μm). The high quality of the fits are demonstrated in Fig. 1. The results show that the flaring of the disks, measured by the flux ratios between 24 μm and 8 μm, is inversely

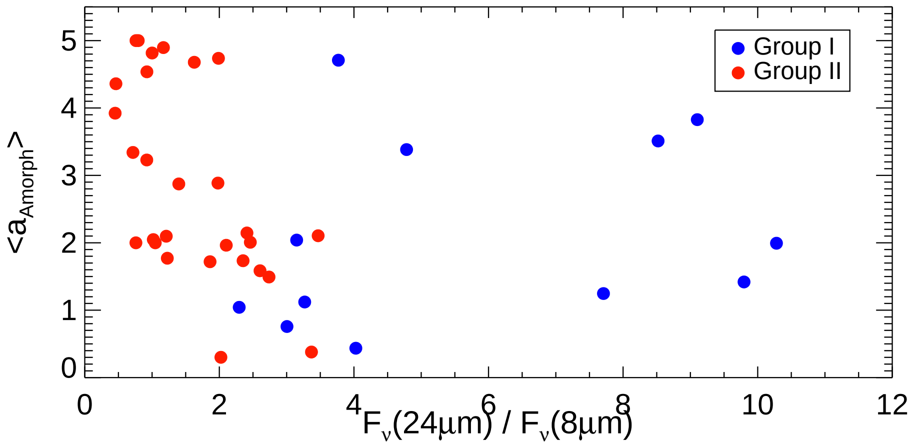

Figure 2: *Mass-weighted average grain size of amorphous silicates as a function of disk flaring. Apart from a few outliers from Group I, there is clearly visible trend that flatter (lower F_{24}/F_8 flux ratios) have larger grains than flared disks. The outliers in Group I have unusual disk structure (e.g. large inner hole, or a wide gap), i.e. the used flux ratio is not a direct measure of the flaring.*

correlated with the average grain size of the amorphous silicates. This is a direct evidence that grain growth and dust settling can turn an initially flared disk onto a flat one. We found that the forsterite over enstatite abundance ratio increases with wavelength (i.e. with radial distance from the star). No correlation has been found between crystallinity and any of the global parameters of the systems (e.g. disk mass, flaring, stellar parameters). None of the so far proposed crystal formation mechanisms can alone reproduce all these observational results. We concluded that probably all of these mechanisms can play an equally important role in the formation of silicate crystals in protoplanetary disks. Although our model can reproduce the observed Spitzer spectra typically on a percentage level, our fits are not perfect (χ^2 is typically a few tens). We concluded that the differences between the model and the observed spectra are due to small variations in the iron content of the crystals and due to grain shape effects. The shape of protoplanetary dust grains is unknown, however optical properties of small grains in the Rayleigh-limit are very sensitive to that. The limits of our analysis are, therefore, likely to be set by the uncertainties in the shape of the grains instead of uncertainties in the measured spectra.

Collaborators are Bram Acke (KU Leuven, Belgium), Mario van den Ancker (ESO, Germany), Gwendolyn Meeus (UAM, Spain), Carsten Dominik (University of Amsterdam, The Netherlands), Michiel Min (University of Utrecht, The Netherlands), Alexander G.G.M. Tielens (NASA Ames, USA), Laurens, B.F.M. Waters (University of Amsterdam, The Netherlands)

References

[1] Juhász, A., Henning, Th., Bouwman, J., Dullemond, C.P., Pascucci, I., Apai, D., 2009, ApJ, 695, 1024

Mid-infrared interferometry of protoplanetary disks with the VLTI

Roy van Boekel, Thorsten Ratzka, Davide Fedele, Alexander Schegerer, Christoph Leinert, and Sebastian Wolf

Introduction

The disks of gas and dust around newborn stars provide a natural laboratory for studying the formation of planetary systems. Due to the large distances toward even the nearest young stars, special methods need to be applied to spatially resolve scales comparable to the (inner) solar system, such as the Adaptive Optics technique that is strongly pursued at the MPIA. An even higher spatial resolution is offered by long baseline interferometry. Observations in the 10 μm atmospheric window allow studying the emission from warm material in the inner $\approx$10 AU of the disk. The MIDI instrument at the VLT Interferometer, built by an MPIA-led consortium, offers a linear resolution of order 1 AU at $\lambda = 10\,\mu$m, at the distance of nearby young stars. In this contribution we report on recent advancements in spatially resolved studies of the planet forming region of young star disks.

A comprehensive MIDI study of 8 protoplanetary disks

In order to investigate the spatial structure of protoplanetary disks, and its evolution, we have selected a sample of 8 T Tauri stars with estimated ages ranging from $\sim$1 Myr to $\sim$10 Myr for a MIDI study. All sources were spatially resolved with MIDI, and we simultaneously model the spectral energy distributions and MIDI visibilities. For this we have adapted the 3D radiative transfer code MC3D (Wolf et al. 1999) to include accretion, an envelope, a multiple-dust layer approach, and a self-consistent solution of the vertical density structure.

For five objects (RY Tau, DR Tau, RU Lup, S Cra N, and S Cra S), the observations are best fit with an active disk model, in which typically 10 to 30% of the total energy output is generated through the release of gravitational energy from accreting material. For the more evolved objects, HD 72106 and HBC 639, a purely passive disk model yields the best fit. Our visibilities are consistent with a gap being present in the inner disk of RU Lup, but we also constructed a model without an inner gap that equally well reproduces the available observations. The 10 μm silicate feature is detected in emission in the infrared spectra of all our sources, showing that small silicate grains are abundant in the disk surfaces. However, if we consider the spectra *in correlated flux* as measured by the interferometer, in which emission on scales larger than the interferometric resolution is filtered out and the spectrum of the inner disk regions can thus be measured directly, we find that the silicate feature is absent in the more evolved objects and we see a featureless continuum instead, pointing at large dust grains of at least $\approx$4 μm. Our results reconfirms that the dust properties in protoplanetary disks are strongly dependent on the distance from the central star. These results have appeared in A&A [1, 2].

The T Tau triplet as seen with MIDI: 3 disks within 1″

The T Tau system consists of the optically visible northern star T Tau N and the southern close binary with components Sa and Sb. All 3 stars exhibit infrared excess emission indicative of circumstellar material. In order to characterize the disks we have observed the system with MIDI. The diffraction limited beams of the 8.2m UTs spatially separate T Tau N from the southern binary, but do not resolve the Sa-Sb pair.

The disk around T Tau N was well resolved in our observations. We simultaneously fitted the SED and interferometric visibilities using the same 3D radiative transfer model as in the previously mentioned study, and confirm this object has an almost face-on disk. The silicate feature is seen in emission, and the dust is found to be more strongly processed close to the central star. Such behavior has been interpreted as the first essential step in the formation of planetary bodies.

The visibilities measured on T Tau S bear the sinusoidal modulation typical of binary sources, from which the relative positions of Sa and Sb, as well as their flux ratio, can be derived. The measured phases indicate that Sa is the brighter source in the N-band. The silicate band is seen in absorption towards both sources and confirms a high foreground extinction of $A_V \approx 15$ mag toward Sb and $A_V \approx 30$ mag toward Sa, which may arise in a circumbinary disk or torus, or in remnant cloud material, which must in any case be very local since T Tau N, at a projected separation of $\approx$100 AU, suffers only $\approx$1 mag of extinction. The interferometric data reveal an elongated structure for Sa, interpreted as a compact disk seen nearly edge-on. The orientation of this disk is almost north-south. Sa might thus be the driving source of the east-west jet.

Our study shows that the orbits and disks in the T Tau triple system have complex orientations. While the disk around Sb might be coplanar with its orbit around Sa, the disk around Sa is not aligned. It is almost perpendicular to the disk around T Tau N. Thus, the picture of a single rotating and fragmenting cloud core, resulting in a multiple (disk) system with aligned angular momentum vectors, clearly does not hold for the T Tau system. The formation history of close multiple systems is more complex, and disk-companion tidal interaction is likely strong (see also the contribution entitled: "The T Tau triplet: a fresh look"). These results have appeared in A&A [3].

The structure of HAe star disks in gas and dust

Studies investigating the structure of circumstellar disks using infrared interferometry and SED modeling trace the dust continuum emission, but do not assess whether the gaseous material follows the dust distribution. We have performed the first direct comparison of the distribution of gas, as traced by the [OI] 6300 Å emission, and the dust, as traced by the 10 μm continuum emission, in the disks around young stars. The distribution of the gas is obtained from VLT UVES spectra with a spectral resolution of 77 000, in which the spectral line profile can be converted to a radial intensity profile, assuming that the disk is in Keplerian rotation (i.e. high spectral resolution is used to indirectly obtain spatial information on small scales). The distribution of the dust is obtained directly from the spatially resolved MIDI observations. We find that in two disks, around HD 101412 and HD 135344, the disk shows a "flat" or "self-shadowed" structure when viewed in dust emission, whereas the gaseous component appears "flared". Our observations may provide the first evidence of gas-dust decoupling in protoplanetary disks. In HD 179218 we find evidence for a disk gap or shadowed region between $\sim$3 and $\sim$15 AU, which is not seen in the gaseous component. We suggest that the three studied systems form an evolutionary sequence: the initially flared dusty disk becomes flat under the combined action of gas-dust decoupling, grain growth and dust settling. These results have appeared in A&A [4].

References

[1] A.A. Schegerer, S. Wolf, Th. Ratzka, and Ch. Leinert 2008, A&A, 478, 799

[2] A.A. Schegerer, S. Wolf, C.A. Hummel, S.P. Quanz, and A. Richichi 2009, A&A, 502, 367

[3] Th. Ratzka, A.A. Schegerer, Ch. Leinert, P. Abraham, Th. Henning, T. Herbst, R. Köhler, S. Wolf, and H. Zinnecker 2009, A&A, 502, 623

[4] D. Fedele, M.E. van den Ancker, B. Acke, G. van der Plas, R. van Boekel, M. Wittkowski, Th. Henning, J. Bouwman, G. Meeus, and P. Rafanelli, 2008, A&A, 491, 809

Do transitional disks bear signs of planet formation?

Jörg-Uwe Pott, Tom M. Herbst

Introduction

Circumstellar disks are a natural outcome of the star-formation process: when a molecular cloud core collapses, it gives rise to a central star surrounded by a rotating circumstellar disk, which transports material towards the star. Possible observational support for inside out disk evolution has been found in a small number of so-called transitional disks. These systems show a strong mid-infrared excess ($\geq 8\,\mu$m) revealing the presence of dust but significantly reduced NIR infrared excess compared to typical classical T Tauri disks, indicating a depletion of optically thick inner dust out to a radius of a few AU. Therefore, these disks might be in the process of dispersing and this has often been assumed to be due to the influence of newly formed planets. Discussed explanations of the transitional disk phenomenon reveal two important features which can be tested directly by high angular resolution imaging observations: (1) The depletion of dust inside of the outer, mid-infrared disk, could be caused by a close (AU-scale) binary system inside of the disk. Binary companions can perturb a circumstellar disk and create inner holes with diameters comparable to the binary separation [1]. To call such a circumbinary disk transitional, would be misleading, since circumbinary disks can be dynamically stable and longer-lasting than the currently assumed short time-scales for the transitional disk phenomenon. (2) While some transitional disks may be completely cleared of material in the inner region, the planet formation hypothesis suggests that disk clearing may often result in gaps between inner and outer dusty regions (e.g. Quillen et al. 2004). Other possible disk clearing mechanisms such as photoevaporation would produce strictly inside-out clearing, so evidence for gaps in disks (in contrast to totally cleared holes) tends to support the planet formation hypothesis. It has been shown for a few systems that this near-infrared excess can be explained by a small amount of emitting dust close to the star at $\sim$ 0.1AU-scales, leaving a gap between this innermost dust, and the outer mid-infrared disk (Fig. 2). Therefore, the near-infrared excess in transitional disk systems might origin from such small size scales, if not emitted by a so far unresolved companion (case 1). To directly assess (1) the presence of close binary companions within transitional disks and (2) the emission size scale of the near-infrared excess over the stellar continuum, we used the Keck Interferometer (KI) to observe 5 transitional disks in the nearby ($\sim$ 140 pc) Taurus-Auriga young star-forming region at a nominal interferometric resolution of $\sim$2.7 mas (Fig. 1).

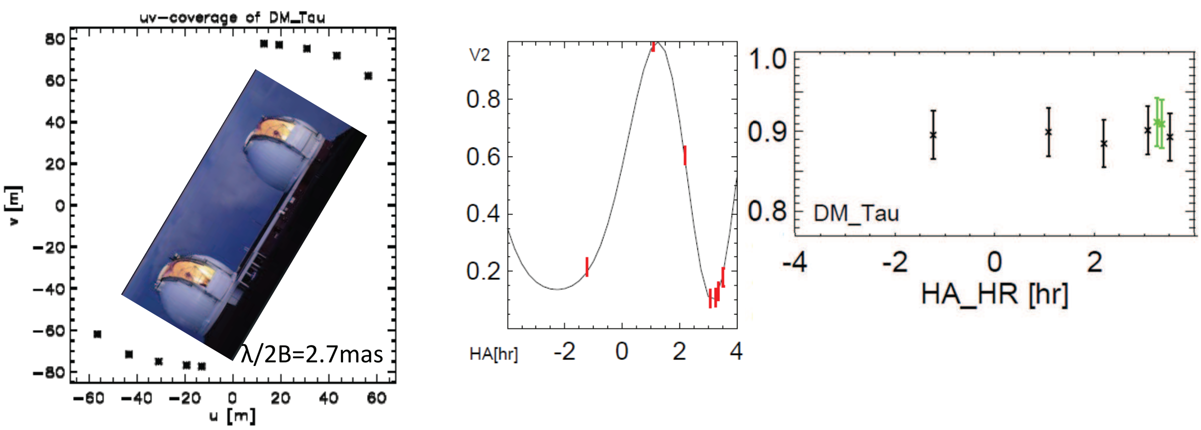

Figure 1: *Left: Typical uv-coverage, sampling and resolution. Center: Expected visibility for equal-mass binary. Right: Flat measured visibilities indicate resolved dust, instead of a binary.*

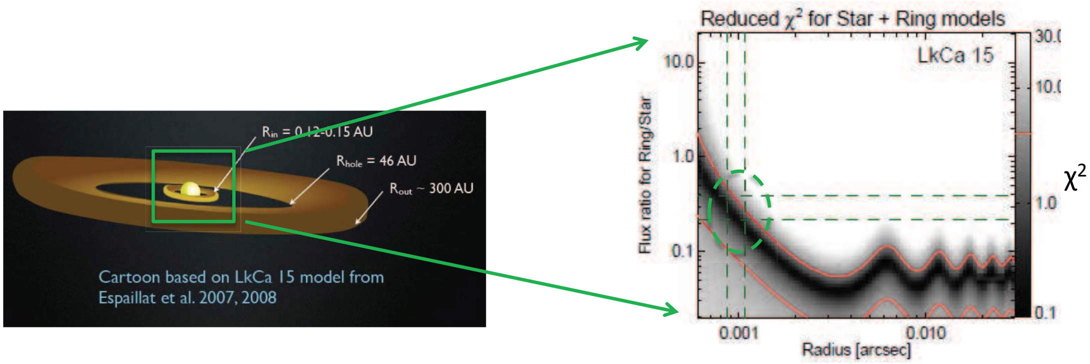

Figure 2: *Left: Sketch of the elements and size scales critical for transitional disks. Right: We resolve the innermost circumstellar disk at 0.1 AU scales. Right: Dark intensities show models consistent with the data, red contours are the 3 σ model rejection limits. The green dashed lines indicate advanced SED models, which coincide with our measurements. The data confirm the presence of a gap, which might have been opened during planet formation.*

Results

The observed visibilities exclude binaries with flux ratios of at least 0.05 and separations ranging from 2.5 to 30 mas (0.35 - 4 AU) over $\geq$ 94% of the area covered. It is shown that the few binary solutions found are likely artefacts of our sparse u, v-sampling. However, a statistical analysis reveals that, unlike in the CoKu Tau/4 system, binarity is in general not responsible for either clearing disk holes to produce transitional-disk-type SEDs, or for the near-infrared excess over the photospheric emission. These interferometric observations extend the finding of similar binary searches, based on diffraction limited 10 m class telescope imaging, down to ten times smaller projected separations.
Instead, we spatially resolve the NIR excess in all five stars. By fitting a toy disk model to the data, we find that this inner disk emission typically comes from radii of about 1 mas (0.15 AU), consistent with previous work. In particular, these findings are consistent with recent disk models fitting spatially unresolved spectro-photometric data of transitional disks (Fig. 2). We confirm that the transitional disk phase is often characterized by several distinct dust zones: an inner (of order 0.1 AU), and an outer part (of order > 10 AU) which are not smoothly connected by a continuous distribtion of optically thick material. In each of our targets, the habitable zones are devoid of optically thick dust emission. The fact that we resolve excess emission very close to the star in a transitional disk, which lacks such emission further out, underlines that the evolution of a primordial disk is not as simple as a clearing from the inside out due to photoevaporation. In fact, the presence of gaps suggests that we may see the effect of planet formation on disks.

Collaborators are: Elise Furlan (JPL), Andrea M. Ghez (UCLA), Stanimir Metchev (Stony Brook), Marshall D. Perrin (UCLA)
The presented results have been *submitted* to the Astrophysical Journal.

References

[1] Meyer, M. R., Beckwith, S. V. W., Herbst, T. M., & Robberto, M. 1997, ApJ, 489, L173

[2] Pott, J.-U., Perrin, M. D., Furlan, E., Ghez, A.M., Herbst, T., Metchev, S., 2010, ApJ, 710, 265

The T Tau triple system: a fresh look

Roy van Boekel, Thorsten Ratzka, Maiken Gustafsson, Thomas Henning, Rainer Köhler

T Tauri has traditionally served as the prototype of young, low-mass stars, and has been extraordinarily well studied. It has proven to be an observer's playground in which many aspects of the star formation process, such as multiplicity, accretion, outflow activity and jets, disk structure and evolution, etc., can be studied in detail due to the relative proximity of the system (148 pc, Loinard et al. 2008). In this contribution we report on new insights in the system, gained from state of the art observations performed with the VLT.

Astrometry of the Sa-Sb orbit

The optically visible star T Tau N has an "infrared companion" (T Tau S) located ≈0.7 arcseconds south of the optically visible star (Dyck et al. 1982). The infrared source itself is a close binary with components Sa and Sb (Koresko 2000), making the whole system at least a triplet. In particular the southern close binary offers an excellent opportunity to spatially resolve the orbital motion and obtain direct and unambiguous mass estimates of both pre-main sequence stars, as well as to study disk-companion interaction (more in the last subsection of this contribution). We have used VLT/NACO to do high-precision astrometric monitoring of the system. The northern component serves a an astrometric reference point, allowing to measure the individual orbits of Sa and Sb, and derive their individual masses, which are found to be: T Tau N $\approx 2.1\,M_\odot$ (indirect); Sa $\approx 2.2\,M_\odot$; Sb $\approx 0.4\,M_\odot$ [2, 3].

H_2 emission from the disk around T Tau N

The T Tau system shows prominent emission lines of molecular hydrogen. In order to characterize this emission, and to clarify its spatial origin and physical emission mechanism, we have observed the T Tau system with the adaptive optics 3D integral-field spectrograph SINFONI at the VLT. We have detected emission from the H_2 v=1-0 S(1) rovibrational line at 2.1 μm and could trace it between $0\farcs1$ (≈15 AU) and $0\farcs7$ (≈100 AU) from T Tau N, around which it appears to arise in a ring-like structure (Fig. 1, left). Radial velocities of the H_2 emitting gas (Fig. 1, right) were obtained by fitting the line centroids in the dispersion direction. The velocities are consistent with the rest velocity of T Tau N and the H_2 emission does not seem to arise in a collimated outflow. Both the morphology and the velocity of the H_2 emitting gas suggest that the emission arises from the disk of T Tau N. This is the first spatially resolved map of H_2 emission from a circumstellar disk around a young star. The total flux of the v=1-0 S(1) line is similar to previous (spatially unresolved) measurements of H_2 in circumstellar disks.

SED modeling shows that the T Tau N system is consistent with an accreting star surrounded by a disk and a torus-like envelope with an opening angle of ∼45°. The disk is likely to have an outer radius of 85 AU consistent with the detection of H_2 at a radius of ≈100 AU. We have also examined the H_2 excitation mechanism. Both shocks impinging on the surface of a disk and irradiation of a disk by UV-photons and X-rays from the central star are plausible candidates for the H_2 excitation mechanism. However, irradiation should not create a large degree of excitation at radii larger than ∼20 AU. Most likely the H_2 emission arises in the atmosphere of a flared disk, where the gas is excited by shocks created when a wide-angle wind impinges on the disk. The H_2 emission could also originate from shock excitation in the cavity walls of an envelope, but this requires an unusually high velocity of the wide-angle wind from T Tau N. These results have appeared in A&A [1].

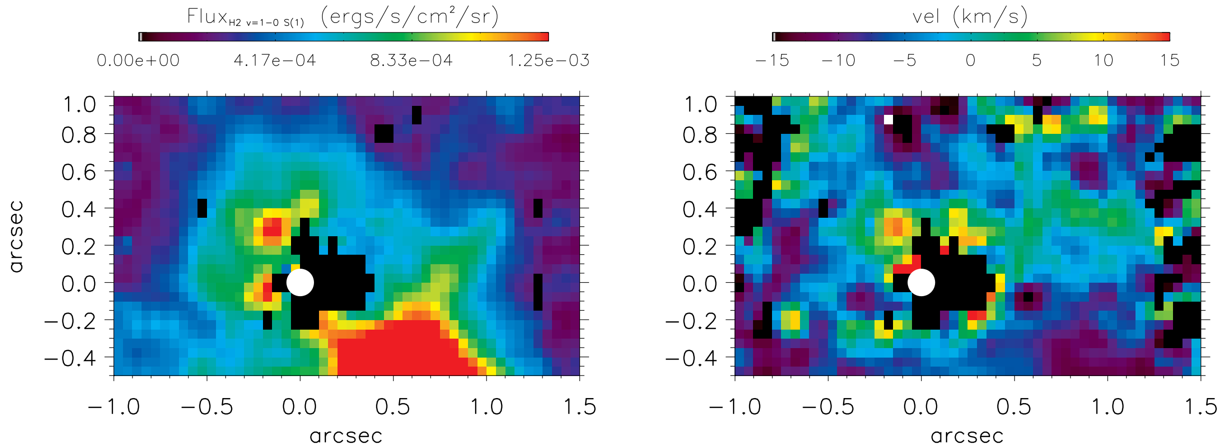

Figure 1: *Left: H_2 v=1-0 S(1) emission surrounding T Tau N observed with VLT/SINFONI. Right: The radial velocity of the H_2 emitting gas relative to the rest velocity of T Tau N. The position of T Tau N is marked by a white circle.*

The variability of Sa: a companion induced accretion outburst?

The apparent brightness of the southern infrared companion was found to vary strongly in time, ≈2−3 magnitudes, at near- and mid-infrared wavelengths (Ghez et al. 1991). High spatial resolution observations have identified Sa as the main variable component. Initially, these brightness fluctuations were attributed to variations in the intrinsic luminosity of the system, caused by a variable accretion rate. However, intensive multi-band photometric monitoring over a number of years has led to a paradigm shift: in recent years the variability of T Tau S has been attributed to variable extinction due to inhomegeneous dust clouds passing through our sightline (Beck et al. 2004).

Based on the rapidity of the brightness variations that we detected at relatively long wavelengths in VLT/VISIR observations of the T Tau system (a brightening of ≈0.25 mag at 12.8 μm within 4 days), we argue that simple variable extinction *cannot* be the mechanism resposible for photometric fluctuations of T Tau S. Instead, rapid and substantial changes in the illumination of the disk surface are required. In a strongly accreting system with a variable accretion rate, this can readily be achieved.

We present updated light curves of the system at near- and mid-infrared wavelengths. We show that, contrary to previous claims, the observed “bluer when brighter” infrared color-brightness behavior of the variability *can* in fact be qualitatively reproduced using a disk model with a variable mass accretion rate. We speculate that the period of high and variable brightness that T Tau S has shown from the early 1990s to the early 2000s is due to gravitational perturbation of the Sa disk during the periastron passage of Sb around ≈1995. If this is so, we predict T Tau S to return to its “low” state soon, and remain there until the highly eccentric orbit of Sb takes it close to Sa once more, in ≈25−100 years. A paper reporting on these results has been submitted to A&A [4].

References

[1] M. Gustafsson, M. et al.,2008, A&A, 488, 235

[2] R. Köhler, T. Ratzka, T.M. Herbst, M. Kasper 2008, A&A, 482, 929

[3] R. Köhler 2008, Journal of Physics, 131, 2028

[4] R. van Boekel, A. Juhasz, Th. Henning, R. Köhler, T. Ratzka, J. Bouwman, and W. Kley 2010, A&A, submitted

The nature of debris disks

Thomas Henning, Veronica Roccatagliata, and Jeroen Bouwman

In circumstellar debris disks dust particles are produced by collisional interactions of planets and minor bodies. Through the study of the dust distribution, debris disks can provide important information on the dynamics of planetary systems. The radial extent and the total dust mass or fractional infrared luminosity are important parameters for the characterization of debris disks.

The dust in debris disk is often confined in ring-like structures as seen prominently in the Formalhaut system. Most known debris disks have a radius of 10-100 AU, resembling the Kuiper Belt in the Solar System. We have comprehensively characterized a large number of debris disks with multi-wavelength observations in order to better characterize their dust evolution. In addition, we have searched for the rare cases of warm debris disks around F-type stars.

Spitzer and Submillimetre Observations of Debris Dust around Solar-type Stars

Within the Spitzer Legacy Program "Formation and Evolution of Planetary Systems (FEPS)" we studied 314 stars in the age range between 3 Myr to 3 Gyr [1]. We used both IRAC and MIPS photometry and IRS low-resolution spectroscopy to search for excess emission from circumstellar disks. The fraction of disks exhibiting a 24 μm excess greater than 10% above the photosphere is 15% for ages smaller than 300 Myr and declines to 3% for older systems. The dust grains are relatively cold, similar in temperature to the dust grains located in the Kuiper Belt of our Solar System. The typical inner radius of the debris disks is at about 10 AU. For sources with detected 70 μm excess emission, the debris disks extend over tens of astronomical units. The lack of excess emission shortward of 16 μm and the relatively flat distribution of the 24 μm excess for ages smaller than 300 Myr is consistent with steady-state collisional models and does not require the occurrence of stochastic events. Another possibility is that the disks were cleared out to 10 AU by dynamical processes.

We also performed very sensitive (sub)millimtre dust continuum observations of about 150 debris disks around solar type-stars selected from the FEPS sample [3]. Despite the sensitivity of the survey most of the debris disks remained undetected, indicating very low dust disk masses (see Fig. 1). Statistical tests demonstrated that younger and older debris disk systems belong to different parent populations in terms of disk mass. In the case of the detected disks, the comparison between collisional and Poynting-Robertson timescales supports the hypothesis that these disks are dominated by collisions.

Discovery of New Warm Debris Disks around F-Type Stars

A very small number of warm debris disks have been detected around FGK-type stars. Most of them are associated with relatively young stars that are members of nearby moving groups. A very small number of warm disks have been identified around older solar-type stars, most notably the system HD 69830 which also harbors three Neptun-mass planets. These old system exhibit high fractional infrared luminosities that cannot be explained by steady-state asteroid belt evolution, where the planetesimals are collocated with the warm dust. Stochastic models are required to explain the properties of these disks with the most likely mechanism of the erosion of planetesimals scattered from an outer reservoir into the inner regions due to a dynamical instability. In a systematic search for debris disks around F-type stars we detected four disks with warm excess emission [2]. Three of the disks have properties consistent with the predictions of steady-state planetesimal disk evolution models. The oldest source, HD 169666, displays a

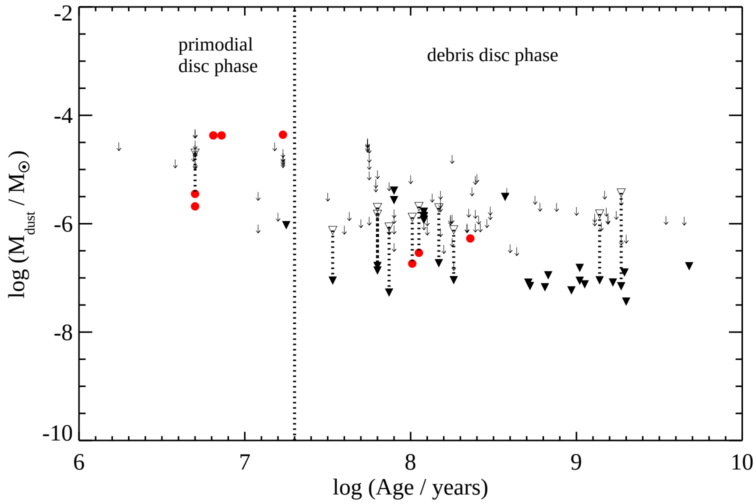

Figure 1: *Disk mass versus age of the systems. Filled circles are the masses determined from the IRAM detections and from the detections presented by Carpenter et al. (AJ 129, 1049, 2005). Upper limits are shown as filled triangles (new IRAM observations), empty and filled triangles (objects measured by Carpenter et al. (2005) and re-observed with higher sensitivity) and down arrows (from Carpenter et al. 2005). The sources observed in both studies are connected by dashed lines. The vertical line separates the sources younger than 20 Myr from older systems.*

dust fractional luminosity much too high to be in a steady state, requiring a recent transient event. The infrared spectra of this disk, separated by approximately three years, shows evidence for submicron- to micron-sized silicate grains. These observations indicate that the production of small grains is continuous over a timescale of a least a few years.

Main Collaborators are D. Apai (Space Telescope Science Institute, Baltimore), A. Moor (Konkoly Observatory, Budapest), J. Carpenter (Caltech, Pasadena), and M. Meyer (Steward Observatory Tucson/ETH Zurich).

References

[1] Carpenter J., Bouwman J., Mamajek E.E. et al.: 2009, Formation and Evolution of Planetary Systems: Properties of Debris Dust around Solar-Type Stars. ApJSS 181, 197.

[2] Moor, A., Apai, D., Pascucci I. et al.: 2009, The Discovery of New Warm Debris Disks around F-type Stars. ApJ, 700, L25.

[3] Roccatagliata, V., Henning, Th., Wolf, S. et al.: Long-Wavelength Observations of Debris Discs around Sun-like Stars. A&A, 497, 409.

The outcome of runaway growth in protoplanetary disks

Chris W. Ormel, Kees Dullemond

Planetesimal growth: runaway growth and oligarchy

Gravitationally-dominated growth becomes important when the velocity dispersion between bodies (u) becomes less than their escape velocity ($v_{\rm esc}$). Collisional cross sections between bodies are then increased by the gravitational focusing factor, $\sim(v_{\rm esc}/u)^2$, over their geometrical cross section. In protoplanetary disks, it is expected that gravity dominates the growth process among bodies of ∼km size or larger.

Gravitationally-dominated growth will be *runaway* when the growth timescale of the massive body *decreases* with increasing mass. This depends on the behavior of $u/v_{\rm esc}$. Initially $v_{\rm esc}$ increases much faster than u. The system is in runaway growth. However, at some point the protoplanets start to *stir up* the planetesimals much faster than they can accrete them. Then, $u/v_{\rm esc}$ increases; runaway growth ceases and so called *oligarchic* growth starts (Kokubo & Ida, 1998, Icarus, 131, 171).

We have modeled the point (e.g. size) where the transition between runaway growth and oligarchic growth takes place. This will be relevant for specifying the initial condition for models that treat the oligarchic growth phase of the protoplanets. Oligarchic growth can generally be well-approximated by a two component model (oligarchs and leftover planetesimals), which is relatively easy to model. However, runaway growth simulations are more challenging.

Runaway growth simulations

An example of a runaway growth calculation is plotted in Fig. 1. Runaway growth is character-

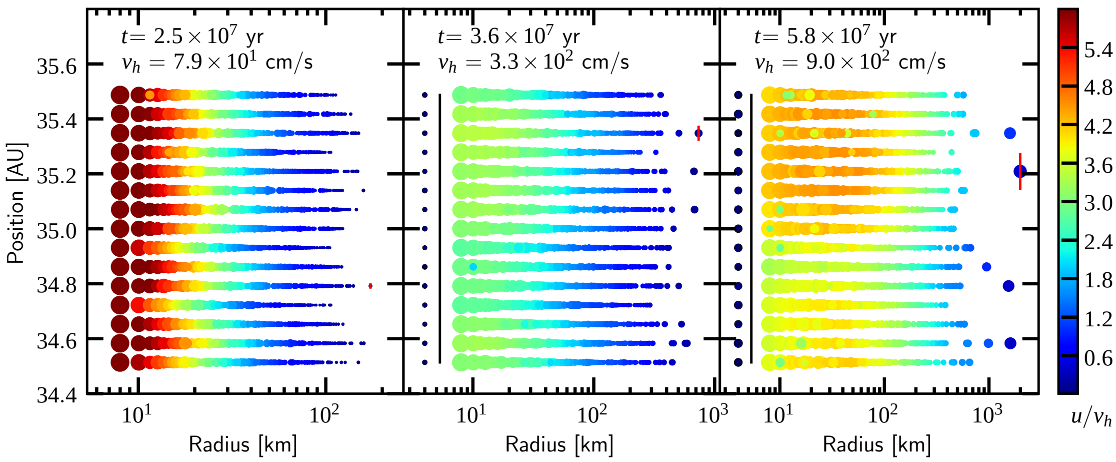

Figure 1: *The growth stages of a population of ∼10 km planetesimals to ∼10^3 km protoplanets. Each panel shows all bodies present in the simulation and indicates their: size (x-axis); radial position (y-axis); mass of the swarm (size of the dots); random velocity (or eccentricity, color shading). Velocities are normalized to the Hill velocity (indicated in the top of the panel). The Hill radius of the biggest body is indicated by a red bar.*

ized by a few high-mass bodies that growth faster ('run away') than the rest of the population. Therefore, it is imperative to *resolve* the high-mass fluctuations more clearly *and* to appreciate the discrete (particle) nature of bodies. As can be seen from the very small dots in the left panel, the Monte Carlo coagulation code resolves the high-mass particles very well. From Fig. 1 it is seen that initially the gravitationally factors decrease (the colors of the low-mass bodies become bluer) but that in the final panel the oligarchs have stirred up the small bodies: gravitational-focussing factors, while still very large, are decreasing. Therefore, at this stage the system is no longer in runaway growth but in oligarchy. One can see from the last panel in Fig. 1 that the big bodies (oligarchs) have separated from the rest of the population: the system can be well approximated by two components.

The Runaway growth/Oligarchy transition

We find that the minimum of the quantity $u/v_{\rm esc}$ (or $u/v_{\rm h}$, which is plotted in Fig. 1) indicates a maximum of gravitational focussing and agrees with the point where runaway growth ceases. Other big bodies will then 'catch up' with the most massive body in the system.

The simulations indicate that this transition occurs typically at radii of the largest object of $R_1 \sim 300$–10^3 km, depending somewhat on the initial conditions, see Fig. 2. However, our

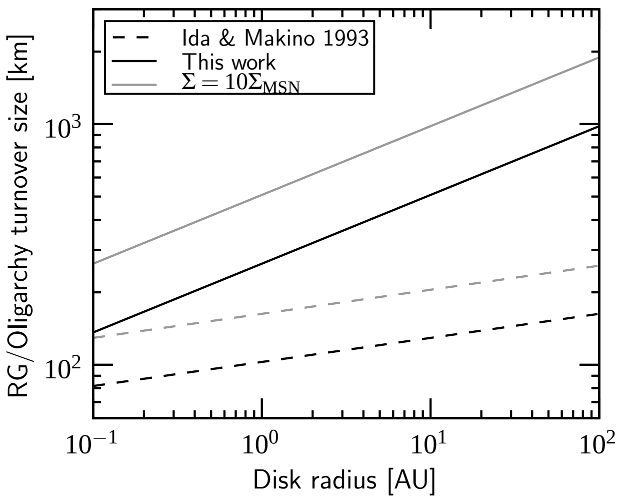

Figure 2: *The runaway growth/oligarchy turnover size as function of position in the disk for Ida & Makino (1993, Icarus, 106, 210) (dashed lines) and the result of the model (solid lines). The grey lines represents the case where surface densities are a factor of 10 larger. The initial planetesimal size is 10 km.*

simulations indicate that the turnover size occurs at a larger size than the criterion given by Ida & Makino (1993, Icarus, 106, 210) especially in the outer parts of the disk. Compared to the oligarchic growth phase, runaway growth is relatively rapid. Therefore, the new results somewhat alleviate the timescale problem for the accretion of massive cores in the outer regions of the disk.

Collaborators: Marco Spaans (Groningen), Rainer Spurzem (ZAH Heidelberg)

References

[1] Ormel, C.W., Dullemond, C.P., Spaans, M., 2010, ApJ, submitted

4 Brown Dwarfs and Exoplanets

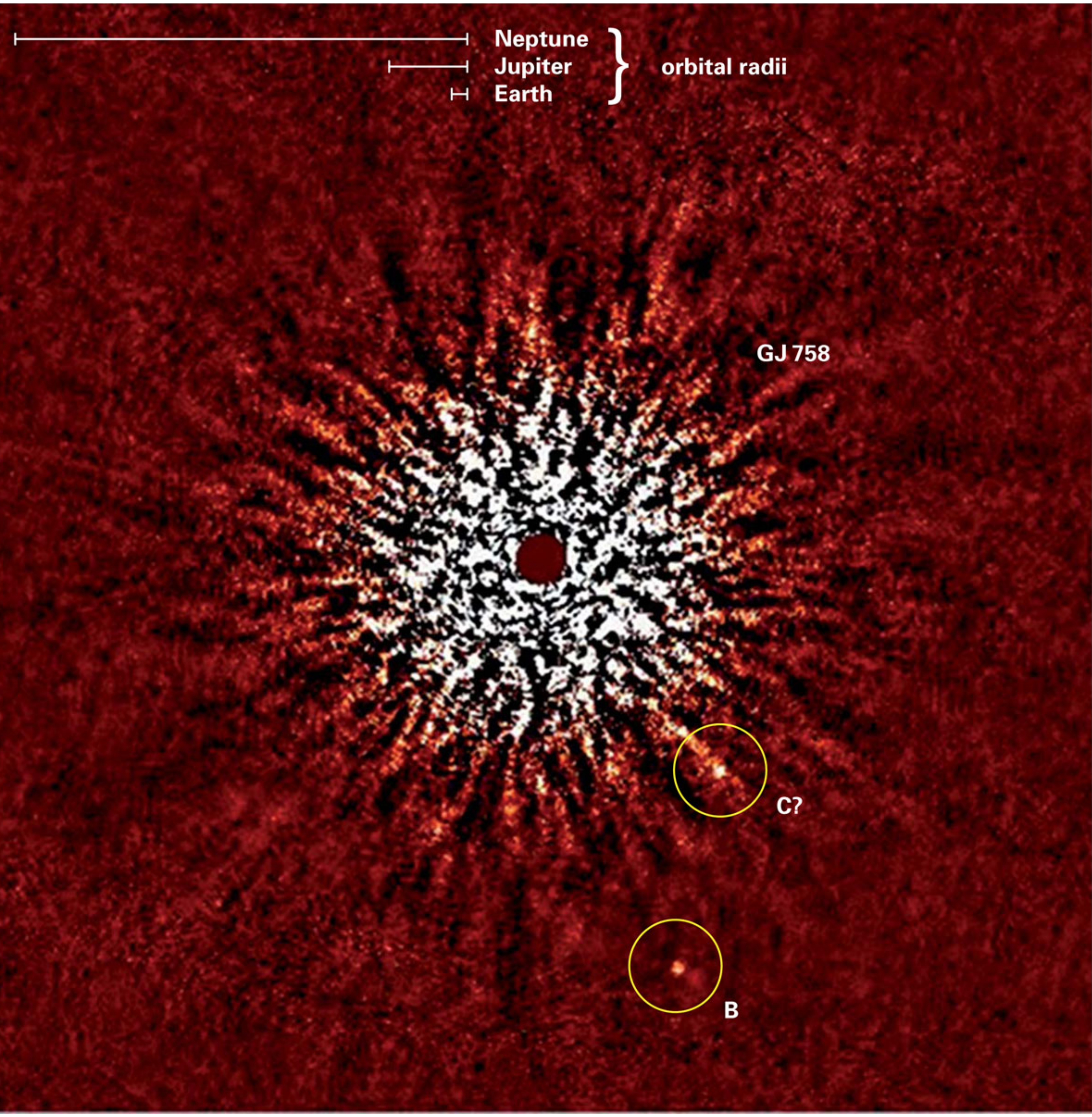

Image on previous page:
The August 2009 discovery image of GJ 758 B, taken with Subaru HiCIAO in the near infrared. Without the special technique employed here (angular differential imaging), the star's glare would overwhelm the signals from the planet candidates.
Credit: C. Thalmann et al. (MPIA) with colleagues from NAOJ

Rotational studies in the Orion Nebula Cluster: from solar mass stars to brown dwarfs.

María Victoria Rodríguez-Ledesma, Reinhard Mundt

Scientific background

Rotational studies at a variety of ages and masses are important for constraining the angular momentum evolution of young stellar objects (YSO). Of particular interest are the very low mass (VLM) stars and brown dwarfs (BDs), because of the significant lack of known rotational periods in that mass range.
The ONC is an excellent target for this kind of study since a large sample of young stellar and substellar objects can be photometrically monitored simultaneously in order to derive rotational periods. Several rotational studies in the ONC have been performed in the past, however they extend only down to masses of about $0.2\,M_{\odot}$ (e.g. [1]). We extend previous studies well down into the substellar regime, providing for the first time information on rotational periods for a large sample of young VLM stars and BDs.

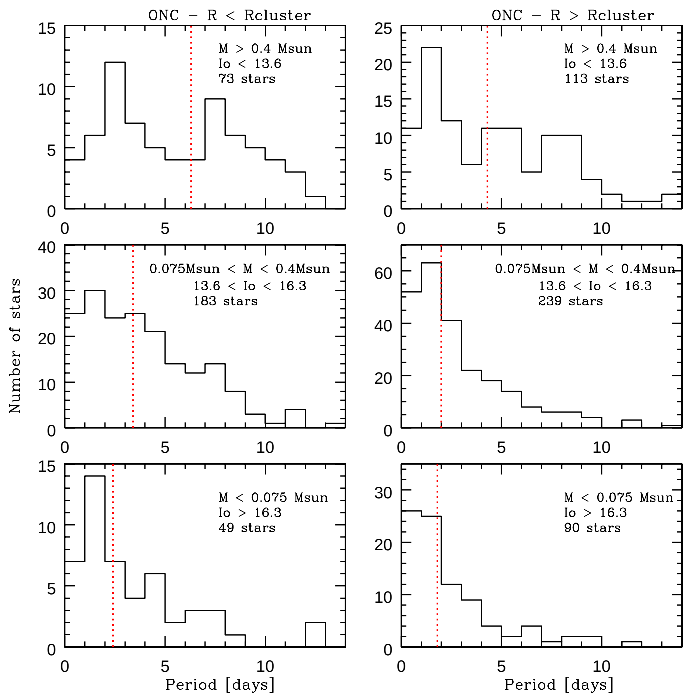

Figure 1: *Period distribution for the stars located inside (left) and outside (right) the cluster radius (∼ 1 pc). The mass regime for each panel is based on models by Baraffe et al. (1998, A&A, 337, 403), assuming a constant* $A_{\rm v} = 1.4$ *mag for all stars(see [3] for details). The medians of the periods for each panel are shown as dashed lines.*

Method and results

This extensive rotational period study of YSOs in the 1 Myr old Orion Nebula Cluster (ONC) is based on a deep photometric monitoring campaign using the Wide Field Imager (WFI) camera on the ESO/MPG 2.2m telescope on La Silla, Chile. Time series data was obtained with about 95 data points spread over 19 nights. Accurate I-band photometry of 2908 stars was obtained

within a magnitude range of 13 to 21 mag, i.e. extending three magnitudes deeper than previous studies in the ONC. Two different power spectral analysis techniques were used to search for periodic variability. In addition, the χ^2 variability test was used for the detection of irregular variables.
We found 487 periodic variables with estimated masses between 0.5 $M_\odot$ and 0.015 $M_\odot$, 124 of which are BD candidates. In addition to the periodic variables, 808 objects show non-periodic brightness variations. We study the dependence of the period distribution on mass and variability level and compare this with known objects in the ONC with masses up to 1.5 $M_\odot$ [1] and with the $\sim$2 Myr old cluster NGC 2264 [2]. As can be seen in Fig. 1, we find that substellar objects rotate on average faster than the VLM stars. In addition, our rotational data suggest a dependence of the rotational periods on position within the field, i.e. different period distribution found for objects inside and outside the so-called cluster radius as shown in Fig. 1 (see [3] for details), which can be explained by a possible age spread in the ONC with a somewhat younger central region. The results of a comparison between the period distributions of the ONC and NGC 2264 favours this hypothesis. An interesting correlation between rotational period and amplitude of the modulation (Fig. 2), in which periodic variables with larger peak-to-peak amplitudes rotate on average slower than those with small peak-to-peak amplitude variations was found, which can possibly be explained by different magnetic field topologies.

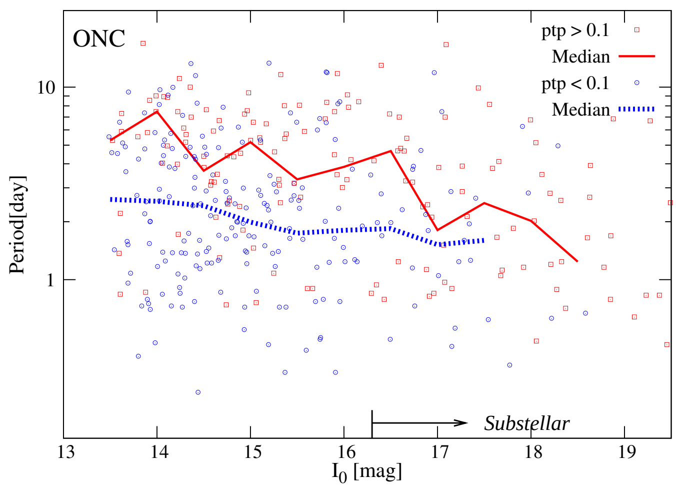

Figure 2: *Period as a function of magnitude (mass) for two different variation amplitudes. The indicated medians of the rotational periods are calculated within 0.5 magnitudes bins.*

This project is done in collaboration with Jochen Eislöffel (LWS Tautenburg).

References

[1] Herbst, W., **Bailer-Jones, C.A.L. Mundt R., Meisenheimer, K.**, Wackermann, R.,2002,ApJ, 396, 513.

[2] **Lamm M., Bailer-Jones, C.A.L., Mundt R.**, Herbst, W., Scholz A.,2004,A&A, 417, 557.

[3] **Rodríguez-Ledesma, M. V., Mundt R.**, Eislöffel, J. 2009,A&A, 502, 883.

Constraints on brown dwarf formation via ejection: radial variation of the stellar and substellar mass function of the young open cluster IC2391

Steve Boudreault & Coryn A. L. Bailer-Jones

Introduction

The origin and evolution of brown dwarfs (BD) remains a fundamental open question. BDs have masses bridging the lowest mass hydrogen-burning stars and giant planets, so any picture of star and planet formation is incomplete if it cannot account for BDs. Several formation mechanisms have been proposed, including star-like formation from the compression and fragmentation of a dense molecular cloud, planet-like formation in a circumstellar disk, and the dynamical interruption of a star-like accretion process. There are observational signatures which may be used to distinguish between these scenarios, such as the distribution of binaries, the presence and properties of circumstellar disks, the (initial) mass function (MF) and kinematics (see [2] for a review of observational signatures on the formation of BDs). Here we present the stellar and substellar mass function of the open cluster IC 2391, plus its radial dependence, and use this to put constraints on the formation mechanism of brown dwarfs.

Observations

The survey consists of 35 34×33 arcmin fields extending to 3 degrees from the center of the cluster and centered on RA=08:40:36 DEC=-53:02:00. The total coverage of our survey is 10.9 sq. deg. The optical observations were carried out in four runs with the Wide Field Image (WFI) on the 2.2m telescope at La Silla. The fields in our survey were observed in four medium bands filters, namely 770/19, 815/20, 856/14 and 914/27 (where the filter name notation is central wavelength on the full width at half maximum, FWHM, in nm) and one broad band filter, R_c. These filters were chosen to sample the spectra of late M and early L dwarfs to improve selection over, say, $R_c - I_c$, and to minimize the Earth-sky background plus any nebular emission (as the filters are in regions of low emission). In order to improve the determination of their low mass status (via a better determination of spectral type and luminosity), we also observed all radial fields, including the outward fields, in the J–band using the *Caméra PAnoramique Proche-InfraRouge* (CPAPIR) on the 1.5m telescope at Cerro Tololo, Chile. Our 10σ detection limit is J=17.7 and 914/27=20.5, which corresponds to $\sim$0.03 $M_\odot$ for both cases.

The spectroscopic observations were carried out with HYDRA, a multi-object, fiber-fed spectrograph on the 4m telescope at Cerro Tololo on two nights. Only two fields could be observed (3 and 2 exposures of 45 minutes respectively). We used the red fiber cable with the KPGLF grating (632 lines mm^{-1}) and a blaze angle of 14.7° (no blocking filter was used) and . This gives us a coverage of 6429–8760 Å centered at 7593 Å and a spectral resolution of 4.0 Å.

Photometric and spectroscopic results

We observed a radial variation in the MF from 0.072 to 0.3$M_\odot$, but we do not observe a significant radial variation in the MF in the substellar regime (Fig. 1). This comparative lack of radial variation below the substellar boundary is what we would expect with the ejection scenario for brown dwarf formation, but considering that IC2391 has an age about three times older than its crossing time we might expect that most of the brown dwarfs with velocity dispersion greater than the escape velocity have already escaped the cluster [3]. On the other hand, the rather homogeneous distribution of the substellar objects and the clustered distribution of stellar objects within $\sim$2° from cluster center could be a signature that mass segregation via dynamical

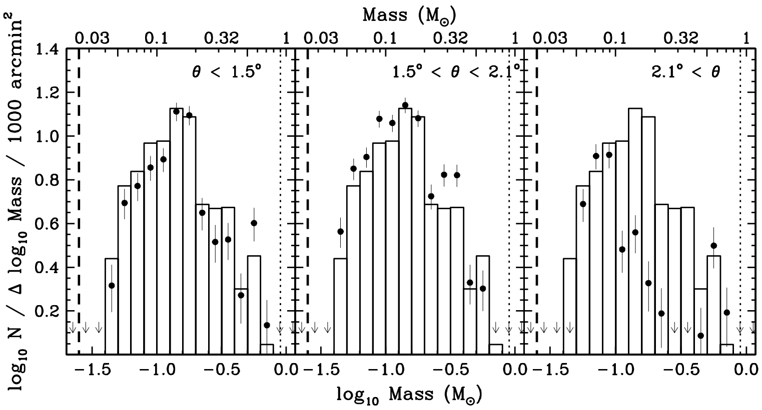

Figure 1: MF based on photometry for all radial fields. The 10σ detection limit is shown as a vertical dashed line. Dots in each panel represent the MF of (*left*) fields within 1.5° of the cluster center, (*center*) fields within the annulus from 1.5° to 2.1° and (*right*) the MF of fields outside of 2.1°. Error bars are Poissonian arising from the number of objects observed in each bin. The histogram is the MF for all fields within 2.1° of the cluster center. The vertical thin dotted line is the mass for which saturation start to occur in the short exposures.

evolution has occurred in IC2391, or that this mass segregation is of primordial nature. We have concluded that if this cluster is dynamically unevolved and if the brown dwarfs have a higher velocity dispersion than the stars, then our observations are consistent with brown dwarf formation by the ejection hypothesis.

In addition to our radial study, we demonstrated that a long spectral baseline permits a better determination of the energy distributions and thus helps the rejection of objects (in particular field M dwarfs) based on observed magnitude vs. predicted magnitude from models. Also, red giant contamination may be reduced by using medium bands such as 770 nm, 815 nm, 856 nm and 914 nm, and theoretical colours of red giants. We saw some variation in the colours of the main (field star) locus in colour-magnitude diagrams, which we attribute to variable extinction affecting the background stars.

Our spectroscopic follow up has confirmed that selection based on these filters resulted in no red giant contaminants among our sample of candidates. From our spectroscopic follow-up, of 17 photometric candidates we confirm 9 objects (i.e. half) as true cluster members. Of these, two are new brown dwarf members of IC2391. We also find that the Hα line cannot be used as a membership criterion from fiber spectroscopy at low spectral resolution (spectral dispersion of 1.14Åper pixel) because of spatially variable diffuse Hα emission. This prevents reliable sky subtraction around this line when using a fiber spectrograph with fibers assigned for sky subtraction and assuming a uniform background at a galactic latitude of b∼-6°.

The results from our work on IC2391 are presented in a publication in the Astrophysical Journal [1].

References

[1] Boudreault, S & Bailer-Jones, C. A. L., 2009, ApJ, 706, 1484

[2] Luhman, K. L., Joergens, V., Lada, C., Muzerolle, J., Pascucci, I. & White, R., 2007, Protostars and Planets V, 443

[3] Moraux, E & Clarke, C, 2005, A&A, 429, 895

Binary frequency of brown dwarfs at separations smaller than 3 AU

Viki Joergens

Where lies the peak of the brown dwarf binary separation distribution?

Searches for companions to brown dwarfs are of primary interest for understanding brown dwarf formation, for which no widely accepted model exists (e.g. Luhman et al. 2007, PPV 443). The frequency and properties of brown dwarfs in multiple systems are fundamental parameters in formation models. In recent years, many brown dwarf binaries were detected through direct (AO or HST) imaging searches, which probe mainly orbital separations greater than 3–10 AU (e.g. Burgasser et al. 2007, PPV 427). The binary frequency found in these surveys is 10-20% and the separation distribution has a peak around 3-10 AU, i.e. close to the incompleteness limit (see Fig. 1). It was therefore suspected that the largest fraction of brown dwarf binaries remained yet undetected, i.e. that the peak of the separation distribution might lie in the unprobed range. A means to study very close separations are radial velocity (RV) surveys for Doppler shifts introduced by unseen companions. First RV surveys of brown dwarfs were started at large telescopes, however, due to limited timely duration or sensitivity they can probe only to separations smaller than 0.1-0.6 AU (e.g. Joergens 2006, A&A 446, 1165; Basri & Reiners 2006, ApJ 132, 663; Maxted et al. 2008, MNRAS 385, 2210) leaving an important range unprobed.

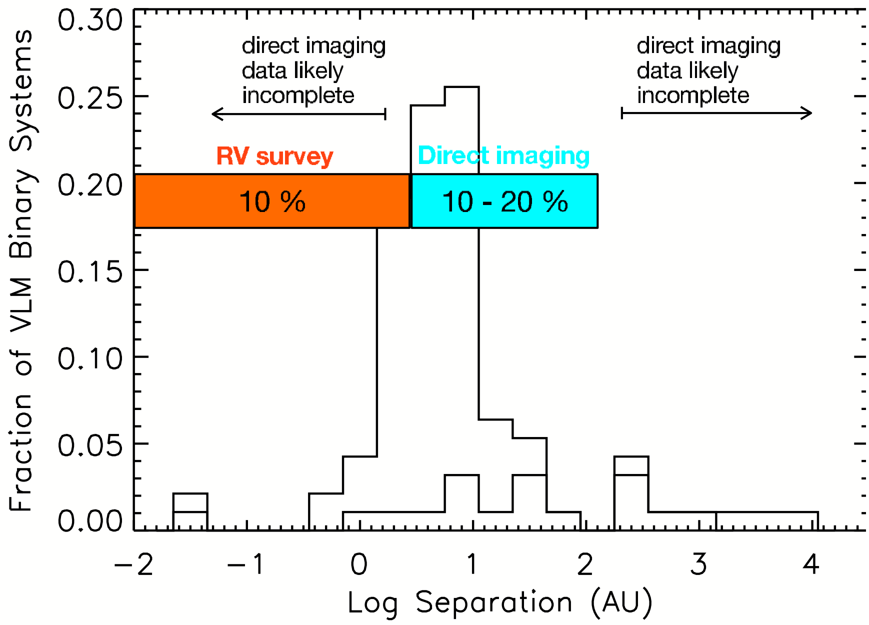

Figure 1: *The separation distribution of currently known brown dwarf and very low-mass stellar binaries found mainly by direct imaging. The peak around 3-10 AU is close to the incompleteness limit. Based on the here described RV survey, it was for the first time possible to study the binary fraction in the whole unprobed range of small separations (red). We find that the fraction of unresolved brown dwarf binaries at separations <3 AU (10%) is not exceeding that at larger separations (10-20%).*

Radial velocity survey of brown dwarfs with the VLT

Recent work for the first time extends high-precision radial velocity surveys of brown dwarfs out to 3 AU [1] with a sensitivity to detect giant planets (e.g. Joergens & Müller 2007, ApJ 666, L113). Based on more than six years UVES/VLT spectroscopy the binary frequency of brown dwarfs and (very) low-mass stars (M4.25-M8) in Chamaeleon I was determined: it is 18^{+20}_{-12} % for the whole sample and 10^{+18}_{-8} % for the subsample of ten brown dwarfs and very low-mass stars (M$\leq$ 0.1 $M_{\odot}$). Fig. 2 shows the superiority of this RV survey compared to other current RV surveys of brown dwarfs and very low-mass stars based on a Monte-Carlo simulation.

Now for the first time companion searches of (young) brown dwarfs cover the whole orbital separation range and the following observational constraints for models of brown dwarf formation can be derived: (i) the frequency of brown dwarf and very low-mass stellar binaries at <3 AU is not significantly exceeding that at >3 AU; i.e. direct imaging surveys do not miss a significant fraction of brown dwarf binaries; (ii) the overall binary frequency of brown dwarfs and very low-mass stars is 10-20 %; (iii) the decline of the separation distribution of brown dwarfs towards smaller separations seem to occur between 1 and 3 AU; (iv) the observed continuous decrease of the binary frequency from the stellar to the substellar regime is confirmed at <3 AU providing further evidence for a continuous formation mechanism from low-mass stars to brown dwarfs. Very recently, in a large observational effort the sample of the survey in Cha I could be substantially enlarged which will allow significant improvements to the statistics.

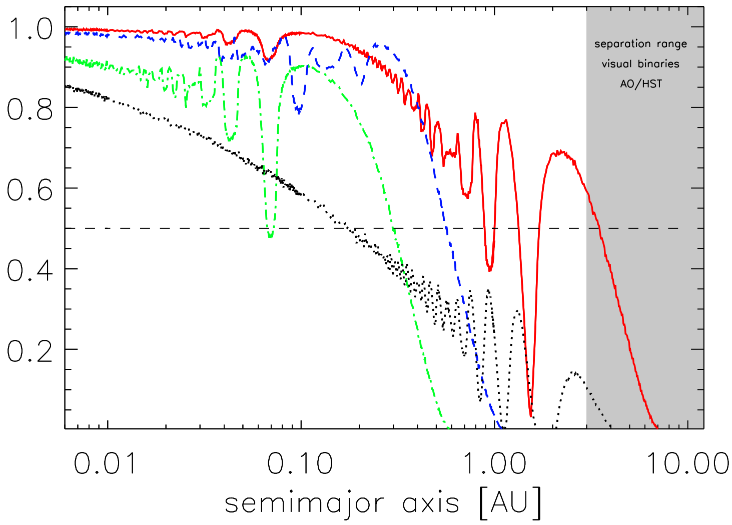

Figure 2: *Detection probability of binary systems in several RV surveys of brown dwarfs and very low-mass stars. The investigation conducted at the MPIA and described above (red) is the most sensitive one. It allows for the first time to investigate the whole range of unresolved brown dwarf binaries and to provide an overlap with current direct imaging surveys with AO/HST. The gray region shows the sensitivity of current direct imaging surveys. From [1].*

References

[1] Joergens, V., 2008, A&A, 492, 545

Kelu-1 AB – a possible brown dwarf triple system: First resolved spectra and dynamical mass estimates

Micaela Stumpf, Wolfgang Brandner, Thomas Henning, Felix Hormuth, Viki Joergens

The degeneracy in the mass-luminosity (age-temperture) relation of substellar objects makes it hard to establish the physical properties of isolated, single brown dwarfs in order to improve and calibrate the evolutionary models and to guide the interpration of the observations. These issues were directly addressed with a detailed study of the benchmark L dwarf binary Kelu-1 AB and its properties, benefitting from the fact that the system components are expected to be coeval, removing part of the mentioned degeneracy.

Orbital parameters and dynamical mass estimate

Continuous high-spatial resolution astrometric and photometric monitoring over three years and an overall observational period of ~ 10 years enabled us to compute the orbital parameters and derive the first dynamical mass measurement for the system with no evolutionary models involved in the calculations. We found a quite eccentric orbit, seen almost edge-on. The period of 38^{+8}_{-6} years and a semi-major axis of $6.4^{+2.4}_{-1.3}$ AU yields a total system mass of $185^{+139}_{-57}\,M_{\rm Jup}$ which is slightly higher than one would expect in a BD-BD binary system (see Fig. 1).

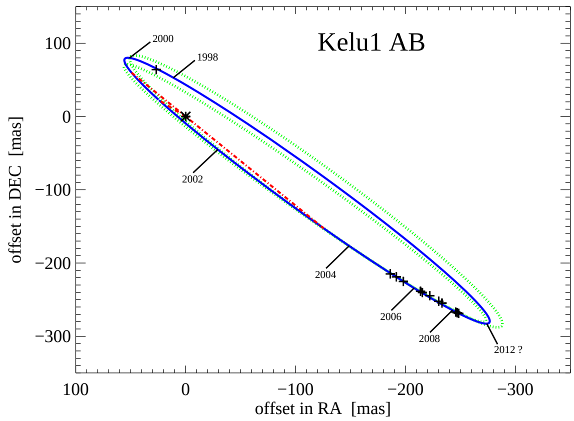

Figure 1: Orbit of the Kelu-1 AB system. The star indicates the position of Kelu-1 A while the measurements for the relative motion of Kelu-1 B around Kelu-1 A are indicated by crosses. Measurement errors are comparable to or smaller than the plotted symbols. The resulting best orbit fit is represented by the solid, blue curve and the green, dotted lines show the orbits at the 90% confidence limit (with periods of 32 and 46 years). The red, dash-dotted line marks the line of nodes and the dashed line indicates the position of the periastron. In addition the positions on January 1^{st} for the years 1998-2008, as well as the predicted position for 2012 are marked.

Spectral types and Photometry

Furthermore, for the first time spatially resolved spectra of the system components were achieved. The near-IR spectra display interesting peculiarities for each component. The spectrum of Kelu-1 A shows a distinct cup-shaped dip from 1.6 - 1.65 μm which did not fit any early, single L dwarf spectrum, but could be best reproduced by a combined spectrum of an early L and late T dwarf (Fig. 2). Our spectral template matching algorithm leads to the result that Kelu-1 A itself is

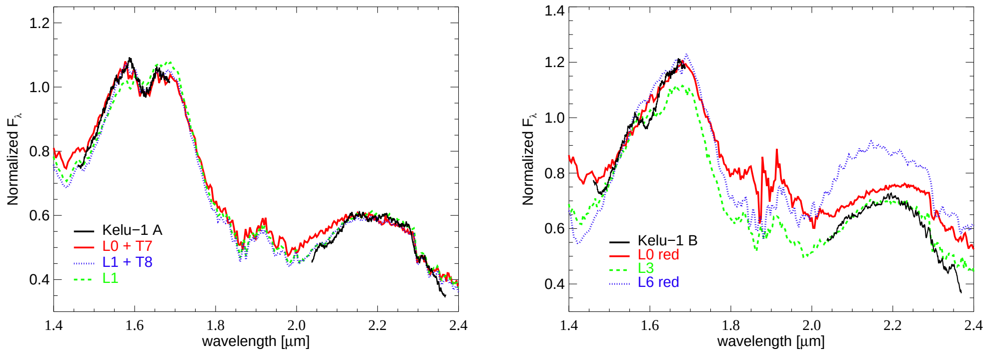

Figure 2: *Left*: H- and K-band spectrum of Kelu-1 A (smoothed to template resolution, solide line) compared to the best-fit binary composites and in addition compared to a single L1 object spectrum. The composites reproduce the deep depression at 1.6 - 1.65 μm to a much higher accuracy. *Right*: Spectrum of Kelu-1 B compared to two single red L dwarfs (L0 and L6) and a field L3 dwarf. The distinct FeH absorption dip around 1.58 μm is present in the L3 spectrum, but not in the L0 pec or L6 spectra, while the overall slope better fits the red objects.

a close unresolved binary with spectral types of L0.5 $\pm$ 0.5 and T7.5 $\pm$ 1. In contrast, Kelu-1 B is characterized by a triangular-shaped continuum, similar to very young red L dwarfs and was classified as L3 pec $\pm$1.5 . The first derived resolved L-band photometry for any L dwarf binary and the resulting near-IR colors supported these spectral type determinations. However, a comparison of the total system mass established from evolutionary models ($116 \pm 4\ M_{\rm Jup}$, for an upper limit of the system age of 0.5 Gyr) with the dynamical mass estimations ($185^{+139}_{-57}\ M_{\rm Jup}$) revealed a discrepancy of $\sim 1.5\,\sigma$.
Interestingly, while for several very low mass (VLM) binary systems the so far derived dynamical mass determinations are in agreement with model predictions, similar discrepancies to the models, like for Kelu-1 AB, have been recently reported also for other brown dwarf binary systems (Cardoso et al. 2008; Ireland et al. 2008; Konopacky et al. 2009). There have been different approaches to interpret these disagreements. In the case of Kelu-1 AB, the explanation for the discrepancy of dynamical masses with model predictions might be completely different: The spectroscopic evidence of a third, yet unresolved, system component, could account for the “missing mass”.

Next steps: Upcoming HST and VLT observations of the Kelu-1 AB system include resolved optical spectroscopy to ascertain in which component Li absorption is present and thus help to better establish the age of the components. In addition, it will extend the individual spectral type determinations into the red optical wavelength regime and provide more insight into the physical properties which cause the peculiar shapes of the components SEDs. A high-resolution near-IR radial velocity monitoring program has been started, with the aim to determine the individual component masses and possibly reveal radial velocity signatures of the potential third component, although this depends critically on the component masses of Kelu-1 Aab. Together with the continuation of the astrometric monitoring, the upcoming results will help to refine the orbital parameters and dynamical mass determination and will make Kelu-1 AB an even more powerful benchmark object for the calibration of evolutionary models.

Collaborators are H. Bouy (IAC, ESAC), R. Köhler (ZAH), M. Kasper (ESO)

References

[1] M. Stumpf et al. 2010, submitted to A&A

An oasis in the brown dwarf desert. A close brown dwarf companion to GJ 1046 (M2.5V)

Martin Kürster

The brown dwarf desert

The paucity of brown dwarf companions to solar-like stars at separations of a few AU or less was already noted by Campbell et al. (1988, ApJ 331, 902) in their early precision radial velocity (RV) survey. This "brown dwarf desert" is currently not well understood. Two distinctive formation mechanisms seem to be at work for planetary ($M \leq 13$ $\mathrm{M_{Jup}}$) and stellar ($M \geq 0.08$ $\mathrm{M_{\odot}}$) companions with relatively little overlap between the two. At wide separations no "brown dwarf desert" is observed. The fact that close-in brown dwarf companions are rare is highly significant since the commonly employed radial velocity (RV) method to search for sub-stellar companions to stars is very sensitive to such objects.

We have found a candidate brown dwarf companion to the M2.5V star GJ 1046 in our precision RV survey carried out with the UVES spectrograph at the ESO VLT in search for planetary and substellar companions to M dwarfs. If this candidate is confirmed, the system would be unique in that it would contain the first close-in ($a = 0.42$ AU) brown dwarf companion to a main-sequence star of spectral type early-M (M0V–M5V).

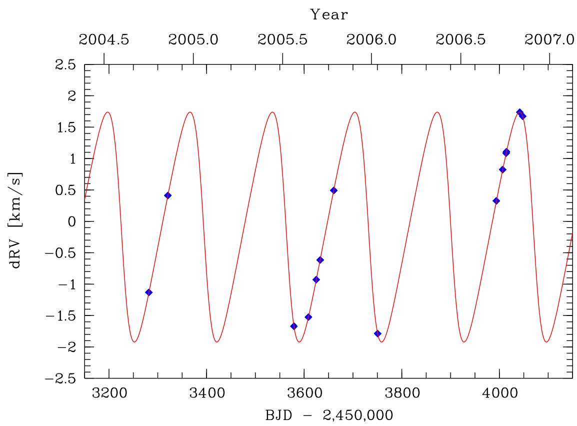

Figure 1: *Time series of UVES RV data for GJ 1046. The solid line corresponds to the Keplerian solution with a period of* 169 d.

Observations and results

Fig. 1 shows our RV time series (14 data points) for GJ 1046 as well as the best-fit Keplerian orbit (solid line). To attain high measurement precision UVES was self-calibrated with its iodine gas absorption cell. The RV measurement error is 3.63 $\mathrm{ms^{-1}}$ on average, much samller than the plot symbols. We find an orbital period of 169 d, an eccentricity of 0.28 and an RV semi-amplitude of 1831 $\mathrm{ms^{-1}}$. Due to the unknown inclination of the orbit only a minimum companion mass of 26.9 $\mathrm{M_{Jup}}$ can be determined (for a stellar mass of 0.398 $\mathrm{M_{\odot}}$). The semi-major axis of the orbit is 0.42 AU. From geometric arguments one can show that there is a probability of just 6.2% that the inclination is less than 20.4° at which value the companion mass would exceed the stellar mass threshold. By simulations we can show that the absence of effects from the secondary spectrum constrains the companion mass to $m \leq 229$ $\mathrm{M_{Jup}}$ (see [1] for details).

Constraining the companion mass via Hipparcos astrometry

Using the Hipparcos parallax (71.11 mas) of GJ 1046 together with the RV-derived orbital parameters we can predict the minimum astrometric signal of the stellar reflex motion to be 3.7 mas peak-to-peak. This corresponds to the full minor axis of the orbit. Since the Keplerian fit to the RV data only permits the determination of the projected orbit of the stellar reflex motion, the true astrometric effect could be considerably higher. For an inclination of 20.4° corresponding to the brown dwarf/stellar mass threshold the full minor axis of the stellar orbit would extend 10.6 mas on the sky.

We have analysed the Hipparcos Intermediate Astrometric Data for GJ 1046 using the new reduction of the raw data by van Leeuwen (2007, A&A 474, 653) and following the approach described in Reffert & Quirrenbach (2006, A& 449, 699). The result is shown in Fig. 2. The combination of RV and Hipparcos data yields a 3σ upper mass limit to the companion mass of 112 M_{Jup} with a formal (but insignificant) optimum value at $m = 47.2\ M_{Jup}$. From the combination of RV and astrometric data, the chance probability that the companion is a star is merely 2.9%. We therefore conclude that the companion is most likely a brown dwarf.

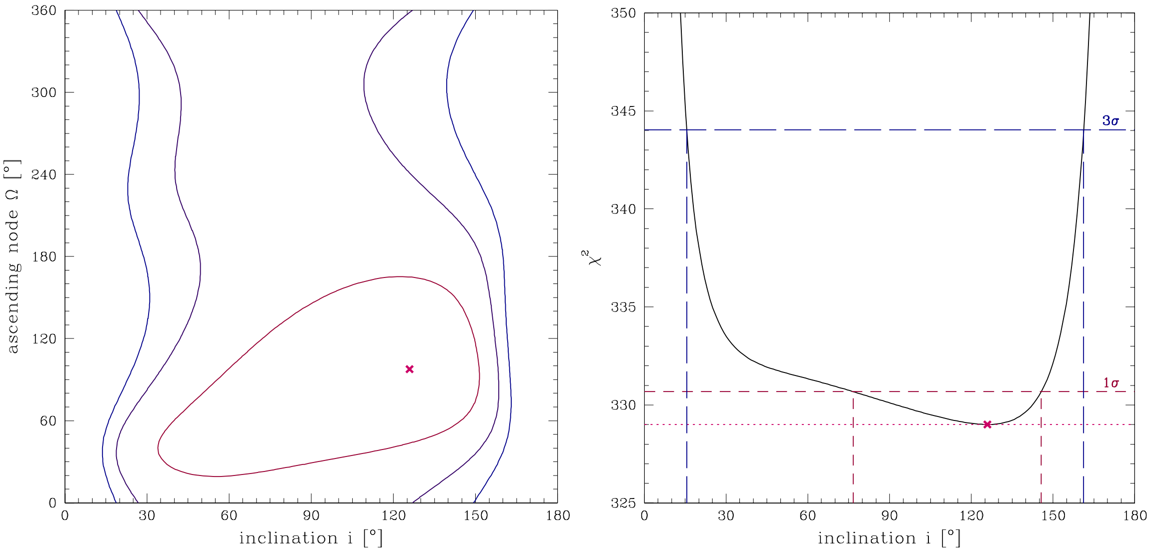

Figure 2: **Left:** χ^2 *contours for fitting a substellar companion to the Hipparcos data of GJ 1046 with spectroscopic parameters fixed at their RV-determined values. The orbital inclination i and the ascending node* Ω *were free parameters of the fit, as were corrections to the standard five astrometric parameters in the Hipparcos Catalogue. The contours represent two-parameter joint confidence levels at* 1, 2, *and* (3σ). *The formal best-fit solution is indicated by a cross.* **Right:** χ^2 *of the astrometric orbit as a function of inclination only. In this case the* 1σ *and* 3σ *confidence levels indicated by the horizontal dashed lines correspond only to the single parameter i (treating* Ω *as uninteresting) Again the formal best fit solution is indicated by a cross.*

Collaborators on this project are Michael Endl (University of Texas at Austin) and Sabine Reffert (ZAH Heidelberg)

References

[1] Kürster, M., Endl, M., Reffert, S., 2008, A&A 483, 869

New ultra-cool brown dwarfs in the solar neighbourhood

Bertrand Goldman, Sylvain Marsat, Thomas Henning

A valuable class of brown dwarfs

Cool brown dwarfs (BDs) with effective temperatures lower than 1800 K are characterized by complicated atmospheric processes that profoundly affect their emerging spectral energy distribution. A valuable sub-class of BDs are those for which we can obtain more information than is usually the case for isolated BDs. As BDs cool with age, it is difficult to disentangle the effects of a higher mass and a younger age; gravity measurements are difficult to obtain for those faint objects, and high-spectral resolution modeling is complex. Objects associated with a cluster, or a brighter companion, may be used as *benchmark brown dwarfs* (Burningham et al., 2008, MNRAS 391, 320).

Recent surveys, such as 2MASS, DENIS or SDSS have brought a wealth of new neighbours of always cooler temperatures. The UKIDSS set of surveys push this research forward (Lawrence et al., 2007, MNRAS 379, 1599). In its high-galactic latitude, shallow component, the Large Area Survey (LAS), more than 30 new T dwarfs have been discovered. We have searched the area newly covered by the data release DR5+ of April 2009 for new BDs of spectral type T, and used the GROND simultaneous multi-band imager on the ESO/MPG 2.2m telescope in La Silla (Greiner et al., 2008, PASP 120, 405), and the Omega2000 infra-red camera on the 3.5m telescope in Calar Alto to confirm our candidates.

Search for ultracool brown dwarfs

Known cool BDs (mid-T type and later) are red in their optical and $Y-J$ colours and blue in their near-IR colours. The former is primarily due to the absorption by alkali elements such as Na I and K I, while the latter is due to the absorption by water and methane.

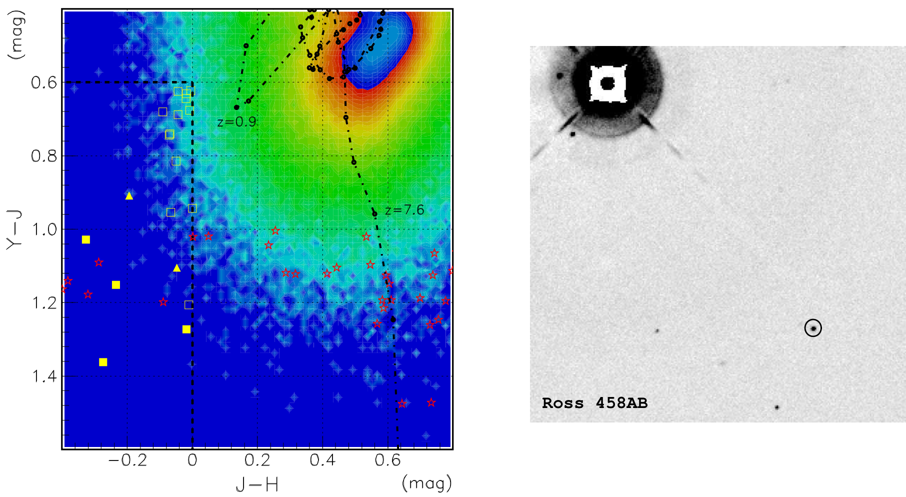

Figure 1: Left: *$Y-J$ vs. $J-H$ colour-colour diagramme for UKIDSS DR5+. The selection cuts are indicated by the dashed lines. The shades scale as the logarithm of the stellar density, with black for the highest density of the stellar locus, selected over the whole area of DR5+ with the same quality cuts as our candidate sample. Empty stars show known brown dwarfs.*
Right: *Finding chart of Ross 458ABC based on Omega 2000 methane off image.*

We search the UKIDSS DR5+ data release of the LAS for point sources with YJH detections and photometric errors smaller than 30 mmag; and colours such as $Y - J > 0.6$ mag, $J - H < 0.0$ mag and either $H - K < 0.25$ mag if the object is detected in the K band, or $H - \mathrm{depth}_K < 0.25$ (Fig. 1). We rejected objects with bright SDSS detections. In April 2009 we obtained broad-band $g'r'i'z'JHK$ imaging data of four brown dwarf candidates out of six remaining objects. Then in May 2009 we obtained Omega 2000 images in the methane on and off filters. Spectra of mid-T dwarfs and later-type brown dwarfs are known to exhibit strong methane (and water) absorption in the red half of the H band. Relatively short exposure times offer a robust confirmation and a preliminary spectral classification of BD candidates. We confirmed three candidates as T5, T7 and T9 BDs, and one likely T4 dwarf [1].

A new late benchmark brown dwarf with extremely low mass

The late T-type dwarf shares its high proper motion with an active M0.5+M7 close binary, Ross 458AB, which establishes their companionship. The separation is 1100 AU. The strong activity of the M0.5 dwarf sets an upper-limit on its age at 1 Gyr. Montes et al. (2001, MNRAS 328, 45) argue that it is a member of the Hyades supercluster, confirming a young age (0.4–2 Gyr). With a parallax of 87.50 ± 1.51 mas, we can place the late T dwarf in the colour-magnitude diagramme (Fig. 2). Compared to Wolf 940B, the object is overluminous, and has a redder colour. We interpret these elements as indication of youth: incomplete contraction and lower gravity, resulting in lower collision-induced absorption in the K band. Evolutionary models give for the methane colour of Ross 458C and an age younger than 1 Gyr indicate a mass as low as 14 Jupiter masses, at the edge of the deuterium burning minimum mass. Ross 458C is a promising target to constrain the evolutionary and atmospheric models of very low-mass BDs. Since then, we have discovered a T5–T6 benchmark BD as well as four mid- to late-T dwarfs.

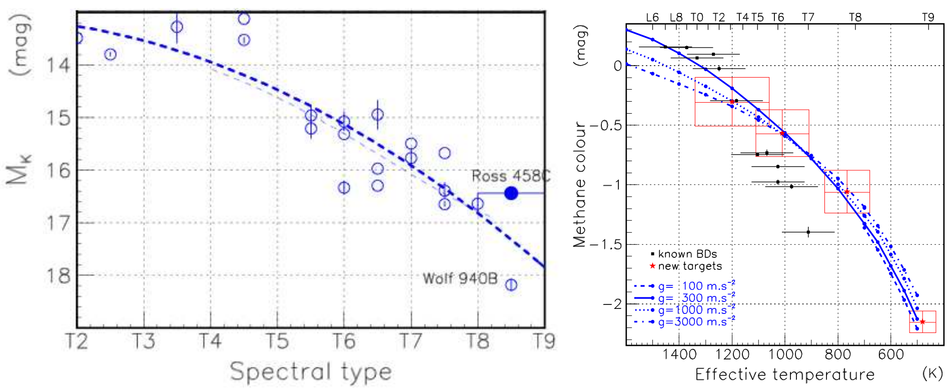

Figure 2: Left: K_{2MASS} *magnitude vs. spectral type diagram for dwarfs later than T2, excluding known close binaries.* Right: *Methane colour for our new objects (stars, with error boxes), and synthetic photometry using the atmospheric models of Saumon & Marley (2008, ApJ 689, 1327).*

Collaborators are Christian Clemens, Jochen Greiner (MPE).

References

[1] Goldman, B., Marsat, S., Henning, T., Clemens, C., Greiner, J., MNRAS accepted

A young brown dwarf at the deuterium-burning minimum mass edge

Bertrand Goldman, Thomas Henning, Wolfgang Brandner

The end of the mass function

Taurus is certainly one of the best studied low-mass star-forming (SF) regions in the northern hemisphere. It lies at a distance of $\sim$140 pc and is very young median age $\sim$1 Myr. The initial mass function (IMF) in Taurus has been studied intensively in the last years using large surveys mostly in the optical. It first seemed as if at the low-mass end the number of brown dwarfs (BDs) was too small compared to the expectations for a typical IMF.

Apart from one exception the least massive objects in Taurus known today have spectral types of M9–M9.5 with corresponding effective temperatures of $\sim$2400 K. Young objects (1–3 Myr) with L and T spectral types and corresponding effective temperatures below $\sim$2300 K could potentially be of planetary mass.

Observations and member selection

We performed a deep JHK survey using the Omega2000 near-infrared camera mounted on the Calar Alto 3.5m telescope. We observed 24 pointings for an effective area of 1.5 sq.deg., with 30-min integration time per filter, down to a $5-\sigma$ detection magnitude of $J \approx 22$ and $K_s \approx 19.5$ (see Fig. 1). The data were obtained in October 2004, December 2005 and January 2006, with FWHM ranging from 1.0” to 2.6”. We reduced the data with the MPIA-developed pipeline dedicated to the instrument, and we extracted the point-source catalogue using the `daophot` package. The catalogues of all three filters were matched within a 2-pixel (0.90”) radius. We then cross-matched the resulting catalogue with the SDSS Orion data set (Finkbeiner et al., 2004, AJ, 128, 2577), with a 2” matching radius, over $\sim$1 sq.deg. We require SDSS detections with signal-to-noise larger than 5 in the i and z bands. Our sensitivity is limited by the SDSS depths.

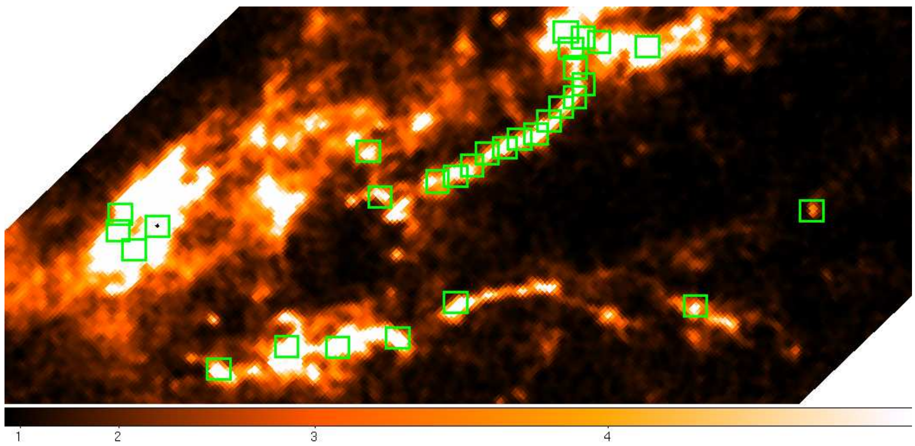

Figure 1: *Omega2000 footprints superimposed on the Taurus A_V extinction map (Alves et al.).*

We searched for Taurus members using optical and near-infrared colour-colour and colour-magnitude diagrams, selecting objects brighter than a 5-Myr isochrone (Baraffe et al., 2003, A&A, 402, 701). Excluding five spurious detections at the edge of the chip, 16 objects satisfied all our constraints, out of which ten proved to be known members of Taurus, while six are new discoveries. One was independently confirmed by Luhman et al (2009, ApJ, 691, 1265) as a young M9.25 companion to FU Tau.

A new very-low-mass brown dwarf

We sought to confirm the youth of our six member candidates using mid-infrared Spitzer/IRAC archive photometry and proper motion. Their near−mid-infrared colours are similar to the detections of Zapatero Osorio et al. (2007, A&A, 472, L9), although the error bars are large. FU Tau B shows a strong IR emission excess. We derived proper motions using Omega2000 and archived CFHT, SDSS, and UKIDSS data, when available. Apart from FU Tau B, four objects have proper motions compatible with typical members' motion, while one does not. With a short time baseline and very different instruments, our statistical error bars and systematics are however too large to draw firm conclusions.

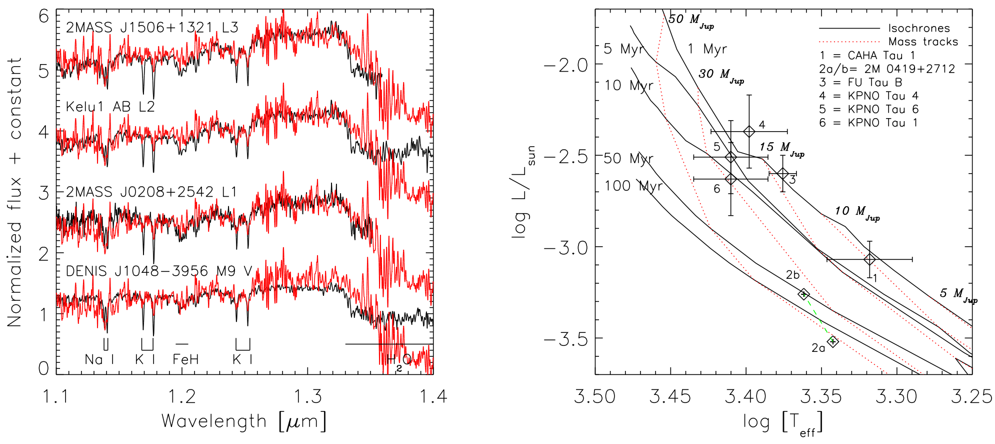

Figure 2: Left: *Comparison of CAHA Tau 1 (in red) to low-mass field reference objects. The best overall agreement is found with Kelu 1 AB, a binary system with the combined spectrum of spectral type L2.* Right: *HR-diagram comparing some of the least massive Taurus members known today.*

We obtained ISAAC J band spectroscopy for two faint candidates, CAHA Tau 1 and 2. The spectrum of the former shows similar features of those of field early L dwarfs, and matches best that of the L2 standard dwarf Kelu 1AB, in terms of slope and water absorption. We estimate the extinction using the map of Dobashi et al. (2005, PASJ, 57, 1). The atomic line strengths are weaker compared to those of that old, high-gravity binary (see Fig. 2, left), a well-known feature of low-gravity, young brown dwarf spectra (Kirkpatrick et al., 2006, ApJ, 639, 1120). CAHA Tau 1 is therefore a very likely Taurus member, the latest-type member known to date. From atmosphere models we find its effective temperature to be 2080±140 K. The luminosity of CAHA Tau 1 is derived from the bolometric correction BC_K and assuming a distance to Taurus of 140 pc and A_V=2.3. We compare its parameters with those of cool known members in the HR diagram (Fig. 2, right), and find a very good agreement with the 1–10-Myr evolutionary models, with a predicted mass of 5–15 Jupiter masses.

Since then we have obtained Subaru J and HK spectroscopy which will allow us to confirm and characterise the whole set of candidates.
Collaborators are S. Quanz (ETH), A. Burrows, L. W. Hofstetter (Princeton)

References

[1] Sascha Quanz, Bertrand Goldman, Thomas Henning, Wolfgang Brandner, Adams Burrows, Lorne W. Hofstetter, 2010, accepted by ApJ.

Correlated spectral variability in brown dwarfs

Coryn A.L. Bailer-Jones

Models of brown dwarf atmospheres suggest they exhibit complex physical behaviour. Observations have shown that they are indeed dynamic, displaying small photometric variations over timescales of hours [1][3][5][6][7]. $v \sin i$ observations obtained with UVES on the VLT have shown that brown dwarfs are rapid rotators, with rotation periods of 3–10 hours [2], yet I have also demonstrated that the variability evolves on this timescale, so it is not the result of a simple rotational modulation [1][5][6].

To explore this phenomenon further I have carred out a programme of infrared (0.95–1.64 μm) spectrophotometric monitoring of four field L and T dwarfs to look for variability over timescales of 0.1–5.5 hrs. This was carried out using the SOFI spectrograph on the 3.5 m ESO NTT telescope at La Silla, following on from a pilot programme carried out at Calar Alto [1]. A time series of spectra was obtained for each source over a period of several hours with a time resolution of about 8 minutes. Each source was observed simultaneously with a reference star in the same slit which is assumed to be constant on the timescales of interest. The spectra are analysed differentially with respect to their reference source in order to remove Earth-atmospheric variations.

The median target and relative spectrum for one of the sources is shown in Fig. 1 (top two panels). These reveal well known brown dwarf features including the KI doublets at 1169/1178 nm and 1244/1253 nm and the FeH Wing-Ford band at 990–994 nm. The bottom two panels show the amount of variability across the spectrum, the significance of which is de-

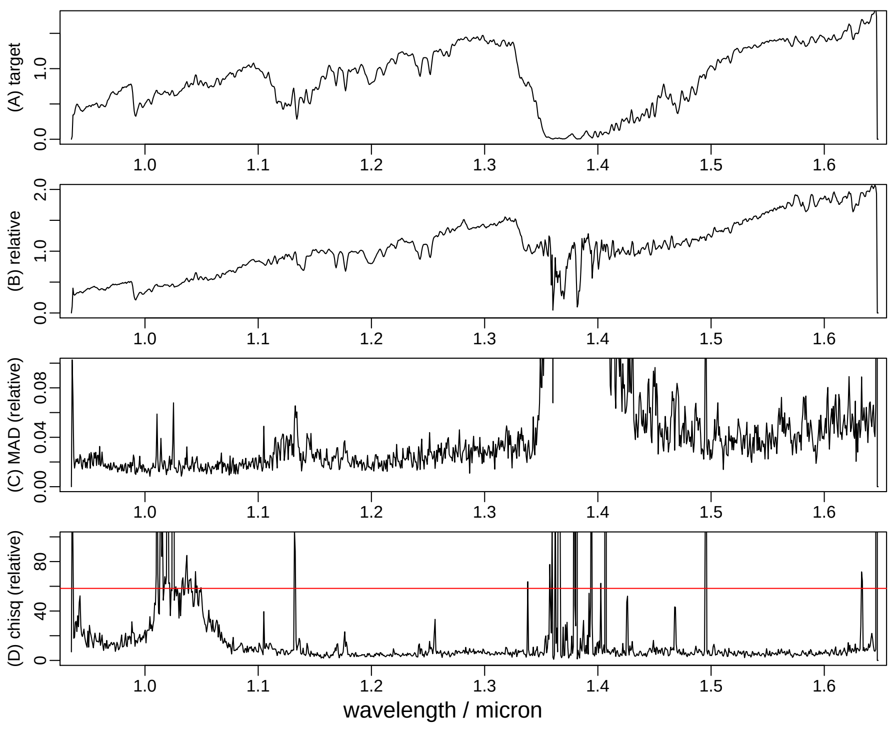

Figure 1: Spectra of the L2 dwarf SSSPM 0828. The flux scale is proportional to photon counts (not energy). From top to bottom: (A) The median target spectrum; (B) the median relative spectrum (median of target divided by reference at each epoch). Both are rectified by dividing by their integrated flux so the vertical scale is dimensionless. (C) The median absolute deviation in the relative spectrum; (D) The χ^2 spectrum. Points in (D) above the horizontal line are variations beyond the estimated errors with a confidence of 99.9% or more per pixel.

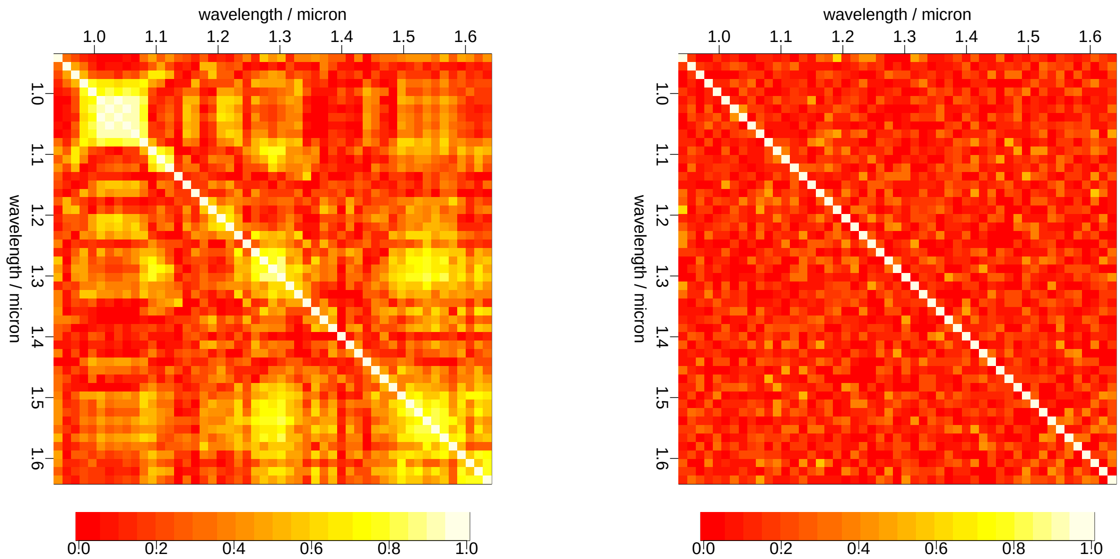

Figure 2: Left: Correlation matrix for the relative spectra of SSSPM 0828 with a binning factor of 20 in wavelength (to improve the SNR). Right: Corresponding correlation matrix for random spectra. Each point shows the absolute value of the correlation coefficient between two pairs of wavelengths on the heat scale indicated at the bottom.

termined by comparison to a photometric noise model. This shows that some of the variability is real. To get better confidence on this I examine the correlation between different wavelengths. The resulting correlation coefficients are plotted as a matrix in Fig. 2 (left panel). When compared to the correlation expected for random spectra (with the same noise properties) shown in the right panel, we see that there are many regions of significant correlation. (This procedure is actually independent of the assumed noise level.)

A significant correlation is also seen in two of the other three sources, with variability amplitudes of 2–10%. Some of the variability in the three sources can be associated with specific features including Fe, FeH, VO and KI, and there is good evidence for intrinsic variability in H_2O and possibly also CH_4. Yet some of this variability covers a broader spectral range which would be consistent with dust opacity variations. The underlying common cause is plausibly localized temperature or composition fluctuations caused by convection. For more details see [4].

Videos of the spectral time series are available at http://www.mpia.de/homes/calj/bdvar5.html

References

[1] Bailer-Jones C.A.L., 2002, A&A 389, 963

[2] Bailer-Jones C.A.L., 2004, A&A 419, 703

[3] Bailer-Jones C.A.L., 2005, in *Proc. 13th Cool Stars Workshop*, F. Favata, G.A.J. Hussain, B. Battrick (eds), ESA, SP-560, 429, astro-ph/0409463

[4] Bailer-Jones C.A.L., 2008, MNRAS, 348, 1145

[5] Bailer-Jones C.A.L., Mundt R., 1999, A&A 348, 800

[6] Bailer-Jones C.A.L., Mundt R., 2001, A&A 367, 218. Erratum: A&A, 374, 1071

[7] Bailer-Jones C.A.L., Lamm M., 2003, MNRAS 339, 477

Weather and dust on ultra-cool dwarfs

Bertrand Goldman, Jan Pitann, Cynthia Knight, Thomas Henning, Coryn Bailer-Jones

The heterogenous distribution of dust in ultra-cool atmospheres

The L spectral type covers effective temperatures of 2200 K to ≈ 1400 K. The optical spectra of L dwarfs show specific features that define the type: strong hybrid bands (FeH and CrH) and alkali lines (Na I, K I, Rb I, Cs I). The oxides TiO and VO produce weak absorption features, which is interpreted to be due to the coagulation of those species into dust grains. Other refractory elements such as Al, Ca, Fe, and Mg condensate into grains and form dust clouds. Through Mie scattering, this dust will produce polarised light.

Several studies have shown that ultra-cool dwarfs are fast rotating. It is therefore likely that the rotation induces a flattening at the poles. Furthermore, the fast rotation may increase the turbulence in their convective atmospheres, leading to possible heterogeneities in the cloud deck. These effects may prevent the polarisation to cancel out when integrating the light over the whole surface.

Sengupta & Krishan (2001, ApJ 561, L123) considered single scattering to predict the net polarisation for various grain sizes, flattenings and spectral types, assuming an homogenous cloud cover. The polarisation arising from rotational flattening is expected to be small, 1% or less. The polarisation arising from many small-scale, randomly-distributed structures would equally cancel out, but large-scale heterogeneities may result in additional polarisation. Gravitational pulling by a close companion could also break the symmetry of the brown dwarf surface, as it is expected rotational acceleration does.

Finally, the grain size distribution affects how the polarisation changes with wavelength, giving us a unique insight into this crucial, and barely constrained, parameter.

Observations and interpretation

We selected nine nearby ultra-cool, on the basis of their brightness, because a high signal-to-noise ratio is needed to obtain accurate polarisation measurements; and of their spectral type, to study dust in atmospheres of various effective temperatures. We also favour targets with measured projected rotational velocity, to seek correlation between the expected flattening and the polarisation; and with previous polaristion detections, in order to confirm them and search for variability.

Ménard et al. (2002) and Zapatero Osorio et al. (2005) had detected polarisation in a handful of L-type dwarfs, using FORS1 on the VLT and CAFOS on the Calar Alto 2.2m, with levels of 0.2% to 2.5%. Using the FORS1 Wollaston prism with the quick, but less accurate, acquisition with four half-wave-plate retarder angles, we obtained polarisation measurements for targets, with spectral types from M9+L0 (DENIS J2200−3038) to T1(+T6) ϵ Indi B. We observed all targets in the I_{Bessel} filter, and a subset in the R_{Bessel} and z_{Bessel}. All targets were found unpolarised within the errors, except LHS 102BC (Goldman et al. 1999). We observed that L5 dwarf in the I_{Bessel} band three times, and obtained an average polarisation of (0.30 ± 0.05)%. This measurement lies about 3.5σ away from the value of Ménard et al. (2002) of (0.10 ± 0.05)%.

We compare our results with models of Sengupta & Kwok (2005, ApJ 625, 996). We do not know the inclination of the stellar rotational axis, but we argue that to first order, the flattening-induced polarisation depends on $v \sin i$: for a small inclination, the larger true rotational velocity compensates the projection effect. Our results are at odds with the model predictions, with much smaller polarisation degrees than expected (see Fig. 1). The possible explanations for this

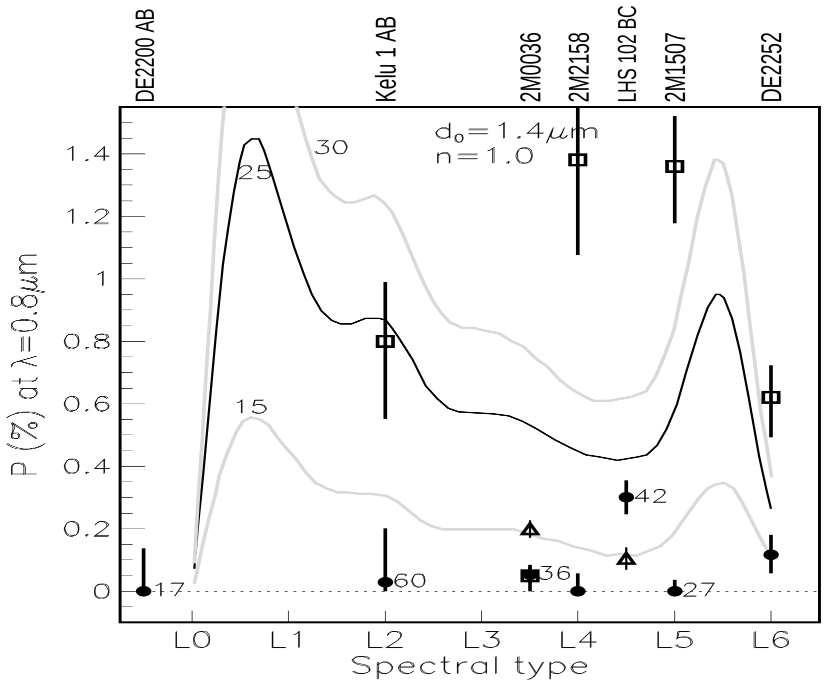

Figure 1: *Polarisation degrees as a function of spectral type for our FORS1 sample (filled circles), ZO05 (empty squares) and M02 (empty triangles), for the same targets. We superimpose the Sengupta & Kwok (2005) predictions for various rotational velocities (starting from the bottom: 15, 25, 30 km/s). We report* $v \sin i$ *measurements (in km/s) when available.*

discrepancy include thicker dust cloud which would increase multiple scattering, non-spherical scatterers, and gain sizes (much) larger than 1.4 μm. We also fail to detect the dependence of the polarisation degree with the spectral type, but our sample size is too small to draw a conclusion.

We also compared our measurements with previous publications. We have two targets in common with Ménard et al (2002, A&A, 396, L35), which also used FORS1. Three measurements are compatible but we found a significantly larger P_Q value for LHS 102BC. We cautiously interpret this result as indication of polarisation variability. We have six targets in common with Zapatero Osorio et al. (2005, ApJ, 621, 445), which used CAFOS with a similar observing set up. We find smaller polarisation degrees six times out of seven, a pattern that cannot be due to intrinsic variability. Checking carefully the reported polarimetric errors, we conclude that two measurements, P_U of the L5 dwarf 2MASS J1507−1627 and P_Q of the L7.5 dwarf 2MASS J2244+2043, may be show real variations, while the other four discrepant measurements are most likely due to instrumental effects or under-estimated errors.

Since then we have reduced polarimetric data obtained with the CAFOS imager mounted on the Calar Alto 2.2m telescope. We find another mid-L-type brown dwarf showing strong indication of polarisation variability.
Collaborators are M. R. Zapatero Osorio (IAC/CSIC-INTA), V. J. S. Béjar (IAC), J. A. Caballero (Universidad Complutense de Madrid).

References

[1] Bertrand Goldman, Jan Pitann, Maria Rosa Zapatero Osorio, Coryn A. L. Bailer-Jones, Víctor J. S. Béjar, Jose A. Caballero, and Thomas Henning, 2009, A&A 502, 929

Planets around intermediate-mass stars

Johny Setiawan, Patrick Weise, Tim Schulze-Hartung and Thomas Henning

Do intermediate-mass stars have planets?

To date, observational and theoretical studies of planet formation are still mainly concentrated on solar-like stars, i.e., stars with masses and ages similar to those of the Sun. In contrary to planet searches around solar-like stars, there are only limited search programs of extrasolar planets around intermediate-mass and massive stars. Additionally, planet formation processes around these stars are poorly known. To explore the characteristics and study the formation of planetary systems with intermediate-mass host stars, a sufficient number of planet detections are necessary to put constraints on the statistics and theoretical models. However, the most popular planet search method, namely the radial-velocity (RV) technique, is ineffective for the majority of early-type (B-F spectral type) main-sequence stars. These stars have only few and broad spectral lines that prohibit high precision RV measurements.

Nevertheless, there is an alternative way that can be applied to search for planets around intermediate-mass stars, as described briefly in the next paragraphs. As there is an extensive RV planet search program in MPIA to detect planetary companions around non solar-like stars, we have a subprogram within this survey to monitor RV variations of G and K giants with the high-resolution spectrographs FEROS and HARPS at ESO La Silla observatory. The main scientific goals of this program are (1) to complete the cencus of planet host stars in the upper stellar mass domain (see Fig. 1) and (2) to study the characteristics of such planetary systems, in comparison to those with solar-like host stars.

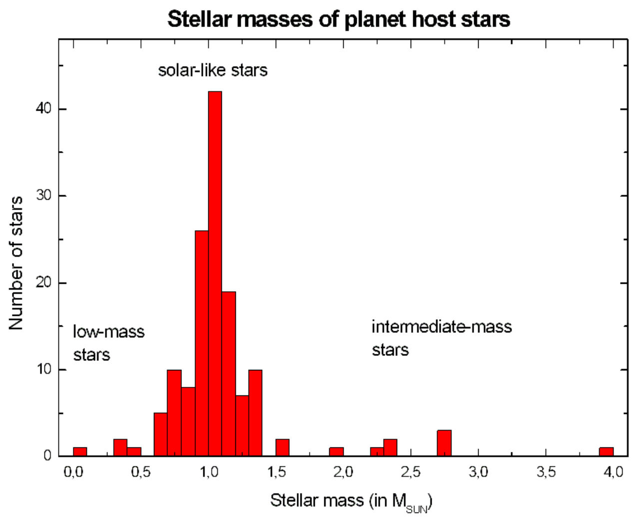

Figure 1: *The mass distribution of the RV planet host stars. It is obviously, that the lower and upper stellar mass domains are still poorly explored.*

G and K giants as planet search targets

A posibility to overcome the difficulties in planet searches around intermediate-mass stars with the RV technique is to use G and K giants as target stars. Intermediate-mass main-sequence stars (B-F spectral type stars) evolve into giants in their later evolutionary stage. These evolved stars, such as G and K giants, are in general slow rotators and possess many narrow absorption lines. Thus, high-precision RV measurements are possible. However, G and K giants exhibit intrinsic stellar activity, so that the observed RV variation can be also due to other sources, like nonradial pulsations and/or rotational modulations. These difficulties are reflected in the low number of the detected planets around giants, in comparison to the solar-like planet host stars. Nevertheless, the first discovery of a planet around an intermediate-mass giant star HD 11977 [2] has shown an indirect evidence that early type main-sequence stars also have planetary companions.

Further results from MPIA G-K giants survey

Following our previous successes [1];[2], we found three more planetary companions around intermediate-mass G-K giants. One of them is HD 110014 which has a stellar mass of 2.2 $M_\odot$ [3]. The two other stars have stellar masses of 1.4 and 3.2 $M_\odot$ (Setiawan et al. in preparation). Our preliminary results show that intermediate-mass stars have more massive planets than solar-type stars. In addition, we did not find planet-metallicity connection as observed in solar-like planet host stars. However, this finding is based on a limited number of statistics. More planet detections around intermediate-mass (giant) stars are still required to confirm this hypothesis.

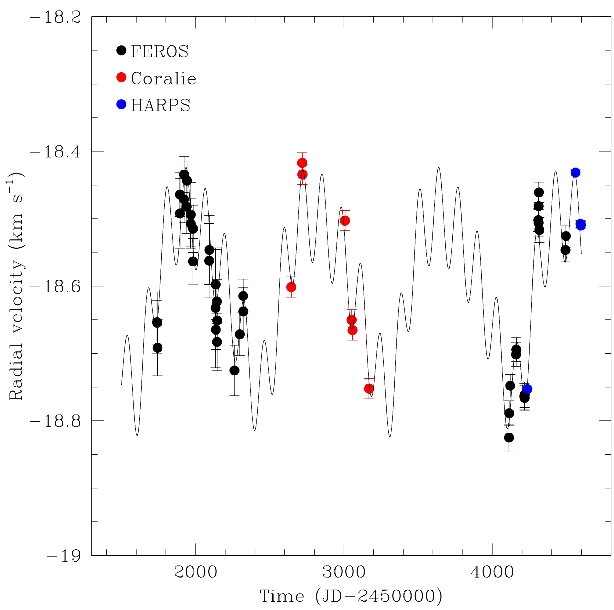

Figure 2: *Radial velocity measurements of the K giant HD 110014 (2.2 $M_\odot$)*

Collaborators are M.P. Döllinger (ESO), L. Pasquini (ESO), A.P. Hatzes (Tautenburg), J.R. de Medeiros (Brazil), L. da Silva (Brazil), L. Girardi (Padova), O. v. Lühe (Freiburg i.Br.).

References

[1] Setiawan, J., Hatzes, A.P., von der Lühe, O., et al. 2003, A&A, 398, L19.

[2] Setiawan, J., Rodmann, J., da Silva, L. et al., 2005, A&A, 437, L31.

[3] de Medeiros, J.R., Setiawan, J., Hatzes, A.P., et al. 2009, A&A, 504, 617.

Search for terrestrial planets in the habitable zone of M dwarfs. The M dwarf planet search programme at the ESO VLT + UVES

Mathias Zechmeister, Martin Kürster

Why M dwarfs?

When searching for terrestrial exoplanets in the habitable zones (HZ) of stars with radial velocity (RV) methods, then M dwarfs are very promising targets. For the RV method they have two advantageous characteristics compared to solar like stars: (i) they have a lower mass (M = 0.1 – 0.6 $M_\odot$) and (ii) the habitable zone is close-in around this cooler and less luminous type of star (L = 0.0008 – 0.06 $L_\odot$). Thus the RV amplitude induced by a planet in the HZ of an M dwarf is higher than that of a solar-like star and therefore easier to detect. However, M dwarfs are faint and require large telescopes to achieve a high RV precision.

Radial velocities

We performed radial velocity (RV) measurements of our sample of 40 M dwarfs from our planet search programme with VLT+UVES begun in 2000 [1]. Although with our RV precision down to 2–2.5 m/s and time baseline of up to 7 years, we are capable of finding planets of a few Earth masses in the close-in habitable zones of M dwarfs, we do not detect of a planetary companion. This is in line with the lower frequency of 1 % or less for Jupiter-mass planets around M dwarfs up to 1 AU orbital radius (compared to 2.5 % for solar like stars) estimated by Endl et al. (2006, ApJ, 649, 436). For Neptune-mass icy giant planets Ida & Lin (2005, ApJ, 626, 1045) even predict a higher frequency in short periodic orbits for M dwarfs than for G type stars based on their accretion model. However, we do not find any such object in our sample.

We identified 6 M dwarfs that host a brown dwarf or low-mass stellar companion. With the exception of these, all other sample stars show low RV variability with an rms < 20 m/s. Some high proper motion stars exhibit a linear RV trend consistent with their secular acceleration (a purely geometric effect reflecting the space motion of the star). As an example Fig. 1 shows the RVs for Barnard's star, one of our best measured targets. This star has an RV dispersion of only 3.3 m/s around its secular acceleration.

Mass detections limits

To demonstrate the sensitity of our planet search we calculated mass detection limits. These limits allow us to exclude Jupiter-mass planets up to 1 AU for most of our sample stars. As an example Fig. 2 shows the mass detection limits for Barnard's star derived from the RV shown in Fig. 1. It illustrates that we are capable to detect terrestrial planets of a few Earth masses in the habitable zone which is below 0.1 AU for Barnard's star.

RV-Hα correlation?

RV variations can also be caused by stellar activity and can be mistaken as planetary companions. We examined our data sets for a possible correlation between RVs and stellar activity as seen in variations of the Hα line strength. For Barnard's star we found a significant anticorrelation. Therefore a significant 45 d period we found in the RV data of Barnards star is likely to be caused by stellar activity. However, such a correlation RVs and Hα index was found here only for a few M dwarfs and most of the sample stars do not show such a correlation.

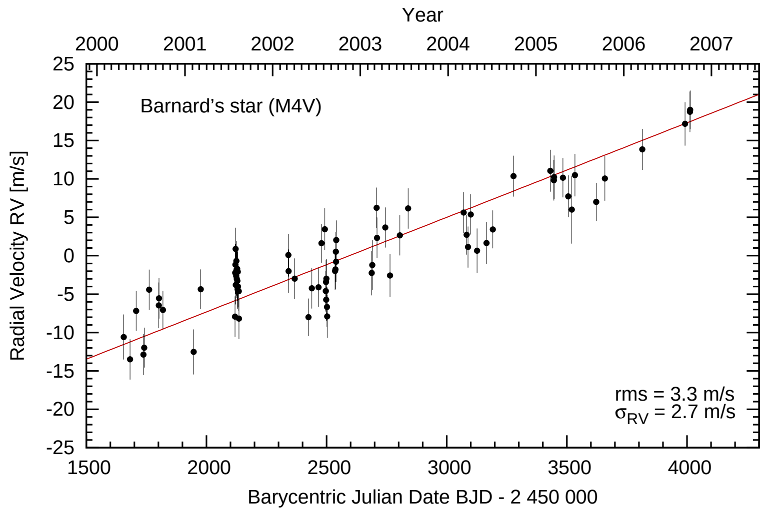

Figure 1: *Radial velocity (RV) times series for the M4Ve dwarf Barnard's star. The trend of 4.5 m/s/yr is due to the high proper motion of Barnard's star (secular acceleration).*

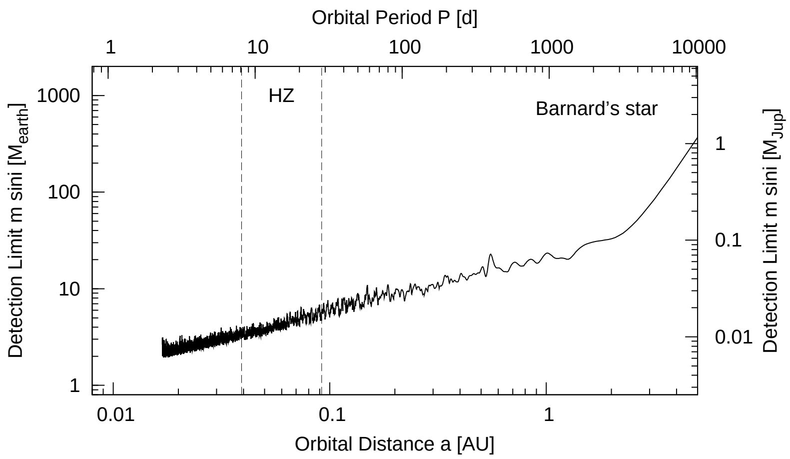

Figure 2: *Mass detection limits ($m \sin i$) for companions to the M4Ve dwarf Barnard's star. The habitable zone (HZ) is depicted by the vertical dashed lines.*

A collaborator on this project is Michael Endl (McDonald Observatory, University of Texas, Austin, USA).

References

[1] Zechmeister, M.; Kürster, M.; Endl, M., 2009, A&A,505,859

Toward detection of terrestrial planets in the habitable zone of our closest neighbour: Proxima Centauri

Martin Kürster

Our nearest neighbour

Ground-based Doppler measurements have attained precision levels that make discoveries of planets with a few Earth masses possible. This is particularly true for M dwarfs that comprise the majority of stars in the solar neighbourhood. Once their intrinsic faintness is overcome, M dwarfs represent attractive targets for high precision Doppler surveys. Because of the lower mass of M dwarfs compared to solar-type stars, a planet of a given mass induces a larger stellar reflex motion that is more easily detectable with radial velocity (RV) measurements.

Our nearest neighbour, the M5Ve star Proxima Centauri, is located at a distance of 1.29 pc and has a mass of 0.12 $M_\odot$. It is still under debate whether Prox Cen is gravitationally bound to the α Cen binary with which it shares common proper motion (e.g. Wertheimer & Laughlin 2006, AJ 132, 1995). Prox Cen exhibits all characteristics of a magnetically active star, like coronal X-ray emission and flare activity. Photometric variability was reported by Benedict et al. (1999, AJ 118, 1086). Its classical liquid-water habitable zone (after Kasting et al. 1993, Icarus 101, 108) is located at separations from 0.022 to about 0.054 AU, corresponding to orbital periods from 3.6 to 13.8 d.

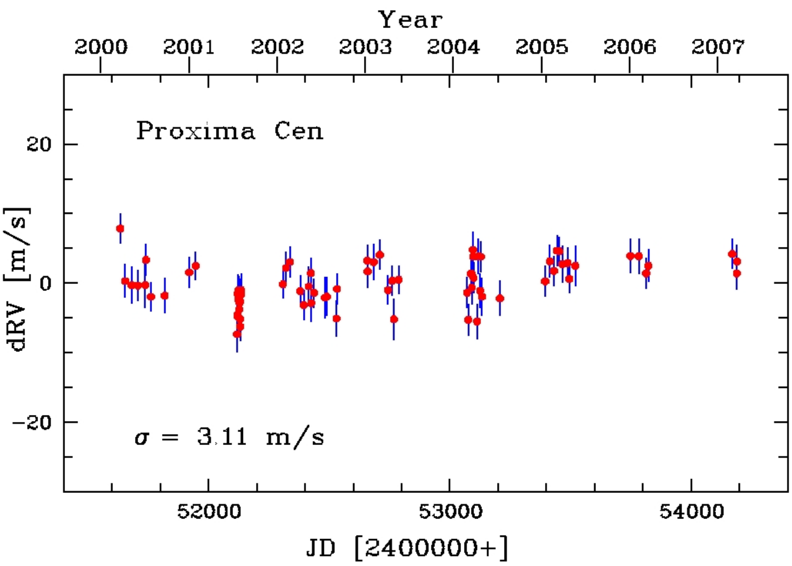

Figure 1: *Seven years of RV measurements for Prox Cen using UVES+iodine cell at the ESO VLT. The data have a total rms of* 3.11 ms^{-1} *and an average uncertainty of* 2.34 ms^{-1}.

Observations and results

We have observed Prox Cen for seven years starting in early 2000 with the ESO VLT+UVES. To attain high RV measurement precision we have self-calibrated the spectrograph with its iodine gas absorption cell that allows to model the instrumental profile and correct for instrumental instabilities. Fig. 1 shows our RV time series data. There is some evidence for a 1-year periodicity that can be attributed by an interplay between the window function of the time series and probably more irregular variability related to stellar activity.

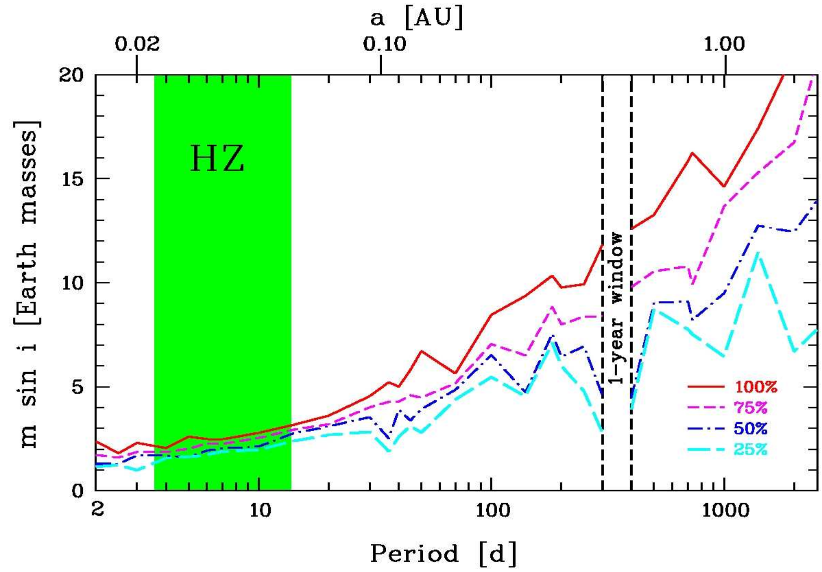

Figure 2: *Upper limits to the projected (minimum) mass* $m \sin i$ *of planets in circular orbits around Prox Cen. All test signals with amplitudes corresponding to projected masses on and above the red solid line were recovered with* $> 99\%$ *significance. The red solid, mangenta dashed, blue dashed-dotted, and cyan long-dashed lines show, respectively, the mass ranges where we successfully recovered* 100, 75, 50 *and* 25% *of the test signals. The green area labelled "HZ" displays the approximate location of the classic liquid water habitable zone (after Kasting et al. 1993, Icarus 101, 108). The region labelled "1-year window" shows the period range that we excluded from our simulations.*

Mass upper limits

Lacking clear evidence for a planetary companion signal we have determined mass upper limits to planets that we would have detected in our data. For this purpose we injected and recovered signals into the original RV data that are assumed to be pure noise. We restrict the simulations to circular orbits. We then use bootstrap randomization to determine the statistical significance of the recovered signal. The result is shown in Fig. 2. We conclude that we would have detected all planets with a projected (minimum) mass $m \sin i = 2 - 3$ $M_\oplus$ in the habitable zone around Prox Cen.

Collaborator on this project is Michael Endl (University of Texas at Austin).

References

[1] Endl, M., Kürster, M., 2008, A&A 488, 1149

A search for planetary mass companions to brown dwarfs with HST

Micaela Stumpf, Wolfgang Brandner, Viki Joergens, Thomas Henning

In the past years, the effort to directly image an extrasolar planet became an area of intensive research, since a successful detection would provide direct access to their physical properties such as brightness, color, effective temperature and composition. While previous direct imaging surveys focused especially on searches for exoplanets around young stars in nearby associations, we obtained high-resolution observations with HST/NICMOS of 12 L dwarfs within 30 pc of the Sun, using the spectral differential imaging technique (SDI) in the two narrow-band filters F108N and F113N. The effort was to optimize the brightness contrast and to be able to find planetary mass objects at small physical separations from their host. To this date, this is the only SDI survey for planetary mass companions around field brown dwarfs (not related to any young association or moving group) conducted from space or ground-based telescopes. Further, it is the only one which uses the spectroscopic feature of water absorption instead of the methane feature.

New brown dwarf binaries

The survey resolved two brown dwarf binaries. The L dwarf system Kelu-1 AB [2] and the newly discovered L/T transition system 2MASS 031059+164815 AB, which could already be confirmed in follow-up observations [3]. An overall binary fraction of $15^{+18}_{-10}\,\%$ for this survey, as well as separations of the binaries smaller than 6 AU are consistent with previous brown dwarf binary statistics [1, 4]. Moreover, their mass ratios of $q \geq 0.8$ confirm the preference of brown dwarfs to form equal mass systems, in contrast to the lower mass ratio main-sequence star binaries. All these results add up important values to the brown dwarf binary statistics.

A planetary companion candidate

Furthermore, tentative evidence was found for a very low mass companion around the L4 dwarf 2MASSW 033703-175807 (Fig. 1), straddling the brown dwarf/planetary mass boundary. This companion has a very low $T_{\rm eff} \approx 600\text{-}630$ K and the system reveals an uncommonly low mass

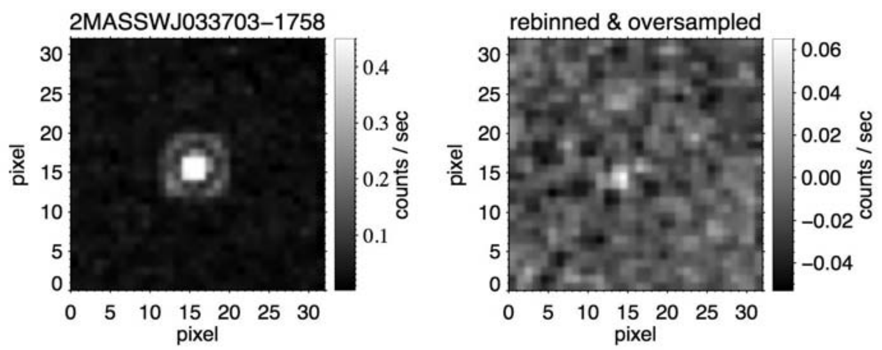

Figure 1: Result image of our spectral differential imaging observations with HST/NICMOS for the L4.5 dwarf 2MASSW 0337-1758. The left image represents the added image of all exposures taken in the F108N filter with the upper cut-level reduced for a better visibility of the background (thus not representing the real peak values). The right image displays the residual image of all exposures after SDI reduction. The remaining positive signal is clearly visible with a S/N ratio of 7 at its peak (pixels: 14,14).

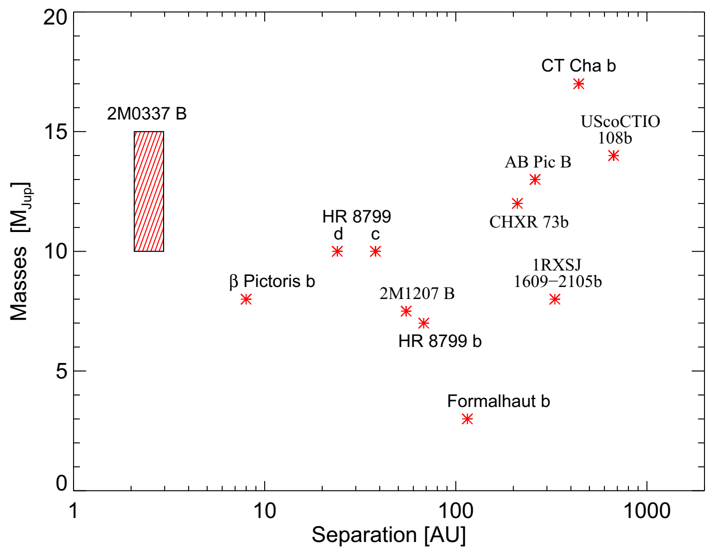

Figure 2: Comparison of mass vs. separation to the primary, of the so far directly imaged planetary mass candidates. The plot shows that our planetary mass candidate 2MASS 0337-1758 B is by far the closest resolved companion ever directly imaged.

ratio ($q \approx 0.2$) compared to the vast majority of previously found brown dwarf binaries. With a derived minimum mass of 10 $M_{\rm Jup}$ to 15 $M_{\rm Jup}$ a planetary nature of the secondary cannot be ruled out yet. It seems, however, more likely to be a very low mass brown dwarf secondary at the border of the spectral T/Y transition regime, primarily due to its similarities to recently found very cool T dwarfs (Leggett et al. 2009).
Follow-up observations are proposed to confirm common proper motion of the system and to derive more physical properties like colors for spectral type classification. In addition, these new observations will provide second epoch astrometry for the determination of orbital parameters and hence an initial dynamical mass estimation. If gravitationally bound 2MASSW 0337-1758 B will be the closest resolved ($0.087'' \pm 0.015''$, corresponding to 2.52 ± 0.44 AU at a distance of 29 pc) planetary mass companion ever directly imaged (see Fig. 2) and depending on the age, the so far coldest and the least massive companion to any L or T dwarf. Therefore, including its multiplicity status, the system will be an important testbed in the newly explored ≤ 700 K temperature regime and might imply new constraints on the existing formation scenarios.

Collaborators are H. Bouy (ESAC), R. Köhler (ZAH), M. Kasper (ESO)

References

[1] Bouy, H., Brandner, W., Martín, E., et al., 2003, AJ, 126, 1526

[2] Stumpf, M.B., Brandner, W., Henning, Th., Bouy, H., Köhler, R., Hormuth, F., Joergens, V., Kasper, M., 2009, A&A, submitted

[3] Stumpf, M.B., Brandner, W., Bouy, H., Henning, Th., Hippler, S., 2009, A&A, submitted

[4] Umbreit, S., Burkert, A., Henning, Th., Mikkola, S., Spurzem, R., 2005, ApJ 623, 940

New parameters and transit timing studies for the exoplanet OGLE2-TR-L9b

Cristina Afonso, Monika Lendl, Nikolay Nikolov and Thomas Henning

Strength and motivation of the transit method

In the study of extrasolar planets, the observation of planetary transits has a prominent position. It allows us to determine several parameters which are not accessible by other means, shedding more light on the nature of the transiting planet. From the transit light curve itself, the planetary radius and the inclination of the orbit can be found by investigating shape and depth of the transit light curve. Together with radial velocity measurements, the knowledge of the inclination allows us to determine the true mass of the planet, which can then be used in conjunction with the radius to find the mean density of the planet, allowing to constrain the planets composition and structure.

The transit timing method has the potential to detect small and/or further-out objects such as moons, Trojans or additional planets which can be extremely difficult with traditional methods. The gravitational impact of these objects on the transiting planets orbit can be measured as dynamical interactions within the system causing the period of the transiting planet to vary and in turn, the transit occurs earlier or later than expected.

The transiting exoplanet OGLE2-TR-L9 - New Parameters and Transit Timing Studies

We re-examined the OGLE2-TR-L9b system with high cadence, multi-color photometry in order to refine the planetary parameters and probe the system for transit timing variations. OGLE2-TR-L9 has been identified as hosting a planetary candidate in the publicly available data of the OGLE-II project (Udalski et al. 1997, Acta Astron., 47, 319). It was recently confirmed as a transiting exoplanet with the observation of a full transit and radial velocity measurements by Snellen et al. (2009, A&A, 497, 545), remaining however largely unstudied. OGLE2-TR-L9b has a mass of $4.5 \pm 1.5\mathrm{M}_{\mathrm{Jupiter}}$ and a period of approximately 2.5 days, orbiting an F3V star, the hottest star known to host a transiting planet.

We observed five transits of OGLE2-TR-L9, using the GROND (Gamma Ray Burst Optical and Near-Infrared Detector) instrument mounted at the ESO/MPG 2.2 m telescope at La Silla Observatory. Designed with the aim of observing gamma-ray-burst afterglows, GROND simultaneously observes in 4 optical ($griz$) and 3 infrared (JHK) channels allowing us to gather 4 optical light curves of each transit event. The observations took place on April 10, 15, 20, 25 and May 15, 2009. During each night, we observed the full transit plus at least 20 minutes of baseline before ingress and after egress (see Fig.1). In our analysis, we included the transit observed with GROND on January 27, 2008 by Snellen et al. (2009, A&A, 497, 545).

These observed transits allowed us to refine the ephemeris to $\mathrm{Tc(E)[HJD]} = 2454492.80046 + 2.4855347(\pm 6.6.10^{-7})\mathrm{E}$. The newly derived parameters are the semi-major axis $\mathrm{a} = 0.0433 \pm 0.002\mathrm{AU}$, the planetary radius $\mathrm{r_p} = 1.75 \pm 0.05\mathrm{R}_{\mathrm{Jupiter}}$ and an inclination equal to $83.31^\circ \pm 0.28$. In addition, we searched for transit timing variations and we did not find any significant indication of a deviation from a constant period or any sign for a particular trend (see Fig.2). However, we plan to perform further observations in the future, since we now determined a precise ephemeris, which can be used as a reference point for transit timing studies.

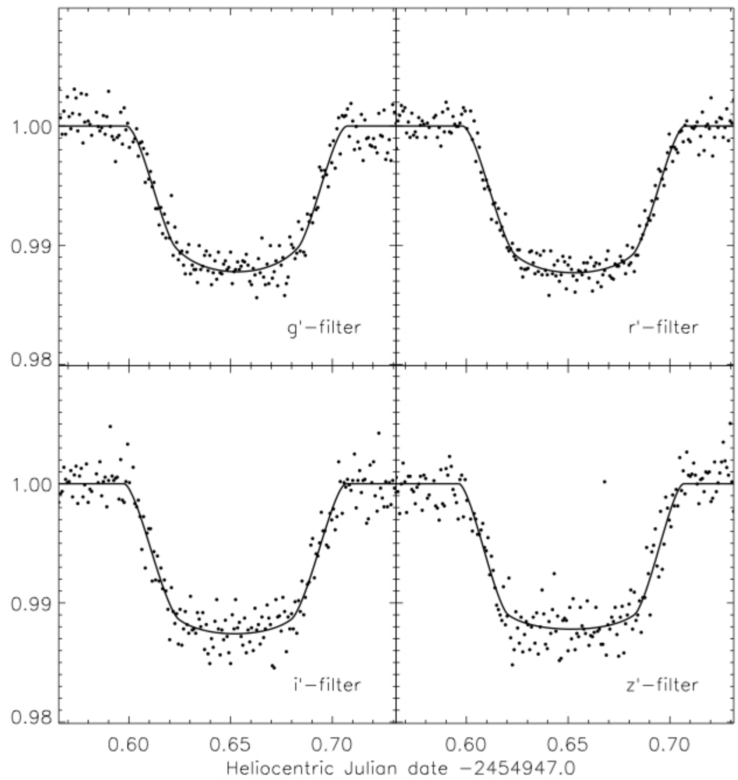

Figure 1: *Example of a light curve recorded in the four optical channels exhibiting the planetary transit of the planet OGLE2-TR-L9. The continuous lines represent the best fit to the data.*

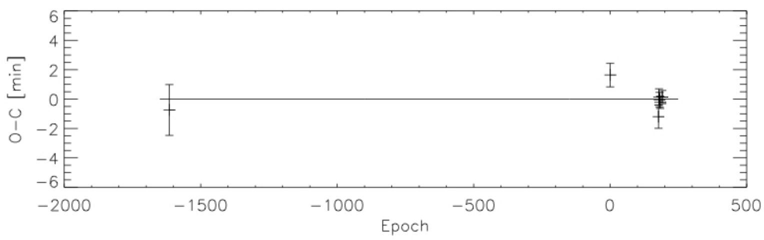

Figure 2: *The O-C diagram (i.e. expected minus calculated values) for the ephemeris calculated from all known mid-transit times of OGLE2-TR-L9 is shown.*

Collaborator is Johannes Koppenhoefer (Max Planck Institute for Extraterrestrial Physics).

References

[1] Lendl, M., Afonso, C., Koppenhoefer, J., Nikolov, N., Henning, Th. 2009, A&A, submitted

Searching for starlight reflected from a hot Jupiter: HD 75289Ab revisited

Martin Kürster, Thomas Henning

Reflected starlight

For exoplanets, the enormous brightness contrast between the star and the planet constitutes a challenge when attempting to observe some kind of direct signal from the planet. Due to the more favourable contrast of close-in planets, hot Jupiters provide the opportunity to attempt detections of starlight reflected from their surfaces and to determine the planetary albedo. When observed spectroscopically the radial velocity (RV) of the planet can be measured and its mass determined even for a non-transiting planet. High-resolution spectroscopy in the optical utilizes the fact that the spectrum reflected from the planet is essentially a copy of the rich stellar absorption-line spectrum. This spectrum is shifted in wavelength according to the orbital RV of the planet and scaled down in brightness by a factor of a few times 10^4 for hot Jupiters.

Observations data modelling and results

We have re-analysed observations of the planetary host star HD 75289A, conducted by Leigh et al. (2003, MNRAS 344, 1271) with UVES at the ESO VLT. These authors did not detect starlight reflected from the hot Jupiter and placed a 99.9% confidence upper limit on the planet-to-star flux ratio of 4.17×10^{-5}, i.e. an upper limit for the geometric albedo of 0.12, for the spectral range $402 - 522$ mn assuming an orbital inclination $i = 60°$. We noticed, however, that this upper limit was based on an erroneous ephemeris of the planet thus warranting re-analysis.

We modelled the starlight reflected from the planet as a copy of the stellar spectrum, strongly scaled down in brightness and Doppler-shifted according to the orbital motion of the planet and the barycentric motion of the Earth. The reflected spectrum from the planet is deeply buried in the noise of the stellar spectra that have signal-to-noise ratios of 300-600 per spectral bin. This weak planetary signal is, however, effectively boosted by the large number of 684 spectra, and more importantly, by the combination of about 1500 absorption lines in a data synthesis approach. Also considered in the modelling is the modulation of the apparent brightness of the planet with orbital phase and the wavelength dependence of its albedo. For the modulation we have adopted a Venus-like phase function; for the albedo function we used the Class IV and Class V atmospheric models for planets with temperatures of 1300 K and ≥ 1500 K, respectively, from Sudarsky et al. (2000, ApJ 538, 885; see there for details, but we note that Class IV models with and without reflective clouds are similar in shape and for our purpose only distinguished by a normalization factor; also in the wavelength regime of our data we are able to approximate the Class V model by a constant "grey" albedo function).

Our modelling results are summarized in Fig. 1, left panel. For both the Class IV and the Class V (grey) models we find formal χ^2 minima for the combination of the two basic model parameters RV semi-amplitude (or orbital inclination) and fraction of reflected light. However, a bootstrap simulation test shows that these minima are not statistically significant.

Upper limits to the planet-to-star flux ratio

Given the non-detection of reflected light we determined upper limits to the fraction of reflected light as a function of RV semi-amplitude/orbital inclination, again employing bootstrap simulation. The result is shown in Fig. 1, right panel. As a consequence of the error in the planetary ephemeris leading to the fact that the HD 75289A planet was not observed at the phases where it

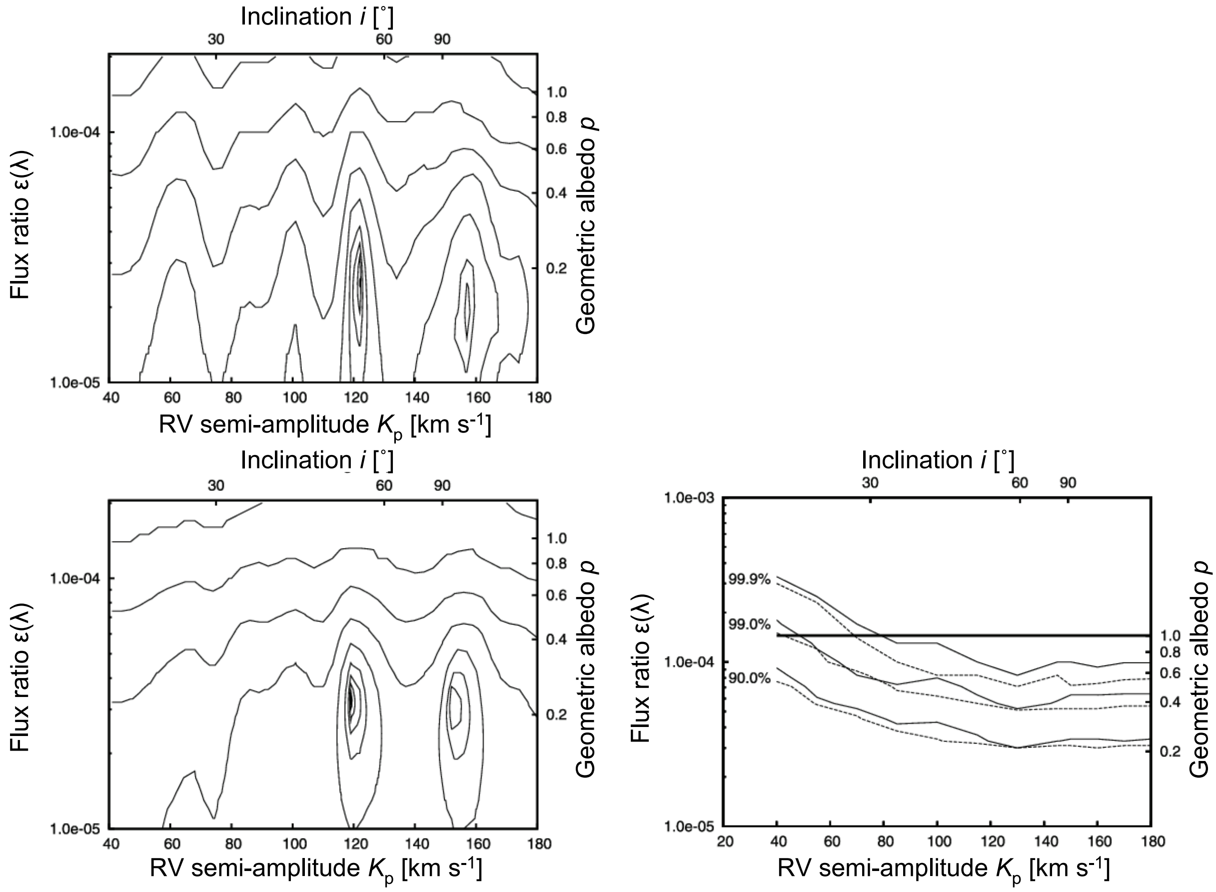

Figure 1: **Left:** *χ^2 contour maps for the parameters of the model fitted to the HD 75289A spectra, i.e. planetary RV semi-amplitude $K_{\rm p}$ and fraction of reflected light $\epsilon(\lambda)$. Upper panel: grey albedo (Class V model); the χ^2 minimum is found at $K_{\rm p} = 121$ km s^{-1} and $\epsilon(\lambda) = 2.9 \times 10^5$ with a false alarm probability of $FAP = 19\%$. Lower panel: Class IV albedo function; χ^2 minimum at $K_{\rm p} = 119$ km s^{-1}, $\epsilon(\lambda) = 3.3 \times 10^5$, and $FAP = 24\%$. In both panels the corresponding orbital inclination i is indicated (upper x-axis) as well as the geometric albedo p assuming a planetary radius of $R_{\rm p} = 1.2$ R$_{\rm Jup}$ (y-axis at the right).* **Right:** *99.9, 99.0, and 90.0% confidence levels for upper limits to $\epsilon(\lambda)$ and p as a function of $K_{\rm p}$ or i. Solid lines: Class IV albedo; dashed lines: grey albedo. The region above the thick horizontal line is excluded, because $p > 1$.*

is brightest, the upper limits resulting from our re-analysis are considerably higher than that of Leigh et al. (2003, MNRAS 344, 1271). These authors had found an upper limit to the geometrical albedo of 0.12 (at $i = 60°$), by far the deepest one determined for hot Jupiters up to now. While they had suggested that they can rule out the Class V "roaster" model for HD 75289Ab, thereby providing an observational constraint on the temperature of the illuminated side of the planet, this conclusion is no longer supported by our re-analysis.

Collaborator on this project is Florian Rodler (now at Instituto de Astrofísica de Canarias, but affiliated with the MPIA during the time of this work).

References

[1] Rodler, F., Kürster, M., Henning, T., 2008, A&A 485, 859

Towards comparative exoplanetology: Atmospheric spectra of transiting planets.

Jeroen Bouwman, Thomas Henning, Cristina Afonso.

Transit spectroscopy

During the last three years several molecules have been detected in the infrared spectra of exoplanets [1, 2, 3, 4]. These detections constitute a major breakthrough in the characterization of exoplanet atmospheres. Molecules serve as probes for the composition, temperature and density structure of the atmospheres and allow us to answer fundamental questions concerning the chemistry, dynamics and formation history. A key role in obtaining the first infrared spectra of exoplanet atmospheres play the so called transiting hot Jupiters: Giant gas planets orbiting their parent star at a very close (∼0.01 AU) orbit, with the orbital plane seen edge on causing the planet to pass in front of (primary eclipse) and behind (secondary eclipse) the central star. The transmission spectra are obtained by taking a spectral time series of the primary eclipse event. During the eclipse the stellar light is attenuated by the atmosphere. This attenuation depends on the optical depth, and thus on the molecular composition of the atmosphere. By measuring the depth of the transit light curve as a function of wavelength, the spectral signature of the molecules present in the atmosphere can be observed. An emission spectrum of the dayside is obtained by taking a spectral time series of the secondary eclipse event. By constructing a difference spectrum from the out of eclipse spectrum, when both the star and planet are visible, and the in eclipse spectrum, when only the star is visible, the emission of the exoplanet can be isolated. An example of dayside emission spectra we obtained with the Hubble and Spitzer Space Telescopes can be seen in Fig. 1.

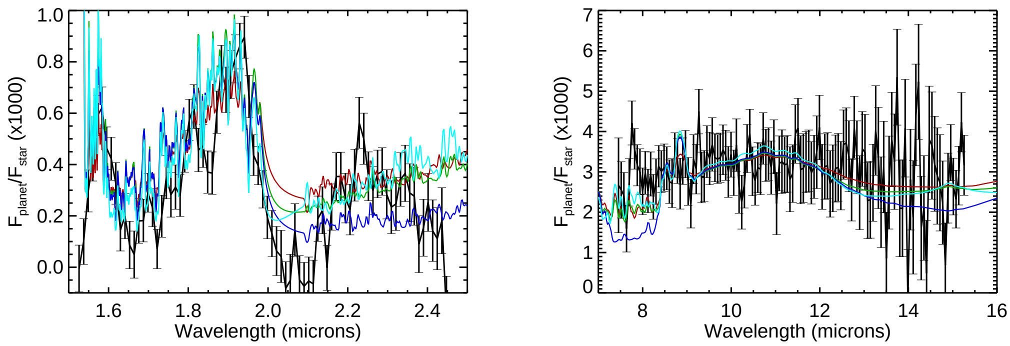

Figure 1: *Near-infrared (Hubble Space telescope [1]) and mid-infrared (Spitzer Space Telescope [2]) observations of the dayside emission of the the transiting exoplanet HD209458b. Also plotted are four model spectra that illustrate the range of temperature/composition possibilities consistent with the data (see also [1]). The blue curves show the best fit model with no temperature inversion within the planetary atmosphere while the red, green and cyan curves show the best fit models with a tropopause at a depth within the planetary atmosphere of 0.001, 0.01, and 0.1 bar, respectively. The smallest residuals between model and observation are achieved with the models which include a tropopause.*

A transmission spectrum is ideal for determining what molecules are present in the exoplanet atmosphere. This is because a transmission spectrum does not require temperature gradients to show the spectral features of molecules. Conversely, an emission spectrum requires the presence of thermal gradients for molecular features to be present in the spectrum. In practice, one uses the transmission spectrum to determine the composition, and the emission spectrum to determine a combination of the pressure-temperature profile and composition.

The atmospheric composition of exoplanets

It is important to realize that all transit spectroscopy results have been made with instruments not specially designed for this purpose. However, with the development of advanced calibration methods, with substantial contributions to this from the MPIA, observations with a dynamical range of upto 10000 could be achieved, making transit spectroscopy possible. Our first result was the mid-infrared daytime spectrum of HD 209458b (Fig 1;[2]) followed by the near-infrared spectrum obtained with Hubble [1]. With these spectra the presence of CH_4, H_2O and CO_2 could be confirmed. A similar result could be obtained for HD 189733b, where next to the same molecules as seen in HD 209458b, also the presence of CO could proven. With the dayside emission spectra of two exoplanets now available the next steps towards comparative exoplanetology can be made. A first comparison of HD 189733b and HD 209458b in terms of the temperature and molecular abundances showed marked differences [1]. Though these first results should be be interpreted as indicative, there is a strong suggestion of enhancement in the abundance of CH_4 and H_2O in HD 209458b relative to HD 189733b. A further difference is that while the presence of a tropopause in the atmosphere of HD 209458b seems certain, a temperature inversion in the atmosphere of HD 189733b seems not to be required.

An exciting new development is that for the first time a ground-based dayside emission spectra in the K- and L-band could be obtained for HD 189733b [4]. While the K-band spectrum is in full agreement with the Hubble observations, the L-band spectrum shows an surprisingly strong emission feature, several times stronger then predicted by current models. The emission feature is most likely non-LTE emission from the CH_4 $\nu 3$ band. This result shows that interpreting emission spectra of hot Jupiters assuming LTE conditions is questionable and improvements to current models have to be made. It is important to note that these observations also show that ground-based transit spectroscopy is possible with mid-sized telescopes and current instrumentation.

The above discussed results show the tremendous progress in the characterization of exoplanet atmospheres made in the last 3 years. With new observations with the re-servised Hubble Space Telescope, further analysis of Spitzer data, the possibility to also use ground based instruments for transit spectroscopy and the construction of the James Webb Space Telescope underway, will establish this decade comparative exoplanetology as an exciting new science field.

Collaborators are Mark R. Swain, Pieter Deroo , Gautam Vasisht, Pin Chen and Yuck Yung (Jet Propulsion Laboratory, USA), Caintlin A. Griffith (University of Arizona, USA), Giovanna Tinetti (University College London, UK), Daniel Angerhausen (German SOFIA Institute, Germany)

References

[1] Swain, M. R.; Tinetti, G.; Vasisht, G.; Deroo, P.; Grifth, C.; Bouwman, J. et al 2009, ApJ 704, 1616

[2] Swain, M. R.; Bouwman, J.; Akeson, R. L.; Lawer, S. ; Beichman, C. A. 2008, ApJ 647, 482

[3] Swain, M. R.; Vasisht, G.; Tinetti, G.; Bouwman, J. et al 2009, ApJ 690, 114

[4] Swain, M. R.; Deroo, P.; Grifth, C.; Tinetti, G.; Thatte, A., Vasisht, G.; Chen, P.; Bouwman, J.; Crossfield, I. J.; Angerhausen, D.; Afonso, C; Henning, Th. 2010, Nature, in press

On the formation of the resonant system HD 60532

Zsolt Sándor

Planetary systems in mean motion resonances

A significant fraction of multi-planet planetary systems contains pairs of giant planets in mean motion resonances (MMR). (Two planets are in a MMR if for their orbital period $T_1/T_2 = (p+q)/q$ holds, where p, q are small integers.) These planets are mainly in the 2:1 MMR, but two planets around 55 Cancri are thought to be in the 3:1 MMR and around HD 202206 the planets are in the 5:1 MMR. Resonant systems can be formed by convergent migration of (at least) two giant planets still embedded in the protoplanetary disk they were born.

The orbital behavior and the formation of the majority of resonant systems were studied thoroughly. It was shown by Kley et al. (2004, A&A 414, 735), that a slow migration of two giant planets ended either in 3:1 or in 2:1 resonant configuration. The formation of systems in the 2:1 MMR was modeled by hydrodynamical and N-body simulations as well; the system GJ 876 was investigated most recently by [1], HD 168311 and HD 73526 by [2] and [3], respectively.

The 3:1 MMR in the system 55 Cancri was already questioned by Naef et al. (2004, A&A 414, 351), and for the system was recently found a non-resonant orbital solution (Fischer et al. 2008, ApJ 675, 790). Thus the discovery of the two planets in 3:1 MMR around HD 60532 by Desort et al. (2008, A&A 491, 883) provided the first 3:1 MMR system. The final confirmation of the 3:1 MMR in HD 60532 was presented in a recent paper of Laskar & Correia (2009, A&A 496, L5) providing orbital solutions calculated from radial velocity observations.

In this work we investigated the formation of the resonant system HD 60532. Using the orbital parameters given by Laskar & Correia (2009, A&A 496, L5) as initial conditions, we integrated numerically the evolution of the 3-body system (star + 2 planets). We found that the behavior of the resonant angles did not match to the theoretical predictions on stationary solutions of the 3:1 MMR found by Beaugé et al. (2003, ApJ 593, 1124). The reason of this unexpected dynamical behavior may be found by studying the formation of the system through migration of the planets embedded in the ambient circumstellar disk. For our investigations we used full hydrodynamical and N-body simulations.

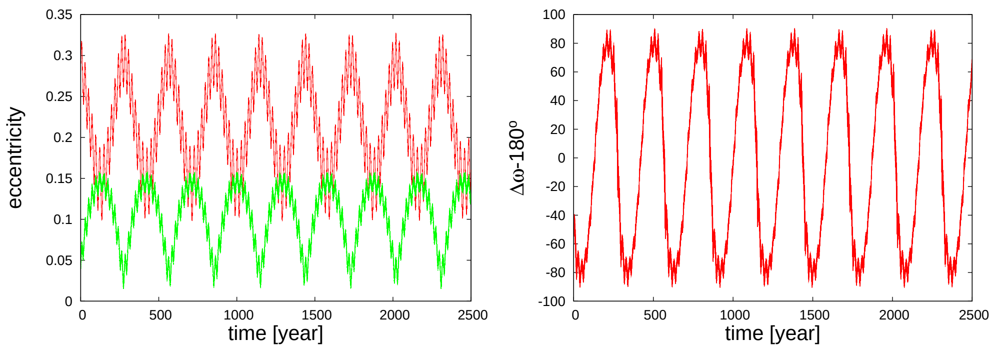

Figure 1: *Left: behavior of the eccentricities, red line corresponds to the inner, the green line to the outer planet. Right: behavior of the corotation angle* $\Delta\omega$.

Orbital behavior and migratory formation of HD 60532

The dynamical behavior of a resonant system can be characterized by the resonant angles, which for the 3:1 MMR are: $\theta_1 = 3\lambda_2 - \lambda_1 - \omega_1 - \omega_2$, $\theta_2 = 3\lambda_2 - \lambda_1 - 2\omega_2$, and $\theta_3 = 3\lambda_2 - \lambda_1 - 2\omega_1$, where λ_i is the mean longitude and ω_i is the argument of the periastron of one of the planets. The corotational angle is $\Delta\omega = \omega_2 - \omega_1$. All of the resonant angles can be expressed with an arbitrarily chosen θ_i and $\Delta\omega$. If one of θ_i-s librates around a constant value, the system is in a $3:1$ MMR, and if $\Delta\omega$ librates additionally, the system is in apsidal corotation as well.

Particularly for HD 60532, we found that all resonant angles librated; θ_1 around $0°$, θ_2, θ_3, and $\Delta\omega$ around $180°$ meaning that the system is in 3:1 MMR and also in apsidal corotation. The eccentricities of the planets show quite large oscillations $e_1 \sim 0.1 - 0.33$ and $e_2 \sim 0 - 0.15$, see Figure 1. Note that index "1" stays for the inner, index "2" for the outer planet.

According to the result on the stationary solutions of the 3:1 MMR of Beaugé et al. (2003, ApJ 593, 1124), the giant planets of HD 60532 are expected to be in an asymmetric apsidal corotation, where instead of 180°, the corotation angle $\Delta\omega$ would librate around $\sim 100°$. However, for HD 60532 this is not true meaning that during the migration of the planets the system did not reach its stationary state. On the other hand, Kley et al. (2004 A&A 414, 735) found that in their hydro simulations a model 3:1 MMR system reached the stationary solution, and therefore $\Delta\omega$ was librating around $\sim 110°$. In their setup the inner disk (the part between the inner planet and the star) was cleared, thus the inner planet moved in gas-free environment.

According to our results the inner disc plays an important role in shaping the dynamics of resonant systems (see [1], [3]), therefore in our present hydrodynamical simulations we assumed that the inner disk is not empty, on the contrary it is filled with dense gaseous material.

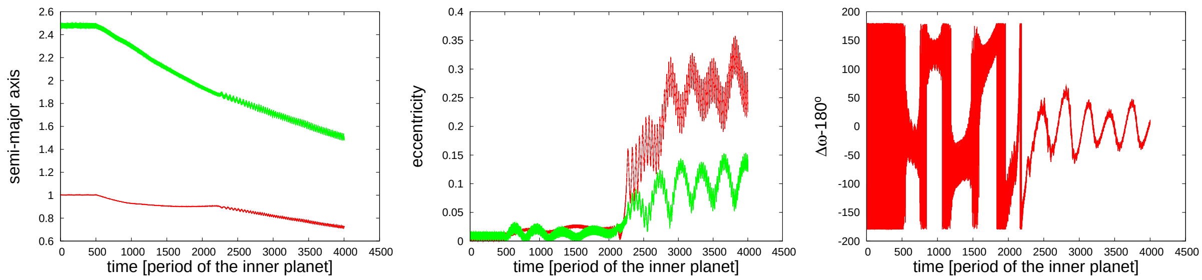

Figure 2: *Behavior of the semi-major axes, the eccentricities and the resonant angle* $\Delta\omega$ *during the migration of the planets.*

The results of our hydro simulations are shown in Figure 2. It can be seen that after the capture into the 3:1 resonance, the eccentricities oscillate very similarly to the numerical solution based on radial velocity data shown in Figure 1. Additionally, the corotation angle $\Delta\omega$ librates around 180° meaning that the dynamical effect of the inner disk impeded the system to reach the stationary solution.

We can conclude that in our hydro simulations we obtained a very silimar behavior of the system to that obtained from observations by numerical integration of the equations of motion. Moreover, the presence of an inner disk may have observable consequences in the post-formation behavior of resonant systems.
My collaborator is Wilhelm Kley from the University of Tübingen.

References

[1] Crida, A., Sándor, Z., and Kley, W., 2008, A&A, 483, 325

[2] Sándor, Z., Kley, W., 2006, A&A, 451, L31-34

[3] Sándor, Z., Kley, W., Klagyivik, P., A&A, 472, 981

Planets on the run

Hubert Klahr, Ana Uribe and Christoph Mordasini

Planets do not only wander around their host star, as their Greek name already implies, they also significantly change their semi major axis during their formation and evolution. They can either interact with the disk gas via tidal forces that can lead to both migration towards the star and away from it, or they gravitationally scatter with each other, if there is more than one planet. In both cases the location where we find a planet today is not necessarily the location where it was formed. This dislocation is a major effect for so called "population synthesis models" where we try to predict typical masses and semi-major axes for planets as a function of the stellar mass and metallicity.

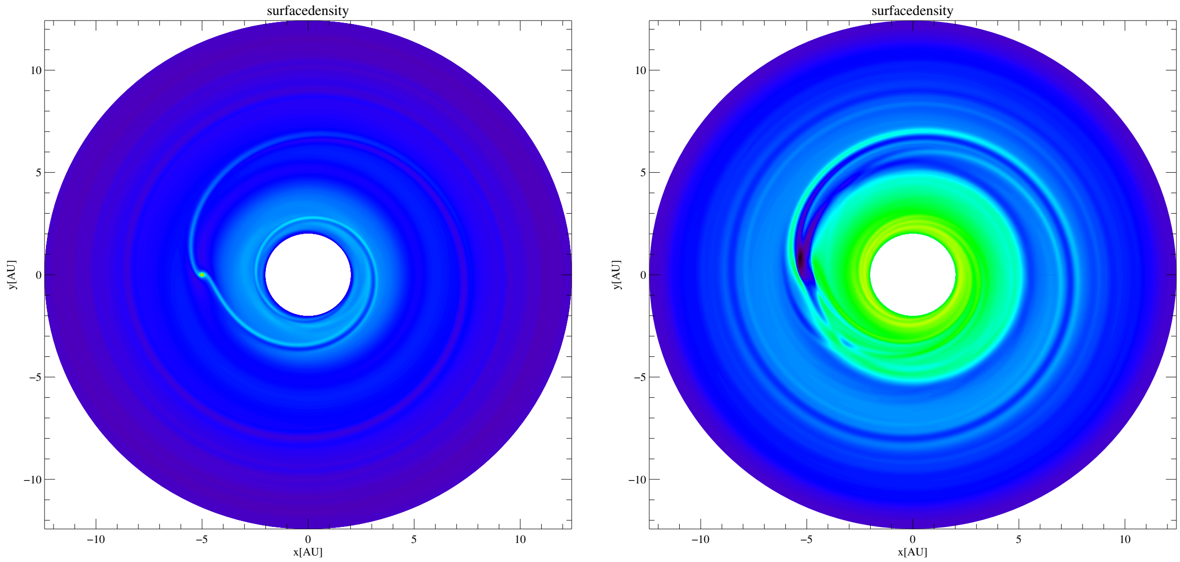

Figure 1: *A 30 Earth mass planet is embedded in a circumstellar disk. Color represents the density. The gravitational pull by the planet in combination with the Keplerian shear in the disk leads to the formation of the stationary spiral pattern. The image on the left shows the situation if the gas is treated as locally isothermal and on the right side if radiation transport and accretion energy is included into the simulation. One sees that the density and then also torques must change.*

In a newborn planetary system there are not only a number of planets interacting with each other via gravity, there is also a significant amount of gas left over from the planet formation process, which forms a wonderful spiral structure that builds up in the disk (see Fig.1a).

The net gravitational torque exerted by the spiral pattern onto the planet is now slightly negative, which means that the planet looses angular momentum and drifts radialy inward. The above shown case would be classified as Type 1 migration and is valid for up to about 100 Earth mass planets. When one is naively using the face value of migration almost no gas giants form at all, but almost all drop into the star, as a result of the fast migration and slow growing. The word of the "Last of the Mohicans" made the round, the idea that many Jupiters formed that all fell into the sun, but the last one, which was saved because the disk evaporated in time. This is a quite unsatisfying explanation and renders the planet formation process as very inefficient, which is somehow in contradiction with the plenty full of planets around our stellar neighbors.

But why should the planets migrate slower than what theory and numerics had demonstrated? Thermodynamics! All migration up until our work in 2004 [1] had been done in the two dimensional approximation or for isothermal disks, which means they have a fixed temperature structure throughout the simulation. Whereas the precise treatment of heating and cooling including radiation transport does little change in the Type 2 migration case is does a lot for Type 1 migration as was first put forward by Pardekooper and Mellema. They found that planets of 5-20 Earth masses should migrate outward instead of inward if only the thermodynamics are non-isothermal but adiabatic. In the last year we extended the numerical simulations of

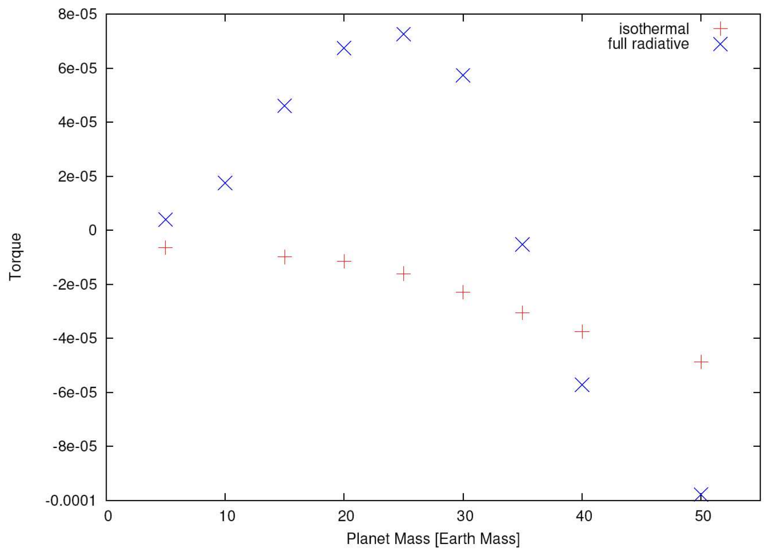

Figure 2: *Migration rate as a function of planet mass: Red crosses are the rate determined in analytic and numerical yet isothermal models. Blue Xes are our new values for full 3D radiation hydro*

Type 1 planet disk interaction to the full 3D case with flux limited diffusion for the radiation transport [2]. Fig. 1b shows the resulting density and temperature structure of the same 30 Earth mass planet that did such a wonderful spiral in the isothermal case (see Fig. 1a). In such a more realistic yet complicated flow field the torques from the material especially in the corotation region with the planet do not so easily cancel out each other anymore. The precise value of the net torque depends now also on the optical depth of the gas (surface density and opacity) and on the angular momentum transport via turbulence in the gas, which is currently studied by Ana Uribe in MHD simulations. In Fig. 2 we give a comparison between migration rates as a function of planet mass in the isothermal case which is always directed inward, and the full radiation hydro case, which is for a certain mass range directed outward. Currently Christoph Mordasini implements this migration behavior into the Population synthesis model he developed, so we will see whether this fix in the migration behavior will be sufficient to eradicate the currently used 1% fudge factor from the population synthesis model and still produce populations that agree with observation.
Collaborators are Willy Kley and Bertram Bitsch (Universität Tübingen).

References

[1] Klahr, H., Kley, W. 2006. A&A, 445, 747-758.

[2] Kley, W., Bitsch, B., Klahr, H. 2009. ApJ, 506, 971-987.

The turbulent birth of planetesimals

Hubert Klahr, Wlad Lyra, Anders Johansen, Andras Zsom

A very attractive way to form the kilometre sized Planetesimals in the early solar system is the "Gravoturbulent Fragmentation" of a cloud of relatively small icy and dusty objects. In a non-turbulent e.g. laminar disk sedimentation of particles leads rather to a Kelvin-Helmholtz instability driven turbulence than to a particle layer dense enough for gravitational collapse (Goldreich- Ward instability). Latest studies on the coagulation efficiency of dust aggregates have shown that cm-sized dust aggregates can rapidly form. However, any further growth seems to be inhibited by either the bouncing or the fragmentation barrier. Hence, we came up with a hybrid scenario in which turbulent concentration of depending on the location in the disk millimetre to meter sized icy and dusty material leads to sufficiently large densities in which self gravity dominates over gas drag and the tidal forces of the star, thus a heap of material collapses spontaneously under its own weight into a many kilometre sized planetesimal [1, 2, 3]. Meanwhile we started to perform extended simulations on the initial fate of colliding

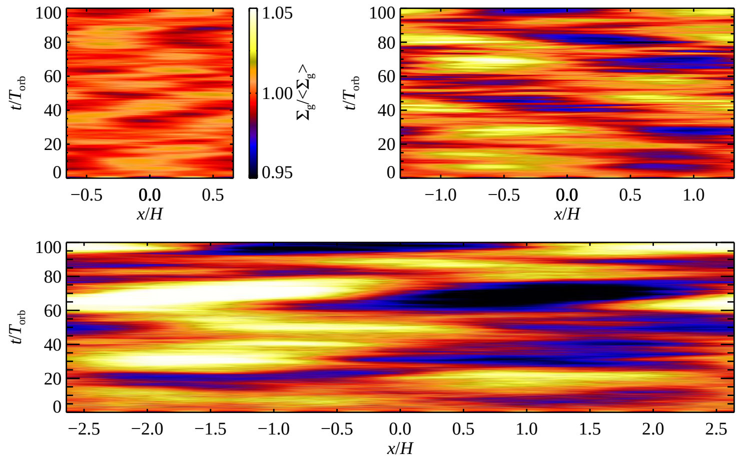

Figure 1: *The gas density of three runs averaged over the y- and z-direction, as a function of radial distance from the center of the box, x, and the time, t, given in orbits. Density structures get higher amplitude and longer lived as the box size is increased from $L_x = L_y = 1.32H$ to $L_x = L_y = 5.28H$. The height of the box stays fixed at $L_z = 5.28H$.*

pre-planetesimals [5] and the features that caused the particle concentration in the first place [9]. Here we find that the amplitude and lifetime of the particle concentrating flow feature increases with the physical size of our simulation domain, e.g. towards global simulations. The space-time plots of the gas density for three runs with increasing radial extent in radius shown in Fig. 1 confirm the dominance of the $k_x/k_0 = 1$ mode. Here we have averaged over the vertical and azimuthal directions and show the gas density as a function of radial coordinate x and time t measured in orbits. Both the density amplitude and the correlation time of the large scale structures increases significantly when making the box size larger.

Also truly global simulations have been performed by us also leading to the formation of planetesimals [4, 6, 7]. In [8] we study in the formation and evolution of vortices in greater detail, focusing on the implications for the dynamics of embedded solid particles and planet formation (See Fig. 2). We also estimate the collisional velocity history of the particles that compose the most massive embryo by the end of the simulation, finding that the vast majority of them never experienced a collision with another particle at speeds faster than 1 ms^{-1}. This result lends further support to previous studies showing that vortices provide a favorable environment for planet formation. Collaborators are A. Youdin (CITA), J. Oishi (Berkley), N. Piskunov

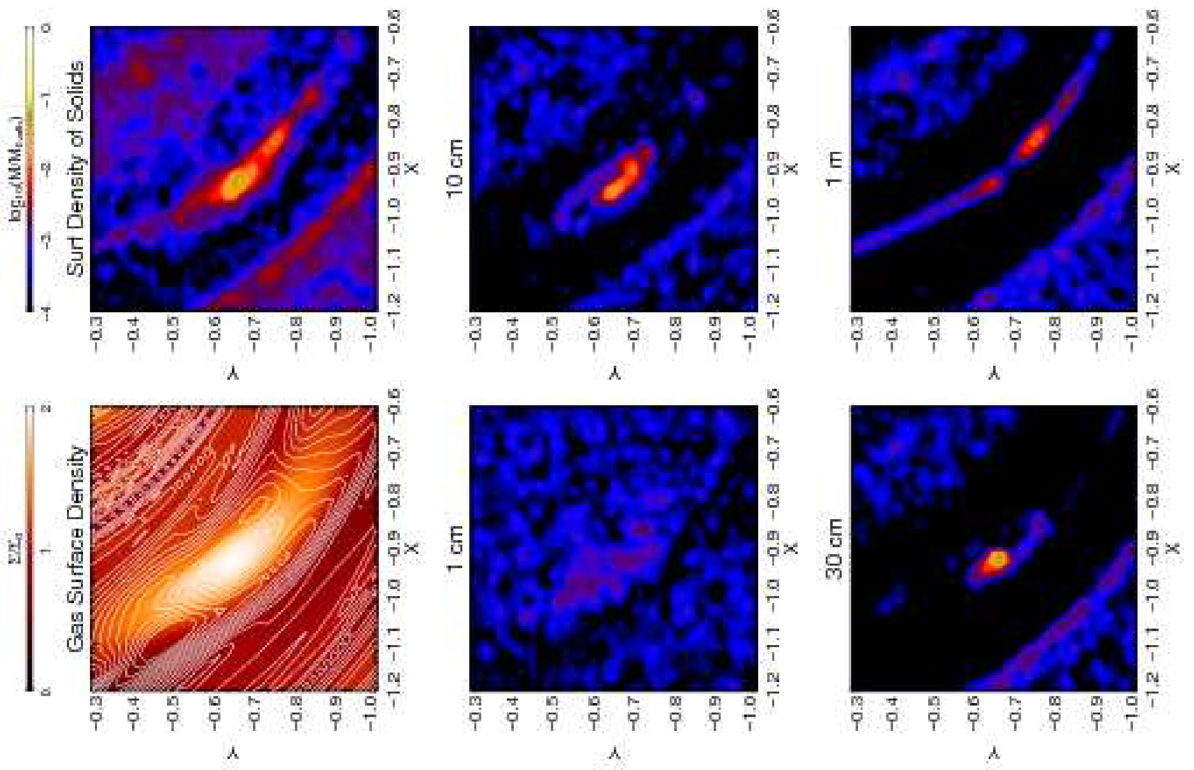

Figure 2: *Enlargement around a vortex in a global simulation of planetesimal formation [8]. Contours of vorticity are superimposed on the gas surface density, showing that the density enhancement is associated with intense vorticity. In the upper left panel we show the total surface density of solids, whereas in the middle and right panels we show the contribution of each particle species. The vortical motion preferentially traps particles of radius a=10 - 30 cm.*

(Upsala), and M.-M. Mac Low (American Museum of Natural History).

References

[1] Johansen, A., Klahr, H., Henning, T. 2006. ApJ 636, 1121-1134.

[2] Johansen, A., Oishi, J. S., Low, M.-M. M., Klahr, H., Henning, T., Youdin, A. 2007. nature, 448, 1022-1025.

[3] Klahr, H., Johansen, A. 2008. Physica Scripta Volume T 130, 014018.

[4] Lyra, W., Johansen, A., Klahr, H., Piskunov, N. 2008. A&A 479, 883-901.

[5] Johansen, A., Brauer, F., Dullemond, C., Klahr, H., Henning, T. 2008. A&A 486, 597-611.

[6] Lyra, W., Johansen, A., Klahr, H., Piskunov, N. 2008. A&A 491, L41-L44.

[7] Lyra, W., Johansen, A., Klahr, H., Piskunov, N. 2009. A&A 493, 1125-1139.

[8] Lyra, W., Johansen, A., Zsom, A., Klahr, H., Piskunov, N. 2009. A&A 497, 869-888.

[9] Johansen, A., Youdin, A., Klahr, H. 2009. ApJ 697, 1269-1289.

Planet formation via disk fragmentation

Hubert Klahr and David Foltin

We cannot really tell by looking at a planet whether it formed around a core or not. Even for Jupiter the existence of a core in its center is still under debate, the unknown properties of the equation of state for Jupiter material have a stronger influence on his size than the existence of this little additional potential of 5-10 Earth mass in its center. Such an alternative scenario, which works without a core, exists indeed.

If the circumstellar disk was at certain distances from the star massive enough for selfgravity to lead to a local gravitational collaps within the disk and on the other hand optical thin enough to cool on the collaps time scale, then one can in principle form pure gas planets of several Jupiter masses in a few hundred years. The conditions for this collaps are usually not given at the radii where we find most of the planets. Even if the disk were massive enough at 5AU where Jupiter could have formed it would not fragment, as the cooling time is many orbital periods. Instead of fragmentation the disk will react with gravitoturbulence and redistribute quickly mass and angular momentum, until the disk is no longer self-gravitating.

Yet at radii larger than 20-30 AU dependent on the stellar mass, metallicity and luminosity one finds the conditions for disk fragmentation fulfilled, as we were able to show recently at the MPIA [1]. As an example for our model we use the beautiful system HR8799 which hosts

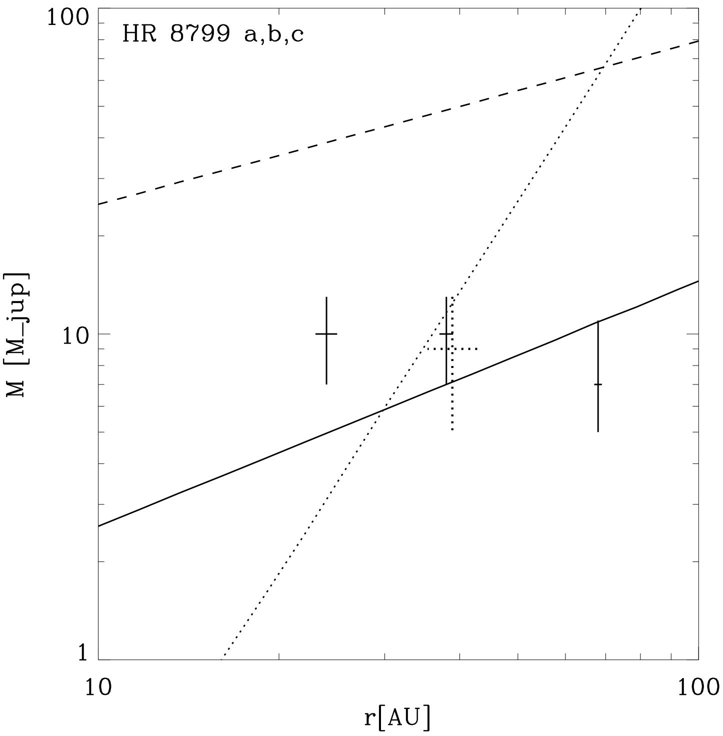

Figure 1: *The actual masses and locations of the system HR8799b,c,d and the allowed area given by the critical surface densities. Solid line = lower limit (i.e. self gravity), dotted line = upper limit (i.e. cooling rate) and dashed line = upper cut off (i.e. disk mass is half the stellar mass).*

three planets of 7 and 10 Jupiter masses at 24, 38 and 68 AU. In our model consiting of hydro static vertical disk atmosphere models we can determine cooling times and Toomre parameters Q (fragmentation occurs for Q$\leq$1). Based on a whole set of local models we can determine what range of surface densities would lead to fragmentation by being high enough for self gravity and low enough for fast cooling. These surface densities can be translated into probable masses of the fragments, which is what we show in Fig. 1. Interestingly only the middle planet is in the allowed region. But if we assume that all planets formed originally with the same semi major axis and calculate this location via the conservation of angular momentum, then the three planets end up right in the possible region for disk fragmentation. So it is conceivable that the planets in fact formed all at about 40 AU and then scattered out to their current location. The remaining disk would then have damped the eccentricity of the relocated planets and circularized them in a short time. Migration in such a self gravitating disk is also possible but has never been explored sufficiently.

We did also apply our method for the system GJ 758 (see Fig. 2), where a team led by MPIA astronomer Christian Thalmann discovered the coldest thermally imaged companion of a sun-like star and were able to show that a formation via disk fragmentation is quite plausible.

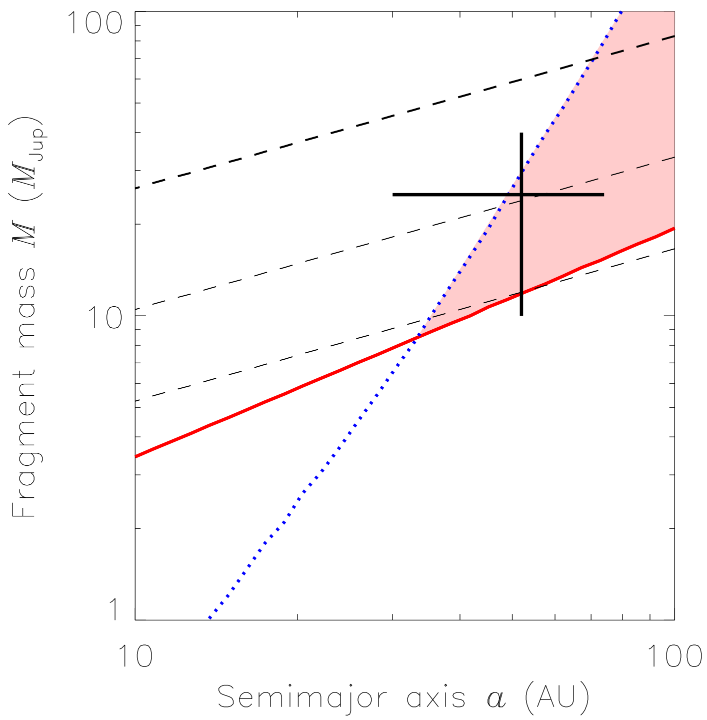

Figure 2: *Theoretical boundaries for objects formed by gravitational instability around GJ 758. The red shaded area shows the range of masses and separations of such objects immediatelyafter collapse. It is bounded by the Toomre criterion for unstable surface density underirradiation from the star (solid red line) and the requirement for sufficiently fast cooling times(dotted blue line). The dashed lines show the achievable masses for disk masses of 0.1, 0.2,and 0.5 stellar masses, from bottom to top. The derived properties of GJ 758 B (black bars) areconsistent with these conditions within 1σ. These calculations assume a radius of 3$R_\odot$, a mass of 0.97$M_\odot$, a metallicity of 0.22 and a temperature of 4200K for the protostar at zero age.*

References

[1] Foltin, D. and Klahr, H., ApJ, submitted.

Planet Population Synthesis: Theory meets observation

Christoph Mordasini, Kai-Martin Dittkrist, Hubert Klahr, Thomas Henning

Planetary population synthesis as a link between astronomical observations

Astronomical observations of the last decade have brought to us an enormous increase of knowledge of two basic types of astronomical objects: Protoplanetary disks and extrasolar planets. For both these classes, we nowadays know many different examples (e.g. more than 400 extrasolar planets). This enables us to study no more just single objects, but also the statistical properties, like for example the distribution of lifetimes of the circumstellar disks, or the distribution of masses and semimajor axes of the extrasolar planets.

Protoplanetary disks are the birth places of planets. They set the initial conditions. But the processes that transform the gas and dust contained in the disk into the planets cannot be observed directly. This planetary formation process can only be modeled theoretically.

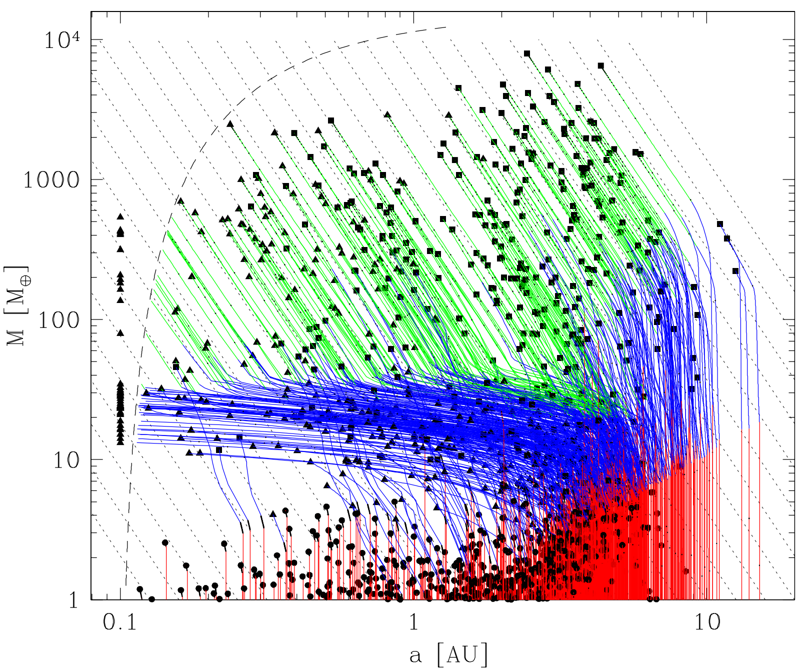

Figure 1: *Planetary formation tracks in the mass-distance plane, illustrating how the diversity of protoplanetary disk causes the diversity of planets. Planets start at a small initial mass, and a given initial semimajor axis. Depending on the disk properties, they then grow and migrate in a certain way to their final positions (large black symbols). Colors indicate migration regimes.*

Planetary population synthesis establishes this link in a statistical way. While population synthesis is a well known technique in stellar astrophysics, its usage for exoplanets is relatively new [1]. It became possible, apart from the mentioned observational progress, also because of the development of complex planet formation models. Its method is the following: One derives distributions of initial conditions from observed protoplanetary disks. A planet formation models is used to calculate the planets forming under given initial conditions. This step is repeated many times, synthesizing a population (see Fig. 1). The properties of the sub-group of detectable synthetic planets are then compared statistically with the ones of the actual exoplanets [2].

In this way, planet population synthesis is a unique tool to understand the formation process: By incorporating the latest theoretical results, one can understand their global consequences and check whether they lead to a synthetic population compatible with the observed one. But one can also use it to estimate the yield of future search campaigns, as it predicts the full underlying planetary population, unbiased from observational selection effects.

Correlations of disk and planetary properties and other current projects

Population synthesis is obviously a powerful tool to study the influence of disk properties on planetary properties. One such correlation is well known: The increase of the detection probability of giant planets with the host star metallicity. But many more correlation exist, as can be seen in the planetary initial mass function (PIMF, Fig. 1). The figure shows for example that a high metallicity causes the formation of a higher number of giant planets, explaining the mentioned observational result. A higher disk mass in contrast leads to the formation of giant planets of a higher mass, but in the same time less giant planets of a smaller mass.

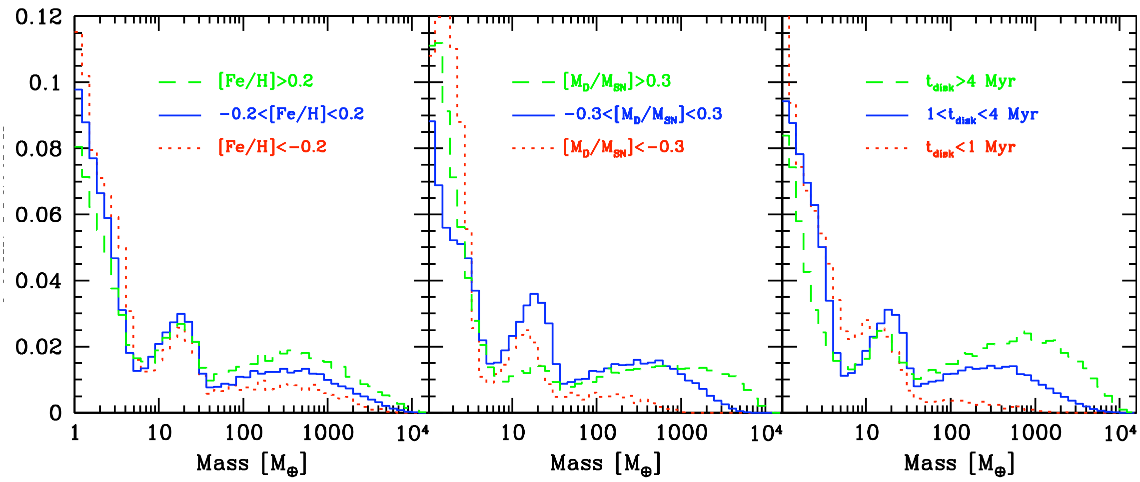

Figure 2: *Effects of disk properties on the planetary initial mass function. Left: Disk metallicity (dust-to-gas ratio). Center: Disk gas mass. Right: Disk lifetime.*

Other current research comprises
• the incorporation of the latest observational results on protoplanetary disk statistics.
• a better description in the model of the stopping mechanisms close to the star, which is important for transiting planets (Afonso group).
• the improvement of the theoretical description of migration, in particular also outward migration, important for direct imaging planets (C. Thalmann, J. Carson et al.).

Collaborators are Yann Alibert (Universität Bern, Switzerland) and Willy Benz (Universität Bern, Switzerland, and external scientific member MPIA).

References

[1] Mordasini, C., Alibert, Y., Benz, W., 2009, A&A, 501, 1139

[2] Mordasini, C., Alibert, Y., Benz, W., Naef, D., 2009, A&A, 501, 1161

5 Interstellar Medium, Circumstellar Envelopes, and Laboratory Astrophysics

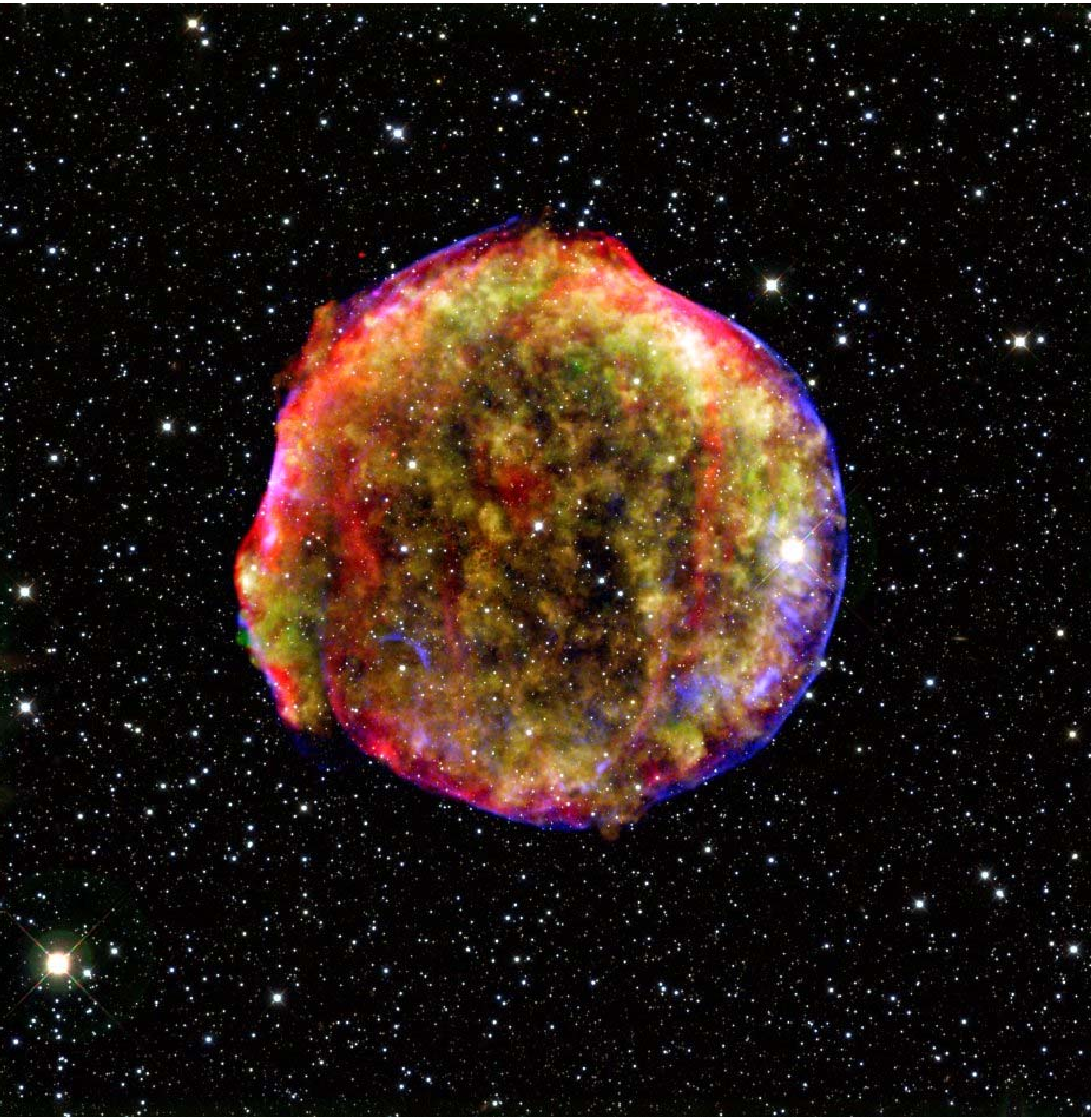

Image on previous page:
Composite image of the Tycho supernova remnant. Combined are infrared and X-ray observations obtained with the Spitzer and Chandra space observatories and the Calar Alto observatory. The thermonuclear explosion of the white dwarf star has left a several million degree hot cloud of expanding debris (green, yellow). The location of the blast's outer shock wave can be seen as blue sphere of ultra-energetic electrons. Newly synthesized dust in the ejecta as well as heated pre-existing dust from the circumstellar medium of the supernova radiates at a wavelength of 24 micron (red).
Credit: O. Krause (MPIA)

A new versatile public software package for 3-D radiative transfer in dust and gas

Cornelis Dullemond

Introduction

The interpretation of astronomical observations often relies on models of radiative transfer. As telescope facilities get larger and more sensitive, the use of simple 1-D models for the interpretation of observations of complex structures such as protoplanetary disks, turbulent molecular cloud complexes, aspherical stellar winds, etc becomes more and more obsolete. In particular because also the numerical hydrodynamic models of such objects are nowadays often fully 3-D, modern radiative transfer tools should be able to deal with 3-D structures. In 3-D models it is common that various kinds of adaptive mesh refinement (AMR) techniques are employed. This allows for high spatial resolution in regions where it is required, while not wasting computer power on regions where low resolution is fine. Currently there are several 3-D computer codes for dust continuum radiative transfer as well as for line radiative transfer in the community. However, with a few notable exceptions, many of these codes remain non-publically available. Also, the vast majority of these codes are *either* continuum *or* line transfer codes. For many applications it is important to be able to treat both within a single framework. This becomes now even more important with the Herschel space telescope, with which far-infrared gas lines and dust continuum are going to be observed originating from the same regions. And at the shortest wavelength bands of ALMA continuum optical depth effects may also play a role even when one focuses on measuring gas lines. There is therefore a clear need for a 3-D AMR-based radiative transfer code package that can handle these processes in an integrated fashion.

My goal was to fill this need with a new code, which will become publically available once it gets beyond the beta-stage, which has a good manual and is reasonably easy to use while still powerful and flexible. We already had an old code for dust continuum radiative transfer, `RADMC`, which was meant for axisymmetric circumstellar nebulae/envelopes/disks, as well as a line transfer code `RADICAL` which is a fully non-LTE transfer code for lines without continuum. Furthermore there is, at our institute, the STEINRAY and MC3D codes available.

I started from some of the ideas from these codes, and code fragments from `RADMC` and `RADICAL`, and built a new code, `RADMC-3D`, basically from scratch. It is written in Fortran-90, is very modular, and includes easy-to-use IDL front-end routines, including an easy-to-use graphical user interface for making images (Fig. 1). It can be used in cartesian coordinates as well as spherical coordinates, and includes the possibility of AMR gridding. This code is currently still in the beta-phase but I expect to publically release a first version before the Fachbeirat.

Dust continuum transfer: A Monte Carlo approach

The objective of the dust continuum part of the code is twofold: to compute dust temperatures and scattering source functions and to compute images and spectra. Before images and spectra can be computed, the dust temperature everywhere has to be calculated self-consistently. Dust grains are usually in thermal equilibrium in the sense that they absorb as much radiation as they emit, keeping them at a constant temperature. Therefore these dust grains are strongly coupled to the radiation field. Computing the dust temperature therefore means that one has to solve it together with the radiation field. In `RADMC-3D` this is done using a relatively standard method: a Monte Carlo algorithm following [1], combined with some ideas of [2].

Once the dust temperature is known everywhere, images and spectra can be made using `RADMC-3D` as a ray-tracer. This can be done with an IDL widget tool that allows on-the-fly

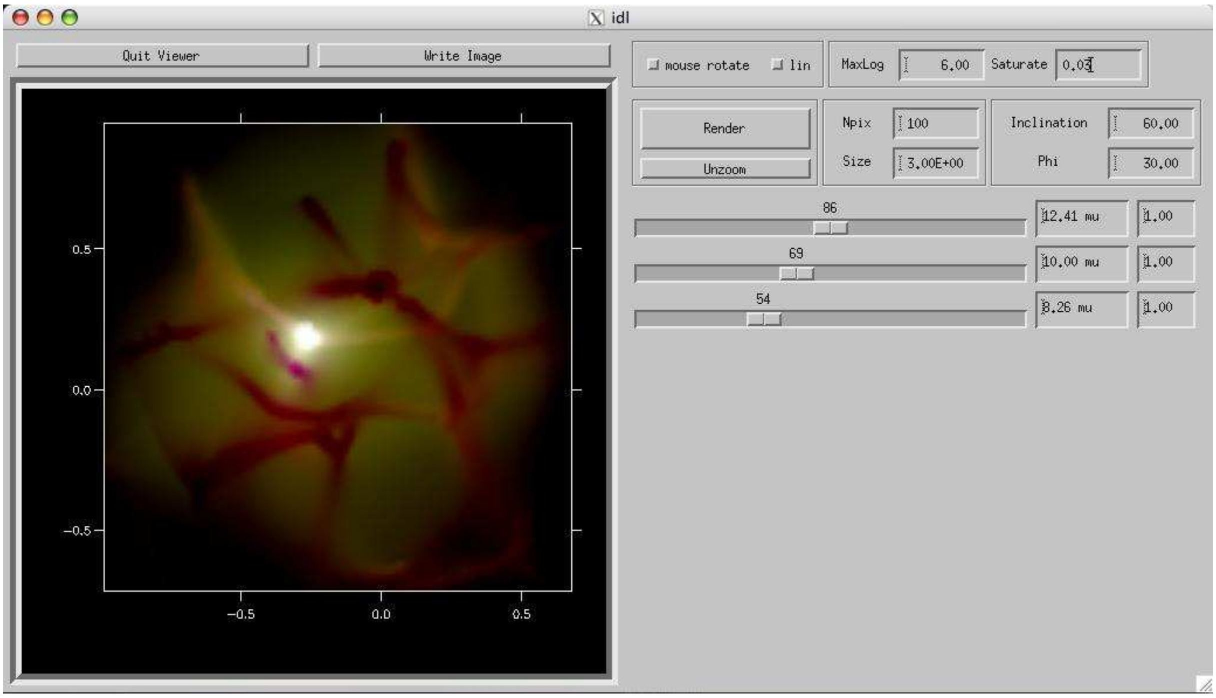

Figure 1: *User interface of* `RADMC-3D` *imager.*

changing of camera position, orientation, zoom-factor, resolution and wavelength (Fig. 1). Care is taken that all the flux is picked up by the algorithm, even if structures exist that are unresolved by the pixels of the image. This is done with a recursive sub-pixeling method. But before the ray-tracing is done, a very quick scattering Monte Carlo computation has to be done to compute the appropriate scattering source function. This second kind of Monte Carlo computation is very fast compared to the thermal Monte Carlo computation. In this way, non-isotropic scattering can be included properly.

Line transfer with dust continuum

In `RADMC-3D` line transfer is done either in local thermodynamic equilibrium (LTE) or with user-specified level populations. A full non-LTE approach is in most cases extremely costly, and there are various arguments that standard non-LTE methods such as Accelerated Lambda Iteration may not be more reliable than clever approximations such as Large Velocity Gradient methods (Sobolev's approximation) or Escape Probability methods. Therefore as an alternative to LTE, we allow the user to specify the level populations directly or via a user-specified subroutine.

From that point onward the lines are included in all images and spectra. The doppler shifts of the lines are taken into account, and so is the dust continuum. In other words: lines and continuum now work hand-in-hand.

References

[1] Bjorkman, J. & Wood, K.,2001, ApJ,554,615

[2] Lucy, L.B., 1999, A&A,344,282

Stochastic simulations of gas-grain chemistry

Anton Vasyunin, Dmitry Semenov, Thomas Henning

Monte Carlo Approach to Model Gas-Grain Chemistry

Chemical processes occur on the surfaces of interstellar grains in the regions of star and planet formation are of crucial importance for the formation molecular hydrogen and complex organic species. Also, they strongly influence the abundances of major gas-phase species – observational tracers of star formation. Chemical rate equations are widely used to model chemical evolution of the interstellar medium. While this approach is reliable for gas-phase chemistry, it may not be valid for grain surface chemistry since each individual grain is tiny and only a handful of molecules can be involved in chemical processes on it. In this case, fluctuations of abundances of species become important and one has to use a stochastic approach instead of deterministic rate equations.

In our work, for the first time we developed the rigorous and robust stochastic approaches to grain surface chemistry applicable to full-scale astrochemical models (up to few thousands reactions) and investigated under which conditions the usage of stochastic techniques is essential in astrochemical modeling. For the first time we build a realistic astrochemical model using

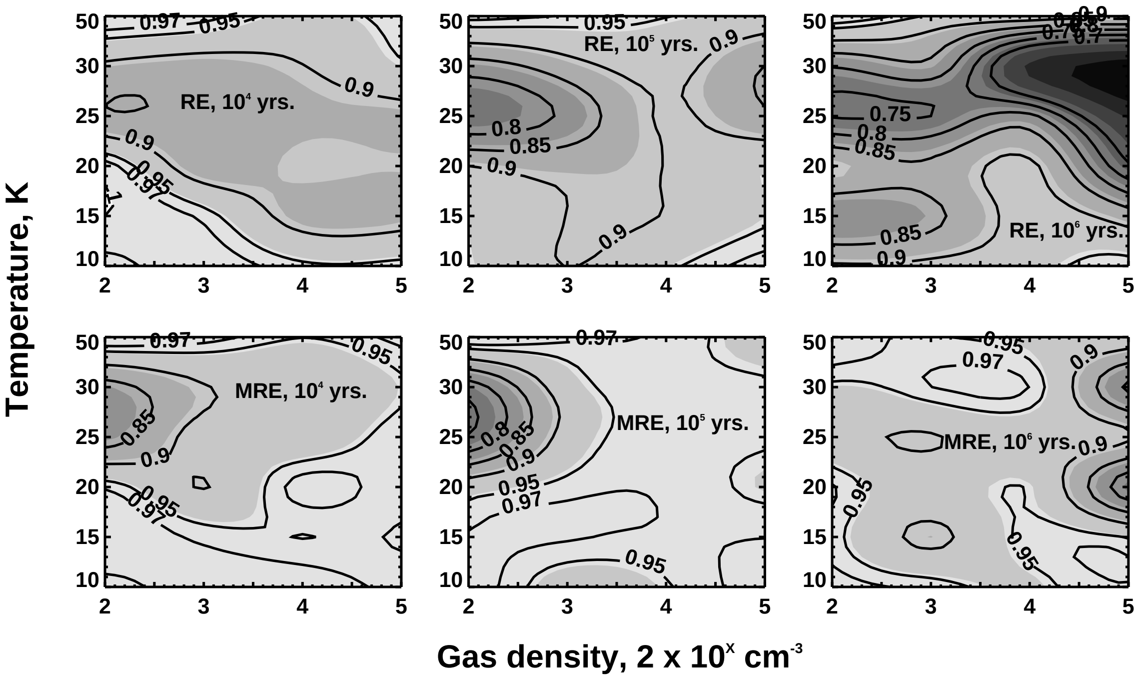

Figure 1: *Global agreement diagrams at three evolutionary times of 10^4, 10^5 and 10^6 yrs. Contour labels show the percentage of species whose abundances computed with rate equations (top row) or modified rate equations (bottom row) differ from those of the Monte Carlo method by no more than one order of magnitude. Grayscale map with arbitrary contours is added for clarity. Darker color corresponds to worse agreement.*

Monte Carlo approach to all – gas phase and grain surface – chemical processes. This allows us to properly take into account the stochastic nature of grain surface chemical reactions. This model includes more that 6000 reactions in total, among them more than 200 grain surface reactions. Using this model, we performed simulations of chemical evolution of the interstellar medium over a grid of physical conditions typical for the regions of star formation: n_H=$2{\cdot}10^2$–$2{\cdot}10^5$ cm^{-3}, T=10–50 K and compared the results with those obtained with rate equations. We found that if quantum tunneling of light species through the potential barriers on grain surface is included in the model, results obtained with rate equations deviate significantly from those of rigorous Monte Carlo approach all over the parameter space considered, especially at late time of $\sim 10^6$ yrs.) (see Fig. 1). While at low temperatures (10–20 K) only abundances of grain surface species are affected, at moderate temperatures of 20–30 K inaccuracies propagate to the gas phase abundances (Fig. 2). This is due to the efficient gas–grain interaction through the processes of accretion and desorption while the surface chemistry is still active at this temperature range.

Modifications to the Rate Equations

The rigorous Monte Carlo method cannot be used in "everyday" astrochemical modeling since it is computationally intensive. Therefore it is of interest to develop modifications to rate equations to enable them to account for stochastic effects in surface chemistry properly.

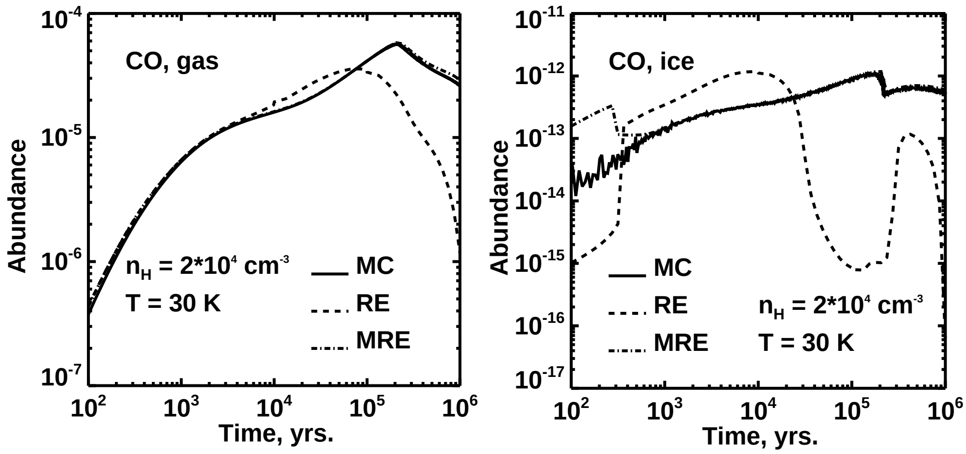

Figure 2: *Gas-phase and grain-surface time-dependent abundances of CO in one of the worst cases for rate equation accuracy: n_H=$2{\cdot}10^4$ cm^{-3}, T=30 K calculated with RE (dashed line), MRE (dotted–dashed line) and Monte Carlo (solid line).*

In our work, we have shown that modified rate equations proposed by Garrod (2008, A&A, 491, 239) show much better agreement with Monte Carlo values (see Fig. 1, bottom row, Fig. 2). Even at critical temperatures of 20–30 K abundances obtained with Monte Carlo and modified rate equations are close to each other, especially at late times. The computational efficiency of the new modified rate equations is much higher than of the Monte Carlo method and comparable with the efficiency of classical rate equations.
Collaborators are Dmitry Wiebe (INASAN, Russia), Robin Garrod (Cornell University, USA)

References

[1] Vasyunin, A. I., Semenov, D. A., Wiebe, D. S., & Henning, T. 2009, ApJ, 691, 1459

[2] Garrod, R. T., Vasyunin, A. I., Semenov, D. A., Wiebe, D. S., & Henning, T. 2009, ApJL, 700, L43

An ultraviolet survey of CO and H_2 in diffuse molecular clouds

Roland Gredel

The CO to H_2 conversion factor in molecular clouds

Molecular hydrogen is the most abundant molecule in the cosmos, but it has no permanent dipole moment and is thus lacking permitted pure rotational transitions that would allow its detection in quiescent molecular clouds. On the other hand, rotational transitions of CO have been extensively observed in molecular clouds, and are used to delineate global distributions of molecular clouds in our Galaxy and in other galaxies. It is an empirical and theoretical foundation of radio mapping that the velocity-integrated emission intensity of the CO (1,0) transition at 115 GHz (I_{CO}, in units of K km s^{-1}) from a molecular cloud is proportional to the total virialized mass of the cloud and hence to its hydrogen content. Radio astronomers thus utilize I_{CO} as a proxy for H_2, by employing a conversion factor $X_{CO} = N(H_2)/ I_{CO}$, where $N(H_2)$ column density of molecular hydrogen. An average value of $X_{CO} = 4 \times 10^{20}$ cm^{-2} (K km s^{-1}) $^{-1}$ is ascribed to giant molecular clouds in the Milky Way.

Direct measurement of the N(CO)/N(H_2) ratio in diffuse clouds

The column densities of CO and H_2 can be measured directly in diffuse molecular clouds. Both CO and H_2 are photo-dissociated by far-UV radiation, resulting in a variable X_{CO} that depends on the efficiency of self-shielding (as well as mutual shielding) of the two species and thus on their column densities. One of our goals is to study the behavior of X_{CO} under diffuse ISM conditions where the molecules are exposed to the UV photons of the interstellar radiation field.

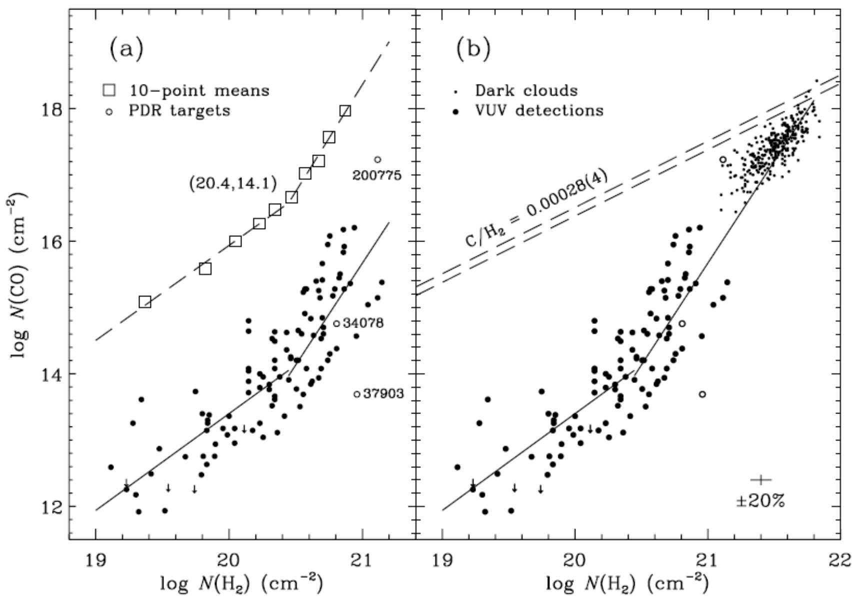

Figure 1: CO vs. H_2 column densities for our sample of diffuse clouds. See text for explanations.

The visual extinction of diffuse molecular clouds (as well as envelopes of dark clouds) is below 5 mag in general, which allows to obtain ultraviolet absorption lines of CO and H_2 in the spectra of background stars. Very accurate measurements of the column densities N(CO) and N(H_2) are obtained this way. We have used archival HST, FUSE and Copernicus data to infer the CO and H_2 column densities towards 106 lines of sight ([1]). The data are plotted in Figure 1. Open circles represent sight lines probing prominent photon-dominated regions. In panel (a) the sample is fitted with two power laws, as revealed by the 10-point means. Panel (b) expands the view to include CO derived for dark clouds (smaller filled circles in the upper right). Practically all CO abundances are found below the limit set by C/H_2 (dashed lines in Fig. 1b with 1σ limits).

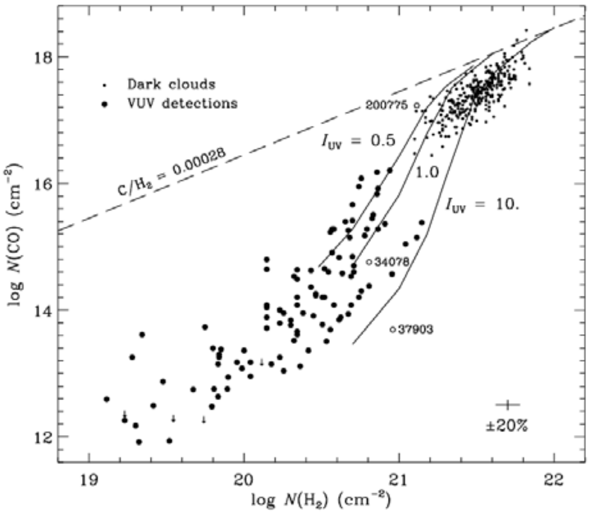

Figure 2: CO vs. H_2 distribution for diffuse and dark clouds compared with models from van Dishoeck and Black (1988, ApJ 334, 771) calculated for I_{UV} = 0.5, 1, and 10 (scaling factor for average interstellar UV radiation field).

Our sample reveals a clear signature of a dual power law correlation between the CO and H_2 column densities, with a break near log N(CO) = 14.1 and log N(H_2) = 20.4. The steeper slope observed for higher H_2 column densities is seen to pass near the center of the dark cloud distribution. Our chemical analysis suggests that the break arises from a change in the production route of CO, due to the variation in the intensity of the UV radiation field. In the low density gas (log N(H_2) < 20), reactions involving CH^+ are found to be the dominant route to CO (see also [3]). At higher densities, reactions involving C+ are dominant. In Figure 2, we show that the theoretical models of van Dishoeck and Black (1988, ApJ 334, 771) are in astonishing agreement with the CO and H_2 column densities derived from our sample.

Collaborators are N.P. Abel, S.R. Federman, D.L. Lambert, M. Rogers, G. Shaw, Y. Sheffer, J.A. Thorburn, and D.E. Welty

References

1. Sheffer, Y., Rogers., M., Federman, S.R., Abel, N.P., Gredel, R., Lambert, D.L., Shaw, G. 2008, ApJ 687, 1075
2. Sheffer, Y., Rogers, M., Federman, S.R., Lambert, D.L., Gredel, R., 2007, ApJ 667, 1002
3. Welty, D.E., Federman, S.R., Gredel, R., Thorburn, J.A., Lambert, D.L. 2006, ApJS 165, 138

Absorption line survey of H_3^+ in the Central Molecular Zone of the Galactic center

Miwa Goto, Thomas Henning

H_3^+ in space

Hydrogen, the most abundant atoms in the universe, has six stable forms: H^+, H, H^-, H_2^+, H_2 and H_3^+. Only three of them H, H_2, H_3^+ are useful as astrophysical probes in the interstellar medium (ISM). H and H_2 were discovered in space in 1951 and 1970, respectively. Search for the third astrophysical probe of hydrogen, H_3^+ was, initiated by Oka (1981, RSPTA, 303, 543) who predicted absorption lines of H_3^+ at 3.7 μm. It was not until 15 years after the prediction that the first H_3^+ ISM detection was successfully carried out by Geballe & Oka (1996, Nature, 384, 334) in a molecular cloud toward AFGL 2136 and W33A. Although it took a long time for the first detection, astronomers quickly realized that H_3^+ molecular ion are ubiquitous. H_3^+ exists not only in dense clouds, but also diffuse clouds. The H_3^+ absorption in the line of sights passing through diffuse clouds are 10 times deeper than is expected from the steady state analysis. McCall et al. (2003, Nature, 422, 500) carefully analyzed the H_3^+ in the diffuse cloud toward ζ Persei with the updated dissociative recombination rate with electron k_e, and concluded that the cosmic ionization rate, which is of prime importance for interstellar chemistry, is one order of magnitude larger than previously thought.

H_3^+ is important for multiple reasons. First, the chemistry of H_3^+ is simple. The number density of H_3^+ is only dependent on the formation of H_2^+ by cosmic ray ionization, and the destruction by recombination with either CO or electrons. The molecular ion therefore serves as an excellent astrophysical probe with minimum uncertainty in the interpretation. Second, as cosmic rays are everywhere, H_3^+ is everywhere, as long as molecular hydrogen is present. H_3^+ is an even better astrophysical probe than H_2, as the high ratio of the dipole to quadrupole transition strength ($\sim 10^9$) overcomes the low fractional abundance of H_3^+ [$n(H_3^+)/n(H_2) > 10^{-7}$]. This is demonstrated by the fact that H_3^+ has been detected in about 100 line of sights by now, while only a handful of sightlines show H_2 absorptions in the infrared (Lacy et al. 1994, ApJL, 428, 69). Third, the neutral-ion reaction is more efficient than the neutral-neutral reaction in the ultra low density environment in the ISM because of the high Langevin rate. H_3^+ is the most fundamental ion molecule. It plays an important role in the interstellar chemistry incomparable with any other ion molecules in the ISM.

H_3^+ in Galactic Center

We will discuss the recent highlight of the H_3^+ study below. We have carried out a small survey of H_3^+ in the Galactic center with high resolution infrared spectroscopy using 8 bright infrared stars in the central and Quintuplet clusters as the background continuum source (Oka at al. 2005, ApJ, 632, 882; [1]). These observations quadruple the number of sources in which H_3^+ has been detected in the Galactic center (Geballe et al. 1999, ApJ, 510, 251). The absorption of $R(1,1)^l$ is detected at 3.715 μm for all sources. The absorption lines are deep, an order of magnitude deeper than the absorption in diffuse clouds in the Galactic disk. The deep absorption of $R(1,1)^l$ in the Galactic center means that either the cloud dimension L or the cosmic ray ionization rate ζ is an order of magnitude larger than in the Galactic disk ($\zeta \sim 10^{-15}$ s^{-1}).

The first H_3^+ absorption from the excited state was discovered by Goto et al. (2002, PASJ, 54, 951). The absorption line $R(3,3)^l$ are all positively detected in 8 sources. The rotational level (J,K)=(3,3) is 331 K higher than the lowest level. The detection of $R(3,3)^l$ at 3.534 μm and the non-detection of $R(2,2)^l$ except GCIRS 3 indicates that there is a large cloud of the size of 30–100 pc in the Galactic center with high temperature (200–350 K) and low density (<50–

200 cm^{-3}; Oka & Epp 2004, ApJ, 613, 349; Fig. 1). The warm and diffuse cloud is possibly an important population in the Galactic center. The central molecular zone (CMZ) of the Galactic center is filled with cold molecular clouds known from radio spectroscopy to have a filling factor of 10% or less. The rest is filled by ultra hot plasma (10^7–10^8 K) detected in x-ray spectroscopy with warm ionized gas in the interface between the dense molecular clouds. The warm and diffuse gas newly detected by H_3^+ with large filling factor might change the fundamental picture of the medium in the CMZ.

The H_3^+ absorption line $R(2,2)^l$ is detected at 3.620 μm for the first time in the ISM in the line of sight toward GCIRS 3. The presence of $R(2,2)^l$ indicates that the gas is dense (175-300 cm^{-3}), which is exceptional among other line of sights observed in this study. GCIRS 3 is also exceptional to show $R(3,3)^l$ absorption deeper than $R(1,1)^l$ in the same positive velocity with $R(2,2)^l$. The gas should be warm and dense, and the cosmic ionization rate is higher than the other sightlines in the Galactic center by yet another order of magnitude. However, the nature of the cloud toward GCIRS 3 remains unclear. The velocity of the absorption line of +50 km s^{-1} associated with the cloud coincides with that of the well-studied "+50 km s^{-1}" cloud near the Galactic nucleus. The velocity of the absorption line is also roughly consistent with the circumnuclear disk at the location near GCIRS 3. Further search for $R(2,2)^l$ is in progress for other sources in the central cluster in order to test if the warm and dense gas is local to GCIRS 3.

Collaborators are Takeshi Oka (University of Chicago), Tom Geballe (Gemini Observatory), Ben McCall, Nick Indriolo (University of Illinois), Tomo Usuda (Subaru Telescope).

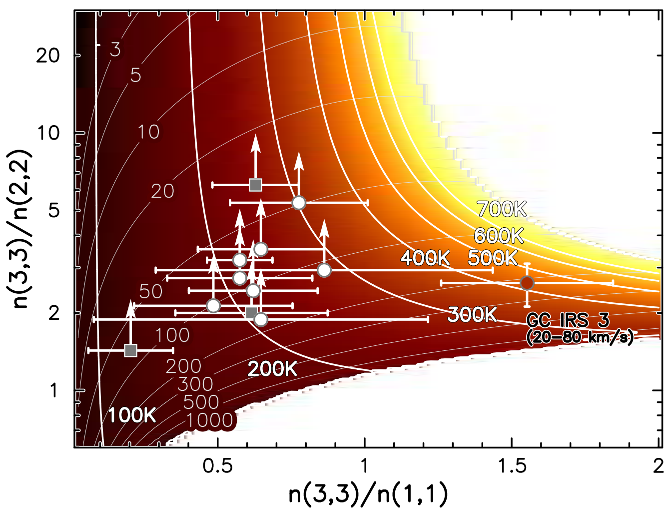

Figure 1: *Temperature and density plot as functions of population ratios n(3,3)/n(1,1) and n(3,3)/n(2,2). Temperature is indicated by thick white lines and density by thin lines.*

References

[1] Goto, M., Usuda, T., Nagata, T., Geballe, T. R, McCall, B. J., Indriolo, N., Suto, H., Henning, Th., Morong, C. P., Oka, T.2008, ApJ, 688, 306

Quantitative optical and near-infrared spectroscopy of molecular hydrogen in HH 91

Roland Gredel

H_2 emission in protostellar jets

Outflows from young stellar objects (YSOs) drive powerful shock waves into the interstellar medium, and the heating associated with the shocks results in emission from molecular hydrogen in general. The total H_2 luminosities are proportional to the accretion rates of the YSO, and the ro-vibrational excitation of H_2 is sensitive to physical conditions in the shocked gas. Emission from ro-vibrational levels in v' = 1 – 5 is detected at near-infrared wavelengths and attributed to arise from hot gas at temperatures of several 1000 K. Signatures of non-thermal excitation processes, such as H_2 fluorescence in strong UV fields created in fast shocks or impact excitations from energetic secondary electrons created by X-rays from embedded TTau stars have been sought as well, but are not detected in general ([1], [2], and references therein).

Optical emission of H_2 in HH91A

It is not widely recognized that H_2 emission may be detectable at optical wavelengths as well. Non-thermal excitation processes such as UV fluorescence populate ro-vibrational levels with v'>5, and emission from these levels may become detectable at wavelengths below 1 µm.

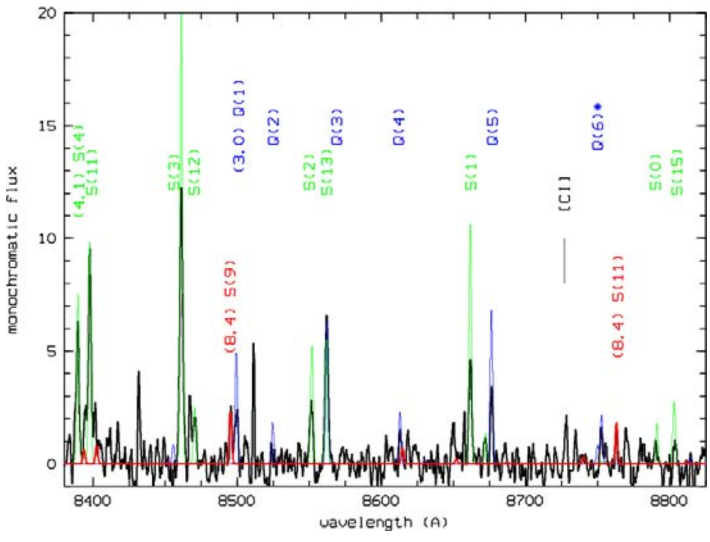

Figure 1: Observed spectrum (black) of HH 91A obtained with PMAS at the CAHA 3.5m telescope. Modeled spectrum obtained for thermal emission from a column of 10^{18} cm^{-2} of gas at 2750K which contains 1% of hot gas at 6000K is reproduced in color.

In a previous study ([3]), we have discovered very strong H_2 emission in HH 91A, which has prompted us to search for signatures of non-thermal excitations in the optical wavelength region. Figure 1 reproduces one of the optical spectra obtained with PMAS at the CAHA 3.5m telescope. Emission from the (8,4) S(9) and S(11) lines are marginally detected. We have complemented the optical studies with deep J, H, and K-band spectra obtained with SOFI at the NTT. An example of the near-infrared spectra is shown in Figure 2, which also reveals emission in high excitation lines such as the (6,4) Q-branch. In total, we have detected about 200 H_2 emission lines towards HH 91A ([1]), In spite of the detected emission from v'>5, the emission spectrum is purely thermal, and well explained to arise from a mixture of gas where the bulk of the gas is at a temperature of 2750K and where 1% is at the very high temperature of 6000K. The total column of H2 towards HH 91A is 10^{18} cm^{-2}. Conditions that would lead to detectable non-thermal excitations of H_2 towards HH 91A are absent. The total column of shocked H_2 is 10^{18} cm^{-2} and is explained to arise from a slow J-type shock which propagates into a low-density medium which has been swept up by previous episodes of outflows which have occurred in the HH 90/91 complex.

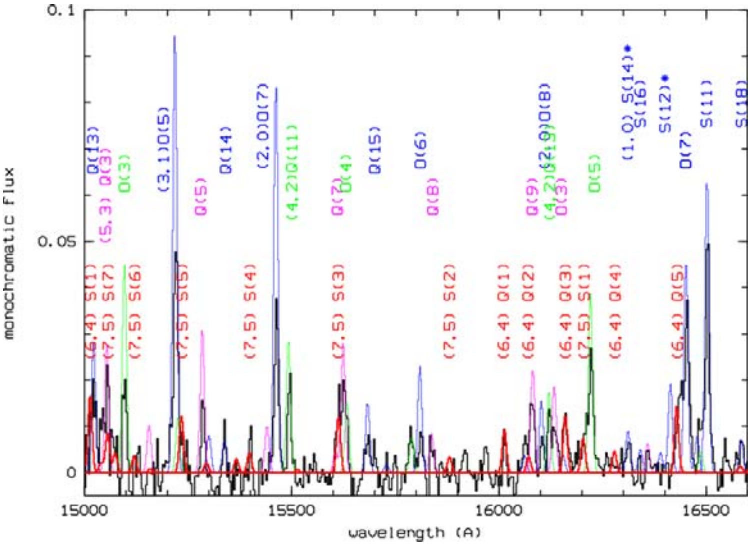

Figure 2: Near-infrared spectrum obtained with the SOFI/NTT (black). Model spectrum (see caption of Figure 1) reproduced in color.

Our conclusions were derived from an analysis of the ro-vibrational population distribution inferred from the manifold of 200 emission lines observed towards HH91A, and are supported by a model spectrum which has been set up for the 2750K+6000K gas mixture. The model spectrum is fully consistent with the observed spectrum, as shown in Figs. 1 and 2. This is the first time that optical emission of H_2 has been detected in interstellar shocks and where the ro-vibrational excitation in levels v'>5 is ascribed to a pure thermal excitation scenario.

References

[1] Gredel, R., 2007, A&A 474, 941
[2] Guedel, M., Skinner, S.L., Cabrit, S., Eisloeffel, J., Dougados, C., Gredel, R., Briggs, K.R., 2009, in *Protostellar Jets in Context*, eds. K. Tsinganos, T. Ray, M. Stute, Berlin, Springer
[3] Gredel, R., Reipurth, B., Heathcote, S. 1992, A&A 266, 439

Light echoes of galactic supernovae

Oliver Krause, Miwa Goto

A supernova (SN) in our own Galaxy is a rare event: Only six SNe were registered during the past millennium. The remnants of these historic Galactic SNe such as the Crab nebula or Cas A have been extensively studied across the electromagnetic spectrum and provide, due to their proximity, the best view of the physical conditions and processes hundreds of years after outburst. However, the exact nature of their original explosions is the subject of debate. If the precise spectroscopic types of the Galactic SNe were known, their remnants can be directly linked to the diverse population of SNe and progenitor systems, and can be compared to explosion models in detail.
Light echoes, i.e. supernova light scattered by dust grains in the vicinity of a SN, provide the unique opportunity to pinpoint the nature of the historic explosions. Since the light path through the scattering dust cloud is longer than the direct way to Earth, light can still be received hundreds of years after explosion. As a rare occasion in astronomy, it becomes possible to study the cause and effect of an event simultaneously. SN light echoes were considered by c and Jan Hendrik Oort already in 1940. However, the secure identification and spectroscopic study of light echoes required the powerful instrumentation of the 21st century: In 2008, our team was successful in obtaining the first two optical spectra of historic Galactic SNe.

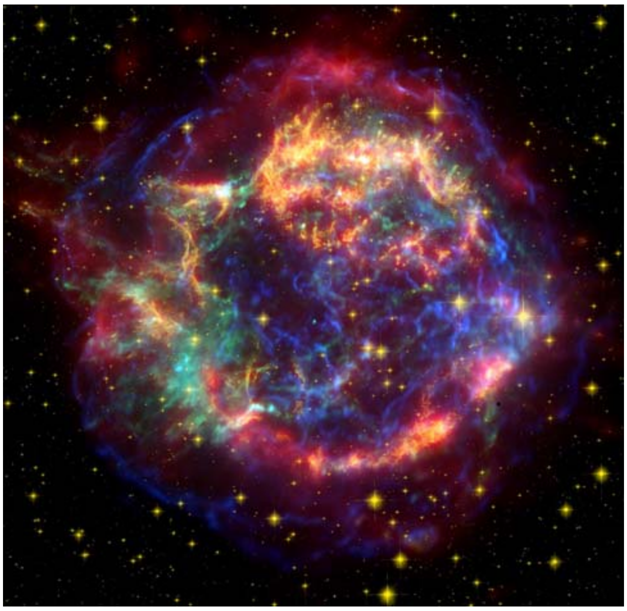
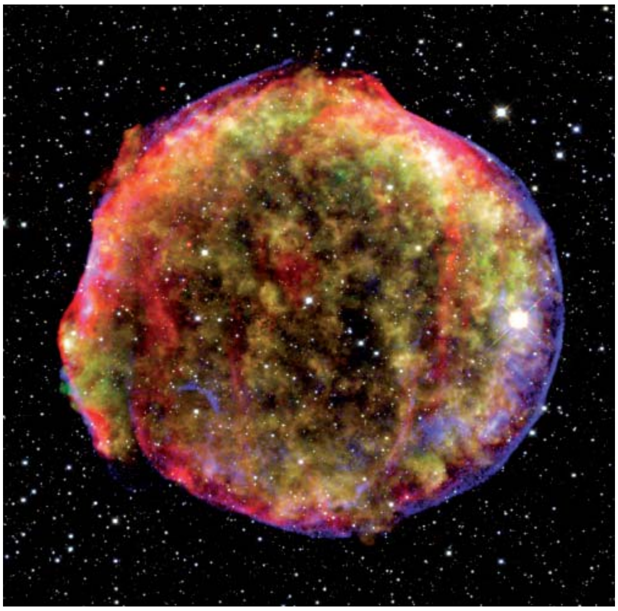

Figure 1: The two supernova remnants for which the original explosion could be studied via light-echo spectroscopy: Cas A (left) and Tycho Brahe's SN1572 (right). Both panels show X-ray, infrared, optical composite images acquired by Chandra, Spitzer and ground-based observations.

Cas A is the youngest known remnant of a core-collapse SN in the Milky Way (Fig. 1). Located at a distance of 3.4 kpc, the outburst occurred around 1680 as derived from kinematical studies of the remnant. Guided by infrared echoes discovered with *Spitzer* - the thermal emission of dust grains heated by the Cas A SN - we obtained optical spectroscopy of the associated faint (R ~23.5 mag arcsec^{-2}) scattered emission. The broad features of the spectrum confirmed a SN origin and enabled a detailed comparison with SN template spectra (Fig. 2). The best match of the Cas A spectrum is provided by the prototypical type IIb SN1993J. This established the origin of Cas A as the explosion of a helium core after stripping of the hydrogen envelope with only little hydrogen left at its surface prior to explosion, presumably as progenitor in a binary system [1].

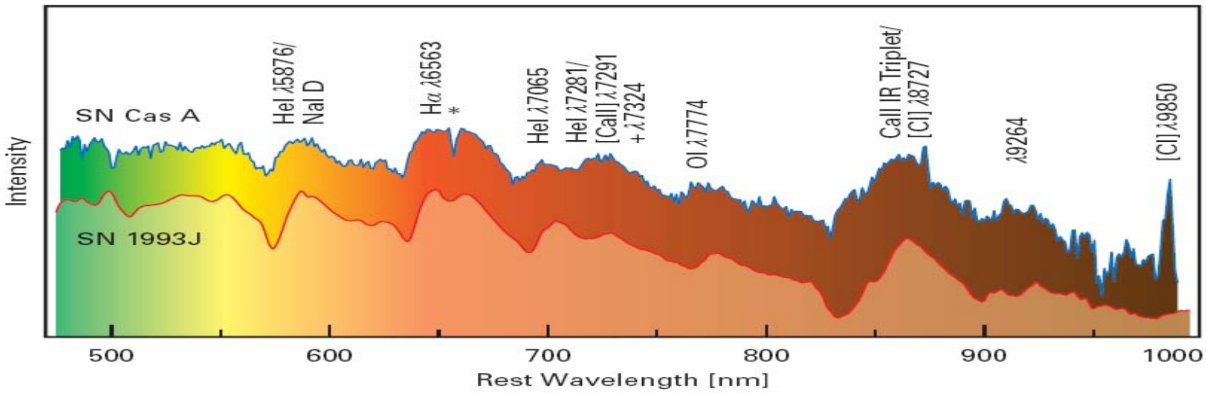

Figure 2: Spectrum of the Cas A SN in comparison with the prototypical type IIb SN1993J.

Tycho's SN 1572 was a milestone for the history of astronomy as one of the key events that led to the revision of the understanding of the universe at the end of the Middle Ages. The historic light curve obtained by Brahe and others and remnant properties have been mostly interpreted in terms of a type Ia SN, the thermonuclear explosion of a white dwarf star. However, as under- and overluminous type Ia SNe have been reported recently, the understanding of the explosion mechanism has come under debate. The comparison of the light echo with different type Ia SNe (Fig. 3) demonstrates that SN1572 belongs to the majority class of normal type Ia and confirms SN1572 as the best example of a normal type Ia SN in our Galaxy [2]. Hints of an aspherical explosion in the spectrum may put new constraints on explosion models for future studies.

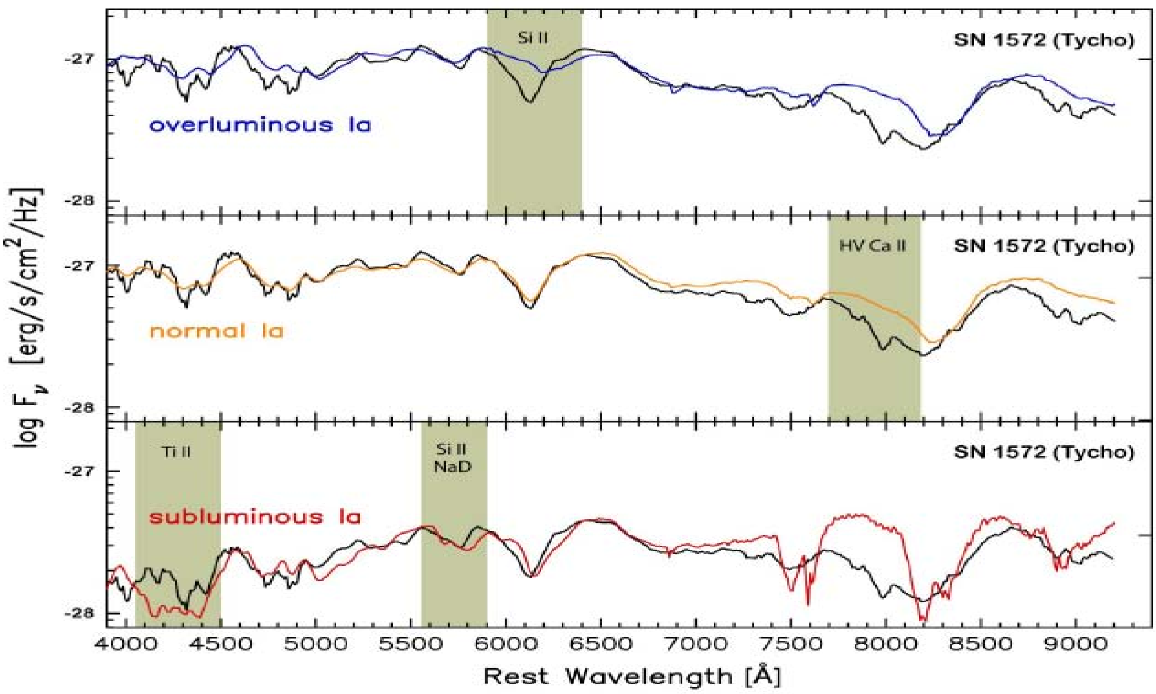

Figure 3: Spectrum of SN1572 (black line) compared to template spectra of subluminous (red), normal (yellow) and overluminous (blue) type Ia SNe.

References

[1] Krause, O., Birkmann, S., Usuda, T. et al., Science 320, 1195 (2008)
[2] Krause, O., Tanaka, M., Usuda, T. et al., Nature 456, 617 (2008)

In collaboration with University of Arizona, University of Tokyo, and NAOJ – Subaru Telescope.

Formation and transformation of hydrocarbon dust near protoplanetary nebulae

Miwa Goto, Thomas Henning

A protoplanetary nebula (PPN) is a low- to intermediate-mass star at the end of its evolution. It has ceased massive mass loss of the AGB phase, but the central star is not hot enough to ionize the circumstellar shell to make a visible planetary nebula. The transition phase to a planetary nebula is short, only lasts 1000 to 10000 yrs. The atmosphere of the old star in this phase is dense and cool, therefore serves as the major interstellar dust formation site. A PPN with carbon rich chemistry is of particular interest, as its atmosphere contains rich organic molecules starting from acetylene to benzene.

Hydrocarbon dust has two major forms in space, aliphatic and aromatic. The former is characterized by saturated, linear or branched carbon chains. The latter is characterized by conjuncted aromatic rings. The goal of the study is to use high angular resolution observing technique to uncover the spatial distribution of the hydrocarbon dust near carbon-rich PPNe to shed light on the formation and post-processing of the carbon dust.

The targets of the observation are "21 μm" PPNe in which unidentified emission feature was found at 21 μm by Kwok et al. (1989, ApJ, 345, 51) in the low-resolution spectra of IRAS. Although the carrier of the 21 μm emission is still debated (e.g. Speck & Hofmeister, 2004, ApJ, 600, 986), PPNe with an emission feature turn out all extremely carbon rich, providing the best laboratory for the study of hydrocarbon dust. The most common hydrocarbon emission in the near infrared regime 1–5 μm is the aromatic emission at 3.3 μm, and is classified as class A by Geballe (1997, ASPC, 122, 199). Only a handful of objects show class B emission of aliphatic hydrocarbon at 3.4 μm. These class B hydrocarbon sources, IRAS 05341+0852, IRAS 04296+3429, and IRAS 22272+5435 all tuned out to be 21 μm PPNe.

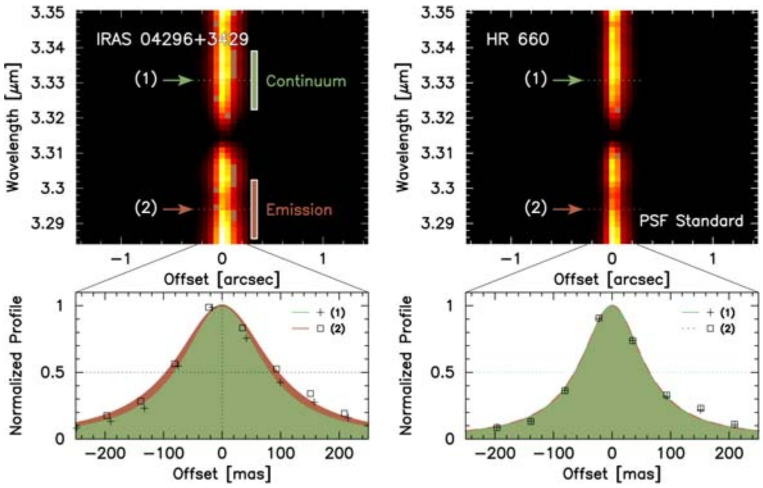

Figure 1: *Spectrogram of IRAS 04296+3429 compared to a point-source standard star HR 660. The one dimensional PSF centered on the emission feature at 3.3 μm is larger than that of continuum emission by 10 %.*

The spectroscopy was carried out at the Subaru Telescope atop Mauna Kea, using the facility spectrograph IRCS. The adaptive optics system was used to feed nearly diffraction limited images to the spectrograph. The spectroscopy covered 2.85–4.05 μm with medium resolution grism ($R \sim 2000$). The distances to the PPNe are 2–7 kpc, therefore a special technique is required to discern the spatial distribution of the hydrocarbon emission. The FWHM of the spectra are measured along the dispersion direction to be sensitive to the spatial extent of the emission lines down to a fraction of the point spread function (PSF). The technique is especially sensitive to the spatial extent of the emission line relative to that of the continuum emission (Fig. 1). The sensitivity is not limited by the PSF, but by atmospheric effects and the signal to noise ratio of the spectra. In the present case, we are able to detect ∼20 mas excess of FWHM in the hydrocarbon emission (the FWHM of the emission feature 170 mas, the continuum emission 150 mas).

The hydrocarbon emission of IRAS 22272+5435 is extended to 600–1300 AU, as is reported in Goto et al. (2003, ApJ, 589, 419). No excess of FWHM is detected at the hydrocarbon emission at 3.3–3.5 μm at the central star, which implies that the circumstellar shell is detached from the star, and the central part of IRAS 22272+5435 is already devoid of hydrocarbon dust (Fig. 2). The hydrocarbon emission from IRAS 04296+3429 is clearly extended when compared to its continuum emission. The size of the hydrocarbon emitting zone is 50–100 mas assuming the continuum emission is unresolved. If we deconvolve IRAS 04296+3429 with the PSF of the reference star recorded separately, the size of the hydrocarbon emitting zone amounts to 150 mas, which is 500 AU at a distance of 4 kpc. IRAS 05341+0852 does not show any excess of FWHM in the hydrogen emission lines. In contrast to IRAS 22272+5435, the spectra extracted from the regions offset from the central star are all identical, which testifies to the fact that PSF halo dominates in these offset regions, and that the hydrocarbon emission region remains unresolved. The upper limit of the size of the hydrocarbon emitting zone is 400 AU at the assumed distance of 7.4 kpc.

The ratio of the intensity of the aromatic emission to the aliphatic emission increases in the order IRAS 05341+0852, IRAS 04296+3429, IRAS 22272+5435. The physical size of the hydrocarbon emitting zone is therefore smaller for the source with more aliphatic chemical composition. The physical scale of the hydrocarbon emitting zone translates to the evolutionary state of PPNe. The chemical composition linked to the evolutionary state lends support to the formation of carbon dust as aliphatic material, and the transformation from aliphatic to aromatic material in the post-processing as the newly formed aliphatic carbon travels outbound from the star, possibly by thermal annealing (Goto et al. 2000, A&AS, 141, 149).

Collaborators are Sun Kwok (Hongkong University), Hideki Takami (Subaru Telescope).

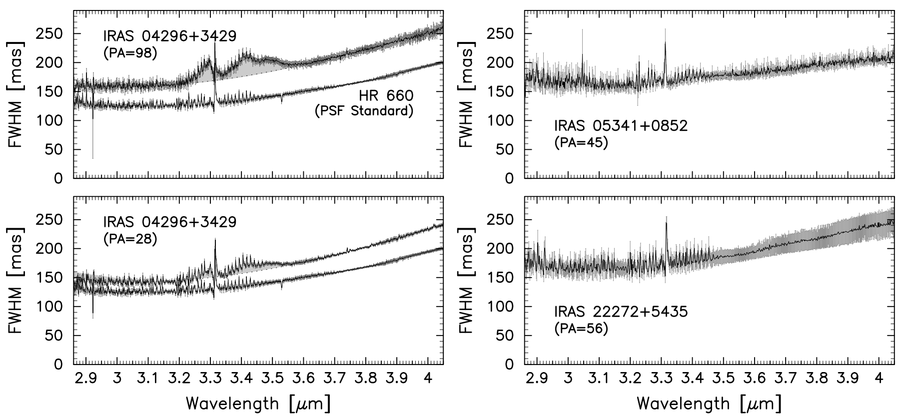

Figure 2: *FWHM Spectra of IRAS 04296+3429, IRAS 05341+0852 and IRAS 22272+5435. The FWHM of IRAS 04296+3429 is larger at the hydrocarbon emission feature at 3.3–3.5* μ*m than that of the continuum emission.*

References

[1] Goto, M., Kwok, S., Takami, H., Hayashi, M., Gaessler, W., Hayano, Y., Iye, M., Kamata, Y., Kanzawa, T., Kobayashi, N., Minowa, Y., Nedachi, K., Oya, S., Pyo, T.-S., Saint-Jacques, D., Takato, N., Terada, H., Henning, Th. 2007, ApJ, 662, 389

From PAHs to carbonaceous dust

Cornelia Jäger, Mathias Steglich, Friedrich Huisken, Thomas Henning

Gas-phase condensation of carbonaceous materials

Most of the primary cosmic carbonaceous material is formed as nanometer-sized particles via gas-phase condensation in envelopes of carbon-rich asymptotic giant branch (AGB) stars. Despite all efforts, the formation process of carbon nanoparticles in astrophysical environments is not sufficiently understood. We have employed gas-phase condensation experiments to produce nanometer- and subnanometer-sized carbonaceous particles in a high-temperature (HT; $T \geq 3500$ K) and low-temperature (LT; $T \leq 1800$ K) condensation regime. These laboratory techniques are able to mimic gas-phase condensation of carbonaceous material in astrophysical environments. The study of the formation pathways of carbonaceous condensates has been performed via analytical characterization of the condensate (particles and by-products), including high-resolution transmission electron microscopy (HRTEM), chromatographic methods, and mass spectroscopy (MS). There are strong morphological and structural differences between the LT and HT condensates accompanied by a considerable spectral diversity that has been discussed in various papers [1, 2]. Fig. 1 shows the internal structure of the formed materials in LT and HT condensation processes.

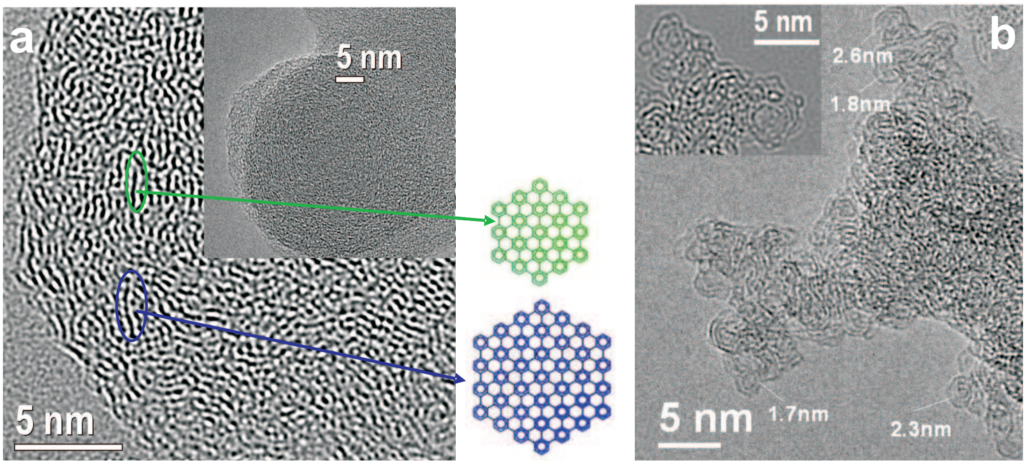

Figure 1: *(a) HRTEM image of a carbon particle formed in a LT condensation process. The rather plane graphene layers show an average length of around 1.8 nm and a maximum size of 3 nm. (b) Particles condensed in a HT process.*

The soot grains formed in HT condensation processes are characterized by very small particles with sizes up to $3-4$ nm. Buckyonions with interleaved fullerene cages, fullerene and elongated fullerene molecules that have been formed as by-products in the condensation process can be observed. However, most of the structural units are cage fragments which can be linked to another fragment either by aliphatic bridges or by van der Waals forces. The formation pathway of the HT condensate is found to be initiated by long and branched carbon macromolecules suggested to be the precursors for cyclic structures (Irle et al. 2003, Nano Letters 3, 1657). A HT condensation process of carbon nanoparticles can be expected in supernovae or in the hot circumstellar environments of carbon-rich stars, such as Wolf-Rayet stars (Cherchneff et al. 2000, A&A, 357, 572). In contrast, LT condensation favors a formation process with PAHs as precursors and particle-forming elements. Since larger PAHs have a lower volatility compared to the smaller ones, a preferred accumulation of large molecules during the surface growth process of particles can be determined. This accumulation process of large PAHs could be confirmed by a detailed analysis of the HRTEM micrographs revealing a mean length of the graphene sheets inside the particles of around 1.8 nm corresponding to PAHs with masses of around 1000 Da. The longest graphene layers that could be determined in the micrographs of the soot particles had extensions of about 3 nm, which corresponds to the highest-mass PAHs detected with MS. As a result, large carbonaceous grains with planar or slightly bent graphene layers in their interior are generated. Low-temperature condensation is a very likely formation process of soot and PAHs in AGB stars. Condensation temperatures in our laboratory studies were found to be very similar to the temperature range for carbon dust condensation in carbon-rich AGB stars predicted to start at temperatures of 1700 K (Cherchneff & Cao 1999, Proceedings of the IAU Symposium 191, San Francisco: ASP, 251).

Composition of the LT condensate

The soluble components of the LT condensates provide a pool of realistic, gas-phase condensed, astrophysically relevant PAHs with interesting spectral properties. Consequently, we have paid our attention to the efficient extraction, separation, and characterization of the PAH components employing chromatographic methods such as high-performance liquid chromatography (HPLC) combined with UV spectroscopy (see Fig. 2b). Matrix-assisted laser desorption/ionization in combination with time-of-flight mass spectrometry (MALDI-TOF) has verified that PAHs with masses up to 3000 Da are formed (Fig. 2a). The studies have revealed the fact that the soluble component of the LT condensate consists of much more than 70 PAHs originally analyzed [3] and that every stable structure including hydrogenated PAHs may exist.

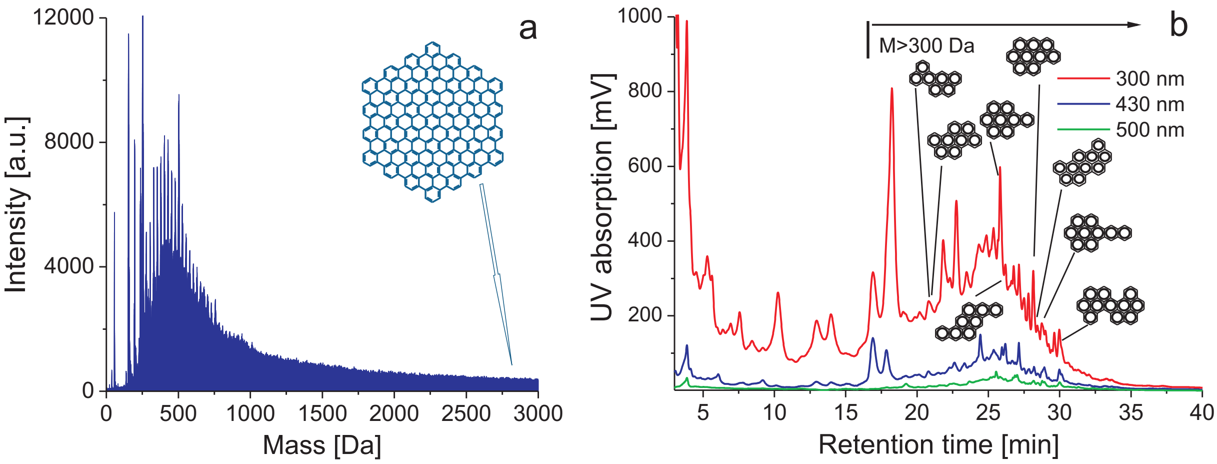

Figure 2: *(a) MALDI TOF spectrum of a LT condensate showing PAHs with masses up to 3000 Da. (b) HPLC chromatograms (UV/Vis absorption at three wavelengths) of separated PAHs.*

Collaborators are H. Mutschke, Astrophysical Institute and University Observatory (FSU Jena) and H.J. Räder, Max Planck Institute for Polymer Chemistry (Mainz).

References

[1] Jäger, C., Mutschke, H., Henning, Th., Huisken, H., 2008, ApJ 689, 249

[2] Jäger, C., Huisken, F., Mutschke, Llamas Jansa, I., Henning, Th., 2009, ApJ 696, 706

[3] Jäger, C., Huisken, F., Mutschke, H., Henning, Th., Poppitz, W., Voicu, I., 2007, Carbon 45, 2981

UV/Vis gas phase spectroscopy of PAHs

Gaël Rouillé, Marco Arold, Mathias Steglich, Cornelia Jäger, Friedrich Huisken, Thomas Henning

Jet-cooled PAHs

The presence of free polycyclic aromatic hydrocarbon (PAH) molecules in space was revealed by their collective infrared emission spectrum. PAHs have also been proposed as possible carriers of phenomena observed in the ultraviolet (UV) and visible (Vis) wavelength ranges. These phenomena include the UV extinction bump at 217.5 nm, the Extended Red Emission, the Blue Luminescence first observed in the Red Rectangle, and the Diffuse Interstellar Bands (DIBs).

The collision-free and low temperature environment of the interstellar medium is best mimicked in the laboratory by supersonic jet expansions. In order to compare them with the DIB spectrum, we have measured jet-cooled absorption spectra of several small PAHs, including the most recent candidate, 2,3-benzofluorene ($C_{17}H_{12}$) [1]. The spectra measured with the cavity ring-down laser absorption spectroscopy technique are shown in Fig. 1. In comparison with the DIBs, the absorption bands of the neutral PAHs are located at shorter wavelengths. On the other hand, their cations exhibit absorptions in the Vis range. They do not appear as likely DIB carriers, however, because their bands are broader than any known DIB.

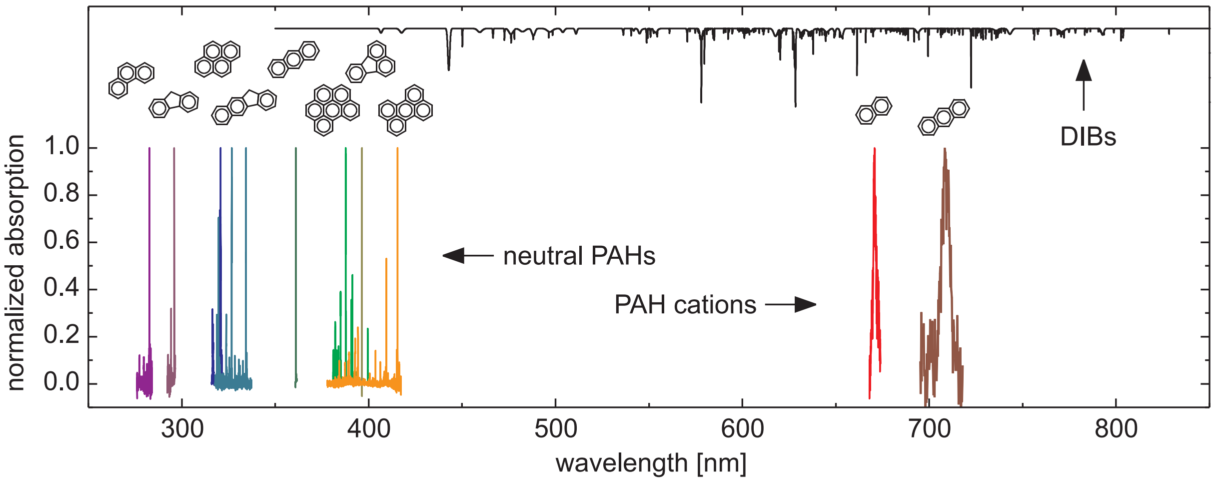

Figure 1: *Absorption spectra of jet-cooled PAHs measured by cavity ring-down spectroscopy. The synthetic DIB spectrum displayed at the top for comparison is based on the data compiled by Jenniskens (http://leonid.arc.nasa.gov/DIBcatalog.html).*

Matrix-isolated PAHs

Large PAHs have absorption bands at longer wavelengths, that is in the same range where the DIBs are observed. As data on the absorption spectra of these large molecules are very limited or not available, matrix isolation spectroscopy (MIS) is used as a first approach. By isolating the species of interest in a cryogenic rare gas matrix, large wavelength ranges can be scanned while consuming little sample. Moreover, band positions can be extrapolated for the gas phase by using different rare gases, e.g., Ne and Ar. Thus, the data obtained by MIS allow us to narrow down the wavelength ranges to be explored in coming supersonic jet experiments.

We reported the UV/Vis spectrum of the bowl-shaped corannulene ($C_{20}H_{10}$) in an Ar matrix [2] and, more recently, we carried out measurements in a Ne matrix. We also measured the spectrum of the large hexa-*peri*-hexabenzocoronene (HBC, $C_{42}H_{18}$) in Ne and Ar matrices [3]. By extrapolation, the strongest UV transitions of corannulene and HBC are expected in the gas phase near 246.5 and 334.2 nm, respectively. The spectra of corannulene and HBC obtained in Ne matrices are shown in Fig. 2(a) and (b).

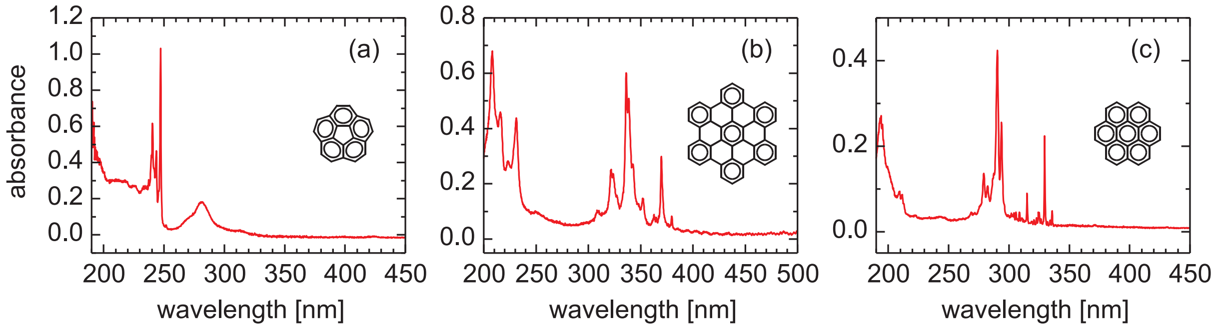

Figure 2: *Absorption spectra of corannulene (a), HBC (b), and coronene (c) isolated in Ne matrices at 6 K. Corannulene and HBC were vaporized by heating in an oven while coronene was laser-vaporized.*

Toward larger PAHs

In our first experiments, the samples were vaporized by heating in an oven. This method is considered to be suitable for PAHs containing up to approximately 50 carbon atoms and it allowed us to study the large HBC (42 C atoms) as shown in Fig. 2(b). As we plan to go beyond this limit, we have tested the laser vaporization technique in conjunction with our supersonic jet absorption spectrometer [4] and with the MIS setup. For instance, we have measured the absorption spectrum of laser-vaporized coronene ($C_{24}H_{12}$) isolated in a Ne matrix. This spectrum is shown in Fig. 2(c). Laser vaporization coupled to MIS is currently applied to study small mixtures of large PAHs that are produced by laser-induced pyrolysis and selected by high-performance liquid chromatography (see the contribution by Jäger et al.).

Collaborators are Klaus Müllen (Max Planck Institute for Polymer Research, Mainz), Hans-Joachim Knölker (Technical University Dresden), and Angela Staicu (National Institute for Laser, Plasma and Radiation Physics, Bucharest, Romania).

References

[1] Staicu, A., Rouillé, G., Scholz, R., Pouladsaz, D., Henning, Th., Huisken, F., 2008, J. Chem. Phys., 129, 074302

[2] Rouillé, G., Jäger, C., Steglich, M., Huisken, F., Henning, Th., Theumer, G., Bauer, J., Knölker, H.-J., 2008, ChemPhysChem, 9, 2085

[3] Rouillé, G., Steglich, M., Huisken, F., Henning, Th., Müllen, K., 2009, J. Chem. Phys., 131, 204311

[4] Rouillé, G., Arold, M., Staicu, A., Henning, Th., Huisken, F., 2009, J. Phys. Chem. A, 113, 8187

Oxidation reactions at very low temperatures in helium droplets

Serge Krasnokutski, Friedrich Huisken

Introduction

Despite the low temperatures encountered in the ISM and in interstellar clouds, there is strong evidence of a rich gas-phase chemistry taking place in these environments. It has been shown that, in general, the extrapolation of high-temperature reaction rates to low-temperature values yields incorrect results. Therefore, it is actually necessary to study the reaction kinetics at low temperatures in the laboratory. This data is urgently needed to explain astronomical observations and to provide input data for astrochemical models.

The most widely used technique to cool gase-phase molecules to temperatures in the order of 10 K is the molecular beam technique based on supersonic jet expansions. However, this method has the disadvantage that the temperature is not unique for all degrees of freedom. Another method to provide cryogenic temperatures but to keep all degrees of freedom in equilibrium is the matrix isolation technique. Here, the disadvantage is that the reactants are locked in the solid matrix and cannot move freely. A third method combining the advantages of both methods is the helium droplet technique which has been explored and developed only very recently [1].

Incorporating two different species A and B into the helium droplet, it is possible to study the reaction between A and B at the ultralow temperature of 370 mK. The simplest way to monitor the reaction is the detection of the products in a mass spectrometer. Another possibility is to detect electronically excited products by measuring the chemiluminescence (CL) light emitted by the hot products. We have used these techniques to study the oxidation reactions of a number of period 3 elements of significant universal abundance (Mg, Si, and Al) with O_2.

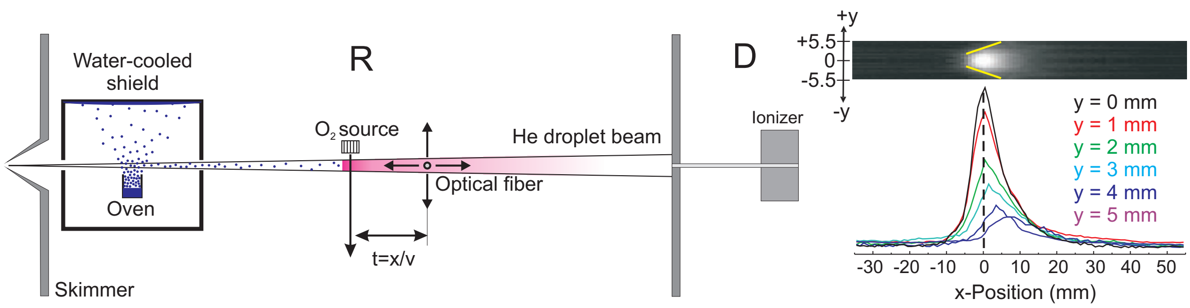

Figure 1: *Schematic view of the experimental setup (left) and two-dimensionally resolved chemiluminescence signal produced in the reaction between Mg complexes and O_2 molecules (right).*

Experiment

A schematic view of the experimental setup is shown in Fig. 1. The helium droplet beam enters the reaction chamber R through the skimmer. Mg (or Si or Al) atoms are incorporated by passing the helium droplets just above a crucible where the respective material is evaporated. The second reactant (O_2) is incorporated further downstream by crossing the helium droplet beam with an effusive beam of O_2. The CL photons generated from electronically excited product molecules are collected by a fiber that can be moved in x- and y-direction and that is coupled to a photomultiplier. Alternatively, the product molecules remaining in the helium droplets or being expelled in forward direction can be detected with a mass spectrometer mounted into the detector chamber D.

Results

A two-dimensional image of the CL light generated upon the reaction of Mg complexes with O_2 molecules is shown on the right-hand side of Fig. 1. The x-coordinate refers to the direction of the helium droplet beam while y indicates the direction perpendicular to it. The interaction with O_2 molecules occurs at $x = 0$ mm. When O_2 is replaced by Ne or N_2O no chemiluminescent light is observed. The observation of CL in general and the emission pattern in particular prove that (i) the chemical reaction takes place with O_2, (ii) up to 3.1 eV are released by the photons (as revealed by measuring the emission spectrum), (iii) the products are expelled from the helium droplets, and (iv) the CL rate is much slower than the reaction rate (as evidenced by the diverging CL pattern). The CL study allows an evaluation yielding an upper limit for the reaction time constant. It is found that the reaction between Mg complexes and O_2 molecules is completed within the first 100 μs after the incorporation of O_2. Thus, we conclude that this reaction may be relevant for the ISM.

Filling the empty p-orbital of the Mg atom with one or two electrons results in the formation of Al or Si atoms, respectively. It will be interesting to see how this change in the electronic configuration will affect the chemical properties of the elements at low temperatures.

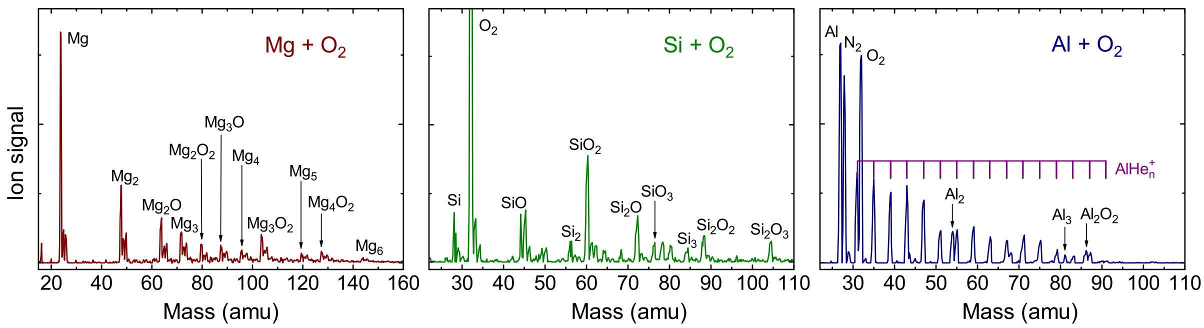

Figure 2: *Mass spectra resulting from the reaction of Mg, Si, and Al atoms with O_2.*

A mass spectrometric study of the reactions Mg + O_2 and Si + O_2 yields similar mass spectra. At low metal vapor pressure, no products are seen in the mass spectra. We only observe the depletion of the reactant's mass peaks indicating that the products are expelled from the beam. Only if the metal vapor pressure is increased such that metal clusters are formed, we do see products of the form M_xO_y (see Fig. 2). In contrast, the incorporation of Al atoms and O_2 molecules does not yield any chemical reaction. The only peak related to an oxide, Al_2O_2, should be attributed to the formation of a van der Waals complex. At the same time, the Al^+ cation produced in the ionizer easily forms complexes with He atoms yielding $AlHe_n^+$ with n up to 16. The present studies allow us to conclude that the reaction of O_2 with Mg and Si atoms or clusters proceeds rather fast at 370 mK [2]. On the other hand, Al atoms or clusters do not react with O_2 at this temperature. These findings are confirmed by monitoring the evaporation of He atoms from the droplets, thus providing information on the energy released during the chemical reaction.

References

[1] Jäger, C., Mutschke, H., Huisken, F., Krasnokutski, S., Staicu, A., Henning, Th., Poppitz, W., Voicu, I., (2006), ApJS, 166, 557

[2] Krasnokutski, S., Huisken, F., 2010, J. Chem. Phys., in preparation

Cold stardust: infrared properties of carbonates and hydrous silicates

Thomas Posch, Thomas Henning, Simon Zeidler, Harald Mutschke

Background

Carbonates (e.g. dolomite and calcite) and hydrous silicates (e.g. montmorillonite) are among the numerous species of cosmic dust grains that we know today. Carbonate grains have been found in interplanetary dust particles, they have been suggested to be components of the Comet 9P/Tempel 1 based on infrared spectroscopy, furthermore they have been tentatively identified in the atmosphere of Mars and in Planetary Nebulae such as NGC 6302. Hydrous silicates occur in primitive meteorites such as the carbonaceous chondrites of the CM and CI classes and also in a corresponding class of interplanetary dust particles.

In many these environments, temperatures considerably below room temperature are prevailing. However, the optical constants and mass absorption coefficients for carbonates and hydrous silicates that could be found in the literature before 2008 were based on measurements performed at room temperature. Consequently, a realistic modeling of the above-mentioned environments was hardly possible – hence the necessity of new experiments performed at cryogenic tempera-tures. This was the starting point of our work, which was a joint project of the MPIA, the AIU Jena and the Institute of Astronomy in Vienna.

Laboratory Measurements

For the measurements which will be described in the following (and which were more exten-sively explained in [1] and [2]), different kinds of samples have been used: in the case of carbonates, nearly transparent natural crystals of calcite and dolomite; in the case of hydrous silicates, powders of sub-micron sized grains of talc, montmorillonite, chamosite and picrolite. The crystals have been cut and polished such as to obtain highly reflective surfaces for infrared spectroscopy. The powders have been embedded in KBr and polyethylene matrices.

Both the reflectance and the transmittance measurements were performed using a Bruker 113v FTIR spectrometer in the wavelength range 2–120 m. To cool down the samples, a continuous-flow liquid-helium cryostat with contact-gas cooling has been used. Spectra have been taken at 300K, 200K, 100K and 10K. The optical constants of calcite and dolomite for 10K, 100K, 200K and 300K have been published in [1] and are also available on the following website:http://www.astro.uni-jena.de/Laboratory/OCDB The mass absorption spectra of hydrous silicates have been published in [2].

Derived infrared properties and their implications

We compared the dolomite and calcite spectra with the far-infrared bands of the Planetary Nebula NGC 6302. The main results are the following: Dolomite has a strong emission band centered at 65 m. Its profile strongly depends on the grain shape and grain temperature.

However, for no combination of particle shapes and temperature, the 65 m band in NGC 6302 can be ascribed to dolomite dust as feature carrier. Calcite has a strong far infrared emission band centered at 90 m. For temperatures below 50 K, the mid-infrared bands of calcite (at 30 m and at 42-43 m) are suppressed and the observed profile of the 90 m band becomes compatible with irregularly shaped CaCO3 grains (see Fig. 1).

For the above mentioned hydrous silicates, we found that they generally have much sharper bands at $\approx$100 m than previously assumed. The very broad dust emission in the spectrum of HD 142527 can no longer be ascribed to montmorillonite dust due to this new insight (Fig. 2).

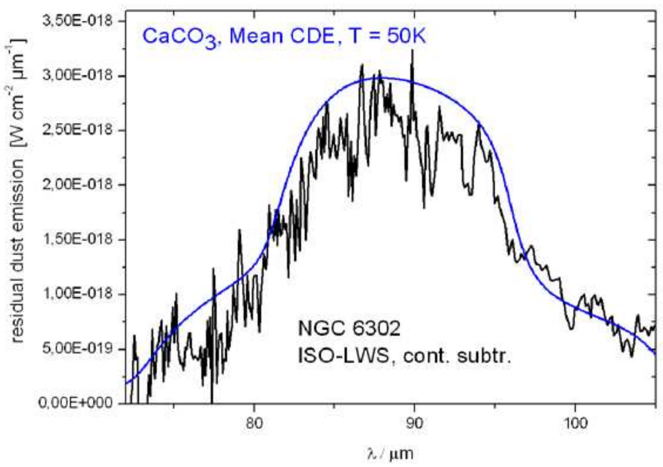

Figure 1: *Comparison of the residual (non-silicate) dust emission of NGC 6302 (ISO-LWS spectrum) with the calculated emission spectrum of cold calcite grains following a continuous distribution of ellipsoids.*

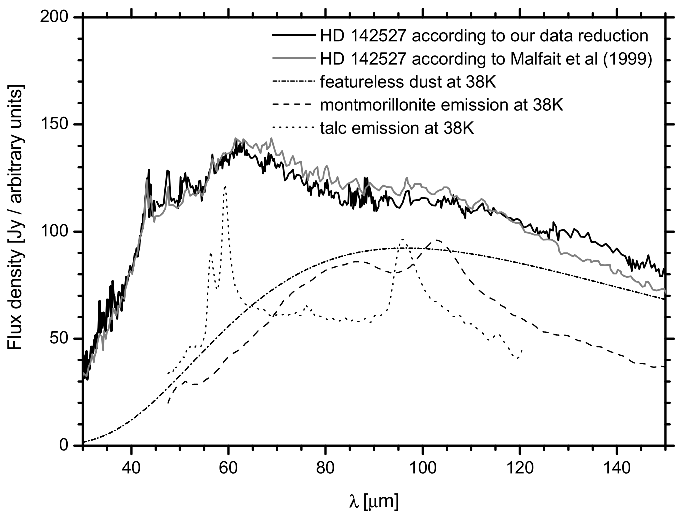

Figure 2: *The ISO spectrum of HD 142527 (solid lines) compared to the emission spectra of cold montmorillonite (dashed line) and talc dust (dotted line). Featureless dust (dash-dotted line) is an alternative carrier of the broad emission in the 100 m region.*

On the basis of the published data, we hope to set further constraints on the existence of carbo-nates and hydrous silicates in space – especially by analyzing upcoming far infrared spectra currently gained by the Herschel satellite.

References

[1] Posch Th., Baier A., Mutschke H., Henning Th., 2007, ApJ 668, 993-1000.

[2] Mutschke H., Zeidler S., Posch Th., Kerschbaum F., Baier A., Henning Th., 2008, A&A 492, 117-125.

6 Gas and Stellar Populations in Galaxies

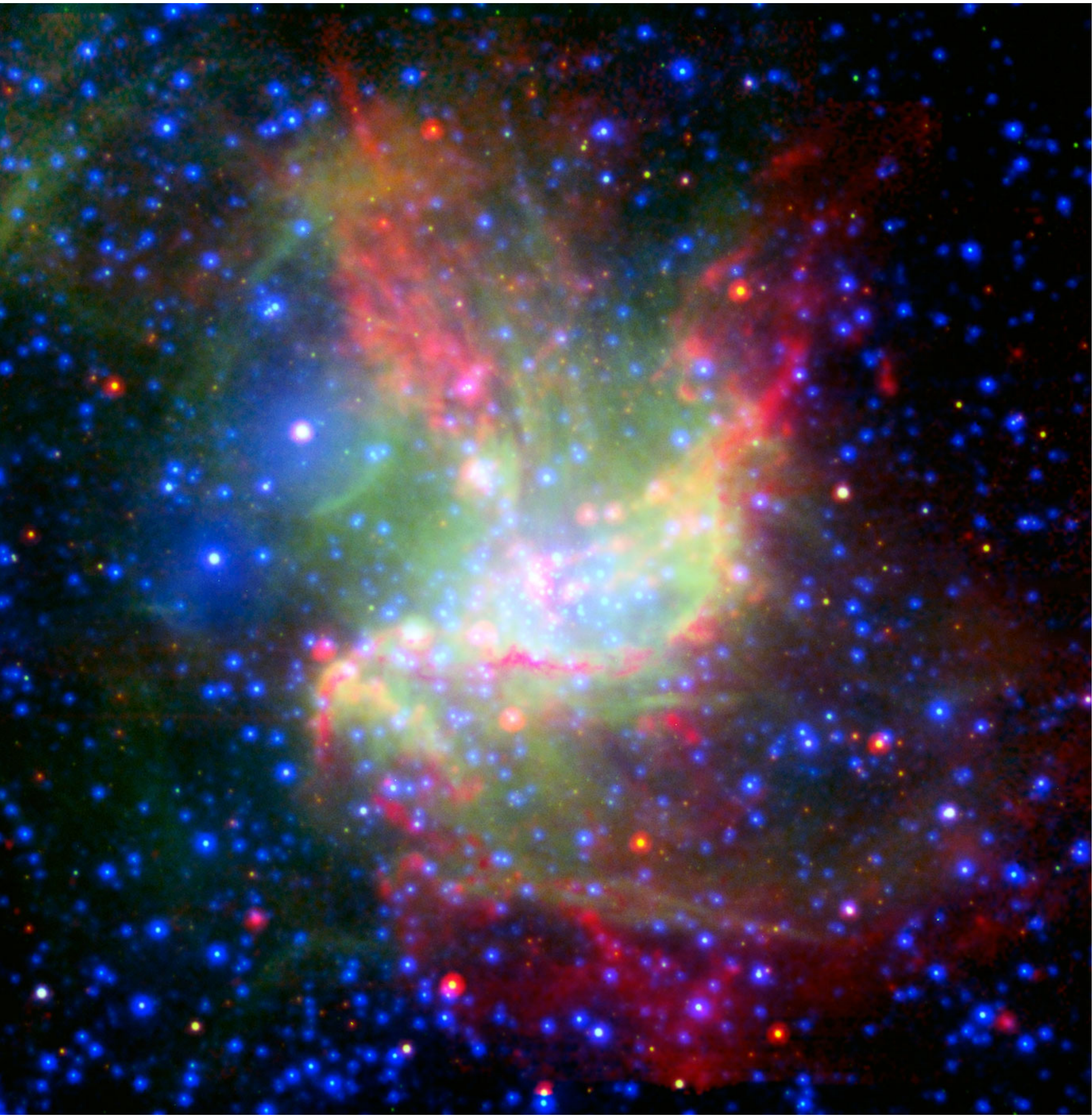

Image on previous page:

The star-forming region NGC 346 in the Small Magellanic Cloud. The image is based on data from ESA XMM-Newton (X-rays; blue), ESO's New Technology Telescope (visible light; green), and NASA's Spitzer (infrared; red). The infrared light shows cold dust, while the visible light denotes glowing gas, and the X-rays represent very hot gas. Credit: ESO/ESA/JPL-Caltech/NASA/ D.Gouliermis (MPIA) et al.

Young, massive clusters in the Galaxy

Wolfgang Brandner, Arjan Bik, Boyke Rochau, Nicola Da Rio, Mario Gennaro, Dimitrios Gouliermis, Natalia Kudryavtseva

Probes for stellar and cluster evolution from μas astrometry

Stars in young, massive clusters like NGC 3603, Westerlund 1, or the Orion Nebula Cluster span the entire range of stellar masses. Hence these clusters are ideal places to study early stellar evolution, to benchmark and calibrate star formation models and theories, and to investigate the formation and dynamical evolution of clusters[1, 2]. Multi-epoch high-precision astrometric observations with HST/WFPC2 and VLT/NACO enable us to discern cluster members from field stars, and to derive both orbital parameters of clusters and internal velocity dispersions[5]. After correcting for instrumental contributions, we determine the internal velocity dispersion of NGC 3603 to $\sigma_{1\mathrm{D}} = 135 \pm 29\,\mu$as/yr (4.7±0.7 km/s at a distance of 6 kpc)[4].

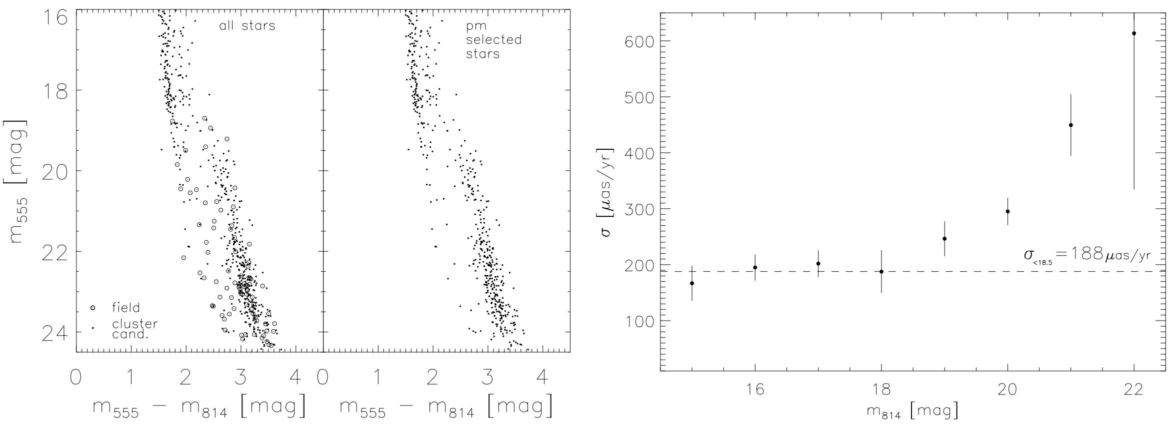

Figure 1: $m_{555} - \mathrm{m}_{814}$ *vs.* m_{555} *CMD of NGC 3603 with proper motion selected cluster members and field stars (left) and only cluster members (center) Right: The observed proper motion dispersion* $\sigma_{1\mathrm{Dobs}}$ *as a function of stellar magnitude. The flat relation* $\sigma_{1\mathrm{Dobs}} = 188\mu as/yr$ *(dashed line) for* $14.5^{\mathrm{m}} < \mathrm{m}_{814} < 18.5^{\mathrm{m}}$ *indicates that there is no equipartition of energy among the cluster members. Hence NGC 3603 is not yet in virial equilibrium.*

Early stages - the rôle of outflows

As the dispersal of remnant cloud material during the first few Myr leads to a rapid dynamical evolution, still earlier stages have to be studied to better understand the formation of massive stars and clusters. Yet, even in the still partially embedded cluster MWC 1080, low-mass pre-stellar clumps are already affected by winds and outflows from massive stars. This suggests that massive stars strongly influence their star formation environment early-on[3, 6].

Revealing the hidden clusters

Massive Young Clusters are very rare in the Galaxy. The fact that they are invisible at optical wavelengths, hidden by walls of extinction makes them difficult to detect. Combining UKIDSS, SPITZER, sub-mm and radio data, we will search new candidate starburst clusters in the Galactic Plane. Ongoing follow-up near infrared spectroscopy and imaging with the new LUCIFER camera at the LBT aims at characterizing their stellar content. From this we derive age and mass of candidate starburst clusters, and study the high-mass end of the IMF, as well as mass

Figure 2: *Composite-colour image of the massive star forming region S255 obtained with LBT/LUCIFER. Colour-coded in green is emission from H_2, which traces shocks and outflows.*

segregation and feedback processes for the most massive young clusters in our Galaxy.

Collaborators are Andrea Stolte (Univ. of Cologne), Benjamin Hussmann (Univ. of Cologne), Morten Andersen (ESA/ESTEC), Hans Zinnecker (AIP/Sofia), Massimo Roberto (STScI), Pier Giorgio Prada Moroni (Univ. of Pisa), Emanuele Tognelli (Univ. of Pisa), Rens Waters (Univ. of Amsterdam), Simon Clark (Open Univ. UK), Shiya Wang (Univ. of Michigan), Leslie Looney (UIUC).

References

[1] Brandner, W., Clark, J.S., Stolte, A., Waters, R., Negueruela, I., Goodwin, S.P., 2008, A&A 478, 137

[2] Da Rio, N., Robberto, M., Soderblom, D.R., Panagia, N., Hillenbrand, L.A., Palla, F., Stassun, K., 2009, ApJS 183, 261

[3] Martín-Hernández, N.L., Bik, A., Puga, E., Nürnberger, D.E.A., Bronfman, L., 2008, A&A 489, 229

[4] Rochau, B., Brandner, W., Stolte, A., Gennaro, M., Gouliermis, D., Da Rio, N., Dzyurkevich, N., Henning, Th., 2009, ApJL, subm.

[5] Stolte, A., Ghez, A.M., Morris, M., Lu, J.R., Brandner, W., Matthews, K., 2008, ApJ 675, 1278

[6] Wang, S., Looney, L.W., Brandner, W., Close, L., 2008, ApJ 673, 315

The Initial Mass Spectrum of NGC 602

Markus Schmalzl, Dimitrios Gouliermis, Thomas Henning

Introduction

In [1] we present our photometric study from data obtained in the filters $F555W$ and $F814W$ with HST/ACS in wide-field mode of the star forming region NGC 602/N 90 in the wing of the SMC. Our aim is to take advantage of the high-resolution efficiency of ACS for the construction of the IMF of the association NGC 602 for the whole observed stellar population of the system. We use the ACS module of the photometric package DOLPHOT, which is especially designed for imaging with the ACS and we provide the full photometric catalog of all stars detected with short and long exposures in one ACS/WFC field that covers a region of about $3\rlap{.}'4 \times 3\rlap{.}'4$ centered on the young stellar association NGC 602. The region is found to host a mixture of stellar populations. Star counts revealed that there are three prominent stellar concentrations in the observed field. The CMDs of all three systems are contaminated by the stellar population of the general field of SMC in the region. We selected the most empty (and less contaminated from dust emission, as seen with *Spitzer*; [2]) part of the observed area as the most representative of the general SMC field. We, then, applied a Monte Carlo method for decontaminating the CMDs of all three identified stellar systems from the contribution of the field.

Colour-Magnitude Diagram

The Colour-Magnitude Diagram (CMD) of NGC 602 reveals that the stellar members of the association belong to a rich upper bright main sequence down to $m_{555} \sim 21$ mag and to a prominent red sequence of faint pre-main sequence stars down to the detection limit (Figure 1). In general, the observed sequence of PMS stars corresponds to an age of roughly 4 Myr. However, there is also a significant amount of PMS stars that can be fitted by a ~ 10 Myr model. Therefore the age cannot be determined exactly, which might be evidence for sequential star-formation. This is also supported by the finding of Spitzer YSO-candidates at the rim of NGC 602 [2].

Initial Mass Spectrum of NGC 602

Concerning the mass spectrum of the association, the PMS stars in the CMD of NGC 602 show a prominent broadening, which does not allow a direct measurement of the masses of these stars through a single Mass-Luminosity-relation (ML-relation). This broadening might be the result of an age spread, but it could also be due to the characteristics of the PMS stars, such as variability and extinction. In any case the accurate measurement of their age and the estimation of their masses becomes a rather difficult task. Therefore, we constructed the Initial Mass Spectrum (IMS) of the association with an age-independent method based on counting the PMS stars between evolutionary tracks (Figure 1). We used the grids of models by both Palla & Stahler (1999, ApJ 525, 772) and Siess (2000, A&A 358, 593). For the bright main sequence stars we used a ML-relation obtained from the evolutionary models by Girardi (2002, A&A 391, 195). The IMS of the association is found to be well represented by a single-power law of slope $\alpha \approx -2.2 \pm 0.3$ (Figure 2) for $1 \lesssim M/M_{\odot} \lesssim 45$, similar to the field IMS in the solar neighborhood (Salpeter 1955, ApJ 121, 161). No significant differences are found between the IMF derived with the use of Palla & Stahler (1999) models and the one from the models by Siess (2000), although these grids of models are found to be quite different from each other for stars with $m_{555} \lesssim 20$ mag.

Collaborator is Andrew Dolphin (Raytheon Corporation, Waltham, MA)

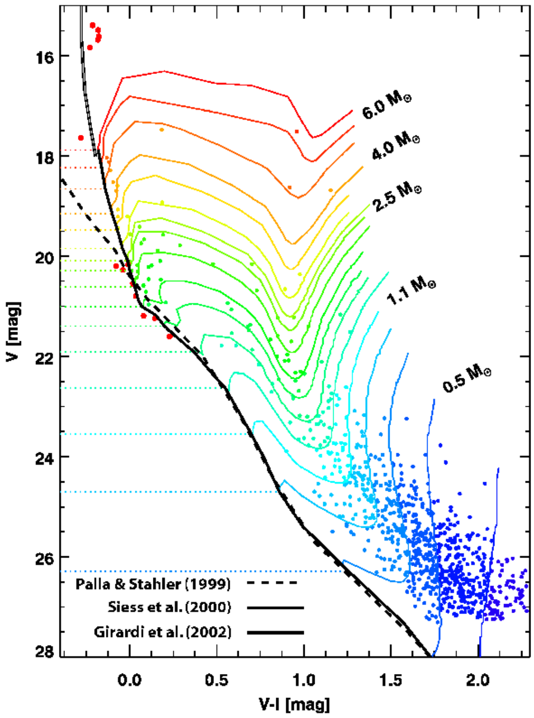

Figure 1: Construction of the Initial Mass Spectrum (IMS) of NGC 602 by counting stars between evolutionary tracks. The PMS tracks by Siess (2000) are shown in this plot. The ZAMS of both Siess (2000) and Palla & Stahler (1999) are shown to demonstrate their differences for stars with $V \lesssim 20$ mag. Different PMS tracks and the stars included between them are plotted in different colors to be easier distinguished.

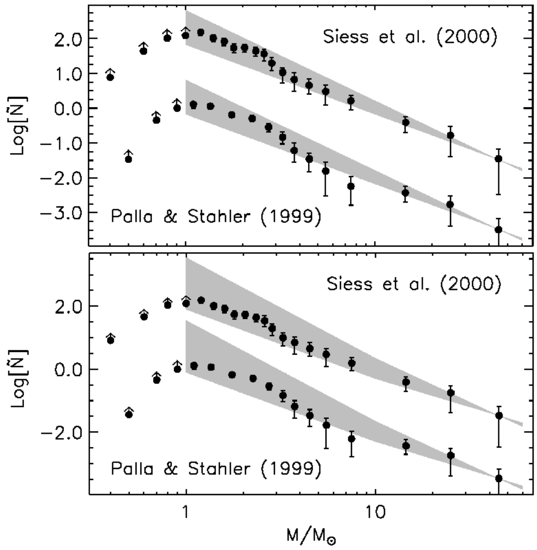

Figure 2: The Initial Mass Spectrum (IMS) of NGC 602 as constructed by counting PMS stars between evolutionary tracks and with the use of a ML-relation from the models by Girardi (2002) for the brightest MS stars. The derived IMS is shown in each panel from counting PMS stars between tracks from both the models of Siess (2000) (top IMS) and Palla & Stahler (1999) (bottom IMS). The shades at the top panel correspond to a Kroupa (2002, MNRAS 336, 1188) IMS with $\alpha = -2.3 \pm 0.3$, while the ones at the bottom panel to a Scalo (1998, ASPC 142, 201) one with $-2.7 \lesssim \alpha \lesssim -2.3$. Stellar numbers $\tilde{N}$ are corrected to a bin-size of $1\,M_\odot$. A slope of $\alpha \sim -2.2 \pm 0.3$ is found to represent very well the IMS as it is constructed with the use of all considered grids of models.

References

[1] Schmalzl, M., Gouliermis, D. A., Dolphin, A. E., & Henning, T. 2008, ApJ, 681, 290

[2] Gouliermis, D. A., Quanz, S. P., Henning, T. 2007, ApJ, 665, 306

Triggered star formation in the star-forming region NGC 346/N66 in the Small Magellanic Cloud from multi-wavelength observations

Dimitrios A. Gouliermis, Thomas Henning, Wolfgang Brandner, Felix Hormuth

Science Case

Stellar feedback, expanding HII regions, wind-blown bubbles, and supernovae are thought to be important triggering mechanisms of star formation. We present evidence based on previous and recent detailed studies that NGC 346/N66, the brightest HII region in the Small Magellanic Cloud (SMC), hosts at least two different events of triggered star formation. Using data that cover the whole extend of the spectrum, from X-rays and optical imaging to far-IR observations, we reveal the complexity of the recent star formation history of this exceptional region.

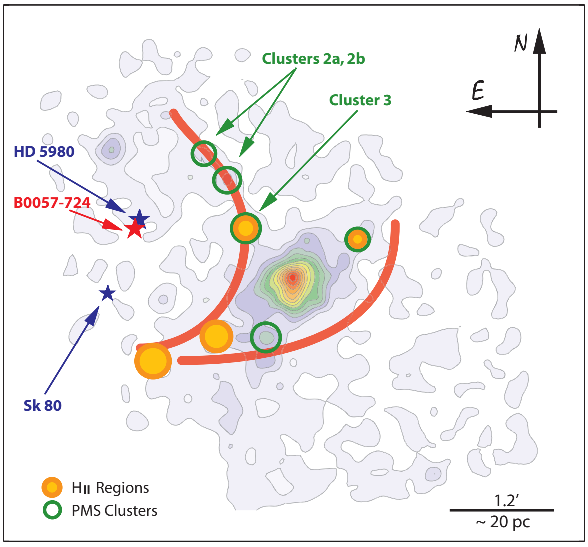

Figure 1: Left*: Color-composite image of the area of NGC 346/N 66 from combination of X-ray observations with XMM-Newton (blue), [O* III*] (501.1 nm) with NTT (green) and at 8μm with* Spitzer *(red). The image covers an area about 6′ × 6′ (∼ 100 × 100 pc^2) wide centered on NGC 346. North is up, East is to the left.* Right*: Schematic representation of the proposed star formation scenario, according to which the massive progenitor of SNR B0057−724 triggered current star formation at the north of the N 66 bar through its wind-blown bubble. The contribution of the most massive stellar object in the area, the LBV HD 5980, is also considered important. The colored iso-density contour map, constructed from star counts of both bright main sequence and faint PMS stars of the region, is shown in the background to demonstrate the geometry of the youngest stellar concentrations. The locations of the SNR, HD 5980, the O-star Sk 80 and significant PMS clusters and H* II *regions are also indicated. Two important dusty features, also visible in the left panel, are drawn with red thick curves. The one to the south, south-west of the bar of N 66 is considered to be the product of the energy output from the OB stars of the association NGC 346. The other to the north and east of the bar coincides very well with a shock-wave coming from the direction of the SNR B0057−724. The synergy of both these strong energy sources seems to define the recent star formation history of the region.*

Results

In our previous studies of the region NGC 346/N66 ([1, 2]) we find that besides the central part of the H II region N66, where the bright stellar content of the association NGC 346 is concentrated, an arc-like nebular feature, north of the association, hosts recent star formation. This feature is characterized by a high concentration of emission-line stars and Young Stellar Objects, as well as embedded sources seen as IR-emission peaks that coincide with young compact clusters of low-mass pre-main sequence stars. All these objects indicate that the northern arc of N66 encompasses the most current star formation event in the region. In this study ([3]) we use multi-wavelength observations of the stellar content, gas and dust in the region to show that the observed northern star formation is the product of a different mechanism than that in the general area of the association, and that it is triggered by a wind-driven expanding H II region (or bubble) blown by a massive supernova progenitor, and possibly other bright stars, a few Myr ago. We propose a scenario according to which this mechanism triggered star formation away from the bar of N66, while in the bar of N66 star formation is introduced by the photo-ionizing OB stars of the association itself (Fig. 1).

Press Releases

- *"Splashy portrait paints picture of how stars form"*,
  ESA *News*, 8 October 2008
  `http://www.esa.int/esaCP/SEMLKL4N0MF_index_0.html`
- *"Born from the Wind - Unique Multi-wavelength Portrait of Star Birth"*,
  ESO Photo Release, 8 October 2008
  `http://www.eso.org/public/outreach/press-rel/pr-2008/pr-34-08.html`
- *"Splashy Portrait Helps Explain How Stars Form"*,
  JPL News Release, 8 October 2008
  `http://www.jpl.nasa.gov/news/news.cfm?release=2008-188`
  NASA/*Spitzer* Release, 8 October 2008
  `http://www.nasa.gov/mission_pages/spitzer/news/spitzer-20081008.html`

Collaborators

- You-Hua Chu (Department of Astronomy, University of Illinois, USA)
- Robert A. Gruendl (Department of Astronomy, University of Illinois, USA)
- Eva Hennekemper (Kirchhoff Institute for Physics, Heidelberg)
- Andrew E. Dolphin (Raytheon Corporation, USA)

References

[1] Gouliermis, D. A., Dolphin, A. E., Brandner, W., & Henning, T. 2006, ApJS, 166, 549

[2] Hennekemper, E., Gouliermis, D. A.; Henning, T., Brandner, W., Dolphin, A. E. 2008, ApJ, 672, 914

[3] Gouliermis, D. A., Chu, Y.-H., Henning, T., Brandner, W., Gruendl, R. A., Hennekemper, E., & Hormuth, F. 2008, ApJ, 688, 1050

The complete initial mass function down to the subsolar regime in the Large Magellanic Cloud with Hubble Space Telescope ACS observations

Nicola Da Rio, Dimitrios Gouliermis, Thomas Henning

Science case

The Magellanic Clouds (MC), our closest neighboring galaxies, are template environments for the study of young stellar systems, especially thanks to the lower dust extinction than in the disk of our Galaxy. Recently high-res HST imaging led to the discovery of PMS populations in the MCs, initiating the study of low-mass star formation outside the Galaxy [1].

Regarding the IMF, several studies have been carried out for the Galaxy, supporting the hypothesis of its universality, and hinting to the possible dependance on metallicity for the lower masses. Increasing the number of observational findings it is therefore critical for improving our understanding of the origins of stellar systems up to entire galaxies. So far this study outside our Galaxy has been limited to the intermediate and high-mass stars, and only recently has been possible to detect low-mass stars from photometry in the Magellanic Clouds.

We use deep HST photometry on the stellar association LH 95 in the MC to investigate, for the first time, the properties of the pre-main sequence population in the sub-stellar regime outside the Milky Way, and in particular the initial mass function [2].

The stellar association LH 95

Located on the edge of the shell LMC-4, LH 95 is an OB association of 10×20 pc of size. We use $V-$ and $I-$band deep HST Advanced Camera for Surveys (ACS) imaging, both for

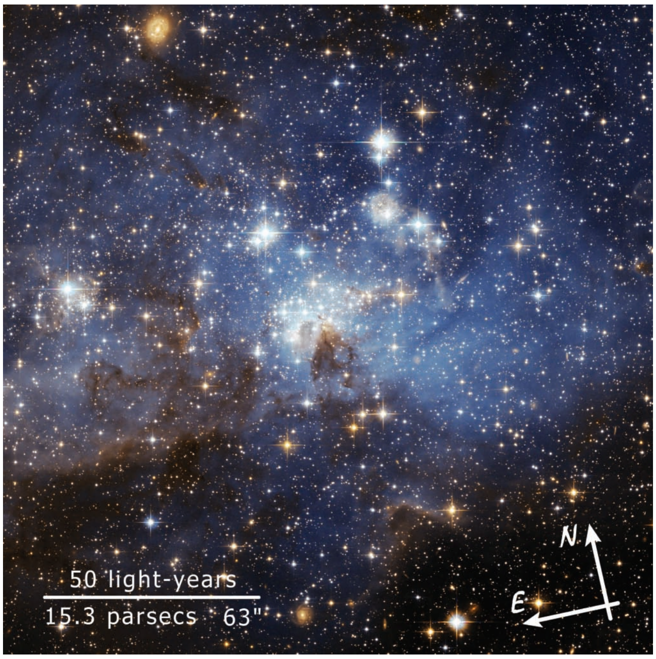

Figure 1: *The young stellar association LH 95 in the LMC seen with the Advanced Camera for Surveys onboard the Hubble Space Telescope. Image credit: NASA, ESA and D.A. Gouliermis (MPIA)*

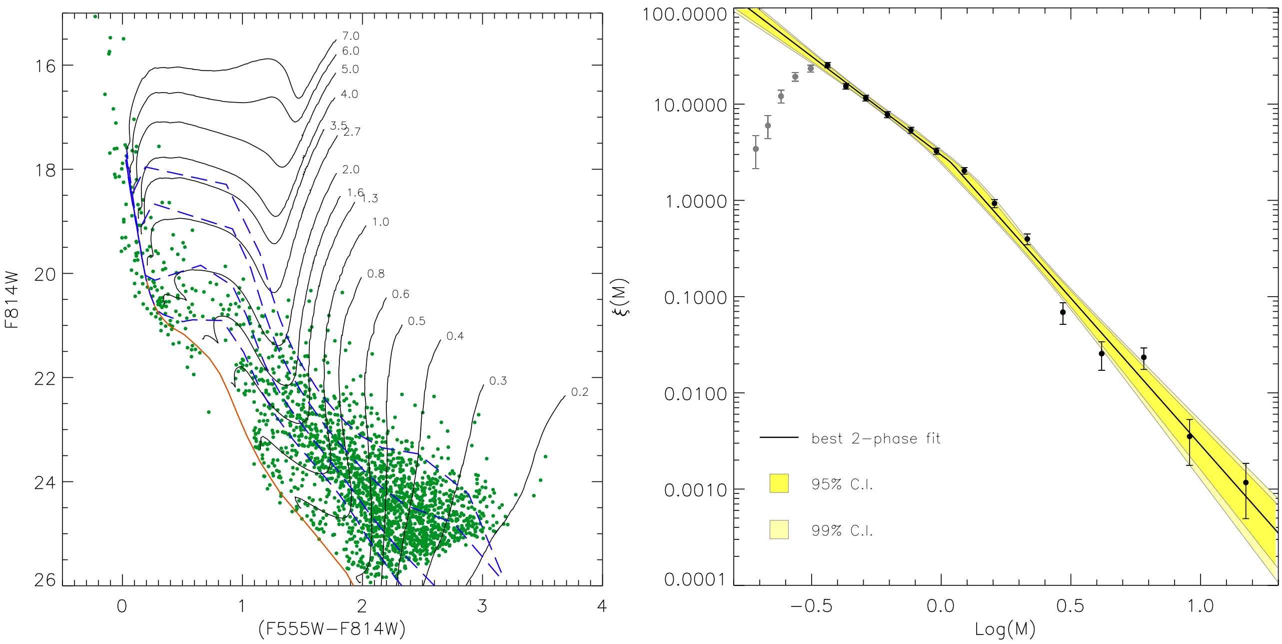

Figure 2: *Left panel: the observed CMD of LH95 after the removal of the contamination from the LMC field, characterized by* ~ 2500 *pre-main sequence members. Model evolutionary tracks are shown as well, denoting the relevant masses. The blue curves are isochrones for the ages of 1, 2, 4 and 10 Myr, while the red curve is the zero-age main sequence. Right panel: The derived IMF, corrected for detection incompleteness down to* $\sim 0.4 M_{\odot}$ *shows a statistical confirmed flattening with a break point at 1M⊙*

the system and a control field selected for the estimation the field contamination of the LMC. The field-subtracted population of LH 95 shows the presence of ~ 2500 young stars in pre-main sequence phase, and bright, massive, upper main-sequence (UMS) members (Figure 2a). The dust extinction we measure from the reddening of the UMS stars is exceptionally low for a star forming region ($A_V \simeq 0.6$ mag), enabling an accurate assignment of the stellar parameters.

The first subsolar IMF in the LMC

Using a new conversions of evolutionary models for the HST/ACS photometric system, we assign masses to all the members, down to the detection limit of $0.2 M_{\odot}$, well below the mass limit of any previous study outside the Milky Way. We derive the IMF (Figure 2b), corrected for incompleteness down to $0.4 M_{\odot}$ We find the IMF well represented by a two-phase power law, with a statistically confirmed change of slope at $1 M_{\odot}$, where the slope decreases from $x = 2.05$ to $x = 1.05$ (compared to the Salpeter value $x = 1.35$). This result, corrected for unresolved binarity is compatible with the Galactic IMF. The IMF does not show spatial variations within the system.

References

[1] Gouliermis, D. A., Henning, T., Brandner, W., Dolphin, A. E., Rosa, M., & Brandl, B. 2007, ApJL, 665, L27

[2] Da Rio, N., Gouliermis, D. A., Henning, T. 2009, ApJ, 696, 528

Recent star formation in the star-forming region NGC 346/N66 in the Small Magellanic Cloud with near-IR VLT/ISAAC imaging

Dimitrios A. Gouliermis, Wolfgang Brandner, Thomas Henning

Science Case

The youthfulness of the region NGC 346/N66 in the Small Magellanic Cloud (SMC) is well documented by studies of the gas and dust emission, and the detection in the optical of a rich sample of pre-main sequence (PMS) stars, and in the mid- and far-IR of Young Stellar Objects (YSOs). However, there is a lack of a comprehensive study of this region in the near-IR that will bridge the previous surveys. We perform a photometric near-IR analysis of the region NGC 346/N66 and a nearby control field of the SMC in order to locate the centers of active high- and intermediate-mass star formation through the identification of near-IR bright objects as candidate stellar sources under formation. Our data comprise deep, seeing-limited VLT images taken with the near-IR camera ISAAC. The striking difference in the appearance of the region NGC 346/N66 as seen in IR wavelengths is demonstrated in Fig. 1.

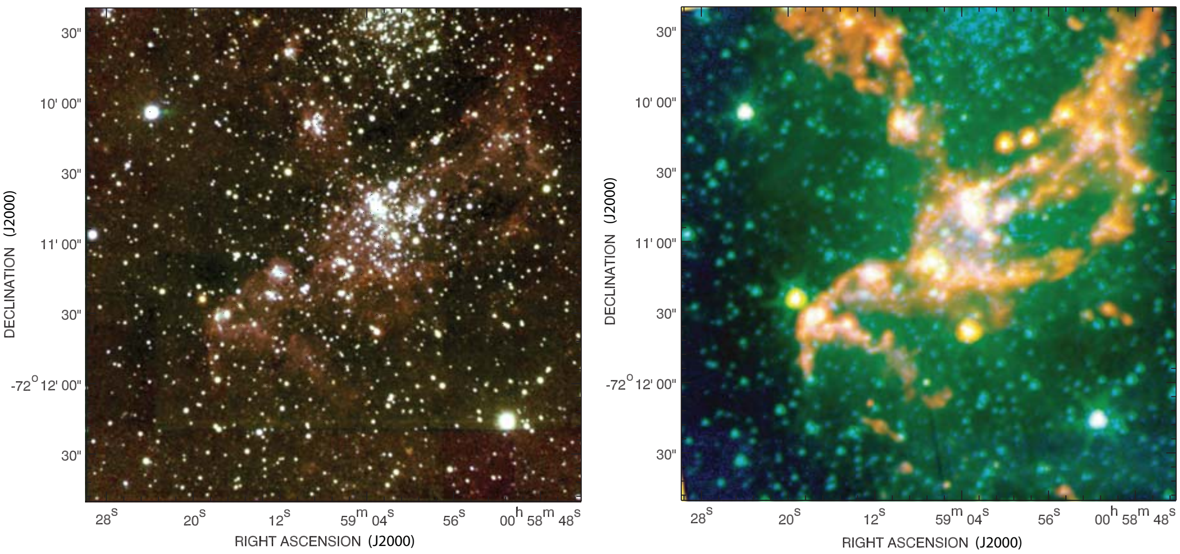

Figure 1: *Color-composite images of the main part of the region NGC 346/N66. Left: Image constructed with the combination of the jittered images in J (blue), H (green), and K_s (red) from VLT/ISAAC imaging. Right: Image composed from the K_s ISAAC image (blue) and Spitzer/IRAC 3.6 μm and 8 μm filters (green and red respectively). The dust emission, seen in the 8 μm band, signifies the centers of the most recent star formation and demonstrates the different information revealed in different wavelengths for the same region.*

Methodology and Results

We use archived imaging data obtained with the high-resolution camera ISAAC at VLT of NGC 346/N66 and we construct the near-IR color-magnitude (CMD) and color-color diagrams (C-CD) of all detected sources. We investigate the nature of all stellar populations in the observed CMDs, and we identify all stellar sources that show significant near-IR excess emission

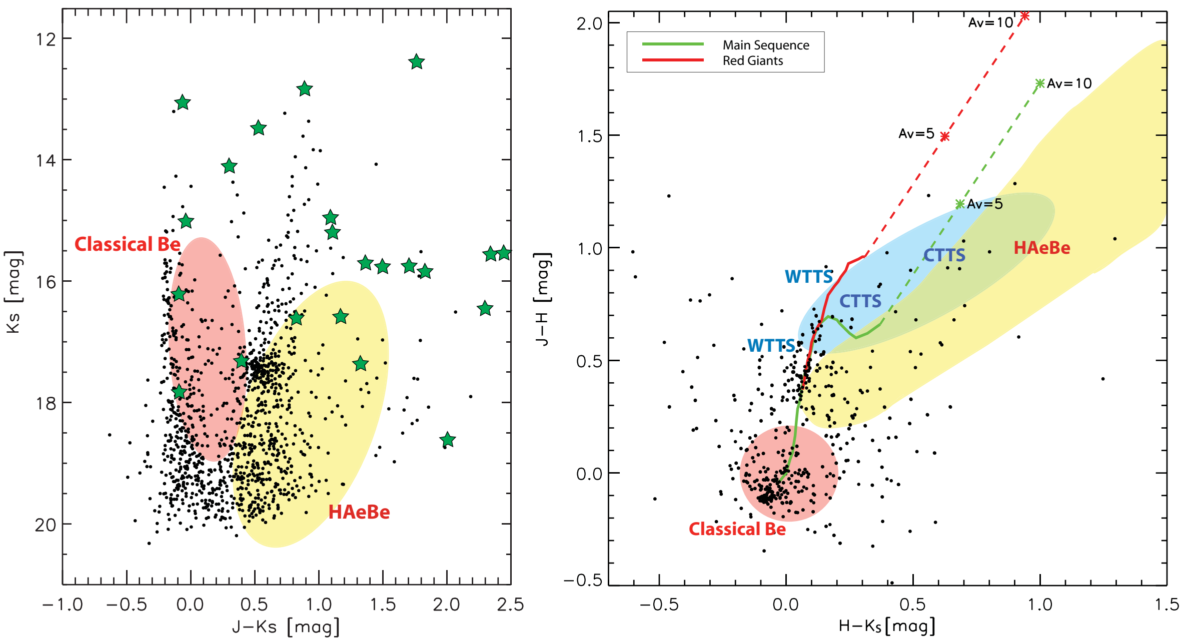

Figure 2: *$J - K_s$ vs. K_s Color-Magnitude Diagram (CMD) and the corresponding $J - H$ vs. $H - K_s$ Color-Color Diagram (C-CD) of all sources found in the main part of the star-forming region NGC 346/N66 with high photometric accuracy ($\sigma \lesssim$ 0.1 mag) from our VLT/ISAAC photometry. Typical locations of Herbig Ae/Be stars (HAeBe; yellow shaded areas), Classical Be stars (red shaded areas) and classical T Tauri stars (CTTS; blue shaded area) are shown based on previous studies. Weak-line T Tauri stars (WTTS) are also shown in the C-CD for completeness. The objects plotted in the CMD with green "⋆" symbols are the extinction corrected positions of the massive YSOs identified in our Galaxy.*

in the observed C-CD (Fig. 2). We select, thus, the best candidates for being young stellar sources. Based on their near-IR colors we select 263 candidate young stellar sources. This sample comprises a variety of objects such as intermediate-mass PMS and Herbig Ae/Be stars and possibly massive YSOs, providing original near-IR colors for them. The spatial distribution of the selected candidate sources shows that they are located along the dusty filamentary structures of N66 seen in mid- and far-IR dust emission and agrees very well with that of previously detected candidate YSOs and PMS stars. Our study provides an original accurate set of near-IR colors for candidate young stellar sources ([1]).

Collaborators

- Joachim M. Bestenlehner (Armagh Observatory, UK)
- Mónica Rubio (Departamento de Astronomía, Universidad de Chile, Chile)
- Rodolfo H. Barbá (Departamento de Física, Universidad de La Serena, Chile)

References

[1] Gouliermis, D. A., Bestenlehner, J. M., Brandner, W., Henning, T., Submitted to A&A (arXiv:0909.1027)

An LBT investigation of star formation and feedback in IC 2574

Anna Pasquali, Hans-Walter Rix, Fabian Walter, Tom Herbst

Young massive stars play a crucial role in the life of galaxies and in their energy budget. Through their winds and supernova explosions, these stars release kinetic energy, in addition to freshly synthethized metals (aka stellar feedback), with the possible effect of locally suppressing the formation of new stars and triggering it on larger scales across their host galaxy. Stellar feedback thus becomes a driving mechanism for galaxy evolution and a key ingredient of models of galaxy formation and evolution. Unfortunately, an accurate measure of its efficiency is difficult to obtain. The ideal targets for the study of stellar feedback are irregular galaxies with on-going star formation, and which are rich in atomic hydrogen (HI) and with no spiral arms, just like the nearby dwarf galaxy IC 2574. IC 2574 belongs to the M81 group at a distance of about 4 Mpc. High-resolution imaging of its neutral hydrogen HI shows a very structured distribution, rich in holes and shells even at large galactocentric radii [3]. These features appear to be expanding with a radial velocity of about 10 km s^{-1}, which, in turn, defines dynamical ages and kinetic energies consistent with being driven by stellar winds and supernova explosions. Nevertheless, no central star cluster has been so far detected in any (but one) of these features that can be responsible for their existence. The question is then whether the lack of a one-to-one correlation between HI holes and star clusters (or OB associations) is due to the limited photometric depth of the data that has been collected so far.

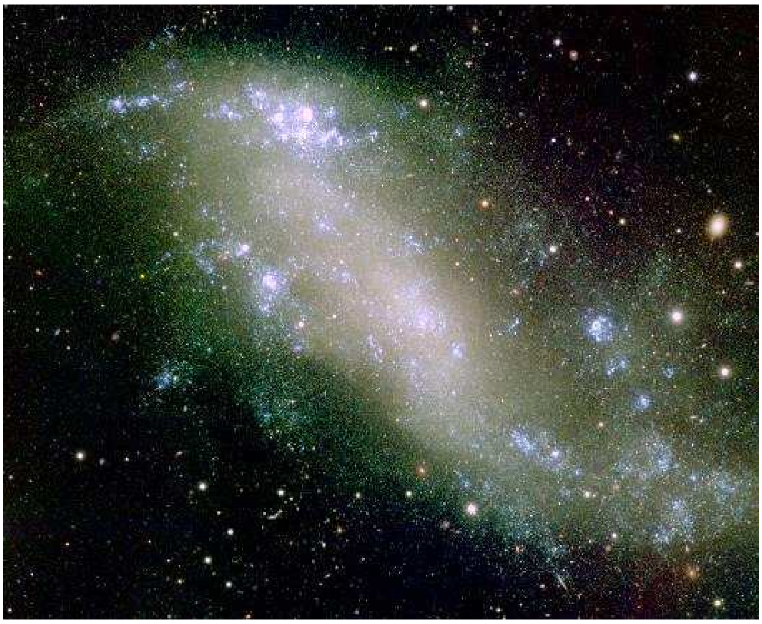

Figure 1: *Colour composite of IC 2574 obtained with the LBT LBC blue camera in the Bessel U, B and V filters, during the Science Demonstration Time of February 2007. North is up and East to the left. The size of the image is 14' × 11', the central one-fourth of the LBC field of view. The mean seeing is 1 arcsec.*

The lesson learned from LBT

We observed IC 2574 with the LBT LBC blue camera in 2007, reaching an unprecedented depth of 26 mag $arcsec^{-2}$ in the UBV bands [2]. Figure 1 shows a wealth of morphological features: the knotty tidal stream oriented East-West, the giant star-forming region in the North coinciding with a giant HI shell [3] and the extended tail of star formation in the South-West. Also visible are faint plumes of stars departing from the eastern and western sides of IC 2574. We computed the observed colours for each pixel within the galaxy extent and compared them with stellar evolutionary tracks [1]. We detected two major epochs of star formation in the galaxy; these are shown in Figure 2.

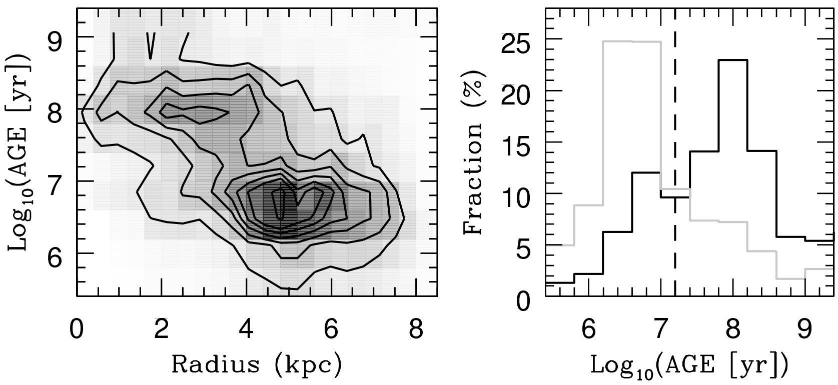

Figure 2: *The pixel stellar age distribution as a function of galactocentric distance (left-hand panel), with the grey shade becoming darker with increasing number of pixels. The right-hand panel plots the normalized age histogram for all pixels at $R < 4$ kpc (black line) and the remaining at $R \geq 4$ kpc (grey line). The black dashed line corresponds to $Log_{10}(AGE) = 7.2$ (16 Myr), the value we use to separate the younger from the older burst.*

The older burst occurred about 100 Myr ago, mainly at $R < 4$ kpc, while the second, younger event took place between 10 and 1 Myr ago, mostly at $R \geq 4$ kpc. Star formation proceeded in between the two bursts, but with a somewhat lower rate. At $R < 4$ kpc, the older burst has occurred over 73% of the pixels while the younger one has involved only 27% of the area. In the outer regions, instead, the younger burst has lit up 70% of the pixels, and the older burst has taken place only in 30% of the area. The older burst is characterized by a mean stellar mass surface density of about 1 $\mathrm{M_\odot pc^{-2}}$, while the younger burst has a characteristic value of about 0.04 $\mathrm{M_\odot pc^{-2}}$. These values translate into a star formation rate of 0.5 and 0.2 $M_\odot \mathrm{yr}^{-1}$ for the younger and older burst respectively. Using the results from the stellar population modelling, we have computed the kinetic energy (stellar winds and supernova explosions) released by the younger burst within the HI holes and compared it with the kinetic energy involved in their expansion. We find that the hole expansion can be sustained with only 10% of the stellar energy, indicating that the efficiency of stellar feedback is $\sim$ 10% in IC 2574. We also find that young stars live preferentially in the outskirts of most holes and not at their centre as we would expect if they drove the hole expansion. In conclusion, it is hard to establish whether stellar feedback is at work in IC 2574. The reasons behind these findings will require further investigation; they may rest either in an overestimate of the stellar mass loss and stellar winds, especially at low metallicity, or in our understanding of how stellar energy interacts with the interstellar medium. Another explanation may be that low-mass galaxies have a poorly-sampled Initial Mass Function (IMF), whose stochastic effects may mislead the comparison of the observations with stellar-populations synthesis codes based on a densely sampled IMF.

Collaborators are Adam Leroy (NRAO, Charlottesville) and Evan Skillman (University of Minnesota).

References

[1] Leitherer, C. et al., 1999, ApS, 123, 3

[2] Pasquali, A., Leroy, A., Rix, H.-W., Walter, F., Herbst, T. et al., 2008, ApJ, 687, 1004

[3] Walter, F., Brinks, E., 1999, AJ, 118, 273

The star formation efficiency in nearby galaxies

Adam K. Leroy, Fabian Walter, Frank Bigiel

A long-standing goal of studying nearby galaxies is to quantify the impact of local conditions on the conversion of gas into stars. Although the scaling relation between the galaxy-averaged surface densities of gas and recent star formation is one of the most widely used in extragalactic astronomy, many competing theories are capable of reproducing the observations. The fact that this relation is non-linear and that it breaks down in dwarf galaxies and the outer disks of spirals implies that environment does affect the conversion of gas to stars; as part of the scientific program for The HI Nearby Galaxies Survey (THINGS) [1] (see separate article in this report) we have been attempting to quantify these variations and identify their drivers.

Quantifying the relationship between gas and star formation obviously requires maps of the atomic (HI) and molecular (H_2) interstellar medium (ISM). To this end, we have created the first systematic set of combined HI and CO[1] maps for a large sample of galaxies. Using the Very Large Array, THINGS mapped the HI in 34 galaxies with high resolution and sensitivity. HERACLES [2], a parallel effort targeting an overlapping using the IRAM 30-m telescope, mapped CO emission from 19 galaxies (an extension to 45 galaxies has since been carried out). Both surveys targeted galaxies that had also been observed in the infrared (IR) observations by the SINGS legacy program using the *Spitzer* Space Telescope and in the far-ultraviolet (FUV) by the Galaxy Evolution Explorer (GALEX) as part of the Nearby Galaxy Atlas. As a result, the distribution of massive young stars (and hence the recent star formation rate) in each target is known in a way that is largely robust to uncertainties in sensitivity and extinction.

Using these data, we carried out a thorough investigation of what drives the *star formation efficiency* (SFE) — the star formation rate per unit gas[2] — in galaxies. We identified a number of proposed drivers (instability, shear, stellar surface density, pressure, orbital time, free-fall time) and measure the SFE as a function of each — both over individual 800 pc resolution elements and in radial profiles. Thanks to the rich multi-wavelength database surrounding the SINGS survey, we were able to estimate most key environmental quantities directly from observations.

Our basic observation is that the SFE in spiral galaxies is roughly constant where the ISM is mostly H_2 and declines steadily with increasing radius where HI makes up most of the mass. This two-part behavior may be seen in the left part of Figure 1, where we plot SFE as a function of radius (magenta points show where $H_2 >$ HI and blue points show where $H_2 >$ HI). There is a high degree of covariance among many environmental factors, and as a result we find a similar result comparing SFE to stellar surface density, orbital timescale, pressure, and the free-fall timescale. Of these, stellar surface density shows the tightest observed correlation — either suggesting our targets are rough equilibrium over timescales of a few Gyr or highlighting the importance of stellar gravity to converting gas to stars.

The simplest explanation for our observations is that stars form from H_2 at a more or less constant rate, while the fraction of the ISM in H_2 (as opposed to HI) varies systematically across a galaxy. The strongest component of this variation is radial; we observe the H_2-to-HI ratio to be a clear, strong function of radius and a variety of covariant parameters. The tightest relationship to a physical quantity is with hydrostatic pressure or stellar surface density, while again large-scale estimates of instability and shear appear to offer little handle on the H_2-HI balance. Our interpretation is that small-scale ISM physics (H_2 destruction and formation, local ISM density) more than large-scale galaxy structure drive star formation. Ongoing work including dust abundance in the analysis appears to bear out this conclusion.

This distinctive two-part behavior led us to focus more closely on the SFE of the H_2 gas alone. Somewhat surprisingly, we found little variation of the star formation rate per unit H_2

[1]Because most H_2 is essentially invisible, CO emission is the standard tracer of molecular gas in galaxies.

[2]This is the conventional extragalactic definition of the star formation efficiency, i.e., the inverse of the gas depletion time. The term unfortunately has another meaning in the context of Milky Way studies.

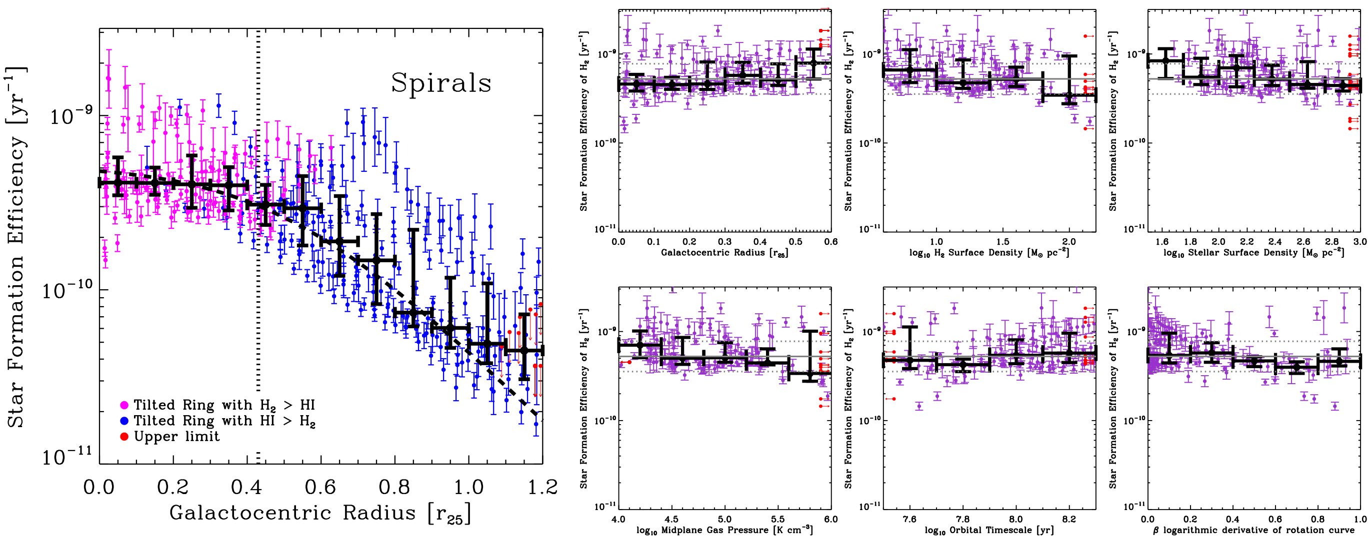

Figure 1: *(left) Star formation efficiency (SFE), star formation rate per gas mass, as a function of radius; (right) SFE of H_2 alone as a function of several environmental diagnostics. We find little variation in SFE (H_2) with environment but variations in the H_2-to-*HI *ratio drive a systematic radial decline in the SFE as a function of radius. Taken from [3].*

mass with any other quantity. This is illustrated in the right part of Figure 1, where we plot SFE(H_2) as a function of a series of other quantities that one might expect to separate our sample into regions that are more or less conducive to star formation in molecular clouds, e.g., due to changes in the pressure at the clouds surface, the rate at which clouds collide with one another or spiral arms, the mode of cloud formation, or the internal structure of clouds.

This observation of a largely invariant SFE(H_2) extends the result of [4], who found an approximately linear relationship between the surface densities of star formation rate and H_2. There are several possible interpretations for this result, including observational selection effects related to the use of CO to trace H_2. Our favored interpretation — and we believe the simplest available — is that the populations of molecular clouds vary little over the range of environments probed (essentially the disks of the dozen nearest spiral galaxies) and that these clouds are mostly insulated from their environment. This interpretation agrees with recent interferometric observations of CO clouds in the nearest galaxies and yields a prediction that will be readily testable with ALMA and an upgraded IRAM interferometer, namely that mass spectrum and scaling relations of giant molecular clouds do not vary much within or among spiral galaxies. This is also a prediction that must break down at some point as this constant SFE(H_2) found in galaxy disks must give way at high surface densities to a well-established non-linear relation relating star formation rate (traced by IR emission) and H_2 (traced by CO).

Collaborators include Elias Brinks (Hertfordshire, UK) and Erwin de Blok (Cape Town, South Africa) as well as Barry Madore (Carnegie Observatories) and Michele Thornley (Bucknell).

References

[1] Walter, F. et al. 2008, AJ, 136, 2563

[2] Leroy, A. K., et al. 2009, AJ, 137, 4670

[3] Leroy, A. K. et al. 2008, AJ, 136, 2782

[4] Bigiel et al. 2008, AJ, 136, 2846

The star formation law in nearby galaxies on sub-kpc scales

Frank Bigiel, Adam Leroy, Fabian Walter

A robust, quantitative measurement of the relationship between star formation rate (SFR) and gas density (SF law) is of major astrophysical importance in the context of galaxy evolution: it describes how efficiently galaxies turn their gas into stars and constrains theoretical models of star formation; in addition, it serves as essential input to simulations and models of galaxy evolution. Direct observations of this relationship at sub-kpc scales are still very rare because measuring the distributions of star formation, atomic gas, and molecular gas at high resolution and sensitivity is challenging and time-consuming.

However, the past few years have seen an explosion in multiwavelength data for nearby galaxies. From the 'GALEX Nearby Galaxy Survey' and the '*Spitzer* Infrared Nearby Galaxies Survey' (SINGS) the distribution of star formation is now known in a large suite of local galaxies. With the MPIA-lead H I nearby galaxy survey THINGS, H I maps that match or exceed the angular resolution and sensitivity of the ancillary datasets are now available for 34 nearby galaxies. From the 'BIMA Survey of Nearby Galaxies' (BIMA SONG) and in particular from the new, MPIA-based 'HERA CO-Line Extragalactic Survey' (HERACLES), which provides very sensitive CO observations across the entire optical disks of many nearby galaxies, the CO distributions of ~ 40 nearby galaxies are also known out to large radii. In this study, we combine this suite of multiwavelength data to measure the surface densities of H I, H_2, and SFR ($\Sigma_{\rm HI}$, $\Sigma_{\rm H2}$, and $\Sigma_{\rm SFR}$) across the entire optical disks of 18 nearby galaxies at 750 pc spatial resolution. Using these measurements, we examine the relationships among these three quantities (SF law) across our sample. These results are shown in Figure 1.

We find two relationships common throughout our data. First, a molecular Schmidt law with index $N = 1.0 \pm 0.2$ relates $\Sigma_{\rm H2}$ to $\Sigma_{\rm SFR}$ in our sample of spirals (compare middle panel of Figure 1). This may also be described as a total gas Schmidt law inside $\sim 0.5\,r_{25}$, where the ISM of all of our spiral galaxies is H_2-dominated. The average molecular gas (including helium) depletion time is $2.0 \cdot 10^9$ years with an RMS scatter of $0.8 \cdot 10^9$ years.

The second common feature of our data is that $\Sigma_{\rm HI}$ saturates at a surface density of ~ 9 $M_\odot$ pc^{-2} (left panel of Figure 1); gas in excess of this value is found in the molecular phase in the spirals . This saturation is common to spiral and H I-dominated galaxies. This is somewhat surprising because conditions in H I-dominated galaxies (such as dwarf galaxies) should be less favorable to the formation of H_2, which may lead one to expect a higher saturation value; a situation that is not observed.

We do not observe a universal relationship between total gas surface density and $\Sigma_{\rm SFR}$ (compare the right panel). Outside the H_2-dominated region, i.e., at $r > 0.5\,r_{25}$, the relationship between gas and star formation varies both within and among galaxies. In some cases, a single power law relates total gas and SFR over many orders of magnitudes in gas surface density. In other cases, we find a wide range of star formation rates at almost the same gas column. As a result of this variation, our best-fit power law index, N, for the total gas in spiral galaxies ranges from 1.1 to 2.7. This agrees well with the range of indices found in the literature, but does not hint at a universal total gas Schmidt law.

We describe variations in the relation between the SFR ($\Sigma_{\rm SFR}$) and the total gas ($\Sigma_{\rm gas}$) in terms of the star formation efficiency (SFE), i.e., star formation rate per unit gas mass ($\Sigma_{\rm SFR}/\Sigma_{\rm gas}$), and the H_2-to-H I ratio ($\Sigma_{\rm H2}/\Sigma_{\rm HI}$). We show that outside of the central, H_2-dominated regime of spiral galaxies, the SFE has a strong gradient with radius, where the highest efficiency points come from the inner disk, and the lowest efficiency points are at larger radii. We also show that the pixel-by-pixel distributions of late-type, H I-dominated galaxies overlap those of the outer disks of the spirals in our sample in $\Sigma_{\rm SFR}$-$\Sigma_{\rm gas}$ parameter space. This implies that similar conditions, i.e., low metallicities, weak potential wells and low dust content,

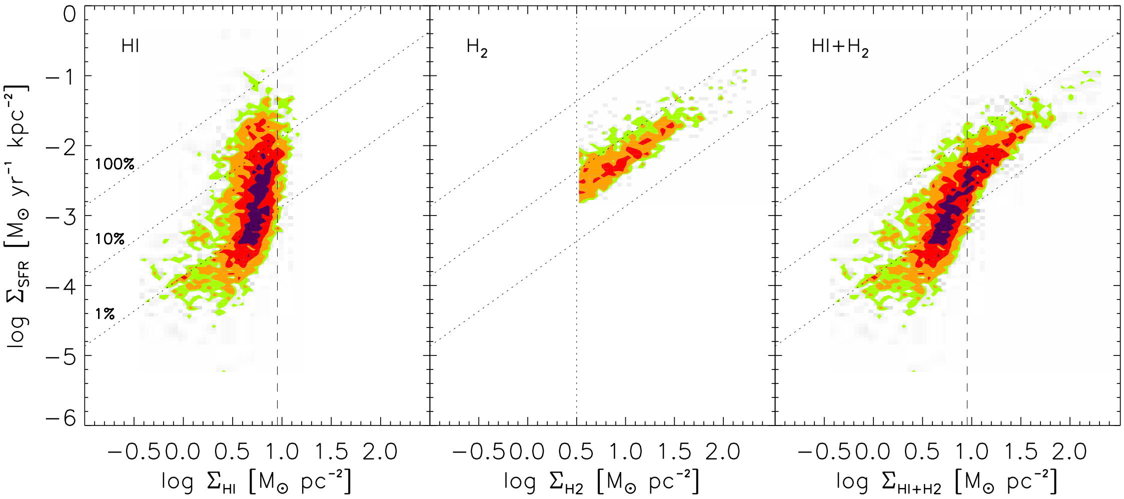

Figure 1: *Pixel-by-pixel data for 7 spiral galaxies plotted together. Left:* $\Sigma_{\rm SFR}$ *vs.* $\Sigma_{\rm HI}$*; middle:* $\Sigma_{\rm SFR}$ *vs.* $\Sigma_{\rm H2}$*; right:* $\Sigma_{\rm SFR}$ *vs.* $\Sigma_{\rm gas} = \Sigma_{\rm HI} + \Sigma_{\rm H2}$*. The contours indicate the density of sampling points (pixels), where the darker contours show where most of the pixel measurements are. The vertical dashed lines indicate the value at which* $\Sigma_{\rm HI}$ *saturates and the vertical dotted line (middle panel) represents the sensitivity limit of the CO data. The diagonal dotted lines are lines of constant star formation efficiency, i.e. SFR per unit gas mass and thus inverse of the gas depletion time, and correspond to depleting* 1%*,* 10% *and* 100% *of the gas in* 10^8 *yrs, including heavy elements.*

might drive the SFE in this regime.

We argue that these observations show a clear link between environment and the relationship between gas and star formation. We suggest the following scenario: the observational star formation 'law', as it is now understood, is a molecular phenomenon. The transition from H I to H_2 and the subsequent formation of stars is not purely a function of the total gas surface density. Instead, other physics sets the ratio of H I to H_2. The critical quantity for these processes is a strong function of radius and appears to be common to both dwarf irregular galaxies and the outer regions of spiral disks. This agrees quantitatively and qualitatively with the ideas of star formation thresholds.

We test these results in several ways and find that our conclusions are robust against variations in the star formation rate tracer used or the applied spatial resolution. Moreover, we find the same results when performing a pixel-by-pixel analysis and when working with azimuthally averaged radial profiles.

Collaborators on this project are Elias Brinks (Univ. of Hertfordshire, UK), Erwin de Blok (Univ. of Cape Town, South Africa), Barry Madore (Carnegie Observatories, USA), Michele Thornley (Bucknell Univ., USA)

References

[1] Bigiel, F., Leroy, A., Walter, F., Brinks, E., de Blok, W. J. G., Madore, B., & Thornley, M. D. 2008, AJ, 136, 2846

THINGS: The HI Nearby Galaxy Survey

Fabian Walter

For the past few decades studies of the atomic interstellar medium (ISM), via observations of the 21–cm line of atomic hydrogen (HI), have proven to be fundamental for our understanding of the processes leading to star formation, the dynamics and structure of the ISM, and the (dark) matter distribution, thereby touching on major issues related to galaxy evolution. Since the detection of the HI line this line has been used as the 'workhorse' for studies of the atomic gas in our own and other galaxies. One of its benefits is that, in contrast to optical or UV radiation, HI emission does not suffer from extinction by interstellar dust. In addition, its Doppler shift provides information about the velocity of the emitting gas. This provides important information on the physical properties of the interstellar gas and the associated kinematics of the ISM.

Before the start of the VLA Large Project THINGS ('The HI Nearby Galaxy Survey') no dedicated HI survey of a significant sample of nearby galaxies has been undertaken. The goal of THINGS was to obtain high quality observations of the atomic ISM of a substantial sample of nearby galaxies, covering a wide range of Hubble types, star formation rates, absolute luminosities, and metallicities to address key science questions regarding the ISM in galaxies. A key characteristic of the THINGS database is the homogeneous sensitivity, as well as spatial and velocity resolution that is at the limit of what can be achieved in studies of extragalactic HI with the VLA. Most of the galaxies in THINGS were drawn from the "*Spitzer* Infrared Nearby Galaxies Survey (SINGS)" (PI: Kennicutt), a multi–wavelength project designed to study the properties of the dusty ISM in nearby galaxies, to ensure that multi–wavelength observations for each galaxy are available for further analysis (see example in Fig. 1).

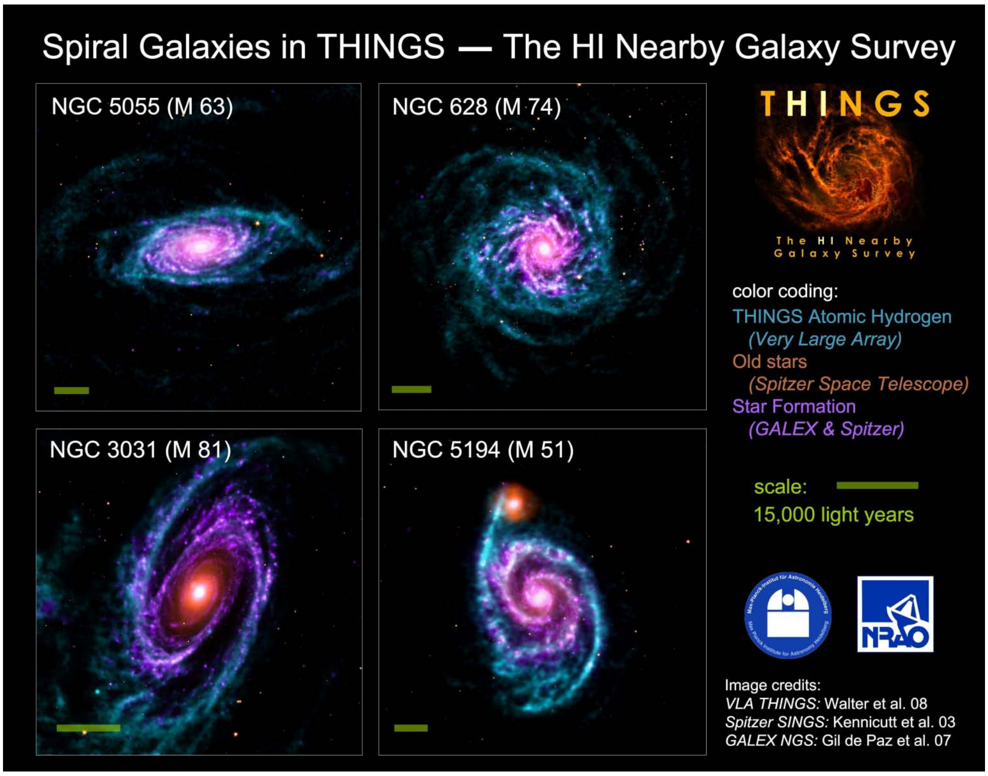

Figure 1: *Multi–wavelength composite of Galaxies observed as part of THINGS.*

In summary, THINGS (Walter et al. 2008, [1]) is a high spectral ($\leq$5.2 km s^{-1}) and spatial ($\sim 6''$) resolution survey of HI emission in 34 nearby galaxies obtained using the NRAO Very Large Array (VLA). The overarching scientific goal of THINGS is to investigate fundamental characteristics of the interstellar medium (ISM) related to galaxy morphology, star formation and mass distribution across the Hubble sequence. Unique characteristics of the THINGS database are the homogeneous sensitivity as well as spatial and velocity resolution of the HI data which is at the limit of what can be achieved with the VLA for a significant number of galaxies. A sample of 34 objects at distances $2 < D < 15$ Mpc (resulting in linear resolutions of $\sim$100 to 500 pc) are targeted in THINGS, covering a wide range of star formation rates ($\sim 10^{-3}$ to $6\,M_{\odot}\,\mathrm{yr}^{-1}$), total HI masses $M_{\rm HI}$ (0.01 to $14{\times}10^{9}\,M_{\odot}$), absolute luminosities $M_{\rm B}$ (–11.5 to –21.7 mag) and metallicities (7.5 to 9.2 in units of 12+log[O/H]).

Science capitalizing on the THINGS data products have been published in a special edition of the Astronomical Journal in December 2008. de Blok et al. (2008, AJ, 136, 2563) present a detailed analysis of high–resolution rotation curves and mass models (including new constraints for the stellar mass–to–light ratio) for the majority of THINGS galaxies. Trachternach et al. (2008, AJ, 136, 2648) present a detailed analysis of the centres of the THINGS targets and perform a harmonic decomposition of the velocity fields to constrain the non–circular motions in these objects. Oh et al. (2008, AJ, 136, 2720) present a new method to remove these non–circular motions from the velocity fields to derive accurate rotation curves unaffected by such motions. The star formation properties are addressed in papers by Leroy et al. ([2]) and Bigiel et al. ([3]) as described in two separate articles in this Report. Tamburro et al. ([4]) use the offset seen between the HI and 24 micron emission to derive an average timescale for star formation to commence in spiral arm environments. Zwaan et al. (2008, AJ, 136, 2886) use the THINGS data to compare the HI properties in nearby galaxies to the HI absorption properties found in Damped Lyman–α Absorbers systems at high redshift. Finally, the THINGS dataset is of sufficiently high quality that alternative data imaging techniques can be explored. This is described in Rich et al. (2008, AJ, 136, 2897) who use the THINGS data to investigate the applicability of the Multi–Scale CLEAN algorithm.

The THINGS data will enable other research projects and all data products are made publicly available through a dedicated webpage at MPIA (www.mpia.de/things). The collection of THINGS papers in the Astronomical Journal can be accessed through:
http://www.iop.org/EJ/journal/-page=extra.things/1538-3881

Collaborators include: Elias Brinks (University of Hertfordshire), Erwin de Blok (University of Cape Town), Adam Leroy (now Hubble Fellow at NRAO Charlottesville), Frank Bigiel (now UC Berkeley) and Rob Kennicutt (Cambridge).

References

[1] Walter, F., Brinks, E., de Blok, W.J.G., Bigiel, F., Kennicutt, R.C., Thornley, M.D., and Leroy, A., 2008, AJ, 136, 2563

[2] Leroy, A., Walter, F., Brinks, E., Bigiel, F., de Blok, W. J. G., Madore, B., Thornlet, M.D., 2008, AJ, 136, 2782

[3] Bigiel, F., Leroy, A., Walter, F., Brinks, E., de Blok, W.J.G., Madore, B., Thornley, M.D., 2008, AJ, 136, 2846

[4] Tamburro, D., Rix, H.–W., Walter, F., Brinks, E., de Blok, W. J. G., Mac Low, M., 2008, AJ, 136, 2872

A library of galaxy spectra

Paraskevi Tsalmantza, Coryn Bailer-Jones

For the classification and parametrization of galaxy observations in photometric and spectroscopic surveys (Gaia, Pan-STarrs etc) the use of suitable libraries of galaxy spectra is very important (i.e. libraries that include realistic spectra and show sufficient variation in intrinsic astrophysical parameters). For this purpose we have produced a library of approximately 30000 synthetic spectra of galaxies at z=0, corresponding to 4 spectral types (E, S, Im and SB).

The library of synthetic spectra of galaxies was produced with the PÉGASE.2 evolutionary model (Fioc & Rocca-Volmerange 1999, arXiv:astro-ph/9912179). For a given evolutionary scenario the model computes the spectrum and the values of the main astrophysical parameters (e.g. SFR and metalicities) of the galaxy for various timesteps, using an extended set of stellar evolutionary tracks from the Padova group and the BaSeL 2.2 stellar library. The resulting spectra cover a wide range of wavelengths from ultraviolet to near infrared with a resolution of R=200.

In previous work (Fioc & Rocca-Volmerange 1999, A&A, 326, 950), eight typical synthetic spectra of galaxies were produced with PÉGASE.2 by adopting the IMF of Rana & Basu (1992, A&A, 265, 499), a SFR proportional to the mass of the gas, the presence of infall and in the case of early type galaxies galactic winds. The spectra correspond to eight galaxy types from Im to E (Im, Sd, Sc, Sbc, Sb, Sa, S0 and E). The age of the galaxies is 13 Gyr except for the case of the irregular galaxy for which the age was assumed to be 9 Gyr. The resulting spectra were compared with observations available at the time and found in good agreement with them. As a first step we repeated this comparison with SDSS. We selected only nearby galaxies (z less than 0.01) with small photometric errors (less than 0.1 mag in all bands). The comparison is shown in Fig. 1 where we present the color-color diagram of the SDSS and model galaxies (yellow points).

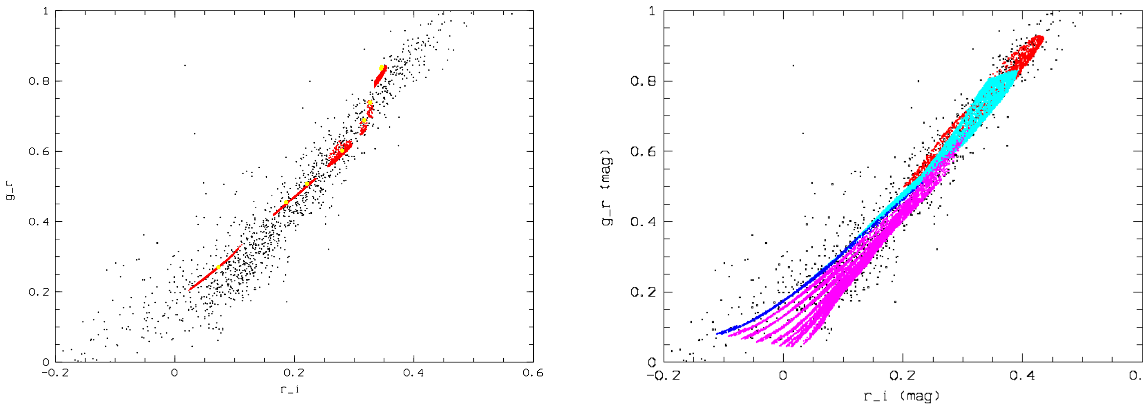

Figure 1: ***Left:*** *The first and* ***Right:*** *the second library of synthetic spectra of galaxies. The black background dots are SDSS galaxies and circles are the 8 typical spectra of PÉGASE.2.*

The good agreement between models and observations allowed us to build our library based on these eight typical models of PÉGASE.2. By expanding the range of the input parameters of the typical models and applying selection criteria for each type we produced our first library of 2700 synthetic galaxy spectra [3]. The color-color diagram of the first library of synthetic spectra at zero redshift is presented in Fig. 1.

Although the photometry produced by the synthetic spectra was in good agreement with the observational data, there were two main problems that we had to overcome before trying to build a second library that would cover most of the SDSS colour-colour diagram and therefore all aspects of the observational data. The first problem is a small deviation between models and observations of early type galaxies. This was solved by changing their SFR scenario from one proportional to the mass of the gas to an exponential one. The second problem was the spread in the blue part of the diagram, where the SDSS data have a large variance, while all the synthetic photometric data are located on one line. To cover this part of the diagram we added models for starburst galaxies, which we modelled as irregular galaxies for which the SF is stopped at various time steps.

By adopting these two new models and extending the parameter range for the irregular and spiral galaxies we created the second library of 28885 synthetic galaxy spectra and covered the majority of the SDSS colour-colour diagram (Fig. 1, [2]). The library consists of four more general galaxy types: starburst, irregular, spiral and early type galaxies. The synthetic spectra of this library were also compared with other observations, both photometric (e.g. LEDA, Paturel et al. 1997, A&AS 124, 109) and spectroscopic (e.g. SDSS and Kennicutt 1992, ApJS, 79, 255). The comparison showed good agreement between synthetic and observed data except in the case of starburst galaxies, where the models do not reproduce the strong emission lines that appear in the observed spectra.

Each spectrum in this library has been further simulated at four random values of redshift each lying in the ranges 0 to 0.05, 0.05 to 0.1, 0.1 to 0.15 and 0.15 to 0.2 respectively. The final library now includes 144425 synthetic spectra produced by a random grid of parameters.

The second library of synthetic spectra was used in the classification and parametrization systems developed for future surveys. More specifically the synthetic spectra were simulated for Gaia low resolution spectroscopy and Pan-STarrs photometry and used to train and test Support Vector Machine (SVM) classifiers in order to separate galaxies from other sources, (for a detailed description of SVM see [1]). For the case of the Gaia mission SVMs were also used to determine the different galaxy types and to estimate the astrophysical parameters that characterise the galaxy spectra, based again on the synthetic library presented here. The first results from SVM tests are promising, indicating that in both surveys galaxies can be separated from other sources with high completness. Additionally, galaxy types can be reliably predicted and several parameters (e.g. redshift, mass to light ratio, present SFR) can be estimated with low bias and variance from Gaia observations [2].

Collaborators from other institutions are Mary Kontizas, Evdokia Livanou (UOA, Greece), Brigitte Rocca-Volmerange, Michel Fioc (IAP, France), Romylos Korakitis (NTUA, Greece), Evagelos Korakitis, Anastasios Dapergolas, Ioannis Bellas-Velidis (NOA,Greece) and Antonella Vallenari (INAF, Italy).

References

[1] Bailer-Jones C. A. L., Smith K. W., Tiede C., Sordo R., Vallenari A. 2008, MNRAS, 391, 1838

[2] Tsalmantza P., Kontizas M., Rocca-Volmerange B., Bailer-Jones C. A. L., Korakitis R., Kontizas E., Livanou E., Dapergolas A., Bellas-Velidis I., Vallenari A., Fioc M., 2009, A&A, 504, 1071

[3] Tsalmantza P., Kontizas M., Bailer-Jones C. A. L., Rocca-Volmerange B., Korakitis R., Kontizas E., Livanou E., Dapergolas A., Bellas-Velidis I., Vallenari A., Fioc M. 2007, A&A 470, 761

7 Structure and Dynamics of Galaxies

Image on previous page:
NGC 6946 in an infrared image taken with the SPITZER Space Telescope.
Credit: N*ASA*/JPL-Caltech, Univ. of Arizona, Univ. of Cambridge, the S*INGS*-Team

Stellar mass-to-light ratios from galaxy spectra: how accurate can they be?

Anna Gallazzi and Eric F. Bell

Stellar masses play a crucial role in constraining the evolution of the galaxy population. Obtaining estimates of stellar mass-to-light ratios (M_*/L) as accurate as possible is thus of primary importance. However there is a number of statistical and systematic uncertainties, including uncertain aspects of populations synthesis models (the necessary tool to interpret galaxy spectro-photometric properties), assumptions on the shape and universality of the initial mass function (IMF) and dust attenuation. In this work (see [1]) we instead assume a fixed population synthesis model and IMF and we neglect dust effects, with the motivation of isolating the contribution of variations in star formation history (SFH) and metallicity on the M_*/L scatter over a range of observables. In particular we wish to explore in depth how M_*/L accuracy depends on the choice of observational constraints, on data quality and on galaxy type. Besides building intuition about the minimum observational requirement for a target accuracy, this approach helps us to gain insight into the questions: how much effort should be placed in creating realistic SFH and metallicity templates? How much should we improve population synthesis models?

Spectroscopic versus photometric estimates

We generate a Monte Carlo library of SFHs (random bursts of SF on top of exponentially declining SFHs) covering a broad range of metallicities (kept fixed along each SFH), as described in [2]. Mock galaxies are created by perturbing with different signal-to-noise ratios (S/N) original model spectra, selected in five different regions of the Hδ−D4000 plane (left plot of Figure 1) corresponding to different typical SFHs: galaxies with either a continuous or bursty SFH and different light-weighted ages. For each mock galaxy at each S/N we derive the probability density function (PDF) of M_*/L by comparing 'observed' spectral absorption features with those predicted by all the models in the library. Figure 1 (right) shows the M_*/L uncertainty (expressed by half of the 68% range of the PDF) against S/N for the five different galaxy types.

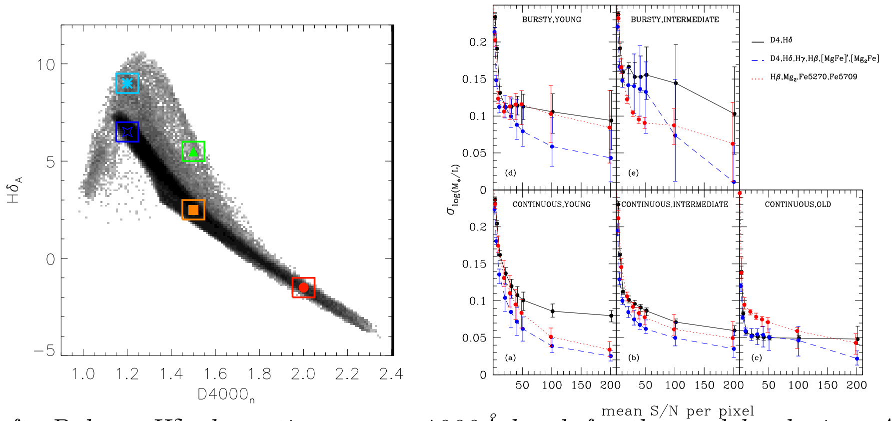

Figure 1: *Left: Balmer Hδ absorption versus 4000Å-break for the model galaxies. According to these two diagnostics of recent SFH we select mock galaxies characterized by either continuous SFH and dominated by old (red circle), intermediate-age (orange square) or young stellar populations (blue diamond) or by bursty SFH with intermediate-age (green triangle) or young stellar populations (cyan asterisk). Right: error as a function of spectral S/N on the M_*/L estimated using different spectral absorption features. Each panel refers to a particular galaxy spectral type.*

The plot shows that the M_*/L of old galaxies is more easily constrained than for other galaxy types. Only two age-sensitive spectral indices are enough to predict the correct M_*/L within 0.05 dex independently of S/N (Figure 1c). At fixed S/N the uncertainties become larger for galaxies with younger stellar populations, which span a larger range in metallicity. It is crucial to add constraints from metallicity-sensitive indices to derive M_*/L with uncertainties < 0.1 dex (Figure 1a,b). The M_*/L of galaxies with bursty SFHs are affected by uncertainties as large as ~ 0.2 dex. There is an intrinsically large spread in M_*/L that is hardly reduced by increasing the number of observational constraints or the S/N (Figure 1d,e). Finally we notice that there are situations in which uncertainties as low as 0.03 dex could in principle be reached. Therefore improvement of the models and control of systematics should remain high priority.

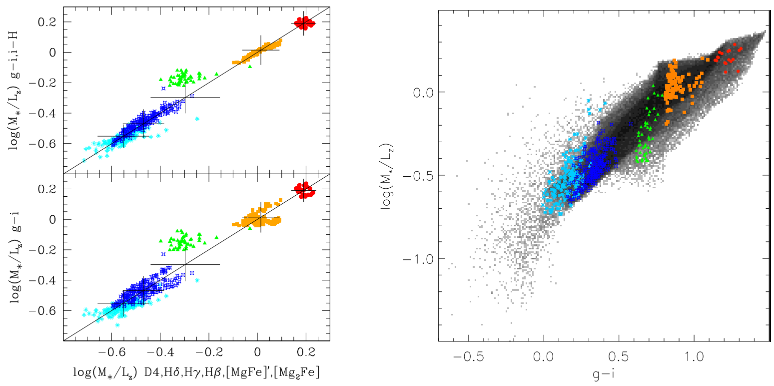

Figure 2: *Left: M_*/L estimates based on either one color ($g-i$; lower panel) or two colors ($g-i$ and $i-H$; upper panel) versus those based on spectral absorption features, for different spectral classes (see Figure 1). The mean M_*/L errors for each class are also shown. Right: M_*/L versus $g-i$ color for the full library (grey density map) and for the mock galaxies color-coded according to their spectral class. Bursty, intermediate-age galaxies have M_*/L lower than the bulk of the models at similar colors. This explains why their estimated M_*/L is biased high.*

We also derive M_*/L estimates with one optical or optical-NIR color. Figure 2 (left) compares spectroscopic estimates with those obtained with $g-i$ color. The use of $g-i$ alone (in the assumption that redshift is known and dust is absent) provides similar uncertainties as absorption indices. This is reflected in the good correlation between M_*/L and optical colors (Figure 2 right plot). However for galaxies with bursty SFH and intermediate ages color-based estimates are biased high by 0.2 dex (green triangles). Adding an optical-NIR color improves slightly the uncertainties but does not remove the bias (upper left panel of Figure 2).

Effects of prior assumptions on SFH and metallicity distribution

In [1] we further explore the effects on M_*/L estimates of any mismatch between the assumed prior distribution in SFH and metallicity and the true distribution, by fitting mock galaxies with libraries that have different prior distributions from the parent library. We find that, while it is necessary to account for bursts of SF in order to reproduce the observed range of absorption features, over-representing them can lead to under-estimate the M_*/L of galaxies with smooth SFHs, both for spectroscopic (0.05 dex) and color-based estimates (0.1 dex). Finally, assuming a fixed metallicity along the SFH does not introduce any bias in the M_*/L estimated from absorption features. On the contrary, the colors of single-metallicity populations do not correctly predict the M_*/L of multi-metallicity populations and tend to under-/over-estimate the M_*/L of old/young galaxies by 0.05 dex more than in the default case.

References

[1] Gallazzi A. & Bell E. F., 2009, ApJS, 185, 253

[2] Gallazzi A., Charlot S., Brinchmann J., White S.D.M., 2005, MNRAS, 362, 41

M51: a great laboratory for local ISM properties

Gaelle Dumas, Eva Schinnerer

The spatially resolved radio-IR correlation at 100pc resolution

The grand-design spiral M51 is an ideal target for detailed studies of the underlying physics in the Interstellar Medium (ISM) because it is nearby (8.4Mpc), has well-defined spiral arms and a nearly face-on orientation (i=20°). The close empirical correlation between the cm-radio emission (>1GHz) and the infrared (IR) luminosity is widely used out to high-z to estimate star formation rates (SFRs), despite the fact that its origin is poorly understood.

We observed M51 at three wavelengths (20cm, 6cm and 4cm) using the VLA (for a total of ~170hrs on-source) and the Effelsberg 100m telescope to obtain the highest quality radio continuum images of a nearby spiral galaxy (Fig. 1 left). These data were combined with deconvolved Spitzer 8μm and 24μm images to investigate the local changes in the radio-IR correlation at 2.4″ (≈ 100 pc) resolution.

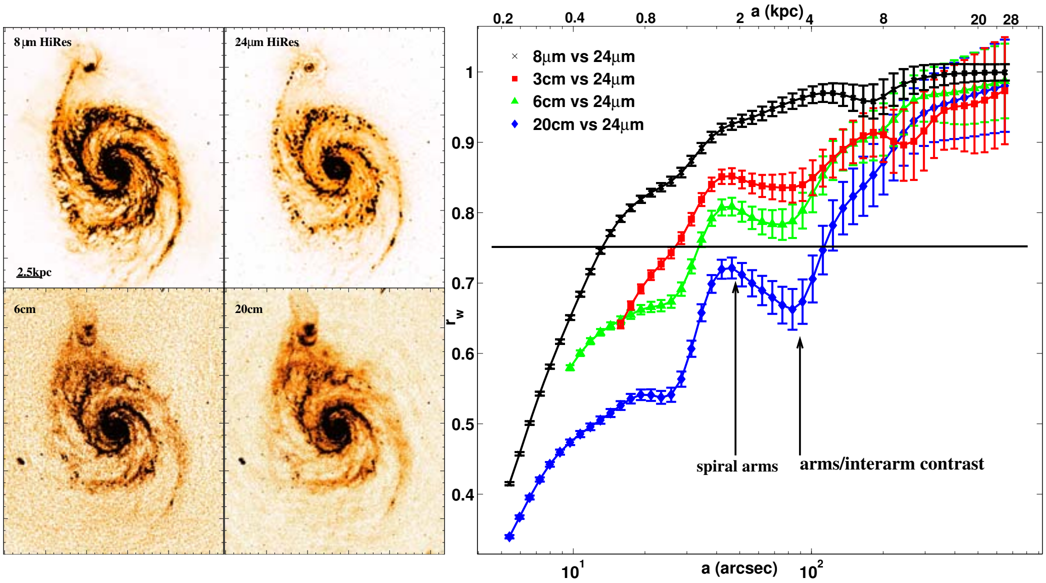

Figure 1: **Left:** *The Spitzer infrared images at 8μm and 24μm (top panels) and the VLA radio images at 6cm and 20cm (bottom panels) of M51 used for a detailed analysis of the spatially resolved radio-IR correlation.* **Right:** *Result of the cross-correlation of the wavelet decomposition showing that the radio-IR relation is changing as a function of spatial scale with local extrema (indicated by the arrows) as well as a function of radio wavelength used. The decrease in correlation for longer radio waves is expected as the radio emission is more and more dominated by synchrotron emission that is caused by cosmic rays and is expected to have a different scale length than dust heated by young stars.*

Our wavelet analysis using cross-correlation of the wavelet spectra shows different predominant structures in the radio of IR maps. For the first time local extrema can be studied revealing that the radio-IR correlation is high within the spiral arms (Fig. 1 right) while it becomes less good for scales encompassing the spiral arms and interarm regions indicating that another process unrelated to star formation might contribute to the radio emission. The global decreases of the cross-correlation spectra towards small scales, e.g. for 20cm and 24μm, is in agreement with the cosmic rays electrons diffusion length.

1 The properties of GMCs in the spiral arms

It is of great interest to establish whether the ISM properties in external galaxies are similar to those observed and studied in detail in our own Galaxy. Molecular clouds have received particular interest as they are the cradles for star formation. In order to investigate the properties of the molecular gas in the spiral arms of M51, we obtained multi-transition observations of the ^{12}CO(1-0), ^{12}CO(2-1, ^{13}CO(1-0) and C^{18}CO(1-0) transition with the OVRO interferometer and the IRAM 30m telescope for two selected regions in the disk of M51a (Fig. 2).

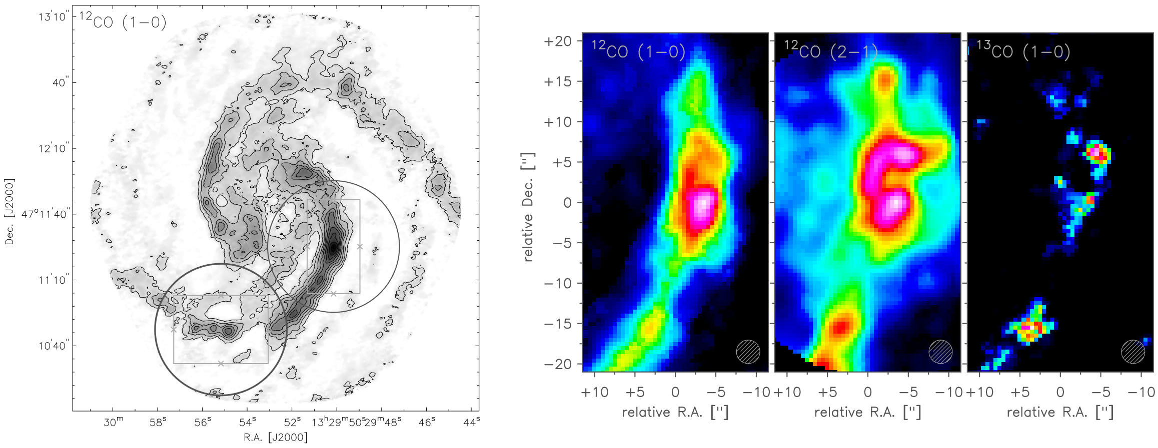

Figure 2: *The two selected region of the multi-transition study in M51 are overlaid onto the CO(1-0) map (left). The ^{12}CO(1-0), ^{12}CO(2-1), and ^{13}CO(1-0) integrated emission maps (right) are presented for the Western region at a resolution of 2.9" (≈ 120 pc). Line ratios derived from these short spacing corrected data indicated that the properties of the molecular gas complexes in the spiral arms are similar to those of GMCs detected in our Galaxy. The beam is shown in the lower right corner of each panel.*

Detailed analysis of the line ratios of ^{12}CO(2-1) and ^{12}CO(1-0) and ^{12}CO(1-0) and ^{13}CO(1-0) employing the Large Velocity Gradient (LVG) analysis shows that the kinetic temperatures and densities of the gas studied at about 120-180 pc resolution are very similar to those seen in the Milky Way suggesting that the properties of Giant Molecular Clouds (GMCs) might be universal. Comparison of the location of the molecular gas to ongoing star forming sites, i.e. HII regions, as traced by their ionizing gas emission shows that the vast majority of HII regions is located outside the gas spiral arms and thus does not have a large impact on the molecular gas properties.

Collaborators are Fatehmeh S. Tabatabaei (MPIfR), Rainer Beck (MPIfR), Thangasamy Velusamy (JPL, CaltTech), Axel Weiß (MPIfR), Susanne Aalto (OSO) and Nicolas Z. Scoville (CalTech).

Stellar mass and SED maps of nearby galaxies

Stefano Zibetti, Hans-Walter Rix

Stellar mass maps

The key role of stellar mass to determine (or predict) the physical properties of present day galaxies has been established by a number of works since the last decade. Stellar mass estimates, however, are generally derived from unresolved photometry, which biases mass-to-light ratios (M/L) towards lower values due to the dominance of young and unobscured stars. Properly weighting all regions of galaxies and resolving the distribution of stellar mass is thus crucial to correctly measure the total stellar mass and to investigate the structure and dynamics of galaxies in an unbiased way. To this goal we have developed a method to construct resolved stellar mass maps from optical and NIR imaging [1]. Accurate pixel-by-pixel colour information (specifically $g-i$ and $i-H$, computed by means of the median adaptive smoothing code ADAPTSMOOTH, [3]) is converted into stellar M/L with typical accuracy of 30%, based on median likelihoods derived from a Monte Carlo library of 50,000 stellar population synthesis models that include dust and updated TP-AGB phase prescriptions. Surface mass densities are computed by multiplying M/L by surface brightness. In a pilot study, we analyze nine galaxies spanning a broad range of morphologies. Their M/L maps are shown in Fig. 1. Looking at mass maps, galaxies appear

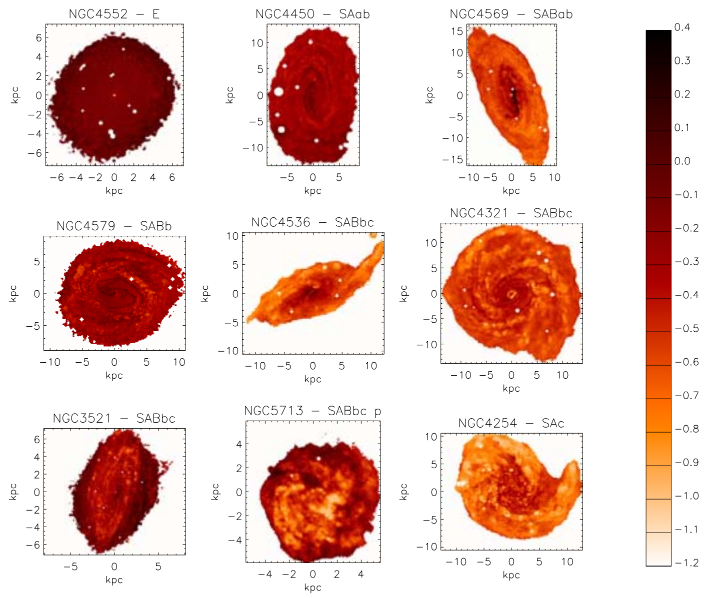

Figure 1: *The M/L maps of the nine galaxies of our sample, sorted from early to late type. Blue star-forming arms appear to have lower M/L, while dust lanes have higher than average M/L.*

much smoother than at any optical or NIR wavelength. Due to stellar population gradients, effective disk scale-lengths measured from light images are over-estimated with respect to the real structure as given by the stellar mass. Moreover we find that the total stellar mass estimates based on unresolved photometry are biased low with respect to the integral of resolved stellar mass maps, by up to 40%, due to dust obscured regions being under-represented in global colours.

Dependence of local SED on stellar mass density

Based on the pixel-by-pixel analysis of the previous section, we study the correlation between the SED (spectral energy distribution) as represented by colours (namely the optical $g-i$) and the surface stellar mass density *within* each galaxy [2]. The distribution of pixels as a function of these two quantities are shown in Fig. 2, where the colour scale denotes the density of pixels. As a general result, we see that the colour positively correlates with surface stellar mass density: higher density regions in galaxies are redder. Although this holds for all galaxies, the slope and the dispersion of the correlation varies a lot along the morphological sequence. For a typical elliptical galaxy the relation is very flat and very tight (consistent with a scatter due to photometric errors only). As we move to later types the colour-mass relation steepens, with low-density regions becoming increasingly bluer, while the highest density regions have roughly constant red colours. We can interpret this as a sign that star formation prefers low density and that the colour-morphology relation is mainly set by the relative weight of the younger stellar populations in the lower density regions with respect to the red high-density 'cores'. In addition, we see that the scatter around the mean relation increases going to later types, which have a more inhomogeneous distribution of physical properties at given surface mass density. The presence of dust also increases the scatter, especially at high surface mass density. These

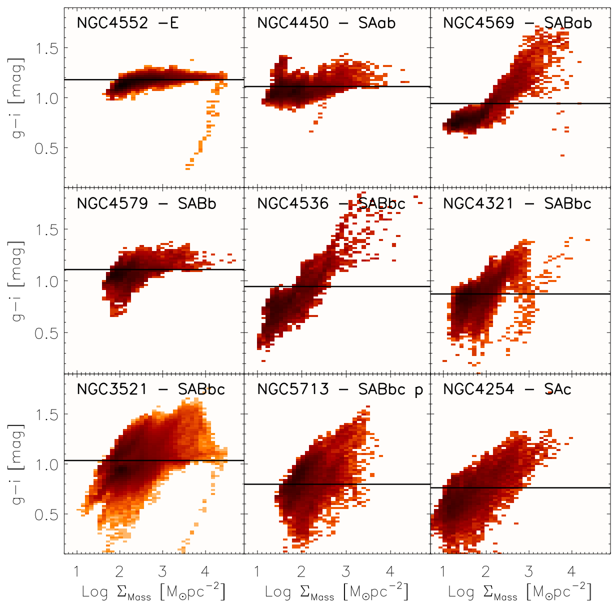

Figure 2: *The distribution of pixels in the* $g - i$ *vs surface stellar mass density plane for the nine galaxies: in colour scale the log of normalized number of pixels per cell. The horizontal line marks the global colour of the galaxy.*

preliminary results based on a small sample of only nine galaxies will be put on a much more solid ground, both from the statistical and physical point of view, by the forthcoming analysis of a larger sample of galaxies for which multiwavelength observations, from UV to radio, are available.

External collaborator: Stéphane Charlot (Institut d'Astrophysique de Paris).

References

[1] Zibetti, S., Charlot, S., Rix, H.-W., 2009, MNRAS in press, arXiv:0904.4252

[2] Zibetti, S., Charlot, S., Rix, H.-W., 2009, proceedings of the IAU Symposium 262, arXiv:0910.4975

[3] Zibetti, S., 2009, MNRAS submitted, arXiv:0911.4956

Galaxy-dark matter connection

Surhud More, Frank van den Bosch & Marcello Cacciato

Introduction

According to the standard picture of galaxy formation, galaxies form and reside in dark matter haloes. The complex physics of galaxy formation and evolution is primarily believed to be governed by the mass of the dark matter halo in which it occurs. Quantifying the connection between galaxy properties and their dark matter halo masses is an important stepping stone towards understanding galaxy formation.

Satellite galaxies are excellent tracers of the dark matter haloes of their central galaxies. Hence, their kinematics can be used to probe the dark matter halo mass. Using central and satellite galaxies identified from the SDSS, we have measured the average scaling relation between mass and light over a wide range of central galaxy luminosities. We have also obtained quantitative constraints on the scatter in this scaling relation which reflects the stochasticity of galaxy formation.

Method and Results

Under the assumption that satellite galaxies are in virial equilibrium, their velocity dispersion (VD), σ, can be used to determine the halo mass M, using the relation: $\sigma^3 \propto M$. Precise measurements of the VD are possible in haloes that host a large number of (detectable) satellites, a requirement that is only satisified in massive haloes. To measure the VD in low mass haloes, one has to stack the satellite galaxies in small bins of their central galaxy luminosities. However, the distribution of halo masses given the central luminosity, $P(M|L_c)$, may not be sufficiently narrow. In such a case, the stacking results in mixing the kinematics of satellites within haloes of different masses which complicates the interpretation of the measured VD signal.

The VD of the stacked satellites can be measured using two weighting schemes, satellite-weighting (each satellite gets unit weight) or host-weighting (each host has unit weight). In [1], we presented an analytical framework to model each of the VDs. We showed that if the distribution $P(M|L_c)$ has non-zero scatter, none of the two schemes can on its own be used to uniquely determine the scaling relation between light and mass due to a degeneracy with the scatter in this relation. We also showed that the ratio of the VD in the two schemes is sensitive to the scatter in $P(M|L_c)$ and hence can be used to break this degeneracy.

We applied this method to a volume-limited sample of galaxies from the SDSS in the redshift range $0.0 \leq z \leq 0.072$. Fig. 1 shows that the VD in the two weighting schemes are systematically different. This points to the presence of a non-negligible scatter in $P(M|L)$. The average halo mass and the scatter in halo masses as a function of central galaxy luminosity determined from the VDs are shown in Fig. 2. Consistent with expectations, we find that bright galaxies on average live in more massive haloes. We also find that the scatter in halo masses of centrals of the same luminosity can be non-negligible at the bright end. This can complicate interpretation of studies involving stacking (e.g. galaxy-galaxy lensing) that usually assume a negligible scatter.

The scaling relation and its scatter that we obtain are in good agreement with predictions from a semi-amalytical model (SAM) of galaxy formation (Croton et al. 2006, MNRAS, 365, 11) and also the conditional luminosity function (CLF) model from [3]. The CLF also reproduces the observed galaxy abundance, galaxy clustering and the galaxy-galaxy lensing signal [3]. We conclude that the scaling relation between the luminosity of the central and its halo mass is well established, is supported by various different astrophysical probes and is fairly well reproduced by models of galaxy formation.

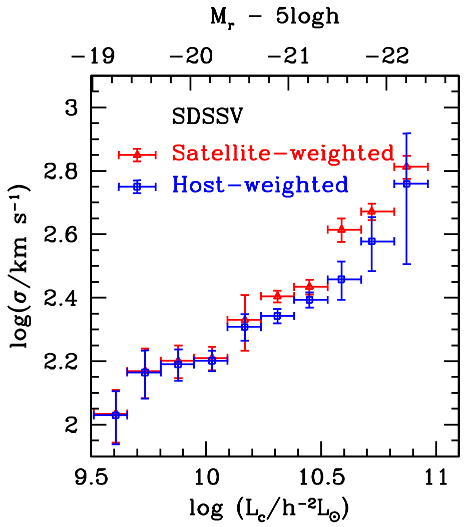

Figure 1: *The velocity dispersions of satellite galaxies as a function of the* $^{0.1}r$*−band luminosity of their centrals measured using two different weighting schemes.*

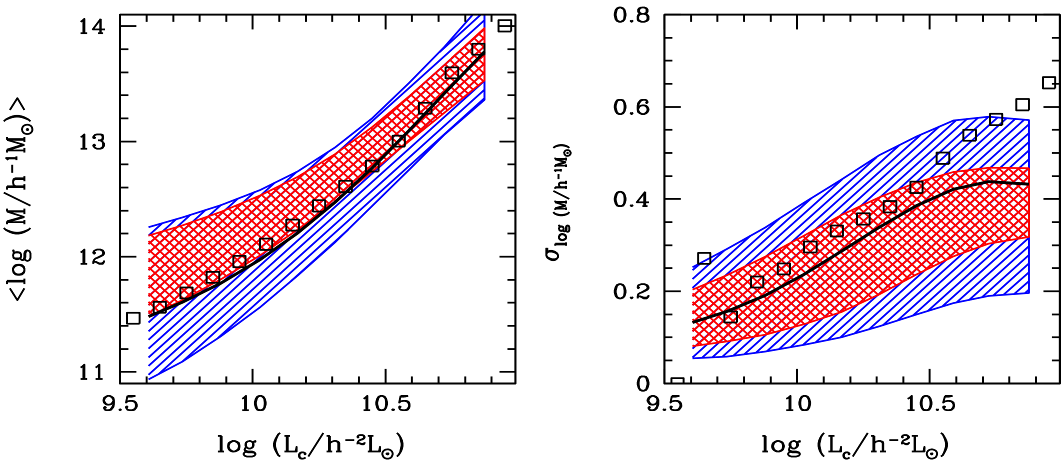

Figure 2: *The 68 percent (red crossed) and the 95 percent (blue slanting lines) confidence estimates of the average halo mass and the scatter in halo masses as a function of the central luminosity obtained via satellite kinematics. The squares show predictions from the SAM of Croton et al. (2006) while the solid lines show predictions of the CLF model from [3].*

Collaborators are Houjun Mo, Ran Li (University of Massachusetts) and Xiaohu Yang (Shanghai Astronomical Observatory).

References

[1] More, S., van den Bosch, F. C., & Cacciato, M. 2009, MNRAS, 392, 917

[2] More, S., van den Bosch, F. C., Cacciato, M., Mo, H. J., Yang, X., & Li, R. 2009, MNRAS, 392, 801

[3] Cacciato, M., van den Bosch, F. C., More, S., Li, R., Mo, H. J., & Yang, X. 2009, MNRAS, 394, 929

Ages and metallicities of central and satellite galaxies: implications for galaxy evolution

Anna Pasquali, Anna Gallazzi

Being able to split the galaxy population of groups/clusters in centrals (the most massive galaxy) and satellites has proven to be extremely useful for investigating the impact of satellite specific transformation processes (e.g., ram-pressure stripping, tidal stripping, strangulation, harassment). Using the SDSS DR4 galaxy group catalogue [5], our team has shown that satellites are redder and more concentrated than centrals of the same stellar mass (M_*), indicating that strangulation (i.e. the removal of hot gas) is most likely the main mechanism for quenching star formation in satellites [3]. An important shortcoming of integrated colours is that they simultaneously depend on stellar age, metallicity and dust extinction, and they are thus degenerate with respect to the age and metallicity of stellar populations. In fact, keeping dust absorption aside, red colours may be due to older ages and/or higher metallicities.

Ages and metallicities of centrals and satellites

We have matched the SDSS DR4 galaxy group with the catalogue of (mass-weighted) stellar ages and metallicities of [1] in order to study how these quantities depend on M_* and the dark matter mass, M_h, of the halo where central and satellite galaxies reside [2]. In Figure 1 we investigate the dependence on M_h at fixed stellar mass and viceversa with the aim of determining which one of these dependencies is casual. The solid, coloured lines show the mean ages and metallicities of satellite galaxies as function of stellar mass for narrow bins in halo mass (left-hand panels), and as function of halo mass for narrow bins in stellar mass (right-hand panels). The errorbars indicate the errors on the mean. In each panel, the grey band depicts the range of ages/metallicities enclosed by the 16th and 84th percentiles of the corresponding distributions for centrals, with the black dotted line indicating the corresponding median. A comparison of panels a and c shows that massive satellite galaxies ($M_* > 3 \times 10^{10} h^{-2} M_\odot$) have luminosity weighted ages that are (i) comparable to those of central galaxies of the same mass, and (ii) virtually independent of the mass of the halo in which they reside. However, in the case of low mass satellites ($M_* < 3 \times 10^{10} h^{-2} M_\odot$), there is a clear dependence on halo mass, such that satellites in more massive haloes have older stellar populations. This halo-mass dependence is most pronounced for the satellites in the lowest stellar mass bin probed here ($9 < \mathrm{Log}_{10}(M_*/h^{-2} M_\odot) \leq 9.5$), whose age increases with M_h. Analogous trends can be seen for the stellar metallicities, shown in panels b and d. Massive satellites with $M_* > 3 \times 10^{10} h^{-2} M_\odot$, which all reside in haloes more massive than $\sim 3 \times 10^{12} h^{-1} M_\odot$, have metallicities that are similar to centrals of the same stellar mass and independent of halo mass. The metallicities of satellites with $M_* < 3 \times 10^{10} h^{-2} M_\odot$, though, increase with the mass of the halo in which they reside. Similar as for the ages, this mass dependence becomes stronger for less massive satellites.

Implication for galaxy evolution

We have compared the above results with the semi-analytical model of [4]. Although the model predicts that satellite galaxies have older stellar populations than central galaxies of the same stellar mass, in qualitative agreement with the data, it yields metallicities that are ~ 0.2 dex too low at the high mass end, and an age-stellar mass relation that is much too shallow. In addition, it fails to reproduce the halo mass dependence of the metallicities of low mass satellites, and predicts that centrals have the same metallicities as satellites of the same stellar mass. We believe that these discrepancies arise from the treatment of supernova/AGN feedback, strangulation and tidal stripping in the model. For example, the data suggest that AGN feedback as well

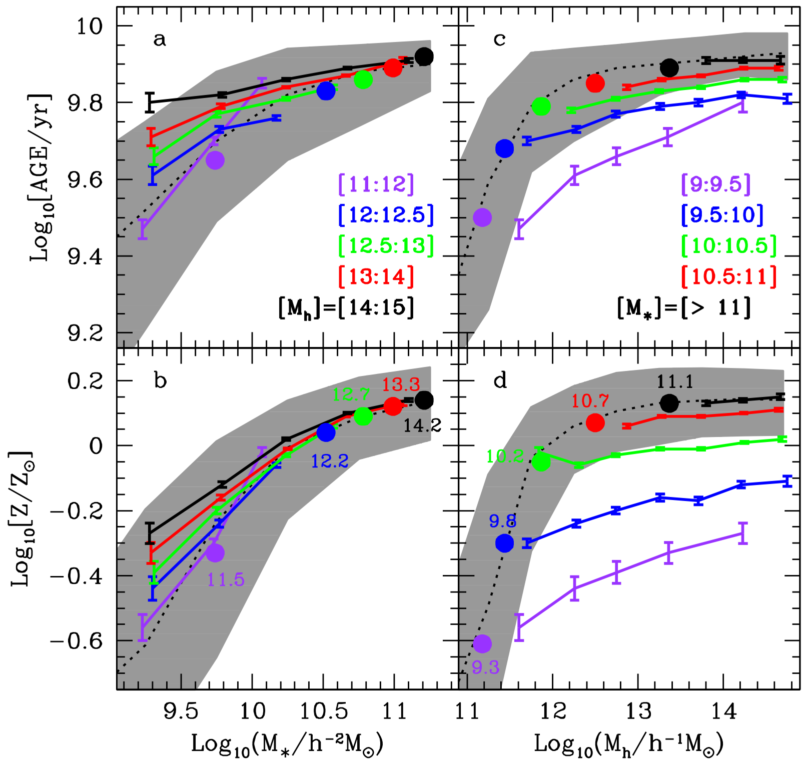

Figure 1: *Ages and metallicities of central and satellite galaxies as function of stellar mass (left-hand panels) and halo mass (right-hand panels). From top to bottom the panels show the mass-weighted ages (panels a and c) and the stellar metallicities (panels b and d). The grey band in each panel marks the 16th-to-84th percentile range of the distribution of centrals, with the dotted line indicating the corresponding median. The coloured solid lines indicate the medians for satellites in logarithmic bins of halo mass (left-hand panels) or stellar mass (right-hand panels), as indicated in panels a and c. The coloured filled circles indicate the corresponding medians for the centrals in those bins, with the associated mean logarithmic values of* $M_{\rm h}$ *and* M_* *indicated in panels b and d, respectively.*

as strangulation should depend more gently on halo mass and/or stellar mass than what is now implemented in the model. Also, the observations indicate that the recipe for supernova feedback should be modified by taking the effects of galactic winds into account. The model should include tidal stripping (i.e. mass loss of a galaxy due to tidal interactions with its host halo potential well) as a plausible explanation for the observed metallicity difference between central and satellite galaxies.

Collaborators are Fabio Fontanot and Gabriella De Lucia (INAF Trieste), Frank van den bosch (University of Utah), H.J. Mo (University of Massachusetts), Xiaohu Yang (Shangai Astronomical Observatory).

References

[1] Gallazzi, A. et al., 2005, MNRAS, 362, 41

[2] Pasquali, A., Gallazzi, A., Fontanot, F., van den Bosch, F.C., De Lucia, G., Mo, H.J., Yang, X., 2009, MNRAS, submitted (astro-ph 0912.1853)

[3] van den Bosch, F.C. et al., 2008, MNRAS, 387, 79

[4] Wang, J. et al., 2008, MNRAS, 384, 1301

[5] Yang, X. et al., 2007, ApJ, 671, 153

Evidence for stellar feed-back in IC 342's nucleus

Eva Schinnerer

Nuclear Stellar Clusters in Late Type Spiral Galaxies

About 75% of late-type disks host distinct nuclear star clusters, most of which have experienced multiple discrete star formation events in their history. So far, it has been unclear whether the repetitive nature of nuclear star formation is due to variability of the gravitational potential (e.g. dissolution/formation of a stellar bar), the clumpy nature of the molecular gas (e.g. inflow of discrete giant molecular complexes – GMCs), or whether nuclear massive star formation itself is disrupting the gas supply.

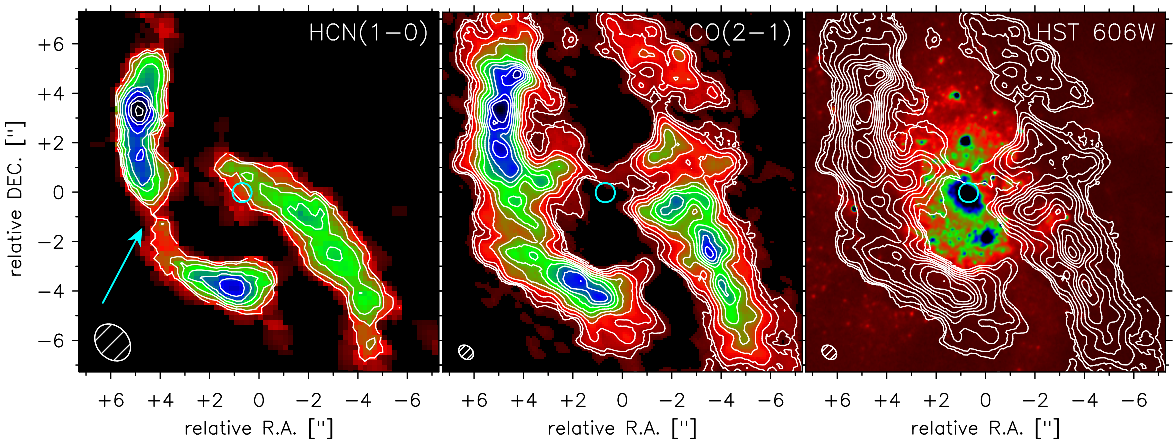

Figure 1: *The distribution of molecular gas in the central 300 pc of IC 342: dense gas traced by HCN(1-0) line emission* **(left)**, *the cold molecular gas reservoir observed in CO(2-1)* **(middle)**, *CO(2-1) in contours overlaid onto the stellar light distribution as observed with HST in the V band (color)* **(right)**. *The nucleus is marked by the cyan circle, while CLEAN beam for each molecular line observation is given in the bottom left corner in each panel. Comparison of the CO(2-1) and HCN(1-0) intensity maps shows that the dense gas follows the overall distribution, but reached closer to the nuclear stellar cluster. The arrow in the left panel points to a pronounced kink in the eastern spiral arm that is present in both emission lines. (See text for details.)*

The Scd spiral IC342 is the nearest proto-type of a late-type spiral harboring a well-studied nuclear star cluster. The nuclear cluster has a stellar mass of $\sim 10^7$ $M_\odot$ and its luminosity is dominated by a recent star formation event which took place 4-30 Myr ago (both corrected for the revised distance of 3.3 Mpc, Böker et al. 1999, AJ, 118, 831). The spiral geometry of the molecular gas in the central 500pc is due to the response of the gas to the large-scale stellar bar.

Our new 0.6" and 1.5" resolution data of the CO(2-1) and HCN(1-0) line emission obtained with IRAM/PdBI allows for a direct comparisons to high resolution HST imaging (Fig. 1) (presented in [1]). The eastern spiral arm has a break and its southern portion exhibits a sharp edge on the side facing the nucleus. The ionized gas seen in Hα fills the central 'cavity' of the molecular gas (Fig. 2). In particular, the Hα shells (or arcs) coincide with the inner edge of the eastern CO(2-1) spiral arm, suggesting that the expanding ionized gas is 'running' into the molecular gas, compressing and/or pushing it in the process. The central cavity also offers a relatively un-obscured view onto the stellar disk, as demonstrated by the comparison to the optical continuum: the stellar disk is substantially dimmed wherever molecular gas is present.

Evidence for Self-Regulation of Star Formation in IC 342's Nuclear Stellar Cluster

The excellent alignment between the Hα shells and the sharp inner edge of the south-eastern molecular spiral arm suggests that stellar winds and supernova explosions produced in the recent nuclear star formation event have pushed the southern portion of the eastern molecular gas spiral arm outward. A first order approximation of timescales and energies involved shows that this is a plausible scenario (Fig. 2) for the latest starburst event in the nuclear stellar cluster. If correct, this scenario implies that models for the gas fueling mechanism (over the innermost 1-100 parsec) cannot rely on the shape of the gravitational potential alone but need to take the mechanical energy released by nuclear activity onto the gas flow into account. The impact of this feedback process will be strongly variable in time and will critically depend on the amount of energy released as well as its geometry.

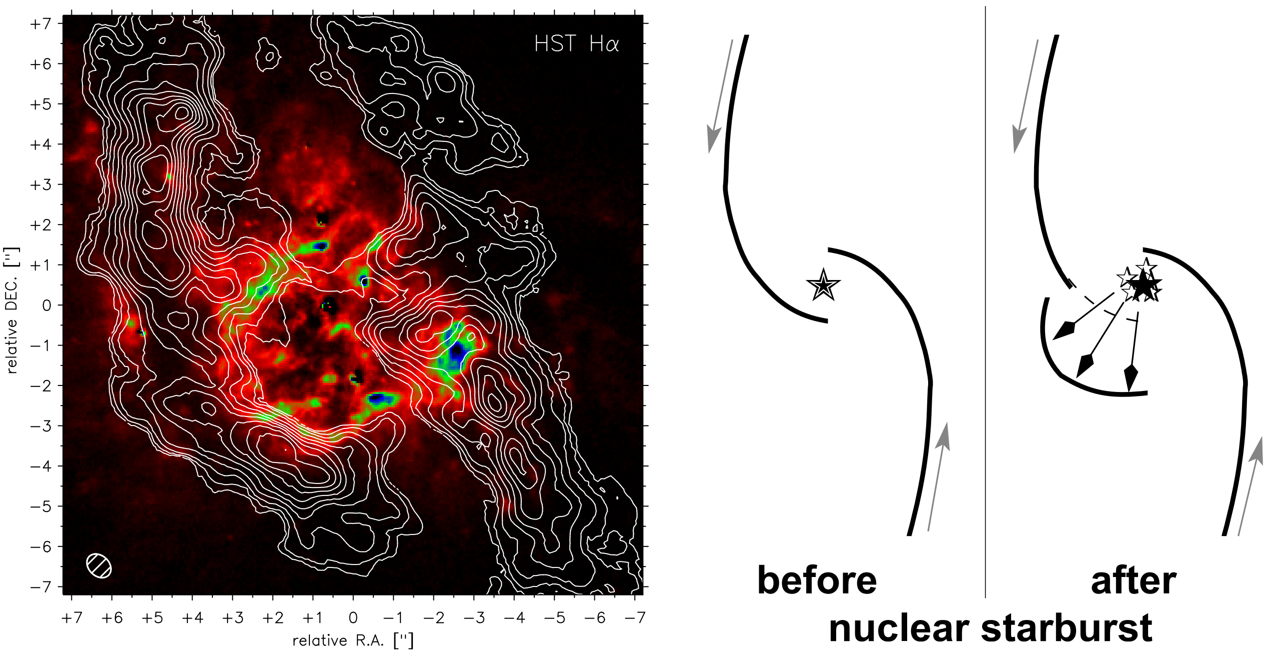

Figure 2: **Left:** *Comparison of the CO(2-1) gas distribution (contours) to the morphology of the ionized gas as traced in Hα emission (color) from HST observations. The shells that apparently originated from the nuclear stellar cluster fit nicely the inner borders of the CO(2-1) distribution, in particular along the inner edge of the south-eastern spiral arm. These shells could be driven by stellar winds and SN from the last starburst event in the nuclear cluster about 30 Myrs ago.* **Right:** *Proposed scenario of stellar feed-back acting in the nucleus of IC 342. The large-scale stellar bar feeds molecular gas towards the central stellar cluster (left panel). When enough molecular material has been accumulated, a new starburst event released mechanical energy in the form of winds that pushes the molecular gas spiral arm(s) off and thus shuts down the supply of gas towards the nucleus causing a self-regulation of nuclear feeding.*

Collaborators are Torsten Böker (ESA/ESTEC), David S. Meier (NMT) and Daniela Calzetti (UMASS).

References

[1] Schinnerer, E., Böker, T., Meier, D.S., Calzetti, D., 2008, ApJL, 684, L21

Can gas prevent the destruction of thin stellar discs by minor mergers?

Benjamin P. Moster and Andrea V. Macciò

Introduction

The large population of merging satellites has raised the question of whether mergers are *too* common in the CDM scenario. Some studies have questioned whether thin, dynamically fragile discs such as the one observed in the Milky Way can survive this bombardment by incoming satellites and found that the answer depends quite sensitively on the mass ratio of the merging galaxies. There seems to be a consensus that the main danger to thin discs is from events with a mass ratio of (∼1:10). However, studies performed so far have only considered the dissipationless components in the galaxy (dark matter and stars), neglecting the presence of a dissipative gas component in the disc. However, the inclusion of gas physics is known to play an important role in stabilizing galactic discs.

Numerical Simulations

We make use of the parallel code GADGET-2 which uses Smoothed Particle Hydrodynamics (SPH) to evolve the gas using an entropy conserving scheme. Radiative cooling is implemented for a primordial mixture of hydrogen and helium and a spatially uniform time-independent local UV background in the optically thin limit is included. Star formation and the associated heating by supernovae (SN) is modelled following the sub-resolution multiphase ISM model described in Springel & Hernquist (2003, MNRAS 339, 289).

Each primary system consists of gas and stellar discs with radial profiles described by an exponential and a spherical bulge embedded in a dark matter halo. The vertical structure of the stellar disc is described by a radially independent sech^2 profile with a scale height z_0, and the vertical velocity dispersion is set equal to the radial velocity dispersion. We construct a set of primary systems, each with a virial mass of $M_{vir} = 10^{12} M_{\odot}$ containing a disc and a bulge, and a satellite system with a virial mass of $M_{vir} = 10^{11} M_{\odot}$ containing only a bulge. For models that also include a gaseous disc component we add gas such that the gas fraction in the disc is 20% and 40% in the two cases. We adopt a "fiducial" value of $z_0 = 0.4$ kpc. Edge-on surface brightness maps for the initial conditions of our primary galaxies are shown in the upper and lower left panels of Figure 1 for $z_0 = 0.4$ and 0.25 kpc, respectively. All simulations were evolved for a total of 6 Gyr [1].

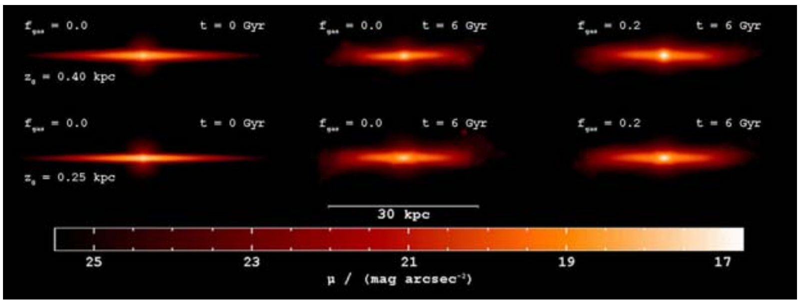

Figure 1: *Edge-on surface brightness maps for galaxies with an initial scale height of* $z_0 =$ 0.40 kpc *(upper row) and* $z_0 = 0.25$ kpc *(lower row). The left column shows the initial models while the centre and the right columns show the final galaxies (t=6* Gyr*) for an initial gas fraction of 0% and 20%, respectively.*

Results

We analyze the surface brightness profiles of the merger simulations with gas, and show the resulting evolution of the scale height in Figure 2 for initial gas fractions of 0%, 20% and 40%, and an inclination of 60° (MA60, MB60 and MC60). This shows that the presence of gas does indeed suppress the thickening of the disc by a minor merger. The final scale height increases by a factor of ~ 1.75 for the 20% gas case, and by only a factor of 1.5 for the 40% gas case, in contrast to the factor of 2 increase in the gas-free case (corresponding to a decrease in the final scale height of 25% and 50%, respectively).

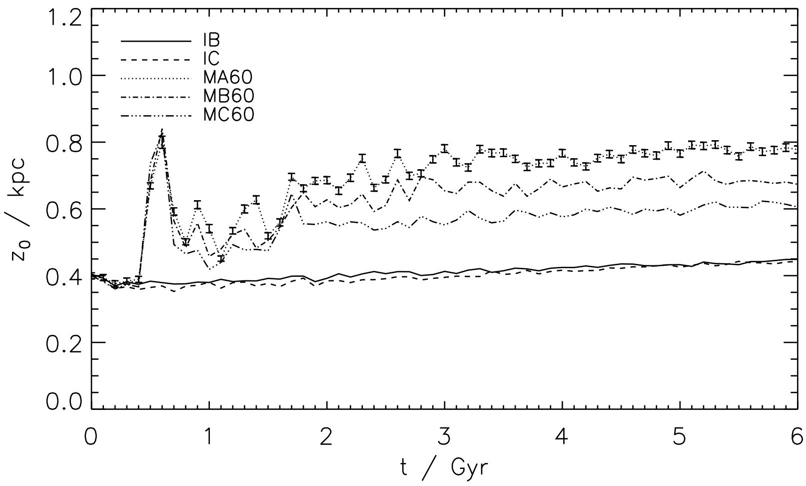

Figure 2: *Evolution of the disc scale height for simulations with gas. The solid and the dashed lines show the isolated case while the other lines illustrate mergers with different gas fractions (0%, 20% and 40% for MA60, MB60 and MC60, respectively).*

In order to gain insights into the physical process that is causing this change in behaviour, we examine the SFR as a function of time. The SFR quickly drops to low values (after 2.5 Gyr for a gas fraction of 40% and 1.5 Gyr for the gas fraction of 20%). This implies that most of the gas is consumed before the merger is complete. Thus, the galaxy is not able to reform a new thin stellar disc after the merger, which could pull heated stars towards the galactic plane again. This means that the dominant process preventing disc heating in the simulations above is the absorption of the kinetic impact energy of the satellite by the gas component.

Another way to demonstrate that the formation of a new disc does not reduce the disc thickening noticeably in our simulations is to compare the scale height of the stellar particles created in the initial conditions (old stars) to the scale height of the stellar particles that form during the simulation through SF (new stars). The new stars clearly form a thinner disc than the old stars, however, the combined sample has a scale height which is only slightly thinner than the old stellar disc.

Collaborators are Rachel S. Somerville, Peter H. Johansson and Thorsten Naab.

References

[1] Moster, B. P., Macciò, A. V., Somerville, R. S., Johansson, P. H., Naab, T., 2010, MNRAS 112

Searching for stellar halo streams in the solar neighborhood

Rainer Klement, Hans-Walter Rix, Coryn Bailer-Jones and Kester Smith

The hierarchical merging scenario predicts a richly structured phase-space distribution of dark matter and stars. Numerical simulations predict that most accreted satellites would spread their tidal debris on eccentric planar orbits into the Milky Way's disk component, so that we can expect to find such "fossil remnants" right in our immediate surroundings. Although no longer spatially coherent and possibly phase-mixed, such stellar streams keep their common origin imprinted into their chemical and dynamical properties and remain detectable in the space of integrals of motion.

We have started to develop new search techniques in phase- and [Fe/H]-space to derive "effective" integrals of motion that are most suitable for a comparison with the observables. These consist of combinations of a stars' Cartesian velocity components that can be shown to approximate the angular momentum, eccentricity and orbital inclination. Stars that move on simiilar orbits show up as clumps in the space spanned by these quantities.

A possible halo stream in the first RAVE data release

Our method has been applied to the first RAVE public data release [1] which contains radial velocity- and proper motion estimates. Having no spectroscopically derived stellar parameters available, we assumed all stars to be main sequence stars and applied a photometric parallax relation that we calibrated on Hipparcos stars to derive distances. Our sample consisted of 7015 stars selected to be within 500 pc of the Sun and to have distance errors better than 25%. We characterized the orbits of these stars through the aforementioned proxies for their angular momentum and eccentricity and compared the observed distribution to the expectations from a smooth distribution. On this basis, we have found a new stream candidate on a slowly rotating orbit ($V \approx -160$ km s^{-1}), suggesting a possible origin external to the Milky Way's disk.

Halo streams in SDSS

We confirmed the detection of this new stream in a sample of 22,321 nearby ($d \leq 2$ kpc), metal-poor ([Fe/H]≤ -0.5) main-sequence stars with six-dimensional estimates of position and space velocity from the seventh SDSS data release [2] (Fig. 1).

Again, we characterized the orbits of these stars through our kinematic proxies for their angular momenta, eccentricities and orbital inclinations and compared the observed distributions to expectations from a smooth distribution in four [Fe/H] bins. In addition to the stream we detected in the RAVE data, we identified at least four other significant "phase-space overdensities" of stars on very similar orbits in the solar neighborhood to which we can assign unambiguously peaked [Fe/H] distributions. Two of them have been identified previously, including the halo stream discovered by Helmi et al. (1999, Nature 402, 53) at a significance level of $\sigma = 12.0$. In addition, we find at least two new genuine halo streams, judged by their kinematics and [Fe/H], at $\sigma = 2.9$ and 4.8, respectively. For one stream the stars even show coherence in the configuration space, matching a spatial overdensity of stars found by Juric et al. (2008, ApJ 673, 864) at $(R, z) = (9.5, 0.8)$ kpc.

And RAVE again

Currently, we are investigating whether we can confirm the detection of the stream made in paper [1] in the recently published second RAVE public data release [3]. This catalog now contains

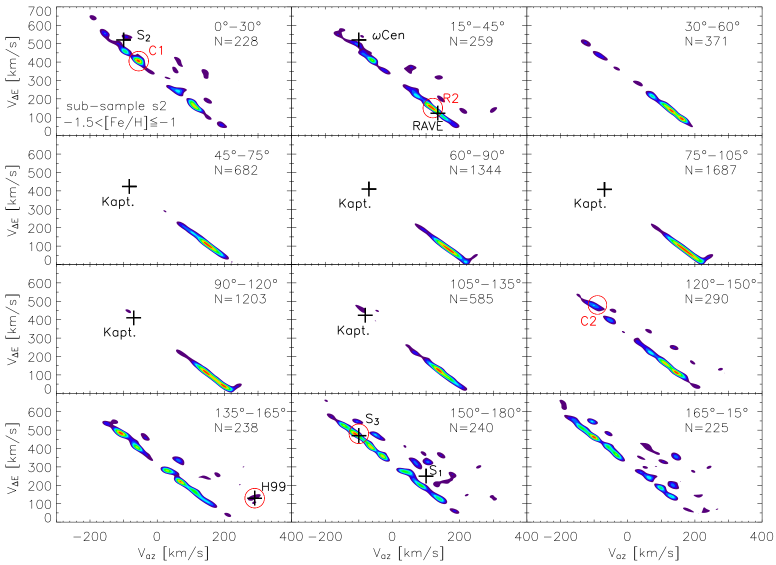

Figure 1: $(V_{az}, V_{\Delta E})$*-distribution of SDSS stars with metallicities* $-1.5 <$ *[Fe/H]* ≤ -1*, shown in bins of different inclination angles of the orbital plane with respect to the direction of the North Galactic Pole. The quantities* $(V_{az}, V_{\Delta E})$ *are given through the Cartesian velocity components; they are proxies of a star's angular momentum and orbital eccentricity. Stellar streams show up as clumps in these "effective" integrals of motion, and we have circled significant detections in red. To accentuate the overdensities, a wavelet transform has been applied to the data.*

spectroscopically derived astrophysical parameters for a subset of $\sim 20,000$ stars. Their $\log g$ estimates allows a classification into dwarfs and (sub-)giants by fitting multicomponent Gaussian mixture models to the observed $\log g$ distribution, thereby accounting for its dependence on color (spectral type) and on Galactic latitude b (in the RAVE magnitude range the density of giants drops rapidly at high latitudes). Our goal is then in a second step to use the photometry of these spectroscopically classified dwarfs and (sub-)giants to classify the stars that lack $\log g$ estimates by a supervised machine learning method (we chose a Support Vector Machine algorithm) into dwarfs and others. The aim is to minimize the fraction of true giants classified as dwarfs (the contamination) and redo the analysis from paper [1] on the pure dwarf sample, for which we can get reliable photometric distance estimates. First results indicate that we can confirm the existence of the stream at $V \approx -160$ km s^{-1} at at a comparable significance level as previously reported (99.7% confidence).

External collaborators are Burkhard Fuchs (ARI Heidelberg), Chris Flynn (Tuorla Obs., Finland), Tim C. Beers (Michigan State Uni., USA) and the SDSS collaboration.

References

[1] Klement, R., Fuchs, B., Rix, H.-W., 2008, ApJ, 685, 261

[2] Klement, R., Rix, H.-W., Flynn, C., Fuchs, B., Beers., T. C., et al. (10 more coathors), 2009, ApJ, 698, 865

[3] Klement, R., Bailer-Jones. C. A. L., Fuchs, B., Rix, H.-W., Smith, K., 2009, ApJ, *submitted, currently revised*

Constraining the Milky Way potential with a 6-D phase-space map of the GD-1 stellar stream

Sergey Koposov, Hans-Walter Rix

How to measure the potential of Milky Way?

Measuring the gravitational potential and therefore the distribution of the matter in the Galaxy is one of the most important tasks in Galactic astronomy. Mapping the 3D distribution of the matter in the Galaxy and especially in its outskirts is interesting because it may give us important clues on the Galaxy formation and the nature of Dark Matter.

There are different ways to measure the Galactic potential. Usually in order to measure the potential we need to see the movements of individual objects to directly measure their acceleration. Unfortunately the objects in the Milky Way (MW) halo are located at large distances, so it is almost impossible to see directly the objects moving and measure their acceleration in the potential. The other possible way to measure the potential is by measuring positions and velocities of objects lying on one particular orbit in the MW halo. And it turns out that there are actually ensembles of stars in the MW halo which lie approximately on the same orbits and therefore can be used to constrain the potential of the MW – these are the stars torn from disrupted objects such as Globular Clusters and dwarf galaxies orbiting around the Galaxy and forming large tidal tails.

In last several years, systematic surveys of the Milky Way halo done with Sloan Digital Sky Survey (SDSS) and Two Micron All Sky Survey (2MASS) have revealed a large number of such streams. One such stream discovered in the MW halo using SDSS dataset is especially suited for the measurements of the Galactic potential. The stream called GD-1, discovered in Grillmair&Dionatos (2006) seems to have been produced by a disrupted globular cluster and spans more than 60 degrees on the sky. We have undertaken a profound study of the stream trying to make a 6-dimensional phase-space map of the stream and use it to constrain the MW's potential[1].

Mapping and fitting of the tidal stream

In order to map the stream we have done:

- Precise measurement of the location of the stream on the sky.
- Measurement of the heliocentric distances to the stream stars using the color-magnitude diagram fit to the SDSS data.
- Measurement of the proper motions of stream stars by combining the SDSS data with the USNO-B1.0 dataset and carefully removing the background contamination from halo stars.
- Measurement of the radial velocities of the stream stars by doing spectroscopic follow-up of the highly probable stream members.

After mapping the stream in 6-D phase-space, we have undertaken the modeling of that dataset by a single orbit in the Galactic potential and tried to constrain two its important parameters: the circular velocity at the Sun's position (V_c) and the flattening of the potential (q_Φ). Four left panels of Fig. 1 show the observed 6-D map of the stream together with the the fit to these data in Galactic potentials with different (V_c, q_Φ). The right panel of the Figure shows the likelihood map and confidence regions for different values of (V_c, q_Φ) and shows the 1-D posterior probability distributions for these parameters.

As a result of the modeling of the dataset on the GD-1 stellar stream we have been able to measure with high accuracy the circular velocity at the solar radius $V_c = 224^{+12}_{-13}$ km/s and the flattening of the overall Galactic potential at $\sim 15\,kpc$ from the Galactic center $q_\Phi = 0.87^{+0.07}_{-0.04}$. The method, which we developed to map and analyze the stream in 6 dimensions should become very useful when the new astrometric surveys such as GAIA will provide us with a wealth of new information on the Galaxy.

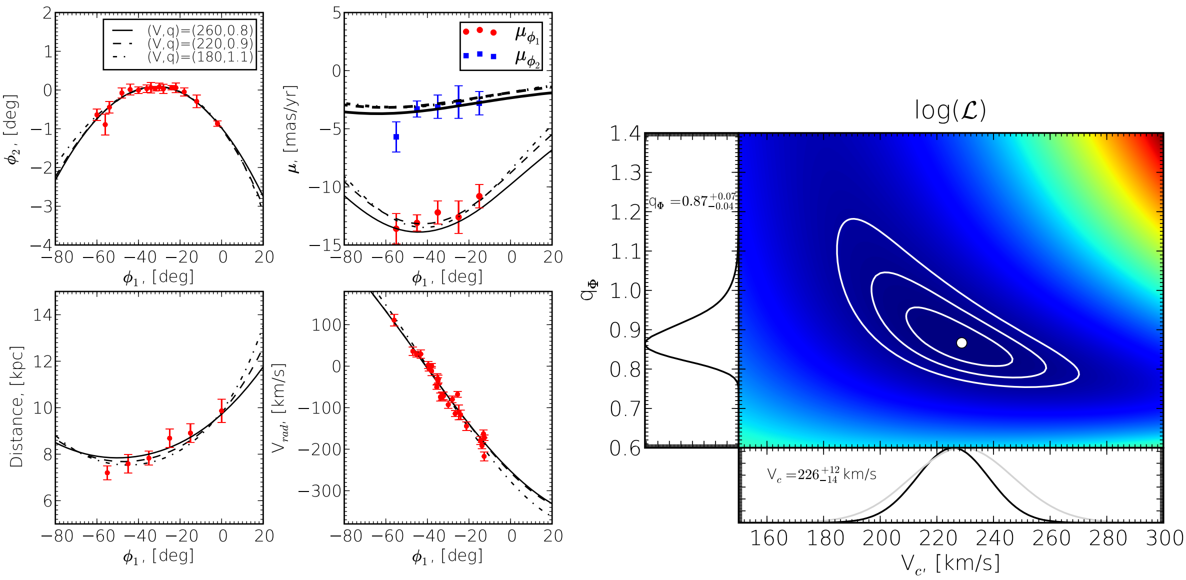

Figure 1: *Left: The data-model comparison for a set of best-fit orbits in different logarithmic potentials* $\Phi = V_c^2\,log(x^2 + y^2 + (z/q_\Phi)^2)$ *with three different* (V_c, q_Φ) *parameters values (180 km/s,1.1), (220 km/s,0.9), (260 km/s,0.8.) The colored data points with error bars show the observational data, while the black lines show the model predictions (different line styles show the orbit models in different potentials). The top left panel shows the positions on the sky, the top right panel shows the proper motions, the bottom left panel shows the distances, the bottom right panel shows the radial velocities. Right: The log-likelihood surface of the orbit fit for the family of flattened logarithmic potentials with different circular velocities* V_c *and flattenings* q_Φ*, with a prior on the* V_c *of 229±18 km/s from Ghez et al. (2008). The likelihood was also marginalized over the Gaussian prior on* $R_0 = 8.4 \pm 0.4$ *kpc. The contours show the* 1σ*,* 2σ *and* 3σ *confidence regions. The inset panels at the bottom and on the left show the 1D marginalized posterior probability distributions for* V_c*,* q_Φ *respectively. The gray line in the bottom panel shows the adopted prior distribution for the* V_c *from Ghez et al. (2008)*

In collaboration with David Hogg (New York University)

References

[1] Koposov S., Rix H.-W., Hogg D. W., 2010, ApJ in press, arxiv:0907.1085

The accretion origin of the Milky Way's stellar halo

Eric Bell, Knud Jahnke, Jelte de Jong, Sergey Koposov, Christine Ruhland, Xiangxiang Xue Hans-Walter Rix

The stellar halo of the Milky Way has low metallicity, alpha element enhancement, and a high degree of support from random motions. Such properties could plausibly indicate that the stellar halo was formed *in situ* in the early phases of the collapse of the Milky Way (Eggen, Lynden-Bell & Sandage 1962; ApJ, 136, 748), or alternatively that the stars were formed outside the Milky Way in satellite galaxies only to be accreted by the Milky Way at a later date (Searle & Zinn 1978; ApJ, 225, 357).

A key discriminant between these pictures is the structure of the stellar halo. *In situ* formation would predict relatively little substructure, as the formation epoch was many dynamical times ago. In contrast, current models of galaxy formation in a hierarchical context predict that the vast majority of stellar halo stars should be accreted from disrupted satellite galaxies, with the general expectation of a significant amount of recognisable halo substructure; furthermore, if such substructure was accreted dwarf galaxy debris, one expects different substructures to have different stellar populations.

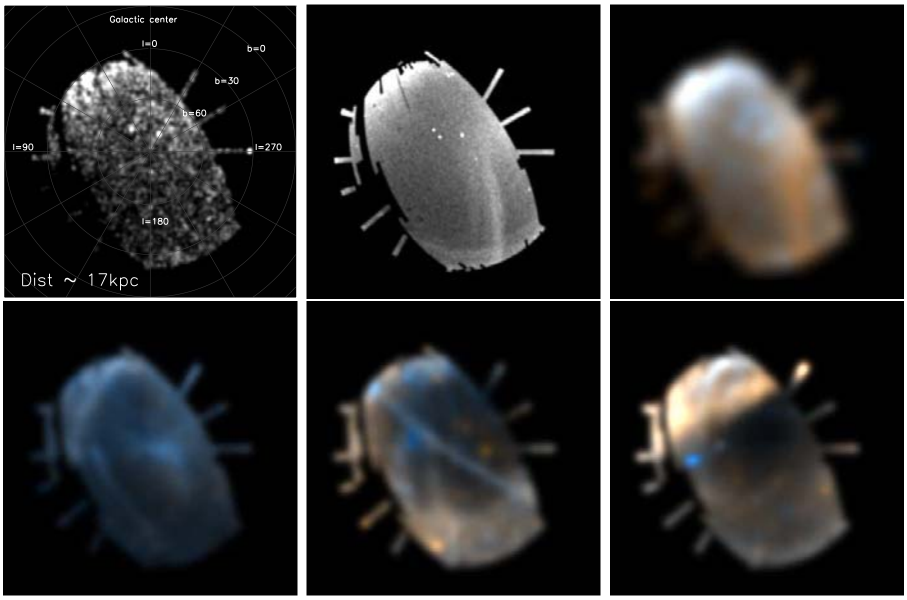

Figure 1: *TOP PANELS: Left: Map of the BHB stars in thick distance modulus slices, where the BHB distances have been 'degraded' to* $\sigma_M = 0.9$ *to match the distance resolution of MSTO stars. Middle: Map of MSTO stars in the same distance modulus slice, assuming a MSTO* $M_r = 4.5$. *Right: Color representation of the BHB/MSTO ratio, smoothed with a 6 degree Gaussian. BOTTOM PANELS: A color representation of the relationship between structure and metallicity in simulated stellar halos of Bullock et al. The three columns show stellar metallicity (where blue denotes* $[\mathrm{Fe/H}] = -1.5$ *and red denotes* $[\mathrm{Fe/H}] = -0.5$*) in halos with relatively low, average, and large amounts of substructure.*

The SDSS and our richly-structured stellar halo

We have used the 5th and 7th Data Releases of the Sloan Digital Sky Survey (SDSS) to probe the structure and stellar populations of the stellar halo of the Milky Way [1, and in a submitted paper]. We have photometrically-isolated both main sequence turn-off stars (MSTO stars; a generic feature of all stellar populations) and candidate blue horizontal branch stars (BHB stars; to first order a feature of old, metal-poor populations) using color and magnitude cuts using the SDSS *ugr* bands.

In the top panels of Fig. 1, we show the distribution of BHB and MSTO stars in a single distance slice in the stellar halo, and the ratio of MSTO to BHB stars in the color panel. One can clearly discern a great deal of substructure; furthermore, it is clear that different substructures have different populations.

Fig. 2 quantifies the degree of substructure using a robust metric — the RMS of the data around a smooth model fit on scales $\gtrsim 100\,\mathrm{pc}$, after accounting for the (known) contribution of Poisson uncertainties.

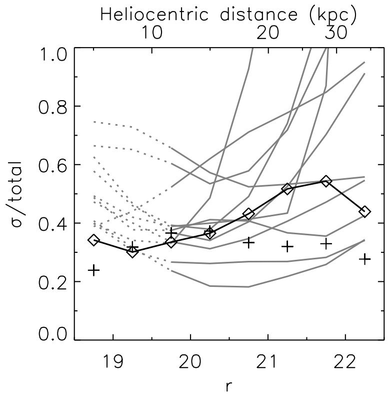

Figure 2: *The run of σ/total as a function of Heliocentric distance for the SDSS data (diamonds: all DR5; crosses: DR5 with the largest structures excised before the analysis) and eleven cosmological simulations of stellar halo formation (grey lines).*

Comparison of our results with models of stellar halo formation in a cosmological context

We compared the observations with simulations of galactic stellar halos formed entirely from the accretion of satellites (Bullock & Johnston 2005; ApJ, 635, 931) in a cosmological context by analysing the simulations in the same way as the SDSS data. While the masses, overall profiles, and degree of substructure in the simulated stellar halos show considerable scatter, the properties and degree of substructure in the Milky Way's halo match well the properties of a 'typical' stellar halo built exclusively out of the debris from disrupted satellite galaxies (see Figs. 1 and 2, where the models show both distinctive populations in different substructures, and a degree of substructure that quantitatively spans the range of values observed in our stellar halo). Our results therefore point towards a picture in which an important fraction of the stellar halo of the Milky Way has been accreted from satellite galaxies.

This work was done in collaboration with D. Zucker, N. Evans and V. Belokurov (Cambridge), S. Sharma and K. Johnston (Columbia), J. Bullock (UC Irvine), D. Hogg and A. Zolotov (NYU), T. Beers (Michigan State), E. Grebel (ARI), Ž. Ivezić (University of Washington), D. Schneider (Penn State), and M. Steinmetz (AIP)

References

[1] Bell, E. F., et al. 2008, ApJ, 680, 295

A comprehensive analysis of the structural properties of faint Milky Way satellites

Nicolas Martin, Jelte de Jong, Hans-Walter Rix

The wide systematic mapping of the Milky Way (MW) surroundings provided by the Sloan Digital Sky Survey (SDSS) has thoroughly changed the knowledge of the MW satellite system. The number of dwarf galaxies known to exist around our Galaxy has more than doubled from the discovery of numerous sparse overdensities of stars, that have since been shown to inhabit massive dark matter sub-halos (Martin et al. 2007, *MNRAS* 380, 281). These new discoveries have extended the realm of galaxies to objects ~ 100 times fainter than were known before. Unfortunately, they are comprised of less than a few hundred stars down to the SDSS limit, with sometimes as little as 30 stars in a single object. This strongly hampers any determination of their properties. As many group have used different assumptions to first characterize them, the comparison of their properties proves difficult. We have therefore embarked on a systematic modeling of the density profile of all the new dwarf galaxies, using a robust maximum likelihood algorithm to derive their centroids, sizes, ellipticities, angles on the sky and background contamination [1]. This constitutes the first effort to create a comprehensive and statistically sound data set of the structural properties of these systems, enabling a relevant comparison of their similarities and differences.

The first striking property of the new dwarf galaxies is that they show no strong separation with the previously know, 'classical' MW dwarf galaxies. In the size–luminosity plane shown in Figure 1, they simply smoothly extend to fainter magnitudes and smaller sizes (one has to recall, though, that faint and large systems are, by definition, more diffuse and more difficult to find, which could well explain the dearth of objects that are in the lower-right part of the figure). Moreover, we have shown that previous claims that some of the new galaxies could be undergoing tidal destruction as they appeared distorted is mainly an artifact of the small number of stars that one has to work with to map them. With only a few tens or hundreds of stars to probe it, the structure of a system will naturally seem irregular, but simply from the effect of 'shot-noise' (see Fig. 2).

Most of our derived parameters are in good agreement with previous determinations but we find that faint satellites are somewhat more elliptical than initially thought (see Fig. 1), and ascribe this effect to the previous use of smoothed maps, which can be dominated by the smoothing (round) kernel. As a result, the faintest half of the MW dwarf galaxies ($M_V > -7.5$) is significantly (4σ) flatter ($\langle\epsilon\rangle = 0.47\pm0.03$) than its brightest half ($M_V < -7.5$, $\langle\epsilon\rangle = 0.32\pm0.02$). We consider three scenarios that could explain the rather elongated shape of faint satellites: rotation supported systems, stars following the shape of more triaxial dark matter subhalos, or elongation due to tidal interaction with the MW. Although none of these is entirely satisfactory, the last one appears the least problematic, but obviously warrants much deeper observations to track evidence of such tidal interaction. We have initiated deep photometric follow-up programs on 8m-class telescopes to investigate this further.

References

[1] Martin N. F., de Jong J. T. A., Rix H.-W., 2008, ApJ 684, 1075

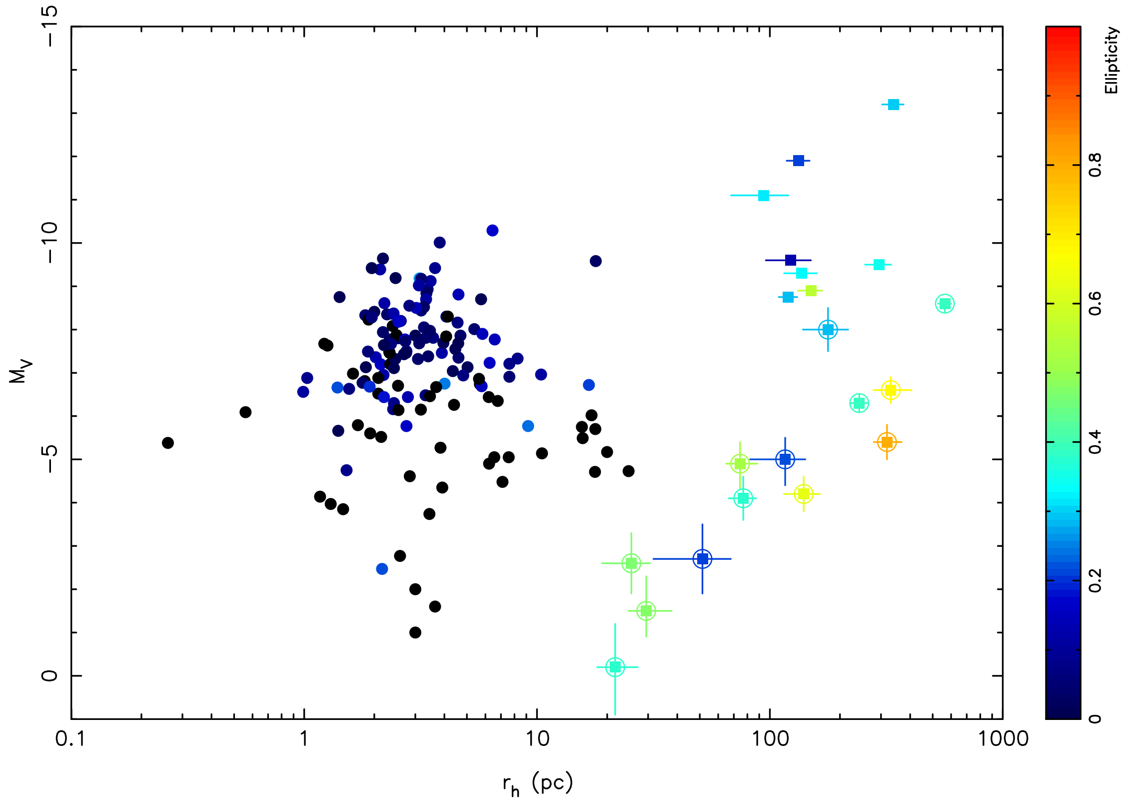

Figure 1: *Distribution of the MW satellites in the size-luminosity plane, color-coded by their ellipticity. The dark systems on the left are the compact globular clusters whilst dwarf galaxies are shown as square for the 'classical', previously known systems, and circled squares for the new ones. These extend to much fainter magnitudes as well as smaller sizes. The lack of objects in the bottom-right corresponds to systems that would be fainter than the SDSS surface brightness limit.*

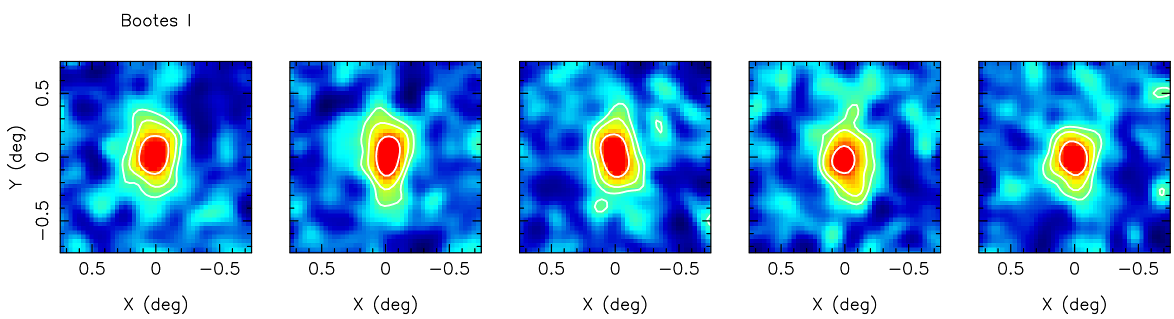

Figure 2: *Smoothed maps of Boötes I, one of the new dwarf galaxies, from the SDSS data (left) and four simulations of the same galaxy, constructed assuming the best parameters determined by the Maximum Likelihood fit. Although Boötes I has a distorted morphology, the purely spheroidal simulated models show as much distortion.*

Photometric identification of Blue Horizontal Branch stars

Kester Smith, Coryn Bailer-Jones, Rainer Klement

Blue Horizontal Branch (BHB) stars are interesting as tracers of halo structure because they are standard candles, with a narrow luminosity distribution, because they are intrinsically bright, and so can be used to probe a large volume, and because they occupy a reasonably well-defined area of narrow-band colour space, and so are easy to identify. Previous studies have often identified samples of BHB stars from colour cuts alone. These samples however show significant contamination both from main sequence stars and from blue stragglers. Some authors (Sirko et al., 2004, ApJ 127,899; Xue et al. 2008, ApJ 684, 1143) have used classification schemes based on spectra to weed out most of these contaminants. Such spectroscopic techniques provide a much purer sample than the simple colour cuts, but because spectra are required, the overall number of available sources is reduced, and also faint, distant sources are systematically lost.

We have investigated several methods to identify BHB stars from SDSS colours alone, using various machine learning techniques. The objective is to obtain a sample that is larger overall than that available from spectroscopy, and also contains more of the fainter sources, whilst mitigating the contamination that would be introduced if a simple colour cut were used.

We have used three standard methods and compared them to identify the most promising. They are: k Nearest Neighbours (kNN), Discriminant analysis by Kernel Density Estimation (KDE), and a Support Vector Machine for classification (SVM). kNN selects the class of a new instance by obtaining the k nearest neighbours in the colour space and using the relative fractions of these to determine the class of the new data. With KDE, we build an estimate of the probability density function for both the BHB stars and the contaminating stars and compare these functions to obtain the probability that a new source is of each class. The SVM uses the training data to determine a separating boundary between the two classes. All of these methods require a training set of known examples from which a model is learned. This model is then applied to unknown data for classification. Our training data were drawn from the sample of Xue et al., whose catalogue includes not only the BHB stars they identified but also the contaminants that were tested but rejected.

The methods can be compared with one another by classifying a test set of data of known type and then measuring the completeness and the contamination (the fraction of non-BHB stars in the output positives). Extensive testing revealed that the SVM and KDE methods were superior to the kNN method. Both these methods delivered samples of a purity of 10-20% up to magnitude $g = 18$ or so. However, the SVM achieved a greater level of completeness across all magnitudes. We therefore adopt the SVM as the method of choice.

We obtained a sample of SDSS DR7 photometry for sources lying in the appropriate colour region and used the SVM method to classify them. Out of a sample of nearly 290,000 sources, we identified just over 27,000 as possible BHB stars. About 11,000 of these are located in the North Galactic cap region, shown in Fig. 1.

As a sanity check, we derived the distances to a selection of globular clusters in the NGC region from their BHB populations. BHB stars were assumed to be associated with a globular cluster if they lay within half a tidal radius of the cluster centre. The mean distance of the BHB population is then compared to the accepted distance of the cluster (Fig. 2). The distance check gives generally good agreement with the catalogue distances, although several of the points lie above the line. This might be an indication that the assigned BHB population contains contaminant stars that are really cluster members, which being less luminous than the true BHB stars will then yield systematically greater distances. A paper based on this work has been submitted to A&A [1].

This work is done in collaboration with X.-X. Xue., National Astronomical Observatories, Beijing, China.

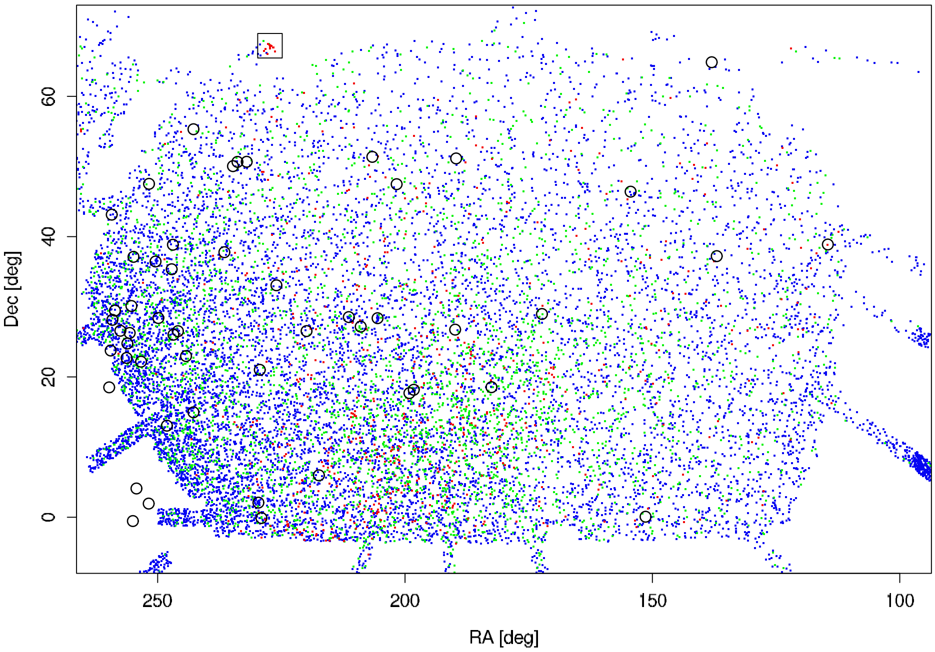

Figure 1: *The North Galactic Cap in BHB stars. Sources closer than 20kpc are coloured blue, sources between 20 and 50kpc are green and sources beyond 50kpc are red. The locations of the Ursa Minoris dwarf galaxy is marked with a box. The locations of a selection of globular clusters in this region are marked with small circles.*

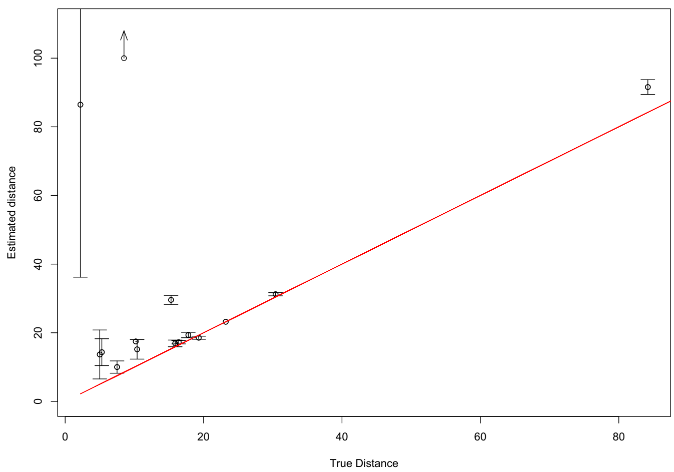

Figure 2: *The distances to a selection of globular clusters derived from BHB populations versus the accepted catalogue distance. Error bars are errors on the mean BHB distance.*

References

[1] Smith, K.W., Bailer-Jones, C.A.L., Klement, R., Xue, X.-X., 2010, submitted to A&A.

Stellar populations of the faintest galaxies

Jelte de Jong, Nicolas Martin, Hans-Walter Rix

The faintest galaxies known are the dwarf spheroidals (dSph), which can have luminosities as low as a few thousand Suns. During recent years over a dozen of previously unknown dSphs have been discovered around the Milky Way, drawing on data from the Sloan Digital Sky Survey (SDSS). These faintest galaxies are astrophysically important for a number of reasons: in the current paradigm of hierarchical galaxy formation they form the building blocks of all larger galaxies, they form the low luminosity limit to the galaxy formation process, they provide the lowest density environments in which star formation occurs, and they are the only regime in which cosmological theories are poorly constrained.

A uniform analysis of the faintest dwarf spheroidals

To study the stellar populations of the faint dSphs recently discovered in SDSS data, we adapted the color-magnitude diagram (CMD) fitting software package MATCH (Dolphin 2002, MNRAS, 332, 91) for application to SDSS data. These data are relatively shallow, but allow a uniform analysis. Only for a subset of these systems a complete star formation history could be recovered, because the CMDs of most are too sparsely populated. For this reason, new ways of using MATCH were developed, allowing us to constrain the overall properties, such as age, metallicity and distance even for very sparse objects. The so-called Single Component (SC) fitting technique compares the goodness-of-fit of simple stellar population templates. Figure 1 shows results of the SC-fitting technique for the two faint dSphs Boötes I and Ursa Major II. The results for twelve new Milky Way satellites were presented in [1] and showed that the majority are dominated by old (<10 Gyr) and metal-poor ([Fe/H]≤ -2) stellar populations. Some of them, however, show evidence for a more complex population make-up: Canes Venatici I, Ursa Major II and Leo T exhibit (from SDSS data alone) signs of multiple epochs of star formation and significant chemical enrichment. These results therefore showed that even at the extreme faint end of the luminosity function galaxies can retain gas and form stars for extended periods of time.

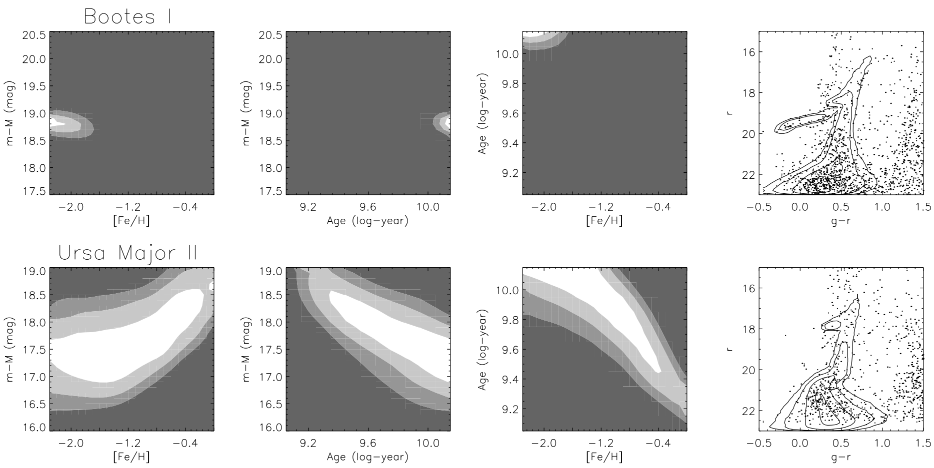

Figure 1: *Stellar population properties of the faint dwarf spheroidals Boötes I (top) and Ursa Major II (bottom), derived using the Single Component fitting technique [1]. From light to dark the grayscale contours show the regions within 1σ, 2σ and 3σ from the best-fit model, which is represented by the contours overplotted on the color-magnitude diagrams.*

Deep LBT photometry of the faintest star-forming galaxy

Perhaps the most remarkable of the dSph galaxies discovered based on SDSS data is Leo T. This isolated system is located at ∼400 kpc from the Milky Way and may be floating freely through the Local Group. Although it is faint ($M_V \sim -8$) it contains gas and already from the SDSS data there are signs of the presence of very young stars.

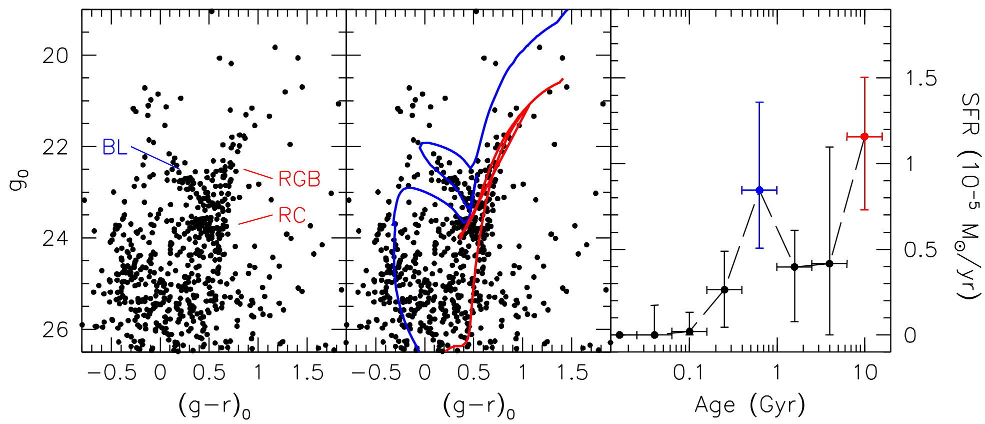

Figure 2: *Deep Large Binocular Telescope photometry of Leo T. Left: color-magnitude diagram (CMD) of the central 1.4′ of Leo T. The locations of the red giant branch (RGB) and red clump (RC), corresponding to an intermediate age to old population are labeled in red, and the blue loop (BL), indicative of young stars, is labeled in blue. Center: the same CMD as on the left, but now with isochrones overplotted for ages of 10 Gyr (red) and 600 Myr (blue), corresponding to the mean ages of the two main epochs of star formation in Leo T. Right: star formation history obtained with MATCH based on the CMDs in the left and central panels. Two distinct peaks of star forming activity are recovered, one old (∼6 to 12 Gyr ago, the red data point) and one very recent (∼400 to 800 Myr ago, the blue data point).*

Using the Wide Field Camera on the Large Binocular Telescope (LBT) we have obtained deep and wide photometry on Leo T in order to study its structure and stellar populations [2]. The CMD of Leo T, shown in Figure 2, clearly shows a red giant branch (RGB) with a red clump (RC) typical of an intermediate age to old population, together with a blue loop (BL) of very young (<1 Gyr) helium burning stars. Fitting the CMD with MATCH yields the star formation history (SFH) shown in the right panel of Figure 2. It confirms that Leo T has a complex star formation history, having formed stars early on in its life from ∼6 to 12 Gyr ago, with another burst of star forming activity occurring several hundred million years ago. Together with the fact that it still contains gas (Ryan-Weber et al. 2008, MNRAS, 384, 535) this unequivocally shows that, under the right circumstances, very faint dwarf galaxies are able to hold on to gas reservoirs and keep star formation going over a Hubble time.

References

[1] J. T. A. de Jong, H.-W. Rix, N. F. Martin, D. B. Zucker, A. E. Dolphin, et al. 2008, AJ, 135, 1361

[2] J. T. A. de Jong, J. Harris, M. G. Coleman, N. F. Martin, E. F. Bell, H.-W. Rix, et al. 2008, ApJ, 680, 1112

The stellar environs of the Milky Way and Andromeda galaxies

Nicolas Martin, Jelte de Jong, Hans-Walter Rix

The Pan-Andromeda Archaeological Survey

The Pan-Andromeda Archaeological Survey, or PAndAS, is a photometric survey that aims at mapping the stellar surroundings of the Andromeda and Triangulum galaxies (M31 and M33) with the 1 deg^2 wide-field camera MegaCam mounted on the 3.6 m Canada-France Hawaii telescope. Building on previous MegaCam surveys conducted by our group, PAndAS has been awarded 220 hours of observing time in the 2008–2011 time-frame. Less than a year after the beginning of the survey, the widest map of the surroundings of Andromeda has already been published (McConnachie *et al.*, 2009, *Nature* 461, 66). Presented in Figure 1, it reveals numerous stellar structures in the halo of M31, out to distances of more than 120 kpc. The survey has also unveiled the presence of metal-poor stars around M33, which are likely to have been stripped from M33's disk during a close passage next to Andromeda. Finally, five new M31 dwarf galaxies have been discovered in the survey [1].

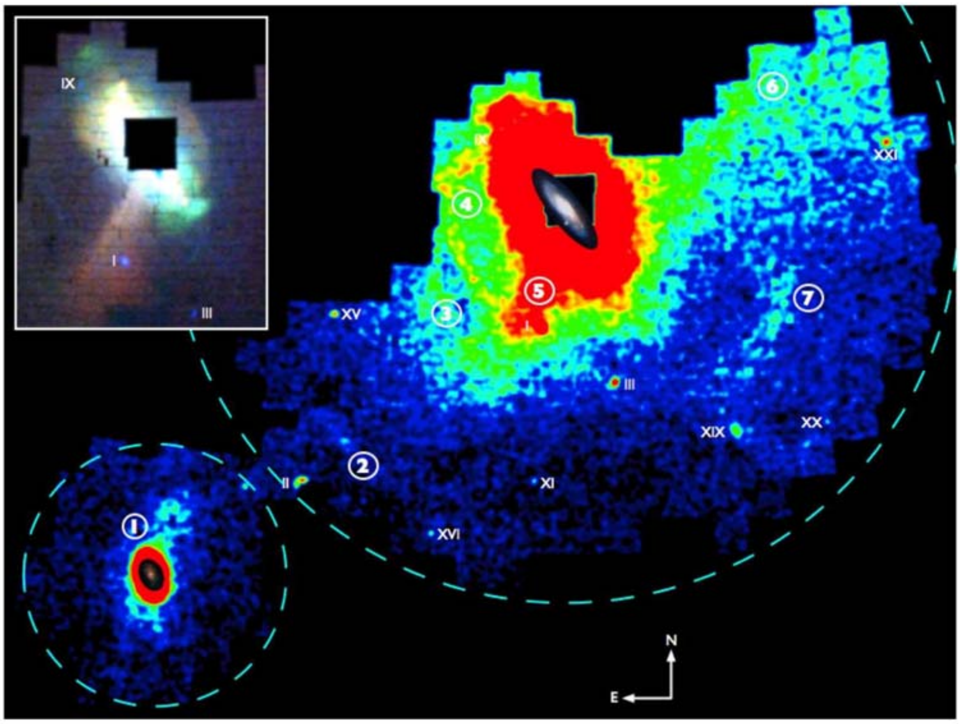

Figure 1: *The current extent of the PAndAS survey. Red-giant branch stars at the distance of M31 were selected to produce this map, where the color represent the stellar density. The dashed light blue circles correspond to the radial extent of the survey, out to distances of 150 kpc from M31 and 50 kpc from M33. Stellar structures and dwarf galaxies have been highlighted. The inset shows the central parts of the survey at higher resolution, and color-coded by metallicity. It reveals many structures of different metallicity and, hence, different origin.*

The outskirts of the Milky Way

The stellar halo and the outer disk of the Milky Way are known to contain a wealth of substructure, such as stellar streams, dwarf galaxies and stellar overdensities of a more obscure nature. Covering a quarter of the sky, the Sloan Digital Sky Survey (SDSS) allowed a sensitive study of a significant fraction of the Galactic halo, revealing many previously unknown structures. Now that the SDSS extension SEGUE (Sloan Extension for Galactic Understanding and Exploration) has added photometric data at low latitudes, a comprehensive analysis of Milky Way structure at both high and low latitudes using uniform SDSS photometry is possible for the first time. We have applied color-magnitude diagram fitting to the SEGUE photometry to build a sparse 3-D map of the stellar mass distribution of the Galaxy [2]. Fitting smooth, axisymmetric galaxy models to this map yields accurate measurements of the structural parameters of the thick disk and the stellar halo, and a first quantified in-situ detection of a metallicity gradient in the halo. Subtracting the best-fit model from the maps reveals a wealth of substructure, as illustrated by Figure 2.

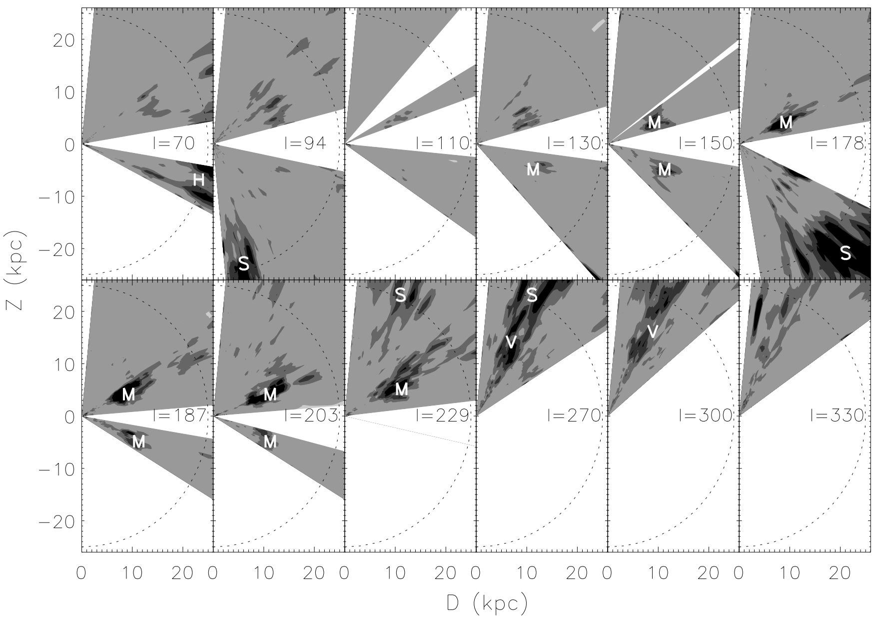

Figure 2: *Stellar overdensities in the outer Milky Way. For twelve constant Galactic longitude slices through the Galaxy, the grayscale shows overdensities over the best-fit smooth, axisymmetric model. Known overdensities are labeled: Sagittarius streams (S), Monoceros stream (M), Virgo overdensity (V), and Hercules-Aquila (H).*

The PAndAS survey is led by Alan McConnachie (HIA, Canada) and includes 29 collaborators from 6 different countries (Australia, Canada, France, Germany, UK, USA). Collaborators on the mapping of the outskirts of the Milky Way are Brian Yanny (Fermilabs, USA) and Andrew Dolphin (Raytheon, USA).

References

[1] Martin N. F., McConnachie A. W., Irwin M. J., Widrow L. M. *et al.*, ApJ 705, 758

[2] de Jong, J. T. A., Yanny, B., Rix, H.-W., Dolphin, A. E., Martin, N. F. & Beers, T. C., 2009, ApJ, subm., arXiv:0911.3900

Milky Way satellites properties in a ΛCDM Universe

Andrea V. Macciò, Xi Kang, Fabio Fontanot, Sergey Koposov

Milky Way as a cosmic laboratory

The Milky Way environment provides an excellent laboratory for astrophysics. It has been used extensively in the past decades to test theoretical models of galaxy formation. In particular, the number density of satellites around our Galaxy has long been considered one of the major problems for the otherwise quite successful ΛCDM paradigm. In recent years the Sloan Digital Sky Survey has changed our view of the Milky Way and its environment. The SDSS has made it possible to carry out a systematic survey for satellite galaxies, which are detectable through their resolved stellar populations down to extremely low surface brightness. As a result the number of known dwarf spheroidals has doubled in the recent past, ,moreover the homogeneous sky coverage of the SDSS enables a robust determination of the detection limits for faint satellites. Recently [1] provided the first determination of the volume corrected Milky Way satellite luminosity function down to these extremely faint limits,

In light of the discovery of the new ultra-faint dwarf population and the improvements in the numerical modelling of galaxy formation, it is now timely to revisit the issue of whether the basic properties of satellite galaxies around the Milky Way, such as their number density, radial distribution, and central mass, can be reproduced within current cosmological ΛCDM-based models. For this purpose we combine merger trees extracted from very high resolution N-body simulations with three different semi-analytic model (SAM) codes. These merger trees describe the hierarchical assembly of a Milky Way-like halo, while the SAMs are used to predict the relationship between the dark matter (sub)haloes and observable galaxy properties, allowing us to make a direct and detailed comparison with observational data.

From dark matter to visible satellites

We selected four candidate haloes with a mass similar to the mass of our Galaxy ($M \sim 10^{12} M_\odot$) from an existing low resolution dark matter simulation (300^3 particles within 90 Mpc) and re-simulated them at higher resolution. The standard high resolution runs are 12^3 times more resolved in mass than the initial simulation: the dark matter particle mass is $m_d = 4.16 \times 10^5 M_\odot$. For the purpose of constructing accurate merger trees for each simulated halo, we analyse 53 output times between $z = 20$ and $z = 0$. We make use of three different semi-analytic model (SAM) codes in order to predict the observable properties of galaxies that inhabit the dark matter haloes and sub-haloes identified in the N-body simulations. All the SAMs considered in this work parametrize in different ways the main physical processes acting on the baryonic component, such as atomic cooling, cosmic reionization, star formation, supernovae feedback, metal production and dust attenuation, an extensive discussion can be found in [2] All three semi-analytic models considered in this work are able to do a reasonably good job of reproducing the observational data. The results for one of the models (described in Kang et al. 2006, MNRAS 234, 1244) are shown in figure 1. All models quite successfully reproduce the observed LF for satellite galaxies over the entire luminosity range $-2 \geq M_V \geq -16$. We find that in our models, the Milky Way satellite luminosity function is shaped by a complex combination of different physical processes including tidal destruction, photo-ionization, and supernova feedback.

It has been pointed out that the Galactic satellites all have a common mass around $10^7 M_\odot$ within 300 pc ($M_{0.3}$), while they span almost four order of magnitudes in luminosity (Strigari et al. 2008, Nature 454, 1096). It is argued that this may reflect a specific scale for galaxy formation or a scale for dark matter clustering. We show that this common mass scale can be explained within the Cold Dark Matter scenario when the physics of galaxy formation is taken

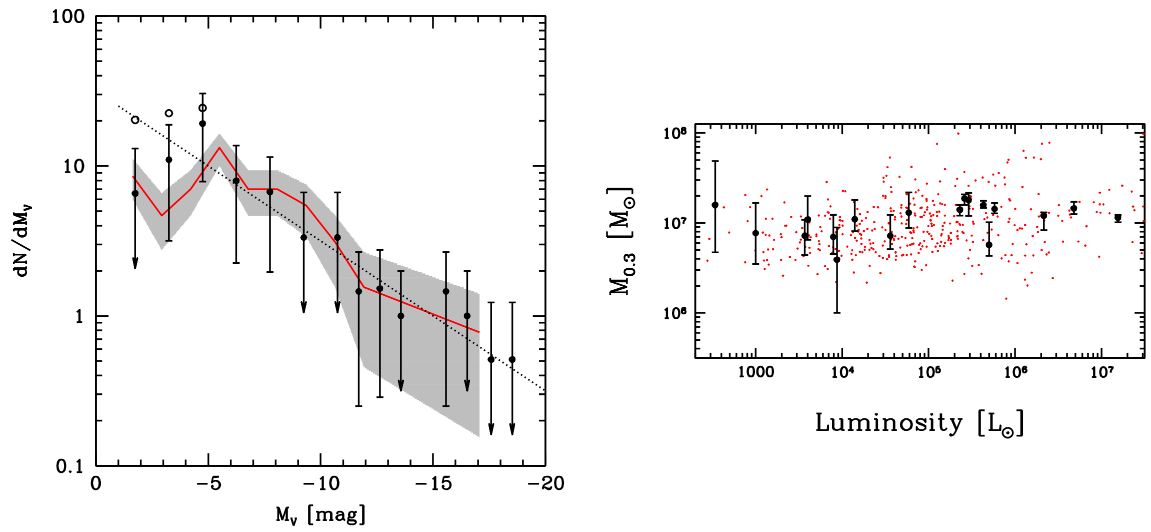

Figure 1: *Left: The Milky Way satellite luminosity function as predicted by one the SAM (Kang et al. 2006, MNRAS 234, 1244) used in our work. The median of the satellite distribution is shown by the solid line, while the shaded area represents the* 1σ *Poisson scatter around the mean. Observational data are taken from [1]. Right: Mass within 300 pc versus luminosity. Red dots show results from our numerical model, black points with error bars are the observational results from Strigari et al 2008.*

into account, as shown in the right panel of figure 1. The narrow range of $M_{0.3}$ comes from the narrow distribution of circular velocities at time of accretion (peaking around 20 km/s) for satellites able to form stars and the not tight correlation between halo concentration and circular velocity [3]. The wide range of satellite luminosities is due to a combination of the mass at time of accretion and the broad distribution of accretion redshifts for a given mass.

- We show that the luminosity function of MW satellites is in agreement with CDM predictions.
- We show that the constant relation between the central mass of MW satellites and their luminosity can be explained within the LCDM model

Collaborators are Rachel Somerville (STSci), Pierluigi Monaco (Univ. Trieste) and Ben Moore (Univ. Zurich). Numerical simulations were performed on the PIA cluster of the Max-Planck-Institut für Astronomie at the Rechenzentrum in Garching.

References

[1] Koposov, S., et al. 2008, ApJ, 686, 279

[2] Macciò, A. V. et al. 2009, MNARS in press

[3] Macciò, A. V., Kang X., Moore B., 2009, ApJL, 692L, 109

8 Surveying Galaxy Evolution

Image on previous page:
This image of the supercluster Abell 901/902 is a combination of a visible-light frame taken with the MPG/ESO 2.2-meter telescope in La Silla, Chile, and a dark matter map (magenta) derived from observations with the Hubble Space Telescope which have been analyzed for weak gravitational lensing (STAGES-Survey).
Credits: NASA, ESA, C. Heymans (University of British Columbia, Vancouver), M. Gray (University of Nottingham, U.K.), M. Barden (Innsbruck), the STAGES collaboration, ESO, C. Wolf (Oxford University, U.K.), K. Meisenheimer (Max-Planck Institute for Astronomy, Heidelberg), COMBO-17 collaboration.

On the size and comoving mass density evolution of early-type galaxies

Arjen van der Wel, Anna Gallazzi, Hans-Walter Rix

Small, yet massive galaxies in the early universe

Early-type galaxies have old stellar populations and are currently not forming new stars. Therefore, they are said to be passively evolving. Their appearance is smooth and symmetric, adding to the impression that these galaxies, which host a good fraction of all the stars, are very old and have remained unchanged for much of the history of the universe.

This image began to erode when it was discovered that their number in fact changes substantially with cosmic time. There is strong evidence that new early-type galaxies have been forming up until relatively recently (see Figure 1, bottom right), and there is no reason to suppose that this process is not continuing today. It was then widely admitted that the population changes, but also widely maintained that early-type galaxies, once formed, do not change thereafter.

However, in the mean time, evidence was steadily accumulating that early-type galaxies had very different structures in the past. In particular, distant, high-redshift early-type galaxies (that is, early-type galaxies in the distant past) are found to be much smaller than equally massive early-type galaxies today (Figure 1, top right). In other words, even after its appearance as an early-type, a galaxy appears to change over time. Not much is left of the old picture in which early-type galaxies all formed early on, and do not change thereafter.

Both the issue of the continued formation of new early-type galaxies, and the issue of their subsequent structural evolution, are at the moment heavily debated in the literature. The paper described here [1] seeks to connect the two phenomena, and attempts to identify the physical mechanism that is responsible for the growth of the early-type galaxy population.

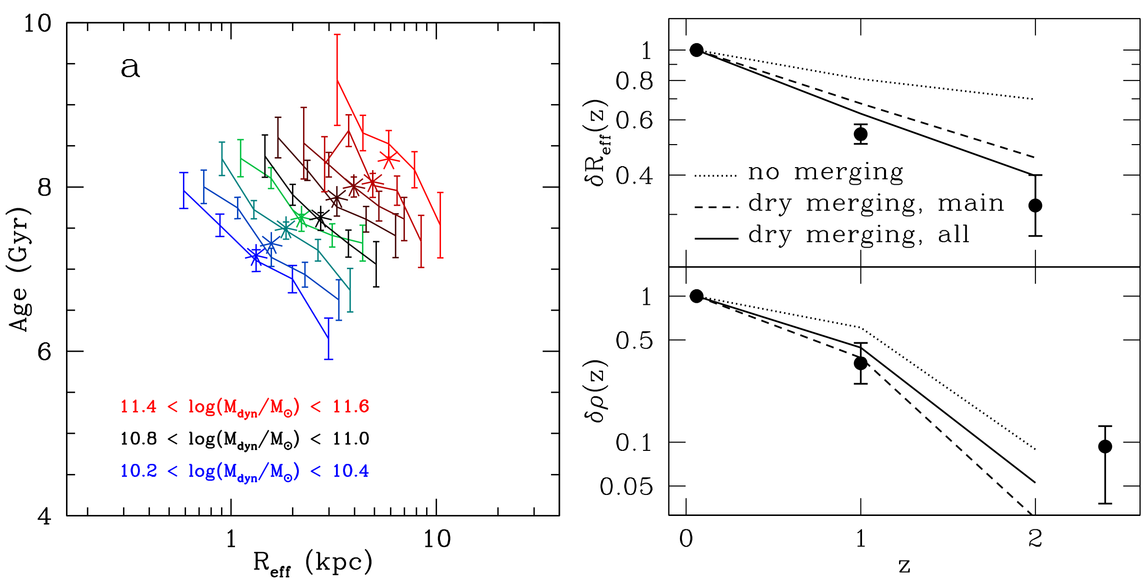

Figure 1: *Left: The relation between size (x-axis) and age (y-axis) of early-type galaxies with a given mass (the color coding indicates galaxy mass). Right: Size evolution (top) and number evolution (bottom) of early-type galaxies with cosmic time (redshift). The symbols represent observations; the lines represent our model, with different assumptions about merging activity.*

A possible explanation

The first issue that we investigate is whether changes in the sizes of individual galaxies are in fact required to explain the observations. If galaxies that form early are smaller than equally massive galaxies that form late, the average size of galaxies with that mass increases with time (decreases with redshift), even without any individual galaxy changing in size.

We test this idea by gathering data on a large number of early-type galaxies from the Sloan Digital Sky Survey, which MPIA has been heavily involved in over the past decade. We find that our hypothesis is correct: small galaxies are older than large galaxies that have the same mass (Figure 1, left). The implication is that at earlier times the average size of early-type galaxies must have been smaller, simply because the larger ones, which are young today, did not yet exist (at least, not as early-type galaxies). Here we see how the two phenomena described above, number evolution and size evolution, are intimately connected.

The next step is to test whether the observed number and size evolution match the amount of evolution implied by the idea that, at a given mass, large galaxies form later. To this end we simulate high-redshift samples of galaxies by excluding those galaxies with young ages in our observed, present-day sample. The implied change in the number of early-type galaxies over cosmic time matches the observed evolution well (Figure 1, bottom right). The implied size evolution, on the other hand, does not match the observations quantitatively, but the observed and predicted trends are, as expected, in the same direction (Figure 1, top right). A good way to describe this discrepancy is that there are too few small galaxies in the present-day universe to match the observed number of small galaxies in the high-redshift universe.

This disagreement leads us to turn to the idea that most researchers invoke to explain the observed size evolution: merging, which can 'puff up' a galaxy. Obviously, merging also cause galaxies to grow in mass. The main concern with the merging picture is that the number of mergers required to explain the strong, observed size evolution is so large that many very massive galaxies are expected to exist today, perhaps more than observed. We are the first to test this quantitatively.

Based on numerical simulations of the growth of cosmological structures (dark matter halos) and several simple assumptions regarding the properties of galaxies in those halos, we predict the number of mergers that each galaxy experiences, and the mass ratio of the progenitors of each merger product. We use this simulation in combination with the already applied technique to exclude young, present-day galaxies from the simulated high-redshift samples, in order to predict how large and how numerous early-type galaxies were in past.

It turns out that the evolution of the number of early-type galaxies is not greatly affected by adding merging to our model: the evolution in the number of early-type galaxies over cosmic time still matches the observed evolution. However, the model prediction for the size evolution changes substantially, and now provides a good fit to the observations.

We conclude that the observed size evolution of early-type galaxies can be explained partially by the continuous emergence of new early-type galaxies, which are larger than pre-existing early-type galaxies with the same mass, and partially by merging among early-type galaxies, which increases their sizes.
Other collaborators, both with MPIA affiliation on the paper described here, are Eric F. Bell (University of Michigan) and Frank C. van den Bosch (University of Utah)

References

[1] van der Wel, A., Eric F. Bell, Frank C. van den Bosch, Anna Gallazzi, and Hans-Walter Rix, ApJ, 698, 1232

Major merging: the way to make a massive, passive galaxy

Arjen van der Wel, Hans-Walter Rix, Aday R. Robaina

What the shapes of early-type galaxies tell us

Early-type galaxies have old stellar populations and are currently not forming new stars. The explanation of their formation is heavily debated, up until the present. Once thought to be simple systems that formed shortly after the Big Bang, with little subsequent changes, the formation and evolution of early-type galaxies is now understood to be complex and ongoing. Here we summarize a paper [1] which uses a very simple approach to constrain the formation mechanism of the very most massive early-type galaxies in the universe, each hosting close to 10^{12} stars.

We measured the axis ratios (the projected shapes on the sky) of thousands of early-type galaxies in the Sloan Digital Sky Survey, which MPIA has been heavily involved in over the past decade. We then examined the axis ratio distribution as a function of galaxy mass (Figure 1).

This exercise reveals that early-type galaxies with a mass, in stars, below $\sim 10^{11} M_\odot$ (for comparison, the Galaxy has a stellar mass of $\sim 5 \times 10^{10} M_\odot$) have a large range in axis ratio. This implies that many of these galaxies have flattened, disk-like stellar components that contribute significantly to the total stellar mass.

The most interesting discovery, visualized in Figure 1, is the absence of elongated early-type galaxies with masses higher than $\sim 10^{11} M_\odot$. Apparently, such massive early-type galaxies do not have disk-like components and are intrinsically round (or, rather, elliptical). The quite abrupt transition in galaxy shape at $\sim 10^{11}$ tells us something about the different evolutionary paths of low- and high-mass galaxies.

Star formation and disk formation are associated. Especially, it is difficult, if not impossible, to create many stars without having a substantial fraction of those ending up in a disk. Since early-type galaxies with mass $< 10^{11} M_\odot$ tend to have disks it is reasonable to suppose that such galaxies are the remnants of gas-rich, star-forming galaxies that, somehow, had their gas removed in order to stop star formation to produce an early-type galaxy.

This picture does not work for early-type galaxies with higher masses: those do not have disks. The process that results in the formation of such a galaxy destroys the disk that once must have existed, as the result of previous star formation. We know of only one way to destroy disks: merging. Our conclusion is straightforward: mergers are necessary in order for early-type galaxies to grow beyond a threshold mass of $\sim 10^{11} M_\odot$.

Hence, galaxies are not allowed to grow much beyond this mass through star formation, because this would produce a disk. A corollary is that the progenitors that lead, after merging, to the formation of a massive early-type galaxy do not contain much gas, as this would lead to the formation of a substantial disk. In addition, cosmological simulations tell us that galaxies grow in mass mostly through mergers between rather equal progenitors, with a typical mass ratio 1:2 to 1:4.

These considerations lead us to conclude that major merging among early-type galaxies are likely responsible for the formation of the most massive early-type galaxies.

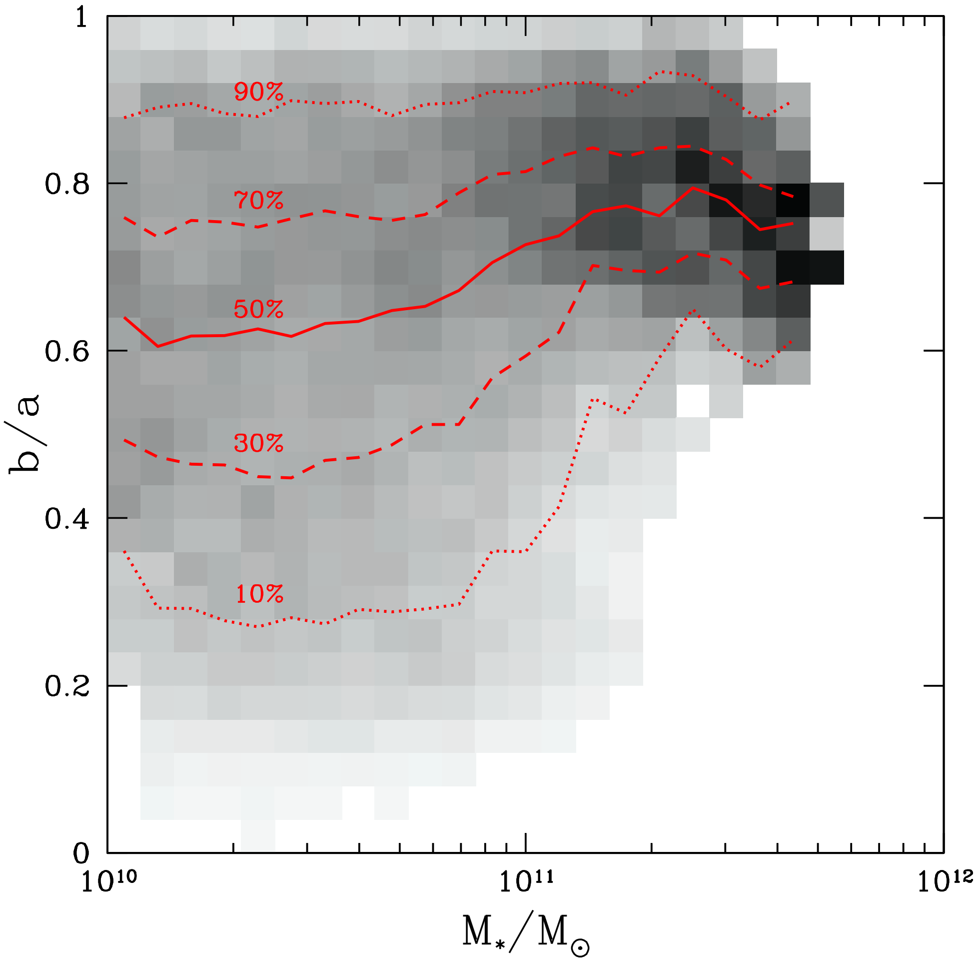

Figure 1: Axis ratio distribution of ∼16,000 galaxies as a function of galaxy mass in stars. Perfectly round galaxies $b/a = 1$; infinitely thin galaxies have $b/a = 0$. The gray scale represents, normalized to the total number of galaxies in narrow bins of stellar mass, the fraction of galaxies with axis ratio b/a. The upper boundaries below which, as a function of mass, 10%, 30%, 50%, 70%, and 90% of galaxies are located, are delineated by the red lines. The lack of elongated galaxies at high galaxy is conspicuous, and forms that backbone of the analysis that we briefly describe in this paper.

Other collaborators are Bradford F. Holden (University of California, Santa Cruz) and Eric F. Bell (University of Michigan, with MPIA as his affiliation on the paper described here.)

References

[1] Arjen van der Wel, Hans-Walter Rix, Bradford P. Holden, Eric F. Bell, Aday R. Robaina, 2009, ApJL, 706, 120

Obscured star formation in intermediate-density environments: a *Spitzer* study of the Abell 901/902 supercluster

Anna Gallazzi, Eric F. Bell, Klaus Meisenheimer, Knud Jahnke, Aday R. Robaina

The IR view of the environmental dependence of star formation

The environment in which galaxies live plays an important role in shaping their star formation activity. Several processes can act on galaxies as they interact with their surrounding environment, with the net effect of a suppression of star formation. However, gas compression or density fluctuations induced by many of these mechanisms can lead to a temporary dust-enshrouded burst of star formation. As a consequence, in environments where such mechanisms are more efficient, star formation can be to a large extent obscured. Star formation indicators unaffected by dust attenuation, such as the infrared (IR) luminosity, are thus needed to get an unbiased view of star formation. In this work [1] we want to quantify the incidence of dust-obscured star formation 'hidden' among red-sequence galaxies, and its dependence on environment. To this purpose we analyze the Abell 901/902 supercluster at $z = 0.165$ in conjunction with a field sample at $z < 0.3$. We complement the UV/optical photometry from the COMBO-17 survey with deep *Spitzer* 24μm data and *HST* imaging from the GEMS and STAGES surveys.

The fraction of red star-forming galaxies

The best indicator of star formation rate (SFR) combines the total IR and UV luminosities, providing a complete census of the luminosity emitted by (obscured and unobscured) young stars. The near-UV/optical COMBO-17 data and the *Spitzer* 24μm data provide us with such an SFR indicator. We define as star-forming (SF) those galaxies whose specific SFR is above a limit of $SFR/M_* = 10^{-10.7} yr^{-1}$ (corresponding to an SFR of $0.2 M_\odot/yr$ at the mass limit of our sample of $10^{10} M_\odot$). We then divide SF galaxies into 'blue' and 'red' according to a magnitude-dependent color cut.

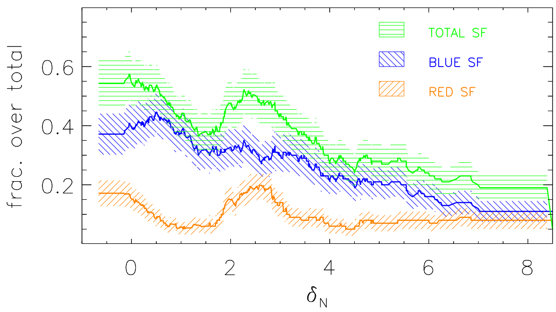

Figure 1: *Fraction of star forming galaxies as a function of galaxy number overdensity.*

Figure 1 shows the fraction of SF galaxies as a function of environment for the combined cluster+field sample. The environment is characterized by the galaxy number overdensity δ_N in a radius of 0.25 Mpc. The overall population of SF galaxies (green) becomes less abundant in higher-density environments. This trend is primarily driven by the decrease in the fraction of *unobscured* SF galaxies (blue). On the contrary, the fraction of red SF galaxies displays an enhancement at intermediate densities ($2 \leq \delta_N \leq 3$) typical of the A901/902 cluster outskirts. At these densities, red SF galaxies constitute 40% of all SF galaxies and contribute about 30% of the total SFR density.

Are red star-forming galaxies old or dusty?

What is the nature of red SF galaxies? Their red colors may indicate either low levels of star formation insufficient to alter the color of the underlying old stellar populations or highly obscured star formation activity. To disentangle the two situations and their relative importance we analyse the specific SFR, dust attenuation and morphology of red SF galaxies in comparison to normal blue SF galaxies. Figure 2 shows the distribution in specific SFR (left panels) and IR-to-UV luminosity ratio (right panels) for red SF (orange), blue SF (blue hatched) and quiescent galaxies (black) in three bins of δ_N. Red SF galaxies are not starbursting and have lower specific SFR than unobscured SF galaxies, regardless of environment. Their dust attenuation, as expressed by L_{IR}/L_{UV} is on average higher than that of blue SF galaxies. The distribution in L_{IR}/L_{UV} suggests the presence of two distinct populations among red SF galaxies:

- About half of red SF galaxies have low dust attenuation, low specific SFR and more bulge-dominated morphologies. They are thus dominated by old stellar populations with low levels of residual SF. Their properties and fraction do not vary with galaxy density: no environmental action in addition to internal feedback processes is required.
- More than 40% of red SF galaxies have high dust attenuations, high specific SFRs and show later-type morphologies with signs of nuclear activity. They are clearly more abundant at intermediate densities. This indicates that they are experiencing the environmental influence through, e.g., tidal interactions, particularly efficient at intermediate densities, which funnel gas toward the center inducing an episode of obscured star formation.

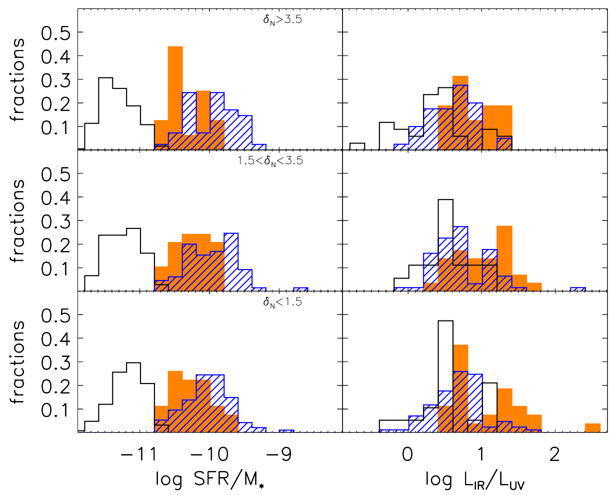

Figure 2: *Distribution in specific SFR (left) and IR-to-UV luminosity ratio (an indicator of dust attenuation; right) for quiescent (black histograms), blue SF (blue hatched histograms) and red SF galaxies (orange histograms) in three bins of increasing galaxy overdensity.*

Collaborators are the STAGES team members, including Christian Wolf (Oxford University), Marco Barden (Innsbruck University), Catherine Heymans (Edinburgh IfA), Boris Haeussler (Nottingham University) all previously at MPIA.

References

[1] Gallazzi A., et al., 2009, ApJ, 690, 1883

Are fossil groups a challenge of the cold dark matter paradigm?

Stefano Zibetti

Fossil groups in a hierarchical Universe

Early numerical simulations suggested that the most compact galaxy groups could merge to form a single elliptical galaxy (hence a 'fossil group') in a few billion years. An elliptical galaxy formed by the merger of such a group retains its X-ray emitting halo of hot gas, which is unaffected by merging. Following this indication, Ponman *et al.*(1994, Nature 369, 462) discovered the archetype fossil group RX J1340.6+4018. It has been suggested that fossil groups constitute a considerable population of objects. Their X-ray extent, bolometric X-ray luminosity ($L_{\rm X,bol} > 10^{42}$ erg s^{-1}), dark matter dominated total mass, and mass in the diffuse hot gas component are comparable to those of bright groups and poor clusters of galaxies ($\sim 10^{13}$–10^{14} M$_\odot$). The brightest member of a fossil group has an optical luminosity comparable to that of a cluster cD galaxy (i.e., $M_{\rm R} < -22.5$) and dominates the galaxy luminosity function of the group such that there is an R-band magnitude gap $\Delta m_{12} > 2$ between the brightest and second brightest members within half virial radius. Fossil groups have become a puzzling problem to cosmology since D'Onghia & Lake (2004, ApJ, 612, 628) showed that the fossil group RX J1340.6+4018 lacks galaxies ('substructures') nearly as luminous as the Milky Way, with respect to the state-of-the-art numerical simulations that accurately describe the frequency of substructures in massive galaxy clusters. In this respect, fossil groups appeared to exacerbate the so-called 'small-scale crisis' of CDM universes.

Real fossil groups: luminosity and substructure functions

To help solving this puzzle, we [1] study six groups and clusters of galaxies suggested in the literature to be 'fossil' systems, each having good quality X-ray data and SDSS spectroscopic or photometric coverage out to the virial radius. After establishing the fossil nature of all but one

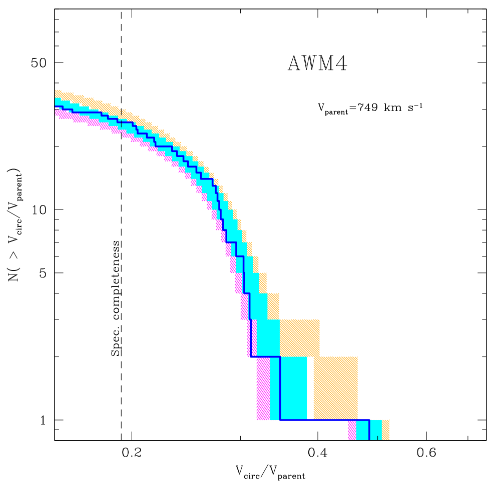

Figure 1: *The cumulative substructure distribution function (CSDF) of AWM4. The blue line is our fiducial estimate, while shades area in different colours show the effects of measurement errors (width of the shaded area) and of systematic uncertainties in scaling relations (different colours identify different assumptions).*

(RX J1552.2+2013) systems, we study their luminosity functions within 0.5 and 1 virial radius and find them to be consistent, within the uncertainties, with the universal luminosity function of clusters. For the five *bona fide* fossil systems, having a mass range $2 \times 10^{13} - 3 \times 10^{14}$ $M_{\odot}$, we compute accurate cumulative substructure distribution functions (CSDFs), that is the number of substructures (i.e. galaxies) up to a given circular velocity normalized by the group/cluster's circular velocity. To do this we need to carefully compute the virial mass of the system from X-ray observations and the circular velocity for each galaxy within the virial radius (also given by X-ray data) by means of optical scaling relations. The CSDF of the newly classified 'fossil' AWM4 is shown in Fig. 1 as illustration.

Fossil vs normal groups and simulations

We compare the CSDFs of our five fossil groups with those of observed and simulated groups/clusters available in the literature. In Fig. 2 we show the CSDFs of the fossils as grey shaded areas (including the confidence interval allowed by uncertainties) and we overlay the CSDFs of 34 real clusters in the SDSS (left panel) and CDM simulated clusters (right panel) as hatched areas. This demonstrates that the CSDFs of fossil systems are consistent with those of normal

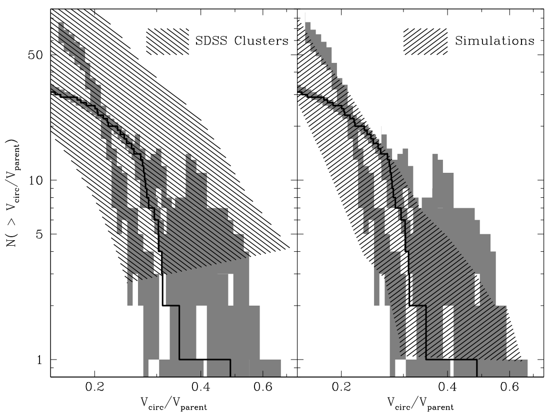

Figure 2: *The CSDFs of our five fossil groups are confronted with those of ordinary real clusters (left) and simulated CDM clusters (right) from Desai et al.(2004, MNRAS, 351, 265). The grey shaded areas are the sum of the confidence intervals of the fossil systems, while hatched areas are used for the comparison samples. The black solid lines highlight the newly established fossil AWM4.*

observed clusters and do not lack any substructure with respect to simulated galaxy systems in the cosmological ΛCDM framework. In particular, this holds for the archetype fossil group RX J1340.6+4018 as well, contrary to earlier claims.

Collaborators are Daniele Pierini and Gabriel W. Pratt (MPE-Garching).

References

[1] Zibetti, S., Pierini, D., Pratt, G. W., 2009, MNRAS, 392, 525

Properties of Dark Matter haloes as a function of the cosmological model

Andrea V. Macciò, Frank van den Bosch

Dark matter haloes properties

In the paradigm of hierarchical structure formation, dark matter (DM) haloes provide the potential well in which galaxies subsequently form. As a consequence the structural parameters of disk galaxies (size and rotation velocity) are tightly coupled with those of their hosting DM halo, such as concentration and spin [1]. In this work we investigate the effects of changes in the cosmological parameters between the WMAP 1st, 3rd, and 5th year results (WMAP1, WMAP3, WMAP5) on the structure of dark matter haloes. We use a set of simulations that cover five decades in halo mass ranging from the scales of dwarf galaxies ($V_c \approx 30$ km/s) to clusters of galaxies ($V_c \approx 1000$ km/s). For each halo in our sample we determine a set of parameters, including the virial mass and radius, the concentration parameter, the angular momentum, the spin parameter and various axis ratios (shape); moreover we payed attention in removing from our sample unrelaxed haloes. Figs. 1 shows the $c_{\rm vir}$-$M_{\rm vir}$ relation for the WMAP1, WMAP3 and WMAP5 cosmologies, and for both the ALL and RELAXED samples, as indicated. For all three cosmologies the c-M relation is well fit by a single power-law (red solid line).

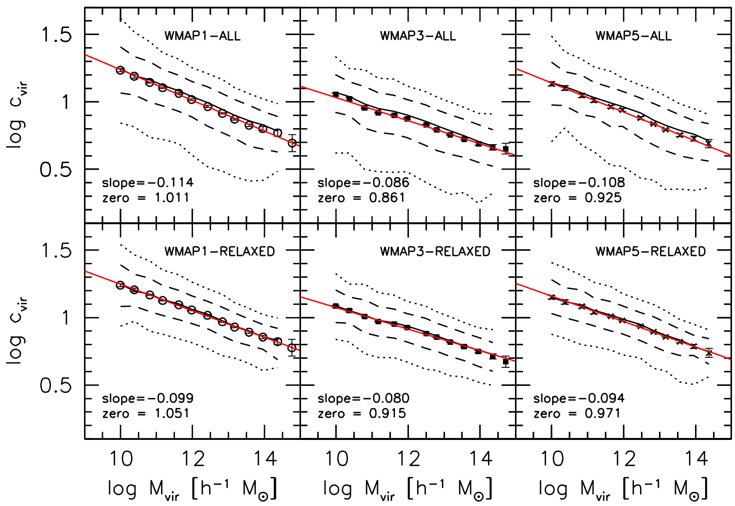

Figure 1: $c_{\rm vir}$ *vs* $M_{\rm vir}$ *for WMAP1 (left), WMAP3 (center) and WMAP5 (right). The upper panels show all haloes with more than 500 particles, while the lower panels show the "relaxed" haloes. The points show the mean concentration in bins of width 0.4 dex in mass, the error bar shows the Poisson error on the mean.*

Comparison with observations

An observationally robust measurement of the central density is given by the dimensionless parameter $\Delta_{V/2}$, defined as the average density of the halo, with respect to the critical density, inside the radius $R_{V/2}$, where the halo circular velocity drops to half its maximum value (see [2] for more details). Fig. 2 shows the relation between $\Delta_{V/2}$ and $V_{\rm max}$ for both observations (symbols) and theory (lines). The observations are for dwarf and LSB galaxies, color coded

according to the reference. These values are calculated based on the pseudo-isothermal halo fits to the observed rotation curves. We have removed a few galaxies with obviously very bad fits, or for which $V_{\rm max}$ was poorly constrained by the data. We have verified that including these galaxies makes no significant difference to the median observed $\Delta_{V/2}$. The $\Delta_{V/2} - V_{\rm max}$ relations for WMAP1, WMAP3 and WMAP5 cosmologies are shown as the short dashed, long-dashed and solid lines, respectively. Note that the data are broadly consistent with all these cosmologies; within the errors, the data seem to prefer a cosmology with $\sigma_8 \simeq 0.8$ and $n \simeq 0.96$.
We conclude therefore, that modulo the caveats of halo contraction and systematic effects (which to first order tend to cancel each other), the central densities of dwarf and LSB galaxies are in good agreement with predictions for a ΛCDM cosmology with parameters favored by the WMAP mission.

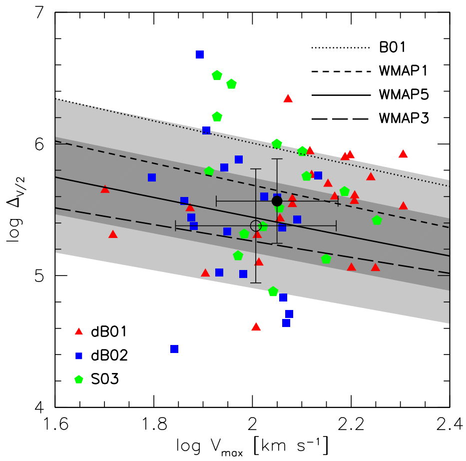

Figure 2: *Comparison between the* $\Delta_{V/2} - V_{\rm max}$ *relation from observations of dwarf and LSB galaxy rotation curves (solid symbols) and the predictions of N-body simulations in a variety of LCDM cosmologies. The shaded region shows the 68.3% and 95.4% range of* $\Delta_{V/2}$ *from our WMAP5 simulations.*

- We provide new, numerical based, relations between dark matter haloes parameters
- We find no clear tension between observational results and numerical predictions

A collaborator to this project is Aaron Dutton (UCO/Lick Observatory), numerical simulations were performed on the PIA cluster of the Max-Planck-Institut für Astronomie at the Rechenzentrum in Garching.

References

[1] Macciò, A. V., Dutton A. A., van den Bosch F. C., Moore B., Potter D., Stadel J., 2007, MNRAS, 378, 55

[2] Macciò, A. V., Dutton A. A., van den Bosch F. C., 2008, MNRAS, 391, 1940

How cold is Dark Matter? Constraints from Milky Way Satellites

Andrea V. Macciò, Fabio Fontanot

Dark matter properties at small scales

The inflationary cold dark matter scenario gives a clear prediction for the initial fluctuation spectrum responsible for the formation of the Large Scale Structure in the Universe, with a considerable power down to very small scales. This prediction can be tested against the smallest galaxies we can observe: the satellites of the Milky Way. In this work we test the luminosity function of Milky Way satellites as a constrain for the nature of Dark Matter particles. We expand the results presented in [1], trying to use a combination of observational data and theoretical predictions to infer significant constraints on the allowed mass of any warm dark matter particle. We perform dissipationless high-resolution N-body simulations of the evolution of Galaxy-sized halo in the standard Cold Dark Matter (CDM) model and in four Warm Dark Matter (WDM) scenarios, with a different choice for the WDM particle mass (m_w). We then combine the results of the numerical simulations with semi-analytic models for galaxy formation, to infer the properties of the satellite population.

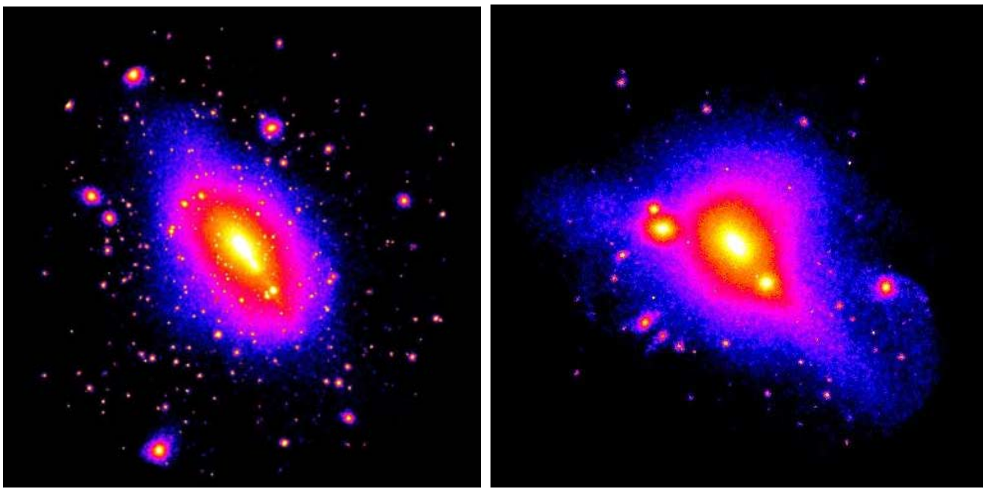

Figure 1: *Dark matter density map within a sphere of radius $R = 360$ kpc. LCDM and LWDM results ($m_w = 1$ keV) are shown in the left and right panel respectively.*

Method and comparison with observations

In this paper we combine merger trees extracted from very high resolution N-body simulations, describing the hierarchical assembly of a MW-like halo, with semi analytic model techniques, to predict the relationship between the dark matter (sub)haloes and observable galaxy properties, allowing us to make a direct and detailed comparison with observational data from SDSS [2]. In particular, for this work we select one specific halo (namely the G1 halo in [1]) and we resimulate it for a suite of WDM models with particle masses $m_w = 10, 5, 2, 1$ keV. To generate initial conditions for WDM, we define a rescaled version of the CDM power spectrum using a fitting function that approximates the transfer function associated to the free streaming effect of WDM particles [3]. In order to predict the expected luminosities of satellite galaxies, we combine the results of the N-body simulations with a state-of-the-art semi analytic model [4], that takes into account the complex physics of gas cooling, star formation and gas reheating. Our main results on the MW satellite luminosity function are presented in the left panel of figure 2. In each sub-panel, we compare the original results for the G1 halo in the LCDM cosmology (shown as a solid line) with the predictions corresponding to the different LWDM cosmologies (dotted lines). Quite surprisingly we find that even WDM models with relatively low m_w values (2-5 keV) are able to reproduce the observed abundance of ultra faint ($M_v < -9$) dwarf galaxies, as well as the observed relation between Luminosity and mass within 300 pc (right panel of figure 2). Our results suggest a lower limit of 1 keV for thermal warm dark matter, in broad agreement with previous results from other astrophysical observations like Lyman-α forest and gravitational lensing.

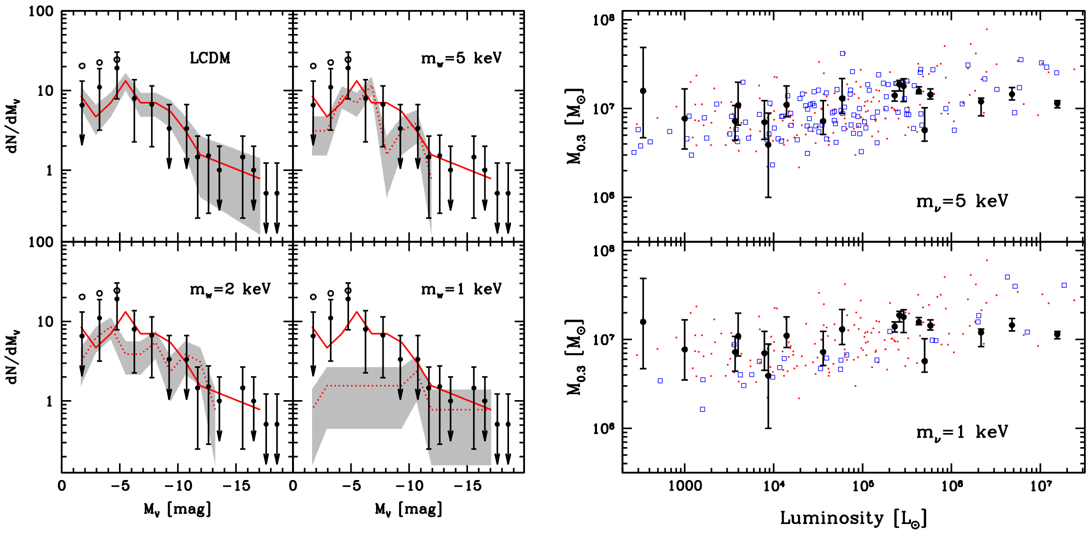

Figure 2: *Left: Milky Way satellites luminosity function in LCDM and LWDM models. In each panel solid line refers to the prediction for LCDM cosmology, while dotted lines refer to the predictions for LWDM realizations. The shaded area represents the* 1σ *Poisson scatter around the mean. Observational data are taken from [2]. Right: Mass within 300 pc versus luminosity. Red dots show results from LCDM numerical simulations. The squares show results for WDM satellites for a* $m_\nu = 5$ *and* 1 *keV in the upper and lower panel respectively. Black points with error bars are the observational results from Strigari et. al (2008, Nature, 454, 1096).*

This paper is mainly a ground test on the feasibility of our approach. New data coming from the most recent multiwavelength surveys like the Panoramic Survey Telescope and Rapid Response System (Pan-STARRS) will provide a better determination of the MW satellite properties and then an optimal data-set to increase our knowledge about the nature of dark matter.
Numerical simulations were performed on the PIA cluster of the Max-Planck-Institut für Astronomie at the Rechenzentrum in Garching.

References

[1] Macciò, A. V. et al. 2009, MNARS in press

[2] Koposov, S., et al. 2008, ApJ, 686, 279

[3] Miranda, M., Macciò, A. V. 2007, MNRAS, 382, 1225

[4] Macciò, A.V. Fontanot, F., MNRAS Letter in press

The many manifestations of downsizing: hierarchical models confront observations.

Fabio Fontanot

Introduction

The current standard paradigm for structure formation predicts that the collapse of dark matter (DM) halos proceeds in a "bottom-up" fashion, with smaller structures forming first and later merging into larger systems. It has been widely claimed that several lines of observational evidence suggest that galaxy evolution follows a different, apparently "anti-hierarchical", trend, for which the term "downsizing" has been coined. In [1] we aimed at determining to what degree these observational trends are in serious conflict with predictions from theoretical models based on ΛCDM cosmology. Among the different definitions found in the literature we consider in detail the evolution with redshift of stellar mass (i.e. more massive galaxies assemble earlier than low-mass counterparts), of the star formation rate (i.e. the mass of typical star-forming galaxies declines with decreasing redshift) and the "archaeological downsizing" (i.e. more massive galaxies host the older stellar populations).

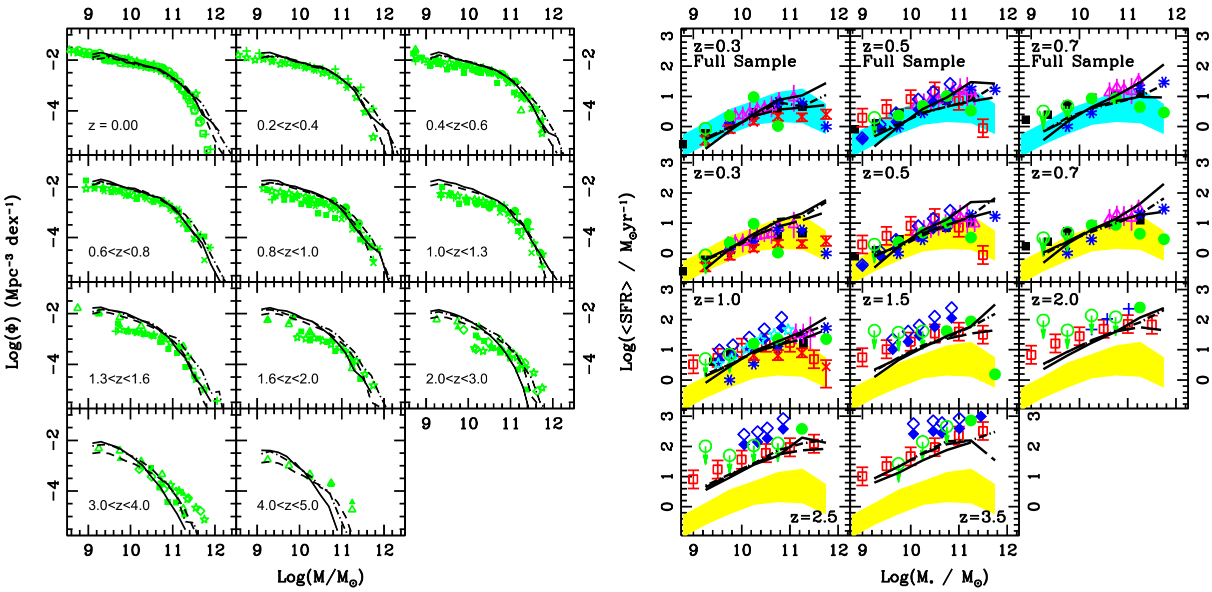

Figure 1: *Right Panels: Galaxy stellar mass function as a function of redshift Left Panels Average SFR of galaxies in bins of stellar mass and redshift. The shaded area represents the confidence region for the lowest redshift bin. Top row: all model galaxies are included in the average; second through fourth rows: Only active (SSFR $> 10^{-11}$ yr^{-1}) model galaxies have been included in the average. The results for active and all galaxies are nearly indistinguishable for the high redshift ($z \geq 1$) bins. In both panels solid, dashed and dot-dashed lines refer to the* MORGANA, *WDL08 and S08 models respectively: model predictions have been convolved with the appropriate error distributions. Data correspond to observational measurements collected in [1].*

In this work we compare the available observational constraints with the predictions of three semi-analytical models of galaxy formation within the LCDM framework, developed independently by different groups: MORGANA [2], WDL08 [3], S08 [4], which include different implementations of the main physical processes acting on the baryonic component. In order to take into account the effect of observational error in the reconstruction of physical properties (such as stellar mass, star formation rates and the mean ages of the stellar populations) we convolved model predictions with a Gaussian error distribution on $\log M_\star$ with standard deviation of 0.25 dex and with a Gaussian error distribution on $\log SFR$ with standard deviation of 0.3 dex.

Results & Conclusions

Despite significant differences in the recipes adopted in the three models to describe the physical processes acting on the baryonic component, the predictions are remarkably consistent both for the evolution of the stellar mass and for the star formation rate as a function of stellar mass (fig. 1). We find that, when observational errors on stellar mass and SFR are taken into account, the previously claimed discrepancies on massive galaxies (stellar mass $> 10^{11} M_\odot$) weaken or disappear. This implies that models acceptably reproduce the evolution of massive galaxies over the entire redshift range that we consider ($0 < z < 4$). On the contrary, the statistical properties of lower mass galaxies (in the stellar mass range $10^9 - 10^{11}$ $M_\odot$) are not correctly recovered. By considering the redshift evolution of the stellar mass function we notice that their number density is nearly constant since $z \sim 2$: we then conclude that these objects formed too early in the models (left panel). At the same time their star formation rates are too low compared with observational data (right panel). These too informations indicate an excess of low-mass passive galaxies. Finally, we show that models predict stellar mass-weighted ages for the stellar populations in low-mass galaxies that are too old with respect to the corresponding results of high-resolution spectroscopy.

We also use models to check the physical properties and environment of the objects responsible for this excess. We thus demonstrate that these discrepancies are mainly connected to the excessively efficient formation of central galaxies in high-redshift halos with circular velocities $\sim 100 - 200$ km/s. We conclude that some physical process operating on these mass scales — most probably star formation and/or supernova feedback — is not yet properly treated in these models.

This work has been done in collaboration with Gabriella De Lucia (INAF-OATs, Italy), Pierluigi Monaco (DAUT, Italy), Rachel Somerville (StSci, USA, former staff member at MPIA) and Paola Santini (INAF-OAR, Italy).

References

[1] Fontanot F., De Lucia G., Monaco P., Somerville R. S., Santini P., 2009b, MNRAS, 397, 1776

[2] Monaco P., Fontanot F., Taffoni G., 2007, MNRAS, 375, 1189

[3] Wang J., De Lucia G., Kitzbichler M. G., White S. D. M., 2008, MNRAS, 384, 1301

[4] Somerville R. S., Hopkins P. F., Cox T. J., Robertson B. E., Hernquist L., 2008, MNRAS, 391, 481

The Importance of Satellite Quenching for the Build-Up of the Galaxy Red Sequence

Frank C. van den Bosch, Daniel Aquino, Anna Pasquali, Xi Kang

The Build-Up of the Red Sequence

In the current paradigm of galaxy formation, it is believed that virtually all galaxies initially form as late-type, disk galaxies. During the subsequent hierarchical evolution, these late-type galaxies are then transformed into early-types via a variety of mechanisms that cause morphological transformations and/or star formation quenching. This has strong support from high-redshift observations, which have shown that the total stellar mass density on the red sequence has roughly doubled over the last 6-8 Gyr (e.g., Bell et al. 2004, ApJ, 608, 752). What is still largely unknown, however, is what the dominant mechanisms are that cause the late- to early-type transition, and in what kind of environments they operate.

In addition to major mergers, which are known to transform disk galaxies into early-type spheroids, a number of different transformation and quenching mechanisms have been proposed that are special in that they only operate on satellite galaxies. These are stripping of a galaxy's hot, diffuse gas ('strangulation'), ram-pressure stripping of the galaxy's cold gas reservoir, and impulsive heating due to high-speed encounters ('galaxy harassment'). Researchers at MPIA have used a large galaxy group catalogue constructed from the Sloan Digital Sky Survey (SDSS) in order (i) to study the impact of these satellite-specific transformation mechanisms, (ii) to determine which process dominates, (iii) to determine the fraction of galaxies that undergo a transition from the blue sequence to the red sequence as satellites, and (iv) to investigate in what kind of environment these transitions take place.

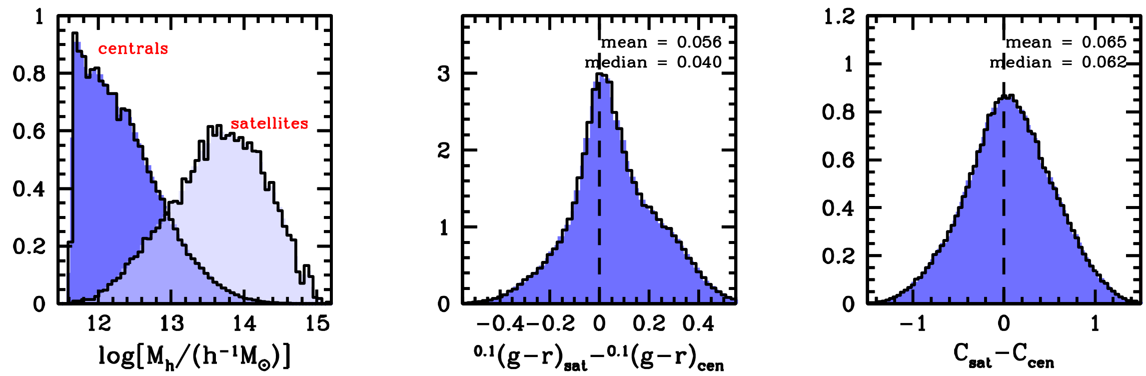

Figure 1: *The left-hand panel shows the halo mass distributions of central and satellite galaxies that are matched in stellar mass. As expected, satellites reside in more massive haloes than central galaxies of the same stellar mass. The middle and right-hand panels show the corresponding distributions of the color and concentration differences between centrals and their matched satellites. The mean and medians of both distributions are indicated. On average, satellites are both redder and more concentrated than centrals of the same stellar mass, but only marginally so.*

The Importance of Satellite Quenching

The MPIA researchers have compared the colors and concentrations of satellites galaxies to those of central galaxies of the same stellar mass, adopting the hypothesis that the latter are the progenitors of the former. They find that, on average, satellite galaxies are redder and more concentrated than central galaxies of the same stellar mass (see Fig. 1), indicating that satellite specific transformation processes do indeed operate. Central-satellite pairs that are matched in both stellar mass and color, however, show no average concentration difference (see Fig. 2), indicating that the transformation mechanisms operating on satellites affect color more than morphology. The color and concentration differences of matched central-satellite pairs are also found to be completely independent of the mass of the host halo of the satellite galaxy (see Fig 2), indicating that satellite specific transformation mechanisms are equally efficient in host haloes of all masses. Based on these results the MPIA researchers argue that strangulation is the main transformation mechanism for satellite galaxies.

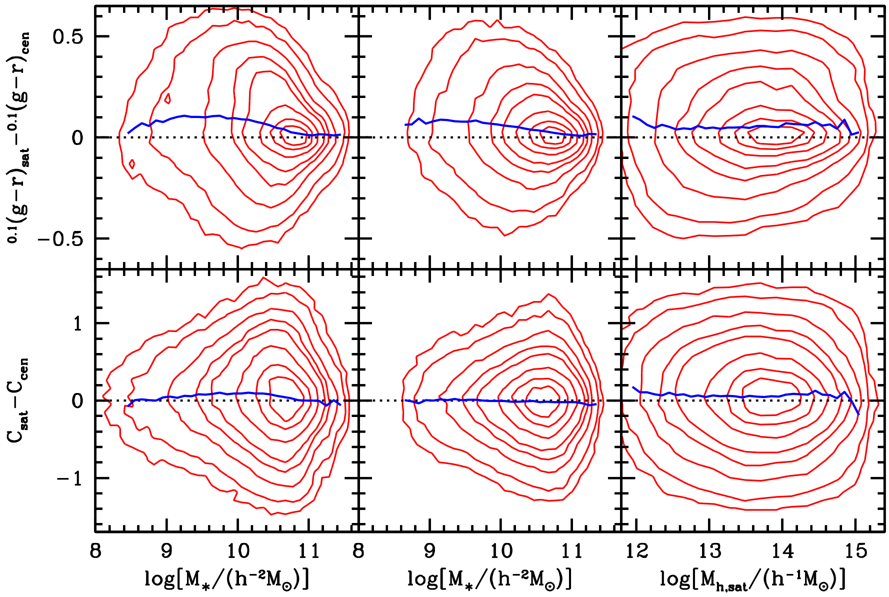

Figure 2: *Contour plots of color-difference (upper panels) and concentration-difference (lower panels) as functions of stellar mass, M_*, and satellite halo mass, $M_{\rm h,sat}$, for central-satellite pairs. In the left- and right-hand panels centrals and satellites have been matched in stellar mass only. In the middle panels they have also been matched in both stellar mass and concentration (upper-middle panel) or in stellar mass and color (lower-middle panel). Blue solid lines indicate the running averages.*

The MPIA researchers also determined the *relative* importance of satellite quenching for the build-up of the red sequence. They find that roughly 70 percent of red sequence satellite galaxies with $M_* \sim 10^9 h^{-2} M_\odot$ had their star formation quenched as satellites. This drops rapidly with increasing stellar mass, reaching virtually zero at $M_* \sim 10^{11} h^{-2} M_\odot$. Therefore, a large fraction of red satellite galaxies were already quenched before they became a satellite.

Collaborators are Xiaohu Yang (SAO, China), Houjun Mo (UMass, USA), Daniel McIntosh (UMKC, USA) and Simone Weinmann (MPA, Germany).

References

[1] van den Bosch, F.C., Aquino, D., Yang, X., Mo H.J., Pasquali, A., McIntosh, D.H., Weinmann, S.M., Kang, X., 2008, MNRAS, 387, 79

The 20 cm VLA COSMOS survey: Deriving a dust-unbiased cosmic star formation history

Vernesa Smolčić (now CalTech), Eva Schinnerer, Knud Jahnke, Eric F. Bell (now UMich)

A new method to separate star forming galaxies from those containing an active galactic nucleus

The use of radio observations for the study of the cosmic evolution of galaxies has the major advantage of bypassing dust-extinction biases. Radio emission from extragalactic sources at 1.4 GHz (20cm) is dominated by the radiation from active-galactic nuclei (AGN) and star-forming (SF) galaxies, hence a reliable SF/AGN identification is the main prerequisite for such studies. Combining the VLA-COSMOS 20 cm survey [1] with the rich COSMOS data-set (X-ray to radio) we have developed a robust method to separate SF from AGN galaxies in the faint radio population. Our method is based on a rest-frame optical color classification [2] that mimics the standard spectroscopic classification tools (Baldwin, Phillips & Terlevich 1981; BPT). The classification method was well-calibrated using a large local sample of galaxies ($\sim 7,000$ SDSS "main" spectroscopic galaxy sample, NVSS and IRAS surveys) representative of the VLA-COSMOS population. We have shown that the method agrees well with other independent classification schemes based on mid-infrared colors and optical spectroscopy (see Fig. 1).

Our newly developed method allowed us for the first time to robustly access the composition of the submilli-Jansky radio population (see [2] for details). We have found that SF galaxies are not the dominant population at sub-mJy flux levels, as previously often assumed, but that they make up an approximately constant fraction of 30% to 40% in the flux density range of ~ 50 μJy to 0.7 mJy (see Fig. 1).

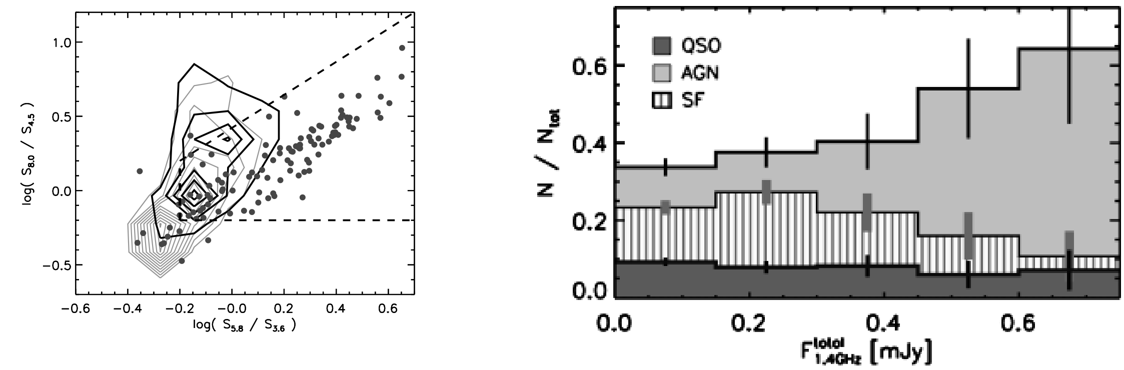

Figure 1: *The left panel illustrates the effectiveness of the star forming vs. AGN galaxy classification method in a mid-IR diagnostic diagram (Lacy et al. 2004, ApJS, 154, 166). As expected, quasars selected by our method (dots) are in the wedge-shaped area, while star forming galaxies (black contours) and AGN (grey contours) occupy different regions of this diagnostic diagram. The right panel shows the distribution of different sub-populations in the submilli-Jansky radio population in the VLA-COSMOS survey as a function of 20 cm flux density. Note that the AGN contribution decreases with decreasing flux density, while the star forming galaxy contribution increases with decreasing flux density, but still does not dominate the counts at the low flux levels (~ 50 μJy) probed here.*

The dust-unbiased cosmic star formation history

Our carefull division of the 20 cm VLA-COSMOS galaxy sample into SF and AGN galaxies [2] enabled a detailed study of the cosmic evolution of the SF galaxy population out to $z = 1.3$ – for the first time based on a statistically significant radio source sample [3]. While the VLA-COSMOS based dust-unbiased cosmic star formation history for all galaxies agrees well with other star formation history estimates (see Fig. 2, left panel), we find that the most intensely star forming galaxies (equivalent to the ultra-luminous infrared galaxies, ULIRGs) evolve slower than previously suggested (based on mid-IR data; le Floc'h et al. 2005, ApJ, 632, 169). The latter likely arises from AGN contamination in the MIR-selected sample, possibly causing an overestimate in the MIR-derived star formation history for ULIRGs. This has subsequently been verified by Magnelli et al. (2009, A&A, 496, 57) who showed that careful extraction of (X-ray bright) AGN from a MIR sample yields results very consistent with our radio-based ones (see Fig. 15 in Magnelli et al. 2009).

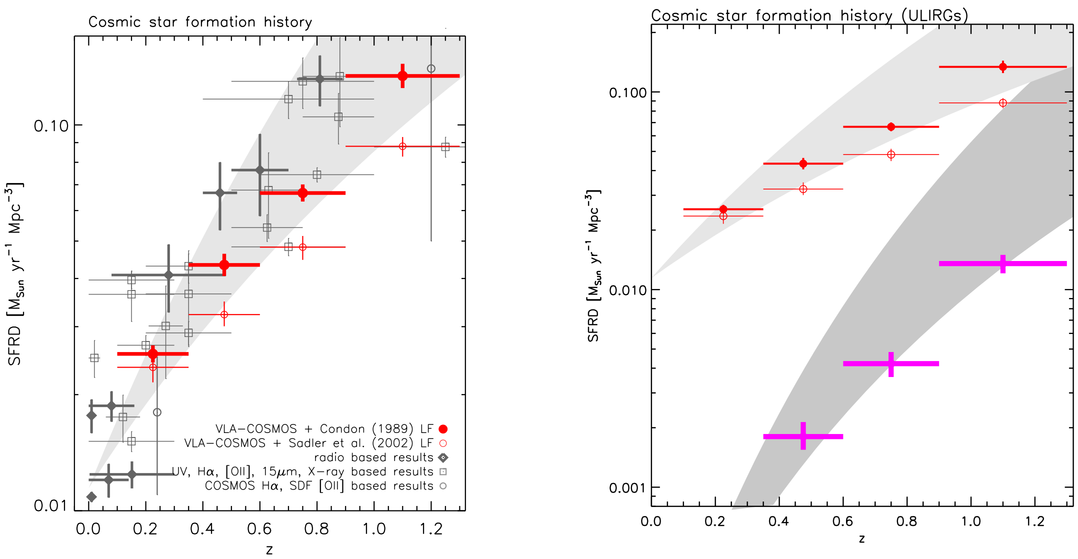

Figure 2: *The dust-unbiased cosmic star formation history out to redshift of $z = 1.3$ for all galaxies (left panel) and intensely (> 100 M$_\odot$/yr) star forming galaxies (ULIRGs) derived based on the 20 cm VLA-COSMOS data (red and purple symbols, respectively). Note that the VLA-COSMOS based cosmic star formation history for all galaxies agrees well with various other star formation tracers (indicated in the left panel), however it indicates a slower evolution for intensely star forming galaxies, compared to mid-IR based results (shown by shaded curves). The latter is likely due to AGN contribution (see text for details).*

Collaborators: Gianni Zamorani, Marco Scodeggio (INAF), Chris Carilli (NRAO), Nicolas Z. Scoville (CalTech)

References

[1] Schinnerer, E., et al. 2007, ApJS, 172, 46

[2] Smolčić, V., et al. 2008, ApJS, 177, 14

[3] Smolčić, V., et al. 2009, ApJ, 690, 610

9 Active Galactic Nuclei

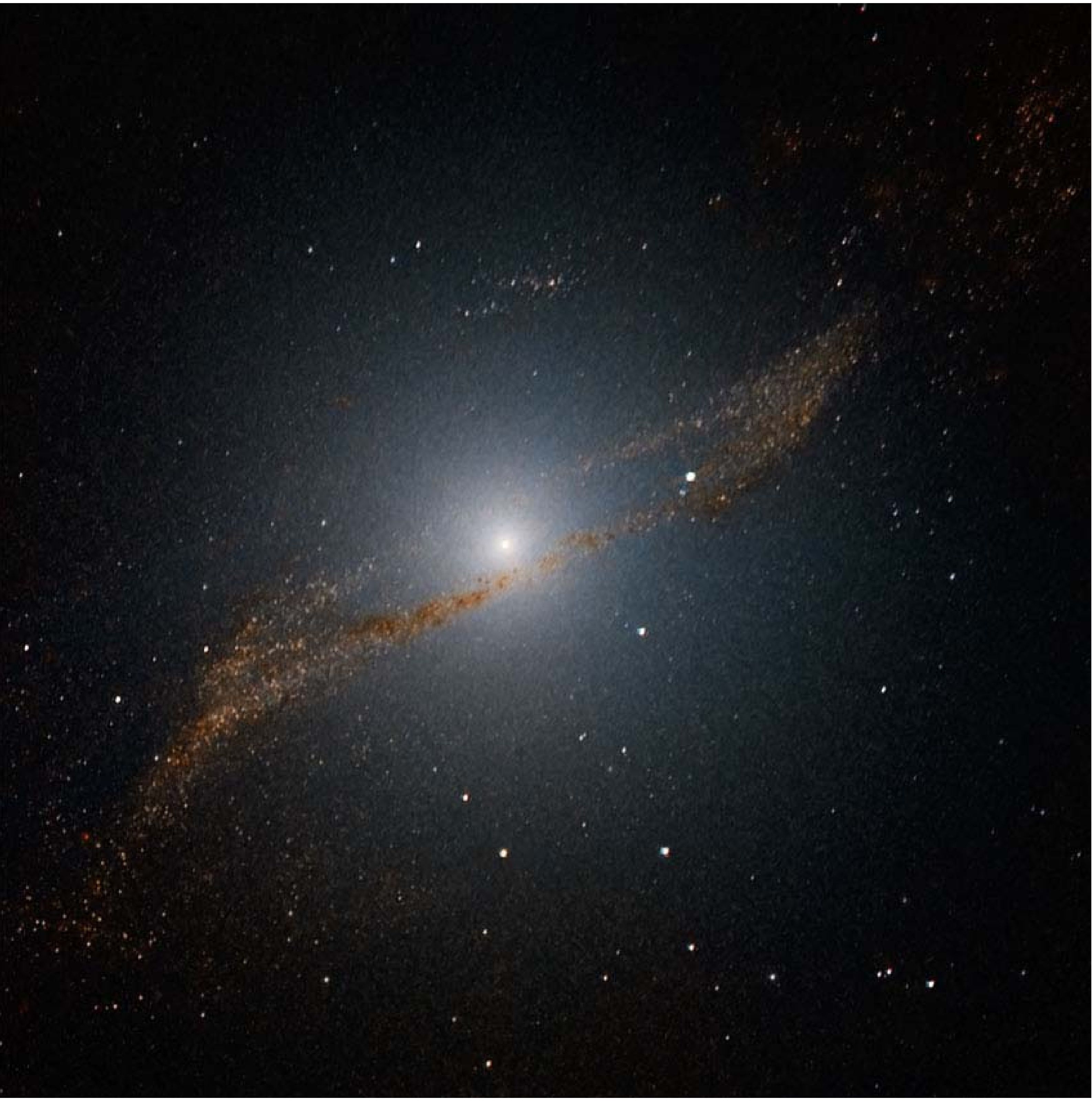

Image on previous page:
This unusual NIR-image (ESO-NTT) of the inner region of the Active Galaxy Centaurus A reveals the remnants of a spiral galaxy (which has been merged with Cen A) as well as numerous star clusters.
Credits: Y. Beletsky (ESO), J. Kainulainen (MPIA and Univ. Helsinki)

MHD jets from AGN and massive young stars

Christian Fendt, Oliver Porth, Bhargav Vaidya

Simulations of relativistic MHD jets

While MHD self-collimation and acceleration of non-relativistic outflows from disks has been successfully approved by numerical simulations, this has not been done for relativistic jets from Active Galactic Nuclei or Micro Quasars. We have therefore initiated a project performing relativistic MHD simulations in order to further investigate this question.

Our simulations use the special relativistic MHD code PLUTO and run for 500 inner disk rotations and on a physical grid size of 100x200 inner disk radii. (Newtonian) gravity is added in order to allow for the physical boundary condition of an underlying disk in centrifugal and pressure equilibrium [2]. Two options for the initial field geometry are applied - a hourglass-shaped potential magnetic field and a split monopole field. We obtain collimated, mildly relativistic

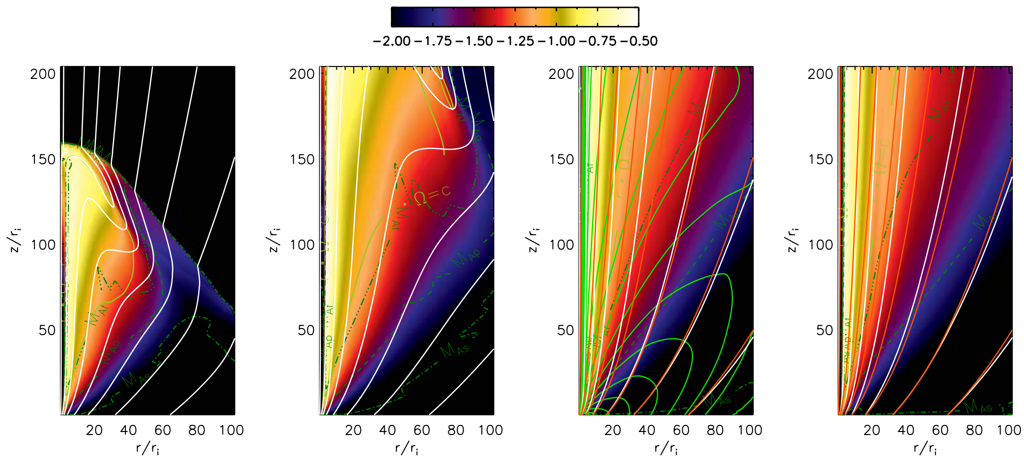

Figure 1: *Evolution of a collimating relativistic MHD jet at time* $t = 25, 50, 250, 500$*. Magnetic field lines (white; red is initial field), electric current lines (green), critical magnetosonic surfaces (dashed green), the light surface (light green), and the Lorentz factor* $log_{10}(\Gamma - 1)$ *(color coding).*

beams with Lorentz factors < 6 and a mass-weighted half-opening angle $< 7°$ (Fig. 1). The split-monopole setup usually provides less collimated jets. The light surface of the outflow magnetosphere tends to align vertically - implying three relativistically distinct regimes in the flow - an inner sub-relativistic domain close to the jet axis, a relativistic jet and a surrounding sub-relativistic outflow launched from the outer disk surface.

Launching of outflows from massive young stars

Jets and outflows are observed also from high-mass young stars. Their launching mechanism is not well understood as a number of parameters cannot really constrained observationally - such as mass loss rate, outflow velocity, or magnetic field.

In order to understand the launching conditions for jets around massive young stars, we first developed a model for the global disk structure applying the steady state model of thin disks [3]. The thin disk equations are solved with proper opacities for dust and gas taking properly into account the huge temperature variation along the disk. For a $10\,M_\odot$ protostar accreting $10^{-4}\,M_\odot \mathrm{yr}^{-1}$, the midplane temperatures of the inner disk reach almost 10^5 K. The inferred dust sublimation radius by turbulent disk self-heating is about 10 AU, which is 3 times larger as compared to stellar irradiation.

Currently we investigate the collimation and acceleration of MHD jets from high-mass young stars considering the radiation forces from the massive protostar and/or its disk.

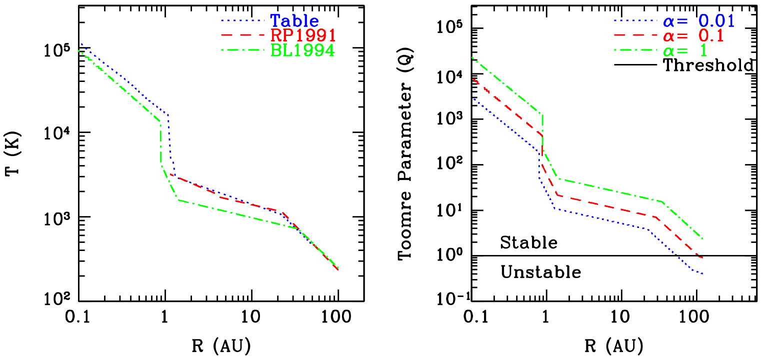

Figure 2: *Radial structure of a massive thin disk. Temperature profile for different opacity models (left), Toomre parameter profile indicating disk stability for different turbulent parameters α.*

Jets forming in a complex magnetic field structure

We have applied axisymmetric MHD simulations to investigate the interrelation of a central magnetosphere and wind with a surrounding magnetized disk outflow and how the overall formation of a large scale jet is affected [1]. The initial magnetic field is superposed of two components - a stellar dipole and a surrounding disk magnetic field, in both either parallel or anti-parallel alignment. Correspondingly, the mass outflow is launched as stellar wind plus a disk wind. Stellar

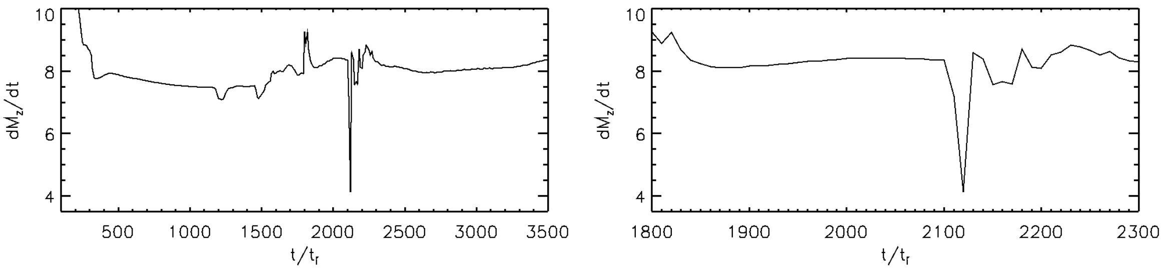

Figure 3: *Time evolution of the outflow mass flux. Dramatic change are due to flaring or reconnection.*

and disk wind evolve in a pair of collimated outflows. The existence of a reasonably strong disk wind component seems to be essential for collimation as the disk jet becomes de-collimated by the central wind. Some simulations show the generation of strong flares - triggering a sudden change in the outflow mass loss rate (factor of two), and a re-distribution in the radial profile of momentum flux and jet velocity across the jet (Fig. 3). Such flares may trigger internal shocks in the asymptotic jet which could then be observed as knots.

Henrik Beuther (MPIA) is observational co-supervisor for B. Vaidya. PLUTO was provided by Andrea Mignone (Torino). We acknowledge the HGSFP and the Klaus Tschira foundation KTS for B. Vaidya's PhD stipend. The research of O. Porth is funded by IMPRS-HD.

References

[1] Fendt, Ch., 2009, ApJ,692,346

[2] Porth, O., Fendt, Ch., 2009, ApJ, revised, 2009arXiv0911.3001P

[3] Vaidya, Bh., Fendt, Ch., Beuther, H., 2009, ApJ,702,567

Evolution of the infrared-radio relation of galaxies?

Mark T. Sargent, Eva Schinnerer, the COSMOS collaboration

Intermediate redshift ($z < 1.4$) starbursts and AGN

In the local universe, the correlation between infrared and radio continuum emission in star forming galaxies defines one of the tightest relations of extragalactic astrophysics (e.g. Yun et al. 2001, ApJ, 554, 80). Since it provides insight on the physics of the interstellar medium and intragalactic magnetic fields, the question of whether or not it still holds at high redshift has attracted much interest.

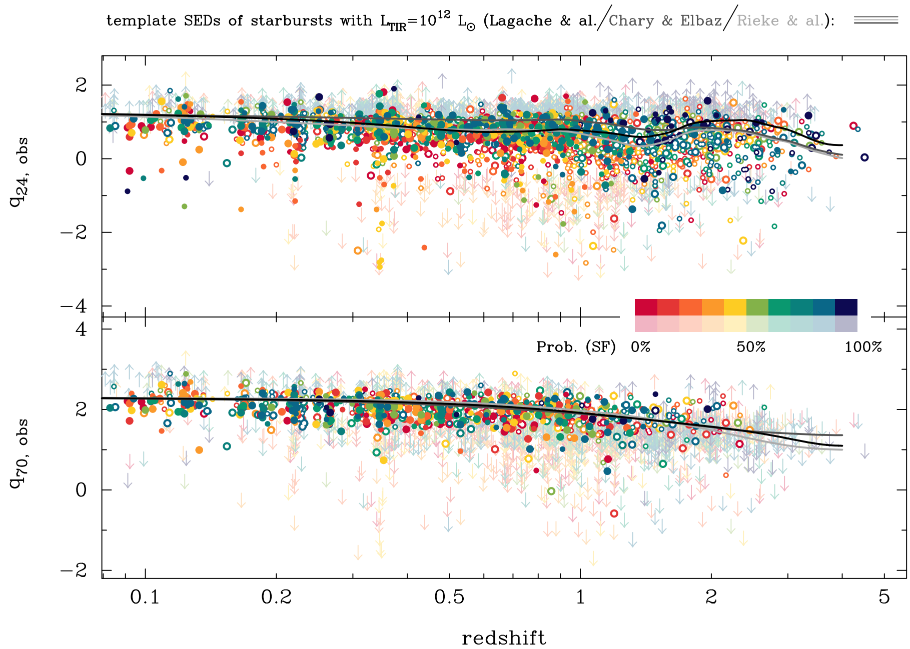

Figure 1: *Observed (i.e. not K-corrected) monochromatic IR/radio flux density ratios* $q_{24,\,\mathrm{obs}}$ *(*top*) and* $q_{70,\,\mathrm{obs}}$ *(*bottom*) as a function of redshift. The measurements are coloured according to their probability of being a star forming system (dark/light colour coding is used for sources with spectroscopic/photometric redshifts, respectively). The black and grey tracks show the IR/radio properties of model starbursts (cf. legend along upper edge). The tracks closely follow the data suggesting no evolution in the infrared-radio relation out to at least* $z \sim 1.4$*.*

This project aims to trace the evolution of the IR-radio relation out to high redshift by taking advantage of the large and diverse COSMOS data set [1]. In our analysis we employ the methods of survival analysis in order to ensure a statistically sound treatment of flux limits arising from non-detections at either infrared or radio wavelengths. We provide firm support [2] for previous findings that the IR-radio relation remains unchanged out to at least $z \sim 1.4$ (see Fig. 1). Moreover, we measured the observed shift in the average IR/radio properties of IR- and radio-selected populations and were able to show that this offset not only agrees with theoretical expectations, but that it can also reconcile previously conflicting measurements of the average IR/radio properties of galaxies at intermediate redshift.
Thanks to the multi-wavelength observations of the COSMOS field it was possible to adopt a probabilistic approach to distinguish [3] between star forming galaxies and active galactic nuclei (AGN). We found that radio-quiet AGN populate the locus of the IR-radio relation in similar numbers as star forming galaxies. Whether or not this means that SF activity dominates the

IR and radio emission of these AGN hosts is the subject of current debate (e.g. Barthel 2006, A&A, 458, 107).

The IR/radio properties of high-redshift galaxies

Our COSMOS sample contains ∼150 sources at $z > 2.5$ and thus represents the largest sample of high-z sources so far, for which it was possible to study the IR-radio relation based on a large

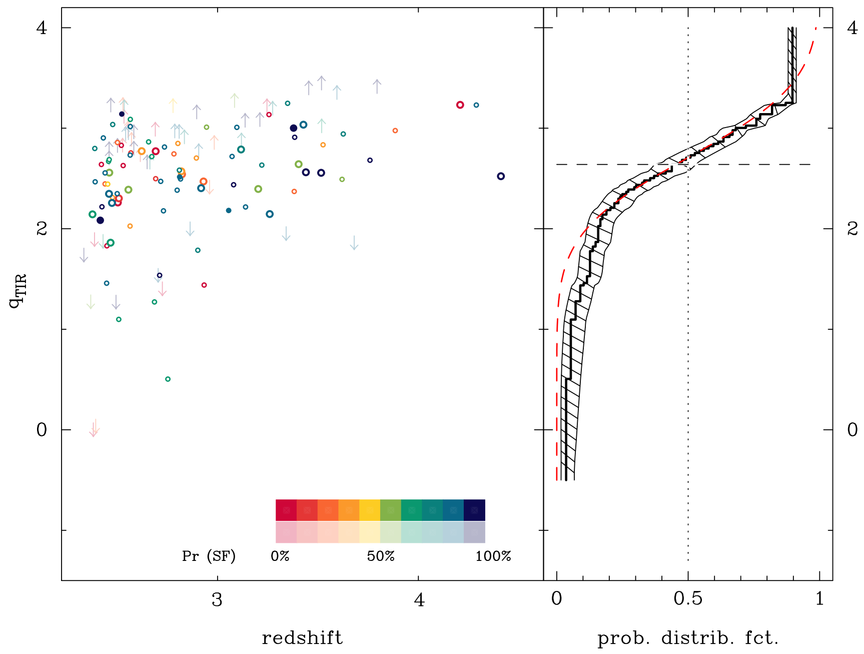

Figure 2: *At the highest redshifts sampled by the COSMOS VLA and Spitzer surveys, the median value of the logarithmic IR/radio ratio* $q_{\rm TIR}$ *is still unchanged in comparison to the locally measured average.* Left *– measured values of* $q_{\rm TIR}$ *in the range* $2.5 < z < 5$. Right *– cumulative distribution function of measured IR/radio ratios (black curve) with best-fitting Gaussian (red dashes) and local average (black dashes; from Bell 2003, ApJ, 586, 794) indicated.*

fraction of direct detections rather than flux limits. The average IR/radio properties of these sources – the most distant of which are detected when the universe was only ∼1.4 Gyr old – are very similar to those in the local universe. This is remarkable, since the synchrotron emission from these highly infrared-luminous sources is expected to be strongly suppressed due to inverse Compton scattering of their cosmic ray particles off the intense microwave background radiation from the Big Bang.

Collaborators are Vernesa Smolčić (Caltech, USA) and Alejo Martínez-Sansigre (U. of Oxford, UK), both previously at MPIA, as well as Eric Murphy (Caltech/SSC, USA), Gianni Zamorani (INAF Bologna, Italy) and Chris Carilli (NRAO, USA).

References

[1] Schinnerer, E., et al. 2007, ApJS, 172, 46

[2] Sargent, M. T., et al. 2010, ApJS, 186, 341

[3] Smolčić, V., et al. 2008, ApJS, 177, 14

NGC4151: fix torus around variable accretion disk

Jörg-Uwe Pott, Tom M. Herbst

Introduction

In this article, we concentrate on the origin of the near-infrared (NIR) emission of NGC 4151, and its relation to the nuclear luminosity. Dust plays an exceptional role among the circumnuclear emission components. It is not only assumed to significantly contribute to the near-to-mid-infrared continuum radiation of an AGN. Also, a non-spherically symmetric dust distribution is widely assumed to explain the type 1 / 2 dichotomy of AGN emission line spectra. The circum-nuclear dust distribution of AGN is now within reach of observations with infrared telescope arrays at mas angular resolution. Mid-infrared data of the VLT interferometer typically find in Seyfert nuclei 10 μm emission sizes of a few parsecs [1, 2]. Radiative transfer models of clumpy distributions of dust clouds are currently the favored explanation of the steadily increasing amount of observational data [3]. In the following, we refer to the circum-nuclear dust distribution as torus, keeping in mind that its detailed morphology is rather uncertain and might not resemble closely a smooth torus.
While it is not in question that the total NIR power originates in the accretion disk, it is uncertain how the emission and size of the torus relates to the direct nuclear emission. After recent sensitivity upgrades at the Keck Interferometer (KI), systematic interferometric 2 μm studies of the innermost dust in nearby Seyfert nuclei are within observational reach. Here we present the analysis of new interferometric data of NGC 4151, discussed in context with the results from recent dust reverberation, spectro-photometric and interferometric campaigns.

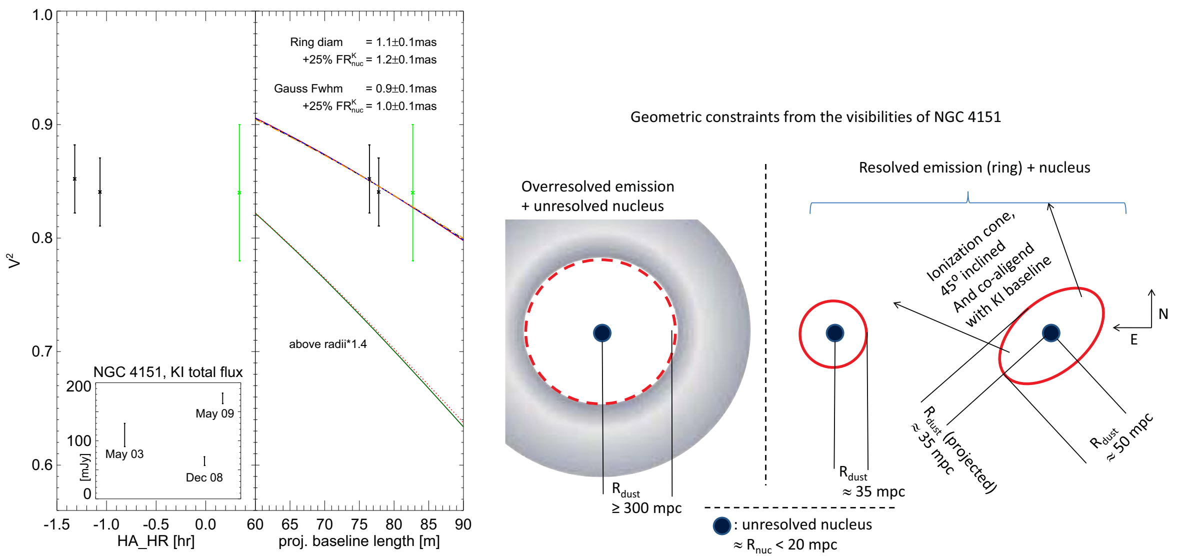

Figure 1: *Left: New (black, Dec 08) and old (green, May 03) 2 μm visibility data of NGC 4151. The inlet shows the nuclear total flux variability in K. The accretion disk fraction of this total flux varies between 10 - 25 %, which does not affect the torus size modeling. The data are precise enough to exclude that the fitted torus models vary in size, following the nuclear luminosity variability as $L^{0.5}$. For instance, model visibilities corresponding to a doubling of the accretion disk illumination are overplotted. Right: Sketches (not to scale) of the torus constraints from our experiment. The inclined torus (rightmost model) fits the inclination and position angle of the NLR ionization cone as well, and is the most likely solution.*

Results

The interferometric visibilities and size estimates were compared to previously published interferometric and single telescope data. The KI data alone indicate two scenarios: the K-band emission is either dominated to $\sim$ 90% by size scales smaller than 20 mpc, which falls short of any dust reverberation measurement in NGC 4151 and of theoretical models of circumnuclear dust distributions. Or contrary, and more likely, the K-band continuum emission is dominated by hot dust (1300 - 1800 K) at linear scales of about 50 mpc, depending on the detailed observed morphology. This is roughly consistent with the expectations from circumnuclear, dusty radiative transfer models, and spectrophotometric modeling. In particular, the derived torus size scales are comparable to V-to-K-continuum reverberation measurements.

The observations show that NIR-interferometry on K $\sim$ 10 mag AGN are now feasible at a high precision of a few percent. Our dataset enables for the first time to study the flux dependence of near-infrared interferometric visibilities of an individual AGN. We did not detect a significant visibility dependence on the K-band emission of NGC 4151, which varied by factors of 2-3 between different observations. This supports the notion, that, for an individual AGN, the size of its circumnuclear NIR emission structure does not strictly depend on the respective momentary nuclear luminosity. The direct interferometric size estimates appear to be more robust estimates of the average location of the dust than continuum reverberation estimates, which did indicate torus size variations (Koshida et al. 09). Being flux-independent, this average location probably relates to the sublimation radii of the AGN at its high activity state. Future dust reverberation campaigns, contemporaneous to direct interferometric measurements are highly desirable to study the circumnuclear NIR emission region, to correctly interpret the reverberation measurements, and to investigate apparent changes in the dust illumination, heating efficiency, and covering factors.

Collaborators are: Matt A. Malkan (UCLA), Moshe Elitzur (Univ. Kentucky), Andrea M. Ghez (UCLA), Rainer Schödel (IAA-CSIC), Julien Woillez (WMKO)
The presented results will be submitted to the Astrophysical Journal.

References

[1] Tristram, K. R. W.; Raban, D.; Meisenheimer, K.; Jaffe, W.; Röttgering, H.; Burtscher, L.; Cotton, W. D.; Graser, U.; Henning, Th.; Leinert, Ch.; Lopez, B.; Morel, S.; Perrin, G.; Wittkowski, M. 2009, A&A, 502, 67

[2] Burtscher, L., Jaffe, W., Raban, D., Meisenheimer, K., Tristram, K. R. W., Röttgering, H. 2009, ApJ, 705, L53

[3] Schartmann, M., Meisenheimer, K., Camenzind, M., Wolf, S., & Henning, T. 2005, A&A, 437, 861

A nuclear star cluster hosting an AGN

J. Shields, J. Walcher, H.-W. Rix

Do galaxies without a bulge host a central super-massive black hole?

The fact that the spheroids of massive galaxies all harbour a super-massive black hole at their center, whose mass can be predicted from the mass-scale of the bulge to better than a factor of 2, is one of the most fascinating – and still unsolved – puzzles in galaxy evolution. One empirical approach to understanding why there are massive black holes in the centers of galaxies at all, is by exploring whether 'bulge-less', pure-disk galaxies also have central black holes. E.g. it is entirely open whether galaxies like the Large Magellanic Cloud has a central black hole and if so where one would find it. As an intermediate step towards addressing this question in irregular galaxies we have expanded a thesis centered on so-called nuclear clusters in pure disk galaxies to look for evidence of black holes; we have found such evidence in the nuclear cluster of NGC1042.

Figure 1. The bulgeless galaxy NGC 1042, as imaged by SDSS . Analogous to M33 is has no bulge but only a central nuclear cluster. VLT spectra from Jakob Walcher's PhD thesis at MPIA have revealed clear evidence for an AGN, presumably an accreting central black hole.

Nuclear star clusters

The centers of galaxies that must have had an extremely quiescent star-formation history and therefore appear to be purely disk galaxies have proven interesting. Many of them – and M33 is the most prominent example – host so-called nuclear star clusters. These are akin to globular clusters, but are somewhat more massive and almost always have multi-age stellar populations, including young stars. In their structural and population properties they sit in between star-clusters and mini-bulges, and apparently are only found at galaxy centers. To understand what role the galaxy center (or, the bottom of the potential well) plays in enabling black hole formation an growth, we looked for AGN (= black hole) evidence in these nuclear clusters, using CAHA TWIN and VLT UVES spectra.

The AGN in NGC 1042

In one of the initially nine sample members, NGC 1042, we found evidence for and AGN: as Figure 2 shows, the emission lines in this galaxy are much broader than expected form the velocity dispersion of nuclear cluster (~30 km/s). The cluster hosts no important young stellar population, so winds and supernovae are unlikely explanations fort these large line-widths.

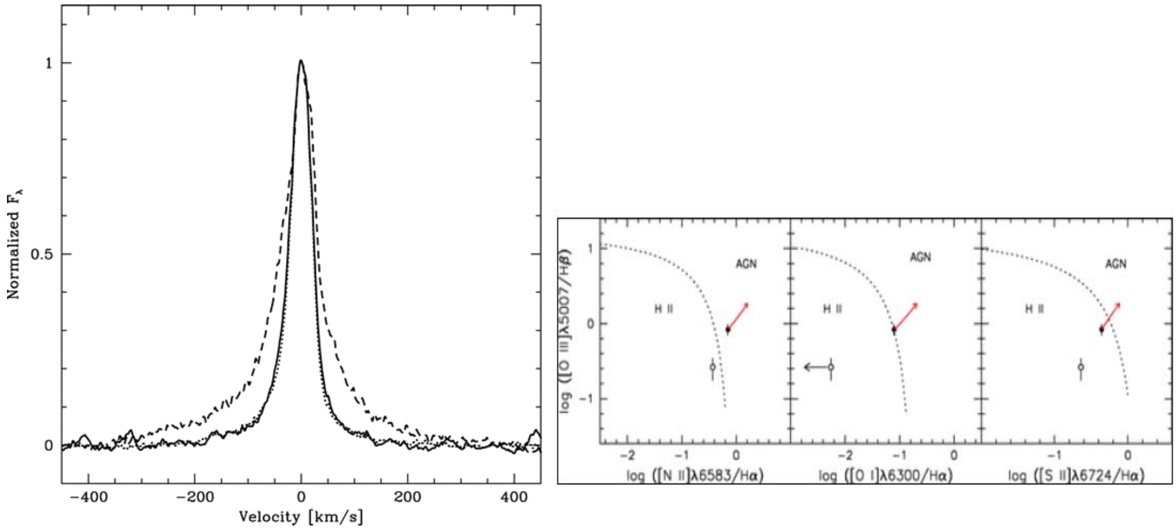

Figure 2. Emission line profiles of the central 1" (i.e. the nuclear cluster) in NGC 1042 (left panel). The dashed line is the NII profiles, the solid line the Hα profile. The nuclear star cluster that hosts this line emission has a velocity dispersion of only 30km/s; nonetheless the NII line extends over ~600 km/s in velocity. The line-ratios, too, argue for a LINER, not an HII region (right panel).

Note only are the lines very broad, also the line ratios argue for an AGN excitation (see Figure 2, right panel). By ruling out all alternatives, we concluded that these phenomena must be attributed to an accreting black hole. Simple arguments imply the $M_{BH} > 60\ M_0$ (with an upper limit of $10^6 M_0$). This makes NGC 1042 the lowest velocity dispersion galaxy with a likely central black hole and a prime candidate for 'intermediate mass' black holes at galaxy centers.

References

[1] Shields, J., Walcher, J, Rix, H.-W. et al., 2008, ApJ, 682, 104.

A kiloparsec-scale hyper-starburst in a Quasar host less than 1 Gigayear after the Big Bang

Fabian Walter, Dominik Riechers

The host galaxy of the quasar SDSS J1148+5251 (at redshift z=6.42, when the Universe was <1 billion years old) has an infrared luminosity of 2.2×10^{13} $L_\odot^{1,2}$, presumably significantly powered by a massive burst of star formation. In local examples of extremely luminous galaxies such as Arp 220, the burst of star formation is concentrated in the relatively small central region of < 100 pc radius. It has been unknown on which scales stars are forming in active galaxies in the early Universe, which are likely undergoing their initial burst of star formation.

Using the IRAM Plateau de Bure interferometer we obtained a spatially resolved image of [CII] emission of the host galaxy of J1148+5251. The forbidden $^2P_{3/2} \rightarrow {}^2P_{1/2}$ fine–structure line of ionized Carbon ([CII]) at 158 microns provides effective cooling in regions where atomic transitions cannot be excited, and therefore helps gas clouds to contract and form stars. [CII] emission is thus known to be a fundamental diagnostic tool of the starforming interstellar medium. Given the very bright continuum emission of the central accreting black hole of quasars in optical and near–infrared wavebands, standard star formation tracers (such as hydrogen recombination lines) cannot be used to study star formation in these systems. The [CII] line is however much brighter than the underlying far–infrared (FIR) continuum, thus making it a prime choice to characterize star formation in quasar host galaxies.

We used the IRAM Plateau de Bure interferometer to resolve the [CII] emission from the z=6.42 host galaxy of J1148+5251 with a linear resolution of ~ 1.5 kpc. At a redshift of z=6.42 the age of the Universe was just ~ 870 million years (or 1/16th of its present age) and 1” on the sky corresponds to 5.6 kpc.

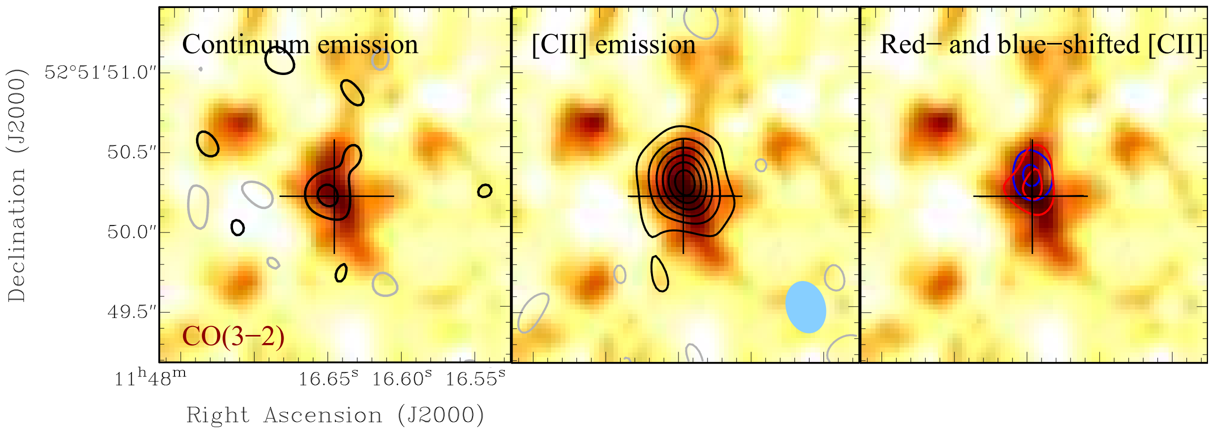

Figure 1: *PdBI observations of the [CII] line in the z=6.42 quasar J1148+5251 (Walter et al. 2009, Nature).*

The distribution of the [CII] emission is shown in the middle panel of Figure 1, taken from [?]. Gaussian fitting to the spatially resolved [CII] emission gives an intrinsic source size of 0.27”±0.05” (1.5±0.3 kpc). The [CII] emission is embedded within the molecular gas reservoir traced by CO (Walter et al. 2003, 2004), however the [CII] emission is offset to the north from the optical quasar and the CO peak by ∼0.1” (∼600 pc). Given the good agreement between the position of the optical quasar and the simultaneous 158 micron continuum observations (Fig. 1, left) we do not attribute this offset to inaccurate astrometry. The significance of the [CII] detection is high enough that it shows spatially resolved velocity structure (red and blue contours in the right panel of Figure 1).

The (rest–frame) FIR continuum emission underlying the [CII] line is detected at 10 sigma significance in the integrated frequency spectrum (Fig. 2, taken from [1]). If the FIR continuum was due to the (unresolved) optical quasar, a 10 sigma point source is expected at the optical position. However, from Figure 1 (left) we only find ~50% of the flux to be coincident with the optical quasar position. This implies that the sensitivity of our observations is not high enough to image the remaining FIR flux that is presumably due to the more extended emission from star formation. This would imply that at most 50% of the FIR emission can be attributed to heating by the central black hole, i.e. the FIR emission is significantly powered by star formation. In the following we thus assume a FIR luminosity due to star formation of $\sim 1.1 \times 10^{13}$ $L_\odot$, i.e., a star formation rate of ~ 1700 $M_\odot\,yr^{-1}$ (assuming a standard initial stellar mass function).

The compactness of the [CII] emission implies that massive star formation is concentrated in the central region with radius 750 pc of the system, even though molecular material is available on larger scales (as discussed in [2]). Given the star formation rate derived above, we find an extreme average star formation rate surface density of $\sim 1000\,M_\odot\,yr^{-1}\,kpc^{-2}$ ($\sim 7 \times 10^{12}$ $L_\odot\,pc^{-2}$) over this central 750 pc radius region. Similarly high starburst surface densities are also found in the centre of local ULIRGs such as Arp 220 (where each nucleus of size $\sim$ 100 pc has $L_{FIR}=3 \times 10^{11} L_\odot$), albeit on spatial scales that are by two orders of magnitudes smaller. For comparison, the Galactic young starforming cluster associated with Orion KL also exhibits such high densities in its central region ($L_{FIR}=1.2 \times 10^5\,L_\odot$, area: $\sim 1\,arcmin^2$, $0.013\,pc^2$, resulting in $\sim 10^{13}\,L_\odot\,kpc^{-2}$), however over an area that is 8 orders of magnitudes smaller than in J1148+5251.

In the context of other galaxies in the early universe, this kpc–scale 'hyper'–starburst has a star formation rate surface density that is one order of magnitude higher than what is found in massive starforming z~2.5 submillimeter galaxies. It is however consistent with recent theoretical descriptions of (dust opacity) Eddington limited star formation of a radiation pressure–supported starburst on kpc scales (Thompson et al. 2005, ApJ, 167) The high star formation rate surface density is also compatible with other theories describing 'maximum starbursts': stars can form at a rate limited by SFR=$\epsilon \times M_{\rm gas}/t_{\rm dyn}$, where ϵ is the star formation efficiency, $M_{\rm gas}$ is the gas within radius r and $t_{\rm dyn}$ is the dynamical (or free–fall) time, given by $\sqrt{r^3/(2\,G\,M)}$. For r=750 pc, $M \sim M_{\rm gas} \sim 10^{10}\,M_\odot$ a star formation efficiency of $\epsilon \sim 0.4$ is required to explain star formation rate density that we observe in the case of J1148+5251. Such high efficiencies may be expected given the high dense gas fractions found in local ULIRGs. In this calculation, we assume that the stellar initial mass function in this object is not significantly different from what is known locally. Such a high star formation efficiency could be expected if J1148+5251 were to undergo a major merger, where the gas is funneled to the central 1.5 kpc on rapid timescales.

These observations provide direct evidence for strong, kpc–scale star formation episodes at the end of Cosmic Reionization that enable the growth of stellar bulges in quasar host galaxies. Such 'hyper starbursts' appear to have an order of magnitude higher star formation rate surface densities on kpc scales than previously studied systems at high redshift. These observations are currently the best means by which to quantify star formation rates and their surface densities in quasars at the earliest cosmic epochs.

Collaborators include: Chris Carilli (NRAO), Pierre Cox, Robert Neri (both IRAM), Dominik Riechers (now Hubble Fellow at Caltech), and Frank Bertoldi (AIfA Bonn)

References

[1] Walter, F., Riechers, D., Cox, P., Neri, R., Carilli, C., Bertoldi, F., Weiss, A., & Maiolino, R. 2009, Nature, 457, 699

[2] Riechers, D. A., Walter, F., et al. 2009, ApJ, 703, 1338

10 High Redshift and Cosmology

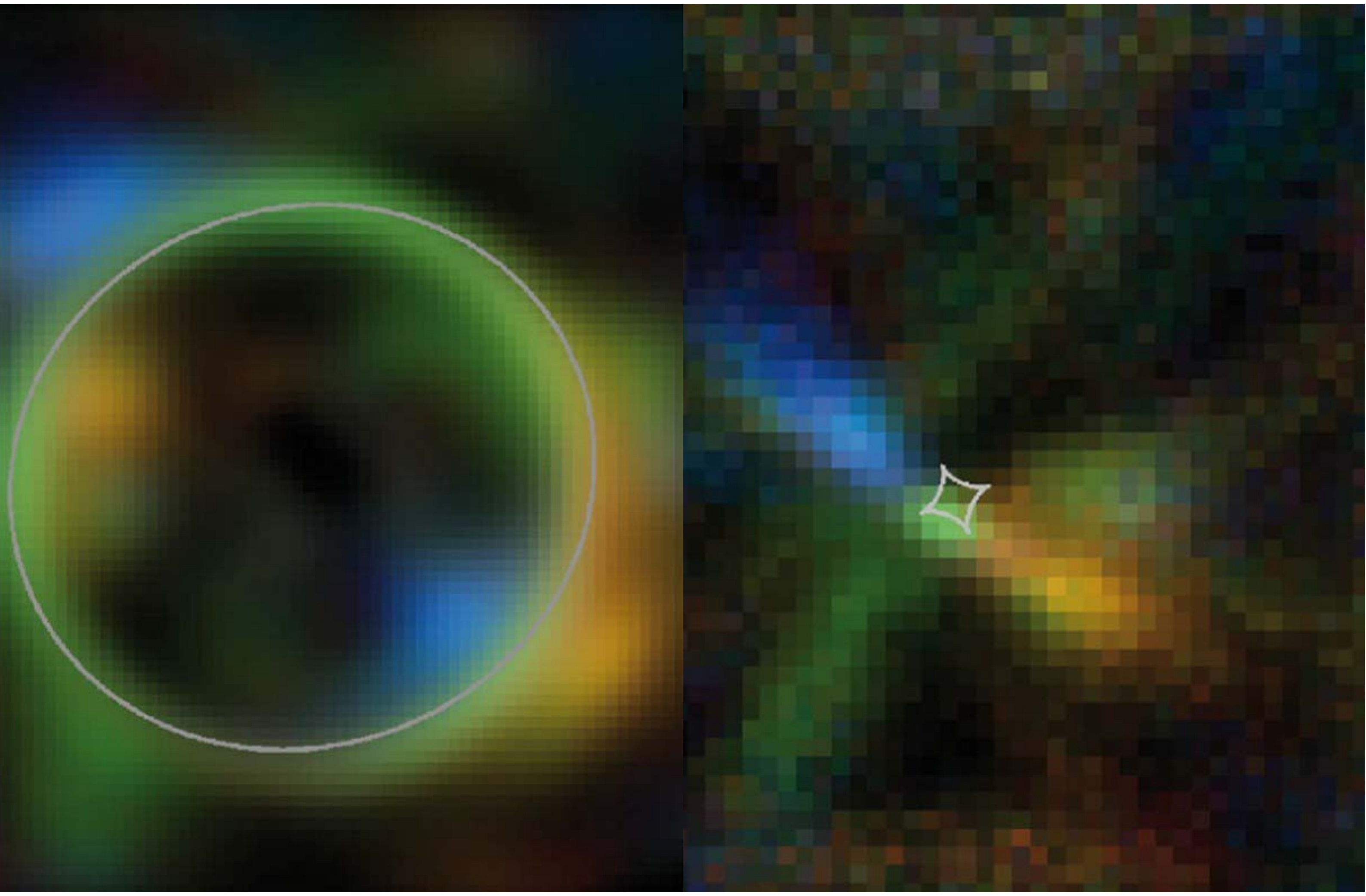

Image on previous page:
The galaxy PSS J2322+1944 at a redshift of 4.12.
Left: The observed image of the galaxy – a deformation into a Einstein Ring due to gravitational lensing. Right: the reconstructed image. The colors red, green and blue correspond to the radial velocities of gas with reference to the distant galaxy.
Credits: D. A. Riechers, F.Walter (MPIA), and colleagues of : Institute of Astronomy, University of Sidney / NRAO / Argelander-Institut für Astronomie, Bonn / IRAM

Finding rare objects and building pure samples: Probabilistic quasar classification from low resolution Gaia spectra

Coryn A.L. Bailer-Jones, Kester Smith

Gaia, the upcoming mission of the European Space Agency, will perform an all-sky astrometric and spectrophotometric survey complete to $G = 20$, expecting to observe some 10^9 stars, a few million galaxies and half a million quasars (e.g. [3]). Its primary mission is to study Galactic structure by measuring the 3D spatial distribution and 2D kinematic distribution of stars throughout the Galaxy and correlating these with stellar properties (abundances, ages etc.) derived from the spectra. With astrometric accuracies as good as $10\,\mu$as, Gaia cannot be externally calibrated with an existing catalogue. Instead, it must observe a large number of quasars over the whole sky with which to define its own reference frame. This quasar sample must be very clean (low contamination) and is itself of intrinsic interest.

Object classification and estimation of astrophysical parameters is an integral part of the overall Gaia data processing [1] and comprises one of the Coordination Units in the Gaia Data Processing and Analysis Consortium (DPAC) [4] [5].

The Discrete Source Classifier (DSC) is the data processing module responsible for classifying all the objects which Gaia detects. As the name suggests, it assigns objects to discrete classes, e.g. star, galaxy, quasar, binary star, in each case it assigning a class probability. Classification is based primarily on the low resolution BP/RP spectra, because (initially at least) there is no morphological information from Gaia. The subsequent stages in the CU8 data processing are concerned with extracting physical parameters for these classes (e.g. stellar temperatures) and classifying the RVS spectra. DSC is based on machine learning methods for pattern recognition, currently a so-called "Support Vector Machine".

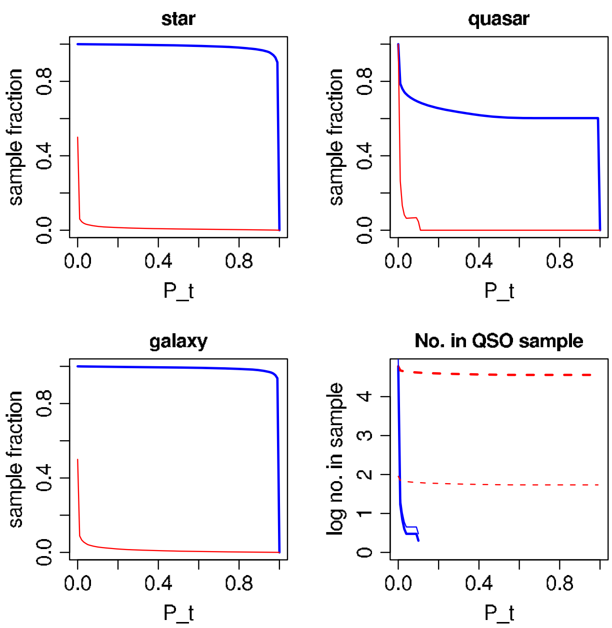

Figure 1: Completeness (blue line) and confusion (red line) of samples of star, galaxies and quasars as function of the classifier threshold

One of the challenges of Gaia is to reliably classify of rare objects, e.g. the expected half million quasars among one thousand million stars. Standard methods for machine learning will often fail to identify them. To address this, the DSC team has developed a method for modifying the output probabilities to accommodate rarity, and applied this in classification experiments on simulated data [2]. Figure 1 shows, for three classes of objects, the completeness (blue

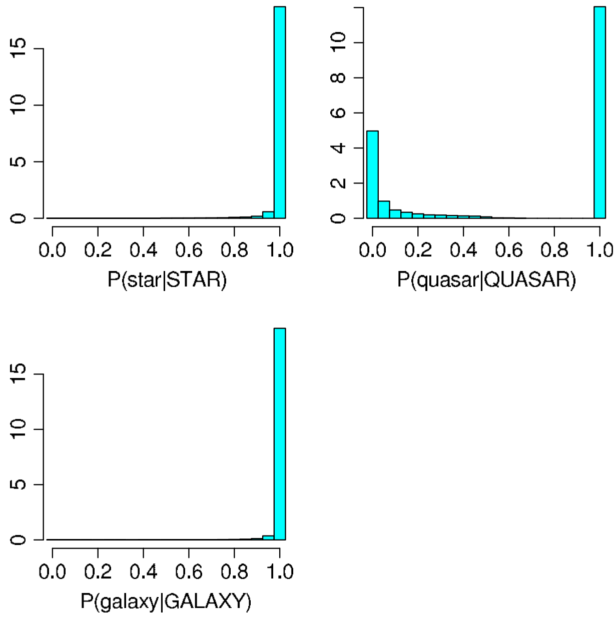

Figure 2: Histogram of probabilites for correctly classified quasars

line) and contamination (red line) of a sample of objects as a function of adjustable probabilty thresholds used to build the sample. We see that we can achieve a zero contamination sample of quasars which still has a completeness of 65%, more than sufficient for Gaia. The corresponding probability outputs from the DSC are shown in Figure 2. With this method we can control the class priors, which allows a single classification model to be applied to any target population without having to tune the training data and retrain the model.

Based on simulations of the universe which Gaia will observe, we find that we are able to achieve a pure sample of quasars (upper limit on contamination of 1 in 40 000) with a completeness of 65% at magnitudes of G=18.5, and 50% at G=20.0, even when quasars have a frequency of only 1 in every 2000 objects. The star sample completeness is simultaneously 99% with a contamination of 0.7%.
For more information see http://www.mpia.de/Gaia

References

[1] Bailer-Jones C.A.L., in *The Three-dimensional universe with Gaia*, C. Turon, K.S. O'Flaherty, M.A.C. Perryman (eds), ESA, SP-576, 393

[2] Bailer-Jones C.A.L., Smith K.S., Tiede C., Sordo R., Vallenari A., 2008, MNRAS 391, 1838

[3] Lindegren L., Babusiaux C., Bailer-Jones C.A.L., Bastian U., Brown A.G.A., Cropper M., Hog E., Jordi C., et al., 2008, Proc. IAU Symposia, vol. 248, 217

[4] Mignard F., Drimmel R. (eds), 2007, *DPAC Proposal for the Gaia Data Processing*, Gaia DPAC Technical note, GAIA-CD-SP-DPAC-FM-030

[5] O'Mullane W., Lammers U., Bailer-Jones C.A.L., et al., in *Astronomical Data Analysis Software and Systems 16*, R.A. Shaw, F. Hill and D.J. Bell (eds), ASP Conf. Ser. 376, 99

The build-up of massive red galaxies around z = 2.

Marie-Hélène Nicol, Klaus Meisenheimer, Christian Wolf, Mathias Jäger

Galaxy evolution as seen by the COMBO–17+4 survey

The optical multi-band survey COMBO–17 delivers very accurate photometric redshifts for galaxies and quasars [4] and has resulted in various studies of galaxy and AGN evolution. However, the use of optical filters only limits the range of accurate redshifts for galaxies to $z < 1.1$. In order to extend the redshift range, the optical data of COMBO–17 were supplemented by photometry in four near-infrared filters – three medium bands and the H-band. Observations were carried out with the survey camera OMEGA2000 at the Calar Alto 3.5m telescope. Thus only the three northern COMBO–17 fields are part of the NIR extension COMBO–17+4. Here we present the results of the first analysed field, containing the super-cluster Abell 901/902 . The H-band selected catalogue contains 10700 galaxies at H< 21.7 with good photometric redshifts out to $z \simeq 2$ [3]. The SED of these galaxies is well sampled by our photometry from the UV out to the rest-frame V band. The entire field is covered by an HST-ACS mosaic (STAGES project, Gray et al. 2009)

Tracing the red sequence out to z = 1.7

Conventionally, color-magnitude diagrams of the rest-frame U-B or U-V (Johnson) versus M_{V} are used to separate the quiescent galaxies in the red sequence from the star-forming galaxies in the blue cloud [1]. In order to minimize the effect of redshift errors (which leads to an unknown fraction of light from $\lambda_{\mathrm{rest}} > 400\,\mathrm{nm}$ contributing to the restframe U-band, we employ the rest-frame color between an artificial top-hat u-band ($\lambda/\Delta\lambda = 280/40\,\mathrm{nm}$) and Johnson V: $u_{280} - \mathrm{V}$. Since the red sequence is strongly tilted in the ($u_{280} - \mathrm{V}$) versus M_{V} diagram, we use the slope of the red sequence in A901 to project the red sequence onto the its location at $M_{\mathrm{V}} = -20$:

$$(u_{280} - \mathrm{V})|_{M_V=-20} = (u_{280} - \mathrm{V}) + 0.3(M_V + 20).$$

When using an "error-weighted" histogram (in which each galaxy is represented by the probability distribution from its error in $u_{280} - \mathrm{V}$), the location of the red sequence can be located very accurately out to $z \simeq 1.7$ (beyond that redshift the number of galaxies is too small to identify the red sequence). In Fig. 1 we plot the location of the red sequence as a function of look back time. The color of the red sequence has evolved almost linearly over the last 10 billion years.

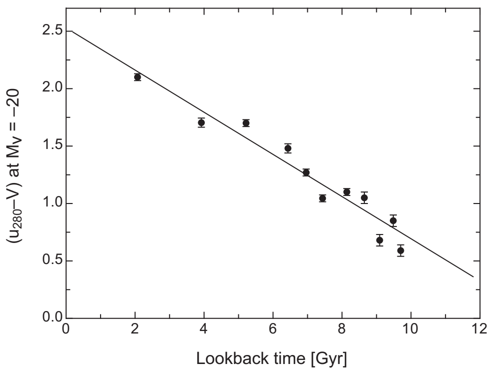

Figure 1: *Evolution of the restframe* $u_{280} - \mathrm{V}$ *color of the red sequence at* $M_{\mathrm{V}} = -20$ *as a function of look back time.*

The scatter around the linear relation is partly caused by the small number of galaxies per bin but could also indicate real variations in metallicity with environment.

Massive red galaxies around redshift 2

The Spectral Energy Distributions (SEDs) are fitted by a 2-dimensional library of templates, parameterized by (1) age of the stellar population and (2) the amount of extinction. Similar to the approach in Borch et al. [2] we describe passive, old galaxies with an exponentially declining burst of star formation ($\tau = 1\,\mathrm{Gyr}$) in the distant past, while young, blue galaxies contain an increasing amount of stars which have formed in a recent second burst. The templates are calculated with the population synthesis code PEGASE (Fioc & Rocca-Volmerange, 1997) and are characterized by their stellar mass-to-light ratio M/L_{V}. Thus, depending on SED the V-band luminosity can be converted into stellar mass directly. Red sequence and blue galaxies are separated at a deviding line at $\Delta(u_{280} - \mathrm{V}) = 0.45$ blue-ward of the red sequence fit (*c.f.* Fig. 1). In our highest redshift bins at $z > 1.55$ we still find several dozen red galaxies with stellar masses $M > 10^{11}\,\mathrm{M}_{\odot}$ (number density: $\sim 10^{-4}/\mathrm{Mpc}^3$). Figure 2 shows a few examples of those massive red high redshift galaxies and demonstrates how well the templates fit the observed photometry, leading to a very accurate photometric redshift. It is obvious that both passive old galaxies (upper row in Fig. 2) and extincted star forming galaxies (lower row) populate the red sequence at $z > 1.5$. NIR spectroscopy with LUCIFER at the LBT will allow us to measure their star formation rates from emission line luminosities.

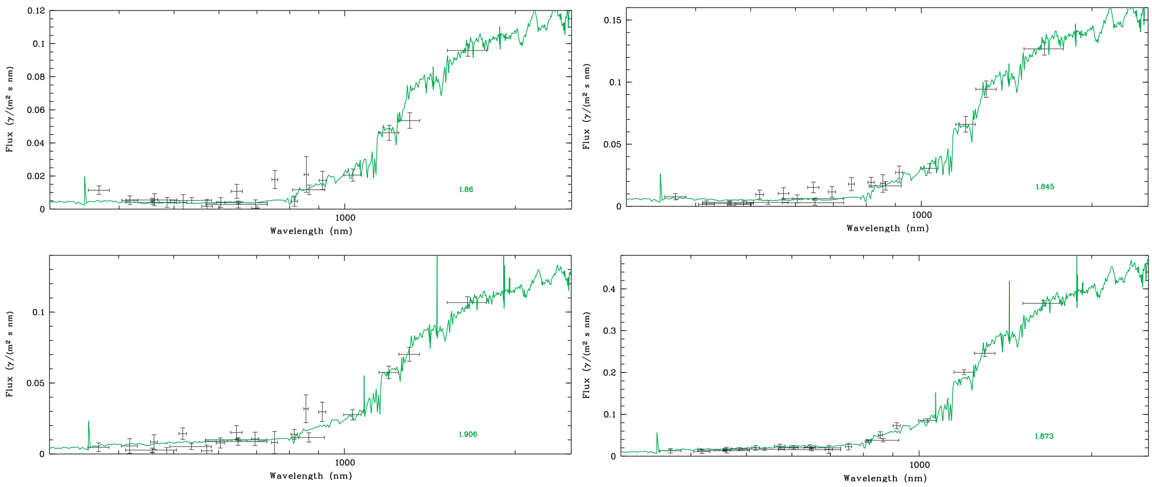

Figure 2: *Spectral Energy Distributions of massive red galaxies at* $z > 1.8$. *Data are shown in black, template spectra in green. Top left:* $z = 1.86 \pm 0.07$, $M = 2.3 \times 10^{11}\,\mathrm{M}_{\odot}$, *top right:* $z = 1.85 \pm 0.07$, $M = 3.4 \times 10^{11}\,\mathrm{M}_{\odot}$, *bottom left:* $z = 1.91 \pm 0.08$, $M = 2.5 \times 10^{11}\,\mathrm{M}_{\odot}$, *bottom right:* $z = 1.87 \pm 0.06$, $M = 1.0 \times 10^{12}\,\mathrm{M}_{\odot}$. *A flux of* $0.1\ \mathrm{ph/s\ m^{-2}\,nm^{-1}}$ *at* $\lambda = 1.65\,\mu\mathrm{m}$ *corresponds to* $\mathrm{H(Vega)} = 20.07$.

References

[1] Bell, E. F., Wolf, C., Meisenheimer, K. et al. 2004, ApJ, 608, 752

[2] Borch, A., Meisenheimer, K., Bell, E. F. et al. 2006, A&A, 453, 869

[3] Nicol, M.-H. 2009, PhD Thesis, University of Heidelberg

[4] Wolf, C., Meisenheimer, K., Kleinheinrich, M. et al. 2004, A&A, 421, 913

Molecular Gas in a Massive Star Former at z=4.5

Eva Schinnerer

A Dusty Star Forming Galaxy at z > 4 in COSMOS

Wide field blank sky surveys at millimeter and sub-millimeter wavelengths have established a population of active star forming galaxies at high redshift. These sources or so-called submillimeter galaxies (SMGs) dominate the (sub-)millimeter background, and represent (50-75)% of the star formation at high redshift causing a significant revision to the optically derived star formation history of the Universe. The bulk of this population lies at redshifts below z=3, with far-infrared (FIR) luminosities of $\geq 10^{13}\mathrm{L}_\odot$, which (if powered by star-formation) imply star-formation rates in excess of $1000\,\mathrm{M}_\odot\ \mathrm{yr}^{-1}$. This is sufficient to build up the stellar mass of a giant elliptical galaxy in about 1 Gyr.

The discovery of such an SMG above a redshift of z=4 indicates that massive galaxy formation is already well under-way when the universe is only 1.5 Gyr old. The recently discovered object J1000+0234 originally selected as a V band drop-out with a weak radio counterpart (Carilli et al. 2008, ApJ, 689, 883) and with a stellar mass of $\mathrm{M}_* > 10^{10}\,\mathrm{M}_\odot$, a young starburst age of 2-8 Myr and a star formation rate of SFR $> 1000\,M_\odot\,yr^{-1}$ is a candidate for such a z>4 SMG, as it was detected in its FIR continuum (Capak et al. 2008, ApJL, 681, L53).

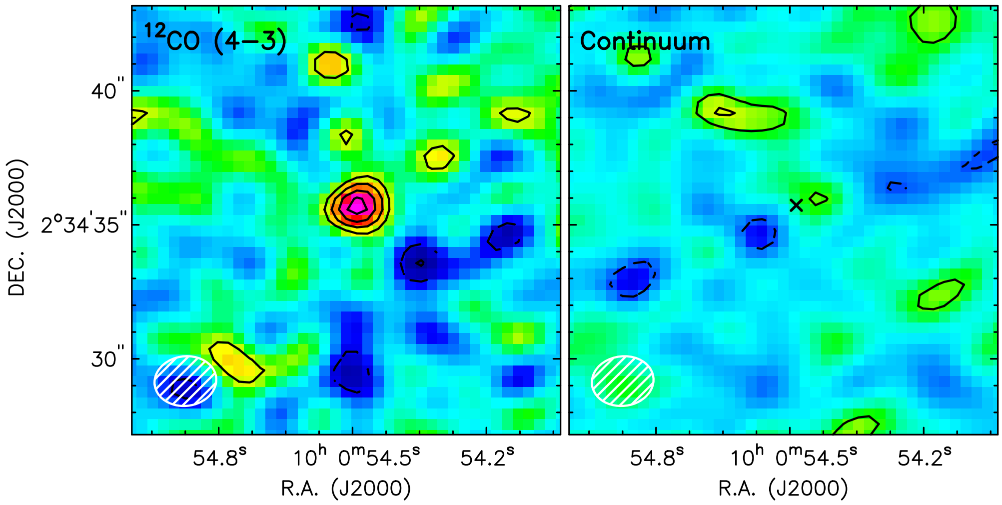

Figure 1: *CO(4-3) line emission and corresponding continuum in the SMG J1000+0234 as observed with the PdBI, shown on the same color scale, but with different contour levels. Continuum emission from J1000+0234 is detected at the 2σ level, while the emission from the CO(4-3) line shows a solid detection at 5.5σ. The integrated CO(4-3) line emission (left) is centered at a redshift of z=4.5423. Contours start at 2σ in steps of 1σ with 1σ = 0.12* $\mathrm{Jy\,beam^{-1}\,km\,s^{-1}}$. *The integrated continuum (right) has the same contour steps, however 1σ corresponds to 0.08 mJy/beam. The cross indicates the position of the CO(4-3) peak. The beam is shown in the lower left corner.*

Are z > 4 SMGs the Progenitors of z∼2 Massive Elliptical Galaxies?

We detected CO molecular line emission in the z=4.5 millimeter-detected galaxy J1000+0234 [1] using the IRAM Plateau de Bure interferometer (PdBI) and NRAO's Very Large Array (VLA). The ^{12}CO(4-3) line as observed with PdBI has a full line width of $\sim 1000\,\mathrm{km\,s^{-1}}$, an integrated line flux of 0.66 Jy km s^{-1}, and a CO luminosity of $3.2\times10^{10}\,L_\odot$ (Fig. 1). Comparison to the 3.3σ detection of the CO(2-1) line emission with the VLA suggests that the molecular gas is likely thermalized to the J=4-3 transition level. The corresponding molecular gas mass is $2.6\times10^{10}\,M_\odot$ assuming an ULIRG-like conversion factor. From the spatial offset of the red- and blue-shifted line peaks (Fig. 2) and the line width a dynamical mass of $1.1\times10^{11}\,M_\odot$ is estimated assuming a merging scenario. The molecular gas distribution coincides with the rest-frame optical and radio position of the object while being offset by 0.5" from the previously detected Lyα emission. J1000+0234 exhibits very typical properties for lower redshift (z∼2) sub-millimeter galaxies (SMGs) and thus is very likely one of the long sought after high redshift (z>4) objects of this population. The large CO(4-3) line width taken together with its highly disturbed rest-frame UV geometry suggest an ongoing major merger about a billion years after the Big Bang. Given its large star formation rate (SFR) of $> 1000\,M_\odot, yr^{-1}$ and molecular gas content this object could be the precursor of a 'red-and-dead' elliptical observed at a redshift of z=2.

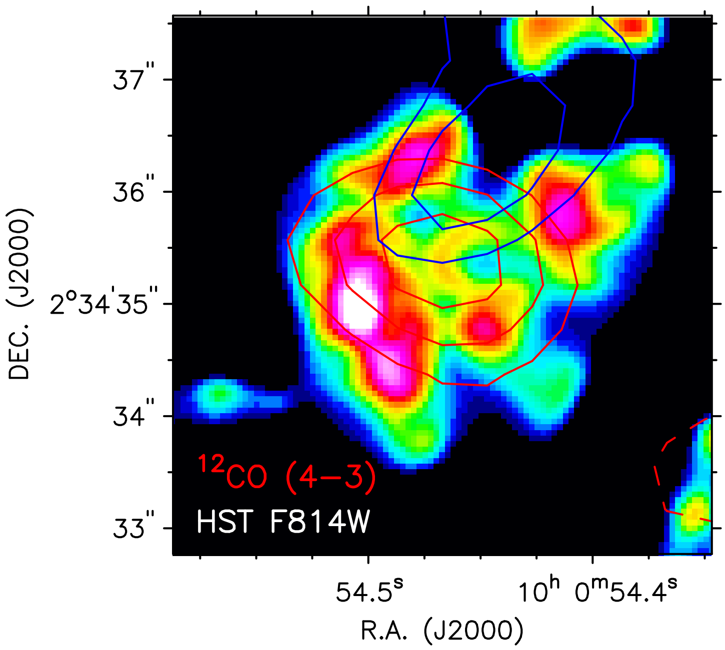

Figure 2: *Integrated red- and blueshifted CO(4-3) line emission in contours overlaid on the adaptively smoothed HST ACS/F814W image of J1000+0234. A motion from southeast to northwest is apparent with an offset of ∼1" (∼ 6.6 kpc) between the peaks of the red- and blueshifted emission. The contours start at 2σ in steps of 1σ with 1σ = 0.085* Jy $beam^{-1}$ km s^{-1} *and 0.084* Jy $beam^{-1}$ km s^{-1} *for the red- and blueshifted line emission, respectively. The object ∼ 0.5" west of the CO emission is a foreground galaxy at z=1.41*

Collaborators are C.L. Carilli (NRAO), V. Smolčić (CalTech), P. Capak (CalTech/SSC), F. Bertoldi (AIfA), N.Z. Scoville (CalTech) and the COSMOS team.

References

[1] Schinnerer et al. 2008, ApJL, 689, L5

Dynamical Dark Energy simulations: high accuracy Power Spectra at high redshift

Andrea V. Macciò

Time evolution of Dark Energy

There seems to be little doubt left that a Dark Energy (DE) component is required to account for cosmological observables. Its first evidence came from the Hubble diagram of SNIa, showing an accelerated cosmic expansion, but a *flat* cosmology with $\Omega_m \simeq 0.25$, $\Omega_b \simeq 0.04$ and $h \simeq 0.7$ is now required by CMB and LSS data and this implies that the gap between Ω_m and unity is to be filled by a smooth non–particle component. If DE evidence seems sound, its nature is perhaps the main puzzle of cosmology. Aside of a cosmological constant Λ, possibly related to vacuum energy, and a scalar self–interacting field ϕ, various pictures have been recently discussed, ranging from a supposed back–reaction of inhomogeneity formation to GR modifications and including even more exotic alternatives. In most of these cases, a DE component, with a suitable $w(a)$ state parameter (a: scale factor), can still be an *effective* description, and a number of observational projects have been devised, aiming first of all at constraining $w(a)$ (e.g., the DUNE–EUCLIDE project, Refregier et al. 2008, arXiv 0802.2522). Some of these studies are likely to be realized in the next decade(s) and, to interpret their outcomes, we need accurate predictions for selected observables. In particular, to fully exploit weak lensing surveys, we need predictions of non–linear power spectra, accurate to $\sim 1\%$.

This calls for high precision simulations, covering the whole functional space of $w(z)$ state equations and taking also into account the admitted ranges of other cosmological parameters; surely a difficult task. A procedure was however suggested, able to match the spectra at $z = 0$, up to $k \sim 3\,h\mathrm{Mpc}^{-1}$, in cosmologies with an (almost) arbitrary $w(z)$, by making use of the results of N–body simulations with $w = \mathrm{const.}$ In this paper we extend such a procedure to high redshift and test our approach through a series of N–body gravitational simulations of various models, including a model closely fitting WMAP5 and complementary data. Our approach detects $w = \mathrm{const.}$ models, whose spectra meet the requirement within $1\,\%$ at $z = 0$ and perform even better at higher redshift, where they are close to a permil precision.

Numerical Simulations and Results

In this paper we run a series of simulations for two cosmological models: (i) a model where $w(a)$ is a polynomial; (ii) a SUGRA model. SUGRA models are an alternative example of a fastly varying state equation; they are true dDE models, where DE is a scalar field ϕ, self–interacting through a SUGRA potential

$$V(\phi) = (\Lambda^{\alpha+4}/\phi^{\alpha}) \exp(4\pi\phi^2/m_p^2), \tag{1}$$

admitting tracker solutions and hence able to solve the fine tuning problem. The aim of our paper is to show that at *any* given redshift ($\bar{z}$) it is always possible for *any* model with an arbitrary dependence on redshift of the equation of state ($w(z)$) to find a model with $w(z) = \mathrm{const.}$ that shares the same power spectrum at $\bar{z}$. This means that for any arbitrary DE model it is always possible to calculate analytically its expected power spectrum (at any redshift) once we know how to map this model into its *auxiliary* model with $w(z) = \mathrm{const.}$ We find that the constant-w model that approaches the power spectrum of the true dark energy model (SUGRA in our case) at a given redshift $\bar{z}$ should share the following parameters with the original model: $d_{\mathrm{LSB}}(\bar{z})$, $\sigma_8(\bar{z})$, $\omega_c(\bar{z})$ and $w_b(\bar{z})$. Where d_{LSB} is the distance last scattering band, σ_8 is the rms of the matter fluctuations smoothed on a scale of 8 Mpc and $\omega_{c,b}$ are the reduced density parameters of dark matter and baryons. We call this requirement the *weak requirement* (W.R. hereafter, see [1] for more details). The main results of this work are described in the Figure 1, where we show the ratio between power spectra for the SUGRA model and the corresponding auxiliary models $\mathcal{W}(z_k)$. Even at small scales ($k \sim 1$) the differences between the two spectra are as low as 1%, with an average difference around 0.3%.

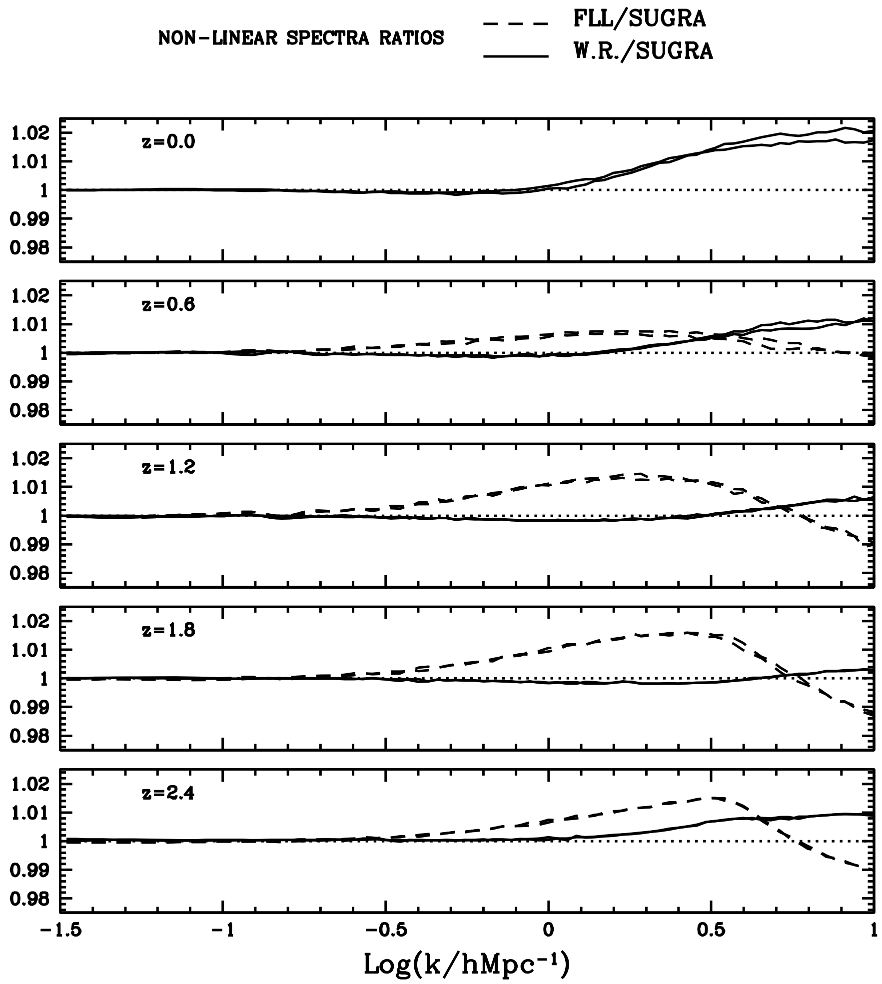

Figure 1: *Ratio between power spectra for the SUGRA model and the corresponding auxiliary models at several reshifts.*

- By using the *"weak requirement"* condition described in this paper, we show that even spectra of models with rapidly varying $w(a)$ are easily obtainable from constant–w spectra. Preliminary evaluations on the possible efficiency of observational techniques probing high redshift spectra, as the planned DUNE–EUCLID experiment, should be reviewed and possibly improved on the basis of the above conclusion.

Collaborators are Luciano Casarini (Univ. Milano) and Silvio Bonometto (Univ. Milano) Most numerical simulations were performed on the PIA cluster of the Max-Planck-Institut für Astronomie at the Rechenzentrum in Garching.

References

[1] Casarini, L., Macciò, A.V., Bonometto, S. 2009, JCAP, 03, 014C

11 Instrumentation

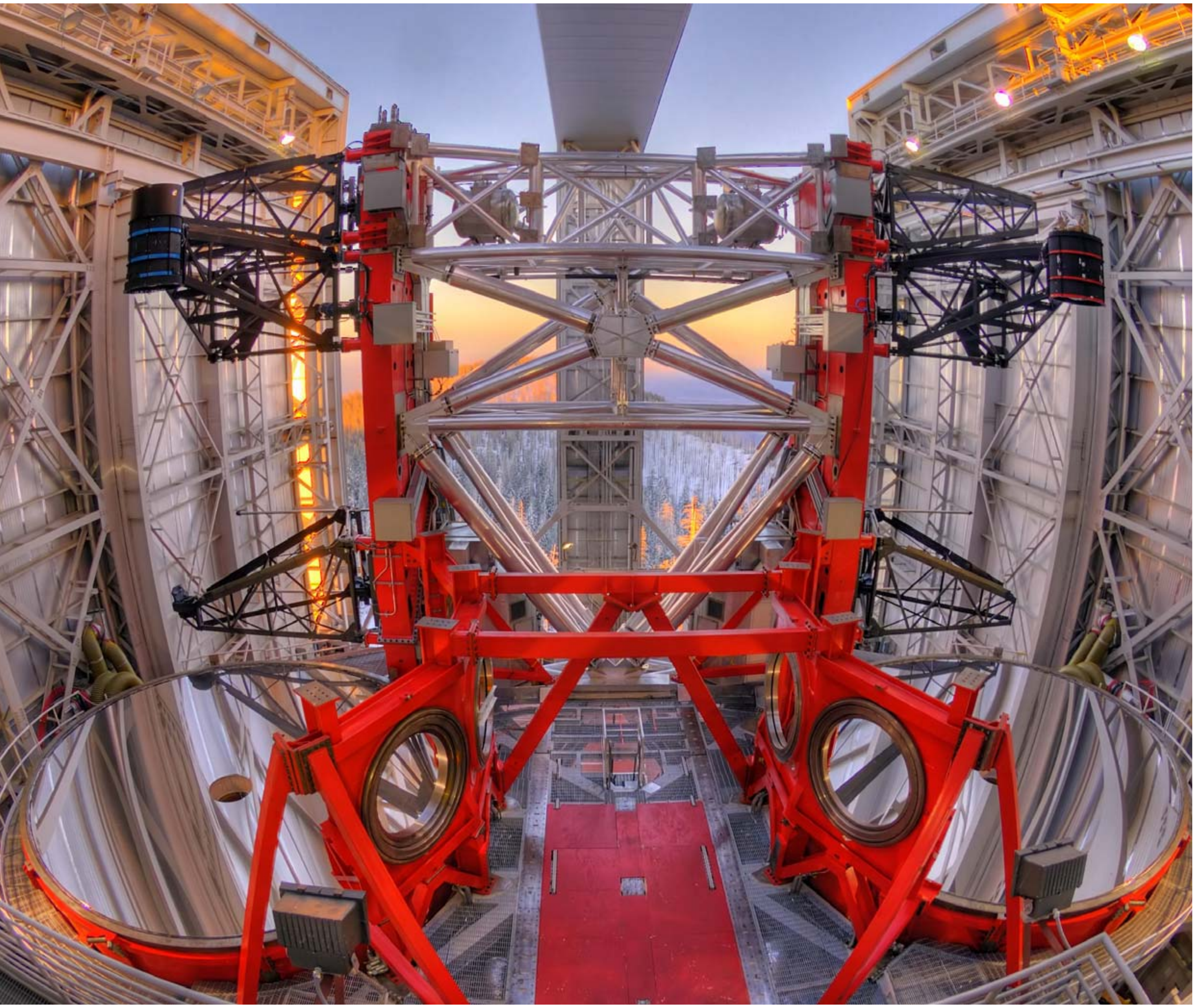

Image on previous page:
The Large Binocular Telescope (LBT) with its two 8.4m main mirrors.
Credit: Marc-André Besel, Wiphu Rujopakarn

METIS, a Mid-Infrared instrument for the E-ELT

Rainer Lenzen, Wolfgang Brandner, Thomas Henning, Stefan Hippler, Vianak Naranjo, Ralf-Rainer Rohloff

Overview

METIS is the name of the '**M**id-infrared **ELT I**mager and **S**pectrograph', the only E-ELT instrument to cover the thermal/mid-infrared wavelength range from 3 – 14 µm. Following an ESO call for proposal, an international team of experts has just (November 2009) finished a phase-A study on observational capabilities and technical feasibility of such an instrument.

The METIS consortium consists of five partner institutions from Germany, Netherlands, France, the United Kingdom, and Belgium. The METIS Science Team consists of two members per partner country, and two adjunct members. In addition, about 25 scientists from within Europe, the United States and Australia have contributed to the science case for METIS.

Science case

The E-ELT with its 42m aperture will undoubtedly open up new perspectives for optical/infrared astronomy. It will not only enable observations of fainter and fainter targets – scaling sensitivity from the VLT to the E-ELT – but also new kinds of observations that have never been possible before. These new perspectives include the thermal and mid-IR range beyond 2.5µm.

The mid-infrared wavelength range is extremely rich in spectral diagnostics, which are complementary to diagnostics found at other wavelengths. It contains emission and absorption lines of virtually all molecules, numerous atoms and ions, and unique solid state features. One of the main METIS science cases MPIA is especially interested in is the study of proto-planetary discs and exo-planets. The large diversity of exo-planetary systems belongs to the most surprising findings in comparative exo-planet research. The origin of this diversity must lie in the structure and evolution of proto-planetary disks out of which they form. The exact process that led to the formation of these planets is largely unknown. METIS will allow us to spatially resolve protoplanetary disks in the mid-IR, to search for the footprints of protoplanets as well as to perform spectral line imaging and spectro-astrometry. METIS may be able to directly detect the signatures of hot, accreting protoplanets and the dynamical structure of the accretion flow onto the planet. The observations will allow us to target the dominant mechanisms for gas dissipation and the chemical content of the planet-forming regions with a statistically significant sample, and clarify the role of water and organic molecules, which are of astrobiological interest.

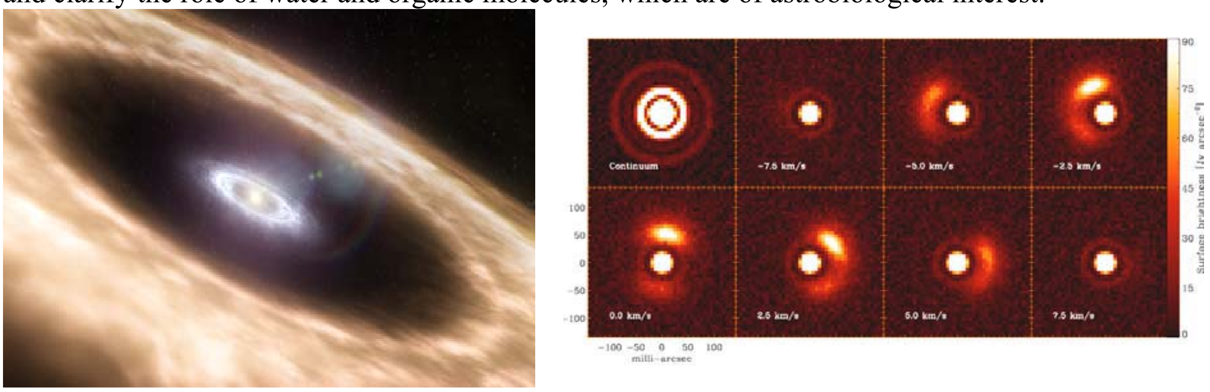

Figure 1: Left: Artist's impressions of a proto-planetary disk showing planet formation (© ESO). Right: Simulation of a METIS image cube of the CO P(8) line from SR 21 for an assumed distance of 125 pc (Pontoppidan et al. 2009).

Description

METIS will add special extremely high spatial and spectral observational capabilities to the existing or planned (JWST) facilities in the mid-infrared wavelength region. The instrument baseline includes the following two main subsystems:

1. A diffraction limited **imager** at L/M, and N band with an approximately 18″×18″ wide FOV and pixel sizes of 17mas and 34mas, respectively. The imager also includes the following observing modes:
   - **coronagraphy** at L and N-band
   - low-resolution (R ≤ 5000) **long slit spectroscopy** at L/M and N band
   - **polarimetry** at N-band.

   Long slit spectroscopy is realized by infrared grisms that can be inserted into the collimated beam. L/M-band and N-band imaging is provided in parallel.
2. An IFU fed, **high resolution spectrograph** at L/M [2.9 – 5.3μm] band. The IFU field of view shall be about 0.4″×1.5″, and the spectral resolution is R ~ 100,000. The small central FOV is picked up near the focal plain, thus, the surrounding FOV can be used in parallel by the imager module.

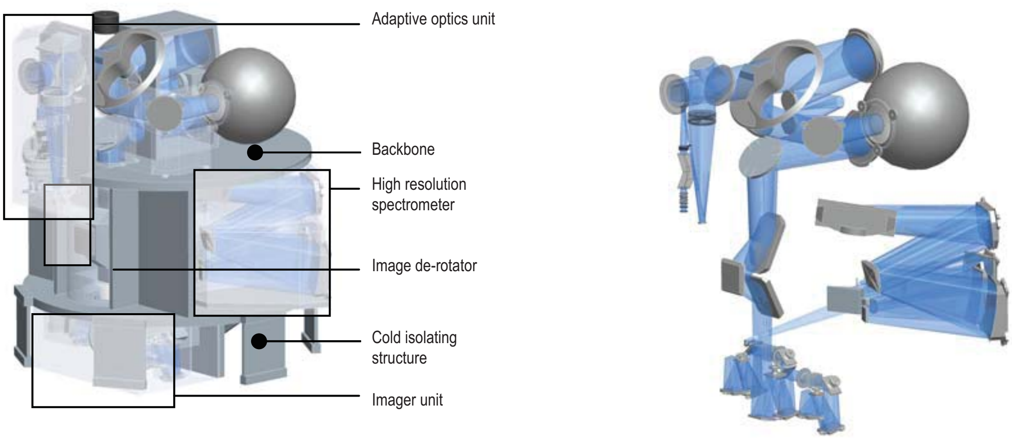

Figure 2: Overview of the packaging of METIS modules into a common cryostat.

The deformable mirror of the E-ELT adaptive optics system is part of the telescope itself, however, for mid-infrared application a special wavefront sensor is planned that will be part of METIS. This allows on-axis NGS AO-operation without adding thermal background by a warm dichroic mirror.

MPIA as one major partner of the METIS project will be responsible for the MIR imager and the wave-front sensor. As soon as METIS will be selected as a first generation instrument for the E-ELT, the METIS team will start developing this exiting observational capability to be prepared to receive first light with a 42m-telescope in 2018.

References

[1] Hippler et al., *Characterization of Exoplanets and Protoplanetary Disks with the proposed E-ELT Instrument METIS*, AIP Conf. Proc. vol. 1158, pp. 333-336 (2009)

The AstraLux Sur Lucky Imaging Instrument at the NTT on La Silla

Stefan Hippler, Carolina Bergfors, Wolfgang Brandner, Sebastian Daemgen (MPIA, ESO), Thomas Henning, Felix Hormuth (MPIA, Calar Alto Observatory), Armin Huber, Markus Janson (Department of Astronomy, University of Toronto, Canada), Boyke Rochau, Ralf-Rainer Rohloff, Karl Wagner

Overview

In July 2006 we installed the Lucky Imaging instrument ASTRALUX at the 2.2-metre telescope of the German–Spanish Astronomical Center at Calar Alto (Hormuth et al., 2007; 2008). The simplicity, robustness and great success of this instrument — around 10 publications so far — resulted, in autumn 2007, in the idea of building a copy of the instrument for the 3.5-metre New Technology Telescope (NTT) at the La Silla Observatory in Chile. In May 2008, eight months after the starter's gun fired, we shipped the heaviest piece of the instrument, now christened AstraLux Sur, to Chile. The 225 kg adapter flange was especially designed for the NTT adapter/rotator counterpart. Accompanied by the camera mount, filter wheel, Barlow lens, an electron multiplying, thinned and back-illuminated CCD (model Andor iXon$^+$), four computers and an electronic rack, everything arrived safely at the observatory. The instrument is sensitive in the visible spectrum and deploys the Lucky Imaging technique with nearly-diffraction-limited performance (~ 0.1 arcseconds) in I'-band and z'-band. The instrument provides a field of view of 16 x 16 arcseconds with a pixel scale of 31 mas.

First light of AstraLux Sur took place on the night of 19 July 2008. The first light target was the ~ 0.7 arcsecond binary system γ Lupi. Even though the observing conditions were rather poor and the NTT was closed for most of the night, with the exception of about half an hour, we could perform basic instrument tests. The opto-mechanical interface with the telescope, as well as our computing equipment, worked as expected.

In summary, after the first two observing runs in 2008, the performance of AstraLux Sur is as expected, in terms of Strehl ratio, but obviously slightly worse than its sister instrument at the 2.2-metre telescope on Calar Alto on account of the larger telescope diameter. The full diffraction limit was reached in I'-band with a FWHM of ~ 50 mas. In general an angular resolution of around 150 mas was achieved in I'-band and z'-band. This is slightly worse than our result on the 2.2-metre telescope at Calar Alto. To understand this behaviour, one should ask if there is an ideal combination of telescope diameter, seeing and filter bandpass for Lucky Imaging. It has been shown by Hecquet & Coupinot (1985) that the Strehl resolution, R, reaches its maximum at $D/r_0 = 7$ if the best 1% of short exposures are selected. The Strehl resolution is defined as the product of the Strehl ratio and the ratio of the telescope diameter to the wavelength squared. The Strehl resolution is a measure of the image quality, including both the Strehl ratio and the image resolution, roughly corresponding to terms like contrast and sharpness. Both higher and lower values for D/r_0 than the supposed optimal value of 7 lead to a loss of image quality. If the telescope diameter is increased at a fixed r_0, equivalent to fixed wavelength and seeing conditions, then the probability for a Lucky Image will decrease, leading to a smaller resulting Strehl ratio. If the telescope diameter is decreased, the higher resulting Strehl ratio is achieved at the cost of image resolution.

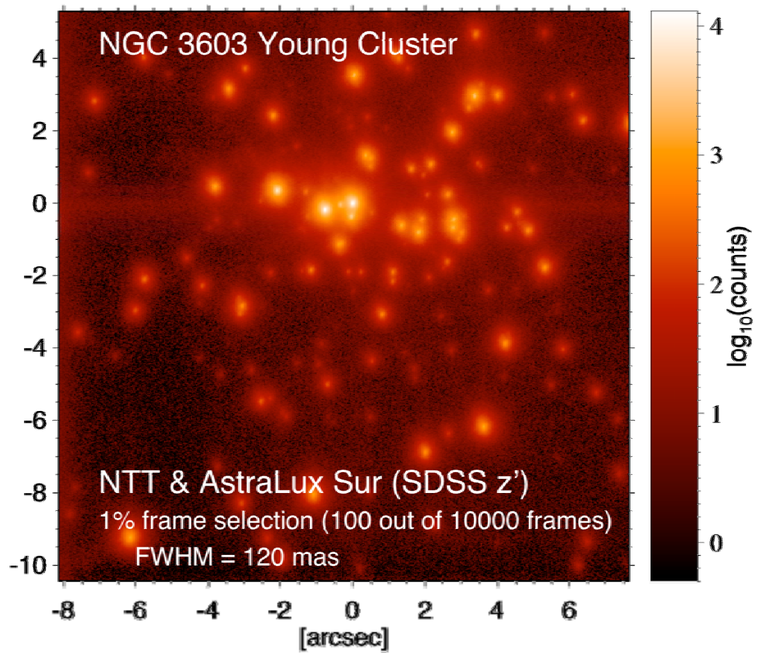

Left: *The AstraLux Sur commissioning team, from left to right: Stefan Hippler, Wolfgang Brandner and Boyke Rochau in July 2008. The AstraLux Sur instrument is attached to the aluminum adapter flange, which itself is connected to the NTT Nasmyth adapter/rotator.*
Right: *The core of the Galactic starburst cluster in the giant HII region NGC 3603, which serves as one of our astrometric calibration targets, as seen by AstraLux Sur in the SDSS z' band at the NTT. The 1% image selection (100 out of 10 000 frames) yields a resolution (FWHM) of 120 mas.*

Science case

With the AstraLux Sur instrument at the NTT visitor focus, we achieved nearly-diffraction-limited imaging performance in the SDSS I'- and z'-band filters, a wavelength range not accessible with other ground-based high-resolution (adaptive optics) instruments. In Period 81 we initiated three science programmes at the NTT with AstraLux Sur. The first programme is a second epoch follow-up of T Tauri binary and multiple systems, which were originally discovered some 15 to 20 years ago. The second epoch observations obtained with AstraLux Sur test if the individual components of each system have a common proper motion, and hence are gravitationally bound. In addition we will derive first estimates of orbital periods and system masses of a statistically significant sample of T Tauri stars. The final observations for this programme were obtained in March 2009, and the analysis has just been completed and we are preparing the findings for publication. A survey of about 800 young, active M dwarfs in the Solar Neighborhood aims at improving binary statistics, identifying very low-mass and substellar companions, finding systems suitable for dynamical mass determination, and establishing a sample of M dwarf binaries suitable for future astrometric exoplanet searches with GRAVITY at the VLT Interferometer. The final observing run for this programme is scheduled for Jan/Feb 2010. A third observing programme surveys transiting exoplanet host stars with the aim of identifying close binary companions. If unresolved, such binary companions bias the determination of planetary parameters from the light curve (see, e.g., Daemgen et al., 2009, for first results obtained with the Northern AstraLux camera). A number of previously unrecognized binary companions were indeed discovered with AstraLux Sur, and the data are currently being analyzed.

References

[1] Hippler et al., *The AstraLux Sur Lucky Imaging Instrument at the NTT*, The Messenger, vol. 137, p. 14-17 (2009) and references therein.

Gravity – interferometric phase referenced imaging and microarcsecond astrometry

Wolfgang Brandner, Stefan Hippler, Ralf Klein, Natalia Kudryavtseva, Rainer Lenzen, Vianak Naranjo, Udo Neumann, Jose Ramos, Ralf-Rainer Rohloff

Overview

This instrument is an adaptive optics assisted second-generation instrument for the VLTI. It will combine the light from all four 8 m Unit Telescopes of the VLT for interferometric phase referenced imaging with a resolution of 4 milli-arcsec, and for narrow-angle astrometry with an accuracy of 10 micro-arcsec for objects as faint as K=20 mag. Gravity will take advantage of the unique 1.7 arcsec diameter field of view of the VLTI. By measuring the angular separation of two objects located within this field, the astrometric accuracy should be improved by a factor of up to 10 beyond the present goal for Prima. To achieve this, GRAVITY will be assisted by adaptive optics. After passing its Phase A review at the end of 2007, the Phase B review will occur in December 2009. First light of GRAVITY at the VLTI is foreseen for 2014. Four partners are developing the instrument:
Max Planck Institute for Extraterrestrial Physics (Principal Investigator Institute), Phase (itself a consortium of French Institutes, including Observatoire de Paris and Observatoire de Grenoble), University of Cologne, and MPIA. MPIA is developing the infrared wavefront sensors as a major instrumental component for GRAVITY. While the interferometric instrumentation of GRAVITY will be in the VLTI laboratory, the near infrared wavefront sensors are located closer to the unit telescopes in order to optimize their sensitivity towards fainter targets. A total of four near-infrared wavefront sensors will be built, one for each of the Coudé rooms of the four Unit Telescopes.

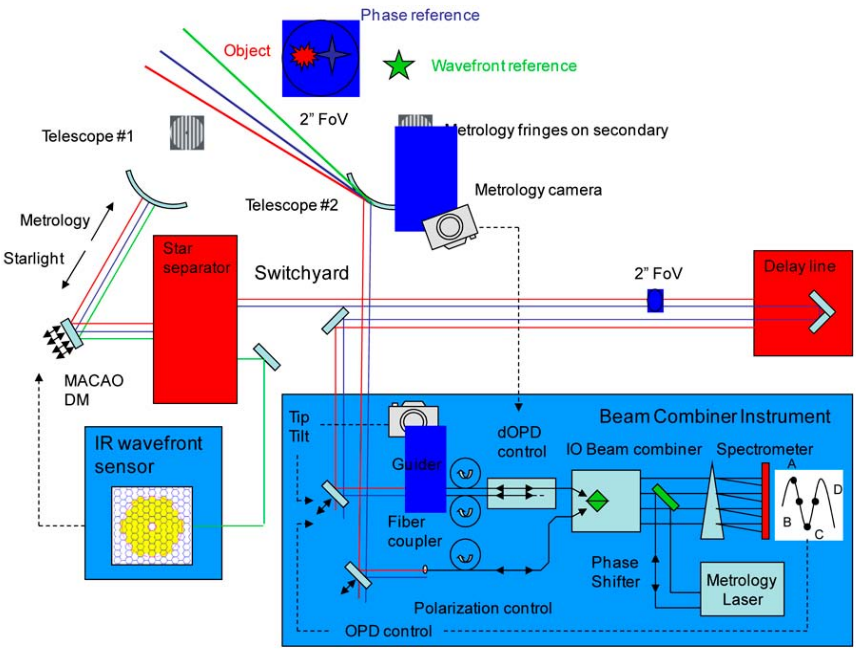

Working principle of GRAVITY

The working principle: NIR-AO, fringe-tracking & dual-feed interferometry
GRAVITY provides four H+K-band infrared wavefront sensors, located at the Coudé rooms of the UTs. Their signal will be used to command the existing MACAO deformable mirrors. The system will compensate atmospheric turbulence and can work on either of the two beams after the star separators. The delay-line induced high-frequency tip/tilt and pupil errors are corrected by means of a laser guiding system. The laser beams are launched at the star separators and trace the optical path down to the beam

combiner instrument. Low frequency drifts of the field and pupil will be measured and corrected with a dedicated acquisition camera. The interferometric instrument will only use the K-band light of one of the two beams. The two objects (fringe-tracking star and science object) for the dual feed thus need to reside within the 2" interferometric field of view. The light of the 4 x 2 objects is coupled into 8 optical fibers for modal filtering, compensation of differential delay and adjustment of polarization. The fibers feed two integrated optics beam combiner, the output of which are two spectrometers. A low-resolution (5-pixels) spectrometer provides internal phase- and group-delay tracking on a bright reference star, so that long integrations become possible on a faint science object. Three spectral resolutions are implemented and a Wollaston prism enables basic polarimetry. The internal path lengths are monitored with a dedicated metrology system, covering the complete path from the beam combiner up to the spider arms of M2 above the primary mirror.

Science case

The defining science case for gravity is an astrometric study of the close environment of the supermassive black hole in the center of the Milky Way. With an accuracy of 10 micro-arcseconds, gravity will be able to study orbits of stars and disk flares as close as a few times the Schwarzschild radius of the black hole, and hence test General Relativity in its strong field limit. MPIA's main science interests include an in-depth study of young, massive starburst clusters with the aim to derive precise masses for the most massive stars, study cluster dynamics, and search for intermediate mass black holes potentially hidden in the very centers of these clusters. In addition, we intend to survey very low mass stars in the solar neighborhood for planetary mass companions.

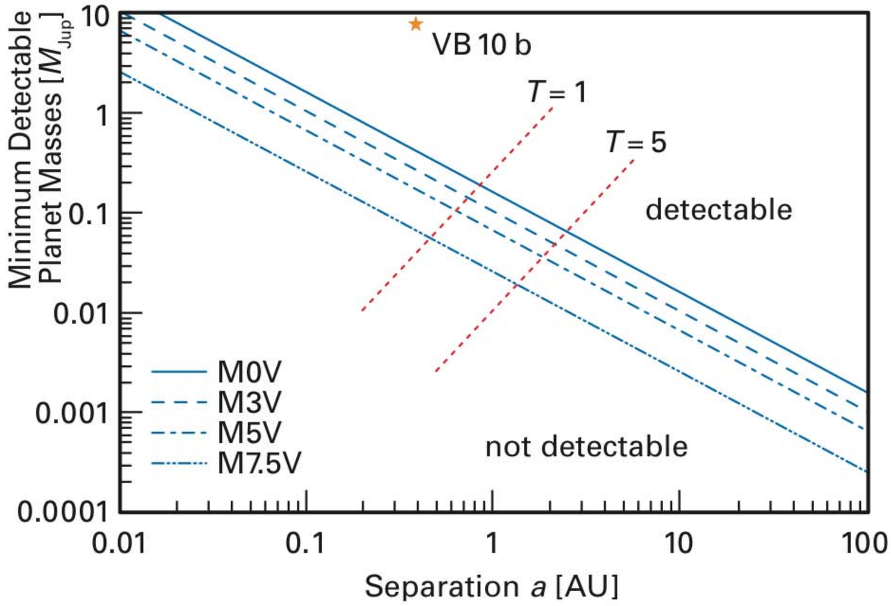

GRAVITY exoplanet detection capabilities around late-type and very-low-mass stars at a distance of 6 pc as a function of semimajor axis of the planet orbit, and for a range of stellar masses between 0.1 (M7.5V) and 0.5 (M0V) times the mass of the Sun. For reference, the location of recently announced exoplanet candidate VB10b, which was also detected by astrometry (Pravdo and Shaklan 2009, astro-ph/0906.0544), is indicated. The two dotted lines indicate the detection limits for a 1 year survey (T □ 1) and a 5 year survey (T □ 5). In a 5 year survey, gravity might be able to detect exoplanets below 10 Earth masses.

References

[1] Eisenhauer, Perrin, Brandner et al., Science with the VLT in the ELT Era, Astrophysics and Space Science Proceedings, Volume . ISBN 978-1-4020-9189-6. Springer Netherlands, 2009, p. 361, and references therein.

SPHERE on track for first light in 2011

Markus Feldt, Alexey Pavlov, Ole Möller-Nilsson, Joe Carson, Christian Thalmann, Thomas Henning

The SPHERE Project

SPHERE Spectro-Polarimetric High-contrast Exoplanet REsearch is a project that results from an idea conceived in 2001 at the ESO workshop on 2nd generation VLT and VLTI instrumentation. On this workshop, the conceptual idea of a Planet Finder instrument for the VLT was presented. After two independent phase-A studies the final consortium formed with institutes from France (PI: Laboratoire d' Astrophysique de Grenoble, LAOG), Germany (Co-PI: MPIA), Italy, Switzerland and the Netherlands. The instrument concept is shown in Fig. 1, it consists of the high-performance AO system SAXO (SPHERE Adaptive optics for eXoplanet Observation), and the advanced coronagraphic devices, the NIR dual-band imager IRDIS, the visual differential polarimeter ZIMPOL, and the NIR 3D spectrograph IFS. The specifications on all parts of SPHERE are extremely tight, the goal for the final wave front error on the coronagraphic focal plane is below 36 nm rms. the final closed-loop Strehl ratios achieved on the focal plane detectors being 84% for IRDIS (at 1600 nm), 74% for IFS (at 1300 nm), and 46% on ZIMPOL (at 800 nm). Tight specifications are also put on other quantities, e.g. the accuracy with which the flat field sensitivity of the NIR detectors, 2 Teledyne HAWAII 2RG arrays, needs to be known: 1%, goal 0.1%. It is in fact this flat field error, that, together with residual static aberrations, will in the end determine the limit of planet detectability.

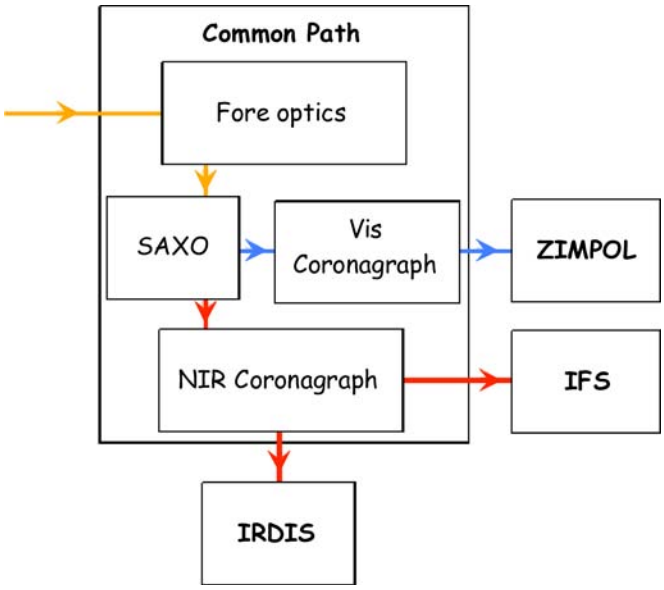

Figure 1: *Instrument concept of SPHERE.*

On Track for First Light

After PDR was passed in 2007 and FDR in 2009, construction of the instrument has now commenced. MPIA's responsibilities in terms of hardware include the SPHERE's two atmospheric dispersion correctors (ADCs), the most expensive parts in the common path, the detector motion stage for IRDIS which will enable lateral shifting of the detector in the focal plane to increase flat field accuracy, and the procurement of the 40×40 lenslet array, the heart of the adaptive optics system (Fig. 2).

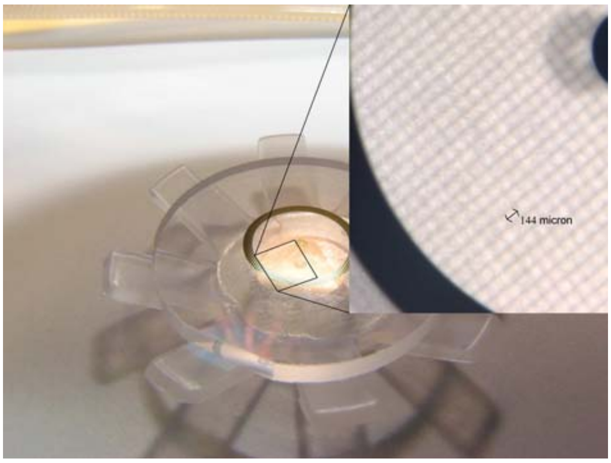

Figure 2: *The 40×40 lenslet array for SAXO.*

An important and well-progressed part of SPHERE is also the data reduction and analysis software, where MPIA is the prime responsible. Unlike any previous instrument, the SPHERE pipeline system consists of 79 so-called recipes[1], a tribute to the enormous calibration effort that will be made when operating SPHERE[2, 3]. For a comparison note that the most complex instrument in terms of calibration so far, the "Visible and wide field imager and multi-object spectrograph" (VIMOS) uses 23 recipes. Prototypes of data reduction pipelines for all three focal plane instruments are already implemented as prototypes and are currently undergoing heavy testing and verification on simulated and early detector characterization data.

The pipeline and the rest of the project are currently on schedule according to the project plan, which foresees first light in 2011.

Primary collaborators in this project are Jean-Luc Beuzit (PI, LAOG), David Mouillet (LAOG), Kjetil Dohlen and Maud Langlois (Laboratoire d'Astrophysique de Marseille), Raffaele Gratton (Osservatorio di Padova), Hans-Martin Schmid (ETH Zürich), and Rens Waters (University of Amsterdam).

References

[1] Pavlov, A.; Feldt, M.; Henning, Th., 2008, ASPC 394, 581

[2] Pavlov, Alexey; Möller-Nilsson, Ole; Feldt, Markus; Henning, Thomas; Beuzit, Jean-Luc; Mouillet, David, 2008, ProcSPIE 7019, 109

[3] Feldt, Markus; Möller-Nilsson, Ole; Pavlov, Alexey I.; Beuzit, Jean-Luc; Mouillet, David; Gratton, Raffaele; Langlois, Maud; Joos, Franco, 2008, ProcSPIE 7019, 100

PYRAMIR

Diethard Peter, Markus Feldt, Stefan Hippler, Thomas Henning

Introduction

Overcoming the atmosphere's perturbing influence on astronomical observations, namely the distortion of the wavefronts of the incoming starlight by the means of adaptive optics (AO) relies on two key elements: the wavefront sensor (WFS), and the deformable mirror (DM) serving as wavefront corrector. This work is concerned with a relatively new type of WFS, the pyramid wavefront sensor (PS). The WFS imposes one main limitation on the AO system: Its working principle and its detector determine the minimum number of photons needed for the analysis of the incoming wavefront in each cycle of the correction loop. This means in turn that it sets the limiting magnitude for the natural guide star required by every AO system, and thus ultimately the sky coverage that can be achieved with the system. It was in this respect, that the PS was predicted by Ragazzoni to act superiorly when compared to a traditional Shack-Hartmann wavefront sensor. The benefit arises especially in a predicted higher suppression of low order modes by the pyramid based system compared to a Shack-Hartmann sensor (SHS) based system. However, a rigorous testing of such a system on sky and a comparison to theory and simulations is still missing. To close this gap we performed on-sky measurements and corrections with our near-infrared PS system PYRAMIR [1] as part of the ALFA AO system on the 3.5m telescope of the Calar Alto Observatory.

On-sky results

During several nights we tested the quality of correction for guide stars of different brightness. We were able to close the loop even under bad (i.e. seeing $\geq 1.''3$ at K') sky conditions.

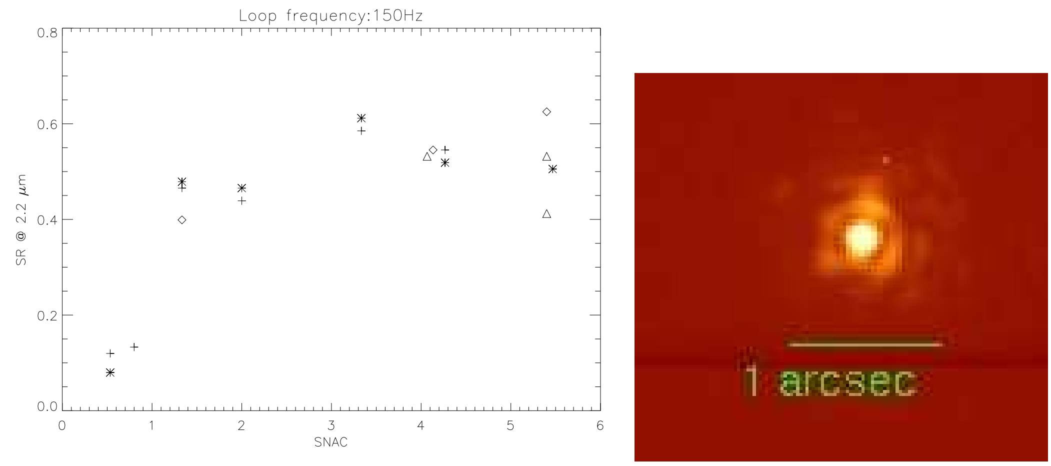

Figure 1: *Left panel: Closed-loop performance (150 Hz, seeing* $0.''6$*, wind speed 3–4 m/s) in dependence of the SNAC obtained during our observations in September 2007. The different symbols denote: Cross: 12 modes , asterisk: 22 modes , diamond: 32 modes, and triangle: 42 modes corrected. Right panel: AO corrected image on Omega Cass. The Strehl ratio is 0.37.*

In Figure 1, left panel, the performance of the WFS is plotted against the signal-to-noise per aperture per loop cycle (SNAC). We use this quantity as the performance of a WFS and/or an entire AO system in a specific set-up critically depends on the incoming flux from the guide star.

The guide star flux results in a certain signal-to-noise ratio measured on the WFS's detector in each aperture in each loop cycle, which in turn governs the overall error of the wavefront determination. Thus the SNAC is the detector and system-independent quantity that should be kept constant when comparing fundamental WFS principles.
We can achieve a maximum SR of 63% in K-band. This stays up to a SNAC of about 3.5 (corresponding to 4.3 mag), then it drops continuously until a limiting SNAC of 0.4 (6.7 mag) in K-band. An example of an AO corrected image is shown in the right panel of Fig.1.

Comparison with the Shack Hartmann sensor

To see the superiority of the PS over the SHS we compare the power spectral density (PSD) of the wavefront after correction by the ALFA system based on the SHS with the PSD after correction by the same system but based on PYRAMIR.
Figure 2 shows the PSD in the case of the faint star for the SHS and PYRAMIR respectively. The PYRAMIR data is plotted as solid line, the SHS data as dashed-dotted line. The mean high order rms is similar for SHS and PYRAMIR but the peak of the curve is smaller for the PS. Thus we can conclude that a PS based system better corrects the low frequencies compared with the SHS based system.

With the demonstrator PYRAMIR we were able to close the AO loop even under bad sky

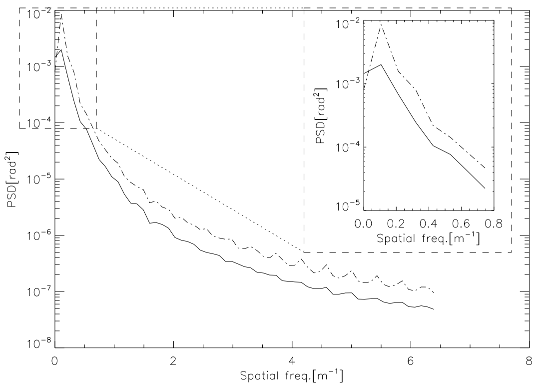

Figure 2: *Circularly averaged PSD for PYRAMIR and the SHS in the faint star regime. The inlay zooms on the regime of the lowest frequencies. In the case of PYRAMIR the loop was closed with 42 modes at 150 Hz. The SNAC was 0.4. PYRAMIR data is plotted as solid line, SHS data as dashed-dotted line. Especially the low frequencies (see inlay) are better suppressed by PYRAMIR.*

conditions. Under good conditions and for bright stars we reached Strehl ratios of ≥ 0.6. A comparison with the ALFA SHS confirmed the theoretical prediction that the PS better suppresses low spatial frequencies and is thus superior to the SHS.
Collaborators are Jesus Aceituno, Luzma Montoya (Calar Alto Observatory, Spain), and Bernhard Dorner (CRAL, France).

References

[1] Peter, D. et al., 2008, PASP, 120, 872

[2] Peter, D. et al., 2010, PASP, accepted

ARGOS - Advanced Rayleigh Ground layer adaptive Optics System

Wolfgang Gaessler (Co-I), Diethardt Peter, Thomas Blümchen, Jose Borelli

The LBT Laser Guide Star Facility

In November 2006 a workshop in Florence launched an initiative to make a Laser Guide Star Facility for the LBT real. In March 2009 the project successfully passed the Preliminary Design review. Currently the team prepares for the Final Design Review in March 2010. The goal defined was to improve the wide field capabilites of LUCIFER for Multi-Object-Spectroscopy and Imaging. The project should focus on a prompt implementation of a ground layer Adaptive Optics System, which provides operability significant over median seeing. The system should be reliable, low maintenance and of reasonable in cost. A strong requirement was to minimize the impact to the telescope and LUCIFER. In addition the team was asked to identify upgrade paths to at minimum on-axis diffraction limited performance

MPIA is responsible for the overall software and control, including some software to reconstruct the Point Spread Function (PSF) at any position in the field from wavefront sensor data, as well as the calibration of the system. A deployable calibration unit is built to test and prepare the adaptive optics during day-time. It will deliver a valuable saving of rare night-time for astronomical observations and will improve the operability of the telescope.

System overview

The overall system consists of three Rayleigh laser system per eye of the LBT launched from the back of the Adaptive Secondary of each side. The lasers are focused at 12km providing a full sampling of the lower atmosphere. One Shack-Hartman wavefront sensor (WFS) for each eye is collecting the information of all three lasers on one low noise detector array. As the laser WFS

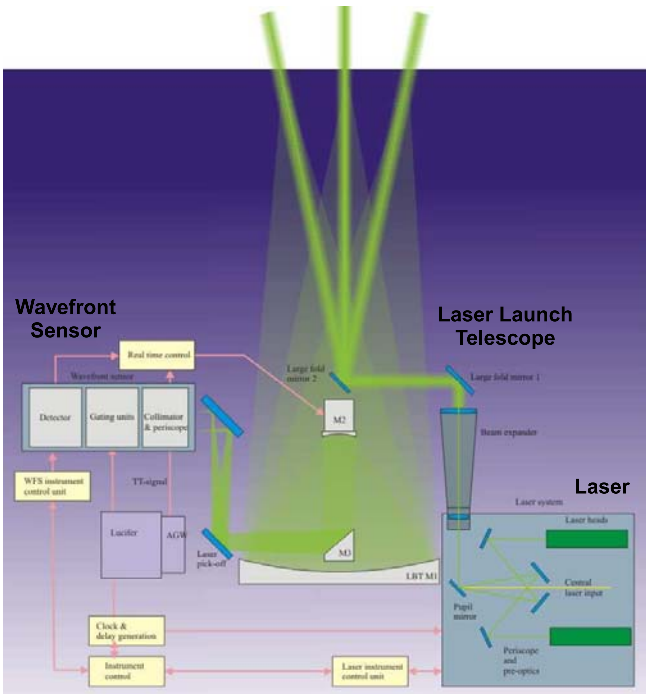

Figure 1: *Schematic of ARGOS.*

is not able to measure the atmospheric tip tilt modes an additional Tip Tilt Sensor is necessary - the existing natural guide star sensor.

1 Calibration Unit

The Calibration Unit allows for day and night time testing and calibration of ARGOS remotely and in short time. The novel concept is shown in Figure 2. It provides an artificial on axis source out of the Adaptive Secondary reflected by the front lense of the calibration unit illuminating LUCIFER and an off-axis source launched through the refractive optic of the unit illuminating the LGS WFS. With the difference of both signals one can calibrate for the non common path errors. With the off-axis source one can also calibrate the interaction between sensor and actuator.

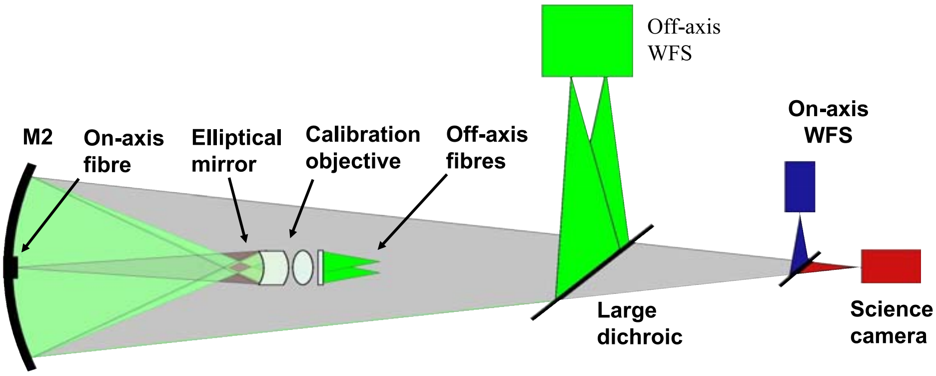

Figure 2: *Schematic of the ARGOS calibration unit.*

2 Point Spread Function (PSF) reconstruction over the field

The PSF on AO-corrected images varies over the field. These variations can contribute strongly to errors in photometry, astrometry, and spectroscopy, especially for larger fields. These variations can be reduced by deconvolution of the image with an accurate (angle depended) model of the PSF. The WFS data is a natural choice, as it delivers detailed and continuous information about the atmosphere simultaneously to the observation.

In the past, several algorithms of PSF retrieval have been proposed and tested. This includes on-axis PSF retrieval from WFS data as well as a correction over the field using a reference PSF. The schemes have been set up for both an AO system using a single natural guide star as well as a system using a laser beacon. For these algorithms to work, a detailed knowledge of the structure of the atmospheric turbulence, i.e. the Cn^2 profile, is crucial. For ARGOS the information for the lower atmosphere is gained from the WFS. The higher atmosphere will be measured with a DIMM/MASS instrument.

The goal of the reconstruction scheme is to gain a contribution of the PSF variation over the field to the photometric and astrometric error of only a few percent.

ARGOS is build in collaboration with the Max-Planck Institute für estraterrestreische Physik (MPE, PI: Sebastian Rabien), Instituto nazionale di astrofisica - Oservatorio astrofisico di Arcetri (INAF-OAA, Co-I: Simone Esposito), Center for astronomical adaptive optics - University of Arizona (CAAO, Co-I: Michael Lloyd-Hardt), Landessternwarte Heidelberg (LSW), Astrophysikalisches Institut Potsdam (AIP), Max-Planck Institut für Radioastronomie Bonn. The project acquired partially funding through the Framwork Program 7 (FP7) as part of OPTICON (Contract No. 226604).

LUCIFERI/II, two multi-mode instruments for the LBT

Rainer Lenzen, Werner Laun, Vianak Naranjo, Karl Wagner

Overview

In 2009, the first of two nearly identical NIR instruments for the LBT, Lucifer I and II, has been successfully commissioned at the Large Binocular Telescope (LBT). The complex systems consist in each case of a highly resolving infrared camera, a long-slit spectrograph, and a multi-object spectrograph – both instruments will be the central infrared devices on the LBT. The second Lucifer instrument should follow in about one year.

Figure 1: Lucifer I being attached to the LBT Gregorian focus.

Lucifer I/II is able to deliver infrared images and spectra both with seeing and diffraction limited angular resolution. The instrument will work at temperatures of less than 70 K. Essentially, the following observation possibilities are available:

- seeing-limited imaging
- diffraction-limited imaging with a field of vision of 0.5 x 0.5 square arc minutes
- long-slit spectroscopy (seeing- and diffraction-limited)
- multi-object spectroscopy (MOS) with slit mask

In addition, a differential imaging mode is in the preparatory phase for Lucifer II, which will be especially useful for studying exo-planets.

Changing the observational mode from direct imaging to spectroscopy takes place by swiveling the lattice unit (exchanging a flat mirror with a grating) and changing the focal mask (from field-limited mask to long-slit or multiple-slit mask). This swap of focal masks is realized by a complicated cryogenic robot system that picks up a certain focal mask out of a magazine and positions it into the focal plain. The mask magazine can be exchanged during daytime without cryo-cycling the instrument.

Project status

In 2009 several commissioning runs have been performed to test and optimize the interaction with the telescope. In addition, the local instrumentation team has been trained in maintaining and operating LUCIFER on the mountain. There is still one last commissioning run planned before the science demonstration time will start in December 2009. Even though the full adaptive optics supported resolution is not yet offered by the telescope, all observing modes have been successfully tested Possibly remaining non common path errors (below the seeing limit) can be taken into account and corrected by the AO system as soon as the deformable mirror will start its operation.

Lucifer II is currently being prepared by the MPE, in spring 2010 it will arrive at MPIA for final integration and testing phase. After acceptance in Europe end of 2010, it will be delivered to the telescope.

Figure 2: Three colour image of the star forming region S255. The field of view is 5.5x5.5 square arc minutes (dithered image, single FOV is 4x4 square arc minutes). Blue corresponds to H-band, green to H2(2.12µm) line and red to the K-band. Publication by Arian Bik et al. in preparation.

References

[1] Rainer Lenzen, Bernd Grimm, Tom Herbst, Werner Laun, Michael Lehmitz, Ralf-Rainer Rohloff, Clemens Storz, Karl Wagner, "Instruments for the LBT: Lucifer I/II: Two Multi-Mode Instruments for the Near-Infrared", MPIA Jahresbericht

LINC-NIRVANA: Interferometric imager for the Large Binocular Telescope

T. M. Herbst (PI), M. Kürster (Project Manager), H. Baumeister, T. Bertram, J. Berwein, P. Bizenberger, A. Böhm, J. Borelli, F. Briegel, M. Brix, F. DeBonis, S. Egner, R. Follert, W. Gässler, R. Hofferbert, F. Kittmann, L. Labadie, W. Laun, U. Mall, T. Maurer, D. Meschke, L. Mohr, N. Münch, V. Naranjo, A. Pavlov, J. –U. Pott, J. Ramos, H. –W. Rix, R. –R. Rohloff, E. Schinnerer, J. Schmidt, C. Storz, J. Trowitzsch, Xiangyu Zhang

LINC-NIRVANA (LN) is a Fizeau-type interferometric imaging instrument with Multi-Conjugated Adaptive Optics (MCAO) for the Large Binocular Telescope (LBT) in Arizona. Operating in the 1.0-2.4 μm wavelength range, LN will combine the light from the two 8.4 meter diameter primary mirrors of the LBT onto a single focal plane, producing panoramic imagery with a sensitivity corresponding to that of a 12-meter telescope and a spatial resolution that would normally require a 23-meter telescope. LINC-NIRVANA is a large (6x5x4.5 m) and complex device. In many ways, it is a precursor for the instrumentation for future Extremely Large Telescopes.

LINC-NIRVANA will sit at one of the shared, bent focal stations of the LBT, receiving light from both optical trains (Figure 1). LN uses visible wavelength sensors for wavefront control, correcting two atmospheric layers using the adaptive secondaries of the LBT and a pair of internal, high performance deformable mirrors. Near-infrared radiation from a star near the science field provides phase information for fringe tracking.

Figure 1 (left): *Computer rendering of LINC-NIRVANA (light grey enclosure at left-center) mounted on the shared instrument platform of the Large Binocular Telescope.*
Figure 2 (right): *Test fitting the large science-channel cryostat on the LINC-NIRVANA optical bench. Note the human figure for scale*

The instrument employs six visible wavelength detectors, two near-infrared arrays, and well over a hundred motorized functions. Such complexity and control is driven by the need to remotely operate what is essentially an interferometric laboratory in the focal plane of a large, moving telescope. To minimize risk, the LINC-NIRVANA team has developed a multi stage implementation plan, interspersed with science exploitation at each stage. This plan begins with small-field, on-axis adaptive optics using proven techniques, and proceeds through steadily more challenging operations to the ultimate goal: full, wide-field, MCAO interferometry.

The LINC-NIRVANA team continues to make good progress on the assembly, integration, and test (AIT) of the instrument in the laboratories at the MPIA, and in the facilities of our collaborators in Italy, Cologne, and Bonn (see Figures 2, 3). The AIT strategy is hierarchical, with individual components and sub-systems being completed and tested in individual, smaller laboratories, before being shipped to MPIA for integration and performance verification in the large assembly hall.
Although LINC-NIRVANA represents a fascinating technical challenge that will prepare us for the next generation of ELT instrumentation, science exploitation of the instrument remains the primary goal. The Design Reference Mission (DRM) science teams, together with the data reduction software groups in Bonn and Genova, have been performing realistic simulations to understand and optimize instrument performance. These simulation exercises have helped refine the LINC-NIRVANA science case, as well as streamline the observation preparation software and the observer interface. With the first light milestone approaching, we have also been working with the LN partners and the observatory in establishing access and publications policies for early science.
Preparation for interferometric operations continues at the LBT Observatory as well. Delivery of the first adaptive optics secondary mirror in 2010 represents a major milestone. With continued good progress, we anticipate shipping LINC-NIRVANA to the observatory in early 2013, with the goal of performing the first interferometric observations in the subsequent months

Figure 3: *Integration and test of the warm optics subsystem in the LBT Lab at MPIA. Completing and verifying these subsystems in a laboratory environment simplifies the eventual integration on the LINC-NIRVANA bench.*

Additional LINC-NIRVANA partners include INAF (Padova, Bologna, Arcetri, Rome, and the University of Genova), Cologne University, and MPIfR Bonn.

LBT infrastructure

Martin Kürster, Tom Herbst, Thomas Bertram, José Borelli, Armin Böhm, Mario Brix, Wolfgang Gässler, Torsten Leibold, Daniel Meschke, Vianak Naranjo, Jörg-Uwe Pott, Ralf-Rainer Rohloff, Johannes Schmidt

LBT Optical Path Difference and Vibration Monitoring System

Characterisation, mitigation and correction of telescope vibrations are crucial for the performance of astronomical infrared interferometers. The project teams of the interferometers for the Large Binocluar Telescope (LBT), LINC-NIRVANA and LBTI, and LBT Observatory (LBTO) have embarked on a joint effort to implement an accelerometer-based vibration measurement system distributed over the optical elements of the LBT. OVMS, the Optical Path Difference and Vibration Monitoring System will serve to (i) ensure conditions suitable for adaptive optics (AO) and interferometric (IF) observations and (ii) utilize vibration information, converted into tip-tilt and optical path difference data, in the control strategies of the LBT adaptive secondary mirrors and of the interferometers. The system hardware is mainly developed by Steward Observatory's LBTI team and its installation at the LBT is underway. Software development and computers are the responsibility of the MPIA LINC-NIRVANA team.

Figure 1: *Left: Vibration measurement equipment at the LBT left tertiary mirror. Blue cables end in accelerometers attached to the back of the mirror support structure at three locations. Right: The DIMM (small telescope on J-shaped mount) located near the top end of the LBT.*

The Differential Image Motion Monitor for the LBT

In 2008, the MPIA delivered a Differential Image Motion Monitor (DIMM) to the LBT. It provides observers with a measure of the current seeing conditions, information essential to the success of scientific observations, as well as test purposes. The DIMM determines the seeing by measuring the differential motion of a stellar image as it takes two different paths through Earth's atmosphere. A small telescope equipped with a mask and glass wedges produces two separated images of the star that are recorded by a high speed digital camera. Because the technique relies on the differential motion of the images, the DIMM is insensitive to vibrations, windshake and tracking errors. Due to construction restrictions at the LBT site, the DIMM is mounted on the telescope itself. This presented significant challenges, since the device must point at and track on a target while the LBT points at and tracks a different target.

LBT Infrared Test Cameras

The LBT is unique in having fully adaptive secondary mirrors as part of the facility infrastructure. These mirrors correct atmospheric turbulence by applying forces to a thin membrane of aluminized glass held by electromagnetic forces close to a thicker reference surface. The adaptive secondaries are extraordinarily complex systems, and require proper test equipment for performance verification and commissioning. To simplify and accelerate this process a pair of infrared adaptive optics test cameras was built by the MPIA and its partners in Bologna. These devices employ fast framing near infrared detectors, which can capture the current delivered telescope image up to one hundred times per second. Three different fields of view allow characterization of the core of the stellar point spread function (PSF), the fainter wings of the PSF, as well as the wider image plane of the telescope. In January 2008, the first of the two cameras was delivered to the adaptive optics test tower in Florence, where it is used to characterize the secondary mirrors before delivery to the telescope. Three months later, the second camera was delivered to the LBT itself to aid in commissioning of the Gregorian foci prior to the arrival of LUCIFER-1.

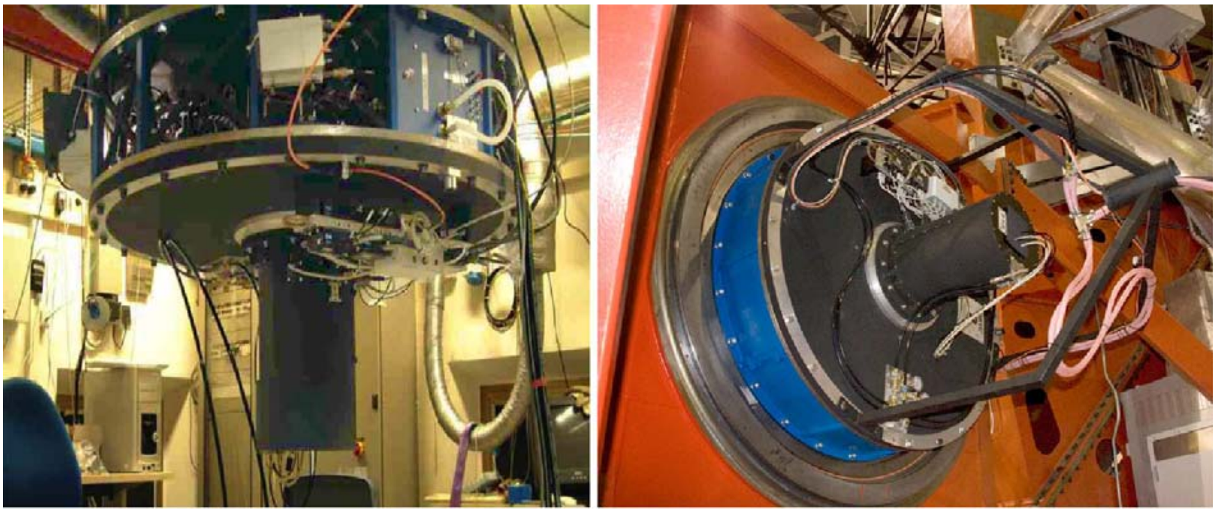

Figure 2: *Test camera #1 (left) mounted on the adaptive optics test tower in Florence. Test camera #2 (right) attached to the Gregorian focal port, now occupied by LUCIFER-1.*

LBT Telescope Control Software

Until mid-2009 MPIA contributed to the construction and development of the LBT with two work packages related to the telescope control software: IIF, the instrument interface software for the communication between the astronomical instruments and the telescope, and GCS, the combined software for telescope guiding and control of the primary mirror active optics. Following routine operations with the two LBC prime focus cameras a modified version of the IIF software was developed for the infrared test cameras. Due to its increased flexibility this new version caught the attention of the other instrument builders and is now employed together with LUCIFER-1 and also foreseen in 2010 for MODS-1 (built by Ohio State University). The GCS package has entered routine operations with LUCIFER-1. It analyzes camera images produced by the Acquisition, Guiding and Wavefront sensing unit.

Collaborators are the LBTI-team of Steward Observatory, Tucson, and the LBT Observatory for the OVMS, the University of Bologna and Bologna Observatory for the IR test cameras, and LBT Observatory for the telescope control software.

Searching Exoplanets by narrow-angle astrometry

Ralf Launhardt, Thomas Henning, Harald Baumeister, Peter Bizenberger, Uwe Graser, André Müller, Vianak Naranjo, Johny Setiawan, Tim Schulze-Hartung, Karl Wagner, Patrick Weise

How to search for exoplanets with narrow-angle astrometry?

Altough the radial velocity (RV) technique has been thus far the most successful method in detecting extrasolar planets, it has a few principle drawbacks. It requires a sufficient number of narrow spectral lines and does therefore not work well with young and active stars. Furthermore, it provides no constraint on the inclination of the orbit ($sin\, i$), and thus only a lower limit on the planetary mass can be derived. These principle drawbacks can only be overcome by invoking another technique: astrometry. However, to play a significant role and open new planet discovery spaces, an astrometric accuracy of order 10–50 muas is needed. This accuracy is out of reach for current-day telescopes and can be achieved from the ground only by performing narrow-angle differential astrometry with a long-baseline interferometer (see Fig. 1) [1].

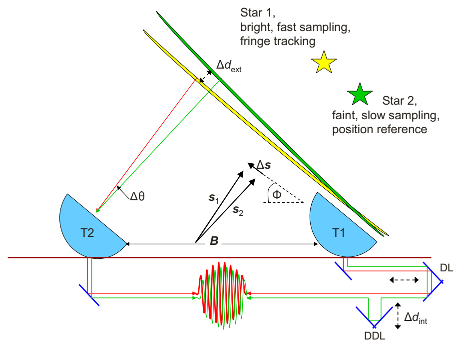

Figure 1: *The differential delay, the primary observable of a dual-star interferometer, is given by* $\Delta d = \Delta\vec{s}\cdot\vec{B} + \Delta C = \Delta s\cdot B\cdot\cos\phi + \Delta C + \Delta d_{\rm inst} + \Delta d_{\rm turb}$, *where* $\Delta\vec{s}$ *is the separation vector between the two stars in the plane of the sky,* $\phi = 90° - \theta$ *is the angle between* $\Delta\vec{s}$ *and* $\vec{B}$, *and* θ *is the angle between* $\vec{B}$ *and the direction towards projected central position between the two stars. The differential instrumental delay,* $\Delta d_{\rm inst}$, *is close to zero and can be calibrated. The metrology zero point,* ΔC, *must either be calibrated or eliminated by periodically exchanging the two stars between the two interferometers.*

Differential Delay Lines for PRIMA

In order to speed up the full implementation of the astrometric capability of the PRIMA facility at the VLTI and to carry out a large astrometric planet search program, a consortium lead by the Max Planck Institute for Astronomy, Landessternwarte Heidelberg, and Observatoire de Genève (Switzerland), has built Differential Delay Lines (DDLs) for PRIMA [2] and is currently developing the astrometric observation preparation and data reduction software [3]. The design of the DDLs has been developed by the consortium in close collaboration with ESO. The optical heart of the DDLs, Cassegrain-type, all-aluminum retro-reflector telescopes (cat's eyes), has been developed at MPIA and was manufactured by Axsys Detroit. The cat's eyes where delivered to MPIA end of 2007. In a dedicated optical laboratory at MPIA they were then extensively tested. In March 2008, the cat's eyes were shipped to Geneva and integrated with the other DDL components. In July 2008, the DDLs successfully passed the provisional acceptance review in Europe (PAE) [4]. Immediately afterwards, the complete DDLs were shipped to Paranal, where they were integrated and aligned in the VLTI Laboratory by a large team of engineers from ESO, Geneva, and MPIA (Fig. 2). At the end of this Assembly and Integration mission, on 3rd September 2008, the team even managed to obtain first fringes with PRIMA on sky with one Fringe Sensor Unit (FSU A). The commissioning of the other PRIMA subsystems will last throughout 2009, and the actual astrometric dual-star commissioning is expected to start in spring 2010. In return for these hardware and software contributions, we were granted guaranteed observing time, which will be used to carry out a systematic astrometric *E*xoplanet *S*earch with *PRI*MA (*ESPRI*) with two ATs, starting in 2011 [5, 6].

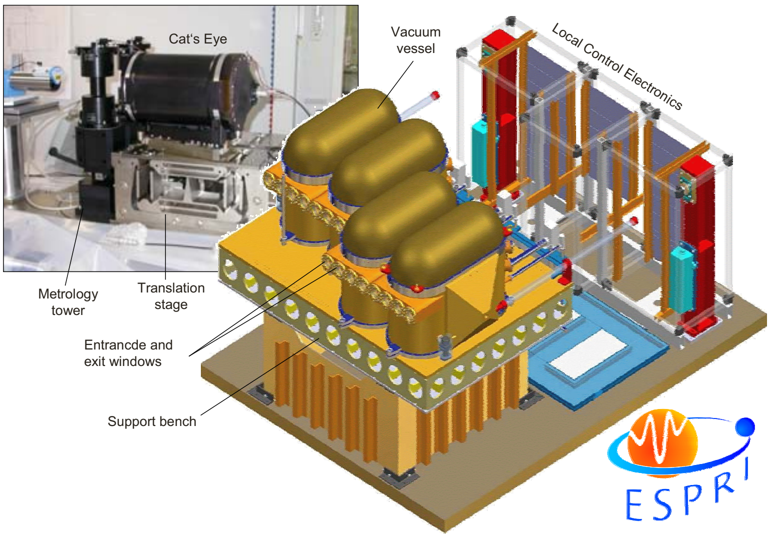

Figure 2: *Schematic view of the Differential Delay Lines as assembled in the VLTI lab. The top left photograph shows one cats eye telescope on the translation stage, with the internal metrology tower in front, set-up for acceptance tests in Geneva. Each vacuum vessel contains two such DDLs. Bottom right: the ESPRI project logo.*

Preparing the exoplanet search program

In accrdance with the main goals of our astrometric planet search program, which are:

1. Resolve the $sin\, i$ uncertainty from planets detected by RV surveys and derive planet masses,
2. Measure the relative orbit inclinations in multiple planetary systems,
3. Inventory of planets around stars with different mass and age,

three lists with potential target stars were preselected for the ESPRI project:

1. **RV**: Stars with known RV planets within ≤ 200 pc around the Sun.
2. **CNS**: Nearby stars of any spectral type within ≤ 15 pc around the Sun.
3. **YS**: Young stars with ages < 300 Myr within ≤ 100 pc around the Sun.

However, narrow-angle astrometry relies on the availability of reference stars within the isopistonic angle around the target object. Since existing sky surveys have a too low dynamic range and suffer from strong saturation and "blind" areas around bright (nearby) stars, we have carried out a large high dynamic range NIR imaging program, using SOFI at the ESO NTT and ΩCass at the Calar Alto 3.5 m telescope, to search for faint ($K \leq 14$ mag) background stars within 20″ around ≈ 900 preselected target candidates. This program is nearly completed and we identified more than 100 good target and reference star pairs for the astrometric planet search.

Collaborators in this project are Observatoire de Genève (D. Queloz et al.), Landessternwarte Heidelberg (A. Quirrenbach et al.), EPF Lausanne (R. Wüthrich et al.), Ècole d'Ingeniuers ARC St. Imier (I. Salvadé et al.), and ESO (F. Delplancke, G. van Belle, F. Derie, et al.).

References

[1] Launhardt, R. 2010, New Astronomy Reviews, in press

[2] Pepe, F., Queloz, D., Henning, Th., et al. 2008, in Proc. SPIE, 7013

[3] Elias, N., et al. 2008, in Proc. SPIE, 7013

[4] Bizenberger, P., Baumeister, H., Graser, U., et al. 2008, in Proc. SPIE, 7014

[5] Launhardt, R., Queloz, D., Henning, Th., et al. 2008, in Proc. SPIE, 7013

[6] Launhardt, R., Henning, Th., Queloz, D., et al. 2008, IAUS 248, 417

The second generation VLTI instrument MATISSE

Uwe Graser, Thomas Henning, Werner Laun, Christoph Leinert, Vianak Naranjo, Udo Neumann, Karl Wagner

The History of MATISSE

MATISSE is a 2nd generation VLTI instrument and can be seen as the successor to MIDI, the Mid-Infrared Interferometric Instrument on the VLTI. Since 2003 first ideas for an add-on to MIDI were discussed to provide MIDI with a four-beam imaging mode. After the ESO workshop on 2nd generation VLTI instruments in April 2005 the plan for this extension to MIDI, called APRES-MIDI., was replaced by a proposition for an entirely new instrument. The following phase-A study for this new mid-IR interferometer with the name MATISSE was successfully concluded in a Phase A review at ESO in July 2007. The official kick-off for the instrument occurred in November 2008. It is planned to install and commission the instrument on Paranal in 2014.

The MATISSE Instrument

MATISSE – the Multi Aperture Mid-Infrared Spectroscopic Instrument – is a mid-IR instrument combining up to four beams of the VLTI. Thus MATISSE will provide for two major break-throughs:

- MATISSE will open two new observing windows at the VLTI, the L and M bands (2.8 – 5.0 µm) in addition to the N-band (7.5 – 13.5 µm). Since MATISSE is composed of 2 cryostats and 2 detectors, the L/M- and the N-band can be observed in parallel.
- MATISSE will measure closure phase relations and thus will offer the possibility of image reconstruction in each of these spectral bands.

With its prisms and grisms MATISSE will allow for spectral resolutions of $20 < R < 1250$ in L at 3.5 µm and for $20 < R < 400$ in N at 10.5 µm. With external fringe tracking the sensitivity of MATISSE will amount to 0.02 Jy (or N=8 and L=10) at the UTs and 0.4 Jy (or N=5 and L=7) at the ATs, respectively.

For both wl-bands the concept of MATISSE is based on a pair-wise 0-π multi-axial recombination (see figure 1). The instrument itself consists of 3 modules, one warm optics table and two separated cryostats which contain the cold optics and the detector for the related wavelength band. For L/M-band we will use a Hawaii 2 RG (Teledyne) and for N-band a 1k x 1k Aquarius detector from Raytheon.

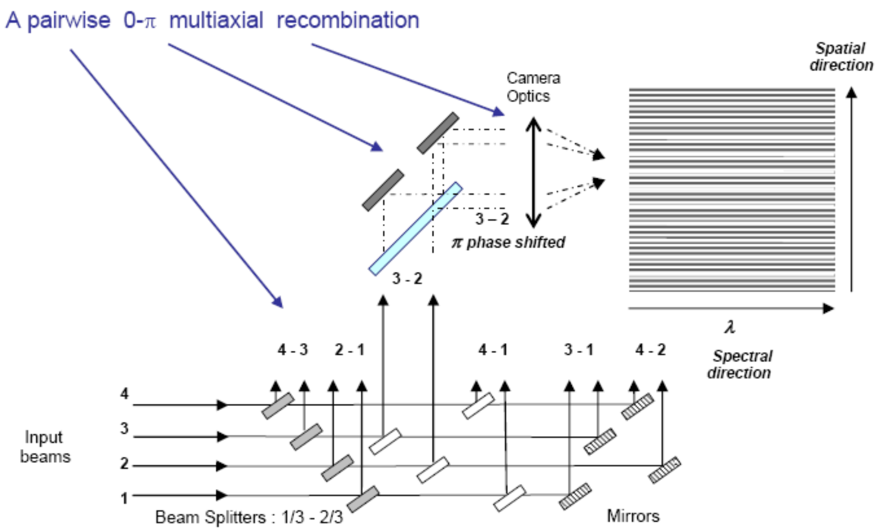

Figure 1: The beam-combining concept. The six pair-wise beams are split with π- phase shifts between the sub-beams. The sub-beams are spectrally dispersed and combined through the camera optics, resulting in 12 spectro-interferometric signals on the detector.

The Consortium

The consortium which builds MATISSE is lead by the Observatoire de la Cote d'Azur (OCA, PI: Bruno Lopez) with major contributions from MPIA in Heidelberg (Co-PI: Thomas Henning), from MPI für Radioastronomie in Bonn (Co-PI: Gerd Weigelt), from ASTRON in Dwingeloo/Netherlands (Co-PI: Walter Jaffe) and from ESO. OCA will build the warm optics and contribute in the field of instrument and data reduction software. MPIfR is responsible for the integration of the detectors as well as for major parts of the data reduction software. ASTRON will deliver the two cold optical benches and ESO will contribute by providing the detectors and the read-out electronics. The contribution of MPIA consists in providing the MATISSE control electronics and both cryostats. In addition MPIA will develop the instrument control software (ICS) and take over some responsibility for the detector integration.

The Science Case

With its spectroscopic and imaging capabilities MATISSE will allow to perform a fundamental analysis of the composition of gases and dust grains in various astrophysical environments on angular scales of 10-20 mas. The key science applications will include star and planet formation processes with their various disk structures, the structure of evolved stars and the tori of AGNs.

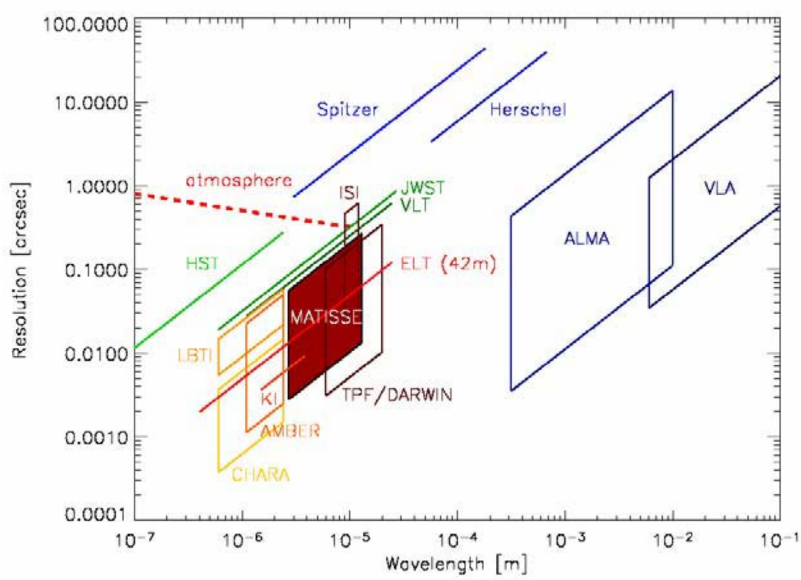

Figure 2: Place of MATISSE in the wavelength – resolution diagram. MATISSE will cover part of the gap between the NIR domain and the (sub)-mm high resolution facility ALMA.

The cryostats for N- and for L/M-band

Because of the sensitivity of the VLTI against vibrations the cooling of the cold optical benches (temperatures: < 40 K for N-band and < 80 K for L/M-band) and the detectors (< 70 K for the HAWAII 2 RG and < 8 K for the Aquarius detector) needs some special design. Since cooling with liquid Helium is not allowed on Paranal we use a pulse tube cooler (CHPT 410 from Cryomech) which reduces the internal vibrations by a factor of 50 – 100 in comparison to a standard closed cycle cooler as used in MIDI and VISIR. Further measures for damping of the induced vibrations will guarantee for stable observations with a temperature stability of 0.1 K. The possibility of using liquid nitrogen for the cooling of the L-band cryostat is still an option depending on the properties of the Hawaii RG 5 micron detector.

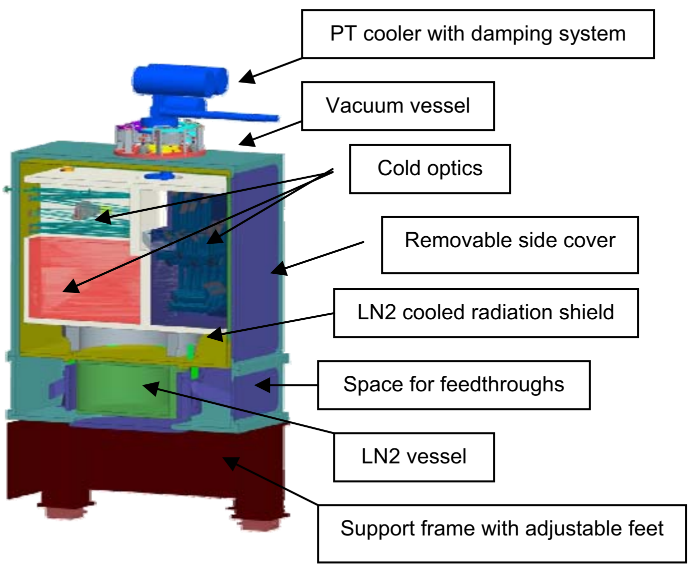

Figure 3: Design of a cryostat:
The cold optics with the detector is distributed into three modules for better access. The size of the cryostat amounts to 110 x 70 x 197 cm and the weight is approximately 1250 kg.
The two-stage pulse tube cooler is currently tested together with the damping system by using a small test cryostat.
Note: The cryostats for the L/M and for the N-band are nearly identical. Only the operating temperature is different.

MICADO - The Multi-AO Imaging Camera for Deep Observations

T. M. Herbst, H.-W. Rix, K. Jahnke

MICADO, The **M**ulti-AO **I**maging **Ca**mera for **D**eep **O**bservations, is a potential first-light near-infrared imager for the European Extremely Large Telescope (EELT), a 42 meter telescope that is approaching the end of Phase B study at the European Southern Observatory. MICADO takes advantage of post focal plane adaptive optics (AO) to deliver a large 53” primary field of view for imaging at the diffraction limit of the EELT. An auxiliary arm provides increased flexibility, with a finer spatial sampling over a smaller field of view and a medium resolution long-slit spectroscopic capability.

MICADO is optimized for photometric sensitivity and astrometric accuracy, allowing MPIA astronomers to measure objects as faint as 30th magnitude (AB) and to follow the motions of celestial objects with unprecedented detail. This capability enables science cases ranging from tracing extremely faint stars at the center of our Milky Way, to the cores and resolved stellar populations of nearby galaxies, to populations of faint galaxies and active galactic nuclei at high redshift.

A team of 15 scientists and engineers from Germany, The Netherlands and Italy, explored the design options and tradeoffs of MICADO in a Phase A study, which began in early 2008. The first part of the study examined various opto-mechanical and cryogenic solutions for the imager and culminated in a mid-term review in December 2008. The second half of the study, which ended with a successful external review in December 2009, concentrated on advanced conceptual design, including plans for construction, implementation, and operation of the instrument..

The instrument is compact, and will be mounted at the output feed of the MAORY multi-conjugated adaptive optics system. The MICADO team has adopted a phased approach, in which the instrument can be initially used with a simpler Single Conjugated AO module, and then seamlessly upgraded to the higher performance AO when it is ready (see Figure 1).

As Europe examines ways to finance and build the EELT, the MICADO team continues to work on the instrument, examining additional options, including advanced airglow suppression filters, a “dual imaging” arm using Fabry-Perot technology, and high time resolution detectors exploiting photon multiplication. We anticipate a go-ahead for EELT construction in early 2011, with a call for instrument proposals following soon thereafter. The science enabled by MICADO makes it an excellent choice for first light capability.

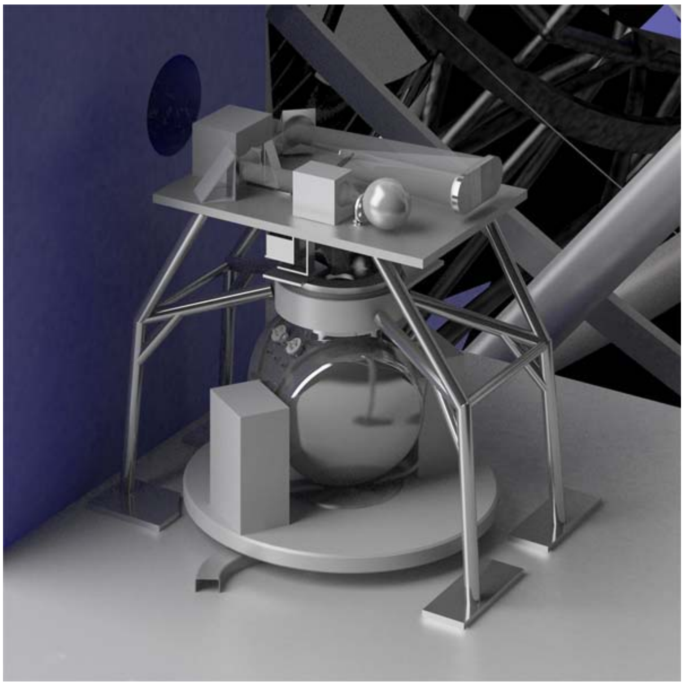

Figure 1: *The MICADO instrument mounted under the optical bench of the Single Conjugated Adaptive Optics Module. The cryostat rotates around a vertical axis to follow the sky. This gravity-stable configuration allows high precision astrometry.*

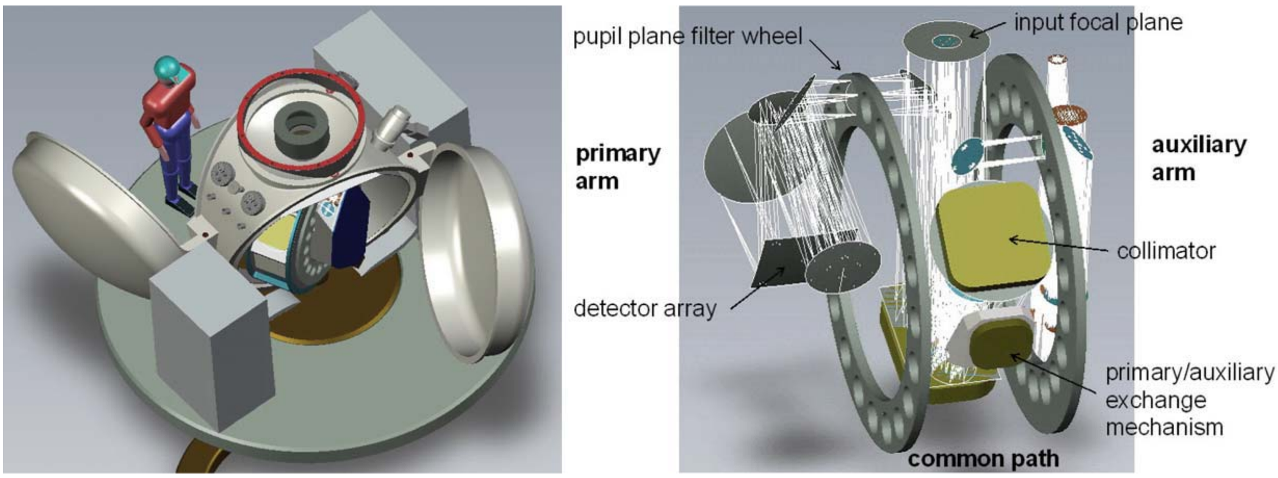

Figure 2: *(left) The MICADO cryostat opened for servicing. The human figure indicates the scale. The internal optical components (right) include a primary imaging arm and an auxiliary arm for high resolution studies and long-slit spectroscopy.*

PANIC - the Panoramic Near Infrared Camera for Calar Alto

Josef Fried, Ralf-Rainer Rohloff, Armin Huber, Harald Baumeister, Werner Laun, Clemens Storz, Ulrich Mall, Karl Wagner, Matthias Alter, Viajanak Naranjo

A wide field imager for the near infrared was identified by astronomers at MPIA and IAA as the most desirable new instrument for Calar Alto. So in October 2006 project PANIC was started and has already been described in the 2007 report. The instrument is an NIR (Z to K bands) wide field imager for the 2.2m telescope; the image scale is 0.45 arcsec/pixel, which results in a 0.5×0.5 degree field of view on a 4096×4096 pixel detector. This is perfectly suited for survey-type of observations. In 2007 we had planned to offer a high resolution pixel scale (0.25arcsec/pixel) by changing some optical components in the beam which would have been mounted on wheels. This had to be dropped because of weight limits. However, PANIC can also be used at the 3.5m telescope: here the image scale is 0.25 arcsec/pixel which is well suited for observations requiring high spatial resolution over a still large field of view of 0.25×0.25 degrees.

The interior of the cryostat is shown in Fig.1. All optical elements are mounted to the cold optical bench (yellow) in order to minimize flexure effects. Tolerances for the mechanics are tight, on the order of 50 microns for several parts. Extensive modelling and finite element analysysis showed that our design actually meets the tolerances. Three mirrors fold the light path to reduce the size of the instrument. The imaging optics is pure lens optics. In order to minimize thermal background a cold stop, located at the image of the telescope mirror, limits the field of view of the detector. In order to optimize the background for both telescopes, two cold stops are mounted on a wheel. Four filter wheels allow 20 filters to be permanently installed. The optics allows to use narrow band (1%) filters, too. Although optimized for wavelengths between 1 and 2.5 microns, the imaging quality is still excellent in the Z-band. The detectors are 4 Hawaii-2RG sensors, mounted in an array (see contribution by Ralf Klein et al.) with a small gap of only 167 pixels which results in a convenient footprint.

Read-out is done simultaneously in 128 channels with our own electronics and MPIA GEIRS software package; tests have shown that hard- and software work very well and stable, we could corroborate the noise values supplied by the manufacturer. The wheels are controlled with our own motor control electronics which is in use in many instruments. Temperature and pressure are monitored and controlled with commercially available devices. An observation tool will make use of PANIC easy, even for the unexperienced user. A quick-look system will allow to check the data online. A pipeline will supply the observer with state of the art reduced data.

Status of the project

Milestones which have been reached are PDR (2007), FDR for optics (2008) and for mechanics (2009). All reviews did not discover major problems.

Current status is as follows: detectors and read-out are working, optimization remains to be done. The cryostat will be delivered in December 2009, internally wired and tested early 2010. Delivery of optics is promised for spring 2010. Assembly and laboratory tests are planned for 2010, final tests early 2011 and first light in May 2011.

PANIC is the first joint instrumental project between IAA and MPIA with IAA responsible for optics and software, MPIA for detectors and read-out, cryotechnique and mechanics. IAA members involved in PANIC are Matilde Fernandez (co-PI), Concepcion Cardenas (optics), Julio Gomez (project management), Antonio Seguras and Jose-Miguel Ibanez (software).

The home page of PANIC: http://www.iaa.es/PANIC

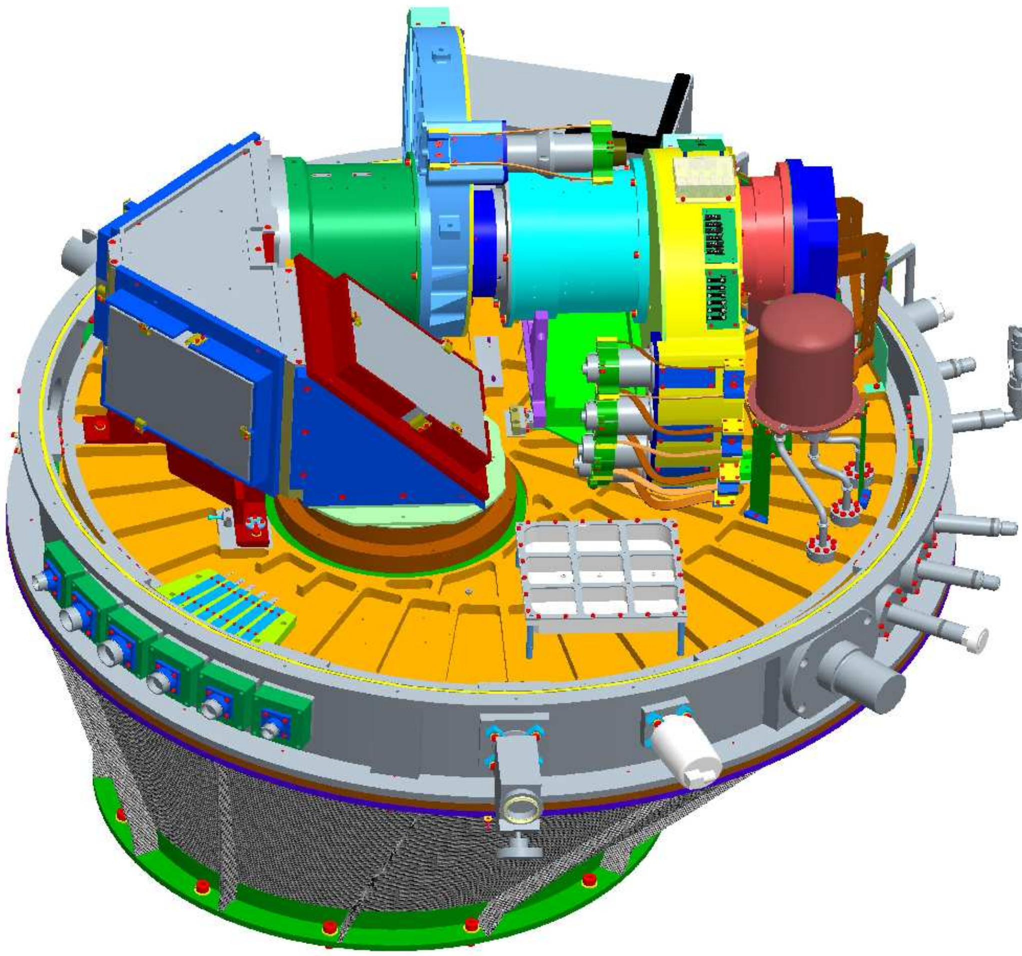

Figure 1: *The interior of the PANIC cryostat, turned up-side down to show the optics. Clearly visible are the optical bench (in yellow) and the folding mirrors. The lenses are mounted in two tubes (green). The cold stop wheel (light blue), the filter wheels (yellow) and detector (blue) are visible.*

LAIWO - An optical camera for the Search for Extrasolar Planets with the Transit Method

Cristina Afonso and Thomas Henning

Abstract

The Max-Planck für Astronomie, the University of Tel Aviv and the Institute für Astrophysik in Göttingen initiated a search program for Jupiter-size extrasolar planets with the transit method. For this aim, a Large Area Imager for the Wise Observatory (LAIWO) was built at the Max-Planck für Astronomie, and successfully installed in November 2008. Data are currently being taken, 8 fields having been monitored up to date with a number of measurements ranging from 600 to 3,000. Here we present the instrument and a brief outline of the scientific goals of the project.

The Project

The Max-Planck-Institut für Astronomie, the University of Tel Aviv and the Institute for Astrophysik in Göttingen, initiated a transit search program, funded by the Max-Planck für Astronomie and the German-Israeli Foundation. The aim of the research project is to detect extra-solar Jupiter-size planets around stars with magnitudes I=14-15 mag, with the transit method. The method relies on the temporary drop in brightness of the parent star, harboring the planet. If the planetary system is in favourable orientation relative to the line of sight, then once per orbit the planet passes between its star and the observer, causing an occultation, or transit, that results in a dip of the light curve. For Jupiter-size planets transiting a sun-size star, the expected dip or transit depth will be about 1%. If three or more transits can be measured and confirmed to be due to the same planet, the orbital period, the radius of the planet and inclination angle can be determined.

In this context, a Large Area Imager for the Wise Observatory - LAIWO, was built at the Max-Planck-Institut für Astronomie (for technical details, see below). The camera was successfully installed in November 2008, being mounted on the 1-m telescope in the Wise Observatory in the Negev desert, Israel. The field of view is one square degree with a 0.43” resolution.

The observing strategy consists of continuously monitoring two fields at any given time, until 3,000 images are acquired per field. We have one week to 10 days per month, for three years. This will allow a sky coverage of about 20 square degrees. Up to date 8 fields have been monitored, with a number of measurements ranging from 600 to 3,000. It has been agreed that observations will be coordinated with the 1.2m MONET telescope located in Texas, USA, operated by the Institut für Astrophysik in Göttingen, Germany, once a larger camera will be installed at the MONET telescope. The expected number of transits over a three year campaing is around 15 planets.

The Instrument

The camera has 4 Lockheed CCD486 devices, 4kx4k pixels, each 15 microns. The CCDs are frontside-illuminated with the following characteristics:

- Quantum Efficiency of about 40% between 600 and 850nm
- Read-out noise < 5 e-
- Full-well $> 85{,}000$ e-

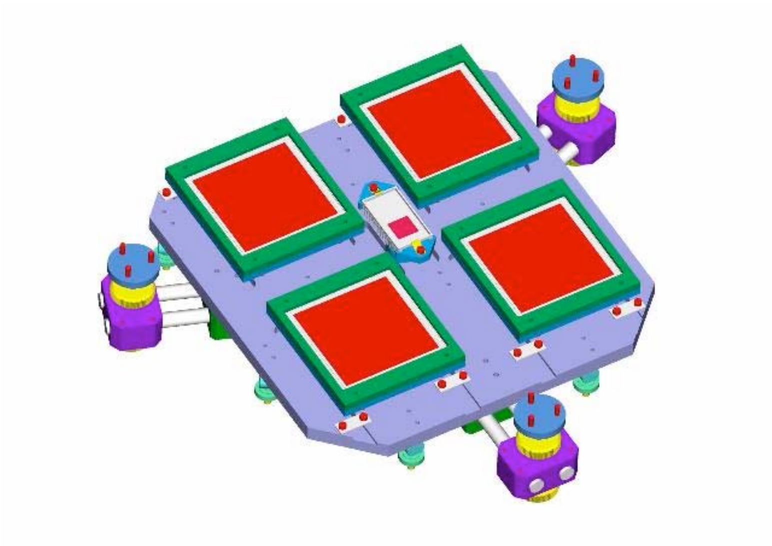

Figure 1: *Layout of the moisac of the CCDs of the LAIWO camera. The center CCD corresponds to the guider camera*

The guider camera contains one CCD located at the center of the mosaic: an eV CCD47-20, 1kx1k frame transfer device, with a pixel size of 13 microns.

A set of 5 filters (U, B, V, R, I, z) is available, mounted on a ruler that fits into a drawer. Three separate plates of sets of filters can be present at the same time. Each plate contains 5 squares, 4 for the imager CCDs and one for the guider CCD.

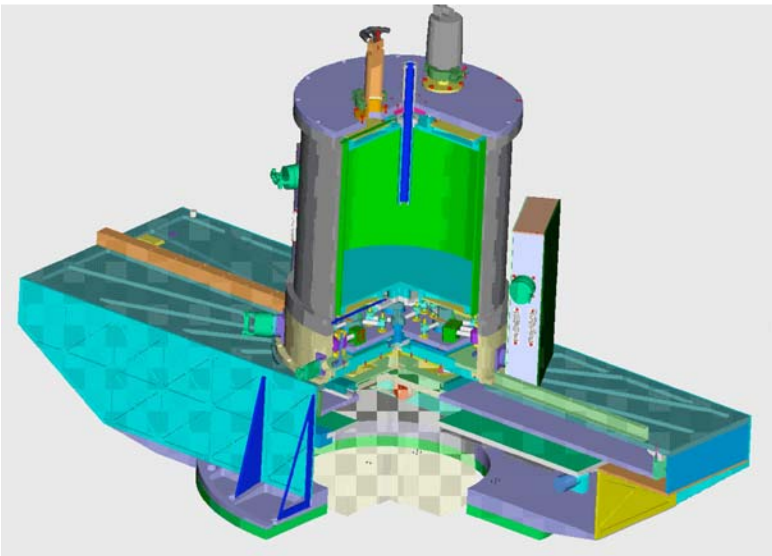

Figure 2: *Layout of the LAIWO camera, where one can see the cryostat and the ruler containing the filters.*

Collaborators are Tsevi Mazeh (University of Tel Aviv) and Stefan Dreizler (Institut für Astrophysik in Göttingen).

The PACS instrument aboard HERSCHEL

Oliver Krause, Ulrich Klaas, Markus Nielbock, Thomas Henning, Jürgen Schreiber, Zoltan Balog, Jeroen Bouwman, Hendrik Linz

Europe's new far infrared and submillimetre space observatory HERSCHEL has started its 3.8 years mission with a picture-perfect launch together with the PLANCK spacecraft aboard an ARIANE-5 rocket on 14th May 2009. The MPIA has been one of the major partners in the development of the PACS instrument which will enable imaging and spectroscopy in the wavelength range from 60 to 210 µm with unprecedented spatial resolution.

The MPIA has been responsible for delivering the PACS focal plane chopper [1] and for characterizing the large Ge:Ga spectrometer cameras and their -270°C readout electronics. After integration of the HERSCHEL 3.5-m-mirror onto the cryostat assembly and cool-down of the instruments to liquid helium temperature at the European Space Agency (ESA) technology centre ESTEC in Noordwijk (NL), a series of tests of all instrument components and software systems was conducted including an end-to-end test simulating the observatory operations with the satellite in the Large Space Simulator Chamber. These tests comprised a large number of short functional tests before and after vibration of the whole satellite and finally after the airplane transport to Kourou (Fig. 1a).

Figure 1: (a) : The HERSCHEL satellite in the cleanroom of the test facility S1B of Europe's space port in Kourou, French Guiana. In front of the satellite, the PACS test team gives green light for launch after a last successful functional test of the instrument. (b): Image of M51 obtained as the first scientific HERSCHEL image during the so called „Sneak Preview“, immediately after cryocover opening, on HERSCHEL's 32nd operational day. This composite image has been created from images in the three PACS bands at 70, 100, and 160 µm.

Dedicated mechanism tuning of the PACS chopper was performed by the MPIA team to verify that the control loop parameters found on instrument level are still valid in the complex satellite environment. Two weeks after the Herschel launch, three MPIA members of the PACS Instrument Control Centre team performed the in-flight verification and optimization of the chopper controller in real time from the Mission Operations Centre at ESOC Darmstadt. The chopper in-orbit behaviour was confirmed to be excellent, even surpassing the last performance measurements on ground.

After successful delivery and check-out of the PACS hardware contributions, MPIA is now heavily involved in many PACS Instrument Control Center tasks. The Instrument Control Centre (ICC), located at the PI institute MPE in Garching, has the responsibility for operations, calibration and data reduction of the PACS instrument. MPIA is one of four institutes of the PACS consortium which are main manpower contributors to the PACS ICC. MPIA coordinates the calibration of the PACS instrument and has been responsible for establishing the PACS Performance Verification Phase plan and the central PACS calibration document. Currently, the MPIA team is building up a corresponding calibration plan for HERSCHEL's routine phase.

During the two months lasting Commissioning Phase the coordination of all PACS instrument activities and their mission planning was executed by the MPIA team. It also ensured the optimum in-flight set-up of the Ge:Ga spectrometer detector arrays following a procedure developed in the MPIA lab [2].

All 64 operational days of the PACS instrument and HERSCHEL telescope pointing performance verification, lasting from mid July until end of November, were coordinated and scheduled by the MPIA ICC team, which also maintained the overall PV Plan. This also included the planning for the first light images of HERSCHEL (Fig. 1b). The performance verification (PV) plan consists of about 2100 individual observations totalling 1300 hours of observing time for performance and sensitivity assessment of the instrument in flight. The PV activity established an initial calibration in space and verified the validity of astronomical observation templates (AOTs), which are the basic observing blocks to be used by all observers later. Setting up the PV plan was a complex and challenging task since a large number of boundary conditions, such as source visibilities and properties as well as interdependencies of observations, had to be accounted for in the mission planning. The MPIA team has exclusively carried out the detailed mission planning of all PACS PV phase operational days, utilizing dedicated software tools, and has delivered the observational data bases to the HERSCHEL Science Center at ESAC in Villafranca (Spain) and the Mission Operations Center at ESOC in Darmstadt (Germany).

By the end of 2009, the PACS spectrometer pipeline, which has been built with significant contributions and under the coordination of MPIA [3], has reached the maturity to populate the HERSCHEL archive with science products.

In collaboration with the partner institutes of the PACS consortium.

References

[1] Krause, O. et al. “The cold focal plane chopper of HERSCHEL's PACS instrument”, SPIE 6273, 66 (2006)
[2] Stegmaier, J. et al. “Preparing Herschel's commissioning phase: Ge:Ga detector tuning”, SPIE 7010, 7 (2008)
[3] Schreiber, J. et al. “The HERSCHEL/PACS Spectrometer Pipeline“, Astronomical Data Analysis Software and Systems XVIII, ASP Conference Series, Vol. 411, 478 (2009)

The MIRI instrument aboard JWST

Oliver Krause, Thomas Henning, Friedrich Müller, Ulrich Grözinger, Silvia Scheithauer, Örs Detre, Ralf-Rainer Rohloff, Armin Böhm, Karl Wagner

The James Webb Space Telescope JWST, to be launched mid 2014, will be the astrophysics flagship mission of the current decade. JWST is jointly being developed by the space agencies of the USA, Canada and Europe. NASA will have the overall responsibility for the mission, which will be launched aboard a European ARIANE 5 rocket.

MIRI is the mid-IR instrument of JWST covering the wavelength range from 5 to 28 μm. The instrument provides imaging over a 1.3 x 1.9 arcmin field of view as well as coronagraphic capabilities on the basis of three 4-quadrant phase mask coronagraphs and one Lyot coronagraph. A complex setup employing 12 individual gratings provides high-resolution ($\lambda/\Delta\lambda$=R=1000-3000) spectroscopy from 5-28 μm while an additional double prism assembly will yield lower-resolution (R=100) spectroscopy over the range from 5 to 10 μm.

MIRI is being developed as a 50-50 partnership between the US and Europe. A European consortium of nationally funded institutes is responsible for building most of the MIRI Optical System while the detectors, focal plane electronics and the cryocooler are contributed by the US. MPIA is a major partner of the MIRI European Consortium led by UK-ATC. The responsibilities of the MPIA are (I) the development of optical wheel mechanisms, (II) leadership of the electrical system engineering team, and (III) strong participation in activities such as instrument testing, software development and preparation of the instrument calibration and commissioning in space.

Wheel mechanisms

In order to provide all observing modes such as broad/narrow-band imaging, coronagraphy and low/medium resolution spectroscopy, the MIRI instrument is equipped with a filter wheel and two dichroic/grating wheel mechanisms. They allow for a re-configuration of the instrument between the different observing modes and wavelength ranges. The lower MIRI operating temperature of T ~ 7K provided by a dedicated cooler, much lower than the passively cooled rest of JWST at a temperature of ~ 40K, implying additional challenges. The main requirements for the three mechanisms with up to 18 positions on the filter wheel (see Fig. 1) include: reliable operation at T ~ 7 K, optical precision of < 4 arcsec, low power dissipation, vibration capability up to 13.5 Grms and full functionality in the temperature range 6 K < T < 300 K.

To meet these requirements, a space-proven mechanism concept based on the European ISO mission and consisting of a central bearing carrying the optical wheels, a central torque motor for wheel actuation, a ratchet system for precise and powerless positioning and a magnetoresistive position sensor has been selected. In order to assure the reliable functionality of the complete wheel mechanisms, they have to undergo extensive testing. All components of the mechanism have been space qualified including 20 cryo-cycles between room temperature and 7 K and radiation testing [1].

The flight model of the MIRI filter wheel (Fig. 1) has been successfully tested and delivered for integration into the MIRIM imager section in September 2009. Currently, the flight models of the dichroic/grating wheel mechanisms are undergoing final tests and are expected to be delivered for integration into the spectrometer unit in March 2009.

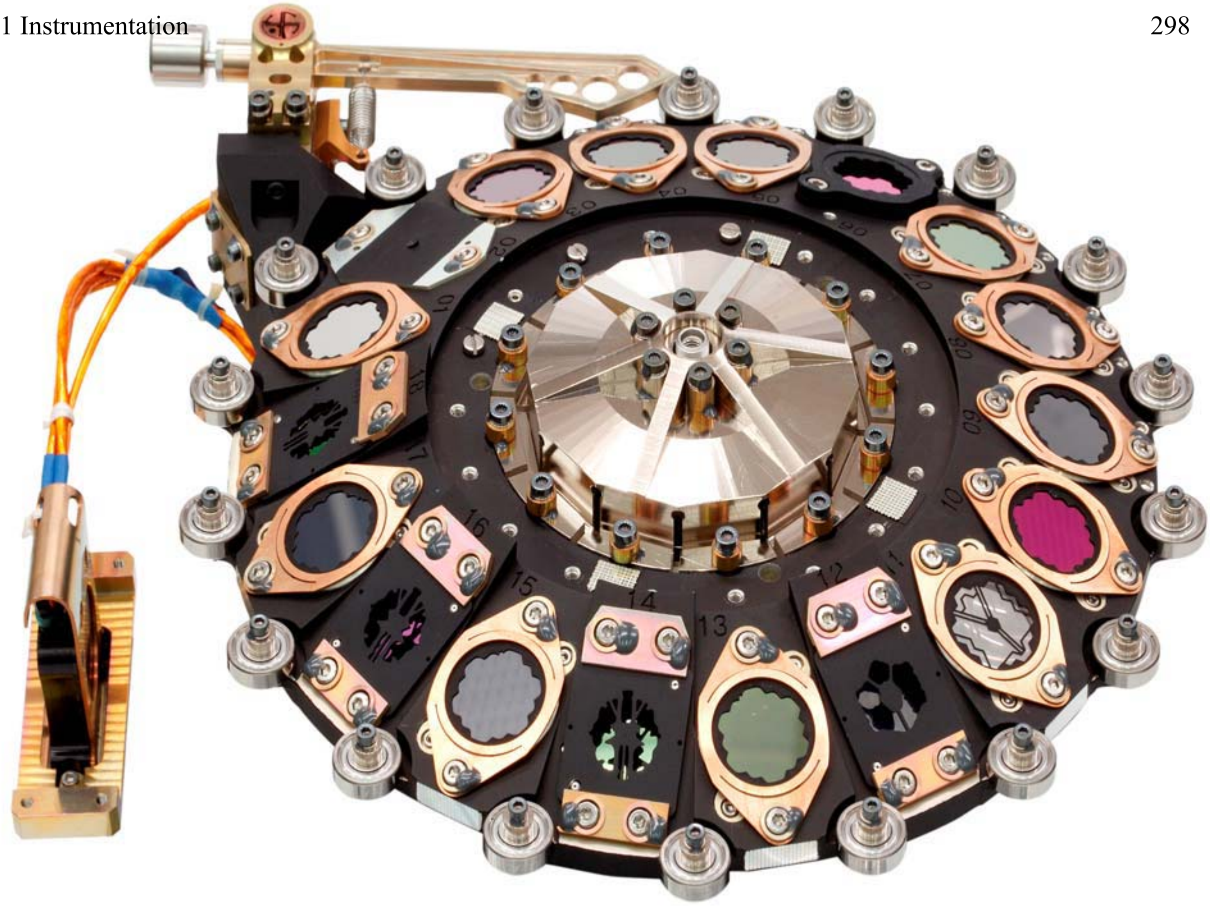

Figure 1: Flight model of the MIRI filter wheel. The optical elements on the wheel are actuated by a central torque motor, with the wheel positions being locked by a ratchet detent latching into the index bearings outer race. The mechanism has a diameter of 30 cm and a total mass of 3.5 kg.

Instrument Testing

A significant milestone for MIRI was reached in 2008 with the extensive testing of the verification model (VM) of the instrument, making MIRI the first of the four JWST instruments to reach this phase of performance testing. The goal of the VM - as a fully functional instrument model - was to verify the scientific performance and all electrical interfaces, to use a telescope simulator as calibration stimulus and to provide additional confidence on the thermal performance of the instrument. The cold MIRI VM test campaign included repeated functional tests under ambient and cryogenic conditions, alignment and thermal balance tests, electromagnetic compatibility tests, characterisation of the MIRI Telescope Simulator (MTS), and MIRI VM performance testing. Members of the MPIA MIRI team prepared, conducted and analysed a significant number of the tests in two cryogenic test campaigns. The VM test campaign was very successful: Among the tested MIRI performance parameters, the image quality nearly met all the flight model requirements, and also the spectrometer performed very well. In addition, all wheel mechanisms were reliably operated during the whole campaign. The lessons learnt from the VM campaign are currently implemented into the flight model test program which is expected to start in June 2010.

References

[1] Krause, O., Birkmann, S., Blümchen, T. et al., SPIE 7018, 67 (2008)

In collaboration with Carl Zeiss Optronics, Oberkochen, and the partner institutes of the MIRI European Consortium.

The NIRSpec instrument aboard JWST

Oliver Krause, Hans-Walter Rix, Thomas Henning,
Ulrich Grözinger, Friedrich Müller

The near-infrared spectrograph NIRSpec is the second instrument aboard the James Webb Space Telescope to which the MPIA is contributing. NIRSpec will be provided by the European Space Agency ESA as one of the major European contributions to JWST. The instrument is currently being built by an industrial consortium led by EADS-Astrium, Germany. Our institute is a member of the industrial consortium, and is represented by Hans-Walter Rix in the NIRSpec Science Team.

Among the primary science objectives for NIRSpec are deep extragalactic surveys. Consequently, the instrument design requires a multi-object spectrograph capable of measuring the spectra of up to 100 objects simultaneously in a 3 x 3 arcminute field of view. In addition, NIRSpec includes fixed slits and an integral field unit which provide high contrast spectra of point-like sources and of extended objects, respectively. Six gratings will provide high-resolution ($\lambda/\Delta\lambda$=R=2700) and medium-resolution (R=1000) spectroscopy over the wavelength range of 1 - 5 µm, while a prism will yield lower-resolution (R=100) spectroscopy over the range 0.6 - 5 µm.

To switch between these different spectroscopic observing modes, NIRSpec is equipped with a grating wheel mechanism carrying the six gratings, the double-pass prism, and also mirror for target acquisition (Fig. 1). The active position in the optical beam is mechanically defined by a ratchet system. An electrical motor moves the next grating into position. The same concept is used for the wheel mechanisms of the JWST-MIRI instrument, yielding synergies between the two projects. The high-precision cryomechanism is jointly being developed by Carl Zeiss Optronics, Austrian Aerospace, and MPIA. The MPIA team is responsible for the procurement of electrical components of the mechanism such as cable harnesses, the DC motor and parts of the position sensor and provides support to both electrical system engineering and cryogenic testing.

Figure 1: The NIRSpec filter wheel mechanism (image credit Carl Zeiss Optronics, Oberkochen).

A filter wheel mechanism houses a set of edge transmission filters for order separation during the different spectroscopic observations. The filter wheel is also equipped with one clear aperture for imaging and a pupil reference/calibration mirror for alignment and instrument self-calibration purposes. Since NIRSpec will be operated at cryogenic temperatures (T ~ 35 K), both mechanisms have been designed to meet an extremely stringent power dissipation constraint, which must not exceed 69 mW in order to maintain the thermo-mechanical stability of the instrument, an important characteristic of this precision spectrograph.

An engineering test unit (ETU) of the NIRSpec instrument has been built which realistically replicates the thermal, mechanical, electrical and optical characteristics of the actual flight model (Fig. 2). The ETU was subjected to a series of vibration, thermal-vacuum and electromagnetic compatibility tests. The ETU will be delivered to NASA later this year for pre-integration testing with the Integrated Science Instrument Module (ISIM) of JWST.

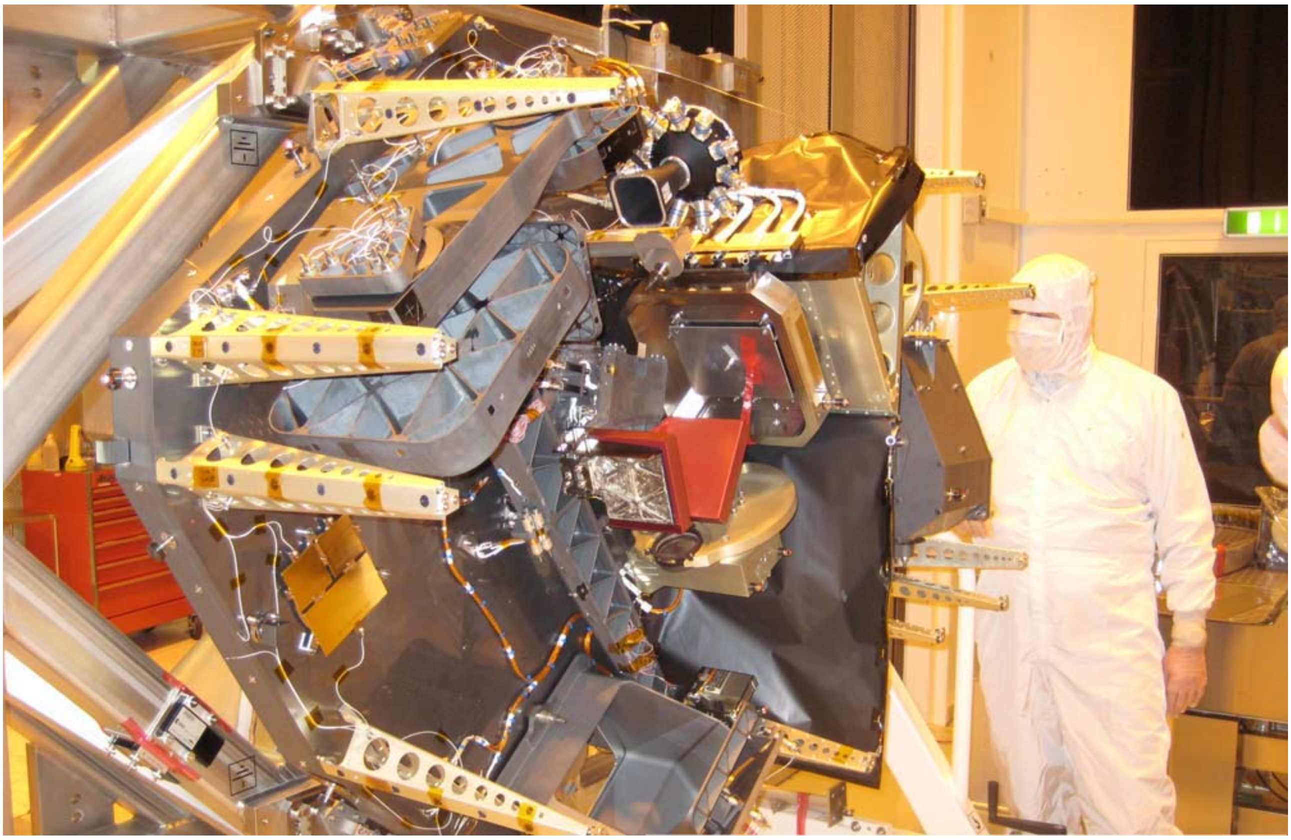

Figure 2: The NIRSpec engineering test unit (ETU) during the gravity-release test at the Astrium facilities in Ottobrunn (image credit EADS Astrium).

The integration of the NIRSpec flight model has started recently. The instrument features a highly modular system, consisting of three optics assemblies, and six main opto-mechanical systems including the grating and filter wheel mechanisms, which can be integrated, aligned and tested independently. The optical assembly, which houses all the opto-mechanical assemblies, is located at the heart of the instrument. Silicon carbide, a ceramic material with very high stiffness-to-mass ratio and a very high thermal stability has been selected. This material has an extremely low coefficient of thermal expansion and matches well with the payload supporting structure ISIM, built from carbon fibre. MPIA has been collaborating with EADS-Astrium to verify mechanical properties of the ceramic at low temperatures – required for the successful space qualification of the material.

In collaboration with EADS-Astrium, Ottobrunn, and Carl Zeiss Optronics, Oberkochen

12 Highlights from our Technical Departments, Public Outreach and Education

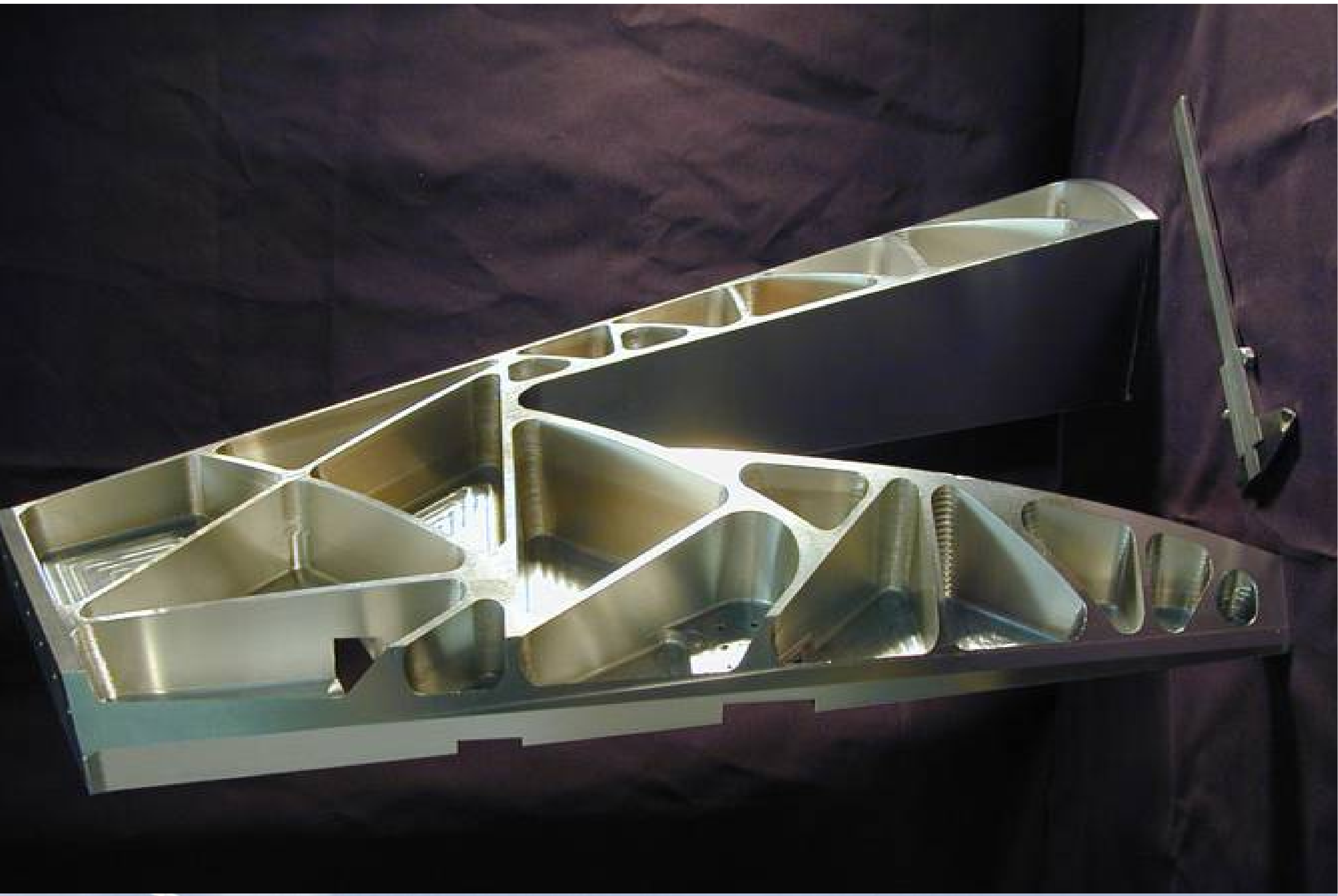

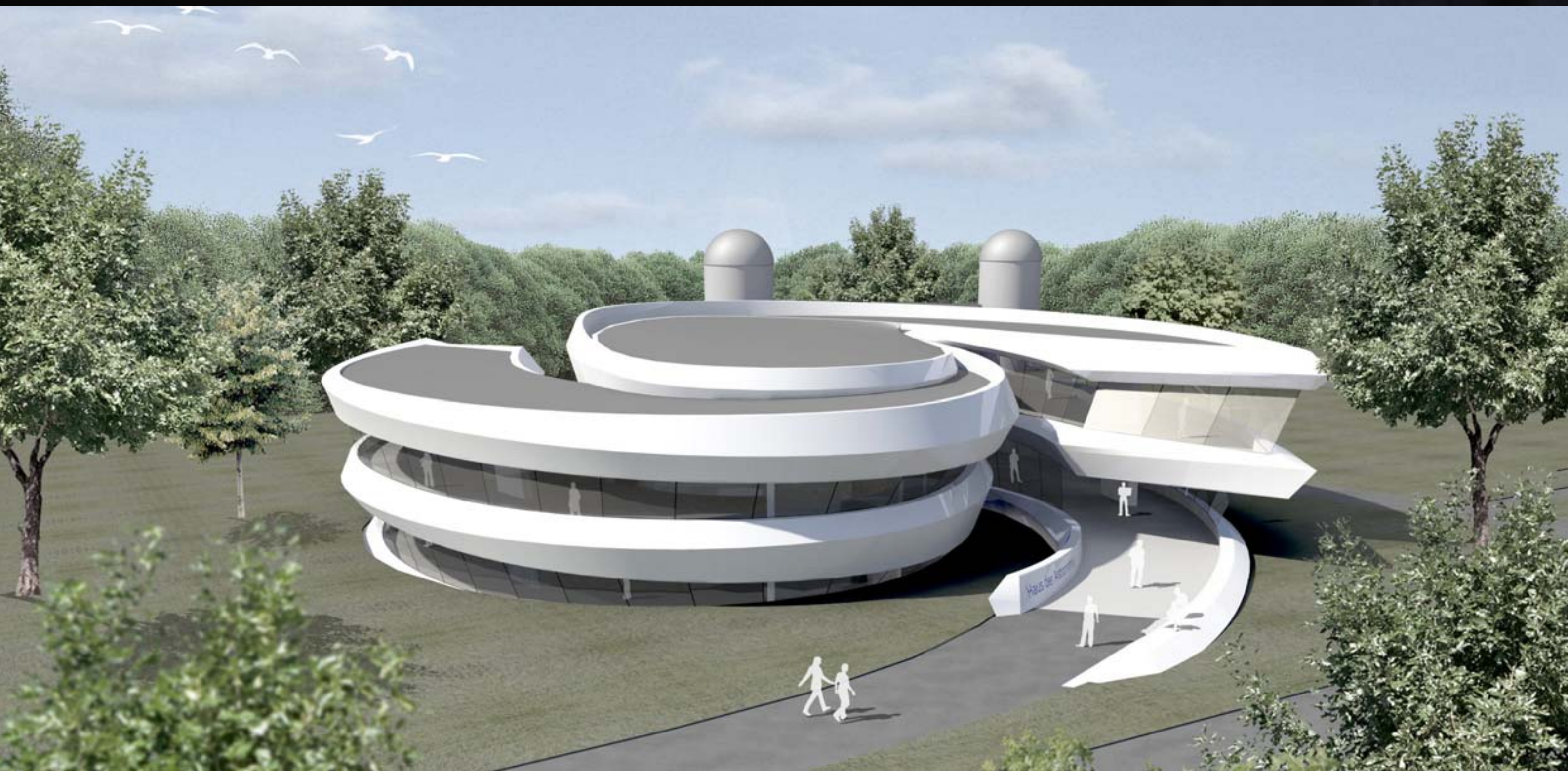

Images on previous page:

Top: Part of the support structure for the cold mechanisms inside the LINC-NIRVANA cryostat fabricated by MPIAs five-axes milling machine.

Bottom: Computer – image of the new “Haus der Astronomie” which is currently under construction. (Credit: Architekten Bernhardt+Partner, Darmstadt)

The technical departments

Martin Kürster

Assignment and expertise

In the technical departments (TD) of the MPIA approximately 50 engineers and technicians work to develop and build astronomical instrumentation for infrared and optical applications. In the past years instruments for gound-based telescopes have been built or continue to be under development for the Large Binocular Telescope (LBT), the Very Large Telescope (VLT) of the European Southern Observatory (ESO), Calar Alto Observatory, and Wise Observatory in Israel. The MPIA has also participated in studies for the European Extremely Large Telescope (E-ELT). Furthermore, the MPIA has made important contributions to instrumentation projects for the space observatories Herschel and JWST and still continues to do so. Figure 1 shows the allocation to MPIA instrumentation projects of TD labour from 2001 to mid-2009.

Among the specialties of the MPIA TD are infrared and CCD detector systems with their pertinent read-out electronics and software, cryogenic cooling systems, the development of new technologies for the machining of materials, and recently also the development of software to support scientific applications. Wide expertise exists in engineering design, precision mechanics manufacture, the design and manufacture of instrument control electronics, the development of instrument control software, and optics calculations which all belong to the standard repertoire of the TD. Larger instrumentation projects can also draw on expertise in project management, systems engineering and control engineering.

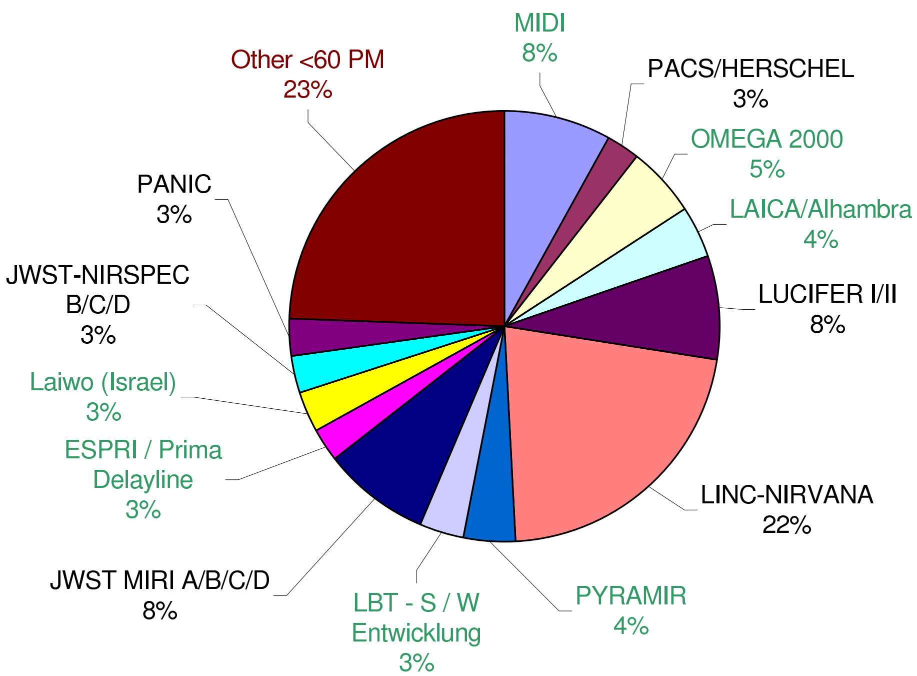

Figure 1: *Usage of labour from the technical departments by the MPIA instrumentation projects for the period 2001 to mid-2009. Projects with green labels were completed (as far as contributions from the MPIA TD are concerned). Projects labelled in black are still ongoing. "Other" subsumes projects that have used* < 60 *person months.*

Organisational structure

The MPIA technical departments are subdivided into five individual divisions each of which has its own department head. They are the engineering design department (or mechanical design office), the precision (or fine) mechanics workshop, the electronics department (comprising both design and workshop), the instrumentation and project software department, and the department of instrumentation and project management.

The five TD together have a general head who acts as the coordinator for the allocation of TD resources (labour, lab space, etc.) to the individual instrumentation projects. Together with the heads of the individual departments he serves as the main interface between the TD and the project leaders and managers. Figure 2 illustrates the organizational structure of the MPIA TD and their subdivisions and main assignments. The five individual TD present themselves in the subsequent contributions to this report.

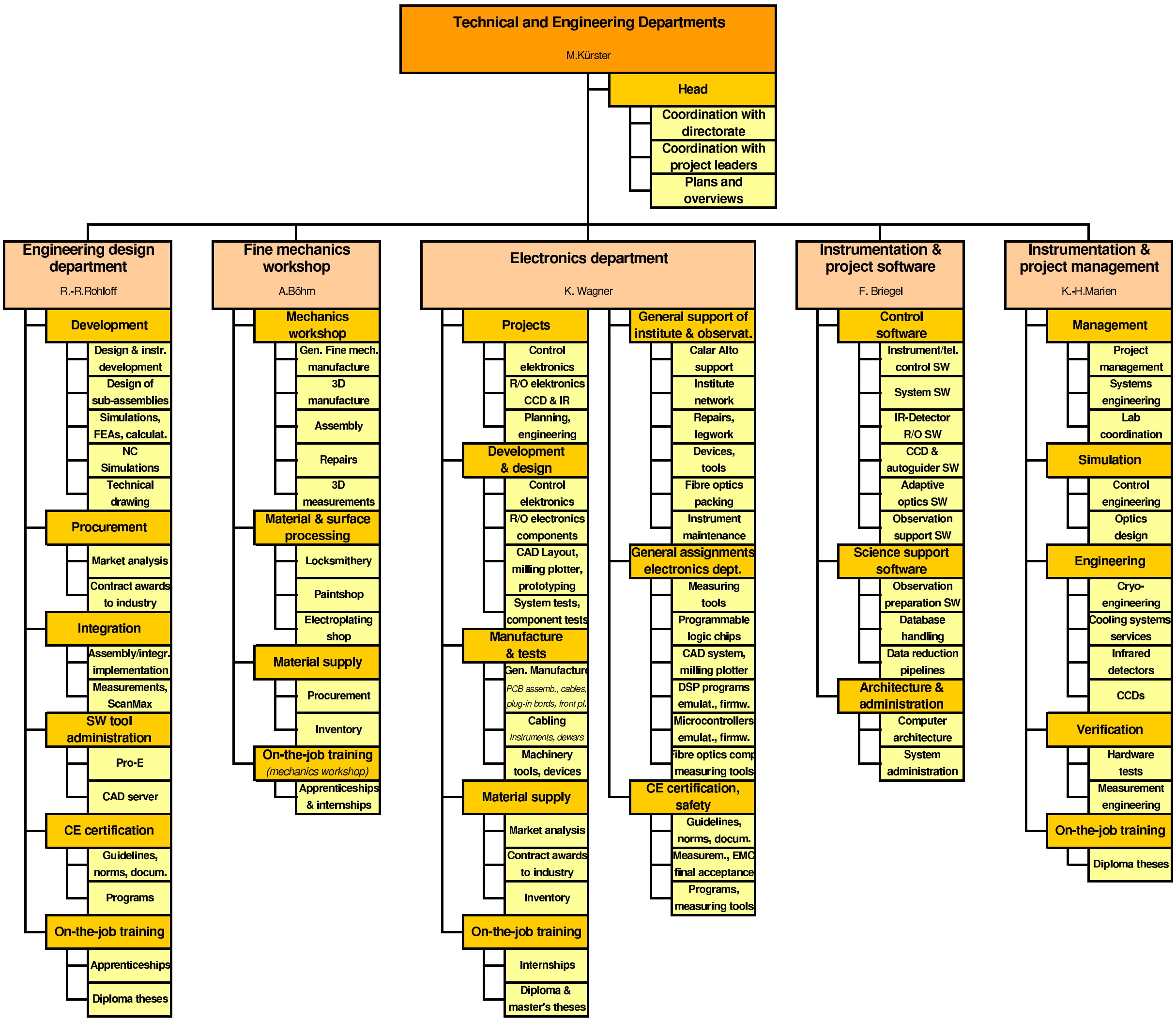

Figure 2: *Organisational structure of the MPIA technical departments. Below the overall coordination level there are five individual departments that are shown together with their subdivisions and functions.*

Engineering Design Department (Mechanical Design Office)

Ralf-Rainer Rohloff, Harald Baumeister, Thomas Blümchen, Monica Ebert, Armin Huber, Norbert Münch

Introduction

The engineering design department produces the mechanical designs of the astronomical instruments built by the MPIA. Department employees also accompany the subsequent phases of instrument building such as manufacture, testing, installation, and commissioning. If required, the behaviour of components under stress is studied in computer simulations which directly impact the design. As far as appropriate, design and/or manufacture are done by external companies on the basis of industry contracts. In this case, the engineering design department manages the interactions with the external companies, monitors the work progress, and takes responsibility for the acceptance of the product.
This report shows the last developments in this field of activity.

Near-infrared camera (PANIC) for Calar Alto

PANIC ((**Pa**noramic **N**ear **I**nfrared Camera for **C**alar Alto) is a joint project between MPIA and IAA Granada. The MPIA is responsible for the complete mechanics, detectors and read-out electronics within the PANIC team. Figure 1 shows a photo-realistic computer rendering of the new instrument.

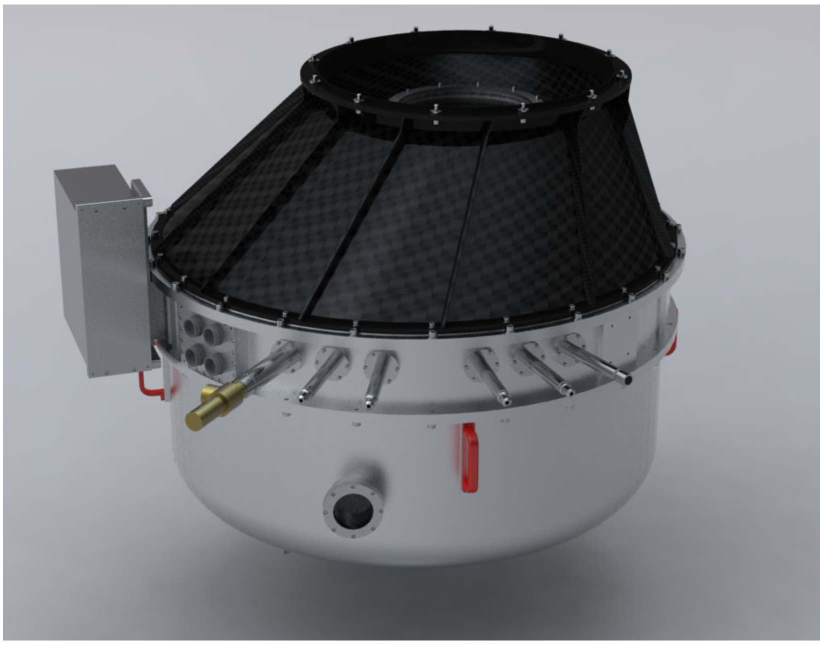

Figure 1: *Computer rendering of the PANIC cryostat including CFRP telescope adapter*

The final mechanical design review for the instrument is planned for mid December 2009. We have already successfully tested critical hardware items like cryogenic motors and gears, mirrors including their mountings and the lens mounting principle.

New calibration swing arm (CSA) for ARGOS at the LBT

ARGOS (**A**dvanced **R**ayleigh **G**round layer adaptive **O**ptics **S**ystem for the LBT) is a laser guide star and wavefront sensing facility, developed in cooperation between MPE Garching, MPIA Heidelberg, INAF Florence, UA and LBTO Tucson, LSW Heidelberg and AIP Potsdam.
MPIA is responsible for the overall software and control, as well as the calibration scheme and calibration unit of the system. The calibration unit, which consists of the retractable CSA carrying a calibration optical unit, permits test and preparation of the adaptive optics mode during day-time. It will deliver a valuable saving of precious night-time for astronomical observations and will improve the operability of the telescope.
The two more than 4 m long CSA's, which have to be rigid, compact and retractable, but also vibration damping, allow for a high positional repeatability above the centres of the telescope main mirrors. The mechanical design of the CSA made of Carbon Fiber Reinforced Plastic (CFRP) was done in the MPIA's mechanical design office in cooperation with a contractor for the special CFRP Finite Element calculations. ARGOS will have its final design review in spring 2010.

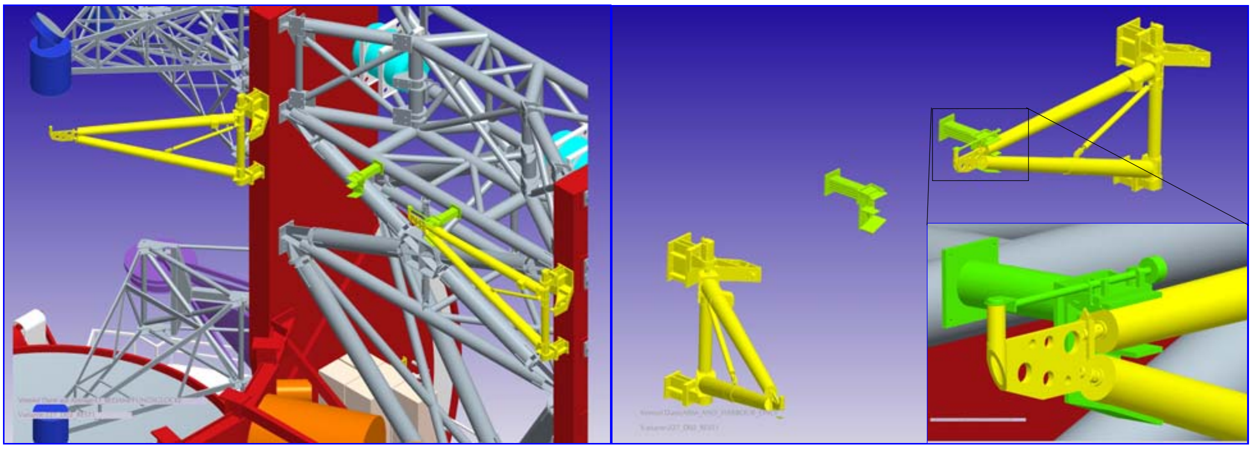

Figure 2: *LBT with CSA (left); CSA with harbour and shelter for optical unit (right)*

GRAVITY wavefront sensor

GRAVITY is one of the 2nd generation instruments for the VLTI. The instrument will combine the light of all four VLT telescopes. MPIA is responsible for the wavefront sensors. Figure 3 shows one of the sensor towers which are located in the VLT Coudé labs. Two optical breadboards are attached to the tower that holds the opto-mechanical components. A mode selection slider is mounted directly to the tower structure.
Phase B review is planned for December 2009.

Figure 3: *GRAVITY wavefront sensor in the VLTI Coudé lab*

Precision Mechanics Workshop

Armin Böhm, Mario Heitz, Tobias Maurer, Stefan Meister, Klaus Meixner, Wolfgang Sauer, Tobias Stadler, Martin Kürster

Precision manufacture in the mechnics workshop

Based on requirements from MPIA scientists as well as from researchers of partner institutes the precision mechanics workshop develops and builds demanding mechnical high-tech equipment for astronomical research and education that cannot be purchased from commercial companies. The workshop is currently involved in the projects LUCIFER, LINC-NIRVANA, JWST/MIRI, JWST/NIRSPEC, MATISSE, GRAVITY, ARGOS, and PANIC. Due to its highly qualified employees the precision mechanics workshop forms an important backbone for support and advise on all mechanics-related issues inclunding material selection and supply. The high standards reached by the MPIA in the development of instruments for astronomical research could not be met without a well-equipped mechanics workshop. Repairs and changes, often to be carried out on short notice, of devices already operational and in use for research constitute another important part of the activities of the workshop.

Figure 1: Steps of the Manufacturing process of an aluminum filter wheel with a diameter of 550 mm for the LINC-NIRVANA instrument. Left: simulted machining process working on a 3D model and creating the control program for the CNC machine. Center: machining of the workpiece. Right: final product.

Besides classical metal working machines the MPIA workshop also has modern computer controlled machine tools at its disposal (computer numerical control or CNC machines). 3D models created with CAD (computer aided design) software in the engineering design office serve as the basis for the manufacturing process by controlling the metal working machines. In many cases paper drawings have been replaced by control software for a CNC machine directly created from the 3D model.

On-the-job training of precision mechanics

The precision mechanics workshop provides opportunities for on-the-job training. At present, there are six trainees working with workshop personnel. Since the founding of the institute a total of 52 apprentices have been trained at the MPIA workshop. The regular duration of the training is 3 ½ years. For trainees with excellent performance the duration can be shortened to three years.

Very good results in school education are a precondition for getting an appenticeship position at the MPIA. Required is either very good credentials (TYP10B) from the nine-year elementary school *(Hauptschule)*, or a general certificate of secondary education *(Realschule)*, vocational school *(Berufsfachschule)*, or grammar scholl *(Gymnasium)*. Besides a general interest for the subject of the training good grades in mathematics, physics, and technology are expected.

After their basic training the apprentices start working in all instrumentation projects (LINC-NIRVANA; PANIC, JWST/MIRI etc.) supervised by workshop personnel. This enables the trainees to relate the components they are manufaturing to specific scientific instruments and to make important contributions to major projects of the institute. The integration of the trainees into instrumentation projects does not only serve to enhance their interest for the job, it also fosters their sense of belonging to the institute. The above-averge level of supervision that the apprentices enjoy from our qualified instructors provides them with the opportunity to acquire expert knowledge. Their regularly good to very good examination performances consitute an impressive proof of this.

In addition to on-the-job training the precision mechanics workshop offers students the possibility for professional pratical training with a duration of up to four weeks. Since 2004 the workshop has hosted 33 internship students.

Opportunities for doing an internship in the workshop exist also for pupils wishing to explore their career options and get acquainted with the job of the precision mechanic. Furthermore, the workshop welcomes a group of school girls every year at Girls' Day in order to introduce them into the job of the precision mechanic.

Figure 2: Basic training: from left to right: rasping, CNC training, Girls' Day activities.

Electronics Department

K. Wagner, R. Klein, M. Lehmitz, U. Mall, L. Mohr, J. Ramos

Introduction

The electronics department has responsibilities in the following areas: system planning and development, manufacture, testing and procurement. The department also supervises students of the Hochschule Mannheim who collaborate in the development of hardware and firmware within the scope a diploma thesis or Master's degree. Together with the engineers and technicians of the department they work on projects and take over general tasks in the areas of electrical engineering and electronics. In order to meet the demands of modern astronomical instruments, electronics hardware has to be compact, efficient, cost-effective, and quickly available. This is achieved by designing modular systems that can be easily adapted to a specific application.

Electronics Development for MIRI and NIRSpec

The MPIA is involved in the development of motorized filter and dichroic/grating wheels for the instruments MIRI and NIRSpec of the JWST. Since the electrical components used in these mechanisms are non-standard and its operation mode is very specific, custom-made test equipment (EGSE) was developed.

Figure 1: The EGSE system on the background being used for tests of the flight model of a MIRI wheel mechanism in a clean room of the Carl Zeiss company.

The company Carl Zeiss received five units from MPIA, which are working successfully in the test campaign of the very special and expensive flight models of the MIRI and NIRSpec wheel mechanisms. Together with these mechanisms EGSE units will be delivered to other consortium partners like CEA (France), ATC (Scotland) or EADS Astrium for further integration of the instruments.

New Electronic Read-out Design for Astronomical Detectors

Current-generation imaging electronics are large, heavy, and dissipate a lot of power. These drawbacks are becoming ever more important, particularly for wide-field instrumentation using mosaicked detector arrays. The electronics department has recently developed new visual and IR electronic Read-out systems for implementation in astronomical cameras. The modular design allows configuration of the electronics for a wide range of currently available IR detectors and CCDs. The new read-out concept can be applied to single or multiple detector systems with up to 144 input channels. The high data-transfer rate, small size ($33 \times 13 \times 31 cm^3$), and low heat dissipation make these electronics ideal for use in relatively large focal-plane detector arrays. The first instruments employing the new system are the Panoramic Near-Infrared Camera (PANIC) for the 2.2m (diameter) telescope at Calar Alto Observatory in Spain and the beam combiner LINC-NIRVANA for the Large Binocular Telescope (LBT) on Mount Graham in Arizona.
Furthermore, we started working on a compact focal plane electronics based on the SIDECAR ASICs from Teledyne in order to be prepared for future oriented large size detector arrays.

Instrument Control Electronics

With steadily increasing telescope sizes and complexity of scientific instruments, there is a growing demand for improved Control Electronics, regulating and controlling all the different subsystems. Among the diverse tasks are on one hand high precision measurements of physical values like temperature, pressure, and acceleration, on the other hand precise detector temperature regulation and the control of well-defined cool-down and warm-up procedures in infrared instrumentation. Water-cooling of the electronics cabinets is required to avoid thermal emission close to the telescope. Extensive interlock systems have been developed to guarantee the safety of equipment and personnel. A competitive control system for the near infrared spectrometer LUCIFER (now installed at the LBT) has been developed at MPIA.

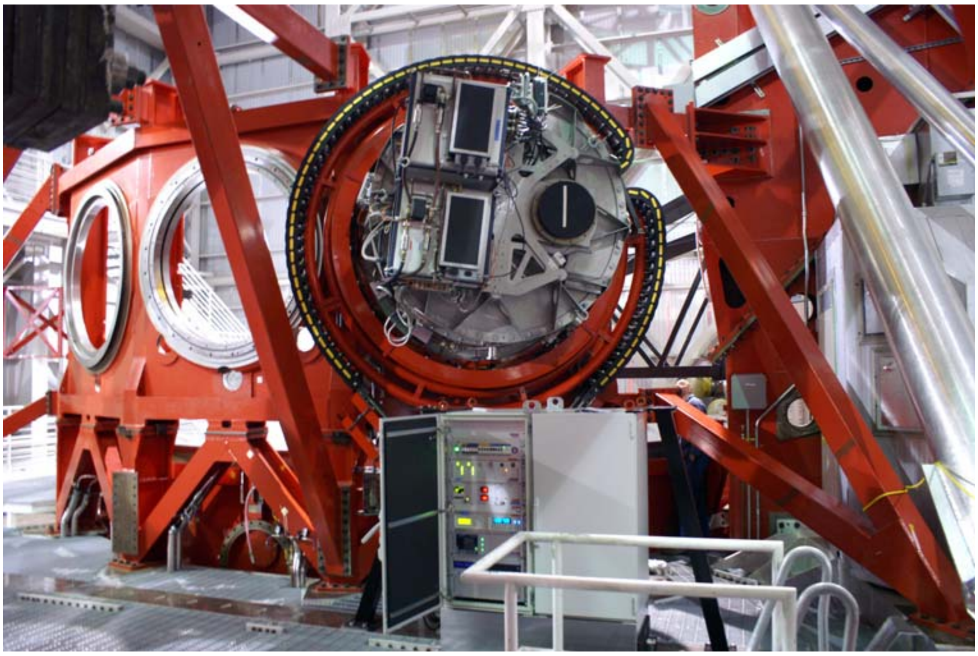

Figure 2: LUCIFER Instrument Control Electronics during commissioning at the LBT

Department of Instrumentation Software

Florian Briegel, Jürgen Berwein, Jose Luis Borelli, Frank Kittmann, Ole Moeller-Nilsson, Udo Neumann, Aleksey Pavlov, Clemens Storz, Jan Trowitzsch

Introduction

In coordination with the scientific project leaders the instrumentation software department develops control, data acquisition and processing software for astronomical instruments. It is only by means of the interface between software and hardware instruments that observational equipment is created which meets the high standards of the observing astronomers.
Nowadays the preparation of observations and the reduction of data is much more tightly connected to the control of the instrument than in traditional astronomy. Such observations need to be carefully planed, taking into account the constraints imposed by scientific objectives as well as features of the instrument. In addition to the development of control software the software group has therefore been involved in the development of observation preparation and data reduction/handling software.

Figure 1: Astronomical workflow of the four software types developed by the department.

The individual branches of software developed by the department are presented in the following:

OPS – Observation Preparation Software

The OPS supports an astronomer (observer) in the complex process of preparing observations, it consists of several software tools to define the overall data structure of an observation program and to provide the observer with information what can be expected under given observation conditions. A more detailed description is available in a separate report in this document.

OSS – Observation Support Software

The OSS is a tool for the scheduling and execution of prepared observation programs. As seen in Figure 1, the OSS is placed between the more scientifically oriented package, the OPS, and the more instrument oriented package, the ICS. The data structure from the OPS are processed, evaluated and sent as instrument level commands to the ICS. The OSS is currently developed for the LINC-NIRVANA project, but can also be used for others instruments.
It has the following modules:

- Repository provides a storage and an access interface for the OPS and the OSS.
- Scheduler designed to semi-automatically assist astronomers in scheduling a set of observation blocks. The conceptional design in was implemented and tested.

- Executor is a program that executes observation blocks containing a set of instrument commands and its parameters. These commands are sent to the ICS for execution.

ICS – Instrument Control Software

The ICS provides the low level functionalities for the instrument hardware and the overlaying processing logic. In normal operation mode, the ICS should not be accessible to the observer. Commands and its parameters are passed over a standard interface to the ICS. Errors and status feedback will be passed from the ICS to the OSS. The ICS is a collection of various software modules for motion control, data acquisition (IR- and CCD cameras) and control loops (AO, guiding, etc) which are used right now and can be reused for future instruments.

1. Design, implementation and test of the Multi Conjugated Adaptive Optics Channels and Ground Wave Sensors Software (LINC-NIRVANA).
2. Design of a laser guide star and wavefront sensing system (Argos).
3. Final test of the pyramid wavefront sensor software for Near-Infrared (Pyramir).

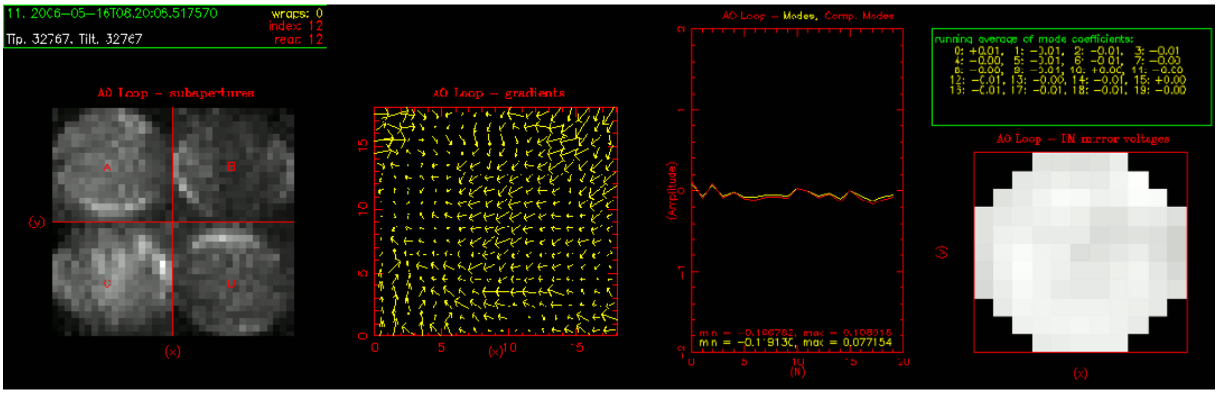

Figure 2: *Snapshot of the adaptive optics monitor while observing with Pyramir.*

4. Generic Infrared Camera software (GEIRS) started with MAGIC - the first infrared camera for Calar Alto (CAHA) in 1992. Since then it has been constantly extended for other IR-camera based projects (MIDI, OMEGA2000, PYRAMIR, LINC-NIRVANA, LUCIFER, PANIC).
5. CCD camera software for one or multi chip CCD cameras (LAIWO), CCD camera based ON/OFF-axis guiding (LBT GCS, CAHA TVG35, LAIWO).
6. Universal motion control software (LINC-NIRVANA, Argos, ..).
7. Common Software designed and implemented as a service oriented architecture used by all ICS and OSS modules (LINC-NIRVANA, CAHA, LAIWO, Argos).

DRHS - Data Reduction Handling System

The data reduction handling system is an instrument pipeline to process calibration and science data. Even though the DRHS is currently being developed for the SPHERE project, it is written with the general instrument types in mind and it is foreseen that it will be also used in other projects.

The SPHERE DRHS is designed and implemented in the form of processing "recipes". It allows processing of calibration and science data from infrared IFU and imaging Instruments as well as reduction of CCD imaging and polarimetry data. The data reduction processes includes both low level calibrations and high level data analysis algorithms for the purpose of direct detection of planets.

Instrumentation and project management

Karl-Heinz Marien, Thomas Bertram, Peter Bizenberger, Mario Brix, Fulvio de Bonis, Wolfgang Gaessler, Uwe Graser, Werner Laun, Vianak Naranjo, Diethart Peter

The department combines three kinds of personalities: specialists with knowledge and skills who work on all projects that need their expertise, engineers who are employed for one project on which they spend 100% of their time, and scientists, who spend part of their time managing one or more projects.

Project Management: Due to the increasing complexity of astronomical instrumentation projects it has become more and more important to apply modern project management methods. The main focus of project management is to organize the interactions between project partners, to ensure the project is accompanied by external reviews, and to manage the financial and human resources. The success of a project is secured by controlling of the project's progress, by utilizing of possibilities for risk minimization, and by the management of complexity.
Systems engineering is an indispensable approach for complex projects such as LINC-NIRVANA. The systems engineer observes the instrument as a whole during all states of instrument development, from the analysis of requirements through all phases of design, manufacture, and verification as well as during the implementation phase. He is a link between the involved disciplines as well as between the contributing project teams.
Control engineering: The LINC-NIRVANA project also applies methods from control engineering in order to characterize the vibration behavior of the LBT, but also to model the various control systems of the instrument. Vibration measurements at the LBT: In order to study various aspects of the LBT environment which are relevant for the performance of the telescope and its instrumentation the effects of vibrations is investigated along with solutions for mitigation. Vibration control is particularly important for interferometer instruments. For this purpose the installation of a dedicated vibration monitoring system has begun at the LBT that will provide a systematic characterization of the vibration behavior of the telescope structure. The development of this system is a joint venture of the two interferometer projects LINC-NIRVANA and LBTI (developed by Steward Observatory, Tucson).
Optical design: In order to build exceptional instruments for very dedicated purposes and/or pushing the limit of feasibility and performance, also the design of these instruments must go beyond conventional strategies. Since optical designs are the backbone for the design of astronomical instruments, also this area of development must be adapted to the high demands. Complex interferometer imaging instruments, partially with cryogenic components and an extended field of view like LINC-NIRVANA, require optical designs which surpass conventional techniques. MPIA deals with this situation either by an adequate division of the design task and introducing optical interfaces or by extending commercial design tools with custom made applications. The optics of the PRIMA differential delay lines are in principle simple but the requirements for micro-arc second astrometry pushes the tolerances close to the limits of feasibility (Figure 1) . This requires a close collaboration of the MPIA with optical companies in order to guarantee a successful operation.
Cryo-engineering: For ground based instrumentation MPIA has built a large variety of cryostats for different projects. Each cryostat has to be adapted for its application where we have to meet the requirements which are not only size and temperature. Also vibrations, mechanical stiffness or weight have to be carefully considered. Cryostats cooled by liquid nitrogen were designed for the Calar Alto instruments OMEGA 2000 and PYRAMIR. The phase A studies of the GRAVITY (ESO VLTI) wave front sensor and for PANIC (Calar Alto) also use nitrogen as the coolant. Cryostats with cooling machines are employed for the LBT instruments LUCIFER and

LINC-NIRVANA (Figure 2). To secure a minimum of vibration transfer the cooling machine for LINC-NIRVANA will be located at a distance from the cryostat transfer gas. For MATISSE (ESO VLTI) a hybrid cooling system with nitrogen and a pulse tube cooler was designed. The MATISSE cryostat is a scaled up version of the MIDI cryostat which was built here a few years ago.

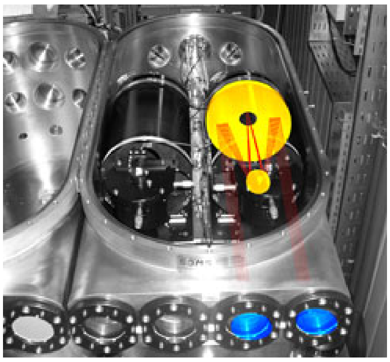

Figure 1(left): Cats-eye optics for the differential delay lines of PRIMA and the optical path.
Figure 2(right): Fit test of the cryostat mounted to the optical bench of LINC-NIRVANA

Metrology, hardware characterization and testing: In the past years LINC-NIRVANA, the NIR / Visible beam combiner for the LBT, has started its integration process. Many components have been delivered and a long characterization process has begun. Most of the prototypes for the cryo-mechanisms that had been designed and manufactured at the MPIA have also been tested with the final unit being fabricated for further integration. The carried out tests do not only aim at the characterization of the behavior of the mechanisms at room temperature, but also at the determination of the achievable precision and reproducibility under cryogenic conditions. The results from these measurements lead to the modification and optimization of the final design.

IR detector systems: Another important field of activity is the characterization and testing of infrared detectors. Through this process, not only the functionality of the detectors is verified, but also important parameters like read-out noise, dark current, sensitivity, stability, etc. are measured. Also, in close collaboration with the Electronics Department, new read-out schemes are being developed and optimised. Examples are the HAWAII-2 detector of the near-infrared spectrograph LUCIFER-1 that is currently being implemented at the LBT and the mosaic of four HAWAII-2RG detectors for the Calar Alto project PANIC (Figure 3).

Figure 3: Mosaic of for HAWAII-2RG infrared detectors for the PANIC wide-field camera for Calar Alto observatory

CCD detector systems: In the last years two wide-field CCD systems were developed and built at the MPIA one on which for Calar Alto observatory (Laica) and one for Wise observatory in Israel (LIAIWO). Both systems are in operation, are being used by MPIA astronomers, and are serviced from here. Each of the two systems consists of four CCDs with 4Kx4K pixels of size 15 µm inside a cryostat cooled with liquid nitrogen, a filter unit, a shutter unit and a control computer. Also integrated into the systems is an auto guider unit for fine guidance of the telescope during the exposure.Some of Calar Alto's CCD systems are currently being modernized by replacing old read-out electronics or integration of modern 4Kx4K CCDs into existing systems. Furthermore, out- dated autoguider units are being exchanged for modern CCD systems developed at MPIA.

Ultra precise metal optics for astronomical applications

Ralf-Rainer Rohloff, Veit Schönherr

Introduction

Single point diamond turning (SPTD) is a common method for the production of metal mirrors but the achieved form accuracy and surface roughness is insufficient for applications at wavelengths shorter than 5 µm. Polishable coatings are necessary, but due to the combination of two different materials, bi-metal effects can occur. This report describes a patented method developed by the MPIA Heidelberg and IOF Jena to overcome this problem.

Recent developments

"Chemical nickel" is an excellent candidate for a polishable coating. However, conventional materials for metal optics such as aluminium either have a considerably higher expansion coefficient than nickel or are very expensive. The sought-after material therefore has to expand and contract in the same manner as the nickel coating when subjected to temperature fluctuations. Otherwise, dissimilar expansion behaviour in the materials would warp the mirrors and impair the image quality.

A newly developed silicon-aluminium alloy adapted for expandability, exhibits properties similar to chemical nickel and is also comparatively economical. This alloy also fulfils the second requirement: its relatively high degree of rigidity makes it ideal to manufacture very stable low-weight structures. The tests conducted thus far confirm the suitability of the material. Combining this alloy with nickel in the so called piston mirror (see Figure 1) for the LBT beam combiner LINC-NIRVANA represents the first of such an application for an optical component [1].

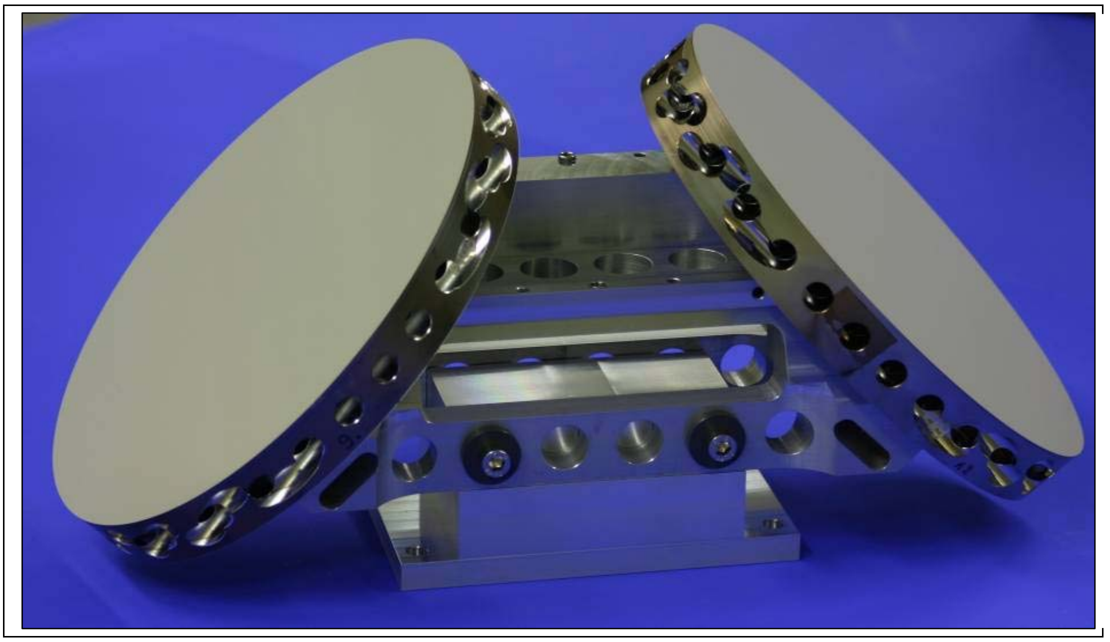

Figure 1: Piston mirror for LBT interferometric beam combiner LINC-NIRVANA

New developments

SPTD manufactured metal mirrors are standard optical components in infrared astronomical instrumentations working at cryogenic temperatures. Instruments like METIS (see Figure 2) planned for the European Extremely Large Telescope (E-ELT) require a higher quality micro-roughness and shape accuracy for the cryogenic mirrors.
Therefore, the MPIA Heidelberg and the Fraunhofer Institute for Applied Optics and Precision Engineering (IOF) in Jena decided to expand their studies to cryogenic temperatures. The Max Planck Society and the Fraunhofer Society support this work financially with € 1,200,000.

First steps in the launched project have been made in sample preparation of both silicon-aluminum and chemical nickel; the latter will be shaped in a cylindrical way by a novel electro-plated method (IOF Jena). Meanwhile, the following measuring instruments are being commissioned at MPIA to analyze material properties under cryogenic conditions:

- Dilatometer: High-precision thermal expansion measurement covering the temperature range of -180°C to room temperature. The measurement system with a high-resolution displacement transducer offers a maximum degree of accuracy, reproducibility and long-term stability.
- Climatic test chamber: Allows observations (-70°C to room temperature) of the shape deviation of a mirror with a FISBA interferometer from outside to the optical surfaces under test inside the climatic chamber.
- Test cryostat: A test cryostat (-180°C) is designed allowing optical characterization of thermally induced strain under cryogenic conditions in vacuum. This test cryostat will be integrated into the FISBA interferometer setup in order to test the thermo-mechanical behavior of the material composites within the scope of cooling cycles.

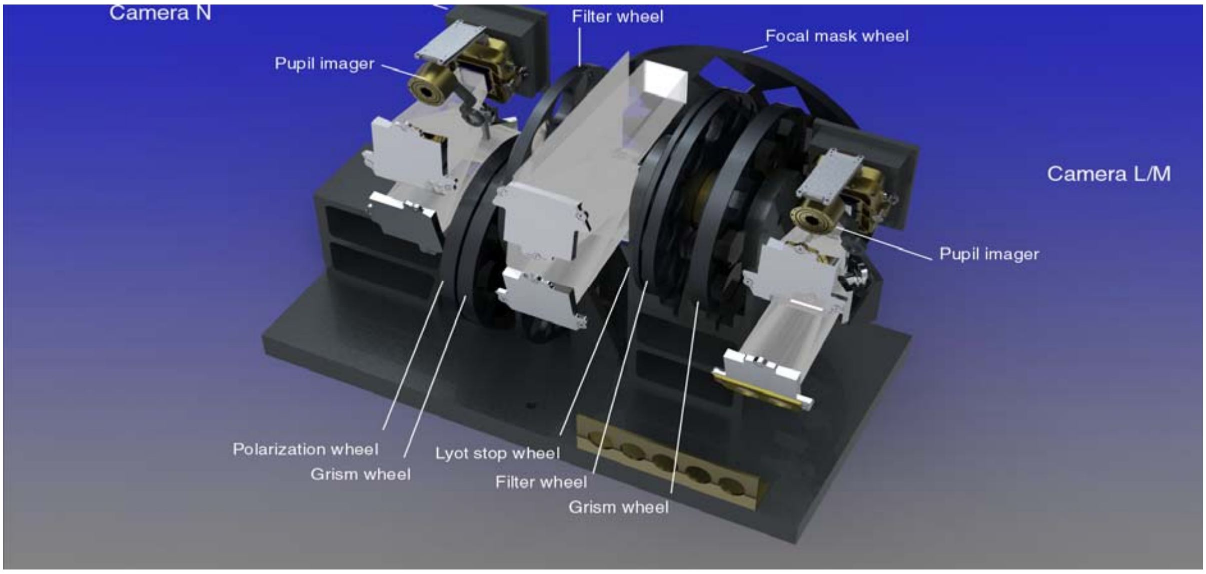

Figure 2: E-ELT METIS imager module with cryogenic metal mirrors

References

[1] Eberhardt, R., Gebhardt, A., Rohloff, R.-R., 2005, Fraunhofer Research News No. 11-2005

Cryo-cooling systems for infrared instrumentation

Werner Laun, Harald Baumeister, Peter Bizenberger, Monica Ebert, Armin Huber, Michael Lehmitz, Ralf-Rainer Rohloff

Introduction

If you look at ground based instruments for IR astronomy in most cases you just see a closed vacuum vessel. All optics, detector and mechanics are hidden in a cryostat. Each instrument has different requirements on the cryostat. The design of the cryostat and the choice of the cooling system depend on those requirements.

Cooling with LN_2 , the PANIC cryostat [1]

One of the most common methods to cool an IR instrument is the cooling with LN_2 (liquid nitrogen). Depending on the shielding a temperature of 77 K at the cold optics and detector can be reached. This is sufficient for most NIR instruments.
Currently, MPIA is building the cryostat for PANIC, the "PAnoramic Near Infrared Camera" for Calar Alto. The instrument will be mounted at the 2.2 m telescope and has therefore a weight limit of only 400 kg including all the electronics and the nitrogen filling. On the weight budget only 180 kg are allowed for the cryostat. To minimize weight a vacuum vessel with dished ends was designed which can be much thinner than with flat ends. The Optics is folded three times so that it can be mounted on a round optical bench with a diameter of about 1 m. The bench is cooled by a nitrogen vessel with a shape similar to the vacuum vessel. Multilayer insulation (MLI) reflects most of the room temperature heat radiation and therefore reduces the necessary volume of the vessel and the weight. For the detector array a separate small nitrogen vessel is used to get a constant detector temperature below 80 K. Besides that, the detector array will have its own temperature control.

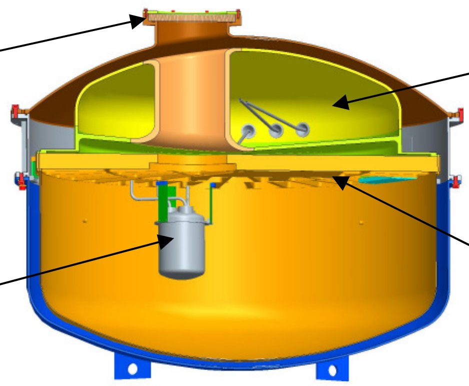

Figure 1: Setup of the PANIC cryostat

Cooling with closed cycle coolers, the LUCIFER cryostat [2]

Since fall 2009 LUCIFER at the LBT is ready for science. The cryostat of this instrument was build under the responsibility of the MPIA. To cool the instrument two powerful Gifford MacMahon (GM) coolers are used which are placed opposite to each other on the side of the instrument. The coolers run with a pulse frequency of 1.2 Hz. To damp out vibrations the coolers are suspended in springs and the thermal coupling to the cold structure is done with flexible copper braids. Furthermore the coolers are synchronized so that they run exactly in phase which almost eliminates the lowest excitation frequency. At the LBT the compressors are placed one level below the telescope. The flexible gas hoses go about 40 m from the compressor along the wall of the building, over a loop to the telescope, along the rim of the mirror cell to the instrument platform, and through a cable rotator to the instrument.

A combination of cooler and LN_2, the MATISSE cryostat [3]

MPIA was PI institute for the ESO VLTI instrument MIDI which is working at mid-IR. Now its successor MATISSE is already in its design and test phase. MPIA is responsible for the design of the cryostat. The cooling concept is quite similar to that of MIDI. To reduce the heat load from room temperature to a minimum, a radiation shield cooled by LN_2 encloses the complete optical bench. For MIDI a GM cooler with a moving displacer was used to cool the cold optics. Now for MATISSE a Pulse Tube (PT) cooler is planned to be used. This type of cooler produces much less vibrations because it does not have a moving displacer. For VLTI, the MATISSE cooler will be the first PT cooler ever used on the mountain. One cooler is already in house and is tested by the MPIA and the ESO teams.

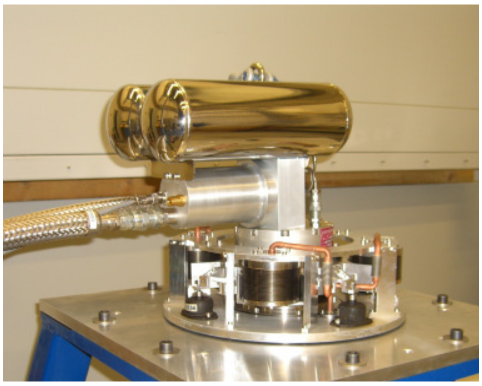

Figure 2: PT-cooler for MATISSE mounted in a damping system

Cooling with a coolant loop, the LINC-NIRVANA cryostat [4]

A very special cooling system is used for the LINC-NIRVANA cryostat. The cooler will be placed far away from the instrument like the compressors for LUCIFER, that is one level below the telescope platform. Here a high capacity industrial Stirling type cooler is used. It cools helium down to 60 K. Through vacuum insulated lines the cold gas is transported to the instrument where it runs through a heat exchanger. The system supplies a high cooling capacity that would be sufficient for even larger cryostats. As far as we know no such system was ever used for astronomy. So we cannot just vary existing systems and adapt them for our application. The performance and the experience we gain from this cooling system will probably be a first step to a cooling system for huge cryostats of future instruments.

References

[1] Harald Baumeister, “PANIC: the new panoramic NIR camera for Calar Alto“, Proc. SPIE, Vol. 7014, 70142R (2008)
[2] Rainer Lenzen: “LUCIFER I/II: Two Multi-Mode Instruments for the Near Infrared”. MPIA Annual report 2007, p92ff
[3] Thomas Henning: “MATISSE and GRAVITY – Second Generation Instruments for the VLTI”, MPIA Annual report 2008, p94ff
[4] Werner Laun: “The LINC-NIRVANA IR Cryostat“, Proc. SPIE, Vol. 6269, 626956 (2006)

Infrared Detector Systems

Ralf Klein, Ulrich Mall, Vianak Naranjo, José Ricardo Ramos, Clemens Storz, Karl Wagner

Introduction

Infrared Astronomy is one of the major research areas at MPIA, thus, the development of Infrared Detector Systems is one of the major technical activities in house.
The MPIA has a specialized expertise in infrared detector systems that brings together engineers from different technical departments: Why? Because an infrared detector system consists of three major key elements: readout electronics, software, and of course, the detector. There has to be harmony between all of these components, and the way to achieve this harmony is done by means of a dedicated optimisation of the system.

Read-out Electronics

The newly developed MPIA Read-out Electronics (ROE) is able to handle single or multiple detector systems with up to 144 input channels, feature high-speed data transfer and low power dissipation. Additionally the system size is small and lightweight.
High data transfer rate, small size and low heat dissipation makes this Read-out Electronics ideal for relatively large focal plane arrays. The first instruments running with the new Read-out Electronics will be PANIC (Panoramic Near Infrared Camera) at the 2.20 m telescope on Calar Alto and the LBT beam combiner LINC-NIRVANA.

Figure 1: New Read-out Electronics for the Panoramic Near Infrared Camera at the 2.20 m telescope on Calar Alto

The ROE from the science camera software point of view

The new ROE meets special requirements and interface implementations which will allow to implement new capabilities for the currently available IR-detectors, besides important features like fast data-path verification possibilities directly at the instrument, frame data protocol with checksum embedded into data flow, all with high speed data output. It will use all advanced capabilities offered by the Hawaii-RG-types of the Teledyne detectors. With the implementation of the requirements by the Infrared-Software-Interface the control of the clocking pattern of the detector allows to react on current needs of astronomical IR-instruments.

For minimisation of persistence effects in IR detectors the new ROE pattern logic will be able to offer different idle-clocking patterns and modes which can be selected and switched, on demand and according to momentary necessity. Idle clocking is automatically done when the detector is not used for some time, to prevent saturation of detector pixels by incoming light.

New clocking schemes for the Hawaii-1 and -2 detectors of Teledyne, the generation before the RG-types of Hawaii detectors, will also be possible with the new MPIA ROE. Beneath MPIA's read-out-modes, which offer nearby 100 percent integration efficiency inside repeated image-cycling, we will for example be able to combine this pattern logic to modify other important read-out modes like 'Fowler-Sampling', and thereby increase the detector integration efficiency.

Some advantages of the Haiwaii-RGs 'Window Readout Mode' can now be emulated with the new ROE to have similar capabilities like the RGs also available with the previous Hawaii-detectors generation. This, for example, will be available for the LINC-NIRVANA science-detector to prevent saturations introduced by bright stars and to reduce crosstalk. And it will extend the capabilities of the RG-detectors in the multi-channel window read-out-mode by allowing high speed multiple sub-windows from anywhere of the science FOV to be interleaved with the read-out of the full-field science frame, in any combination of the fast-read-out (at about 1 MHz until 5 MHz) and the standard clocking of about 100 kHz.

Infrared Detector Characterization

An infrared detector cannot operate alone: as a complex unit of an infrared system the detector serves as a connection between the readout electronics and the software. The characterization process is the way of understanding how the detector works and how it behaves, and it is the key to guarantee the best performance of an instrument during operation.

The MPIA counts with special equipment and laboratories that make up the perfect environment for efficient detector characterization together with revolutionary readout electronics and up to date software. The measurement of important parameters like readout noise, dark current, gain, linearity, sensitivity, etc. are only some of the tasks that the MPIA has been carrying out in this area, not to forget the verification of the detector functionality, fine-tuning and optimisation, whose results are reflected in the future performance of the instrument.

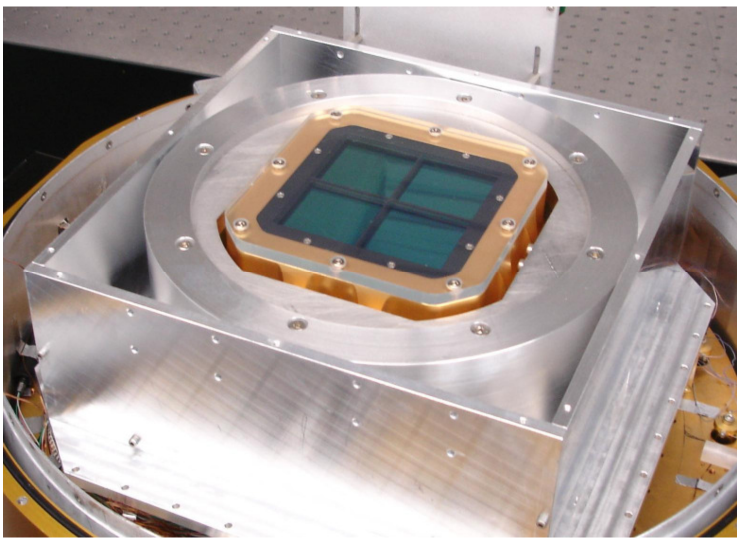

Figure 2: HAWAII-2RG Detector Mosaic for PANIC

Observation Preparation Software

Jan Trowitzsch, Alexey Pavlov, Wolfgang Gässler

Overview

The **L**INC-NIRVANA(LN) **O**bservation **P**reparation **S**oftware (LOPS) supports an astronomer (observer) during the complex process of preparing the observations. LN [1] is a near-infrared imaging interferometer for the Large Binucular Telescope (LBT). LOPS consists of several software tools to specify the overall data structure of an observation program. Information is provided to the observer about what can be expected under given observing conditions. Data relevant for the execution of observing programs like observational constraints and division into multiple observation blocks, depending e.g. on the number of parallactic angles needed for an observation will be also examined there. A first prototype of the LOPS software was successfully presented at the LN science meeting (June 24th 2009). The LOPS underlying framework is very flexible by design so that it can be adapted to prepare observations with other instruments [2].

LOPS Data Model

The observer sets up all observations to achieve a scientific goal in terms of **O**bservation **P**rograms (OPs). An OP contains all the information associated with one *observing program* including multiple targets. In the framework of LOPS an **O**bservation **T**arget **U**nit (OTU) that contains all the information associated with one target is introduced. This means that for each target there is a separate OTU. Each OTU is a self-contained entity and possesses a target, pre-defined observing constraints, scientific objective, multiple instrument configurations including multiple calibrations and exposure times. Astronomers specify OTUs, defining a target with the number of paralactical angles at which it is observed. Within an OTU certain parameters are shared among its **O**bservation **B**lock (OB) elements. Each OB is composed of a number of instrument-mode-specific procedures which are grouped in a procedure sequence table. Each procedure contains a number of parameters which are defined by the user.

LOPS Modules

The main GUI of the LOPS is the Observation Program Editor (see Figure 1). It contains a navigator area on the left side which shows the OPs components in hierachical structure and the corresponding modules for each component on the right side.

The specific software tools within the LOPS are called modules. Each module provides tools and editors for a specific OP component. The module plug-in framework of LOPS ensures persistent data handling between the modules since each module is inter-connected with related modules. Several types of modules have already been implemented [3] or are currently under construction [4].

Overview modules for OTUs, targets, OBs, and guide stars are implemented. The Target Selector module is a catalog navigator that is used to search and extract objects (targets and guide stars) from available remote (or local) catalogs and images. The Elevation Plot module provides a panel for displaying a plot of the elevation, airmass and parallactic angles vs. time for a given target. It will be extended with features to define interactively a number of OBs and the suitable time slot for each of them. It also can provide the *perfect* point-spread function (PSF) and the modulation transfer function (MTF) of the ideal LBT interferometer.

The Observation Block Editor module as depicted in Figure 1 is a key module within LOPS. It allows to create an OB and to manage its procedures including detailed editing of parameters. Each Observation Block describes the observing sequence in terms of pre-defined

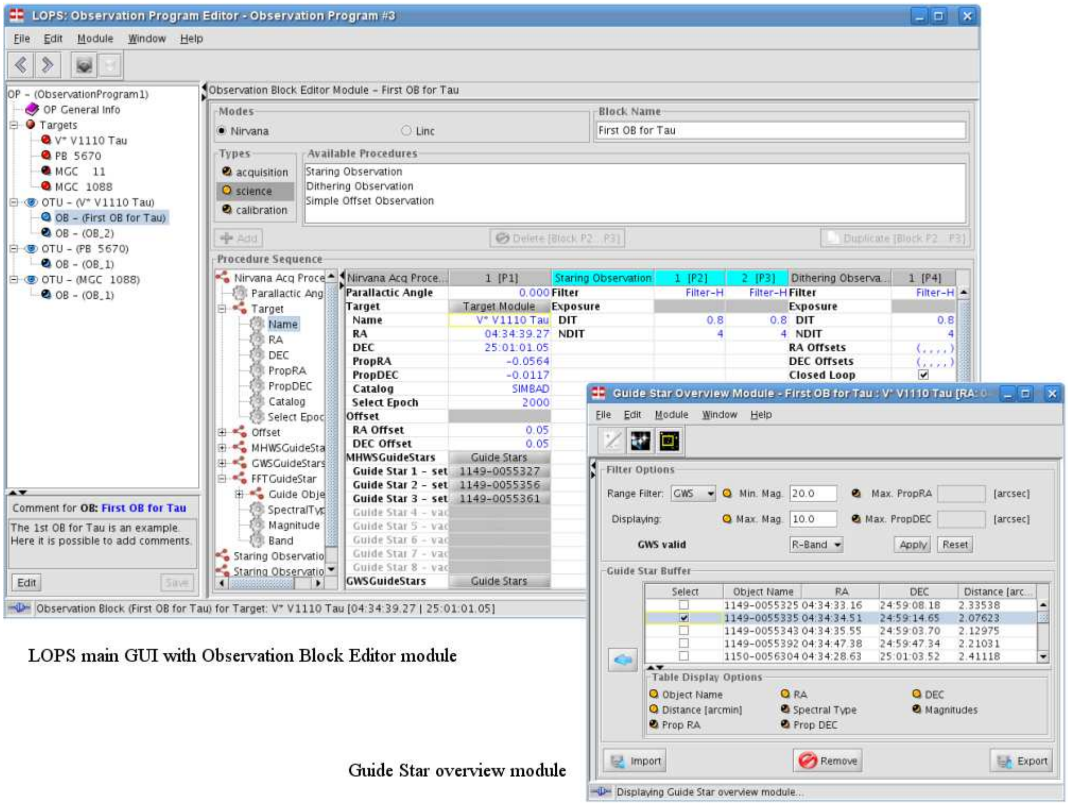

Figure 1: *The LOPS main GUI, OB Editor and Guide Star overview module are shown.*

procedures/scripts (similar to templates in ESO's P2PP). The user can select specific procedures according to their type (acquisition, science, or calibration). The OB editor is connected to other modules so that complex parameters of the procedure can be edited in a related module.

The **G**uide **S**tar (GS) related modules enable detailed specification of the LINC-NIRVANA MCAO and fringe/flexure tracker (FFT) guide star parameters. It provides connections to the external multi-magnitude catalogs and allows the selection available guide star constellations according to the main instrument characteristics such as the geometry and orientation of the field-of-views for the MCAO and FFT system. The GS Overview module provides an astronomer with a tool to select natural guide stars based on the main instrument constraints. This module will later-on communicate with a Performance Estimator module in order to propose the best asterism based on the estimates of Strehl-ratio and fringe contrast. In this context the Exposure Time Calculator (ETC) module allows the calculation of the exposure time for a given S/N ratio or vice versa, based on magnitude, Strehl-ratio and filter.

All components of LOPS are subject of ongoing improvements. The following new modules will be introduced in the near future: Advanced Elevation Plot, Visualization, Performance Estimator, Repository Browser and Pattern Selector/Generator.

References

[1] Herbst, T. M., Ragazzoni, R., Eckart, A., Weigelt, G., Proc. SPIE, Vol. 7013, 701326, 2008

[2] Pavlov, A., Trowitzsch, J., Gässler, W., Berwein, J., Proc. SPIE, Vol. 7013, 701336, 2008

[3] Trowitzsch, J., Pavlov, A., Gässler, W., ADASS XVIII, ASP Conf. S. Vol. 411, p.518, 2008

[4] Pavlov, A., Trowitzsch, J, Gässler, W., ADASS XIX, 2009 (in press)

Educational and public outreach activities

Markus Pössel, Klaus Jäger and Jakob Staude

When it comes to public outreach and education, astronomy provides a gateway to the natural sciences and technology in general. MPIA can look back on a long and successful outreach tradition, from media outreach to a successful public lecture series and to large-scale events such as “Open Days” with on the order of 10,000 visitors (see Figure 1). This tradition has continued in force, in particular during the International Year of Astronomy 2009. Young audiences, including students of all grades, have always been a key target group of MPIA outreach work.

When it comes to outreach, MPIA has gone above and beyond the ordinary. A prime example is “Wissenschaft in die Schulen!” (WiS, literally “Science into [our] schools!”), a highly successful joint venture between MPIA and Germany's most popular astronomy magazine, *Sterne und Weltraum* (literally “Stars and Space”, now published by the German subsidiary of Scientific American, Inc., a part of the Nature Publishing Group), supported by the Klaus Tschira Foundation gGmbH (one of the largest privately funded foundations in Europe), and in cooperation with the Academy for Advanced Teacher Training of the state of Baden-Württemberg. Every month, WiS provides two units of custom-made classroom materials (one unit suitable for middle schools, one for high schools). Each unit’s theme is taken from current astronomical research, and each unit complements one specific article in that month’s edition of *Sterne und Weltraum*. The fact that, since 1982, the journal has been edited at the MPIA is a key element of close collaboration. Several times a year, WiS material is presented in special teacher training courses.

A new Center for Astronomy Education and Outreach

A few years ago, MPIA’s successful outreach activities inspired the idea of a dedicated Center for Astronomy Education and Outreach on Königstuhl. In 2007, MPIA and the University’s Center for Astronomy (ZAH) were able to win the Klaus Tschira Foundation as a major partner in this endeavour, and over the following months, a MPIA project group made detailed plans and started negotiations with other potential partners. A December 2008 press conference presented the partnership for the new Center for Astronomy Education and Outreach, the “Haus der Astronomie” (HdA, literally the “House of/for Astronomy”) to the public. Co-founders are the Klaus Tschira Foundation, which committed to constructing a dedicated building for the Center (see Figure 1) and to providing for basic technical equipment, and the Max Planck Society, which will operate the facility via the Max Planck Institute for Astronomy. Additional partners are the City of Heidelberg (via its Foundation for Youth and Science), the State of Baden-Württemberg and Heidelberg University. The center will closely cooperate with all of Heidelberg’s astronomical institutions, in particular with the University’s Center for Astronomy (ZAH) and with the Astronomieschule e.V., a local volunteer organization dedicated to the popularization of astronomy.

The HdA is set to play a major role in communicating astronomy, and in particular the research done at Heidelberg’s astronomical institutions, to the general public and to the media, and also to further communication between local and external scientists. Its activities will include the development of simulations and visualizations, of exhibits and exhibitions, of printed and online material for use by the general public and in classrooms. The HdA will organize public lectures and tours; it will take an active part in the astronomical training of Heidelberg university’s teacher students and organize and/or contribute to workshops for teachers, students and more general audiences throughout Germany and beyond.

Figure 1: Computer rendering of the Haus der Astronomie by the building's architects, Bernhardt+Partner, Darmstadt

The HdA's dedicated building will have the shape of a spiral galaxy, and will feature an exhibition area, a digital planetarium seating a hundred people, as well as workshop and seminar rooms, and office space for staff, visitors and the editorial team of *Sterne und Weltraum*. The ground-breaking ceremony took place in October 2009; construction has progressed steadily, and the building is slated for completion in the fall of 2011. In parallel, the Center's organizational development gathered pace with the appointment of the Center's head, Markus Pössel, who took up his post in January 2009. As of March 2010, the HdA has a staff of four scientists, and development of HdA programs and activities, procurement of equipment, and the development of new partnerships, cooperations and funding opportunities is progressing at a steady pace. Notably, since early 2009, the HdA acts as the German node for ESO's Science Outreach Network; in spring 2009, we were able to secure a EUR 38,000 grant from the W. E. Heraeus Foundation for telescopes suitable for public viewing and student work; in summer 2009, the "Kepler Days" served as a test-run for a mixed event for students, teachers and the general public; in the fall of 2009, we organized a small astronomy exhibition that went on display at the Frankfurt Book Fair, and in November, we cooperated with Baden-Württemberg's Ministry for Education, Youth and Sports in organizing an astronomy workshop for almost a hundred teachers on the occasion of the IYA 2009. The project has been presented both in a national and an international context, e.g. at the IAU General Assembly in Rio de Janeiro, at the annual meeting of the Astronomische Gesellschaft in Potsdam, and INSAP IV in Venice.

Haus der Astronomie staff: Markus Pössel, Olaf Fischer, Carolin Liefke and Cecilia Scorza;

Collaborators: Jakob Staude, MPIA public relations head until 2009 and initiator of the "Haus der Astronomie" together with the HdA working group at MPIA, consisting of Thomas Henning and Hans-Walter Rix (the Directors), Klaus Jäger (the Scientific Coordinator), Mathias Voss (the Head of Administration), and Frank Witzel (technical service).